Models and Methods
in
Few- and Many-Body Systems

Models and Methods

in

Few- and Many-Body Systems

Proceeding of the DST-UNISA-JINR Symposium

Skukuza, Kruger National Park,

South Africa

February 5-9, 2007

Edited by: S.A. Sofianos

SKUKUZA

What is this life
If full of care
We have no chance
To drive and stare,

No chance to see
In bush we pass
Where rhinos find
Their good in grass,

No chance to see
In broad day-light
Streams full of stars
Like skies at night.

A poor life is
If full of care
We have no time
While drive, to stare.

S.B. Gerasimov

CONTENTS

PREFACE

This symposium was motivated by the quest for establishing a solid research collaboration in the field of theoretical nuclear physics, and in related areas, between the Physics Department of the University of South Africa (UNISA) and the Joint Institute of Nuclear Research (JINR) as envisaged in the recently-signed agreement between the South African Department of Science and Technology (DST) and the JINR.

The number of participants in the symposium was limited to 28, with 10 invited speakers being selected from each side. Researchers from Venda and Rhodes Universities were also included. Speakers were requested to provide somewhat extended details of their research topic, the questions addressed, and future trends in the field. The resulting proceedings are, thus, intended to serve as guidance for the pending collaboration and as substrate material for the students and young researchers who will be brought into the joint ventures. With this in mind, these proceedings will be made available to all interested researchers and students. It is hoped that the DST-JINR research collaboration will become more inclusive, long-lasting, and fruitful as a result.

I would like to acknowledge here the pioneers of this collaboration, namely Profs. R.M. Adam, V.G. Kadyshevsky, and A.N. Sissakian. Special thanks goes to Dr D.V. Kamanin, Prof. V.V. Voronov, and Prof. T.S. Maluleke who enthusiastically endorsed this endeavor, and to my colleagues at UNISA and Ms K. Tadi for their assistance in administrative matters.

S.A. Sofianos

Dispersion Total Photoproduction Sum Rules for Nucleons and Few-body Nuclei Revisited

S.B. Gerasimov*

Joint Institute for Nuclear Research,141980 Dubna, Russia

Questions on the presence and quantitative role of the constant terms in the real part of the high-energy photon-nucleon and photon-nucleus amplitudes representing the contribution of the non-Regge (the fixed j=0-pole) singularities in the finite-energy sum rules (FESR) for the photoabsorption cross sections on nucleons and the lightest atomic nuclei are discussed. New testable relations are presented for relevant combinations of the Compton scattering amplitudes. The importance of more detailed and precise data on the pion photoproduction off the neutron is stressed as the prerequisite for an analysis of newly derived integral sum rules for the nucleon and lightest nuclei total photoabsorption cross sections including the presently poorly known values of the pionic "sigma-terms" and the j=0 fixed-pole residues in the real part of respective Compton scattering amplitudes. Combining the spin-depending dispersion–the GDH and Cabbibo-Radicati sum rules, and the relativistic dipole-moment-fluctuation sum rules with only main valence quark configuration of nucleons taken into account, the distribution and correlation functions of the quark electric dipole moment operators in the nucleon ground state are expressed via the experimentally measurable resonance nucleon photoexcitation amplitudes. These functions are of interest for checking detailed quark-configuration structure of the nucleon state vector.

I. INTRODUCTION

In this report the following topics will be touched upon. First we propose and discuss a new version of the finite-energy integral sum rules both for nucleons and lightest ($A = 2, 3, 4$)–nuclei which may serve to be the source of information on the scalar pion densities inside nuclei being at the same time the counterparts of the well-known non-relativistic Thomas-Reiche-Kuhn (TRK) sum rules for the electric-dipole nuclear photoeffect. Then the relativistic "bremsstrahlung-weighted" sum rules will be discussed following from both the dispersion relations and the current-algebra-type approaches which enable to estimate the asymmetry degrees of the different flavour-parton distribution and correlation functions of the nucleon. Let us remind that in the 1954 seminal paper of Gell-Mann, Goldberger, and Thirring (GGT) [1] on the use of the causality condition in quantum theory the idea of the "superconvergence" sum rule technique was first suggested and applied to the photonuclear absorption processes.

The GGT sum rule follows from the assumption of validity of the unsubtracted dispersion relations for the difference, presumably vanishing as $\nu \to \infty$,

$$\Delta T = T_{\gamma A}(\nu) - ZT_{\gamma p}(\nu) - NT_{\gamma n}(\nu) \tag{1}$$

of the forward Compton scattering amplitudes on the nucleus with atomic number $A = Z + N$ and the sum of amplitudes on the Z free protons and N free neutrons. After inclusion of the Thompson value $-(\alpha Q^2)/M$ (M and Q being the hadron mass and electric charge in units of the electron charge), for every hadron amplitude $T(\nu = 0)$ at zero photon energy, the sum rule

*Electronic address: gerasb@theor.jinr.ru

reads

$$2\pi^2\frac{\alpha}{M_n}(\frac{-Z^2}{A}+Z)+\int_{\nu_{\gamma\pi}}^{\infty}\mathrm{d}\nu[Z\sigma_{\gamma p}(\nu)+N\sigma_{\gamma n}(\nu)-\sigma_{\gamma A}(\nu)]=\int_{\nu_{thr}}^{\nu_{\gamma\pi}}\mathrm{d}\nu\sigma_{\gamma A}(\nu) \tag{2}$$

The first term in left hand side of (2) practically coincides with the "kinetic" part of the long-known TRK sum rule for the electric dipole nuclear photoabsorption

$$\begin{aligned}\sigma_0(E1) &\equiv \int_{\nu_{thr}}^{\infty}\sigma_{E1}(\nu)\,\mathrm{d}\nu=4\pi^2\Sigma_n(E_n-E_0)|\langle n|D_z|A\rangle|^2=2\pi^2\langle A|[D_z[H,D_z]]|A\rangle\\ &= (2\pi^2\alpha NZ)/(AM_n)+2\pi^2\langle A|[D_z[\hat{V}_{NN},D_z]]|A\rangle\end{aligned} \tag{3}$$

where the first term results from the double commutator with the kinetic energy operator of the nuclear hamiltonian H. The present work originates partly from earlier papers of the author [2–4] dealing with sum rules for total photon-hadron cross-sections and aims to present some new experimentally testable and theoretically interesting relations emerging from the dispersion FESR phenomenology.

II. TOWARDS GENERALIZED GGT SUM RULE

It was always tempting and rewarding to combine the power of dispersion relation approach, which is based on very general underlying assumptions and explains many general properties of the scattering amplitudes as well as provides useful relations between them in a rather simple way, with particular dynamical ingredients of a given quantum system such as, for instance, implications of the broken chiral symmetry and pionic dynamics dominating peripheral properties and low-energy interactions of hadrons and nuclei.

A. A glance at a possible role of pion degrees of freedom on GGT sum rule

In [2, 4] an attempt was maid to introduce corrections to the GGT approach understood as a familiar Impulse Approximation (IA) scheme applied to the γA -forward scattering amplitude. The approximate relevance of IA is seen from the fact that it corresponds to taking into account the singularities closest to the physical region of the peripheral scattering process ($t \leq 0$, $t = (k-k')^2$ is the invariant 4-momentum transfer for elastic scattering).

The respective cut in the complex t-plane is defined by the diagrams schematically represented in Fig. 1a, while the next to the leading "anomalous" threshold, given by Fig. 1b, will be the "normal" 2π -exchange diagrams, with the cut starting at $t = 4m_\pi^2$.

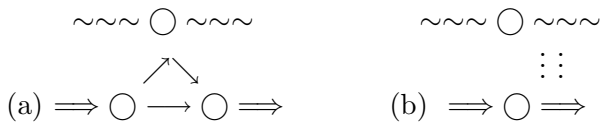

Fig. 1: (a) Cut in the complex t-plane, (b) Leading "anomalous" threshold ("normal" 2π -exchange diagram.)

In Fig. 1a the solid lines refer to nucleons and nuclei, the wavy (dotted) lines represent photons and pions. Thus this graph represents the impulse approximation (IA), while Fig. 1b defines the correction related with the nuclear "collective" pion cloud and thus is effective due to

short-ranged NN-correlation inside nuclei. Their relative role can qualitatively be characterized by the ratio

$$\frac{t_0(IA)}{t_0(2\pi)} \simeq \frac{8m_n\varepsilon_b}{(A-1)\,4m_\pi^2} \tag{4}$$

where t_0 refers to the beginning of the respective cut in the complex t-plane, m_n is the nucleon mass, ε_b is the nuclear binding energy. For instance, this ratio is ~ 0.22 (0.40 and 0.66) for the D (^{3}He and ^{4}He respectively).

This indicates that, naturally, for ^{3}He and ^{4}He the "pionic" contributions will be significantly more important compared to deuteron. Equation (4) also signals that, in the considered respect, the situation for heavier nuclei is expected to be much alike the ^{4}He case because of nearly equal binding energy per nucleon.

B. Towards the measurement and systematization of $\langle A|\phi^*\phi|A\rangle$

A further step in implementing the relevant pionic degrees of freedom into the GGT sum rule was an observation inferred from models providing the convergence of the $\sigma_0^{\rm tot}$-integral. It was first suggested [3] and then perturbatively (to one-loop order) checked [5] in scalar, ϕ^3-type "super-renormalizable" model that the generalized Thomas-Reiche-Kuhn is valid for total photoabsorption cross section

$$\sigma_0 = \int {\rm d}\nu\sigma^{\rm tot}(\nu) = 2\pi^2\langle\phi_1|[D[H,D]]|\phi_1\rangle, \tag{5}$$

where the charged scalar field ϕ_1 is locally connected with two scalar fields, ϕ_2 being charged one and the other, ϕ_3, neutral. The double commutator is then interpreted via the known Schwinger-term, *i.e.*, the equal-time commutator of the time- and spatial-component of the electromagnetic current operator. Hence, the generalized, "GGT$'$"-sum rule, implicitly including the integrals of the absorptive parts of the amplitudes presented by the diagrams with 2π-exchanges, was written [4] in the form

$$\sigma_0^{\gamma A} - Z\sigma_0^{\gamma p} - N\sigma_0^{\gamma n} = 2\pi^2\alpha\left[\frac{NZ}{Am} + \int {\rm d}\vec{x}\,(\langle A|\phi^*\phi|A\rangle - \Sigma_i\langle N_i|\phi^*(x)\phi(x)|N_i\rangle)\right]. \tag{6}$$

The photonuclear sum rule including the terms $\langle A|\phi^*\phi|A\rangle$ and $\langle N|\phi^*\phi|N\rangle$, represented by the Feynman diagram in Fig. 2, was later rediscovered [6], found to be a useful exploration tool [7], and widely discussed (*e.g.*, [8] and further references therein) in view of the interesting idea about possible partial restoration of the chiral symmetry in real nuclei.

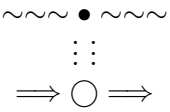

Fig. 2: Feynman diagram representing photonuclear sum rule.

The matter is that, up to constant factors, the matrix element corresponding to the seagull graph of Fig. 2, which in the forward direction is gauge invariant and may have a direct bearing to measurable quantities, is essentially of the same structure as the matrix element presented in Fig. 3.

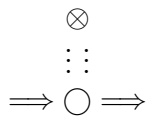

Fig. 3: Matrix element corresponding to the seagull graph of Fig. 2.

The symbol $\otimes$ denotes the local, scalar quark-current and therefore it is directly connected with the Σ_π-term, hence with the chiral symmetry breaking and its possible (partial) restoration in nuclear matter.

C. FESR and problem of "Big Circle" contribution

The standard FESR technique enables one to deal with the amplitudes defined in the finite region of the complex energy plane

$$f(\nu) = \frac{1}{2\pi\imath}\oint \mathrm{d}z \frac{f(z)}{z-\nu} \tag{7}$$

where $f(\nu)$ is the spin-averaged, forward Compton scattering amplitude and the integration contour includes both sides of the cuts along the real axes $-R \leq \nu \leq R$ closed by a circle of a "big" radius R. As usual the problem consists in the justified and economical choice for the representation of amplitudes in the complex energy plane to fulfill the integration over the large but finite-radius circle in the complex plane. We keep the original GGT idea of a relation between the photon-nucleus scattering amplitude and a relevant combination of the photon-nucleon amplitudes at sufficiently large photon energies, but our choice of the "superconvergent" combination of Compton amplitudes $f_{\gamma A(p,n)}$ is different from GGT. It includes amplitudes of two nuclei with $A_1 = Z_1 + N_1, A_2 = Z_2 + N_2$ and is assumed to satisfy the condition

$$\lim_{|\nu|\to R}\left[\frac{1}{A_1}f_{A_1} - \frac{1}{A_2}f_{A_2}\right] = \frac{Z_1N_2 - N_1Z_2}{A_1A_2}(f_p - f_n)|_{\nu=R} + \frac{S_\pi(A_1)}{A_1} - \frac{S_\pi(A_2)}{A_2} \tag{8}$$

where

$$S_\pi(A_i) \simeq \frac{\alpha}{3}\int \mathrm{d}^3x \langle A_i|\vec{\phi}(x)\vec{\phi}(x)|A_i\rangle \tag{9}$$

and the scalar product in the integrand is understood to be in the isospin space. The upper limit $\nu_{max} \equiv R$ in all integrals should be chosen from the compromise provisions.

The first term derived in the approximation linear in A_i, $(i = 1, 2)$ is parameterized through the $a_2(J^P;\, I^G = 2^+; 1^-)$ -Reggeon exchange in the t-channel and includes in addition the real constant term seemingly taking place [9] in the $Re\, f_p$ and referring as the residue of the $j = 0$ fixed-pole in the complex angular momentum plane. Hence one should put $R \geq 1.5 \div 2.0$ GeV to apply the Regge-pole phenomenology with the commonly used parameters [11]

$$\begin{aligned} Im[f_p(\nu) - f_n(\nu)] &= \frac{\nu}{4\pi}(\sigma_p^{\mathrm{tot}} - \sigma_n^{\mathrm{tot}}) = b_{a_2}\nu^{1/2} \\ Re(f_p(\nu) - f_n(\nu)) &= \frac{1}{4\pi}b_{a_2}(-\nu^{1/2}) + C_p - C_n \\ \sigma_p^{\mathrm{tot}}(\nu) - \sigma_n^{\mathrm{tot}}(\nu) &= \frac{24.6}{\nu^{1/2}} \end{aligned} \tag{10}$$

Following [9], we accept $C_p \simeq -3.0\,\mu\mathrm{b}\cdot\mathrm{GeV}$ and put the C_n-value rather arbitrarily to be either $C_n = (2/3)C_p$ or $C_n = 0$ for the sake of further numerical estimations.

Due to the dominant scalar-isoscalar nature of the pionic operators we accept $S_\pi(p) \simeq S_\pi(n)$ while $S_\pi(A_i) \neq 0$ will disclose its essential nonlinear dependence on the atomic number A of real nuclei.

III. ESTIMATION OF THE NEUTRON-TO-PROTON RATIOS FOR INTEGRAL PHOTOPRODUCED PION YIELDS

The meson photoproduction cross-sections on the neutron are largely unknown and should be extracted *e.g.* from the deuteron data. Of all possible photo-meson reactions, the best known is the single pion photoproduction. Therefore we treat the neutron cross-sections entering our sum rules as follows. The $\sigma^{\rm tot}_{\gamma n}(\nu)$ is split into two parts:

$$\sigma^{\rm tot}_{\gamma n} = \sigma(\gamma n \to \pi N) + \sigma(\gamma n \to 2\pi N) + \cdots$$

The single pion production cross-section is taken according to theoretical calculation with fairly good multipole amplitudes of the MAID Collaboration [10].

The detailed experimental study of the meson photoproduction on the deuteron target can be performed at a number of the "intermediate-energy" electron accelerators (*e.g.*, JLab(USA), MAMI-C(Mainz, FRG)). So, anticipating the appearance of a new γn-data, needed for the checking of FESR sum rule for the difference of the γp- and γn- Compton amplitudes and extracting the value $C_p - C_n$, required further for definition of the nuclear sum rules, we present first the dependence of the experimentally measurable ratios $R^{\rm tot}_{n/p}(R^{\rm non-res}_{n/p})$, defined as,

$$R^{\rm tot(non-res)}_{n/p} = \frac{\sigma^{\rm tot}_0(\gamma n \to 2\pi + X)}{\sigma^{\rm tot}_0(\gamma p \to 2\pi + X)} \left(\frac{\sigma^{\rm non-res}_0(\gamma n \to 2\pi + X)}{\sigma^{\rm non-res}_0(\gamma p \to 2\pi + X)}\right) \tag{11}$$

as the function of several plausible values of C_n, taking $C_p = -3.0\,\mu{\rm b}\cdot{\rm GeV}$ for granted. The results are presented in Table I.

TABLE I: The $R^{\rm tot}_{n/p}$ and $R^{\rm non-res}_{n/p}$ as the function of several plausible values of C_n.

C_p	C_n	$R^{\rm tot}_{n/p}$	$R^{\rm non-res}_{n/p}$
0	0	0.95	0.98
-3	-2	0.72	0.62
-3	0	0.60	0.39

For illustrative reasons, we indicate the results of the modelling the neutron-to-proton ratios as follows from the ratios of the electric dipole moment fluctuation in the lowest hadronic Fock-components of the nucleon with at least one charged pion,

$$N \leftrightarrow \pi + N, 2\pi + N, \pi + \Delta(1231)\,,$$

Then

$$\frac{\langle \vec{D}^2(n \leftrightarrow p\pi^-)\rangle}{\langle \vec{D}^2(p \leftrightarrow n\pi^+)\rangle} \simeq 1 + 2\varepsilon, \varepsilon = \frac{m_\pi}{m_N} \tag{12}$$

$$\frac{\langle \vec{D}^2(n \leftrightarrow n\pi^+\pi^-)\rangle}{\langle \vec{D}^2(p \leftrightarrow p\pi^+\pi^-)\rangle} \simeq \frac{(1+4\varepsilon)\langle \vec{r}^{\,2}_{\pi^+\pi^-}\rangle}{(1+2\varepsilon)\langle \vec{r}^{\,2}_{\pi^+\pi^-}\rangle + 2\varepsilon\langle(\vec{r}_{\pi^+\pi^-}\cdot\vec{r}_{p\pi^-})\rangle} \geq 1, \tag{13}$$

and, analogously to (12),

$$\frac{\langle \vec{D}^2(n \leftrightarrow \pi\Delta)\rangle}{\langle \vec{D}^2(p \leftrightarrow \pi\Delta)\rangle} \simeq 0.66\ (0.41) \tag{14}$$

The first value in (14) refers to the sum over all possible charge $\pi\pi$-states produced in the final decay stage $\pi\Delta \to \pi\pi N$, while the second ratio corresponds to the selection of the $\pi^+\pi^-$ final states. The numerical relevance of (14) to the last two rows in Table I testifies on the crucial importance of the correlation of the valence and nonvalence partonic composites of the nucleon in producing of the ultimate characteristics of the Compton scattering amplitude.

IV. SOME NUMERICAL RESULTS AND DISCUSSION OF THE PHOTONUCLEAR SUM RULES

As an example of the generalized nuclear sum rule applications, we choose a pair of lightest nuclei - the deuteron and ^{3}He. While in the deuteron case the total photoabsorption cross section is known well above our taken $\nu_{\max} \simeq 1.6\,\mathrm{GeV}$, the $\sigma_{\mathrm{tot}}(\gamma^3\mathrm{He})$ is known to 0.8 GeV [12], hence, in this case, we have to take $\nu_{\max} = 0.8\,\mathrm{GeV}$. The major purpose of using these new types nuclear sum rules may be the extraction of information about the value of difference of the nuclear matrix elements:

$$\Delta\left(\frac{\Sigma_\pi(A)}{A}\right) = \frac{\alpha}{3}\int \mathrm{d}\vec{x}\frac{m_\pi^2}{2}\left[\frac{1}{A_1}\langle A_1|\vec{\phi}(x)\cdot\vec{\phi}(x)|A_1\rangle - \frac{1}{A_2}\langle A_2|\vec{\phi}(x)\cdot\vec{\phi}(x)|A_2\rangle\right].$$

The term $\Delta\Sigma_\pi(A)$ can thus be extracted from experimentally measurable quantities to give useful information on the values closely related with the chiral symmetry characteristics in real nuclei. Of special interest is the situation when $Z_1N_2 - N_1Z_2 = 0$ in (8) (deuteron- and ^{4}He-pair for example). The contribution of the a_2-Reggeon is then absent and the optimal value of $\nu_{\max} = R$ in dispersion integrals of cross sections could probably be taken at a lower value. Qualitatively, this newly chosen R-value should provide a reasonable balance between the contribution of the same group of most important nucleon resonances into the real parts of nuclear Compton amplitudes represented by the terms $S_\pi(A_i)$ and the respective imaginary parts entering into dispersion integrals in the form of the corresponding nuclear photo-pion production cross sections. For arbitrary $A_1 = Z_1 + N_1$ and $A_2 = Z_2 + N_2$ our general sum rule reads

$$2\pi^2\left[\frac{f_{A_1}(\nu=0)+S_\pi(A_1)}{A_1} - \frac{f_{A_2}(\nu=0)+S_\pi(A_2)}{A_2} + \frac{Z_1N_2 - Z_2N_1}{A_1A_2}\cdot\left(\frac{2b_{a_2}\nu_{\max}^{1/2}}{2\pi^2} - C_p + C_n\right)\right] = \frac{\sigma_0^{\nu_{\max}}(\gamma A_1)}{A_1} - \frac{\sigma_0^{\nu_{\max}}(\gamma A_2)}{A_2} \tag{15}$$

where $f_{A_i}(\nu=0) \simeq -(\alpha Z_i^2)/(A_i m_n)$ is the Thompson zero-energy amplitude, $S_\pi(A_i)$ is defined in Eq. (9) and the integration in $\sigma_0^{\nu_{\max}}$ extends from the photodisintegration threshold to the upper bound $\nu_{\max}$. In the case of ^{3}He and deuteron the integration was carried out with the cross-sections tabulated in [12] up to $\nu_{\max} = 0.8\,\mathrm{GeV}$. The low-energy integrals up to the pion photoproduction thresholds $\nu_{\gamma\pi}$ were approximated by

$$\sigma_0^{\nu_{\gamma\pi}} = 60\frac{NZ}{A}(1+\kappa_A^{\exp})\ [\mu\mathrm{b}\cdot\mathrm{GeV}] \tag{16}$$

where $\kappa^{\rm exp}_{{\rm He}-3(d)} = 0.75 \pm .10\ (0.37 \pm 0.11)$, following [13]. To have an idea about the scale of S_π for the nuclei considered, we confronted the calculated values of

$$(2\pi^2\alpha)/(3)[(1/3)S_\pi(^3{\rm He}) - (1/2)S_\pi(d)] \simeq 7.75\ (1.17)\,\mu{\rm b}\cdot{\rm GeV}$$

for $C_p = -3,\ C_n = -2\ (0)$ with the value

$$60[(2/9)\kappa_{^3{\rm He}} - (1/4)\kappa_d] = (1/3)40(0.75 \pm 0.10) - (1/2)30(0.37 \pm 0.11) \simeq 4.4 \pm 2.1\,\mu{\rm b}\cdot{\rm GeV}$$

representing the "potential parts" in the difference of non-relativistic TRK sum rules

$$2\pi^2\alpha[(1/3)\langle^3{\rm He}|[D,[V_{NN}]]|^3{\rm He}\rangle - (1/2)\langle d|[D,[V_{NN}]]|d\rangle]$$

The correspondence looks reasonable because the non-relativistic value is in between two values following from a more general sum rule with different values of C_n. We also draw the attention to a strong dependence of the abovementioned estimations on two chosen numerical values of C_n, which emphasizes the significance of the sum rule as a source of new interesting information. The pion-nucleon sigma-term

$$\sigma = \frac{\hat m}{2m_p}\langle p|\bar u u + \bar d d|p\rangle, \qquad \hat m = \frac{1}{2}(m_u + m_d),$$

and, generally, sigma-terms of a given hadron are proportional to the scalar quark currents

$$\langle A|m_q\bar q q|A\rangle\,, \qquad q = u,d,s\,, \qquad A = \pi, K, N,\ {}^Z A_N - \text{nuclei}.$$

These are of great physical significance because they are related to the hadron masses, to the meson scattering amplitudes [14], to the strangeness content of A, and to the properties of nuclear [15] and dark [16] matter. Our derived and discussed photoabsorption sum rules are focused on the comparison of the scalar pion densities, hence on important part of the pionic σ-terms for different nuclei, to trace their dependence on the atomic number. In particular, the deuteron sum rule provides thereupon the situation most close to free nucleons while the helium-4 would play the role of a drop of the real nuclear matter.

In view of the above discussion the following looks to be practically important: i) To extend measurements of the total photoabsorption on the ^{3}He and ^{4}He-nuclei at least up to energy of photons $1.5 \div 2.0\,$GeV. ii) To complete calculation of $\langle A|[D[H,D]]|A\rangle$, $A = {}^{3(4)}$He, with best modern potentials and respective wave functions as well as with estimation of relativistic corrections.

V. QUARK-HADRON DUALITY SUM RULES FOR SPIN-DEPENDENT PHOTOABSORPTION CROSS SECTIONS AS CONSTRAINTS ON THE NUCLEON WAVE FUNCTION STRUCTURE

As it is known, while many sum rules were first derived from the dispersion approach [17–20], it was demonstrated that the same relations can be obtained with the help of current algebras and the $p_z \to \infty$ techniques. Here, we intent to use the valence quark approximation and the infinite momentum frame (IMF) approach to bridge between the results following from sum rules and those pertinent to mainly the dynamical approaches based on the three-quark relativistic equations relating description of the ground and excited baryon states. Following formally to the $p_z \to \infty$ techniques derivation of the Cabibbo-Radicati [21] or GDH sum rule [22], one can obtain the relation

$$4\pi^2\alpha\left(\frac{1}{3}\langle\vec D^2\rangle - (\frac{\kappa_N}{2m_N})^2\right) = \int\frac{d\omega}{\omega}\sigma^{\rm res}_{\rm tot}(\omega), \tag{17}$$

formally alike the relation obtained by Gottfried [23] which, however, should be assumed as based on the three active valence quark approximation providing the convergence of the right-hand-side integral (*i.e.*, exemplifying the resonance-(nonvacuum) Reggeon-duality [24, 25]) but leaving for the left-hand-side entries the status of directly non-measurable quantities. Leaving the discussion of nonvalence degrees of freedom for future development, we concentrate on what can be found from such truncated relations. The next idea is to relate the electric dipole moment correlator and the mean-squared radii operators sandwiched by the nucleon state vectors in the "infinite - momentum frame". With the definitions

$$\hat{D} \;=\; \int \vec{x}\hat{\rho}(\vec{x})\;\mathrm{d}^3x = \sum_{j=1}^{3} Q_q(j)\vec{d_j}, \tag{18}$$

$$\hat{r_1^2} \;=\; \int \vec{x}^2\hat{\rho}(\vec{x})\;\mathrm{d}^3x = \sum_{j=1}^{3} Q_q(j)\vec{d_j}^{\,2} \tag{19}$$

where $Q_q(j)$ and $\vec{d_j}$ are the electric charges and configuration variables of point-like interacting quarks in the infinite-momentum frame of the bound system, *i.e.* the nucleon, we have

$$\langle r_1^2\rangle_P \;=\; \frac{4}{3}\alpha - \frac{1}{3}\beta; \langle r_1^2\rangle_N = -\frac{2}{3}\alpha + \frac{2}{3}\beta \tag{20}$$

$$\langle \hat{D^2}\rangle_P \;=\; \frac{8}{9}\alpha + \frac{1}{9}\beta + \frac{8}{9}\gamma - \frac{8}{9}\delta \tag{21}$$

$$\langle \hat{D^2}\rangle_N \;=\; \frac{2}{9}\alpha + \frac{4}{9}\beta + \frac{2}{9}\gamma - \frac{8}{9}\delta \tag{22}$$

$$\langle \hat{D_S^2}\rangle_{P,N} \;=\; \frac{1}{36}(2\alpha + \beta + 2\gamma + 4\delta), \tag{23}$$

where $\langle \vec{d_1}^{\,2}\rangle = \langle \vec{d_2}^{\,2}\rangle = \alpha$, $\langle \vec{d_3}^{\,2}\rangle = \beta$, $\langle \vec{d_1}\cdot\vec{d_2}\rangle = \gamma$, $\langle \vec{d_1}\cdot\vec{d_3}\rangle = \langle \vec{d_2}\cdot\vec{d_2}\rangle \;= \delta$, indices "1" and "2" refer to the like quarks (i.e. to the $u(d)$- quarks inside the proton (neutron)), and the "3", to the odd quark. Our valence approximations assume that all cross sections are understood as the nucleon resonance excitation cross sections; all radii $\langle r_1^2\rangle_{p,n}$, as the valence quark distribution radii $\langle r_1^2\rangle^b_{p,n}$, not including the sea quark and/or meson current effects. Next use the dipole moment algebra in the "$p_z \to \infty$" - frame and the GDH sum rule for the anomalous magnetic moments of nucleons.

$$\frac{4}{3}\pi^2\alpha\langle \hat{D^2}\rangle_{P(N)} \;=\; J_p^{\gamma P(N)}(\frac{1}{2}) + J_p^{\gamma P(N)}(\frac{3}{2}) \tag{24}$$

$$\frac{4}{3}\pi^2\alpha\langle \hat{r_1^2}\rangle^b_N \;=\; J_a^{\gamma P}(\frac{3}{2}) - J_p^{\gamma P}(\frac{1}{2}) + 4J_p^S(\frac{1}{2}) \tag{25}$$

$$J^{V(S)}_{p,a}(I) \;=\; \int_{\nu_{thr}}^{\infty}\frac{\mathrm{d}\nu}{\nu}\sigma_{p,a}(\gamma^{V(S)}N \to N^\star(I)) \tag{26}$$

Not touching many relations checked perturbationaly in field-theoretic models [5], we only mention below one more sum rule checked approximately but *non-perturbationly* within the QED, that is the sum rule for the photoelectric absorption on hydrogen-like system (^{Ze}A) of the electron bound on the Coulomb center with electric charge $+(eZ)$ and obeying the Dirac equation

$$4\pi^2\alpha[\frac{1}{3}\langle r_1^{e2}\rangle - (\frac{\mu_e}{2m_e})^2] = J_{\mathrm{tot}}(\gamma \;+\; {}^{Ze}A)\,. \tag{27}$$

The inclusion of μ_e and evaluation of left hand side via the Dirac equation diminishes the difference of about 7% between left hand side earlier written [26] without the μ_e, and the right hand side, calculated numerically in [26], to quite acceptable level $\mathcal{O}(1\%)$.

Evaluation of the relativistic electric dipole moment fluctuation sum rules for the nucleon was carried out with the PDG compilation [27] of the pion photoproduction data on the proton and neutron $A_{1/2}^{P(N)}$ and $A_{3/2}^{P(N)}$. With the pionic degrees of freedom omitted explicitly in our calculations, we calculated all integrals over photoexcited nucleon resonances in the narrow resonance approximation, when

$$J_{p(a)}^{res} \simeq \frac{4\pi m_n |A_{3/2(1/2)}^{res}|^2}{m_{res}^2 - m_n^2}, \tag{28}$$

where $m_{n(\mathrm{res})}$ is the nucleon (or resonance) mass. The final results are

$$\alpha = \frac{3}{2}J_p^{\mathcal{P}}(\frac{1}{2}) + 3J_p^{\mathcal{N}}(\frac{1}{2}) - 2J_p^V(\frac{1}{2}) + J_p(\frac{3}{2}) - -\frac{3}{2}J_a(\frac{3}{2}) \simeq 0.62 \pm 0.06 \text{ fm}^2 \tag{29}$$

$$\beta = 3J_p^{\mathcal{P}}(\frac{1}{2}) + 6J_p^{\mathcal{N}}(\frac{1}{2}) - 8J_p^V(\frac{1}{2}) + J_p(\frac{3}{2}) \simeq 0.78 \pm 0.12\,\text{fm}^2 \tag{30}$$

$$\gamma = \frac{3}{2}J_p^{\mathcal{P}}(\frac{1}{2}) - \frac{3}{2}J_p^{\mathcal{N}}(\frac{1}{2}) - 2J_p^V(\frac{1}{2}) - \frac{1}{2}J_p(\frac{3}{2}) + \frac{3}{2}J_a(\frac{3}{2}) \simeq -0.18 \pm 0.04\,\text{fm}^2 \tag{31}$$

$$\delta = \frac{9}{4}[J_p^{\mathcal{P}}(\frac{1}{2}) + J_p^{\mathcal{N}}(\frac{1}{2})] - 5J_p^V(\frac{1}{2}) - \frac{1}{2}J_p(\frac{3}{2}) \simeq -0.25 \pm 0.07\,\text{fm}^2 \tag{32}$$

The Dirac rms of the valence quark distribution are

$$\langle r_1^2\rangle^{\mathcal{P}} = \frac{4}{3}\alpha - \frac{1}{3}\beta \simeq .57 \pm 0.06\,\text{fm}^2, (\exp: 0.662\,\text{fm}^2) \tag{33}$$

$$\langle r_1^2\rangle^{\mathcal{N}} = -\frac{2}{3}\alpha + \frac{2}{3}\beta \simeq +.105 \pm 0.052\,\text{fm}^2\,,$$

$$\exp: \ \langle r_{ch}^2\rangle^{\mathcal{N}} - \frac{3\mu_{\mathcal{N}}}{2m_{\mathcal{N}}} = -.113 + .126 = +.013\,\text{fm}^2 \tag{34}$$

At the same time

$$\langle r_1^2\rangle^S = \frac{1}{2}[\langle r_1^2\rangle^{\mathcal{P}} + \langle r_1^2\rangle^{\mathcal{N}}] = \ .34 \pm 0.04 \text{ fm}^2\,, \qquad (\exp: \ .336(1 \pm 0.1)\,\text{fm}^2) \tag{35}$$

The missing dynamical ingredient which defines the negative sign of $\langle r_{ch}^2\rangle^{\mathcal{N}}$ and provides the needed positive contribution to the $\langle r_1^2\rangle^{\mathcal{P}}$ is the isovector 2π-intermediate state in the "current channel" of the nucleon form-factors (it was qualitatively demonstrated, *e.g.*, in Refs. [28, 29]). We conclude with the following remarks:

1. (Hopefully) useful constraints on the "asymmetry" of the nucleon relativistic wave function are obtained that give a hint of a role of the spin-dependent dynamics in the distribution and correlation of valence quarks in the nucleon.

2. As a prospect for the future: Possible extension of derived relations to the virtual photon interactions looks promising (e.g., for probing the higher twist contributions, etc.)

3. The accumulation of more detailed and accurate neutron data is highly desirable to diminish the uncertainties of the presented results.

Acknowledgments

The author is grateful to Dr. S.S. Kamalov for providing some additional MAID data and helpful discussions.

---

[1] M. Gell-Mann, M.L. Goldberger and W. Thirring, Phys. Rev. **95**, 1612 (1954).
[2] S.B. Gerasimov, Phys. Lett. **5**, 259 (1963).
[3] S.B. Gerasimov, Phys. Lett. **13**, 240 (1964).
[4] S.B. Gerasimov, in Proc. Int. Conf. on Electromagnetic Interactions at Low and Medium Energies, AN USSR, Moscow **3**, 382 (1972).
[5] S.B. Gerasimov and J. Moulin, Nucl. Phys. B **98**, 349 (1975).
[6] S.A. Kulagin, TRK 91-39, Uni. Regensburg (1991).
[7] M. Ericson, M. Rosa-Clot, and S.A. Kulagin, Nuovo. Cim. A **111**, 75 (1998).
[8] M. Ericson, G. Chanfray, J. Delorm, and M.Rosa-Clot, Nucl. Phys. A **663&664**, 369c (2000).
[9] M. Damashek and F.J. Gilman, Phys. Rev. D **1**, 1319 (1970).
[10] D. Drechsel, S.S. Kamalov, and L. Tiator, Nucl. Phys. A **645**, 145 (1999).
[11] W.P. Hesse, *et al.*, Phys. Rev. Lett. **25**, 613 (1970).
[12] M. MacCormick, *et al.*, Phys. Rev. C **53**, 41 (1996).
[13] D. Drechsel and Y.E. Kim, Phys. Rev. Lett. **40**, 531 (1978).
[14] M.E. Sainio, PiN Newslett. **16**, 138 (2001).
[15] J.N. Ginocchio, Phys. Rep. **414**, 165 (2005).
[16] A. Bottino, *et al.*, Astropart. Phys. **18**, 205 (2002).
[17] M.L. Goldberger, H. Miyazawa, and R. Oehme, Phys. Rev. **99**, 986 (1955).
[18] S.B. Gerasimov, Sov. J. Nucl. Phys. **2**, 430 (1966).
[19] S.D. Drell and A.C. Hearn, Phys. Rev. Lett. **16**, 908 (1966).
[20] S.B. Gerasimov, Yad. Fiz. **5**, 1263 (1967).
[21] N. Cabibbo and L. Radicati, Phys. Lett. **19**, 697 (1966).
[22] M. Hosoda and K. Yamamoto, Prog. Theor. Phys. **36**, 425 (1966).
[23] K. Gottfried, Phys. Rev. Lett. **18**, 1174 (1967).
[24] R. Dolen, D. Horn and C. Schmidt, Phys. Rev. **166**, 1768 (1968).
[25] H. Harari, Phys. Rev. Lett. **22**, 1395 (1968); P.G.O. Freund, Phys. Rev. Lett. **20**, 235 (1968).
[26] J.S. Levinger and M.L. Rusgi, Phys. Rev. **103**, 439 (1956); J.S. Levinger, M.L. Rustgi, and K. Okamoto, Phys. Rev. **106**, 119 (1957).
[27] Particle Data Group, Phys. Rev. D **45**, II.25 (1992); Eur. Phys. J. C **15**, 1 (2000).
[28] N. Isgur, Phys. Rev. Lett. **83**, 272 (1999).
[29] G.A. Miller, Nucl-th/0206027; 0301041.

Four-Nucleon System: The Doorway to Nuclear Physics

S.A. Sofianos*

Department of Physics, University of South Africa,
P O Box 392, Pretoria 0003, South Africa

Four-nucleon scattering, photo-, and electro-disintegration processes are considered within the integral equation approach to few-body systems. Various open questions related to these processes are discussed. These include questions related to the construction of nucleon-trinucleon interactions, the ratio of the ^{4}He$(\gamma, \mathrm{p})^3$H and ^{4}He$(\gamma, \mathrm{n})^3$He cross sections in the giant dipole resonance region, and the existence or not of a dip (dip-puzzle) in the five-fold differential cross-section of the electro-disintegration at high missing momenta.

I. INTRODUCTION

^{4}He is the lightest nucleus with well-established properties. Being also the first close shell nucleus, it became the subject, since early fifties, of numerous theoretical and experimental studies related to bound, scattering, photo-, and electro-disintegration processes. These studies continued unabated till today especially on the latter two topics. While for the bound state problem several methods exist for exact calculations with realistic interactions (Faddeev-type, Hyperspherical, Monde Carlo, etc.), the handling of reaction processes is far from being satisfactory. Although for energies below the three-body (2+1+1) break-up threshold calculations can be carried out, for higher energies one faces formidable numerical problems arising mainly from the three-body break-up threshold.

It is, therefore, clear that to study at present scattering problems, reasonable approximations to exact formalisms should be employed in conjunction with the use of traditional methods of Nuclear Physics such as the employment of effective interaction between the various clusters. One, however, should be extremely careful in constructing such interactions, since for light nuclei the collective characteristics of the many body problem are manifested in a different way and one has, instead, strong dependence of the underlying interactions, on parity, orbital angular momentum, energy, and mass. Furthermore, this could only be done at low energies as no enough experimental data are available at high energies, to construct them in an unambiguous way. Such constructions have a number of drawbacks in any case. Prejudices in shape and range enter the choice of the potentials and, most importantly, they fit the available data in a collective way and thus incorrect on- and off-shell effects may enter the calculations.

Another strategy is to start the construction of the potentials by using phase shifts obtained via a reliable theoretical model. In the present work we solved the Alt, Grassberger, and Sandhas (AGS) scattering equations [1, 2] for the 3+1 $\rightarrow$ 3+1 process, using the K-matrix approximation [3] and then we employed the inverse scattering method of Fiedeldey and Lipperheide [4], to obtain the required interactions. In this way we may avoid using arbitrary optical potentials and, in addition, we naturally account for the ℓ-, E-, and parity-dependence of these potentials.

Similarly to scattering, the two-fragment electro-disintegration process ^{4}He$(\mathrm{e}, \mathrm{e}'\mathrm{p})^3$H has been the subject of several experimental investigations for various kinematics (see, for example, [5–9]). On the theoretical front, the exact treatment of this process and the inclusion of the final state interactions (FSI) entails the same problems encountered in the scattering. Therefore,

*Electronic address: sofiasa@science.unisa.ac.za

calculations have been simplified by approximations and model assumptions [10–12]. In Plane-Wave Impulse Approximation calculations exhibit a characteristic dip, actually zero, in the five-fold differential cross-section around a missing momentum of $\sim 450\,\mathrm{MeV}/c$, which does not show up in the experimental data. Laget [11] included FSI effects and meson exchange currents (MEC) by means of a Feynman diagrammatic approach. Although this resulted in a partial filling of the dip, these investigations also underestimated the data considerably in this region. Similar results were obtained when FSI was taken into account via effective nucleon-trinucleon interactions [10, 12, 13]. The same behavior was found by Nagorny *et al.* [14] who incorporated the FSI via the pole contribution of the $\mathrm{p}^3\mathrm{H}\rightarrow\ \mathrm{p}^3\mathrm{H}$ scattering matrix [15]. The agreement with the data is again fairly satisfactory, but the zero is exhibited as well [9]. At lower missing momenta, less than $300\,\mathrm{MeV}/c$, calculations show a good agreement with the data and the PWIA performs reasonably well in this region where the FSI could be expected to be more important than in the higher missing momenta region. In contrast, in the region $300\,\mathrm{MeV}/c < Q < 600\,\mathrm{MeV}/c$ the results strongly depend on the way the FSI effects are included. For example, as pointed out in [9] the Laget results underestimate the cross section by a factor of 4 and those of Schiavilla by a factor of 2. At even higher missing momenta, above $600\,\mathrm{MeV}/c$, where the MEC contribution is becoming important, the agreement with the data is again fair. We, therefore, conclude that the zero in the PWIA cross section is not necessarily a manifestation of strong FSI or MEC effects. Instead, one should look for other explanations, such as the dependence of the results on the model used, the interaction forces employed, the determination of the bound state wave functions, etc.

The photo-disintegration of ^{4}He into various channels, especially into n+^{3}He and p+^{3}H, is yet another interesting and controversial topic and numerous experimental and theoretical works were carried out during the last 50 years. The field is rich in physics and the various investigations were focused mainly on understanding the reaction mechanism, the possibility of extracting information on the short range interaction between nucleons, the charge symmetry breaking question, the electromagnetic structure of the nucleon, and on the importance of contributions stemming from the various ingredients involved in the process. However, this problem for a long time has been a controversial topic in photonuclear physics. For example, early data for incident photon energies around 30 MeV appeared consistent with the picture of a giant dipole resonance at low energies, a picture also supported by various model calculations such as by shell [16] and resonating group [17] models. However, AGS calculations [18, 19] for these photo-processes do not show any pronounce giant dipole resonance. The controversy is still raging and many experimental as well as theoretical works appear regularly which show, alternatively, the existence of a pronounced giant dipole resonance or otherwise for both the $^4\mathrm{He}(\gamma,\mathrm{n})^3\mathrm{He}$ and $^4\mathrm{He}(\gamma,\mathrm{p})^3\mathrm{H}$ reactions.

In the present work we discuss, in brief, all these open questions and show that in fact they can be addressed in a unified way. In Sec. II we present the formal AGS theory for the three reactions, in Sec. III we present and discuss our results while in Sec. IV we summarize our main conclusions.

II. FORMAL THEORY

A. Bound and Scattering Equations

Let us briefly recall the Faddeev formalism for three nucleons which is based on the assumption that the particles interact via pairwise forces, *i.e* $V = \sum_{i<j\leq 3} V(r_{ij}) \equiv \sum_\gamma V_\gamma$. Then the

Schrödinger equation for the three-body bound system is written as

$$|\Psi_3\rangle = G_0(z)V|\Psi_3\rangle = G_0(z)\sum_{\gamma=1}^{3} V_\gamma|\Psi_3\rangle \tag{1}$$

or, after some simple rearrangements, as

$$|\Psi_3\rangle = \sum_{\gamma=1}^{3} G_0(z)T_\gamma(z)G_0(z)|F_\gamma\rangle\,. \tag{2}$$

where $z = E_3$ is the three-particle binding energy, $T_\gamma(z)$ is the two-body T-matrix operator in three-body space,

$$T_\gamma(z) = V_\gamma + V_\gamma G_0(z)T_\gamma(z)\,, \tag{3}$$

while the form factors $|F_\gamma\rangle$ obey the three coupled, six-dimensional, Faddeev equations

$$|F_\gamma\rangle = \sum_{\beta\neq\gamma} T_\beta(z)G_0(z)|F_\beta\rangle, \tag{4}$$

The corresponding AGS equations for the transition matrix $U_{\beta\alpha}$ are given by [2]

$$U_{\beta\alpha}(z) = (1-\delta_{\beta\alpha})\,G_0^{-1}(z) \,+\, \sum_{\gamma}(1-\delta_{\beta\gamma})\,T_\gamma(z)G_0(z)\,U_{\gamma\alpha}(z)\,. \tag{5}$$

Similarly to the three-body case, the Schrödinger equation for the bound state of four particles reads

$$|\Psi_4\rangle = G_0(z)\sum_{\gamma=1}^{6} V_\gamma|\Psi_4\rangle \tag{6}$$

where now $z = E_4$ is the four-particle binding energy. In this equation the sum is running over the six two-body potentials, and $G_0(z)$ is the free four-particle resolvent operator. Unlike the three-body system, however, in the four-body we have two-fragment partitions of the form (i, jkl)) and (ij, kl)) (usually referred to as 3+1 and (2+2) partitions respectively). It is useful to label these partitions (1)(234),(4)(123), (12)(34), $\cdots$, by $\sigma,\ \tau$. The notation $\gamma \subset \sigma$ means considering only those two-body indices γ that are part of the three-body or the (2+2)-subsystem contained in partition σ, e.g., (23), (34), (42) for (1)(234), but not (12), (13), (14); or (12) and (34) for (34)(12), but not (13), (14), (23), (24). Quite similarly to the three-particle case, cluster functions $|\mathcal{F}_\beta^\sigma\rangle$ are defined as [2]

$$|\mathcal{F}_\beta^\sigma\rangle = \sum_{\tau\neq\sigma}\sum_{\gamma}(1-\delta_{\beta\gamma}^\tau)\,V_\gamma\,|\Psi_4\rangle\,, \tag{7}$$

with $\delta_{\beta\gamma}^\tau = \delta_{\beta\gamma}$ if $\beta,\gamma \subset \tau$, or $\delta_{\beta\gamma}^\tau = 0$ otherwise. Then Eq. (6) is replaced by the 18 coupled nine-dimensional integral equations for the form factors $\mathcal{F}_\beta^\sigma$

$$|\mathcal{F}_\beta^\sigma\rangle = \sum_{\tau\neq\sigma}\sum_{\gamma} U_{\beta\gamma}^\tau(z)\,G_0(z)T_\gamma(z)G_0(z)\,|\mathcal{F}_\gamma^\tau\rangle \tag{8}$$

with $\beta \subset \sigma$ and $\gamma \subset \tau$, and where $U_{\beta\gamma}^\tau(z)$ are the AGS transition operators for (2+2)- or the three-body subsystems obtained from the respective AGS equations

$$U_{\beta\alpha}^\tau(z) = (1-\delta_{\beta\alpha}^\tau)\,G_0^{-1}(z) \,+\, \sum_{\gamma}(1-\delta_{\beta\gamma}^\tau)\,T_\gamma(z)G_0(z)\,U_{\gamma\alpha}^\tau(z)\,. \tag{9}$$

We emphasize that in Eq. (8) both $U^\tau_{\beta\alpha}(z)$ and $T_\beta(z)$ are operators in the four-body space. The four-nucleon bound state wave function is obtained from the solutions of Eq. (8) via

$$|\Psi_4\rangle = \sum_\sigma \sum_{\beta\gamma} G_0 T_\beta G_0 U^\sigma_{\beta\gamma} G_0 T_\gamma G_0 |\mathcal{F}^\sigma_\gamma\rangle \qquad \beta,\gamma \subset \sigma \tag{10}$$

The scattering equations for the four-body AGS transition operators are [2]

$$\begin{aligned} U^{\sigma\rho}_{\beta\alpha}(z) &= (1-\delta_{\sigma\rho})\,\delta_{\beta\alpha}\,G_0^{-1}(z)T_\beta^{-1}(z)G_0^{-1}(z) \\ &+ \sum_\tau \sum_\gamma (1-\delta_{\sigma\tau}) U^\tau_{\beta\gamma}(z)\,G_0(z)T_\gamma(z)G_0(z)\,U^{\tau\rho}_{\gamma\alpha}(z)\,. \end{aligned} \tag{11}$$

The above equations are of course exact but multi-dimensional and thus the computational complexity is enormous. Simplifications, however, can be accomplished by going over to effective two-body equations which after partial wave decomposition become one-dimensional integral equations. This reduction is achieved in two steps. In the first step one employs a separable expansion of the two-body T-matrix $T_\alpha(z)$,

$$T_\alpha(z) = \sum_{nm} |\alpha n\rangle\, t_{\alpha,nm}(z)\, \langle \alpha m|\,. \tag{12}$$

Inserting (12) in (11) leads, after multiplication with $\langle \alpha n|G_0|$ and $G_0|\beta m\rangle$, to the effective three-body equation

$$\widetilde{U}^{\sigma\rho}_{\alpha n,\beta m}(z) = (1-\delta_{\sigma\rho})\,\widetilde{G}^{-1}_{0_{\alpha n,\beta m}}(z) + \sum_{\tau\neq\sigma}\sum_{\gamma m'} \widetilde{T}^\tau_{\alpha n,\gamma m'} \widetilde{G}_{0_{\gamma m',\gamma m'}} \widetilde{U}^{\tau\rho}_{\gamma m',\beta m}(z)\,. \tag{13}$$

with

$$\widetilde{U}^{\sigma\rho}_{\alpha n,\beta m} = \langle \alpha n|G_0 U^{\sigma\rho}_{\alpha,\beta} G_0|\beta m\rangle\,, \qquad \widetilde{T}^\tau_{\alpha n,\beta m} = \langle \alpha n|U^\tau_{\alpha\beta} G_0|\beta m\rangle\,, \qquad \widetilde{G}_{0_{\alpha n,\beta m}} = \delta_{\alpha\beta}\delta_{nm} t_{\alpha,nm} \tag{14}$$

The second step then consists of introducing a separable expansion of the resulting three-body and (2+2)-body subsystem amplitudes [20–22]

$$\widetilde{T}^\sigma_{\alpha n,\beta m} = \sum_s \sum_{\mu\nu} |\Gamma^{\sigma s,\mu}_{\beta n}(z)\rangle\, h^{\sigma s}_{\mu\nu}(z)\, \langle \Gamma^{\sigma s,\nu}_{\alpha m}(z)|\,. \tag{15}$$

As in the first step, one multiplies by $\langle \Gamma^{\sigma s,\mu}_{\alpha n}|\widetilde{G}_0$ and $\widetilde{G}_0|\Gamma^{\rho r,\mu}_{\beta\mu}\rangle$ to obtain the Lippmann-Schwinger type equation

$$\mathbb{T}^{\sigma s,\rho r}_{\mu\nu} = \mathbb{V}^{\sigma s,\rho r}_{\mu\nu} + \sum_{\tau,t}\sum_{\mu'\nu'} \mathbb{V}^{\sigma s,\tau t}_{\mu\mu'} \mathbb{G}^{\tau t}_{0,\,\mu'\nu'}\, \mathbb{T}^{\tau t,\rho r}_{\nu'\nu} \tag{16}$$

with obvious notation and with s, r, and t representing three-body subsystem channels.

Further to the above formal description one has to include also spin and isospin and to antisymmetrize the amplitudes (see, for example, [19]). For central forces, the total angular momentum J, the total spin S and isospin I, and their corresponding three-components as well as the total orbital angular momentum L are conserved. Thus (16), after antisymmetrization and partial wave expansion, reduces to

$$\begin{aligned} {}^{ISL}\mathbb{T}^{r,s}(q,q';z) &= {}^{ISL}\mathbb{V}^{r,s}(q,q';z) \\ &+ \sum_{j=t,qu} 4\pi \int_0^\infty q''^2 \mathrm{d}q''\, {}^{ISL}\mathbb{V}^{r,j}(q,q'';z)\mathbb{G}^j_0(z-\frac{2}{3}q''^2)\,{}^{ISL}\mathbb{T}^{j,s}(q'',q';z) \end{aligned} \tag{17}$$

where r and s stand for the three-body doublet state t and quartet state qu respectively. Explicit arguments and other details for the above relations can be found, for example, in [3, 19–22]. The effective potentials are given by

$$ {}^{ISL}\mathbb{V}^{r,s}(q,q';z) = {}^{ISL}\mathbb{A}^{r,s}(q,q';z) + \sum_{j=dd,\phi\phi} 4\pi \int_0^\infty q''^2 \mathrm{d}q'' \, {}^{ISL}\widetilde{\mathbb{B}}^{ii,r}(q,q'';z)\mathbb{G}_0^{ii}(z-\frac{1}{2}q''^2)\, {}^{ISL}\mathbb{B}^{ii,s}(q'',q';z) \quad (18) $$

where the $\mathbb{A}$, $\widetilde{\mathbb{B}}$ and $\mathbb{B}$ corresponds to the effective interactions for the processes $3+1 \to 3+1$, $2+2 \to 3+1$, and $3+1 \to 2+2$ and are calculated from the expansion functions Γ for the $3+1$ and $2+2$ sub-amplitudes [21]. The most important aspect in the last equation is that the effective interaction is a sum of a genuine (direct) $3+1 \to 3+1$ scattering term and a rescattering, via $2+2$, term which contributes in a collective way.

B. Electro-processes

The perturbative Hamiltonian H' for the interaction between the electron and the nucleons of the α-particle can be chosen to be that of McVoy and van Hove [23], which was also employed in the electro-disintegration of the trinucleon system [24–26]. This Hamiltonian, correct to the order of $\hbar^2 Q^2/M^2c^2$, is given by

$$ H' = -\frac{4\pi \mathrm{e}^2}{q_\mu^2}\langle v_f| \sum_{j=1}^{4} \Bigg\{ F_{1N}(q_\mu^2)\mathrm{e}^{-i\mathbf{Q}\cdot\mathbf{x}_j}\frac{q^2}{8M} - \frac{F_{1N}(q_\mu^2)}{2M}[(\mathbf{p}_j\cdot\boldsymbol{\alpha})\mathrm{e}^{-i\mathbf{Q}\cdot\mathbf{x}_j} + \mathrm{e}^{-i\mathbf{Q}\cdot\mathbf{x}_j}(\mathbf{p}_j\cdot\boldsymbol{\alpha})] \quad (19) $$

$$ -i\left[\frac{F_{1N}(q_\mu^2)+\kappa F_{2N}(q_\mu^2)}{2M}\right]\boldsymbol{\sigma}_j\cdot(\mathbf{x}_j\times\boldsymbol{\alpha})\ \mathrm{e}^{-i\mathbf{Q}\cdot\mathbf{x}_j} + \frac{q_\mu^2}{8M^2}\ [F_{1N}(q_\mu^2)+2\kappa F_{2N}(q_\mu^2)]\ \mathrm{e}^{-i\mathbf{Q}\cdot\mathbf{x}_j}\Bigg\}|u_i\rangle\,. $$

Here $\mathbf{x}_j$ and $\mathbf{p}_j$ are the position and momentum operators of the j-th nucleon, $\boldsymbol{\sigma}_j$ is the nucleon spin operator, $\boldsymbol{\alpha}$ is the Dirac matrix acting on the free electron spinors $|v_i\rangle$ and $|v_f\rangle$, while q_μ^2 is the exchanged four-momentum squared. Furthermore, F_{1N} and F_{2N} are the form factors of the nucleon, κ is the anomalous moment of the nucleon in nuclear magnetons, and M is the nucleon mass.

When the scattered electron and the ejected nucleon are measured in coincidence, the electron-proton coincidence cross section is given by

$$ \frac{\mathrm{d}^5\sigma}{\mathrm{d}E_f d\Omega_p \mathrm{d}\Omega_e} = \frac{\sigma_\mathrm{M}}{(\hbar c)^3(2\pi)^3}\frac{\rho_f}{4E_iE_f\cos^2\dfrac{\theta}{2}}|\mathcal{M}(\mathbf{q})|^2 \quad (20) $$

where σ_M is the Mott differential cross section, $\sigma_\mathrm{M} = e^4\cos^2\frac{\theta}{2}/4E_i^2\sin^4\frac{\theta}{2}$, $E_i(E_f)$ is the energy of the incoming (outgoing) electron, and ρ_f is the relativistic density of states. The transition matrix, properly antisymmetrized with respect to the four nucleons [27], is given by

$$ \mathcal{M}(\mathbf{q}) = 2\ {}^{(-)}\langle \mathbf{q};\Psi_3|H'|\Psi_4\rangle\,, \quad (21) $$

where the factor of 2 stems from antisymmetrization of the scattering states, H' is the Hamiltonian describing the interaction between the electron and nucleons, Eq. (19), ${}^{(-)}\langle \mathbf{q};\Psi_3|$ is the scattering state for the ejected proton that moves away with momentum $\mathbf{q}$ with respect to the residual three-nucleon bound state $|\Psi_3\rangle$, and $|\Psi_4\rangle$ is the four-nucleon bound state. For proton knock-out, the transition matrix reduces to

$$ \mathcal{M} = -\langle v_f|v_i\rangle\mathcal{M}_Q + \langle v_f|\boldsymbol{\alpha}|v_i\rangle\cdot(\mathbf{M}_\mathrm{elec}+\mathbf{M}_\mathrm{mag})\,, \quad (22) $$

where

$$\mathcal{M}_Q = 2\,{}^{(-)}\langle \mathbf{q};\Psi_3|\mathcal{H}_Q|\Psi_4\rangle\,, \quad \mathbf{M}_{\rm elec} = 2\,{}^{(-)}\langle \mathbf{q};\Psi_3|\mathbf{H}_{\rm elec}|\Psi_4\rangle\,, \quad \mathbf{M}_{\rm mag} = 2\,{}^{(-)}\langle \mathbf{q};\Psi_3|\mathbf{H}_{\rm mag}|\Psi_4\rangle$$

The Hamiltonians $\mathcal{H}_Q$, $\mathbf{H}_{\rm elec}$, and $\mathbf{H}_{\rm mag}$ are given by

$$\mathcal{H}_Q \;=\; F^p_{\rm ch}(1+\frac{q^2_\mu}{8M^2})\sum_{j=1}^{4}{\rm e}^{-i\mathbf{Q}\cdot\mathbf{x}_j}\,\lambda_j \tag{23}$$

$$\mathbf{H}_{\rm elec} \;=\; \frac{F^p_{\rm ch}}{2M}\sum_{j=1}^{4}(\mathbf{p}_j{\rm e}^{-i\mathbf{Q}\cdot\mathbf{x}_j}+{\rm e}^{-i\mathbf{Q}\cdot\mathbf{x}_j}\mathbf{p}_j)\,\lambda_j\,, \tag{24}$$

$$\mathbf{H}_{\rm mag} \;=\; \frac{i}{2M}F^p_{\rm mag}\sum_{j=1}^{4}{\rm e}^{-i\mathbf{Q}\cdot\mathbf{x}_j}\boldsymbol{\sigma}_j\times\mathbf{Q}\lambda_j\,, \tag{25}$$

Here the superscript p refers to the proton and $\lambda_j = e/2\ (1+\tau^3_j)$ is the isospin operator for nucleon j while $F^p_{\rm ch}$ and $F^p_{\rm mag}$ are the charge and magnetic form factors of the proton defined by

$$F^p_{\rm ch} = F_{1p}+\frac{q^2_\mu}{4M^2}\kappa_p F_{2p}\,, \qquad F^p_{\rm mag} = F_{1p}+\kappa_p F_{2p}\,. \tag{26}$$

The analytical fit to the proton form factors F_{1p} and F_{2p} given by Janssens *et al.* [28] can be used in the calculations.

Squaring the matrix element, summing and averaging over the electron spin, and inserting the resulting expression in Eq. (20), we obtain

$$\frac{{\rm d}^5\sigma}{dE_f\,d\Omega_p\,d\Omega_e} \;=\; \frac{\sigma_{\rm M}}{(\hbar c)^3(2\pi)^3}\;\frac{|\mathbf{p}_p|E_p}{1-\dfrac{E_p}{E_{^3H}}\dfrac{\mathbf{p}_p\cdot\mathbf{p}_{^3H}}{|\mathbf{p}_p|^2}}\Big\{|\mathcal{M}_Q|^2 \tag{27}$$

$$-\frac{1}{2}\sec^2\frac{\theta}{2}(\mathcal{M}^*_Q\mathbf{J}+\mathbf{J}^*\mathcal{M}_Q)\cdot(\hat{k}_i+\hat{k}_f)\frac{1}{2}\sec^2\frac{\theta}{2}(\mathbf{J}\cdot\hat{k}_i\mathbf{J}^*\cdot\hat{k}_f+\mathbf{J}\cdot\hat{k}_f\mathbf{J}^*\cdot\hat{k}_i)+|\mathbf{J}|^2\tan^2\frac{\theta}{2}\Big\}\,,$$

where $\mathbf{J} = \mathbf{M}_{\rm elec}+\mathbf{M}_{\rm mag}$. The determination of the coincidence cross section is thus reduced to the determination of the nuclear matrix elements $\mathcal{M}_Q$ and $\mathbf{J}$. However, this presupposes the knowledge of the scattering states ${}^-\langle\Psi_{\sigma s};\mathbf{q}_\sigma|$ where again σ is the two-fragment channel and s the three-nucleon or the $2+2$–subsystem bound states in this channel.

Alternatively, the amplitude $\mathcal{M}$ can be obtained using an integral equation reduced via the use of Møller operators. We demonstate this in the simple two-body case where the transition amplitude is defined by

$$M(\mathbf{p}) = {}^-\langle\mathbf{p}|H'|\Psi_D\rangle = \langle\vec{p}|\Omega^{(-)\dagger}H'|\Psi_D\rangle\,. \tag{28}$$

Using the relation

$$\Omega^{(-)\dagger} = 1+VG^\dagger_0\Omega^{(-)\dagger} \tag{29}$$

we obtain

$$\begin{aligned} M(\mathbf{p}) \;&=\; \langle\mathbf{p}|H'|\Psi_D\rangle+\langle\mathbf{p}|VG^\dagger_0\Omega^{(-)\dagger}H_{E1}|\Psi_D\rangle \\ &=\; \langle\mathbf{p}|H'|\Psi_D\rangle+\int\langle\vec{p}|VG^\dagger_0|\mathbf{p}\rangle\,{\rm d}\mathbf{p}\,\langle\mathbf{p}|\Omega^{(-)\dagger}H'|\Psi_D\rangle \end{aligned} \tag{30}$$

which is of the form

$$M = B + VG_0M \tag{31}$$

In the multichannel case one defines Møller-type operators by [29]

$$\Omega^{\sigma(-)\dagger}_{\beta\alpha}(z) = \delta_{\beta\alpha} + \sum_{\tau}\sum_{\gamma}(1-\delta_{\sigma\tau})U^{\tau}_{\beta\gamma}(z)G_0(z)T_{\gamma}(z)G_0(z)\Omega^{\tau(-)\dagger}_{\gamma\alpha}(z) \tag{32}$$

or in matrix form in the $\alpha\beta$-space

$$\mathbf{\Omega}^{\sigma(-)\dagger}(z) = \mathbf{1} + \sum_{\tau}\mathbf{K}^{\sigma\tau}\mathbf{\Omega}^{\tau(-)\dagger}(z) \tag{33}$$

where the kernel $K^{\sigma\tau}_{\beta\gamma}$ is the same as in the four-body transition operator (11). The scattering states are then written as

$${}^{(-)}\langle \mathbf{q}_\sigma;\Psi^{\sigma s}_3| = \langle \mathbf{q}_\sigma;\Psi^{\sigma s}_3|\mathbf{\Omega}^{\sigma(-)\dagger}(z) \equiv \langle \mathbf{q}_\sigma| < \Psi^{\sigma s}_3|\left[\mathbf{1} + \sum_{\tau}\mathbf{K}^{\sigma\tau}\mathbf{\Omega}^{\tau(-)\dagger}(z)\right] \tag{34}$$

which leads, after some straightforward algebra, to the integral equation

$$\mathcal{M}^{\sigma s}_{\rm elec}(\mathbf{q}_\sigma;z) = \mathcal{B}^{\sigma s}_{\rm elec}(\mathbf{q}_\sigma;z) + \sum_{\rho r}\int \mathrm{d}^3\mathbf{q}'_\rho\, \mathbb{V}^{\sigma s,\rho r}(\mathbf{q}_\sigma,\mathbf{q}'_\rho;z)\mathbb{G}^{\rho r}_0(z-\frac{q'^2}{2M_\rho})\,\mathcal{M}^{\rho r}_{\rm elec}(\mathbf{q}'_\rho;z) \tag{35}$$

where we have introduced the notation

$$\mathcal{M}^{\sigma s}_{\rm elec}(\mathbf{q}_\sigma;z) = \sum_{\beta\subset\sigma,n}\langle \mathbf{q}_\sigma|\,\langle G^{\sigma s}_{\beta n}|\,t_{\beta n}\,\langle g_{\beta n}|G_0\,\Omega^{\sigma(-)\dagger}_{\beta}H'|\Psi_4\rangle \tag{36}$$

for the full electromagnetic transition amplitude and

$$\mathcal{B}^{\sigma s}_{\rm elec}(\mathbf{q}_\sigma;z) = \sum_{\beta\subset\sigma,n}\langle \mathbf{q}_\sigma|\,\langle G^{\sigma s}_{\beta n}|\,t_{\beta n}\,\langle g_{\beta n}|G_0H'|\Psi_4\rangle \tag{37}$$

for the corresponding Born term.

C. Photo-processes

Here, the electromagnetic Hamiltonian is much simpler,

$$H' = -\frac{\hbar}{mc}\sum_{j,\nu}e_j\,\mathrm{e}^{i\mathbf{k}_\gamma\cdot\mathbf{x}_j}\hat{\epsilon}_{\gamma,\nu}\cdot\mathbf{k}_j\,, \tag{38}$$

the expansion of which provide us the various electric and magnetic multiples. In the above, e_j is the charge of the particle j, $\hat{\epsilon}_{\gamma,\nu}$ is the polarization direction of the incident photon, x_j the position coordinate, k_γ the incident photon energy, and $\nu = 1,2$ corresponds to the two polarizations directions of the photon.

Take, for example, the expansion

$$\mathrm{e}^{i\mathbf{k}_\gamma\cdot\mathbf{x_j}}\hat{\epsilon}_\gamma\cdot\mathbf{k} \sim \underbrace{\hat{\epsilon}_\gamma\cdot\mathbf{k}}_{E1} + i\mathbf{k}_\gamma\cdot\mathbf{x_j}\,\hat{\epsilon}_\gamma\cdot\mathbf{k} \tag{39}$$

The second term can be written as

$$
\begin{aligned}
i\mathbf{k}_\gamma \cdot \mathbf{x_j}\, \hat{\epsilon}_\gamma \cdot \mathbf{k} &= \frac{i}{2}(\mathbf{k}_\gamma \cdot \mathbf{x_j}\, \hat{\epsilon}_\gamma \cdot \mathbf{k} - \hat{\epsilon}_\gamma \cdot \mathbf{x_j} \mathbf{k}_\gamma \cdot \mathbf{k}) + \frac{i}{2}(\mathbf{k}_\gamma \cdot \mathbf{x_j} \hat{\epsilon}_\gamma \cdot \mathbf{k} + \hat{\epsilon}_\gamma \cdot \mathbf{x_j} \mathbf{k}_\gamma \cdot \mathbf{k}) \\
&= \underbrace{\frac{i}{2}(\mathbf{k}_\gamma \times \hat{\epsilon}_\gamma)(\mathbf{x_j} \times \mathbf{k})}_{M1} + \underbrace{\frac{i}{2}(\mathbf{k}_\gamma \cdot \mathbf{x_j} \hat{\epsilon}_\gamma \cdot \mathbf{k} + \hat{\epsilon}_\gamma \cdot \mathbf{x_j} + \hat{\epsilon}_\gamma \cdot \mathbf{x_j} \mathbf{k}_\gamma \cdot \mathbf{k})}_{\mathrm{E2}}
\end{aligned} \tag{40}
$$

To proceed, one has to transform the coordinates into Jacobi ones. This can be easily done by defining the operator $\lambda_j = e/2\,(1 + \tau_j^3)$. Since

$$
\tau^3|p\rangle = |p\rangle \qquad \tau^3|n\rangle = -|n\rangle \tag{41}
$$

we have

$$
\lambda_j|p\rangle = 1|p\rangle_j\,, \qquad \lambda_j|n\rangle = 0|n\rangle_j\,, \tag{42}
$$

where $|p\rangle \equiv |+\tfrac{1}{2}\rangle$ and $|n\rangle \equiv |-\tfrac{1}{2}\rangle$.

Using the above relations in the electromagnetic Hamiltonian results in the following operators in the CM system for the 3+1 coordinates

$$
\hat{I}_p \equiv \lambda_1 - \lambda_2\,, \qquad \hat{I}_q \equiv \frac{1}{2}(\lambda_1 + \lambda_2 + 2\lambda_3)\,, \qquad \hat{I}_u \equiv \frac{1}{3}(\lambda_1 + \lambda_2 + \lambda_3 - 3\lambda_4) \tag{43}
$$

where p, q, and u represent the $[ij]$, $[(ij),k]$, and the $[[(ij),k],l]$ Jacobi coordinates. In this notation the Hamiltonian for the E1 transition for the 3+1 coordinates read

$$
H_{E1} = -\frac{\hbar}{mc}\left[\hat{I}_p\, \hat{\epsilon}_\gamma \cdot \mathbf{p} + \hat{I}_q\, \hat{\epsilon}_\gamma \cdot \mathbf{q} + \hat{I}_u\, \hat{\epsilon}_\gamma \cdot \mathbf{u}\right] \tag{44}
$$

Similar relations can be easily derived for the 2+2 coordinates and for other photo-transitions.

The Siegert theorem can be easily applied using the relation $\mathbf{k}_i = \imath\, m\,[H, \mathbf{x}_i]$. Remembering that this relation is squeezed between the three and four bound state wave functions we obtain

$$
\langle \Psi_3 | H_{\mathrm{E1}} | \Psi_4 \rangle \sim (E_3 - E_4)\mathbf{x}_i = E_\gamma \mathbf{x}_i \tag{45}
$$

The differential disintegration cross section, for unpolarized incident photon beam and for a specific fragmentation $\sigma = (ijk, l)$ is given by

$$
\frac{\mathrm{d}\sigma^\sigma}{\mathrm{d}\Omega} = \frac{\mu q}{2\pi\hbar^2} \sum_{\nu=1}^{2} |M^{\nu,\sigma}(\mathbf{q})|^2\,, \tag{46}
$$

where μ is the reduced mass of the outgoing fragments. The amplitude $|M^{\nu,\sigma}|$ is defined as usual via

$$
|M^{\nu,\sigma}(\mathbf{q})| = 2\,{}^{(-)}\langle \mathbf{q}_\sigma; \Psi_3 | H_{\mathrm{EM}} | \Psi_4 \rangle \tag{47}
$$

Using the same procedure as in the electro-disintegration we then obtain

$$
\mathcal{M}^{\sigma s}_{\mathrm{pho}}(\mathbf{q}_\sigma; z) = \mathcal{B}^{\sigma s}_{\mathrm{pho}}(\mathbf{q}_\sigma; z) + \sum_{\rho r} \int \mathrm{d}^3\mathbf{q}'_\rho\, \mathbb{V}^{\sigma s, \rho r}(\mathbf{q}_\sigma, \mathbf{q}'_\rho; z) \mathbb{G}_0^{\rho r}(z - \frac{q'^2}{2M_\rho})\, \mathcal{M}^{\rho r}_{\mathrm{pho}}(\mathbf{q}'_\rho; z) \tag{48}
$$

The above equations include all subsystem information and coupling of the corresponding (2+2)- and (3+1)-channels in the most transparent and unambiguous way.

D. Unification of the Reaction Processes

From the above theoretical description, it is obvious that the scattering, electro-disintegration, and photo-disintegration processes for the two-, three-, and four-body systems can be cast into effective Lippmann-Schwinger equations schematically written as

$$\mathcal{T} = \mathcal{V} + \int \mathcal{V}\mathcal{G}_0\mathcal{T}\,, \qquad \mathcal{M}_{\rm elec} = \mathcal{B}_{\rm elec} + \int \mathcal{V}\mathcal{G}_0\mathcal{M}_{\rm elec}\,, \qquad \mathcal{M}_{\rm pho} = \mathcal{B}_{\rm pho} + \int \mathcal{V}\mathcal{G}_0\mathcal{M}_{\rm pho} \quad (49)$$

where $\mathcal{M}$ is the relevant transition amplitude and $\mathcal{B}$ the corresponding Born term. The FSI effects are, therefore, included via the kernel which is exactly the same in all three types of reactions, namely $\mathcal{V}\mathcal{G}_0$. The only differences among these processes are those introduced by selection rules, mainly in the photo-disintegration reactions.

III. RESULTS AND DISCUSSION

A. Scattering

The low energy scattering (below the three-body break-up) can be tackled using the Faddeev, Hyperspherical Harmonics, and AGS formalisms (see, for example, Refs. [30–32]). Beyond the break-up threshold, however, calculations have not yet been satisfactorily performed. Efforts to describe four-body reaction cross sections with optical potentials were also unsatisfactory. One such effort was that of Podmore and Sherif [33] who introduced an ℓ-dependence in the interaction; another was that by Neudachin *et at.* [34] based on symmetry arguments. However, the constructed potentials have dubious off-shell characteristics and the question of constructing them reliably is far from being properly addressed.

To get some information on the characteristics of the effective 3+1 interaction we employed the AGS formalism in the K-matrix approximation [3] to obtain the phase shifts for the various channels. In Fig. 1 (left) we demonstrate the strong ℓ-dependence of the real part of these phase shifts for the spin $S = 0$ and isospin $I = 0$ 3+1 channel at $E_{\rm Lab}$=50 MeV incident nucleon energy. It is seen that for even partial waves the δ_ℓ are positive while for odd partial waves negative, implying that the underlying interaction is attractive and repulsive respectively. Thus any effort to describe cross-sections with a single potential could be catastrophic if this feature is not taken into account. Using the phase shifts at $E_{\rm Lab} = 50\,$MeV and 88 MeV incident nucleon energies and the inverse scattering procedure of Lipperheide and Fiedeldey [4] at fixed energy, we constructed potentials shown in Fig. 1 (right). The exhibited E- and ℓ-dependence are manifested in all channels and in different way. Thus any attempt to use effective interactions in order to include FSI effects in the various reactions should include these characteristics, by starting, for example, from the above potentials and improve them by fitting experimental data.

B. Electro-processes

The kinematics of the two-body disintegration reaction ^{4}He(e, e′p)^{3}H considered is shown in Fig. 2 (left). Since the complicated cut structure prevents solving Eq. (35) at energies beyond the break-up thresholds, we work in the PWIA, *i.e.* we compute (37) in order to obtain the transition matrix elements $\mathcal{M}_Q$ and $\mathbf{J}$. For this we insert $\mathcal{H}_Q$ and $\mathbf{H}_{\rm elec}$ into Eq. (37), anti-symmetrize, and evaluate the resulting expressions at on-shell energies. Furthermore, in order to bring the problem into manageable proportions we choose the nucleon-nucleon interaction

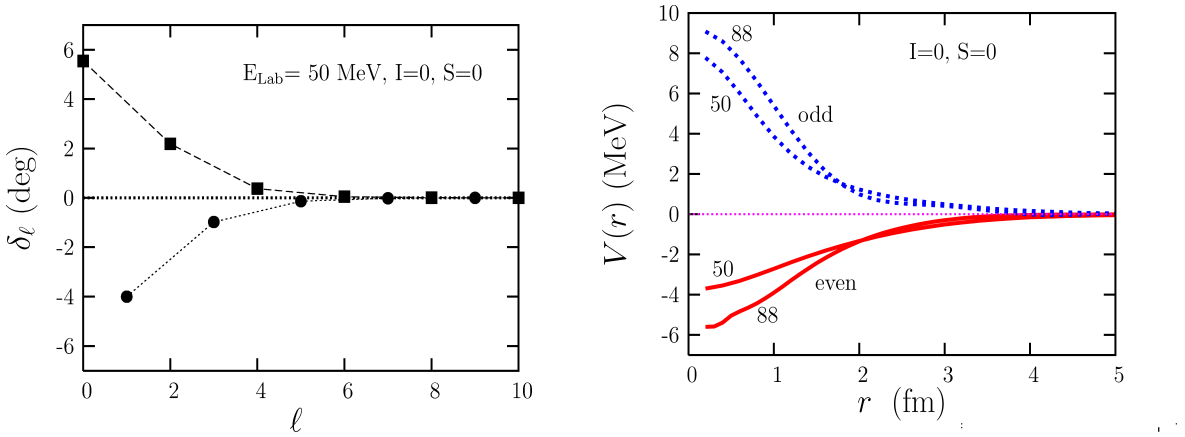

FIG. 1: Phase shifts for the $S = 0$ and $I = 0$ 3+1 channel at $E_{\rm Lab}$=50 MeV incident nucleon energy (left) and the 3+1 interactions generated by inversion of the even and odd partial waves for $E_{\rm Lab}$=50 MeV and 88 MeV (right).

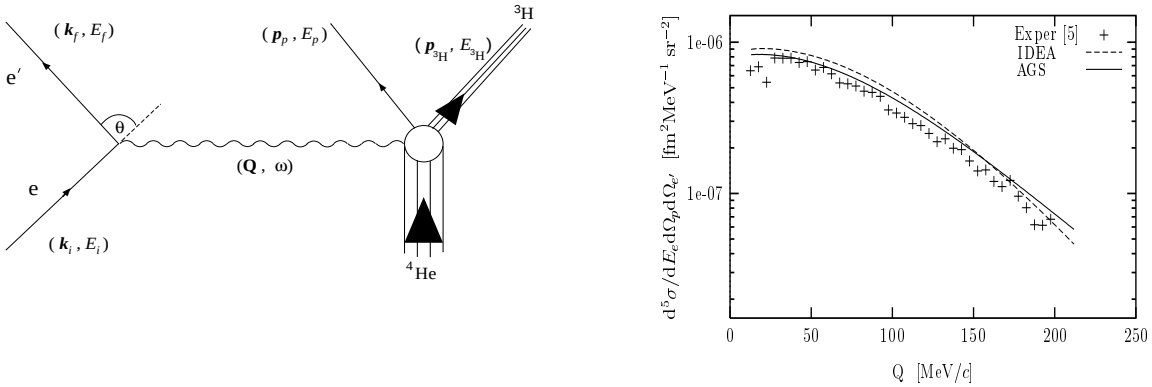

FIG. 2: Kinematics for the process ^{4}He(e,e′p)^{3}H , left, and the five-fold differential cross section as a function of the missing momentum Q for the kinematics of Ref. [6], right.

to be the Malfliet-Tjon (MT I+III) potential [35] which is proved, all along, to give very good scattering results at energies below the three-body break-up threshold.

In Fig. 2, right, we present our AGS results and compare them with the experimental data of van den Brand *et al.* [6]. It is seen that the PWIA results obtained within the AGS formalism at these low missing momenta reproduce the data well except in the lower region where the FSI effects are expected to be important. Similar results were obtained also using the integro-differential equation approach (IDEA) formalism [36]. The results for higher missing momenta **Q** are shown in Fig. 3. The kinematics and the experimental data are those of [8, 9] for the $\omega = 215$ MeV case (left) and for the Saclay kinematics (right) [7] . For comparison we also included the PWIA results of [12], obtained with wave functions constructed via the IDEA of Ref. [36] and of Laget (see Refs. [8, 9, 11]). The latter were obtained using the Urbana potential and wave functions constructed with the variational Monte Carlo (MC) method. The agreement of our AGS calculations with the experimental data, is remarkable, and in disagreement with the results obtained by other methods based on variational wave functions. This holds true also in comparison with other results reported in [9].

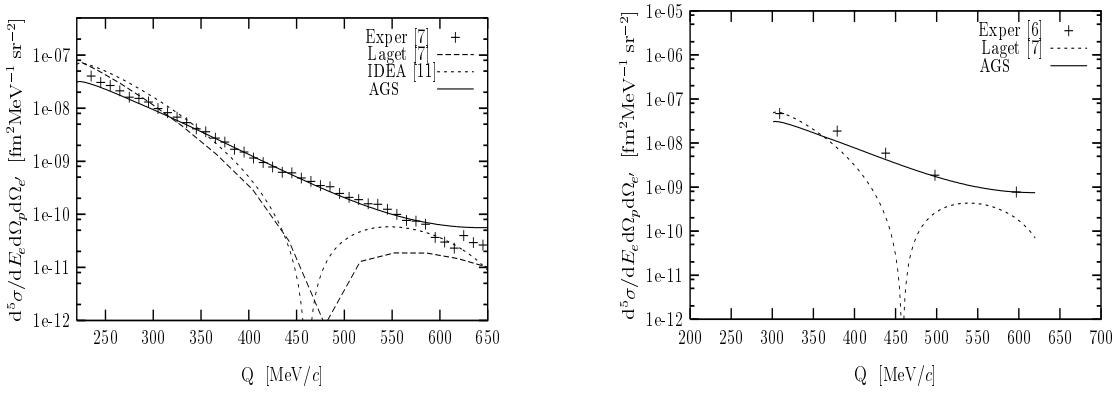

FIG. 3: Five-fold ^{4}He(e,e′p)^{3}H differential cross section as a function of the missing momentum Q for the NIKHEF kinematics [8, 9] (left) and for the Saclay kinematics [7] (right).

C. Photo-processes

For decades experimental measurements and theoretical model calculations for the total cross section σ_T , were wildly varied especially around 30 MeV incident photon energies where, for either or both the n and p, σ_T was ranging from 1 mb/sr to 3 mb/sr. In Fig. 4 we present the results obtained by solving the full photo-disintegration AGS-type integral equations for energies below the three-body break-up threshold. We see that there is no sign of existence of a pronounce giant resonance which is in disagreement with other theoretical results in the field (the latest being those of Ref. [37]) but in good agreement with the experimental data of [38–40]. In the same figure, Fig. 4 (right), we present results for incident photon energies in the

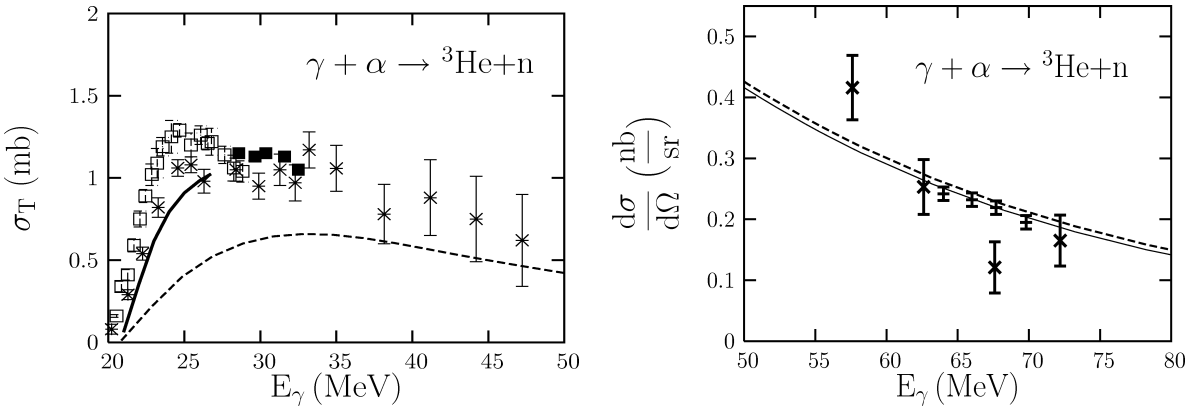

FIG. 4: Total cross section for ^{4}He$(\gamma, n)^3$He at low energies (left): Full solution (E1+E2) with exchange currents (—) and without (- - -)(Born term only); the experimental data are from [38], □, [39], ■ , and [40], ∗. For higher energies (right): (—) Born term (E1+E2), (- - -) (E1+E2+M1); the experimental data are from [40], □, and [41], ○.

region 50-80 MeV and compare the with the results of [40] and [41]. These results were obtained using only the Born amplitude and the agreement with the data indicates that the FSI are small in this region and beyond.

From the above results as well as from those obtained for the (γ,p) reaction show that there is no significant charge symmetry breaking, at least to the extend that it generates a factor of 2 or more in the ratio σ_p/σ_n. A small difference between σ_p and σ_n is of course expected due to Coulomb effects and in the details of the spin-isospin projections. Indeed in the latter case

we found that the E2 contribution to the photo-proton differential cross section is 25 larger as compared to the contribution to the photo-neutron. While this has relatively small contribution to the total cross section the effects of E2 on differential cross sections is important.

In Fig. 5 (left) we present the differential cross section for (γ, n) at 51 MeV in comparison with the results of Sims *et al.* [42]. In the same figure, right, we demonstrate the importance of E2 contribution to the (γ, p) and the (γ, n) reactions by plotting the differential cross sections at $\mathrm{E}_\gamma = 64$ MeV incident photon energy. The effects for E2 stemming from spin-isospin projections for the (γ, p) reaction distinguish the p and n data quite well.

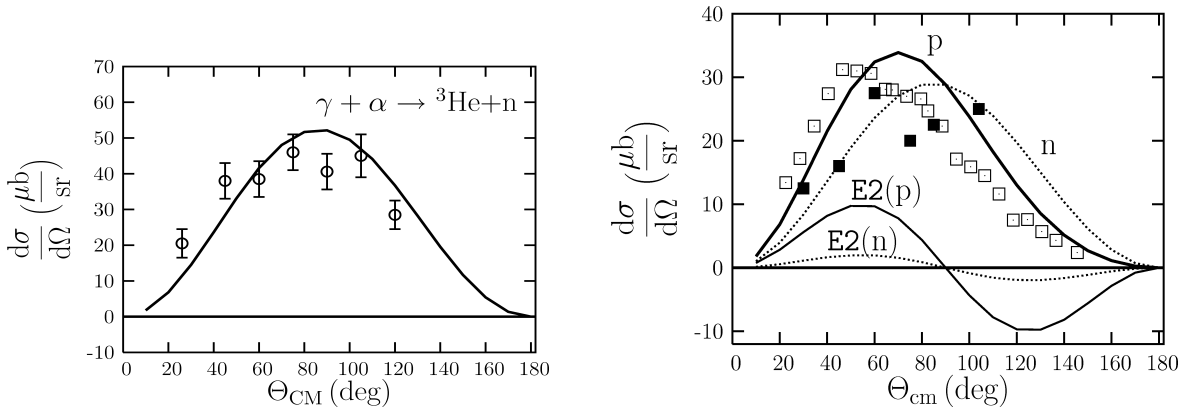

FIG. 5: Differential cross section: □ (γ,p) [41], ■ (γ,n) [42]. The upper curves are for p and n as indicated while the lower correspond to the E2 contribution only.

IV. CONCLUSIONS

Our conclusions can be summarized as follows: i) The construction of effective interactions among light clusters should be carried out with care by taking into account the ℓ-, E-, parity-, and the overall channel dependence. While for the E-dependence one requires all important phase shifts at even and odd partial waves ℓ and for a specific spin-isospin channel, the construction of E-independent but ℓ-dependent potential requires the knowledge of phase shifts for the corresponding ℓ at all energies. Any other construction could results to a non-unique potential. ii) The use of our potentials obtained using exact methods, can serve as starting point for further improvements. iii) The PWIA is quite good in describing the scattering, electro-, and photo-disintegration data and for energies beyond the 'giant' dipole resonance region. This comes as no surprise to us as the FSI is included in the same way in all three processes via integral equations derived using the exact AGS formalism and Møller-type operators. iv) The main reason for the agreement of our results with the data appears to be the use of wave functions obtained from the AGS integral equations with their complete coupling scheme and duly antisymmetrized. iv) Another reason is the way of calculating the nuclear matrix elements. Consider, for example, the electro-disintegration Born term. This is a sum of purely 3+1 components and rearrangement 3+1→2+2→3+1 terms and therefore it is highly unlikely that the two terms have a simultaneous zero at a specific missing momentum which generates the dip found by other methods.

The overall conclusion is that the study of reaction processes for four-body systems using exact methods is, at present, a very difficult task. The alternative way of using effective interactions, although possible, requires extreme care in their construction. Otherwise all sort of

ambiguities could creep in which, in turn, could results in dubious conclusions concerning the reaction mechanisms involved.

---

[1] P. Grassberger and W. Sandhas: Nucl. Phys. B **2**, 181 (1967); E.O. Alt, P. Grassberger, and W. Sandhas, Phys. Rev. C **1**, 85(1970).
[2] E.O. Alt, P. Grassberger, and W. Sandhas, Joint Institute of Nuclear Research (Dubna) Report No. E4-6688, 1972; W. Sandhas, Acta Phys. Austriaca, Suppl. **13**, 679 (1974).
[3] S.A. Sofianos, H. Fiedeldey, and W. Sandhas, Phys. Rev. C **32**, 400 (1985).
[4] R. Lipperheide and H. Fiedeldey, Z. Phys. A **286**, 45 (1978); Z. Phys. A **301**, 81 (1981).
[5] J.F.J. van den Brand *et al.*, Phys. Rev. Lett. **60**, 2006 (1988).
[6] J.F.J. van den Brand *et al.*, Phys. Rev. Lett. **66**, 409 (1991); Nucl. Phys. A **534**, 637 (1991).
[7] J.M. Le Goff *et al.*, Phys. Rev. C **50**, 2278 (1994).
[8] J.J. van Leeuwe, Ph.D. thesis, University of Utrecht, ISBN 90-393-1204-4, 1996.
[9] J.J. van Leeuwe *et al.*, Phys. Rev. Lett. **80**, 2543 (1998).
[10] R. Schiavilla, Phys. Rev. Lett. **65**, 835 (1990).
[11] J.M. Laget, Nucl. Phys. A **579**, 333 (1994).
[12] L.L. Howell, Ph.D. thesis, University of South Africa, 1997.
[13] W. Sandhas, W. Schadow, G. Ellerkmann, L.L. Howell, and S.A. Sofianos, Nucl. Phys. A **631**, 210c (1998).
[14] S.I. Nagorny, Yu. A. Kasatkin, E.V. Inopin, and I.K. Kirichenko, Sov. J. Nucl. Phys. **49**, 465 (1989).
[15] A.A. Zayatz, V.A. Zolenko, Yu. A. Kasatkin, and S.I. Nagorny, Sov. J. Nucl. Phys. **55**, 178 (1992).
[16] D. Halderson and R.J. Philpott, Nucl. Phys. A **359**, 365 (1981), Phys. Rev. C **28**, 1000 (1983).therein.
[17] B. Wachter, T. Mertelmeier, and H.M. Hofmann, Phys. Rev. C **38**, 1139 (1988).
[18] G. Ellerkmann, W. Sandhas, S.A. Sofianos, and H. Fiedeldey, Phys. Rev. C **53**, 2638 (1996).
[19] G. Ellerkmann, Ph.D. thesis, University of Bonn, 1995 (unpublished).
[20] S.A. Sofianos, N.J. Mc Gurk, and H. Fiedeldey, Nucl. Phys. A **318**, 295 (1979)
[21] S.A. Sofianos, H. Fiedeldey, and H. Haberzettl, Phys. Rev. C **22**, 1772 (1980).
[22] S.A. Sofianos, H. Fiedeldey, H. Haberzettl, and W. Sandhas, Phys. Rev. C **26**, 228 (1982).
[23] K.M. McVoy and L. Van Hove, Phys. Rev. **125**, 1034 (1962).
[24] D.R. Lehman, Phys. Rev. C **3**, 1827 (1971).
[25] C.R. Heimbach, D.R. Lehman, and J.S. O'Connell, Phys. Rev. C **16**, 2135 (1977).
[26] C.D. Epp and T.A. Griffy, Phys. Rev. C **1**, 1633 (1970).
[27] W. Böttger, A. Casel, and W. Sandhas, Phys. Lett. B **92**, 11 (1980).
[28] T. Janssens *et al.*, Phys. Rev. **142**, 922 (1966).
[29] W. Sandhas, Invited Lect. on Few-Body Problems in Nucl. Physics, 13-16 March 1978, ICTP, Trieste.
[30] F. Ciesielski, J. Carbonel, and C.Gignoux, Nucl. Phys. A **631**, 653c (1998).
[31] M. Viviani, S. Rosati, and A. Kievsky, Phys. Rev. Lett. **81**, 1580 (1998).
[32] R. Lazauskas, J. Carbonell, A.C. Fonseca, M. Viviani, A. Kievsky, and S. Rosati, Phys. Rev. C **71**, 034004 (2005).
[33] P.S. Podmore and H.S. Sherif, in *Few-Body Problems in Particle Physics*, ed. by R.J. Slobodrian *et al.* (Laval Univ. Press., Quebec, Canada, 1975) p517; H.S. Sherif, Phys. Rev C **19**, 1649 (1979).
[34] V. G. Neudachin et at., Yad. Fiz. **52**, 402 (1990) [Sov. J. Nucl. Phys. **52**, 258 (1990)]; S.B. Dubovichenko, A.V. Dzhazairov-Kakhramanov, arXiv:nucl-th/9803041 v1 20 Mar 1998 and references therein.
[35] R.A. Malfliet and J.A. Tjon, Nucl. Phys. A **127**, 161 (1969); Ann. Phys. (N.Y.) **61**, 425 (1970).
[36] M. Fabre de la Ripelle, H. Fiedeldey, and S.A. Sofianos, Phys. Rev. C **38**, 449 (1988).
[37] S. Bacca, arXinv:nucl-th/0612016 v1 4 Dec 2006.
[38] L. Ward, D.R. Tilley, D.M. Skopik, N.R. Roberson, and H.R. Weller, Phys. Rev. C **24**, 317 (1981).
[39] J. Asai, G. Feldman, R.E.J. Florizone, E.L. Hallin, D.M. Skopik, J.M. Vogt, R.C. Haight, and S.M. Sterbenz, Few-Body Systems, Suppl. **7**, 136 (1994).
[40] A.N. Gorbunov,*Proceeding of the P. N. Lebedev Physics Institute*, **71**, 1 (1976).
[41] R.T. Jones, D.A. Jenkins, P.T. Debevec, P.D. Harty, and J.E. Knott, Phys. Rev. C **43**, 2052 (1991).
[42] D.A. Sims et. al, Phys. Let. A **435**, 257 (1998).

Electromagnetic Excitations in Baryons

I.P. Matamba[1],* R.M. Adam[2], and S.A. Sofianos[3]

[1] *Physics Department, University of Venda, Private Bag X5050, Thohoyandou 0950, South Africa*

[2] *Nuclear Energy Corporation of South Africa, P.O. Box 582, Pretoria 0001, South Africa and*

[3] *Department of Physics, University of South Africa, P.O. Box 392, Pretoria 0003, South Africa*

Electromagnetic excitations in baryons are investigated within the constituent quark model (CQM). The required configuration space three-quark wave functions are constructed using the Integrodifferential Equation Approach (IDEA) and the hypercentral approximation (HCA) while the properly antisymmetrized total wave functions by using, in addition, the underlying SU(6) spin-flavor symmetries. A relativistic generalization of the HCA in momentum space is also presented and applied. The results obtained for the photoexcitation cross-sections for the E1, E2, and M1 transitions are compared with the experimental data as well as with the results of other methods.

I. INTRODUCTION

The static properties of baryons within the CQM can be studied using various approaches. Among them, the Hyperspherical Harmonics (HH) method is perhaps the most suitable [1–3]. Within this formalism, the baryon spectrum, for instance, can be described quite well and three-body wave functions can be easily constructed using the spatial and the underlying SU(6) spin-flavor symmetries [4] allowing us to investigate electromagnetic excitations, form factors, etc.

An interesting version of the HH formalism is the two-dimensional IDEA [5, 6] method in which two-body correlations are taken into account exactly. In the case where the correlations are weak, one may use instead of the IDEA the much simpler HCA [7–11] to study baryon properties in a simple and transparent way. Both the IDEA and HCA reproduce the spectrum of baryons quite well, and provide us with reliable three-quark wave functions [6].

HCA has the big advantage that it depends only on the hyperradius which is a collective coordinate and its success is due to the fact that the two-quark correlations are indeed weak. This approximation has been extensively used by Giannini and collaborators in a variety of investigations concerning baryons [12, 13]. The most appealing feature of the HCA, however, lies in the fact that one may employ it not only in non-relativistic calculations but also in relativistic ones. This becomes possible by transforming it in momentum space where one can introduce relativistic generalizations to obtain an one-dimensional integral equation. As in the genuine two-body case [14, 15], the reduce equation is well-defined even when confining potentials are introduced.

We recall here that, disregarding intrinsic spin, the Schrödinger equation can be altered in three ways to take relativistic effects into account: (i) The relativistic kinetic energy operator must be used. (ii) The interaction must be replaced with a Lorentz-invariant form, which

*Electronic address: Imatamba@univen.ac.za

introduces retardation effects. (iii) In an integral equation approach, a Lorentz-invariant measure is required. These relativistic corrections are easily taken into account within the HCA and using a reduction scheme in which all particles are on mass shell, as in [15] and [16].
In the present work we are concerned with the electromagnetic excitations of baryons which are studied using various quark-antiquark potentials and by employing the IDEA and HCA methods to extract the relevant wave functions.
In Sec. II we describe our formalism. In Sec. III we give details on how the M1, E1, and E2 transition amplitudes are calculated while in Sec. III we discuss how relativistic effects are taken into account. Finally, in Sec. IV we present our results and discussions. Some details on the Jacobi coordinates are given in Appendix A.

II. FORMALISM

The photoexcitation process is described by the transition amplitude

$$M_{fi} = \langle \Psi_f | H' | \Psi_i \rangle, \tag{1}$$

where Ψ_i is the initial baryon ground state wave function, Ψ_f is the final excited state wave function, and H' is the perturbative Electromagnetic Hamiltonian which consists of the electric and the magnetic multipoles which in our case are taken to be the E1, E2, and M1, i.e

$$H' = H_{\rm E1} + H_{\rm E2} + H_{\rm M}\,.$$

In what follows we shall discuss this process in some detail starting from the description of the relevant wave functions.

A. The Wave Functions

The total antisymmetric wave function for a three-quark system can be expressed as a product of the symmetric ($\mathcal{S}$) and the antisymmetric ($\mathcal{A}$) components:

$$\Psi^{\mathcal{S}}_{\rm total} = \underbrace{\psi_{\rm space} \times \Phi_{\rm flavor} \times \chi_{\rm spin}}_{\mathcal{S}} \times \underbrace{C_{\rm color}}_{\mathcal{A}}\,. \tag{2}$$

The color wave function is totally antisymmetric. The structure of the symmetric component depends on the transition considered and can be constructed using the various symmetries involved.
The space wave functions for the three-quark system can be obtained using the IDEA [5]. In the IDEA method the fully symmetric configuration space wave function for the $L = 0$ and $L = 2$ states are [6]

$$\Psi^S_L(\vec{\rho},\vec{\eta}) = \frac{1}{r^{5/2}}\left[P^S_L(z_{12},r) + P^S_L(z_{23},r) + P^S_L(z_{31},r)\right]\,, \tag{3}$$

where $\vec{\rho}$ and $\vec{\eta}$ are the Jacobi coordinates (see Appendix A), r is the hyperradius, and $z_\alpha = 2\rho^2_\alpha/r^2 - 1$, $\alpha = 12, 23, 31$. The explicit form of the mixed symmetric and mixed antisymmetric states, $\Psi^{M^S}_1(\vec{\rho},\vec{\eta})$ and $\Psi^{M^A}_1(\vec{\rho},\vec{\eta})$, for $L = 1$ are given in [4].
In terms of the Young tableau [17], the fully symmetric three-quark spin states are constructed using

$$\boxed{1}\boxed{2}\boxed{3}\,, \qquad \sigma = 3/2\,, \qquad \mu = -3/2,\, -1/2,\, 1/2,\, 3/2$$

with states $|\chi^{\sigma}_{S_{12}s_3}\rangle = |(s_1s_2)S_{12}, s_3; \sigma\rangle$ so that, for example, when $\sigma = 3/2$ $S_{12} = 1$ and $\mu = 1/2$ we have

$$\chi^{S}_{\frac{3}{2}\,\frac{1}{2}} = \frac{1}{\sqrt{3}}(|\alpha_1\alpha_2\beta_3\rangle + |\alpha_1\beta_2\alpha_3\rangle + |\beta_1\alpha_2\alpha_3\rangle)\,, \tag{4}$$

where $\alpha(\beta)$ stand for spin up(down). For the mixed symmetry spin states when the first tableau is symmetric with respect to the interchange of particles 1 and 2 we have

$$\begin{array}{|c|c|}\hline 1 & 2 \\ \hline 3 \\ \cline{1-1}\end{array}\,, \qquad \sigma = 1/2\,, \qquad \mu = -1/2,\, 1/2$$

such that if $\sigma = 1/2$ and $\mu = 1/2$ then

$$\chi^{\mathcal{M}^S}_{\frac{1}{2}\,\frac{1}{2}} = \frac{1}{\sqrt{6}}(2|\alpha_1\alpha_2\beta_3\rangle - |\alpha_1\beta_2\alpha_3\rangle - |\beta_1\alpha_2\alpha_3\rangle)\,. \tag{5}$$

When the second tableau is antisymmetric with respect to the interchange of particles 1 and 2 we have, for $\sigma = 1/2$ and $\mu = 1/2$ for example,

$$\chi^{\mathcal{M}^A}_{\frac{1}{2}\,\frac{1}{2}} = \frac{1}{\sqrt{2}}(|\alpha_1\beta_2\alpha_3\rangle - |\beta_1\alpha_2\alpha_3\rangle)\,. \tag{6}$$

The SU(3) flavor states are constructed from the quark states, as in the spin case, the corresponding dimensions and symmetry types being [18]

$$\begin{array}{|c|}\hline\ \ \\ \hline\end{array} \otimes \begin{array}{|c|}\hline\ \ \\ \hline\end{array} \otimes \begin{array}{|c|}\hline\ \ \\ \hline\end{array} = \begin{array}{|c|}\hline\ \ \\ \hline\ \ \\ \hline\ \ \\ \hline\end{array} \oplus \begin{array}{|c|c|}\hline\ \ & \ \ \\ \hline\ \ \\ \cline{1-1}\end{array} \oplus \begin{array}{|c|c|}\hline\ \ & \ \ \\ \hline\ \ \\ \cline{1-1}\end{array} \oplus \begin{array}{|c|c|c|}\hline\ \ & \ \ & \ \ \\ \hline\end{array}$$

$$\begin{array}{lccccccc} SU(3): & 3\otimes 3\otimes 3 = & 1 & \oplus 8 & \oplus & 8 & \oplus & 10 \\ & & \mathcal{A} & \mathcal{M}^S & & \mathcal{M}^A & & \mathcal{S} \end{array} \tag{7}$$

In the case of non-strange baryons, the resulting states coincide with the standard isospin states. For the decuplet states there are 10 fully symmetric states where, e.g., for one of the deltas we have

$$|\Phi^{\mathcal{S}}_{\Delta^+}\rangle \equiv |\Phi^{\mathcal{S}}_{\frac{3}{2},\,\frac{1}{2}}\rangle = \frac{1}{\sqrt{3}}\left(|uud\rangle + |udu\rangle + |duu\rangle\right)\,. \tag{8}$$

There are two types of linearly independent mixed symmetry octet states, each type having a total of 8 states. The first type is symmetric under the interchange of the flavor indices of the first two quarks, while the second is antisymmetric under this interchange. For instance, in the proton case we have

(i) Symmetric Octet State:

$$\left|\Phi^{\mathcal{M}^S}_P\right\rangle \equiv \left|\Phi^{\mathcal{M}^S}_{\frac{1}{2}\,\frac{1}{2}}\right\rangle = \frac{1}{\sqrt{6}}\left(2|uud\rangle - |duu\rangle - |udu\rangle\right)\,. \tag{9}$$

(ii) Antisymmetric Octet State:

$$\left|\Phi^{\mathcal{M}^A}_P\right\rangle \equiv \left|\Phi^{\mathcal{M}^A}_{\frac{1}{2}\,\frac{1}{2}}\right\rangle = \frac{1}{\sqrt{2}}\left(|udu\rangle - |duu\rangle\right)\,. \tag{10}$$

For the spin-flavor functions, combining the three fundamental representations of SU(6) we get the following dimensions and symmetry types:

$$SU(6):\ 6\otimes 6\otimes 6 = \underset{\mathcal{A}}{20}\oplus \underset{\mathcal{M}^S}{70}\oplus \underset{\mathcal{M}^A}{70}\oplus \underset{\mathcal{S}}{56} \tag{11}$$

The completely symmetric, the symmetric with respect to (12), and the antisymmetric with respect to (12) SU(6) octet states formed from the SU(3) states Φ and SU(2) states χ are

$$\mid \xi^S \rangle \ = \ \frac{1}{\sqrt{2}}\left[|\Phi^{M^S}\rangle|\chi^{M^S}\rangle + |\Phi^{M^A}\rangle|\chi^{M^A}\rangle\right] , \tag{12}$$

$$|\,\xi^{M^S}\rangle \ = \ \frac{1}{\sqrt{2}}\left[|\Phi^{M^S}\rangle|\chi^{M^S}\rangle - |\Phi^{M^A}\rangle|\chi^{M^A}\rangle\right] , \tag{13}$$

$$|\,\xi^{M^A}\rangle \ = \ \frac{1}{\sqrt{2}}\left[|\Phi^{M^S}\rangle|\chi^{M^A}\rangle + |\Phi^{M^A}\rangle|\chi^{M^S}\rangle\right] . \tag{14}$$

Finally, the singlet, antisymmetric color state is

$$C^A_{color} = \frac{1}{\sqrt{6}}(RBY - BRY + BYR - YBR + YRB - RYB), \tag{15}$$

where R, B and Y stand for Red, Blue and Yellow respectively. This state does not enter into the calculations and therefore, in what follows will be suppressed.
The initial total wave function for the proton ground state, with $L = 0$, $S = 1/2$, and $J = 1/2$ is given by

$$|\Psi_i\rangle = \left|\xi^S\right\rangle \left|\Psi^S_0\right\rangle . \tag{16}$$

The final total wave function for the first excited state, with $L = 1$, $S = 1/2$, and $J = 1/2$ or $3/2$, of the proton is

$$|\Psi_f\rangle = \frac{1}{\sqrt{2}}\left[\left|\xi^{M^S}\right\rangle \left|\Psi^{M^S}_1\right\rangle + \left|\xi^{M^A}\right\rangle \left|\Psi^{M^A}_1\right\rangle\right] \tag{17}$$

while that of the second excited state, with $L = 2\,, S = 1/2$, and $J = 3/2$ or $5/2$, has the form

$$|\Psi_f\rangle = \left|\xi^S\right\rangle \left|\Psi^S_2\right\rangle . \tag{18}$$

For the $M1$ transition $(S = 1/2) \rightarrow (S = 3/2)$ [24] where the proton and $\Delta^+(1232)$ both have an angular momentum of $L = 0$, the total wave function for the initial state of the proton is still given by Eq. (16), while the final wave function for the delta is

$$\left|\Psi_f\right\rangle = \Phi^S_\Delta \chi^S_\Delta \left|\,\Psi^S_\Delta\right\rangle . \tag{19}$$

The flavor wave function, Φ^S_Δ, for this transition is given by Eq. (8) while the spin wave function, χ^S_Δ, is given by Eq. (4).

B. Electromagnetic Transitions

1. *Electric Dipole Transitions*

The Hamiltonian for the electric dipole (E1) transition, in the case of three quarks of equal mass m, is given by

$$H_{E1} = -\frac{1}{c}\sum_{j=1}^{3}\lambda_j \hat{\epsilon}_\gamma \cdot \vec{x}_j\,, \tag{20}$$

where $\hat{\epsilon}_\gamma$ denotes one of the polarization directions of the incident photon and $\vec{x}_j = \vec{p}_j/m$ with $\vec{p}_j$ being the momentum of quark j.
For u and d quarks, the charge operator of the j-th quark has the form

$$\lambda_j = \frac{e}{6}(1 + 3\tau_j^z)\,, \tag{21}$$

where τ_j^z is the third component of the isospin of the j-th quark.
Going over to Jacobi coordinates (see Appendix A) we may express H_{E1} in terms of $\vec{\rho}_N$ and $\vec{\eta}_N$ as

$$H_{E1} = -\frac{1}{c}\hat{\epsilon}_\gamma \cdot \left[\vec{\rho}_N(\lambda_2 - \lambda_1) + \vec{\eta}_N(2\lambda_3 - \lambda_2 - \lambda_1)\right]\,. \tag{22}$$

Similarly to the nuclear case [19], we introduce the operators $\mathbb{I}_p$ and $\mathbb{I}_q$

$$\mathbb{I}_p = -(\lambda_2 - \lambda_1) = \frac{e}{2}(\tau_1^z - \tau_2^z)\,, \qquad \mathbb{I}_q = \frac{1}{2}(\lambda_1 + \lambda_2 - 2\lambda_3) = \frac{e}{2}(\frac{\tau_1^z + \tau_2^z)}{2} - \tau_3^z) \tag{23}$$

in terms of which the Hamiltonian takes the form

$$H_{E1} = \frac{1}{c}\hat{\epsilon}_\gamma \cdot \left[\vec{\rho}_N\ \mathbb{I}_p + 2\vec{\eta}_N\ \mathbb{I}_q\right] = \frac{1}{c}\hat{\epsilon}_\gamma \cdot \left[\frac{1}{2}\vec{\rho}\ \mathbb{I}_p + \frac{\sqrt{3}}{3}\vec{\eta}\ \mathbb{I}_q\right]\,, \tag{24}$$

i.e., instead of the form (20) where the Hamiltonian is expressed in terms of the individual particle charge and coordinate, in the last relation it is written in terms of the more appropriate Jacobi coordinates and the charge operators $\mathbb{I}_p$ and $\mathbb{I}_q$ acting on quasiparticles [19]. Similar relations can be derived for higher transitions.

2. Magnetic Dipole Transitions

The magnetic dipole (M1) causes the transition $\gamma P \to \Delta^+(1232)$, in which the proton (P), after absorbing a photon (γ), is excited to the delta (Δ^+). The corresponding Hamiltonian is expressed as

$$H_{\rm M1} = -i\sum_{j=1}^{3}\mu_q^j(\vec{\sigma}_j \times \vec{k}_\gamma)\cdot\hat{\epsilon}_\gamma\,, \tag{25}$$

where the quark magnetic moments are assumed to be of the Dirac form,

$$\mu_q^j = \frac{\lambda_j e\hbar}{2mc} = \frac{\lambda_j M_p}{m}\mu_{nm}\,, \tag{26}$$

with $\mu_{nm} = \dfrac{e\hbar}{2M_p c}$ being the nuclear magneton and M_p the proton mass. Using the identity

$$\left(\vec{\sigma}_j \times \vec{k_\gamma}\right)\cdot\hat{\epsilon}_\gamma = -\vec{\sigma}_j\cdot\left(\hat{\epsilon}_\gamma \times \vec{k_\gamma}\right) \tag{27}$$

we obtain

$$H_{\rm M1} = i\sum_{j=1}^{3}\mu_q^j\vec{\sigma}_j\cdot\left(\hat{\epsilon}_\gamma \times \vec{k_\gamma}\right)\,. \tag{28}$$

Since M1 does not contain any orbital operators, in this transition the spin must change instead.

III. TRANSITION AMPLITUDES

In what follows we shall discuss the various transition amplitudes starting with the electric dipole one.

A. Electric Dipole Transition Amplitude

In order to express the transition amplitude in terms of the conjugate momenta $\vec{p},\vec{q}$ of $\vec{\rho},\vec{\eta}$ we use the reduced masses $\mu_{12}=m/2$ and $\mu_{12,3}=2m/3$. For the H_{E1} Hamiltonian we get

$$H_{E1}=\frac{1}{mc}\hat{\epsilon}_\gamma\cdot\left[\vec{p}\,\mathbb{I}_p+\frac{\sqrt{3}}{2}\vec{q}\,\mathbb{I}_q\right], \tag{29}$$

where $\vec{p}=\mu_{12}\mathrm{d}\vec{\rho}/\mathrm{d}t=m/2\dot{\vec{\rho}}$ and $\vec{q}=\mu_{12,3}\mathrm{d}\vec{\eta}/\mathrm{d}t=2/3\,m\dot{\vec{\eta}}$. The Siegert theorem is applied using the commutation relations

$$\vec{p}=-i\mu_{12}\frac{1}{\hbar}[\vec{\rho},H]\,,\qquad \vec{q}=-i\mu_{12,3}\frac{1}{\hbar}[\vec{\eta},H]\,. \tag{30}$$

Then

$$\langle\Psi_f|\vec{p}|\Psi_i\rangle=i\frac{m}{2\hbar}(E_f-E_i)\langle\Psi_f|\vec{\rho}|\Psi_i\rangle\,,\qquad \langle\Psi_f|\vec{q}|\Psi_i\rangle=i\frac{2m}{3\hbar}(E_f-E_i)\langle\Psi_f|\vec{\eta}|\Psi_i\rangle\,, \tag{31}$$

where E_i and E_f are the energies of the initial and final states respectively. Working out the spin and flavor projections we obtain, for the matrix element,

$$M_{\mathrm{E1}}=\frac{eE_\gamma}{2\sqrt{6}i\hbar c}\left\langle\Psi_1^{M^A}\,|\hat{\epsilon}_\gamma\cdot\vec{\rho}|\,\Psi_0^S\right\rangle-\frac{eE_\gamma}{2\sqrt{6}i\hbar c}\left\langle\Psi_1^{M^S}\,|\hat{\epsilon}_\gamma\cdot\vec{\eta}|\,\Psi_0^S\right\rangle, \tag{32}$$

where $E_\gamma=E_f-E_i$
The integrals in (32) were evaluated using Euler angles α, β, γ as external and ρ, η, $x=\vec{\rho}\cdot\vec{\eta}/\rho\eta$ as internal coordinates. Here the $\hat{\rho}$ is chosen to coincide with the z' axis and $\hat{\eta}$ is in the $x'-z'$ plane. Thus only a five dimensional integration has to be done numerically since both Ψ_0^S and the two components of Ψ_1 are invariant with respect to a rotation about the z-axis and thus do *not* depend on α. After averaging over the direction of $\vec{k}$ and the two polarization directions [20] one obtains the following expression for the absolute square of the transition matrix elements

$$\overline{|\mathcal{M}_{E1}|^2}=\frac{e^2E_\gamma^2}{72\,(\hbar c)^2}\left|\langle\Psi_1^{M^A}|\rho_z|\Psi_0^S\rangle-\langle\Psi_1^{M^S}|\eta_z|\Psi_0^S\rangle\right|^2. \tag{33}$$

Therefore, the following integrals are required

$$\begin{aligned}\left\langle\Psi_1^{M^A}|\rho_z|\Psi_0^S\right\rangle &= 2\pi\int_0^\pi\sin\beta\mathrm{d}\beta\int_0^{2\pi}\mathrm{d}\gamma\int_0^\infty\rho^2\mathrm{d}\rho\int_0^\infty\eta^2\mathrm{d}\eta\\ &\times\int_{-1}^1\mathrm{d}x\Psi_1^{M^A}(\rho,\eta,x,\beta,\gamma)\rho\cos\beta\,\Psi_0^S(\rho,\eta,x)\,, \qquad (34)\\ \left\langle\Psi_1^{M^S}|\eta_z|\Psi_0^S\right\rangle &= 2\pi\int_0^\pi\sin\beta\mathrm{d}\beta\int_0^{2\pi}\mathrm{d}\gamma\int_0^\infty\rho^2\mathrm{d}\rho\int_0^\infty\eta^2\mathrm{d}\eta\int_{-1}^1\mathrm{d}x\\ &\times\ \Psi_1^{M^S}(\rho,\eta,x,\beta,\gamma)\eta(\cos\beta\cos\theta-\sin\beta\cos\gamma\sin\theta)\,\Psi_0^S(\rho,\eta,x)\,. \qquad (35)\end{aligned}$$

The corresponding integrated photoabsorption cross section for a single excited electric dipole state i.e, in the long wavelength limit [21, 22], is

$$\Sigma_1=\int\mathrm{d}E_\gamma\eta_\gamma^{E1}=\frac{4\pi^2c}{\omega}\,\overline{|\mathcal{M}_{E1}|^2}\,. \tag{36}$$

B. Electric Quadrupole Transition Amplitude

Similarly to the E1 case, the use of commutation relations in the amplitude for the E2 transition yields

$$M_{E2} = \langle \Psi_f | H_{E2} | \Psi_i \rangle \equiv -\frac{E_\gamma}{2\hbar c} \langle \Psi_f | \hat{\epsilon}_\gamma \cdot \vec{\rho}\, \mathbb{J}_\rho | \Psi_i \rangle - \frac{\sqrt{3} E_\gamma}{6\hbar c} \langle \Psi_f | \hat{\epsilon}_\gamma \cdot \vec{\eta}\, \mathbb{J}_\eta | \Psi_i \rangle \tag{37}$$

where $\mathbb{J}_\rho$ and $\mathbb{J}_\eta$ are the isospin E2 operators corresponding to the ρ and η coordinates configuration. The $M_{\rm E2}$ transition amplitude for the proton can now be written as

$$M_{E2} = \frac{e}{6\hbar c} E_\gamma \left\langle \Psi_2^S \right| (\hat{\epsilon}_\gamma \cdot \vec{\rho})(\vec{k}_\gamma \cdot \vec{\rho}) + (\hat{\epsilon}_\gamma \cdot \vec{\eta})(\vec{k}_\gamma \cdot \vec{\eta}) \left| \Psi_0^S \right\rangle \tag{38}$$

For a single excited electric quadrupole state, the integrated photoabsorption cross section [21, 22] is

$$\Sigma_2 = \int dE_\gamma \eta_\gamma^{E2} = \frac{\pi^2 c}{3\,\omega} \left| \mathcal{M}_{E2} \right|^2 . \tag{39}$$

C. Magnetic Dipole Transition Amplitude

The matrix element of the magnetic transition is expressed as

$$M_{M1} = \langle \Psi_f | H_{M1} | \Psi_i \rangle = i \left(\hat{\epsilon}_\gamma \times \vec{k_\gamma} \right) \sum_{j=1}^{3} \langle \Psi_f | \mu_q^j \sigma_j^z | \Psi_i \rangle \,, \tag{40}$$

where Ψ_i and Ψ_f are given by Eqs.(16) and (19) respectively.
The process $\gamma P \rightarrow \Delta^+(1232)$ ($\frac{1}{2}^+ \rightarrow \frac{3}{2}^+$) can take place by interaction with either the magnetic dipole ($M1$) or electric quadrupole ($E2$). In the quark model the latter transition is forbidden [23] because it is proportional to the charge operator which cannot cause transitions between quark spin 1/2 and 3/2 states, and hence the matrix element vanishes by orthogonality of the quark spin wave functions.
The $M1$ transition involves the quark magnetic moments – hence the spin operator – and this can lead to transitions $(S = 1/2) \rightarrow (S = 3/2)$ [24]. The transition matrix can be written as

$$M_{\rm M1} = i \left(\hat{\epsilon}_\gamma \times \vec{k_\gamma} \right) \langle \Psi_f | \mu_q^1 \sigma_1^z + \mu_q^2 \sigma_2^z + \mu_q^3 \sigma_3^z | \Psi_i \rangle \,. \tag{41}$$

Using the flavor, spin and configuration space wave functions we obtain

$$M_{\rm M1} = i(\hat{\epsilon}_\gamma \times \vec{k}_\gamma) \frac{2\sqrt{2}}{3} \mu_P \left\langle \Psi_\Delta^S | \Psi_0^S \right\rangle \,, \tag{42}$$

where $\mu_P = \mu_u - \mu_d$.
Averaging over the two polarization directions we obtain for the M1-matrix element

$$\overline{|\mathcal{M}_{\rm M1}|^2} = \frac{2\alpha}{9} \frac{E_\gamma^2 \hbar c}{(mc^2)^2} I_{\rm M1}^2 \,, \tag{43}$$

where $I_{\rm M1}$ is the overlap integral given by

$$I_{M1} = 8\pi^2 \int_0^\infty \rho^2 {\rm d}\rho \int_0^\infty \eta^2 {\rm d}\eta \int_{-1}^{1} {\rm d}x\, \Psi_\Delta^S(\rho, \eta, x) \Psi_0^S(\rho, \eta, x) \,. \tag{44}$$

Like in the electric transitions, the photoabsorption cross section for a single excited magnetic dipole state is

$$\Sigma_{\rm M1} = \int {\rm d}E_\gamma \eta_\Delta^{M1} = \frac{4\pi^2 \hbar c}{\hbar\omega} \overline{|\mathcal{M}_{\rm M1}|^2} \,. \tag{45}$$

IV. RELATIVISTIC EFFECTS

Relativistic effects can be incorporated via the momentum space representation of the HCA. This involves the Fourier transformation, in the D-dimensional space, of the Schrödinger-like equation

$$\left[-\frac{\hbar^2}{m}\nabla^2 + \hat{\mathcal{V}}(r,\Omega_r) - E\right] Y_{[L_0]}(\Omega_r)\Phi_{[L_0]}(r) = 0. \tag{46}$$

The conjugate of the D-dimensional Jacobi vector $\vec{\xi}(\vec{\xi}_1,\vec{\xi}_2,\ldots,\vec{\xi}_{A-1})$ is $\vec{\kappa}(\vec{\kappa}_1,\vec{\kappa}_2,\ldots,=\vec{\kappa}_{A-1})$, where the Jacobi coordinates $\vec{\kappa}_i$ are defined in an identical manner to those in position space

$$\begin{aligned}
\vec{\kappa}_{A-1} &= \vec{k}_2 - \vec{k}_1 \\
\vec{\kappa}_{A-2} &= \frac{2}{\sqrt{3}}\left(\vec{k}_3 - \frac{\vec{k}_1+\vec{k}_2}{2}\right) \\
&\cdots \\
\vec{\kappa}_{A-I} &= \sqrt{\frac{2I}{I+1}}\left(\vec{k}_{I+1} - \frac{1}{I}\sum_{j=1}^{I}\vec{k}_j\right) \\
&\cdots \\
\vec{\kappa}_1 &= \sqrt{\frac{2(A-1)}{A}}\left(\vec{k}_A - \frac{1}{A-1}\sum_{j=1}^{A-1}\vec{k}_j\right) \\
\vec{K} &= \frac{1}{A}\sum_{j=1}^{A}\vec{k}_j,
\end{aligned}$$

where the $\vec{k}_i$ are the conjugates of the individual particle coordinates $\vec{r}_i$. The Zernike-Brinkman (ZB) hyperspherical coordinates in momentum space can be defined in the same way as in position space [25]. In particular, the definition of κ, the analogue of the hyperradius r in wave number space, should be noted:

$$\kappa^2 = \sum_{j=1}^{A-1}\kappa_j^2. \tag{47}$$

The Fourier transform of the HCA to the wave function in the D-dimensional space is given by

$$\mathcal{F}\left\{Y_{[L_0]}(\Omega_r)\Phi_{[L_0]}(r)\right\} = \frac{1}{(2\pi)^{D/2}}\int \mathrm{e}^{i\vec{\kappa}\cdot\vec{\xi}} Y_{[L_0]}(\Omega_r)\Phi_{[L_0]}(r)\,\mathrm{d}\Omega_r\; r^{D-1}\,\mathrm{d}r\,, \tag{48}$$

while the expansion in hyperspherical harmonics of the plane wave by

$$\mathrm{e}^{i\vec{\kappa}\cdot\vec{\xi}} = \frac{(2\pi)^{D/2}}{(\kappa r)^{(D-2)/2}}\sum_{[L]0}^{\infty} i^L Y_{[L]}(\Omega_\kappa)Y^{\dagger}_{[L]}(\Omega_r)J_{\mathcal{L}+\frac{1}{2}}(\kappa r), \tag{49}$$

where $\mathcal{L} = L + (D-3)/2$ and with $\{\Omega_\kappa\}$ the set of $D-1$ angles and hyperangles in κ-space. Substituting (49) into (48), results in

$$\mathcal{F}\left\{Y_{[L_0]}(\Omega_r)\Phi_{[L_0]}(r)\right\} = i^L Y_{[L_0]}(\Omega_\kappa)\Theta_{[L_0]}(\kappa), \tag{50}$$

where

$$\kappa^{\frac{D-2}{2}}\Theta_{[L_0]}(\kappa) = \int_0^\infty r^{\frac{D-2}{2}}\Phi_{[L_0]}(r)J_{\mathcal{L}+\frac{1}{2}}(\kappa r)\,\mathrm{d}r\,, \tag{51}$$

using the orthonormality of the hyperspherical harmonics. The functions $r^{(D-2)/2}\Phi_{[L_0]}(r)$ and $\kappa^{(D-2)/2}\Theta_{[L_0]}(\kappa)$ are therefore related to each other by means of the Hankel transform of order $\mathcal{L}_0 + \frac{1}{2}$ [26].

Fourier transformation of Eq. (46), followed by pre-multiplication by $Y^{\dagger}_{[L_0]}(\Omega_\kappa)$ and integration with respect to Ω_κ yields the following equation for bound states in the HCA,

$$(\kappa^2 + \kappa_E^2)\, f_{[L_0]}(\kappa) + \frac{A(A-1)}{2} \int_0^\infty U_0(\kappa,\kappa') f_{[L_0]}(\kappa')\ \kappa'\, \mathrm{d}\kappa' = 0, \tag{52}$$

where $\hbar^2\kappa_E^2/m = -E$ and $f_{[L_0]}(\kappa) = \kappa^{(D-2)/2}\Theta_{[L_0]}(\kappa)$ and where

$$U_0(\kappa,\kappa') = \frac{m}{\hbar^2} \int_0^\infty J_{\mathcal{L}_0+\frac{1}{2}}(\kappa' r) V_0(r) J_{\mathcal{L}_0+\frac{1}{2}}(\kappa r) r\, \mathrm{d}r\,. \tag{53}$$

To include relativistic effects due to kinetic energy, the kinetic energy term in Eq. (46) must be replaced by its relativistic counterpart, i.e

$$\left[\sum_{j=1}^{A} \sqrt{-\hbar^2 c^2 \nabla_j^2 + m^2 c^4} + V(r,\Omega_r) - Mc^2\right] Y_{[L_0]}(\Omega_r)\Phi_{[L_0]}(r) = 0\,, \tag{54}$$

where $M = Am + E$ is the total mass of the system of A particles. Using the relations

$$\vec{\kappa}\cdot\vec{\xi} + 2A\vec{X}\cdot\vec{K} = 2\vec{k}\cdot\vec{x} \tag{55}$$

and

$$\vec{\kappa_{1_{(j)}}} = \sqrt{\frac{2A}{A-1}}(\vec{k}_j - \vec{K}), \tag{56}$$

where $\vec{X} = \frac{1}{A}\sum_{i1}^{A}\vec{r}_i$, $\vec{x} \equiv (\vec{r}_1, \vec{r}_2, \ldots, \vec{r}_A)$ and $\vec{k} \equiv (\vec{k}_1, \vec{k}_2, \ldots, \vec{k}_A)$, we find that the hypercentral component $T_0(\kappa)$ of the kinetic energy is given by

$$T_0(\kappa) = \int Y^{\dagger}_{[L_0]}(\Omega_\kappa) \left(\sum_{j=1}^{A} \sqrt{\hbar^2 c^2 \frac{2(A-1)}{A}\kappa^2_{1_{(j)}} + m^2c^4}\ \right) Y_{[L_0]}(\Omega_\kappa) d\Omega_\kappa \tag{57}$$

and can be evaluated numerically for small numbers of particles. Moreover, analytic expressions are available [10] to determine matrix elements of an operator which is a symmetric sum of terms over the index j. The relativistic generalization of Eq. (52) is therefore

$$\frac{m}{\hbar^2}\left[T_0(\kappa) - Mc^2\right] f_{[L_0]}(\kappa) + \frac{A(A-1)}{2} \int_0^\infty U_0(\kappa,\kappa') f_{[L_0]}(\kappa')\ \kappa'\, \mathrm{d}\kappa' = 0\,. \tag{58}$$

It is possible to show that Eq. (58) reduces to its non-relativistic counterpart (52) by performing a Taylor expansion of the square root in Eq. (57), and applying (56), as well as the momentum space generalization of the hyperradius r

$$r = \sqrt{\sum_{j=1}^{A-1} \xi_j^2} = \sqrt{\frac{2}{A}\sum_{\substack{i=1\\ i<j}}^{A} (\vec{r}_i - \vec{r}_j)^2} = \sqrt{2\sum_{j=1}^{A} (\vec{r}_j - \vec{X})^2}\,. \tag{59}$$

A. Linear Confining Potential in Momentum Space

Confining potentials may be treated in momentum space [14, 15] by recognizing that the Fourier transform of a linear confining potential does indeed exist in a distributional (if not a classical) sense. For example, the linear potential is derived from the Yukawa potential in the following way:

$$V_{\rm linear} = \lambda \lim_{\mu\to 0} \frac{\partial^2}{\partial \mu^2} \frac{e^{-\mu r}}{r}. \tag{60}$$

The strategy in this work is to extend the two-body formalism of Hersbach [15] to the HCA, and hence to many-body calculations. To begin with, it should be noted that the hypercentral potential corresponding to a linear two-body potential is linear in the hyperradius r. The potential matrix element (see (53)) corresponding to the linear confining potential in the HCA is therefore

$$\begin{aligned} U_0(\kappa,\kappa') &= \Lambda \lim_{\mu\to 0} \frac{\partial^2}{\partial \mu^2} \int_0^\infty J_{\mathcal{L}_0+\frac{1}{2}}(\kappa r) \frac{{\rm e}^{-\mu r}}{r} J_{\mathcal{L}_0+\frac{1}{2}}(\kappa' r)\, r{\rm d}r \\ &= \frac{\Lambda}{\pi(\kappa\kappa')^{\frac{3}{2}}} \lim_{\mu\to 0} \frac{\partial}{\partial \mu} \mu\, Q'_{\mathcal{L}_0}\left(\frac{\kappa^2+\kappa'^2+\mu^2}{2\kappa\kappa'}\right), \end{aligned} \tag{61}$$

where $Q_{\mathcal{L}_0}(x)$ is a Legendre function of the second kind of order $\mathcal{L}_0$. Note that $\mathcal{L}_0$ is integral for even A and half-integral for odd A.
The behavior of $U_0(\kappa,\kappa')$ at the singularity $\kappa\kappa'$ for the case where $\mathcal{L}_0$ is an integer is completely analogous to that in the two-body case, and is discussed in detail in [14] and [15]. The relation [27]

$$Q_{\mathcal{L}_0}(x) = \frac{1}{2}\log\left(\frac{x+1}{x-1}\right) P_{\mathcal{L}_0}(x) + F(x), \tag{62}$$

where $P_{\mathcal{L}_0}(x)$ is a Legendre function of the first kind of order $\mathcal{L}_0$, and $F(x)$ is a function which is finite and smooth at $x=1$, may be used to show that the behavior of the Legendre functions $P_{\mathcal{L}_0}(x)$ at $x=1$ is not qualitatively different for integer and non-integer values of $\mathcal{L}_0$. The singularity in $Q'_{\mathcal{L}_0}(z)$ at $z=1$ is therefore removable for all values of $\mathcal{L}_0$. The two-body result of Hersbach [15] can therefore be adapted and Eq. (58) written as

$$\begin{aligned} \frac{m}{\hbar^2}\left[T_0(\kappa) - Mc^2\right] f_{[L_0]}(\kappa) + \frac{A(A-1)}{2}\frac{\Lambda}{\pi}\Bigg\{ & \frac{f_{[L_0]}(\kappa)}{\kappa} \\ & + \Pr\int_0^\infty \left[\frac{Q'_{\mathcal{L}_0}\left(\frac{\kappa^2+\kappa'^2}{2\kappa\kappa'}\right)}{(\kappa\kappa')^{\frac{3}{2}}} f_{[L_0]}(\kappa') + \frac{f_{[L_0]}(\kappa)}{\kappa'(\kappa'-\kappa)^2}\right]\kappa'{\rm d}\kappa'\Bigg\} = 0\,, \end{aligned} \tag{63}$$

where $\Pr\int$ denotes the principal part of the integral. Coulomb and constant terms can be included in the potential without introducing additional complications, but will be omitted for the sake of simplicity here.

B. Retardation Effects

The Yukawa potential used in the definition of the linear confining potential in (60) has the following form in the momentum representation:

$$U_{\rm Yukawa}(\vec{k},\vec{k}') = \frac{4\pi\lambda}{|\vec{k}-\vec{k}\,'|^2+\mu^2} \tag{64}$$

and needs to be replaced by the Lorentz-invariant expression

$$U_{\text{Yukawa}}(\vec{k},\vec{k}') = \frac{4\pi\lambda}{-q\cdot q+\mu^2}, \tag{65}$$

where

$$q \equiv (k^0 - k'^0, \vec{k} - \vec{k}\,'). \tag{66}$$

In the two-body case, we introduce a retardation

$$\tau(k,k') = \left(\frac{t(k)-t(k')}{2\hbar c}\right)^2, \tag{67}$$

where $t(k) - 2m$ is the kinetic energy operator for the two-body system. We now define an average retardation for the A-body system by generalizing (67), i.e.

$$\tau(\kappa,\kappa') = \left(\frac{T_0(\kappa)-T_0(\kappa')}{A\hbar c}\right)^2, \tag{68}$$

where $T_0(\kappa)$ is given by (57). Using this definition, the term $Q'_{\mathcal{L}_0}\left((\kappa^2+\kappa'^2)/(2\kappa\kappa')\right)$ in equation (63) needs to be replaced by $Q'_{\mathcal{L}_0}\left((\kappa^2+\kappa'^2-\tau(\kappa,\kappa'))/(2\kappa\kappa')\right)$. Note that at low momentum transfer, $\tau \simeq (\hbar/2mc)^2\,(\kappa^2-\kappa'^2)^2$ while at high momentum transfer $\tau \simeq (\kappa-\kappa')^2$. In the latter case, the argument of Q' in Eq. (63) approaches unity.

V. RESULTS AND DISCUSSIONS

The three–quark potential is assumed to be a sum of local two-body potentials between the valence quarks $V = \sum_{i,j<i} Vij$ where V_{ij} is the quark-quark potential V_{qq}. These potentials have as main characteristics their confining nature at large distances and the Coulomb-like behavior as $r \to 0$, which is due to the asymptotic freedom of QCD and the dominance of one-gluon exchange between the colored constituents of the baryon at small distances.
The quark-quark potential can be expressed as a sum of the central and the spin-spin parts $V_{qq} = V^c + V^s$, where V^c contains, as usual, the confinement and the coulombic parts while V^s is of the general form $V^s = f_{ij}(r)\vec{\sigma}_i\cdot\vec{\sigma}_j$. In our investigation we performed calculations with the V^c term alone and also with both terms included. For the calculations with the V^c part only, we used various potentials. In Table I we present the results obtain for the ground and orbitally excited states of the nucleon with spin-independent potentials and by using the IDEA and HCA methods. These results were obtained with the Fabre [28] and the Lichtenberg [29] potentials. For the calculations with both terms included we used the Ono-Schöberl potential [30] and two

TABLE I: Non-relativistic and relativistic nucleon masses in MeV for orbital excitations.

			Expt	IDEA		HCA		HCA (Relat)	
				Potentials		Potentials		Potentials	
L	S	J^P		Fabre	Lichtenberg	Fabre	Lichtenberg	Fabre	Lichtenberg
0	1/2	$\frac{1}{2}^+$	940	1086	1085	1089	1088	1008	1043
1	1/2	$\frac{3}{2}^-$	1520	1744	1730	1744	1730	–	–
2	1/2	$\frac{5}{2}^+$	1680	2245	2218	2251	2224	–	–

of Silvestre-Brac potentials [31], namely the AP1 and AP2 versions. The results obtained are shown in Table II.

TABLE II: Delta masses in MeV obtained with spin-dependent potentials.

Quantum numbers				IDEA			HCA		
				Potentials			Potentials		
L	S	J^P	Expt	AP1	AP2	Ono-Schöberl	AP1	AP2	Ono-Schöberl
0	3/2	$\frac{3}{2}^+$	1232	1300	1307	1224	1300	1308	1225

TABLE III: The integrated photoabsorption cross sections Σ_1 and Σ_2 for the N(1520) and N(1680) proton resonances respectively.

		IDEA			HCA			
	Expt	Potentials			Potentials			
	values	Martin	Fabre	Lichtenberg	Martin	Fabre	Lichtenberg	
E1-E0 (MeV)	580	591	658	645	586	655	642	
Σ_1 (MeVmb)	33[a]	30	31	31	31	31	31	
E2-E0 (MeV)	740	986	1159	1133	986	1162	1136	
Σ_2 MeVmb)	19[a]	18	23	23	10	13	13	
		OTHER METHODS						
		I.K.	h.o.	h.o. (ret)	h.o. $(\rho + j)$	3q	bag	I.K.
E1-E0 (MeV)	580	595[b]	167	167	167	144	349	595[b]
Σ_1 (MeVmb)	33[a]	92[c]	40[c]	38	43	27	13	26[c]
E2-E0 (MeV)	740	775[b]	334	334	334	203	–	–
Σ_2 (MeVmb)	19[a]	6.9[c]	13[c]	9	15	1.5	–	–

[a]ref. [32]; [b]ref. [33]; [c]ref. [21].
ret : retardation; ρ : classical charge density; j : current density.

These transition energies and the corresponding wave functions were used to calculate the integrated photoabsorption cross sections due to the E1 and E2 transitions. Our results are shown in Table III together with experimental values and those of other methods. For both the IDEA and the HCA the cross sections are in good to very good agreement with the experimental values.

TABLE IV: The integrated photoabsorption cross section Σ_{M1} for the $\Delta(1232)$ resonance obtained with the spin-dependent Ono-Schöber potential.

		IDEA	HCA	OTHER METHODS
	Expt	Ono-Schöberl	Ono-Schöberl	Ref. [33]
$[E_\Delta - E_N]$ MeV	292	304	285	300[b]
Σ_{M1} (MeVmb)	63[a]	54	58	52

The results obtained by other methods for the transition energies are generally very low as compared to the experimental ones except those obtained via the Isgur-Karl (I.K.) model [33], which, nevertheless, can not reproduce the experimental photoabsorption cross sections. This mainly implies that the corresponding wave functions are not adequate to describe the photoabsorption cross sections.
The results for the delta mass obtained with the spin-dependent Ono–Schöber potential and the corresponding transition energy together with the cross section are presented in Table IV. The cross sections are in good agreement with the experimental data.
The relativistic results for the nucleon ground state masses are presented in Table I and they are in fairly good agreement with the non-relativistic ones. The accuracy of the Fourier transformations (going from one space to the other) is exhibited in Fig. 1. The shapes of the non-relativistic wave functions, as compared to the relativistic ones are shown in Fig. 2. It is seen that they are in good agreement and the small shifting of the shape should not affect the overlap integral for the various transitions significantly. More work, however, is required in this respect.

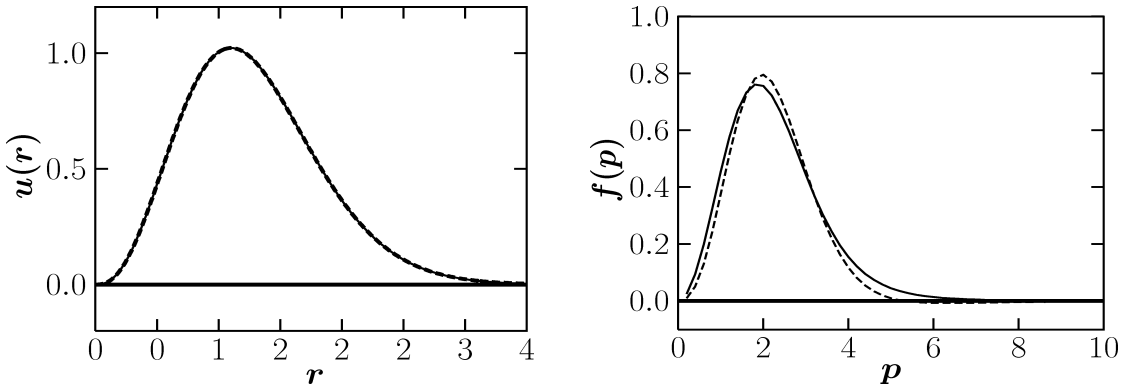

FIG. 1: Fourier transformations from r– to p–space and vise versa.

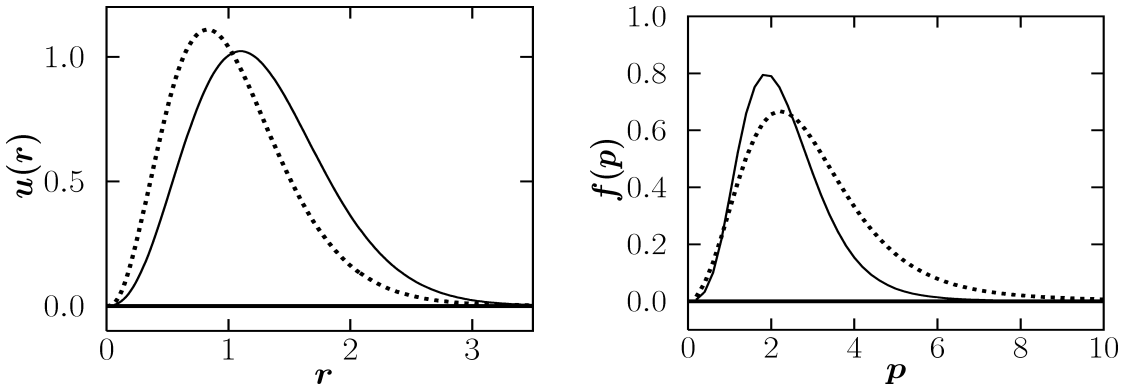

FIG. 2: Non-relativistic wave functions, (—), compared to relativistic ones, (- - -).

To summarize, in this work we show that the IDEA method and its simplified version, HCA, provide us wave functions for three quark systems which produce results for the photoexcitation cross-sections for the E1, E2, and M1 transitions that are in good agreement with the experimental data. Furthermore, a formalism has been developed to transform the very useful and computationally economic HCA from position space to momentum space which render itself to relativistic considerations. The relativistic generalization achieved here yields good spectra for quark systems, and thus it is expected that it will provide an excellent model for hadronic and

multiquark calculations. The use of a relativistic HCA should also remove justified criticism that high energy systems are being investigated with a low energy tool.

APPENDIX A: JACOBI COORDINATES

The three-quark configuration space wave function is written as a function of the three coordinates $\vec{r}_i$ of the individual quarks: $\psi(\vec{r}_1, \vec{r}_2, \vec{r}_3)$. However, to separate the center of mass motion it is customary to use the Jacobi coordinates, which are defined as follows

$$\begin{aligned} \vec{\rho}_{12} &= \vec{r}_2 - \vec{r}_1 \equiv \vec{\rho}, \\ \vec{\eta}_{12} &= \frac{2}{\sqrt{3}}\left(\vec{r}_3 - \frac{\vec{r}_1 + \vec{r}_2}{2}\right) = \sqrt{3}\left(\vec{r}_3 - \vec{X}\right) \equiv \vec{\eta} \end{aligned}$$

where $\vec{X}$ is the center of mass, $\vec{X} = \frac{1}{3}\sum_{i=1}^{3} \vec{r}_i$. The hyperradius r is defined by

$$r^2 = \rho^2 + \eta^2 = 2\sum_{i=1}^{3}\left(\vec{r}_i - \vec{X}\right)^2 \tag{A1}$$

Fixing $\vec{X}$ at the origin, the inverse coordinates are given by

$$\begin{aligned} \vec{r}_1 &= -\frac{1}{2}\vec{\rho} - \frac{\sqrt{3}}{6}\vec{\eta}, \\ \vec{r}_2 &= \frac{1}{2}\vec{\rho} - \frac{\sqrt{3}}{6}\vec{\eta}, \\ \vec{r}_3 &= \frac{\sqrt{3}}{3}\vec{\eta}. \end{aligned}$$

Thus we may express the $\vec{\rho}_{ij}$, needed in constructing the wave functions, in terms of $\vec{\rho}$, $\vec{\eta}$ as follows

$$\begin{aligned} \vec{\rho}_{12} &= \vec{r}_2 - \vec{r}_1 = \vec{\rho}, \\ \vec{\rho}_{23} &= \vec{r}_3 - \vec{r}_2 = -\frac{1}{2}\vec{\rho} + \frac{\sqrt{3}}{2}\vec{\eta}, \\ \vec{\rho}_{31} &= \vec{r}_3 - \vec{r}_1 = \frac{1}{2}\vec{\rho} + \frac{\sqrt{3}}{2}\vec{\eta} \end{aligned}$$

These can be used to express any Faddeev component $\psi(z_{ij}, r)$ in terms of the Jacobi vectors $\vec{\rho}$ and $\vec{\eta}$ using $z_{ij} = 2\rho_{ij}^2/r^2 - 1$.

---

[1] M. Fabre de la Ripelle, Phys. Lett. **B 205**, 97 (1988).
[2] A.M. Badalyan, D.I. Kitoroage, and D.S. Pariyski, Nucl. Phys. **46**, 226 (1987).
[3] M.I. Haysak, V.I. Lengyel, S. Chalupka, and M. Salak, Czech. J. of Physics, **41**, 799 (1991).
[4] I.P. Matamba, M. Braun, and S.A. Sofianos, II Nuovo Cim. **111**, 1 (1998).
[5] M. Fabre de la Ripelle, H. Fiedeldey, and S.A. Sofianos, Phys. Rev. C **38**, 449 (1988); Few-Body Systems **6**, 157 (1989); Few-Body Systems Suppl. **2**, 488 (1987).
[6] W. Oehm, S.A. Sofianos, H. Fiedeldey, and M. Fabre de la Ripelle, Phys. Rev. C **44**, 81 (1991); C **43**, 25 (1991).
[7] M. Fabre de la Ripelle, H. Fiedeldey, and S.A. Sofianos, Few-Body Systems, Suppl. **2**, 493 (1987).

[8] J.P. McTavish, H. Fiedeldey, M. Fabre de la Ripelle, and P. du T. van der Merwe, Few-Body Systems **3**, 99 (1988).
[9] M.M. Giannini, Nucl. Phys. A **497**, 537c (1989).
[10] M. Fabre de la Ripelle and J. Navarro, Ann. Phys. (N.Y.) **123**, 185 (1979).
[11] J. Ballot and M. Fabre de la Ripelle, Ann. Phys. (N.Y.) **127**, 62 (1980).
[12] M.M. Giannini, E. Santopinto, and A. Vassalo, arXinv:nucl-th/0302019, 2003; arXinv:nucl-th/0310041 2003 (and references therein).
[13] M. De Sanctis, E. Santopinto, and M.M. Giannini, Eur. Phys. J. A **2**, 403 (1998).
[14] D. Eyre and J.P. Vary, Phys. Rev. D **34**, 3467 (1986).
[15] H. Hersbach, Phys. Rev D **47**, 3027 (1993).
[16] E.H. de Groot and Th. W. Ruijgrok, Nucl. Phys. **B101**, 95 (1975); Th. W. Ruijgrok, Acta. Phys. Pol. B **7**, 43 (1976); Th. W. Ruijgrok and E.H. de Groot, Acta Phys. Pol. B **17**, 365 (1986).
[17] M. Hammermesh, Group Theory (Addison Wesley, Reading, Massachusetts, 1963).
[18] F.E. Close, An Introduction to Quarks and Partons (Academic Press, 1979).
[19] W. Böttger, A. Casel, and W. Sandhas, Phys. Lett. B **92**, 11 (1980).
[20] G. Ellerkmann, PhD thesis, Bonn Univ., 1995.
[21] R. Brizolara and M.M. Giannini, Few–body Systems **3**, 49 (1987); **5**, 1 (1988).
[22] J.M. Eisenberg and W. Greiner, Excitation Mechanisms of the Nucleus (Amsterdam, North Holland, 1970).
[23] C. Becchi and G. Morpurgo, Phys. Lett. **17**, 352 (1965).
[24] R.H. Dalitz and D. Sutherland, Phys. Rev. **146**, 1180 (1966).
[25] F. Zernike and H.C. Brinkman, Proc. K. Ned. Akad. Wet. **33**, 3 (1935).
[26] G.N. Watson, A Treatise on the Theory of Bessel Functions (Cambridge University Press, 2nd edition, 1944).
[27] Higher Transcendental Functions, Volume I, edited by A. Erdélyi et al, (Robert E. Krieger, reprint edition, 1985).
[28] M. Fabre de la Ripelle, Phys. Lett. B **199**, 267 (1987).
[29] D.B. Lichtenberg and L.J. Tassie, Phys. Rev. **155**, 1601 (1967).
[30] S. Ono, F. Schöberl, Phys. Lett. **118B**, 419 (1982); F. Schöberl, P. Falkensteiner, and S. Ono, Phys. Rev. D **30**, 603 (1984).
[31] B. Silvestre-Brac, Few-Body Systems **20**, 1 (1996).
[32] T.A. Armstrong, et al., Nucl. Phys. B **41**, 445 (1972).
[33] N. Isgur and G. Karl, Phys. Rev. D **18**, 4187 (1978); D **19**, 2653 (1979).

Adiabatic Movement of Three Charged Particles in Continuum at Astrophysical Conditions

V.B. Belyaev[1],* S.B. Levin[2], and E. Truhlík[3]

[1] *N.N Bogolyubov Laboratory of Theoretical Physics, Joint Institute for Nuclear Research, Dubna 181980, Russia*

[2] *V.A. Fock Institute of Physics, St. Petersburg State University, St Petersburg, Russia and*

[3] *Institute of Nuclear Physics, Academy of Sciences of the Czech Republic, Řež CZ–250 68, Czech Republic*

A treatment of three charged particle systems in continuum, based on the Coulomb-Fourier transformation of the three-particle Hamiltonian, is presented. For systems with two heavy and one light particle an adiabatic expansion is developed and applied to the description of electron capture in the process

$$\mathrm{p} + \mathrm{e} + {}^7\mathrm{Be} \to {}^7\mathrm{Li} + \mathrm{p} + \nu$$

which is thought to occur at the center of Sun.

I. INTRODUCTION

The quantitative description of systems with three charged particles in the continuum at low energies is still difficult. Hamiltonians of such a systems are very far from being hypercentral and thus hyperspherical harmonics expansions have, in general, a bad convergence. Apart from that, the Sommerfeld parameter $\eta = Z_1 Z_2 e^2/\hbar v$ is usually greater than 1 and this creates additional difficulties. Indeed, only some special cases with specific properties of the system have been considered in the literature. In this respect one should mention the papers [1, 2] where the asymptotic solution for the three-body wave function has been obtained for configurations where all interparticle distances are much larger than the characteristic size of the system. An alternative limiting case, considered in [3], corresponds to configurations where one Jacobi coordinate is much larger than the other one. The near threshold breakup of hydrogen by a proton (or electron), studied in [4], is yet another example of an approximate solution of the three body Schrödinger equation obtained so far for three charged particles in the continuum.

Our purpose is to develop a new adiabatic expansion for a three-body Hamiltonian for a system consisting of one light and two heavy particles. For this, we use the Coulomb-Fourier (CF) transform formalism proposed in [6] to make a unitary transformation of the Hamiltonian, which leads to a convenient representation, in which one long-range interaction is eliminated. The explicit form of the obtained eigenfunctions allows us to construct a useful integral representation of the interaction potentials for the transformed Hamiltonian. The important feature of this representation for potentials is the appearance of a universal integral with the integrand containing an exponential factor which is proportional to the square root of mass ratio $\tau \sim \sqrt{m_e/m_p}$ of light (electron) and heavy (proton) particles. The natural power series in τ of this integral generates a power series representation of the transformed Hamiltonian which is the basis for our new variant of the adiabatic representation of the problem [5].

*Electronic address: belyaev@theor.jinr.ru

II. EXPANSION FOR THE THREE-BODY HAMILTONIAN

In what follows we use units such that $\hbar = c = 1$ and for the unit electric charge the symbol e is used. Three-dimensional vectors are denoted by $\mathbf{x}, \mathbf{y}, \mathbf{k}, \mathbf{p}, \ldots$ and thir magnitudes and respective unit vectors by $x, y, k, p, \ldots$ and by $\hat{\mathbf{x}}, \hat{\mathbf{y}}, \hat{\mathbf{k}}, \hat{\mathbf{p}}, \ldots$. Sometimes we combine pairs of three-dimensional vectors and six-dimensional ones. These are denoted by, for example, $\mathbf{X} = \{\mathbf{x}, \mathbf{y}\}$ and $\mathbf{P} = \{\mathbf{k}, \mathbf{p}\}$. The Hilbert space of functions depending on vectors $\mathbf{X}$, which in our paper play the role of configuration space vectors, will be denoted by $\mathcal{H}$. The Hilbert space $\hat{\mathcal{H}}$ will be associated with functions depending on momentum variables $\mathbf{P}$.

Consider the *ppe* system, where p is proton of mass m_p and e is electron of mass m_e ($m_p \gg m_e$). We assign the number 1 to the electron, and 2, 3 to the protons. The Hamiltonian of the system in the center of mass frame, using mass-renormalized Jacobi coordinates, can then be written as

$$H = -\Delta_{\mathbf{x}_1} - \Delta_{\mathbf{y}_1} + V_s(x_1) + \frac{n_1}{x_1} + \frac{n_2}{x_2} + \frac{n_3}{x_3}\,.$$

Here $V_s(x_1)$ is a short-range potential describing strong *pp* interaction. Mass-renormalized charge factors n_i are defined by the formulas $n_i = e_j e_k \sqrt{2\mu_{jk}}$, where $e_1 = -e$, $e_2 = e_3 = e$ are the charge of the electron and proton and μ_{ij} stands for the reduced mass of a pair of particles ij, i.e. $\mu_{ij} = m_i m_j/(m_i + m_j)$. Introducing proton and electron masses into this formula we get $\mu_{23} = m_p/2$, $\mu_{31} = m_e m_p/(m_e + m_p)$, $\mu_{12} = \mu_{31}$.

Before proceeding further, let us make three clarifying comments. First, throughout the paper we systematically use a convention that indices of any pair of particles ij are considered as a part of triad ijk which itself is a cyclic permutation of $1, 2, 3$. Second, we define the mass-renormalized Jacobi set $\mathbf{x}_i$, $\mathbf{y}_i$ in such a way that the vector $\mathbf{x}_i$ up to the factor $\sqrt{2\mu_{jk}}$ is proportional to the relative position vector of particles j and k and the vector $\mathbf{y}_i$ is the position vector of particle i with respect to the center of mass of corresponding two-body sybsystem. There are three possible sets $\mathbf{x}_i$, $\mathbf{y}_i$, $i = 1, 2, 3$ and different sets are related to each other by the kinematic rotation matrix elements

$$\begin{aligned} \mathbf{x}_i &= c_{ij}\mathbf{x}_j + s_{ij}\mathbf{y}_j \\ \mathbf{y}_i &= -s_{ij}\mathbf{x}_i + c_{ij}\mathbf{y}_j \end{aligned} \tag{1}$$

with coefficients being defined in terms of particle masses by the formulas

$$c_{ij} = -\sqrt{\frac{m_i m_j}{(m_i + m_k)(m_j + m_k)}}, \tag{2}$$

$s_{ij} = \epsilon_{ijk}\sqrt{1 - c_{ij}^2}$, where ϵ_{ijk} is fully antisymmetric tensor normalized as $\epsilon_{123} = 1$. Third, in all mass factors we keep general situation, i.e. not neglecting m_e with respect to m_p, making sometimes simplifications for illustrative purposes, as for example $\mu_{31} = m_e m_p/(m_e + m_p) = m_e(1 + O(m_e/m_p))$.

Let us now turn to the solution of the Schrödinger equation

$$H\Psi = E\Psi \tag{3}$$

for three particles in the continuum ($E > 0$). For this we will construct a special representation in which the basis consists of eigenfunctions $\Psi_{c0}(\mathbf{X}, \mathbf{P})$, $H_{c0}\Psi_{c0} = P^2\Psi_{c0}$, of the operator

$$H_{c0} = -\Delta_{\mathbf{x}_1} - \Delta_{\mathbf{y}_1} + \frac{n_1}{x_1}$$

with repulsive Coulomb potential i.e, $n_1 > 0$. It is obvious that this eigenfunction has the form

$$\Psi_{c\,0}(\mathbf{X},\mathbf{P}) = \psi^c_{\mathbf{k}_1}(\mathbf{x}_1)\psi^0_{\mathbf{p}_1}(\mathbf{y}_1)$$

where

$$\psi^0_{\mathbf{p}_1}(\mathbf{y}_1) = \frac{1}{(2\pi)^{3/2}}\mathrm{e}^{i\mathbf{p}_1\cdot\mathbf{y}_1} \tag{4}$$

is the normalized plane wave and

$$\psi^c_{\mathbf{k}_1}(\mathbf{x}_1) = \frac{1}{(2\pi)^{3/2}}\mathrm{e}^{i\mathbf{p}_1\cdot\mathbf{y}_1}\mathrm{e}^{-\pi\gamma_1/2}\Gamma(1+i\gamma_1)\Phi(-i\gamma_1,1,ik_1\xi_1) \tag{5}$$

is the normalized Coulomb wave function. The standard notations for Sommerfeld parameter $\gamma_1 = n_1/2k_1$, parabolic coordinate $\xi_1 = x_1 - \langle\mathbf{x}_1,\hat{\mathbf{k}}_1\rangle$, Gamma function $\Gamma(z)$, and Confluent Hypergeometric function $\Phi(a,c,z)$ have been used.

Using (5) we immediately obtain the transformed Hamiltonian $\hat{H}$,

$$\begin{aligned}\hat{H}(\mathbf{P},\mathbf{P}') \;\equiv\; & \langle\psi^0_{\mathbf{p}_1}\psi^c_{\mathbf{k}_1}|H|\psi^0_{\mathbf{p}'_1}\psi^c_{\mathbf{k}'_1}\rangle = (\mathbf{k}_1^2+\mathbf{p}_1^2)\delta(\mathbf{k}_1-\mathbf{k}'_1)\delta(\mathbf{p}_1-\mathbf{p}'_1)\\ & +\; \hat{v}_s(\mathbf{k}_1,\mathbf{k}'_1)\delta(\mathbf{p}_1-\mathbf{p}'_1) + W_2(\mathbf{P},\mathbf{P}') + W_3(\mathbf{P},\mathbf{P}')\end{aligned} \tag{6}$$

operating on CF-transformed wave function $\hat{\Psi}(\mathbf{P})$. Here the first term corresponds to the kinetic energy operator $\hat{H}_0 = \mathbf{k}_1^2 + \mathbf{p}_1^2$, $\hat{v}_s$ stands for the CF-transformed short-range *pp* interaction potential

$$\hat{v}_s(\mathbf{k}_1,\mathbf{k}'_1) = \langle\psi^c_{\mathbf{k}_1}|v_s|\psi^c_{\mathbf{k}'_1}\rangle = \int \mathrm{d}\,\mathbf{x}_1\,\psi^{c*}_{\mathbf{k}_1}(\mathbf{x}_1)\,v_s(\mathbf{x}_1)\,\psi^c_{\mathbf{k}'_1}(\mathbf{x}_1)$$

where $*$ means complex conjugation; W_j are Coulomb potentials n_j/x_j in CF representation. Note that the contribution from the n_1/x_1 potential has been eliminated by the CF transform. The functions $W_j(\mathbf{P},\mathbf{P}')$, $j = 2,3$ have the following structure

$$W_j(\mathbf{P},\mathbf{P}') = |s_{j1}|^{-3}\hat{v}^c_j(s^{-1}_{j1}(\mathbf{p}-\mathbf{p}'))\mathcal{L}_j(\mathbf{P},\mathbf{P}'),$$

where

$$\hat{v}^c_j(\mathbf{q}) = \frac{1}{2\pi^2}\frac{n_j}{|\mathbf{q}|^2}$$

is the familiar Fourier transform of Coulomb potential n_j/x_j and the functions $\mathcal{L}_j(\mathbf{P},\mathbf{P}')$, $j = 2,3$ are given by the integrals

$$\mathcal{L}_j(\mathbf{P},\mathbf{P}') = \lim_{\lambda\to+0}\int \mathrm{d}\,\mathbf{x}_1\,\mathrm{e}^{i\tau_j\langle\mathbf{x}_1,\mathbf{p}-\mathbf{p}'\rangle-\lambda|\mathbf{x}_1|}\psi^{c*}_{\mathbf{k}_1}(\mathbf{x}_1)\psi^c_{\mathbf{k}'_1}(\mathbf{x}_1). \tag{7}$$

The parameters τ_j, $j = 2,3$, have a kinematical origin and are represented in terms of kinematic rotation matrix elements (1) as

$$\tau_j = c_{j1}/s_{j1}.$$

Noting that $\tau_3 = -\tau_2$ which is the consequence of equality of heavy particles (protons) masses and using the definition (2) and the fact that $m_e \ll m_p$ we get

$$\tau_2 = \sqrt{m_e/2m_p}(1+O(m_e/m_p)),$$

which shows that τ_j are small. This allows us to expand the exponential factor in the integrand of (7) and obtain the general expression

$$\mathcal{L}_j(\mathbf{P},\mathbf{P}') = \delta(\mathbf{k}_1-\mathbf{k}_1') + \frac{i\tau_j}{1!}L^{(1)}(\mathbf{P},\mathbf{P}') + \frac{(i\tau_j)^2}{2!}L^{(2)}(\mathbf{P},\mathbf{P}') + \frac{(i\tau_j)^3}{3!}L^{(3)}(\mathbf{P},\mathbf{P}') + ... \qquad (8)$$

Here $L^{(l)}(\mathbf{P},\mathbf{P}')$ are integrals

$$L^{(l)}(\mathbf{P},\mathbf{P}') = \lim_{\lambda\to+0}\int \mathrm{d}\,\mathbf{x}_1\,\mathrm{e}^{-\lambda|\mathbf{x}_1|}\,\psi^{c*}_{\mathbf{k}_1}(\mathbf{x}_1)\langle\mathbf{x}_1,\mathbf{p}_1-\mathbf{p}_1'\rangle^l\,\psi^{c}_{\mathbf{k}_1'}(\mathbf{x}_1) \qquad (9)$$

which are independent of j. This last fact and the property $\tau_3 = -\tau_2$ leads to the following expansion for the sum of the CF transformed Coulomb potentials W_2+W_3, which contains only even power terms

$$W_2(\mathbf{P},\mathbf{P}')+W_3(\mathbf{P},\mathbf{P}') = \hat{v}^c_{\mathrm{eff}}(\mathbf{p}_1,\mathbf{p}_1')\left\{\delta(\mathbf{k}_1-\mathbf{k}_1') - \frac{\tau^2}{2!}L^{(2)}(\mathbf{P},\mathbf{P}') + \frac{\tau^4}{4!}L^{(4)}(\mathbf{P},\mathbf{P}') - \cdots\right\} \qquad (10)$$

where $\tau = |\tau_2|$. The quantity $\hat{v}^c_{\mathrm{eff}}(\mathbf{p}_1,\mathbf{p}_1')$ stands for the Coulomb potential corresponding to the interaction between the electron and effective particle with charge $2e$ and mass $2m_p$ and has the form

$$\hat{v}^c_{\mathrm{eff}}(\mathbf{p}_1,\mathbf{p}_1') = \frac{1}{2\pi^2}\frac{n_{\mathrm{eff}}}{|\mathbf{p}-\mathbf{p}'|^2} \qquad (11)$$

with $n_{\mathrm{eff}} = -2e^2\sqrt{2m_e} \sim -2e^2\sqrt{2m_e 2m_p/(m_e+2m_p)}$. Inserting (10) into (6) we arrive at the representation of the CF-transformed Hamiltonian $\hat{H}$ which plays a central role in the solution of the problem

$$\hat{H} = \hat{H}_0 + \hat{V}_s + \hat{V}^c_{\mathrm{eff}} + \tau^2\hat{W}. \qquad (12)$$

The kernels of the operators involved in (12) read

$$\begin{aligned}
\hat{H}_0(\mathbf{P},\mathbf{P}') &= \left(\mathbf{k}_1^2+\mathbf{p}_1^2\right)\delta(\mathbf{P}-\mathbf{P}'),\\
\hat{V}_s(\mathbf{P},\mathbf{P}') &= \hat{v}_s(\mathbf{k}_1,\mathbf{k}_1')\delta(\mathbf{p}_1-\mathbf{p}_1'),\\
\hat{V}^c_{\mathrm{eff}}(\mathbf{P},\mathbf{P}') &= \hat{v}^c_{\mathrm{eff}}(\mathbf{p}_1,\mathbf{p}_1')\delta(\mathbf{k}_1-\mathbf{k}_1')
\end{aligned}$$

and

$$\hat{W}(\mathbf{P},\mathbf{P}') = \hat{W}^{(0)}(\mathbf{P},\mathbf{P}') - \tau^2\hat{W}^{(2)}(\mathbf{P},\mathbf{P}') + \tau^4\hat{W}^{(4)}(\mathbf{P},\mathbf{P}') - \cdots, \qquad (13)$$

$$\hat{W}^{(l)}(\mathbf{P},\mathbf{P}') = \hat{v}^c_{\mathrm{eff}}(\mathbf{p}_1,\mathbf{p}_1')\frac{1}{l!}L^{(l)}(\mathbf{P},\mathbf{P}'), \qquad (14)$$

where in the last case we have factored out the small parameter τ^2 to show explicitly that the last term in (12) is as small as τ^2.

The structure of the Hamiltonian (12) now suggests the natural perturbative scheme for solving the Schrödinger equation (3). Let us represent the wave-function $\hat{\Psi}$ as power series in τ^2, i.e.

$$\hat{\Psi} = \hat{\Psi}_0 + \tau^2\hat{\Psi}_2 + \tau^4\hat{\Psi}_4 + \cdots. \qquad (15)$$

Inserting (15) into (3) one obtains a recursive set of equations for $\hat{\Psi}_k$, namely

$$\left(\hat{H}_0 + \hat{V}_s + \hat{V}^c_{\mathrm{eff}}\right)\hat{\Psi}_0 = E\hat{\Psi}_0\,, \qquad (16)$$

$$\left(\hat{H}_0 + \hat{V}_s + \hat{V}^c_{\rm eff}\right)\hat{\Psi}_{2l} = E\hat{\Psi}_{2l} - \sum_{s=0}^{l-1}(-1)^{l-s}\,\hat{W}^{(2l-2s)}\,\hat{\Psi}_{2s} \qquad l = 1, 2, 3, \ldots \tag{17}$$

The scheme (16) and (17) has the remarkable property that the solution of the three-body problem, within the framework of this scheme, can be obtained in terms of solutions of two-body problems. Indeed, Eq. (16) allows the separation of variables, so that its solution is reduced to the solution of the respective two-body equations, at the same time the solution of the inhomogeneous equations (17) can be obtained in terms of Green's function of the operator $\hat{H}_0 + \hat{V}_s + \hat{V}^c_{\rm eff}$ which can be constructed from two-body Green's functions due to separability of variables.

For the specific case of three particles in the continuum the above scheme yields the following results. The solution of the first equation (16) reads

$$\hat{\Psi}_0(\mathbf{P}, \mathbf{P}^{\rm in}) = \hat{\psi}^+_{\mathbf{k}_1^{\rm in}}(\mathbf{k}_1)\,\hat{\psi}^{c\,e}_{\mathbf{p}_1^{\rm in}}(\mathbf{p}_1), \tag{18}$$

where the initial state momentums $\mathbf{k}_1^{\rm in}$ and $\mathbf{p}_1^{\rm in}$ are related to the energy E by the formula $\mathbf{P}^{\rm in\,2} = \mathbf{k}_1^{\rm in\,2} + \mathbf{p}_1^{\rm in\,2} = E$. The function $\hat{\psi}^{c\,e}_{\mathbf{p}_1^{\rm in}}(\mathbf{p}_1)$ is the momentum space Coulomb wave function corresponding to the potential $\hat{v}^c_{\rm eff}(\mathbf{p}_1, \mathbf{p}_1')$. The inverse Fourier transform of $\psi^{c\,e}_{\mathbf{p}_1^{\rm in}}(\mathbf{p}_1)$ we will denote by $\psi^{c\,e}_{\mathbf{p}_1^{\rm in}}(\mathbf{y}_1)$ whose explicit form can be obtained from (5) when $n = n_{\rm eff}$ and by replacing $\mathbf{k}_1^{\rm in}, \mathbf{x}_1$ by $\mathbf{p}_1^{\rm in}, \mathbf{y}_1$, respectively. The term $\hat{\psi}^+_{\mathbf{k}_1^{\rm in}}(\mathbf{k}_1)$ is the scattering solution to the two-body Schrödinger equation with the potential $\hat{v}_s(\mathbf{k}_1, \mathbf{k}_1')$ and is conventionally represented as the solution of the Lippmann-Schwinger integral equation

$$\hat{\psi}^+_{\mathbf{k}^{\rm in}}(\mathbf{k}) = \delta(\mathbf{k} - \mathbf{k}^{\rm in}) - \frac{1}{\mathbf{k}^2 - \mathbf{k}^{\rm in\,2} - i0}\int \mathrm{d}\,\mathbf{q}\,\hat{v}_s(\mathbf{k}, \mathbf{q})\,\hat{\psi}^+_{\mathbf{k}^{\rm in}}(\mathbf{q}). \tag{19}$$

The solutions of the inhomogeneous equations (17) are given by recursive formulas starting from $\hat{\Psi}_0(\mathbf{P}, \mathbf{P}^{\rm in})$,

$$\hat{\Psi}_{2l} = -\hat{G}_{s,eff}(E + i0)\sum_{s=0}^{l-1}(-1)^{l-s}\,\hat{W}^{(2l-2s)}\,\hat{\Psi}_{2s}. \tag{20}$$

Here the kernel of the operator $\hat{G}_{s,\rm eff}(z) = \left(\hat{H}_0 + \hat{V}_s + \hat{V}^c_{\rm eff} - z\right)^{-1}$ is represented by two-body Green's functions $\hat{g}_s$ for the potential $\hat{v}_s$ and $\hat{g}^c_{\rm eff}$ for the potential $\hat{v}^c_{\rm eff}$, by the counter integral

$$\hat{G}_{s,\rm eff}(\mathbf{P}, \mathbf{P}', z) = \frac{1}{2i\pi}\oint_C \mathrm{d}\,\zeta\,\hat{g}_s(\mathbf{k}_1, \mathbf{k}_1', \zeta)\hat{g}^c_{\rm eff}(\mathbf{p}_1, \mathbf{p}_1', z - \zeta)$$

with counter C encircling the cut of $\hat{g}_s$ in anticlockwise direction.

So far, we have constructed the formal solution to the CF transformed Schrödinger equation for the system *ppe* in the continuum. The configuration space wave function which obeys (3) can be obtained from $\hat{\Psi}$ by the CF transform

$$\Psi(\mathbf{X}, \mathbf{P}^{\rm in}) = \int \mathrm{d}\,\mathbf{P}\,\Psi_{c\,0}(\mathbf{X}, \mathbf{P})\,\hat{\Psi}(\mathbf{P}, \mathbf{P}^{\rm in}). \tag{21}$$

One can see, that the structure of our solution (15) and respective series in τ^2 for $\Psi(\mathbf{X}, \mathbf{P}^{\rm in})$ generated from (21) by (15) and the structure of the representation for the Hamiltonian (12) outline the framework of our approach as an alternative to the Born-Oppenheimer approach. It is worth mentioning here, that the formalism given above is rather general. With minor

self-evident modifications it is applicable to any three charged particle systems with different masses, as long as the mass of one particle is significantly smaller than the masses of the other two.

Before proceeding further, let us give some explicit approximate formulas the wave function, $\Psi(\mathbf{X}, \mathbf{P}^{\rm in})$ generated by our complete formal solution. (We will use these formulas in the next section where we discuss astrophysical reactions.) Introducing (18) and (20) into (21) we get

$$\Psi(\mathbf{X}, \mathbf{P}^{\rm in}) = \psi^{+}_{\mathbf{k}_1^{\rm in}}(\mathbf{x}_1)\, \psi^{c\,e}_{\mathbf{p}_1^{\rm in}}(\mathbf{y}_1) + \tau^2 \Psi_2(\mathbf{X}, \mathbf{P}^{\rm in}) + O(\tau^4) \tag{22}$$

where

$$\psi^{+}_{\mathbf{k}_1^{\rm in}}(\mathbf{x}_1) = \int \mathrm{d}\,\mathbf{k}_1 \psi^{c}_{\mathbf{k}_1}(\mathbf{x}_1)\, \hat{\psi}^{+}_{\mathbf{k}_1^{\rm in}}(\mathbf{k}_1)$$

and $\Psi_2(\mathbf{X}, \mathbf{P}^{\rm in})$ is given by the transform (21) of $\hat{\Psi}_2$ calculated through $\hat{\Psi}_0$ from (18) using

$$\hat{\Psi}_2 = -\hat{G}_{e,\rm eff}(E + i0)\, \hat{W}^{(2)}\, \hat{\Psi}_0. \tag{23}$$

It is possible to show, that $\Psi_2(\mathbf{X}, \mathbf{P}^{\rm in})$ has the following asymptotic form

$$\Psi_2(\mathbf{X}, \mathbf{P}^{\rm in}) \sim \mathcal{A}(\mathbf{x}, \mathbf{k}^{\rm in}, \mathbf{p}^{\rm in}, \hat{\mathbf{y}}) \frac{\exp\left\{ip^{\rm in} y - i\dfrac{n_{\rm eff}}{2p^{\rm in}} \log 2p^{\rm in} y\right\}}{4\pi y} \left(1 + O\left(y \frac{k^{\rm in}}{p^{\rm in}}\right)\right) \tag{24}$$

where the amplitude $\mathcal{A}$ has the explicit form

$$\mathcal{A}(\mathbf{x}, \mathbf{k}^{\rm in}, \mathbf{p}^{\rm in}, \hat{\mathbf{y}}) = -\frac{1}{2} N_{\rm eff}\, \psi^{c}_{\mathbf{p}^{\rm in}}(0)\; \frac{\partial^2}{\partial t^2} \left[t^2 \mathcal{L}^{(2)}(t, k^{\rm in})\, \psi^{c}_{t\hat{\mathbf{k}}^{\rm in}}(\mathbf{x})\, \psi^{ce*}_{-\sqrt{E-t^2}\hat{\mathbf{y}}}(0)\right]\Big|_{t=k^{\rm in}}$$

The order of terms $O\left(y\, k^{\rm in}/p^{\rm in}\right)$ shows the range of validity of the asymptotics (24), i.e. $y\, k^{\rm in}/p^{\rm in}$ has to be small, which in terms of masses, must be equivalent to the fact that $y\tau^2$ has to be small. Let us emphasize that the above treatment is devoted to three charged particles with kinetic energies comparable to the corresponding potential energy. This means that Coulomb interactions are essential. In this situation, and for systems consisting of heavy and light particles, one can develop the adiabatic description, which actually means small ratio of heavy and light particles momenta $k^{\rm in}/p^{\rm in}$.

III. ASTROPHYSICAL EXAMPLES AND RESULTS

Let us apply the above analysis to the process of electron capture by ^{7}Be nucleus in the center of Sun. This process is important since it contributes to the low energy part of the spectrum of neutrinos radiated by the Sun. Besides, it is obvious that the balance of the disappearance channels of ^{7}Be in the Sun regulates the amount of the nucleus ^{8}B which is the source of the high energy solar neutrinos. This is the main reason why this process attracted considerable attention over many years [7–13].

Practically all the discussion so far, of the electron capture in ^{7}Be, concentrated on the electron wave function in the vicinity of the nucleus and on the screening effects on it (a study of this capture in the plasma can be found in Ref. [13]).

In what follows we will estimate the role of the process that is usually not included in the standard theory of the *pp* cycle in the Sun. Let us first note that in the standard theory of this cycle the destruction of the nucleus ^{7}Be takes place in the following binary reactions

$$\mathrm{p} + {}^7\mathrm{Be} \;\rightarrow\; {}^8\mathrm{B} + \gamma\,, \tag{25}$$

$$\mathrm{e}^- + {}^7\mathrm{Be} \;\rightarrow\; {}^7\mathrm{Li} + \nu\,. \tag{26}$$

Since the nucleus ^{7}Be participates in both processes, instead of the binary reactions (25) and (26) we consider the contribution to the electron capture rate from the three-particle initial state $\mathrm{p} + \mathrm{e}^- + {}^7\mathrm{Be}$. In this case the following reactions can take place

$$\begin{aligned} & \nearrow \ {}^7\mathrm{Li} + \nu + \mathrm{p}\,, && (27)\\ \mathrm{p} + \mathrm{e}^- + {}^7\mathrm{Be} \ & \rightarrow \ {}^8\mathrm{B} + \gamma + \mathrm{e}^-\,, && (28)\\ & \searrow \ {}^8\mathrm{B} + \mathrm{e}^-\,. && (29) \end{aligned}$$

As it was shown in Ref. [8] the screening corrections for the electrons in the continuum are rather small. Therefore, we consider in the initial state the bare Coulomb interaction in all two-body subsystems $e^- + p$, $\mathrm{p} + {}^7\mathrm{Be}$, and $\mathrm{e}^- + {}^7\mathrm{Be}$. In this case one can immediately realize that there is a qualitative difference between the binary and ternary mechanisms[1] of the electron capture. Indeed, if one starts from the three-body initial state, then the processes (25) and (26) should be interdependent because the wave function of three charged particles cannot be presented as a product of pair wave functions, as is required by the binary processes (25) and (26)[2].

As shown above, the continuum wave function of three charged particles can be expanded in terms of a small parameter

$$\epsilon \ = \ \left[\frac{M m_e}{(M+m_p)(m_p+m_e)}\right]^{1/2} \ \approx \ \left[\frac{m_e}{m_p}\right]^{1/2}\,, \qquad (30)$$

where in addition to the electron mass, proton mass, and M, the mass of the nucleus ^{7}Be enters. The expansion of the wave function of the system under consideration is then

$$\Psi(\vec{r},\vec{R}) \ \approx \ \Psi_0(\vec{r},\vec{R}) \ + \ \epsilon\,\Psi_1(\vec{r},\vec{R}) \ + \ \cdots\,. \qquad (31)$$

Since the parameter $\epsilon \approx 0.0233$ one expects the effects of the second term on the right hand side of Eq. (31) to be of the order of 2% in comparison with the first term.

It was found in [15] that, in the limit $\epsilon \ \rightarrow \ 0$, the Jacobi coordinates $\vec{r}$ and $\vec{R}$ (see Fig. 1) separate. It means that the structure of the wave function $\Psi_0(\vec{r},\vec{R})$ is given by

$$\Psi_0(\vec{r},\vec{R}) \ = \ \Psi^C(\vec{R})\,\Psi^C(\vec{r}, Z = Z_1 + Z_2)\,, \qquad (32)$$

where $\Psi^C(\vec{R})$ is the Coulomb wave function describing the relative motion of the proton and the nucleus ^{7}Be and $\Psi^C(\vec{r}, Z = Z_1 + Z_2)$ is the Coulomb wave function that describes the motion of the electron in the field of the effective Coulomb potential of the charge $Z = Z_1 + Z_2$. The crucial point is that the wave function $\Psi^C(\vec{r}, Z = Z_1 + Z_2)$ depends on the distance between the electron and the center of mass of the subsystem of heavy particles. Thus even if the distance between the electron and the nucleus ^{7}Be is zero, as is required by the Hamiltonian of the weak interaction, the wave function $\Psi^C(\vec{r}, Z = Z_1 + Z_2)$, defining the probability of the electron capture by the nucleus ^{7}Be, should be taken at a non-zero distance $|\vec{r}| = \beta|\vec{R}|$, where $\beta = 1/7$ is the ratio of the proton and ^{7}Be masses.

It is clear that this phenomenon appears due to the electron movement in the Coulomb field of two charged particles with positive charges. Following the arguments presented above we now consider two effects which are manifested in opposite directions. On the one hand, increasing

[1] We use the terms binary- and ternary- reactions as synonyms for the reactions in the two- and three- qe component systems.

[2] There is only one exception corresponding to the case when all three particles are at very large distances between themselves [14], which is not applicable to the electron capture.

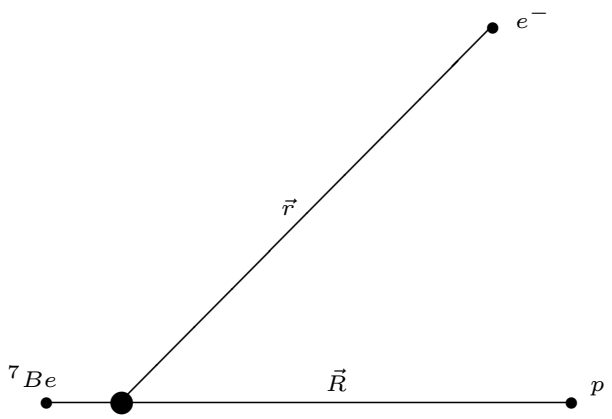

FIG. 1: The Jacobi coordinates for the $\mathrm{p} + \mathrm{e}^- + {}^7\mathrm{Be}$ system.

the effective positive charge of the heavy particles system by one unit will enlarge the electron capture rate. On the other hand, using the Coulomb wave function at finite distances, instead of the function taken at zero distance, should damp the capture rate.

Taking into account that the nuclear matrix elements of the reactions (26) and (27) are the same, as a measure of influence of the third particle (the proton in this case) on the capture rate of electrons by the nuclei ^{7}Be, we introduce the ratio $\varsigma(R,T)$ which is a function of the distance R between the particles and the temperature T,

$$\varsigma(R,T) \;=\; \frac{\displaystyle\int_0^\infty |\Psi_E^C(\beta R, Z=5)|^2\, \mathrm{e}^{-E/kT}\, \mathrm{d}\, E}{\displaystyle\int_0^\infty F(Z=4,\nu)\, \mathrm{e}^{-E/kT}\, \mathrm{d}\, E}\,. \tag{33}$$

The denominator in Eq. (33) contains the quantity that enters the electron capture rate from the continuum for the reaction (26) [7]. $F(Z,\nu)$ is the Fermi function given by

$$F(Z,\nu) \;=\; \frac{2\pi\nu}{\mathrm{e}^{2\pi\nu}-1}\,, \tag{34}$$

which is obtained from the solution of the Dirac equation with the Coulomb potential [16]. Here the parameter ν is given by $\nu = -Z\alpha\, m_e/p = -Z\alpha/v$, α is the fine structure constant, and $p = \sqrt{2m_e E}$ is the electron momentum.

Analogously the integral in the numerator should reflect the effect of the Coulomb potential on the electron in the continuum for the reaction (27). For the wave function $\Psi_E^C(\vec{r},Z)$, we use the Coulomb continuum wave function for the state with zero angular momentum

$$\Psi_E^C(\rho) \;=\; \frac{F_0(\eta,\rho)}{\rho} \tag{35}$$

where the function $F_0(\eta,\rho)$ satisfies the equation

$$\frac{\mathrm{d}\,^2 F_0}{\mathrm{d}\,\rho^2} \;+\; [\,1 \;-\; \frac{2\eta}{\rho}\,]\, F_0 \;=\; 0\,, \tag{36}$$

with $\rho = p\beta R$, and $\eta = -Z\alpha\sqrt{m_e/E} = -Z\alpha\sqrt{2}/v$ is the Sommerfeld parameter. The function $F_0(\eta,\rho)$ can be expressed in terms of the Kummer function M (see Ref. [17], Ch. 14) as

$$F_0(\eta,\rho) \;=\; C_0(\eta)\, \rho\, \mathrm{e}^{-i\rho}\, M(1-i\eta, 2, 2i\rho)\,, \tag{37}$$

where $C_0^2(\eta) = 2\pi\eta/(e^{2\pi\eta} - 1)$.

Instead of the quantity $\varsigma(R,T)$, one can consider

$$\varsigma_C(R,T) \;=\; \frac{\displaystyle\int_0^\infty |\Psi_E^C(\beta R, Z=5)|^2\, \mathrm{e}^{-E/kT}\, \mathrm{d}\, E}{\displaystyle\int_0^\infty |\Psi_E^C(0, Z=4)|^2\, \mathrm{e}^{-E/kT}\, \mathrm{d}\, E}\,. \tag{38}$$

Using Eq. (36), one obtains

$$|\Psi_E^C(0,Z)|^2 \;= \frac{2\pi\eta}{\mathrm{e}^{2\pi\eta} - 1}\,, \tag{39}$$

which is of the same form as the Fermi function (34) with $\eta = \sqrt{2}\nu$. For the Kummer function one can use the following integral representation (see Ref. [17], Ch. 13)

$$M(1 - i\eta, 2, 2i\rho) \;=\; \frac{sh\pi\eta}{\pi\eta} \int_0^1 \mathrm{e}^{2i\rho t} \left(\frac{1-t}{t}\right)^{it} \mathrm{d}\, t\,. \tag{40}$$

In the numerical calculations of the integral over energy in Eqs. (33) and (38), we used this representation of the Kummer function for energies $E > 0.1\,\mathrm{keV}$. For energies $E < 0.1\,\mathrm{keV}$, the function under the integral in Eq.(40) strongly oscillates which makes the calculations difficult. Instead of it we applied the program PFQ developed in Ref. [18]. Let us note that for energies $E > 0.1\,\mathrm{keV}$ the program PFQ and Eq. (40) provide the same results to a high degree of accuracy.

We also introduce the mean value $\langle\varsigma(R_0,T)\rangle$ of the function $\varsigma(R,T)$

$$\langle\varsigma(R_0,T)\rangle = N \int \mathrm{e}^{-(R-R_0)^2/2R_0^2} \varsigma(R,T) \mathrm{d}\, \vec{R} = 4\pi R_0^3 N \int_0^\infty \mathrm{e}^{-(x-1)^2/2}\, x^2\, \varsigma(R_0 x, T) \mathrm{d}\, x \tag{41}$$

where

$$N^{-1} = \int \mathrm{e}^{-(R-R_0)^2/2R_0^2} \mathrm{d}\, \vec{R} = \frac{4\pi R_0^3}{\sqrt{e}} [\,1 \,+\, \sqrt{2\pi e}\,(\,1 \,-\, \phi(-\frac{1}{\sqrt{2}})\,)\,]\,, \tag{42}$$

is the normalization constant. In Eq. (42), the function $\phi(y)$ is the error function (see Ref. [17], Ch. 7). It is seen from Eq. (41) that the quantity $\langle\varsigma(R_0,T)\rangle$ depends on the mean distance R_0 between the particles defined by the density in the Sun and on the temperature T. The mean value $\langle\varsigma_C(R_0,T)\rangle$ is defined analogously by using $\varsigma_C(R,T)$.

We checked the precision of numerical calculations of the quantities $\langle\varsigma(R_0,T)\rangle$ and $\langle\varsigma_C(R_0,T)\rangle$ by using Mathematica and also independent numerical procedures. The results of these two independent ways of calculations agree within the required accuracy of $\sim 0.1\,\%$.

The results of the calculations are presented in Table I and in Figs. 2–4. In Fig. 2, the dependence of the mean value $\langle\varsigma(R_0,T)\rangle$ as given by Eq. (41), on the temperature T and the mean distance R_0 is shown. A weak dependence of $\langle\varsigma(R_0,T)\rangle$ on T means, according to Eq. (33), that the temperature dependence of the electron capture by ^{7}Be is almost the same for the ternary and binary reactions. Such a behavior can be understood from the fact that in both cases only rarely all the kinetic energy is carried by the electron. On the other hand, the dependence of $\langle\varsigma(R_0,T)\rangle$ on the value of R_0 shows that the contribution to the capture rate of the ternary reaction is presumably suppressed in stars, but that it can be at the same level as the contribution to the capture rate for the binary reaction or even prevail over it at very high densities. This is natural since at short distances between the particles, the factor of the larger effective charge acting on the electron will dominate. The same conclusion can be drawn from

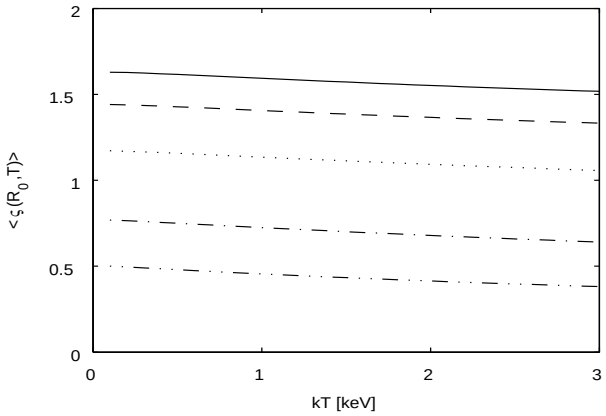

FIG. 2: Dependence of the mean value $\langle\varsigma(R_0,T)\rangle$ on the temperature T and the mean distance R_0. Solid line: $R_0 = 0.1\times10^4$ fm; dashed line: $R_0 = 0.25\times10^4$ fm; dotted line: $R_0 = 0.5\times10^4$ fm; dashed and dotted line: $R_0 = 1.0\times10^4$ fm; dashed and double dotted line: $R_0 = 1.5\times10^4$ fm.

Fig. 3. In this figure the solid and dashed curves practically coincide. This again shows a very smooth dependence of $\langle\varsigma(R_0,T)\rangle$ on the temperature.

Let us note that the values of the R_0, considered in Fig. 2, correspond to rather dense stars. For example, the value of $R_0 = 10^4$ fm corresponds to the proton density $\rho_p = 1673$ g/cm^3 which is about 11 times larger than in the center of the Sun. Let us further discuss the electron capture in the Sun by ^{7}Be alone. In Table I, we show the influence of the protons on the electron capture

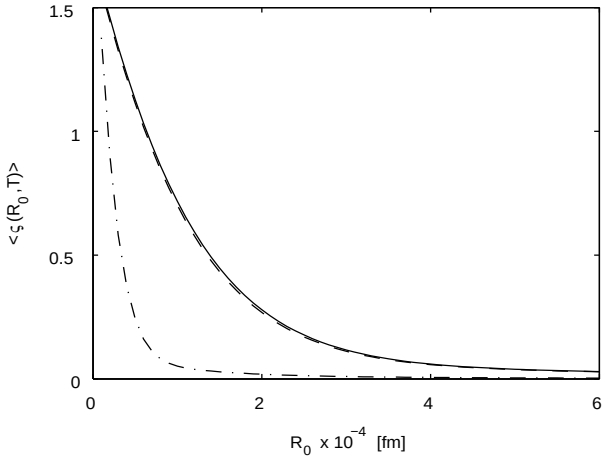

FIG. 3: The dependence of $\langle\varsigma(R_0,T)\rangle$ on the mean distance R_0; solid curve: $kT = 1.161$ keV, $\beta = 1/7$, $Z = 5$; dashed and dotted curve: $kT = 1.161$ keV, $\beta = 4/7$, $Z = 6$; dashed curve: $kT = 1.5$ keV, $\beta = 1/7$, $Z = 5$. The dashed and dotted curve corresponds to analogous calculations for the nuclei ^{4}He.

in the Sun in more detail. For the Standard Solar Model, we choose the model SSMBP2004 [19]. According to Fig. 6.1 of Ref. [20], the maximal intensity of the electron capture by the nuclei ^{7}Be takes place at distances $R_s/R_\odot \approx 0.06$, where $R_\odot$ is the radius of the Sun, and it drops to one half at $R_s/R_\odot \approx 0.03$ and $R_s/R_\odot \approx 0.1$. Using the data on the temperature, density, and the fraction of the hydrogen in this area of the Sun, we obtain the mean values $\langle\varsigma(R_0,T)\rangle$ and $\langle\varsigma_C(R_0,T)\rangle$ presented in Table 1. In the second column, we add the mean value calculated at $R_s/R_\odot = 0.007$ which is close to the center of the Sun. It is seen that the change of the average quantities $\langle\varsigma(R_0,T)\rangle$ and $\langle\varsigma_C(R_0,T)\rangle$ is very smooth. From the first row of Table I and from Fig. 4 one can see that the contribution to the capture rate of the ternary reaction at the Sun

TABLE I: The mean values $\langle\varsigma(R_0,T)\rangle$ and $\langle\varsigma_C(R_0,T)\rangle$ for the electron capture by nuclei ^{7}Be in the Sun.

$\langle\varsigma(R_0,T)\rangle$	0.0991	0.0991	0.0965	0.0913
$\langle\varsigma_C(R_0,T)\rangle$	0.0718	0.0717	0.0696	0.0658
$R_s/R_\odot$	0.007	0.03	0.06	0.1
kT [keV]	1.353	1.300	1.161	1.088
ρ_p [g/cm^3]	52.1	51.6	48.9	44.9
$R_0 \times 10^{-4}$ [fm]	3.179	3.188	3.250	3.340

is about 10 % of the binary one [3]. This means that it should increase sensibly the burning out of the nuclei ^{7}Be in comparison with the binary reaction, thus decreasing the concentration of the nuclei ^{8}B that appear after the capture of protons by ^{7}Be. As discussed by Gruzinov and Bahcall [13] (see Eq. (6) and the related discussion) the total electron capture rate should be calculated using a density enhancement factor w_{IKSBM} with the screening effects included. For $Z = 4$, this factor is $w_{IKSBM} = 3.85$ which is 16% smaller than its unscreened value $w = 4.59$. If one takes into account the 10 % enhancement discussed above, one obtains $w_{IKSBM} = 4.15$ and $w = 4.90$. Here we suppose that the screening effect is the same as for the binary reaction. This assumptions needs to be verified. However, such a study goes beyond the scope of this work.

Comparison of the first and second rows of Table I shows a difference of 3 % between the values of $\langle\varsigma(R_0,T)\rangle$ and $\langle\varsigma_C(R_0,T)\rangle$. This variation arises from the difference between the relativistic and non-relativistic estimations of the electron wave function at zero distance for the binary reaction (26).

In Fig. 4 we show the variation of $\langle\varsigma(R_0,T)\rangle$ for the reaction (27) for larger intervals of T and R_0. One can consider in analogy the influence of the nuclei ^{4}He on the electron capture

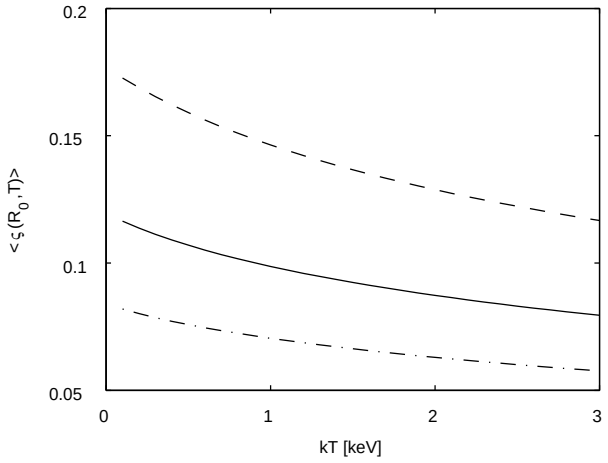

FIG. 4: The dependence of the mean value $\langle\varsigma(R_0,T)\rangle$ on the temperature T and the mean distance R_0. Solid line: $R_0 = 3.25 \times 10^4$ fm; dashed line: $R_0 = 2.75 \times 10^4$ fm; dashed and dotted line: $R_0 = 3.75 \times 10^4$ fm.

by ^{7}Be in the Sun. In this case, $Z = 6$, $\beta = 4/7$ and at the radius $R_s/R_\odot = 0.06$ the mean distance between the nuclei ^{4}He is $R_0 = 5.34 \times 10^4$ fm. Then one obtains from Eq. (41) that $\langle\varsigma(R_0,T)\rangle$=0.0036, which is about 27 times smaller that the analogous value of $\langle\varsigma(R_0,T)\rangle$ for the

[3] The next term in the expansion of Eq. (31) is expected to change it only by ≈ 2 %.

protons given in the fourth column of Table I. Evidently, this influence on the electron capture is negligible. This conclusion is also inferred from Fig. 3.

The main conclusion following from our calculations is that the three-body process due to the presence of the proton in the vicinity of the nucleus ^{7}Be will result in increasing the rate of the electron capture from the continuum by ^{7}Be in the Sun by $\approx 10\,\%$ and therefore, it will reduce the concentration of the nuclei ^{8}B that appear after the capture of protons by ^{7}Be.

---

[1] R.K. Peterkop, Zh. Eksp. Teor. Fiz **43**, 616 (1962) (in Russian) [Sov. Phys. JETP **14**, 1377 (1962)].
[2] S.P. Merkuriev, Theor. Math. Phys. **32**, 680 (1977); M. Brauner, J.S. Briggs, and H.J. Klar, J. Phys. B **22**, 2265 (1989).
[3] E.O. Alt, A.M. Mukhamedzhanov, JETP Lett. **56**, 435 (1992); Phys. Rev. A **47**, 2004 (1993); Y.E. Kim, A.L. Zubarev, Phys. Rev. A **56**, 521 (1997).
[4] J.H. Macek, S.Yu. Ovchinnikov, Phys. Rev. A **54**, 1 (1996); M.Yu. Kuchiev and V.N. Ostrovsky, Phys. Rev. A **58**, 321 (1998).
[5] V.B. Belyaev, S.B. Levin, S.L. Yakovlev, J. Phys. B **37**, 1369 (2004).
[6] E.O. Alt, S.B. Levin, and S.L. Yakovlev, Phys. Rev. C **69**, 034002, (2004); E.O. Alt, S.B. Levin, and S.L. Yakovlev, Few-Body Systems Suppl. **14**, 221 (2003); E.O. Alt, Few-Body Systems Suppl. **14**, 179 (2003); E.O. Alt, S.B. Levin, and S.L. Yakovlev, Book of Abstracts, Few Body 17, Durham 2003, p. 283, 287.
[7] J.N. Bahcall, Phys. Rev. **C 128**, 1297 (1962).
[8] J.N. Bahcall and C.P. Moeller, Astrophys. J. **155**, 511 (1969).
[9] L.S. Brown and R.F. Sawyer, Astrophys. J. **489**, 968 (1997).
[10] I. Iben, Jr., K. Kalata and J. Schwartz, Astrophys. J. **150**, 1001 (1967).
[11] C.W. Johnson, E. Kolbe, S.E. Koonin and K. Langanke, Astrophys. J. **392**, 320 (1992).
[12] W.D. Watson and E.E. Salpeter, Astrophys. J. **181**, 237 (1973).
[13] A.V. Gruzinov, J.N. Bahcall, Astrophys. J. **490**, 437 (1997).
[14] M. Brauner, J.S. Briggs, and H.J. Klar, J. Phys. B **22**, 2265 (1989).
[15] V.B. Belyaev, S.B. Levin and S.L. Yakovlev, J. Phys. B **37**, 1369 (2004).
[16] M. Morita, Beta Decay and Muon Capture (W.A. Benjamin, London, 1973).
[17] M. Abramowitz and I.E. Stegun, Handbook of Mathematical Functions, National Bureau of Standards, Applied Mathematics Series 55, (1964).
[18] W.F. Perger, A. Bhalla and M. Nardin, Comp. Phys. Comm. **77**, 249 (1993).
[19] J.N. Bahcall and M.H. Pinsonneault, Phys. Rev. Lett. **92**, 121301 (2004).
[20] J.N. Bahcall, Neutrino Astrophysics (Cambridge University Press, Cambridge, 1989).

Resonant States of the Three-body Systems Λnn and $\Lambda\Lambda n$

V.B. Belyaev[1,2], S.A. Rakityansky[1,2], and W. Sandhas[3]

[1] *Laboratory of Theoretical Physics, JINR, Dubna 141980, Russia*
[2] *Department of Physics, University of South Africa, P.O. Box 392, Pretoria 0003, South Africa*
[3] *Physikalisches Institut, Universitat Bonn, D-53115 Bonn, Germany*

The hypernuclear systems Λnn and $\Lambda\Lambda n$ are studied within the framework of the hyperspherical approach with local two-body S-wave potentials describing the nn, Λn, and $\Lambda\Lambda$ interactions. Possible bound and resonant states of these systems are sought as zeros of the corresponding three-body Jost functions on the complex energy surface. For both systems, it was found that zeros closest to the origin correspond to very wide near-threshold resonances. Bound states appear only if the potentials are multiplied by a factor of ~ 1.5. The positions of these zeros turned out to be sensitive to the choice of the Λn-potential.

I. INTRODUCTION

The Λ-hyperon belongs to a wide class of particles that are not in abundance in this world and therefore are not freely available for scattering experiments. The properties of their interaction with other particles are studied indirectly. For example, the most important and established way of studying the ΛN interaction consists in measuring and calculating the spectral properties of the so called Λ-hypernuclei [1–3], which are bound states of Λ-particles inside atomic nuclei. The most convenient for this purpose are very light nuclei with $A \lesssim 10$. Firstly, because such simple systems have simple spectra with only few well separated levels, and secondly, because they allow a reliable theoretical modeling based on rigorous few-body methods.

So, the ΛN-potentials are usually constructed in such a way that the calculations with these potentials reproduce experimentally known bound states of the hypernuclei. One may ask: What about scattering? Unfortunately, it is very difficult to do scattering experiments with the Λ-particles because of their short lifetime ($\sim 10^{-10}$ sec) and extremely low intensity of the beams that can be obtained.

It is well known that even when scattering data are available in full, it is impossible to construct an interaction potential in a unique way. One can always obtain different but phase-equivalent (generating the same scattering phase shifts) potentials (see, for example, Ref. [4]). In this respect the ΛN-case is beyond any hope since only few experimental points for the Λp scattering are available [5]. During the decades of studying hypernuclei many features of the ΛN-interaction have been revealed. However the comparison of the theoretical and experimental spectra remains inconclusive. Different potentials lead to almost the same spectra of the hypernuclei. So, we need an additional tool for testing the potentials.

In principle, such a tool could be based on studying the Λ-nucleus resonances, if they do exist [6, 7]. Indeed, while the scattering and bound states mostly reflect the on-shell properties of the interaction, the resonances strongly depend on its off-shell characteristics, which may be different for phase-equivalent potentials.

Our present work is an attempt to attract the attention of both theoreticians and experimentalists to the low-energy resonances in the Λ-nuclear systems. As an example, we consider the three-body systems Λnn and $\Lambda\Lambda n$ in the minimal approximation, $[L] = [L_{\min}]$, of the hyperspherical harmonic approach. By locating the S-matrix poles on the second (unphysical) sheet of the complex energy surface, we show that these systems have near-threshold resonant states. The position of the poles turns out to be strongly dependent on the choice of the ΛN-potential.

This fact supports the idea that the study of the Λ-nucleus resonances could be very important in finding an adequate ΛN-potential.

II. QUANTUM RESONANCES

There are several different ways of locating quantum resonances. The most adequate methods are based on the rigorous definition of resonances as the S-matrix poles at complex energies. This definition is universal and applicable to the systems involving more than just two colliding particles. Of course, the problem of locating the S-matrix poles is not an easy task, especially for few-body systems. There are different approaches to this problem. To the best of our knowledge, so far only one of them has been applied to study the hyperon-nucleus resonant states. This was done in Ref. [6] using an analytic continuation of the rigorous three-body equations proposed by Alt, Grassberger, and Sandhas [8] and known as the AGS-equations. In this paper, we follow a different approach based on the direct calculation of the Jost function using the method suggested in Ref. [9].

To begin with, let us consider a simple two-body system with a central short-range potential $U(r)$. The wave function describing such a system at a collision energy E obeys the Schrödinger equation, which after the partial wave decomposition reads

$$\left[\partial_r^2 + k^2 - \frac{\ell(\ell+1)}{r^2}\right] u_\ell(k,r) = V(r) u_\ell(k,r) \ , \tag{1}$$

where $V(r) = 2\mu U(r)$, μ is the reduced mass, and

$$k = \pm\sqrt{2\mu E} \tag{2}$$

is the relative momentum. At large distances the potential vanishes and the right hand side of Eq. (1) tends to zero. Therefore when $r \to \infty$, the general solution of this equation is a linear combination of the Riccati-Hankel functions $h_\ell^{(\pm)}(kr)$ that obey the free Schrödinger equation,

$$\left[\partial_r^2 + k^2 - \frac{\ell(\ell+1)}{r^2}\right] h_\ell^{(\pm)}(kr) = 0 \ . \tag{3}$$

From the asymptotic behavior of the Riccati-Hankel functions,

$$h_\ell^{(\pm)}(kr) \underset{|kr|\to\infty}{\longrightarrow} \mp i \exp\left[\pm i(kr - \ell\pi/2)\right] \ , \tag{4}$$

one can easily see that they describe incoming and outgoing spherical waves. Therefore, far away from the point $r = 0$, the general solution of Eq. (1) can be written as a linear combination of the incoming and outgoing waves,

$$u_\ell(k,r) \underset{r\to\infty}{\longrightarrow} f_\ell^{(\mathrm{in})}(E) h_\ell^{(-)}(kr) + f_\ell^{(\mathrm{out})}(E) h_\ell^{(+)}(kr) \ , \tag{5}$$

where $f_\ell^{(\mathrm{in/out})}(E)$ are the energy-dependent amplitudes of the waves. These amplitudes play an important role in the scattering theory and have a special name, the Jost functions [1]. The S-matrix is just their ratio,

$$S(E) = f_\ell^{(\mathrm{out})}(E) \left[f_\ell^{(\mathrm{in})}(E)\right]^{-1} \ . \tag{6}$$

[1] It should be mentioned that our notation $f_\ell^{(\mathrm{in/out})}(E)$ for the Jost functions (and generally Jost matrices) is different from the traditional notations. There are two reasons for this. First of all, we do not fix their normalization which can be chosen arbitrarily since it does not affect any observable quantities. Indeed, when

Actually, the Jost functions (and therefore the S-matrix) depend on the energy via the momentum (2). As a result there is a square-root branching point for these functions at the threshold energy $E = 0$. In simple words, the Jost function has two different values at each point E, corresponding to the two choices of the sign in front of the square root in Eq. (2). As is usual in the complex analysis, the Jost function becomes a single-valued function of the energy on the so-called Riemann surface consisting of two parallel sheets. The first one, where the momentum (by definition) has a positive imaginary part, is called the physical sheet. And the second sheet (where $\mathrm{Im}\, k < 0$) is called unphysical (see Fig. 1). When doing the first circle around the

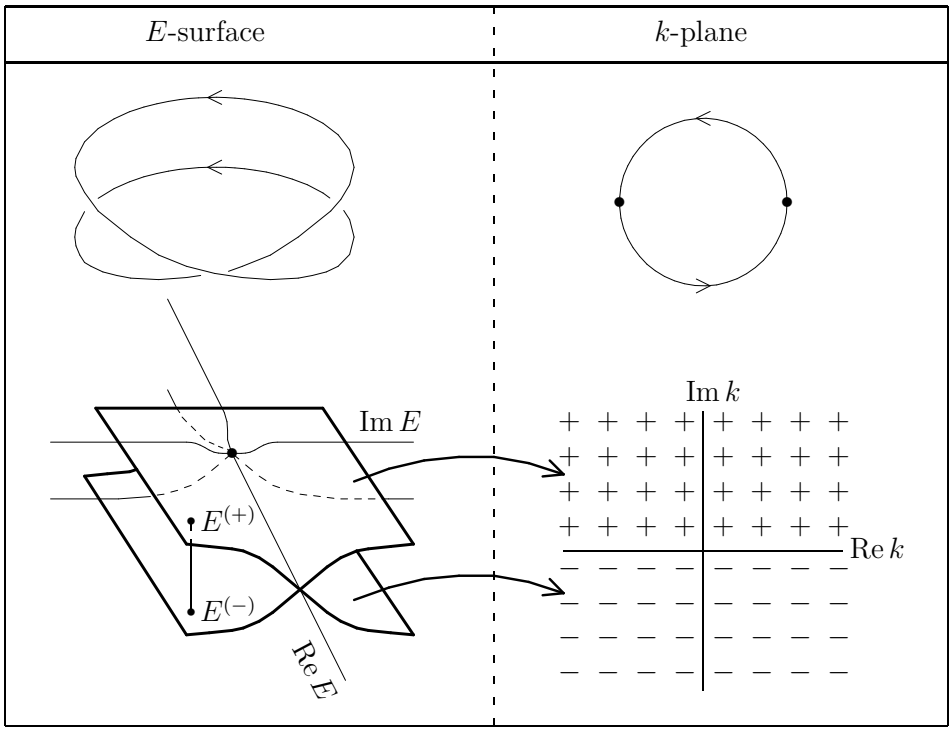

FIG. 1: Correspondence between the complex energy surface and the momentum plane. Any two points $E^{(+)}$ and $E^{(-)}$ situated one above the other, represent the same value of the energy, but correspond to different values of k and thus to different values of the Jost function.

branching point, we are moving on the first sheet and then continue on the second one until coming back to the first sheet after completing the full two circles. Such continuous transition from one sheet to another is possible if we make a cut from the branching point to infinity, and connect opposite rims of the cuts on the two sheets (see Fig. 1).

The asymptotic coefficients $f_\ell^{(\mathrm{in/out})}(E)$ that determine the long-range behavior (5) of the wave function $u_\ell(k, r)$, are not independent. They are the amplitudes of the incoming and outgoing waves which swap their roles when the momentum k changes its sign and also under

calculating observables, we either look for zeros of $f_\ell^{(\mathrm{in})}(E)$ or use the ratio of $f_\ell^{(\mathrm{out})}(E)$ and $f_\ell^{(\mathrm{in})}(E)$. The second reason is that the superscripts (in) and (out) are unambiguous since they clearly indicate which of these functions are the asymptotic amplitudes of the incoming and outgoing waves. Thus we avoid possible confusion caused by the existence of notations with opposite signs for the same Jost functions. In addition to this, the notations used here remain unchanged irrespective of how many channels are involved. In multichannel problems, where it is impossible to introduce a single momentum k, the energy-dependent functions $f^{(\mathrm{in/out})}(E)$ simply become matrices.

the operation of complex conjugation. These amplitudes are therefore related to each other. It can be easily proved that they are equal to each other at the symmetrical points shown in Fig. 2.

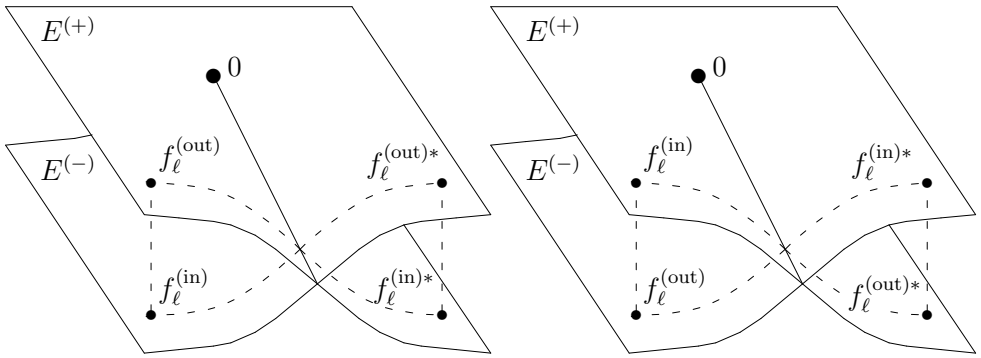

FIG. 2: Symmetry properties of the Jost functions on the E-surface. The dashed lines connect the points at which the values indicated next to them are identical.

At certain points E_n the incoming Jost function may have zeros,

$$f_\ell^{(\mathrm{in})}(E_\mathrm{n}) = 0 \ . \tag{7}$$

At such values of the energy, we have the S-matrix poles and only the outgoing wave in the asymptotic behavior of the wave function. If we find such a zero of the Jost function at a real negative energy on the physical sheet, the corresponding wave function vanishes when $r \to \infty$ and therefore describes a bound state. On the other hand, if such a zero is found at a complex energy

$$E_\mathrm{n} = \mathcal{E}_\mathrm{n} - \frac{i}{2}\Gamma_\mathrm{n} \tag{8}$$

on the unphysical sheet, the corresponding wave function describes a resonance. The real part of E_n is the energy, around which the resonance is centered, while the imaginary part gives us its width. It can be proved that the only zeros that $f_\ell^{(\mathrm{in})}(E)$ may have are those shown in Fig. 3.

So, in principle, the Jost function offers a very nice way of locating bound and resonance states: simply as zeros of the Jost function. But how to calculate the Jost function? For this purpose, we replace the Schrödinger equation with an equivalent system of first order differential equations that enable us to calculate the Jost functions directly [9–14].

To this end we look for the general solution of the Schrödinger equation (1) in the following special form

$$u_\ell(k,r) = F_\ell^{(\mathrm{in})}(E,r)h_\ell^{(-)}(kr) + F_\ell^{(\mathrm{out})}(E,r)h_\ell^{(+)}(kr) \ , \tag{9}$$

where the incoming and outgoing waves are included explicitly. The functions $F_\ell^{(\mathrm{in/out})}(E,r)$ are new unknown functions. Since instead of one unknown functions u_ℓ we introduce two unknown functions $F_\ell^{(\mathrm{in/out})}$, they cannot be independent. We therefore can impose an arbitrary condition that relates them to each other. As such condition, it is convenient to choose the following equation

$$h_\ell^{(-)}(kr)\partial_r F_\ell^{(\mathrm{in})}(E,r) + h_\ell^{(+)}(kr)\partial_r F_\ell^{(\mathrm{out})}(E,r) = 0 \ , \tag{10}$$

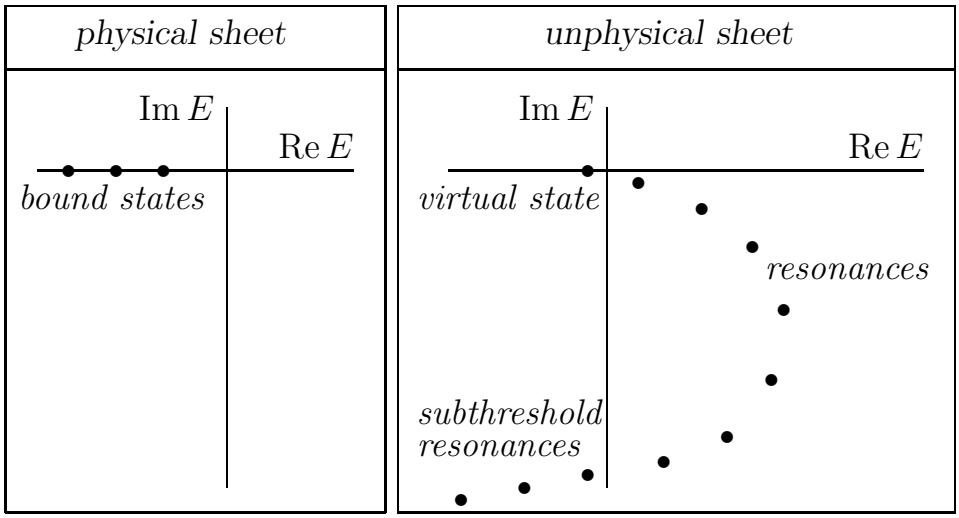

FIG. 3: Typical distribution of the Jost function zeros on the two sheets of the complex energy Riemann surface.

which is standard in the variation parameters method and is called the Lagrange condition. Substituting the ansatz (9) into the Schrödinger equation (1) and using the condition (10), we obtain the following system of first order equations for these unknown functions

$$\begin{cases} \partial_r F_\ell^{(\mathrm{in})} = -\dfrac{1}{2ik} h_\ell^{(+)} V \left[h_\ell^{(-)} F_\ell^{(\mathrm{in})} + h_\ell^{(+)} F_\ell^{(\mathrm{out})} \right] , \\ \partial_r F_\ell^{(\mathrm{out})} = \quad \dfrac{1}{2ik} h_\ell^{(-)} V \left[h_\ell^{(-)} F_\ell^{(\mathrm{in})} + h_\ell^{(+)} F_\ell^{(\mathrm{out})} \right] , \end{cases} \tag{11}$$

where all the functions are written without their arguments for the sake of clarity. A physical solution of these equations can be obtained with the boundary conditions

$$F_\ell^{(\mathrm{in})}(E,0) = F_\ell^{(\mathrm{out})}(E,0) = 1 , \tag{12}$$

which follow from the requirement of regularity of the physical wave function at $r = 0$, i.e. from the condition $u_\ell(E,0) = 0$.

When the energy is real, the right hand sides of Eqs. (11) vanish at large distances because the potential vanishes. This means that $F_\ell^{(\mathrm{in/out})}(E,r)$ become constants (independent of r), i.e. converge to the corresponding Jost functions defined by Eq. (5),

$$\begin{cases} F_\ell^{(\mathrm{in})}(E,r) \underset{r\to\infty}{\longrightarrow} f_\ell^{(\mathrm{in})}(E) , \\ F_\ell^{(\mathrm{out})}(E,r) \underset{r\to\infty}{\longrightarrow} f_\ell^{(\mathrm{out})}(E) . \end{cases} \tag{13}$$

With complex energies however, there is a technical complication. The problem is that one of the Riccati-Hankel functions on the right hand side of Eqs. (11) is always exponentially diverging when $\mathrm{Im}\, k \neq 0$. Therefore, if at large distances the potential vanishes not fast enough, the convergence (13) is not achieved. This problem can be easily circumvented by using different path to the far-away point (see Fig. 4). This is known as the complex rotation of the coordinate. Details concerning convergence of the limits (13) and the use of complex rotation for this purpose can be found in Refs. [9–14].

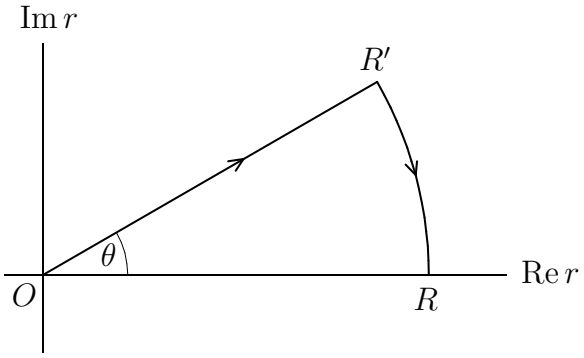

FIG. 4: Deformed contour for integrating Eqs. (11) from $r = 0$ to $r = R$ when the energy is complex.

Therefore, the procedure of calculating the Jost functions is rather simple. Starting from the origin, we integrate Eqs. (11) outwards until at $r = R$ the solutions converge to constant values. If the energy is complex, we simply use an appropriate integration path of the type shown in Fig. 4.

So, this is how we can locate resonances in two-body systems. Can it be generalized for many-body systems? Yes it can, at least for certain systems, namely, for those that cannot form clusters. Some authors call them "borromean" systems. The wave functions describing such systems behave asymptotically as linear combinations of the incoming and outgoing hyperspherical waves. The systems we consider in the present paper, namely, Λnn and $\Lambda\Lambda n$, belong to this category because there are no bound states in any of the pairs nn, Λn, or $\Lambda\Lambda$.

III. HYPERSPHERICAL APPROACH

Although the two-body potentials and masses for the three-body systems Λnn and $\Lambda\Lambda n$ are different, they can be treated using exactly the same equations. Indeed, in both of these systems we have two identical particles with spin 1/2 and a third particle of the same spin. Let us therefore consider a general system of this type.

To describe the spatial configuration of the system, we use the so called hyperspherical coordinates, among which only one (the hyperradius) runs from zero to infinity while all the others (the hyperangles) vary within finite ranges. Within this approach, the wave function is expanded in an infinite series over the hyperspherical harmonics (similarly to the partial wave decomposition in the two-body problem), and we end up with an infinite system of coupled hyperradial equations, which is truncated in practical calculations. All the details of the hyperspherical approach can be found in the review by M. Fabre de la Ripelle [15].

Let m_1 be the mass of one of the identical particles, and m_2 be the mass of the third particle. Then the total mass of the system is $M = 2m_1 + m_2$ and the reduced masses for the identical pair and for the third particle are $\mu_1 = m_1/2$ and $\mu_2 = 2m_1m_2/M$, respectively. With the Jacobi coordinates shown in Fig. 5, the three-body Schrödinger equation can be written as

$$\left(\partial_r^2 + \frac{5}{r}\partial_r - \frac{1}{r^2}\mathcal{L}^2 + k^2 - V\right)\Psi^{[s]}_{\vec{k}_1,\vec{k}_2}(\vec{r}_1,\vec{r}_2) = 0\ , \tag{14}$$

where

$$V = 2M(U_{12} + U_{13} + U_{23}) \tag{15}$$

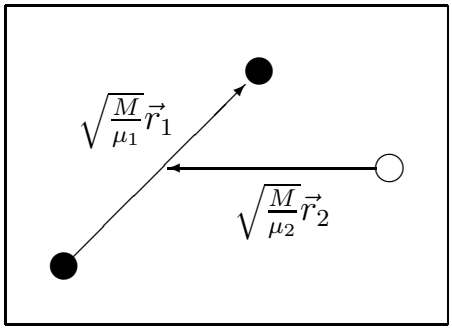

FIG. 5: Jacobi vectors defining the spatial configuration of a three-body system of two identical (filled circles) and one different (open circle) particles.

is the sum of the two-body potentials, $\{\vec{k}_1, \vec{k}_2\}$ are the incident momenta of the three-body collision along the corresponding configuration vectors $\{\vec{r}_1, \vec{r}_2\}$, the superscript $[s] = \{(s_1 s_2)s_{12}, s_3, \sigma m_\sigma\}$ denotes the spin quantum numbers, r is the hyperradius,

$$r = \sqrt{r_1^2 + r_2^2}\ , \tag{16}$$

that gives the "collective" size of the system, k is related to the total energy, $k^2 = 2ME$, and can be called the hypermomentum, and the operator $\mathcal{L}^2$ absorbs all the angular variables. It is defined as

$$\mathcal{L}^2 = -\frac{\partial^2}{\partial\alpha^2} - 4\cot(2\alpha)\frac{\partial}{\partial\alpha} + \frac{1}{\cos^2\alpha}\vec{\ell}^{\,2}_{\vec{r}_1} + \frac{1}{\sin^2\alpha}\vec{\ell}^{\,2}_{\vec{r}_2} \tag{17}$$

with $\alpha = \arctan(r_2/r_1)$, $\quad 0 \le \alpha \le \pi/2$, and $\vec{\ell}_{\vec{r}_i}$ being the operators of the angular momenta associated with the corresponding Jacobi coordinates. The solutions of the eigenvalue problem

$$\mathcal{L}^2 Y_{[L]}(\omega) = L(L+4)Y_{[L]}(\omega) \tag{18}$$

are well known functions of the hyperangles $\omega = \{\Omega_{\vec{r}_1}, \Omega_{\vec{r}_2}, \alpha\}$ including the spherical angles $\Omega_{\vec{r}_i}$ of the vectors $\vec{r}_i$ and the angle α that determines the ratio r_2/r_1. These functions, $Y_{[L]}(\omega)$, are called the hyperspherical harmonics. The subscript $[L]$ is the multi-index $[L] = \{L, \ell_1, \ell_2, \ell, m\}$ that includes the grand orbital quantum number,

$$L = \ell_1 + \ell_2 + 2n\,, \qquad n = 0, 1, 2, \dots\ , \tag{19}$$

as well as the angular momenta associated with the Jacobi vectors and the total angular momentum ℓ together with its third component m. Combining $Y_{[L]}(\omega)$ with the spin states $\chi_{[s]}$, we obtain the functions

$$\Phi^{jj_z}_{[L]}(\omega) = \sum_{m\sigma}\langle \ell m s\sigma | jj_z\rangle Y_{[L]}(\omega)\chi_{[s]} \tag{20}$$

that constitute a full set of states with a given total angular momentum j in the spin-angular subspace.

Similarly to the two-body partial wave decomposition, we can expand a solution of Eq. (14) in the infinite series over the hyperspherical harmonics,

$$\Psi^{[s]}_{\vec{k}_1,\vec{k}_2}(\vec{r}_1, \vec{r}_2) = \frac{1}{r^{5/2}}\sum_{[L][L']jj_z} u^{jj_z}_{[L][L']}(E, r)\Phi^{jj_z}_{[L]}(\omega_{\vec{r}})\Phi^{jj_z *}_{[L']}(\omega_{\vec{k}})\ . \tag{21}$$

After substituting this expansion into Eq. (14) and doing the projection onto the functions $\Phi^{jj_z}_{[L]}$, we end up with the following system of hyperradial equations

$$\left[\partial_r^2 + k^2 - \frac{\lambda(\lambda+1)}{r^2}\right] u_{[L][L']} = \sum_{[L'']} V_{[L][L'']} u_{[L''][L']} \ , \tag{22}$$

where for the sake of simplicity we dropped the superscripts jj_z (indicating the conserving total angular momentum). In Eq. (22),

$$V_{[L][L']}(r) = 2M \int \Phi^{jj_z*}_{[L]}(\omega) \left(U_{12} + U_{13} + U_{23}\right) \Phi^{jj_z}_{[L']}(\omega) d\omega \ , \tag{23}$$

and $\lambda = L + 3/2$. Since we consider a system that cannot form clusters, the asymptotic behavior of its wave function may only involve the incoming and outgoing hyperspherical waves $\sim \exp(\mp ikr)$, which are the products of the corresponding spherical waves along the Jacobi radii r_1 and r_2,

$$e^{ik_1 r_1} e^{ik_2 r_2} = e^{ikr\cos^2\alpha} e^{ikr\sin^2\alpha} = e^{ikr} \ .$$

We therefore look for the solution of matrix equation (22) as

$$u_{[L][L']}(E,r) = h^{(-)}_\lambda(kr) F^{(\mathrm{in})}_{[L][L']}(E,r) + h^{(+)}_\lambda(kr) F^{(\mathrm{out})}_{[L][L']}(E,r) \tag{24}$$

with the Lagrange condition for the unknown matrices $F^{(\mathrm{in/out})}_{[L][L']}$,

$$h^{(-)}_\lambda(kr) \partial_r F^{(\mathrm{in})}_{[L][L']}(E,r) + h^{(+)}_\lambda(kr) \partial_r F^{(\mathrm{out})}_{[L][L']}(E,r) = 0 \ . \tag{25}$$

Similarly to the two-body case, we end up with the following system of first order equations for them

$$\begin{cases} \partial_r F^{(\mathrm{in})}_{[L][L']} &= -\dfrac{h^{(+)}_\lambda}{2ik} \displaystyle\sum_{[L'']} V_{[L][L'']} \left[h^{(-)}_{\lambda''} F^{(\mathrm{in})}_{[L''][L']} + h^{(+)}_{\lambda''} F^{(\mathrm{out})}_{[L''][L']} \right] \ , \\ \partial_r F^{(\mathrm{out})}_{[L][L']} &= +\dfrac{h^{(-)}_\lambda}{2ik} \displaystyle\sum_{[L'']} V_{[L][L'']} \left[h^{(-)}_{\lambda''} F^{(\mathrm{in})}_{[L''][L']} + h^{(+)}_{\lambda''} F^{(\mathrm{out})}_{[L''][L']} \right] \ , \end{cases} \tag{26}$$

which are equivalent to the second order Eq. (22). The regularity of a physical wave function at $r = 0$ implies the following boundary conditions

$$F^{(\mathrm{in})}_{[L][L']}(E,0) = F^{(\mathrm{out})}_{[L][L']}(E,0) = \delta_{[L][L']} \ . \tag{27}$$

With these conditions, the columns of matrix $u_{[L][L']}(E,r)$ are not only regular but linearly independent as well. Therefore any regular column $\phi_{[L]}(E,r)$ obeying Eq. (22), can be written as a linear combination of its columns. In other words, the matrix $u_{[L][L']}(E,r)$ is a complete basis of the regular solutions.

At large hyperradius, the matrices $F^{(\mathrm{in/out})}_{[L][L']}(E,r)$ converge to the energy-dependent constants,

$$f^{(\mathrm{in/out})}_{[L][L']}(E) = \lim_{r\to\infty} F^{(\mathrm{in/out})}_{[L][L']}(E,r), \tag{28}$$

that by analogy with the two-body case can be called the Jost matrices. The convergence of these limits depends on how fast the potential matrix $V_{[L][L']}(r)$ vanishes when $r \to \infty$. Due to

the same reason as for the two-body case, when doing calculations with a complex energy, we have to deform the integration contour as is shown in Fig. 4.

As was said before, the columns of the matrix function $u_{[L][L']}(E,r)$ constitute the regular basis using which we can construct a physical solution $\phi_{[L]}(E,r)$ with given boundary conditions at infinity,

$$\phi_{[L]}(E,r) = \sum_{[L']} u_{[L][L']}(E,r) C_{[L']} \ , \tag{29}$$

where $C_{[L]}$ are the combination coefficients.

The spectral points are those at which the physical solution has only outgoing waves in its asymptotics, i.e. when

$$\sum_{[L']} f^{(\mathrm{in})}_{[L][L']}(E_{\mathrm{n}}) C_{[L']} = 0 \ . \tag{30}$$

This homogeneous system has a non-trivial solution if and only if

$$\det f^{(\mathrm{in})}_{[L][L']}(E_{\mathrm{n}}) = 0 \ , \tag{31}$$

which is a generalization of Eq. (7) for a three-body case.

IV. TWO-BODY POTENTIALS

In our calculations, we used (as input information) certain two-body potentials describing the interaction between two neutrons, Λ and neutron, and between two Lambdas. For all these three potentials, we used the same functional form, namely,

$$U(r) \ = \ \left[A_1(r) - \frac{1+P^\sigma}{2} A_2(r) - \frac{1-P^\sigma}{2} A_3(r) \right] \left[\frac{\beta}{2} + \frac{1}{2}(2-\beta) P^r \right] \ , \tag{32}$$

$$A_i(r) \ = \ W_i \exp(-a_i r^2) \ , \qquad i = 1,2,3 \ , \tag{33}$$

where P^σ and P^r are the permutation operators in the spin and configuration spaces, respectively. The form of $U(r)$ as well as the parameters were taken from Ref. [16]. In order to explore how sensitive the positions of the three-body resonances are to the choice of underlying two-body potentials, we did the calculations with three different sets of parameters for the Λn-potential. All the sets of parameters we used, are given in Table I.

V. THE MINIMAL APPROXIMATION

The system (26) consists of infinite number of equations. For any practical calculation, one has to truncate it somewhere. Before going any further, it is very logical to try the simplest approximation, namely, when only the first terms of the sums on the right hand sides of Eqs. (26) are retained. This corresponds to the minimal ($n = 0$) value of the grand orbital number (19) and is called the hypercentral approximation, $[L] = [L_{\min}]$. We assume that the two-body subsystems are in the S-wave states ($\ell_1 = \ell_2 = 0$), which means that

$$\lambda = \lambda_{\min} = \frac{3}{2} \ .$$

TABLE I: Parameters of the potential (32) for the pairs nn, $\Lambda\Lambda$, and Λn. For the system Λn, three different sets of parameters (denoted as A, B, and C) are given. All the parameters are taken from Ref. [16].

Parameter	nn	$\Lambda\Lambda$	Λn (A)	Λn (B)	Λn (C)
W_1 (MeV)	200.0	200.0	200.0	600.0	5000
W_2 (MeV)	178.0	0	106.5	52.61	47.87
W_3 (MeV)	91.85	130.8	118.65	66.22	61.66
a_1 (fm^{-2})	1.487	2.776	1.638	5.824	18.04
a_2 (fm^{-2})	0.639	0	0.7864	0.6582	0.6399
a_3 (fm^{-2})	0.465	1.062	0.7513	0.6460	0.6325
β	1	1	1	1	1

So, in the minimal approximation, instead of the infinite system (26), we remain with only one equation,

$$\left[\partial_r^2 + k^2 - \frac{\lambda_{\min}(\lambda_{\min}+1)}{r^2}\right] u(E,r) = 2M\langle U\rangle u(E,r) \ , \tag{34}$$

where all unnecessary subscripts are dropped, and the brackets on the right hand side mean averaging over the minimal hyperharmonics,

$$\langle U\rangle(r) = \int \Phi^{jj_z*}_{[L_{\min}]}(\omega)\,(U_{12}+U_{13}+U_{23})\,\Phi^{jj_z}_{[L_{\min}]}(\omega)d\omega \ . \tag{35}$$

From mathematical point of view, Eq. (34) looks exactly like the two-body radial Schrödinger equation. The only difference is that the angular momentum is not an integer number.

The hypercentral potentials $\langle U\rangle$ for the systems Λnn and $\Lambda\Lambda n$ are shown in Figs 6 and 7. With these hyperradial potentials the corresponding differential equations determining the three-body Jost functions, were numerically solved with complex values of the energy. The results of these calculations are discussed next.

VI. NUMERICAL RESULTS

When looking for zeros of the three-body Jost functions, we found that there were no such zeros at real negative energies. In other words, neither the system Λnn nor $\Lambda\Lambda n$ have bound states.

The only zeros we found were located on the unphysical sheet of the energy surface, in the resonance domain. The resonance energies are given in Tables II and III and shown in Fig. 8. As is seen, the positions of the resonances depend on the choice of the Λn potential. For the choice "C", the resonances become even sub-threshold.

TABLE II: Complex resonance energies $E_0 = E_{\rm r} - \frac{i}{2}\Gamma$ for the system Λnn with the three choices of Λn-potential.

Λn-potential	A	B	C
E_0, (MeV)	$0.551 - \frac{i}{2}4.698$	$0.456 - \frac{i}{2}4.885$	$-0.149 - \frac{i}{2}5.783$

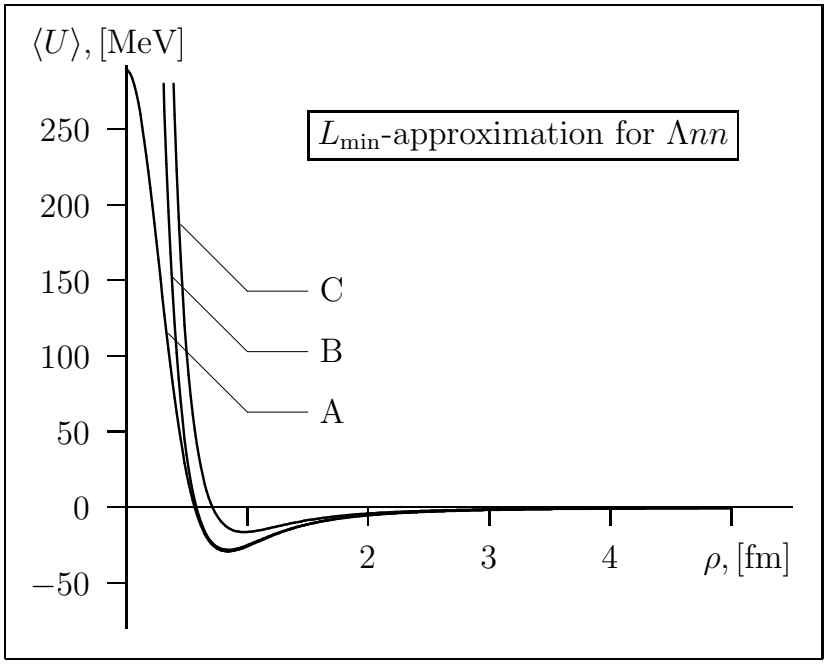

FIG. 6: The hypercentral potential given by Eq. (35) for the system Λnn with the three choices (A, B, and C) of the Λn interaction.

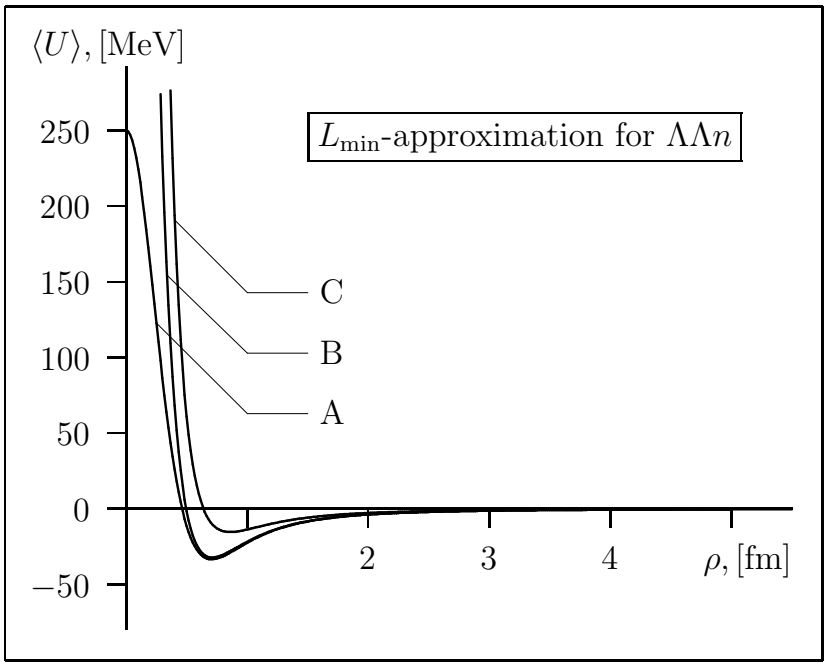

FIG. 7: The hypercentral potential given by Eq. (35) for the system $\Lambda\Lambda n$ with the three choices (A, B, and C) of the Λn interaction.

In order to estimate how far our three-body systems are from being bound, we artificially increased the depths of the potentials by multiplying them by a scaling factor. When this factor was increased from 1 upwards, the Jost function zeros moved towards the origin of the energy surface. At the value of approximately 1.5, the zeros crossed the threshold and moved onto

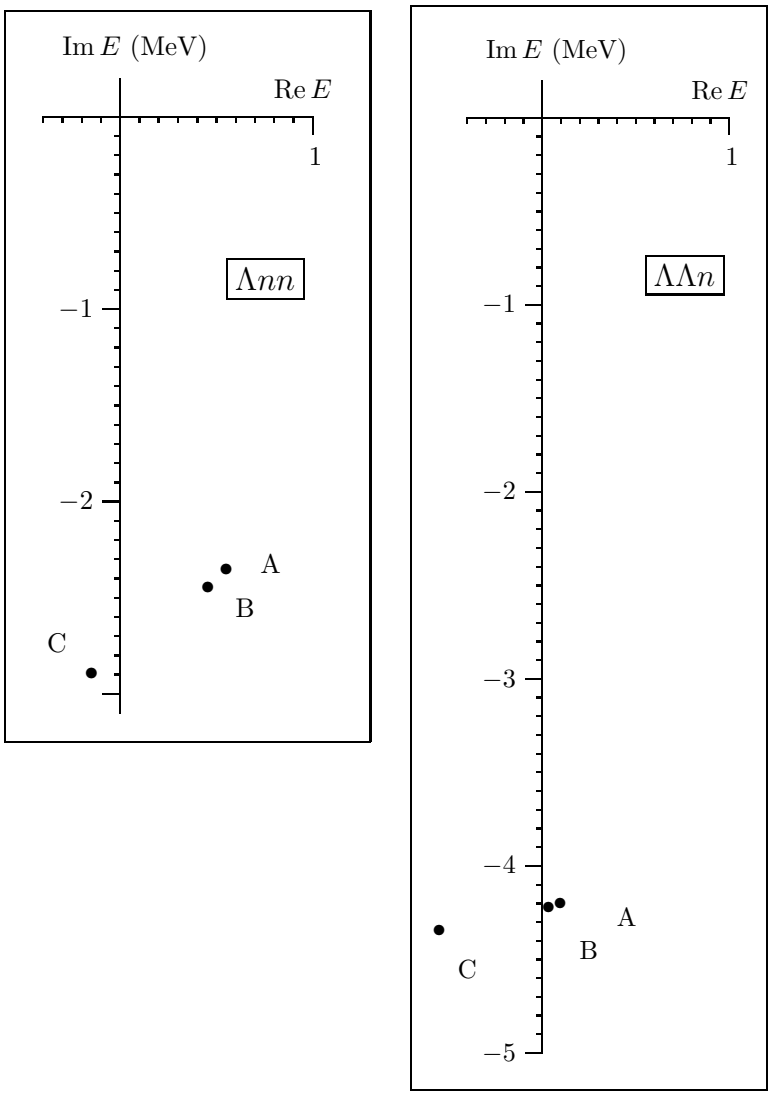

FIG. 8: Resonance points for the systems Λnn and $\Lambda\Lambda n$ found with the three sets (A, B, and C) of parameters of the Λn-potential given in Table I.

TABLE III: Complex resonance energies $E_0 = E_{\rm r} - \frac{i}{2}\Gamma$ for the system $\Lambda\Lambda n$ with the three choices of Λn-potential.

Λn-potential	A	B	C
E_0, (MeV)	$0.096 - \frac{i}{2}8.392$	$0.034 - \frac{i}{2}8.438$	$-0.552 - \frac{i}{2}8.681$

the real negative axis. In other words, the bound states can appear if the potential strength is increased by $\sim 50\%$.

What we found is, of course, an estimate. But it clearly shows that there are near-threshold resonances of the systems Λnn and $\Lambda\Lambda n$. The positions of these resonances depend on the choice of Λn-potential. If such resonances are observed experimentally, they may serve as an additional

instrument for constructing an adequate hyperon-nucleon potential.

---

[1] A. Gal, arXiv: physics/0701019 (2007).
[2] A. Nogga, H. Kamada, and W. Glöckle, Phys. Rev. Lett. **88**, 172501 (2002).
[3] H. Nemura, Y. Akaishi, and Y. Suzuki, Phys. Rev. Lett. **89**, 142504 (2002).
[4] V.B. Belyaev, Lectures on the theory of few-body systems (Springer-Verlag, Berlin Heidelberg, 1990).
[5] H.H. Ansari, M. Shoeb, and M.Z. Rahman Khan, J. Phys. G: Nucl. Phys. **12**, 1369 (1986).
[6] I.R. Afnan and B.F. Gibson, Phys. Rev. C **47**, 1000 (1993).
[7] D.E. Kahana, S.H. Kahana, and D.J. Millener, Phys. Rev. C **68**, 037302 (2003).
[8] E.O. Alt, P. Grassberger, and W. Sandhas, Nucl. Phys. B **2**, 167 (1967).
[9] S.A. Rakityansky, S.A. Sofianos, and K. Amos, Nuovo Cim. B **111**, 363 (1996).
[10] S.A. Sofianos and S.A. Rakityansky, J. Phys. A: Math. Gen. **30**, 3725 (1997).
[11] S.A. Sofianos, S.A. Rakityansky, and G.P. Vermaak, J. Phys. G: Nucl. Part. Phys. **23**, 1619 (1997).
[12] S.A. Rakityansky and S.A. Sofianos, J. Phys. A: Math. Gen. **31**, 5149 (1998).
[13] S.A. Sofianos, S.A. Rakityansky, and S.E.Massen, Phys. Rev. A **60**, 337 (1999).
[14] S.A. Rakityansky and S.A. Sofianos, Few-Body Systems Suppl. **10**, 93 (1999).
[15] M. Fabre de la Ripelle, Ann. Phys. **147**, 281 (1983).
[16] H. Nemura, Y. Suzuki, Y. Fujiwara, and C. Nakamoto, Prog. Theor. Phys. **103**, 929 (2000).

Description of ^{12}C Nucleus in the α-cluster Model and the Role of Effective Interactions

S.I. Fedotov, O.I. Kartavtsev, and A.V. Malykh*

Joint Institute for Nuclear Research, Dubna 141980, Russia

The properties of the ^{12}C(0^+) states in the α-cluster model and the choice of effective potentials are discussed. The effective α-α potentials are adjusted to fit the experimental energy and width of the $\alpha - \alpha$ resonance (^{8}Be ground state) and to reproduce the energy dependence of the α-α s-wave elastic-scattering phase shift up to 12 MeV. The effective three-α potential is introduced to incorporate the effects of the α-particle distortions and non-α-cluster structure, including those connected with antisymmetrization in the 12-nucleon wave function, which are not accounted for by the α-α potential. The three-body potentials are adjusted to fit the experimental energies of the ground and excited 0^+ states and the ground-state root-mean-square radius. Using these potentials, properties of the excited 0_2^+ state are considered and the relation between the excited-state width, the excited-state root-mean-square radius, and the monopole $0_2^+ \to 0_1^+$ transition matrix element is determined.

I. INTRODUCTION

As the α-particle is the most tightly bound nucleus, a variety of low-energy nuclear properties can be successfully described within the framework of the α-cluster model. In this respect, the famous nuclear reaction for the formation of the ^{12}C nucleus in triple-α low-energy collisions should be mentioned. This reaction is of key importance for stellar nucleosynthesis [1, 2] providing helium burning and, thereby, further synthesis of heavier elements. Both the α-α resonance (the ground state of ^{8}Be) and the near-threshold three-body resonance (0_2^+ state of ^{12}C) are crucially important for the low-energy triple-α reaction as the helium burning in stars goes through the sequential reaction

$$3\alpha \to {}^8\mathrm{Be} + \alpha \to {}^{12}\mathrm{C}(0_2^+) \to {}^{12}\mathrm{C} + \gamma\,.$$

The latter resonance was predicted in Ref. [2] as the only explanation for the observed abundance of elements in the universe. Following this the ^{12}C(0_2^+) state [3, 4] was thoroughly studied; in particular, the decay mechanism was experimentally investigated in Ref. [5]. Most recently the ^{12}C(0_2^+) state was discussed as an example of α-particle condensation (see, for example, Refs. [6, 7]).

From a general point of view, complicated processes with few charged particles (three or more) in the initial or final state have not so far been understood completely. The main difficulty stems from the necessity to describe the continuum wave function of few charged particles. Thus even a qualitative understanding of the reaction mechanism would be highly desirable. Interesting examples are the double-proton radioactivity which has been a subject of thorough experimental and theoretical investigations during the last years (more details can be found in the recent reviews [8, 9]) and the decay of the long-lived 1^+ state of ^{12}C nucleus [10, 11]. The Coulomb-correlated penetration of outgoing particles through a multidimensional potential barrier has also been considered (Ref. [12]) in order to describe qualitative features of multicluster decay of atomic nuclei. Besides the resonant triple-α reaction, the study of the non-resonant reaction is of

*Electronic address: maw@theor.jinr.ru

principal importance since it is responsible for the helium burning at ultra-low temperatures and high densities, which takes place in accretion of helium on white dwarfs and neutron stars [13]. Although model calculations are available [14–17], a consistent three-body treatment is needed because the error in the previously calculated non-resonant reaction rate can reach a few orders of magnitude.

For reliable description of nuclei within the framework of the α-cluster model, the effective two-body and (at least) three-body interactions [18–22] must be determined. It is assumed that all effects connected with both the internal structure of α-particles and the identity of nucleons are incorporated in the effective potentials. Fitting the main characteristics of the 3α-cluster ^{12}C nucleus to the experimental values allows one to obtain the three-body potential and to reduce ambiguity in the two-body potential which can not be determined merely from two-body data.

The present report discusses, using both the results of Ref. [20, 22] and recent calculations, the description of the lowest 0^+ states of ^{12}C within the framework of the α-cluster model. One of the questions addressed is to what extent the α-cluster model is able to reproduce the experimental characteristics of a few lowest nuclear states. A more challenging problem is to describe fine characteristics of the 3α-system, such as the width of the near-threshold 0_2^+ state and the monopole $(0_2^+ \to 0_1^+)$-transition matrix element (MTME), which are sensitive to the variation of the potentials. The two- and three-body effective potentials are chosen by comparing the results of three-body calculations and the experimental data for a given set of ^{12}C characteristics.

II. METHOD

The aim of the present report is to describe both the bound state and the resonance state of the $L^\pi = 0^+$ states of three α-particles. The interaction is described by local two- and three-body potentials having a simple Gaussian form. Numerical results are obtained by using the same approach and a similar numerical procedure as in our previous papers [20, 22]. The units $\hbar = m = e = 1$ are used throughout the paper.

A. Hyper-radial equations

The method of calculations is based on the expansion of the total wave function in a set of eigenfunctions on the hypersphere [23]. Scaled Jacobi coordinates are introduced as $\mathbf{x}_i = \mathbf{r}_j - \mathbf{r}_k$, $\mathbf{y}_i = (2\mathbf{r}_i - \mathbf{r}_j - \mathbf{r}_k)/\sqrt{3}$, where the indexes $\{ijk\}$ must be chosen as a permutation of $\{123\}$ and $\mathbf{r}_i$ is the position vector of the ith particle. The hyper-spherical variables ρ, α_i, and θ_i are defined via the Jacobi coordinates by the relations $x_i = \rho\cos(\alpha_i/2)$, $y_i = \rho\sin(\alpha_i/2)$, and $\cos\theta_i = (\mathbf{x}_i \cdot \mathbf{y}_i)/(x_i y_i)$.

The Schrödinger equation for three α-particles is

$$\left(-\Delta_{\mathbf{x}} - \Delta_{\mathbf{y}} + \sum_{j=1}^{3} V(x_j) + V_3(\rho) - E\right)\Psi = 0\ , \tag{1}$$

where $V(x_i)$ and $V_3(\rho)$ are the two-body and three-body potentials, respectively. With the expansion of the total wave function

$$\Psi = \rho^{-5/2}\sum_n f_n(\rho)\Phi_n(\alpha,\theta,\rho) \tag{2}$$

in a set of the normalized eigenfunctions Φ_n satisfying the equation on the hypersphere,

$$\left[\frac{\partial^2}{\partial\alpha^2}+2\cot\alpha\frac{\partial}{\partial\alpha} \;+\; \frac{1}{\sin^2\alpha}\left(\frac{\partial^2}{\partial\theta^2}+\cot\theta\frac{\partial}{\partial\theta}\right) - \frac{\rho^2}{4}\sum_{j=1}^{3}V\left(\rho\cos\frac{\alpha_j}{2}\right)+\lambda_n(\rho)\right]\Phi_n(\alpha,\theta,\rho)=0\ , \tag{3}$$

Eq. (1) is routinely transformed into a system of hyper-radial equations (HRE)

$$\left[\frac{\partial^2}{\partial\rho^2}-\frac{1}{\rho^2}\left(4\lambda_n(\rho)+\frac{15}{4}\right) \;-\; V_3(\rho)+E\right]f_n(\rho) + \sum_m\left(Q_{nm}(\rho)\frac{\partial}{\partial\rho}+\frac{\partial}{\partial\rho}Q_{nm}(\rho)-P_{nm}(\rho)\right)f_m(\rho)=0\ , \tag{4}$$

where

$$Q_{nm}(\rho)=\left\langle\Phi_n\;\middle|\;\frac{\partial\Phi_m}{\partial\rho}\right\rangle\ ,\qquad P_{nm}(\rho)=\left\langle\frac{\partial\Phi_n}{\partial\rho}\;\middle|\;\frac{\partial\Phi_m}{\partial\rho}\right\rangle, \tag{5}$$

and the notation $\langle\cdot|\cdot\rangle$ stands for integration on the hypersphere. To get rid of the numerical calculation of the derivatives $\dfrac{\partial\Phi_n}{\partial\rho}$, $Q_{nm}(\rho)$ are calculated by using the exact expression,

$$Q_{mn}(\rho) \;=\; \frac{3}{4}\left(\lambda_n-\lambda_m\right)^{-1}\left\langle\Phi_m\left|\frac{4}{\cos\frac{\alpha}{2}}+2\rho V_s(\rho\cos\frac{\alpha}{2})+\rho^2\frac{\partial V_s(\rho\cos\frac{\alpha}{2})}{\partial\rho}\right|\Phi_n\right\rangle \tag{6}$$

and $P_{nm}(\rho)$ are calculated by using the approximation

$$P_{mn}(\rho) \;=\; \sum_{l=1}^{N}Q_{ml}(\rho)Q_{nl}(\rho) \tag{7}$$

of the exact sum rule $\mathrm{P}=-\mathrm{Q}^2$ on the limited basis of N trial functions.

Solutions of the eigenvalue problem and the $\alpha+{}^8$Be scattering problem for HRE (4) provide the properties of the ground 0_1^+ state and the excited 0_2^+ resonance state, respectively. The resonance position E_r and width Γ are determined by fitting the energy dependence of the phase shift δ_E for $\alpha+{}^8$Be scattering to the Wigner form,

$$\cot(\delta_E-\delta_{bg})=\frac{2}{\Gamma}(E_r-E)\ , \tag{8}$$

where the background phase shift δ_{bg} is of no interest in the present calculation. The phase shift δ_E is defined by the asymptotic form of the first-channel function

$$f_1^{(E)}(\rho)\sim F_0(\eta,k\rho)+\tan(\delta_E)G_0(\eta,k\rho)\ , \tag{9}$$

where $F_0(\eta,k\rho)$ and $G_0(\eta,k\rho)$ are the Coulomb functions with the parameter $\eta=8/(\sqrt{3}k)$ and the wave number in the first channel $k=\sqrt{E-E_{2\alpha}}$. Eq. (9) follows from the two-cluster asymptotic form of the first-channel potential

$$U_1(\rho)=\frac{1}{\rho^2}\left(4\lambda_1(\rho)+\frac{15}{4}\right)+V_3(\rho)+P_{11}(\rho)\to E_{2\alpha}+\frac{\tilde{q}}{\rho} \tag{10}$$

near the turning point ρ_t defined as $U_1(\rho_t) = E$, $E_{2\alpha}$ is the energy of the ^{8}Be and the Coulomb parameter $\tilde{q} = 16/\sqrt{3}$. In fact, the right hand side of Eq. (10) is the energy of the two-cluster system $\alpha + {}^8$Be for large distance between α and ^{8}Be.

It is suitable to treat the ultra-narrow 0_2^+ resonance state on equal footing with the ground state. Therefore, its wave function is defined as the scattering solution at the resonance energy E_r normalized on the finite interval $0 \le \rho \le \rho_t$. Thus, the r.m.s. radii $R^{(i)}$ of the ground ($i = 1$) and excited ($i = 2$) states and the MTME M_{12} are defined by the expressions

$$R^{(i)} = \sqrt{R_\alpha^2 + \frac{1}{6}\bar{\rho}_i^2}\ , \qquad \bar{\rho}_i^2 = \sum_n \int_0^{\rho_t} \left| f_n^{(i)}(\rho) \right|^2 \rho^2 \mathrm{d}\rho\ , \tag{11}$$

where $R_\alpha = 1.47\,\mathrm{fm}$ is the r.m.s. radius of the α-particle, and

$$M_{12} = \sum_n \int_0^{\rho_t} f_n^{(2)}(\rho) f_n^{(1)}(\rho) \rho^2 \mathrm{d}\rho\ . \tag{12}$$

B. Variational method for solution of the equation on the hypersphere

The coefficients $\lambda_n(\rho)$, $Q_{nm}(\rho)$, and $P_{nm}(\rho)$ of the HRE (4) are calculated using the variational method for the solution of the eigenvalue problem (3). The variational basis consists of N trial functions χ_i with the same symmetry under permutations of particles as the eigenfunctions $\Phi_n(\alpha, \theta, \rho)$. In view of an essentially different structure of the eigenfunctions $\Phi_n(\alpha, \theta, \rho)$ at different values of ρ, it is necessary to use a flexible basis of trial functions which allows one to describe the two-cluster ($\alpha + {}^8$Be) and three-cluster (3α) structure of the wave function in the asymptotic region.

The variational basis contains a set of the symmetric hyperspherical harmonics (SHH) H_{nm} which are the eigenfunctions of the equation

$$\left[\Delta^* + K(K+2)\right] H_{nm} = 0\,, \tag{13}$$

where Δ^* is the differential operator in Eq. (3), $K = 2n + 3m$, the non-negative numbers n and m enumerate SHH, and $2K$ is the order of SHH. For explicit construction of SHH it is convenient to use another set of the hyperspherical variables $0 \le \xi \le \dfrac{\pi}{2}$, $-\pi \le \varphi_i \le \pi$ [24, 25] defined by

$$\begin{aligned} \sin\xi &= \sin\alpha_i \sin\theta_i\,, \\ \cos\xi \cos\varphi_i &= \cos\alpha_i\,, \\ \cos\xi \sin\varphi_i &= \sin\alpha_i \cos\theta_i\,. \end{aligned} \tag{14}$$

In the variables ξ and φ

$$H_{nm}(\xi, \varphi) \sim \cos^{3m}\xi P_n^{(0,3m)}(\cos 2\xi) T_{3m}(\cos\varphi) \sim d^{n+3m/2}_{3m/2,3m/2}(2\xi)\cos 3m\varphi\ , \tag{15}$$

where $P_n^{(\alpha,\beta)}(x)$ and $T_n(x)$ are the Jacobi and Chebyshev polynomials and $d^j_{mk}(\beta)$ is the Wigner function. The variable ξ is invariant under permutations of particles, i.e., independent of the index i enumerating the Jacobi variables. On the other hand, φ_i changes to $\varphi_i \pm 2\pi/3$ under the cyclic permutations as $\mid \varphi_i - \varphi_j \mid = 2\pi/3$ and $\varphi_i \to -\varphi_i$ under the permutation of particles j and k. As follows from Eq. (15) and the above properties of the variables ξ and φ_i, the SHH are completely symmetric under any permutation.

In the numerical calculations, the basis of trial functions contains a set of all SHH $H_{n_i m_i}(\xi, \varphi)$ with those indices n_i and m_i for which K does not exceed the maximum value K_{max}, i. e., $K_i = 2n_i + 3m_i \leq K_{max}$. One can count that the total number of such SHH for which $2n_i + 3m_i \leq K$ equals $K(K+6)/12 + 1$ for K being a multiple of 6 and $([K/6]+1)(K - 3[K/6])$ otherwise. Here $[x]$ stands for the entire part of x. Usage of SHH in the basis of trial functions provides an excellent description of the eigenfunctions at small ρ, where the kinetic energy term dominates, and quite a good description up to large ρ, where the cluster effects essentially come into play.

The two-cluster configuration $\alpha + {}^8$Be of the wave function can be hardly described by a set of SHH due to rather slow convergence that hinders the calculation at sufficiently large ρ. Therefore, the basis contains also a ρ-dependent trial functions

$$\chi_i = \sum_{j=1}^{3} \phi_i(\rho \cos \frac{\alpha_j}{2}) \,, \tag{16}$$

which are the symmetrized combinations of the two-body functions $\phi_i(x)$. Explicitly, a set of $\phi_i(x)$ includes a few Gaussians, which provides a description of the ^{8}Be wave function within the range of the nuclear potential $V_s(r)$, and the function $\phi(x) = x^{1/4} \exp(-4\sqrt{x}(1 + ax))$, which is used for a better description in the sub-barrier region.

III. RESULTS

A. Two-body effective potentials

A set of local two-body potentials is taken in a simple form $V(x) = V_s(x) + V_c(x)$, where the nuclear potential, as proposed in [26], is a sum of two Gaussians

$$V_s(x) = V_r \, \mathrm{e}^{-\mu_r^2 x^2} - V_a \, \mathrm{e}^{-\mu_a^2 x^2} \tag{17}$$

and $V_c(x) = 4/x$ is the Coulomb potential. Bearing in mind the complicated task of reliable calculation of the ^{12}C(0_2^+) width and the MTME, it is ultimately necessary to chose those two-body effective potentials, which provide the energy and width of ^{8}Be coinciding with the experimental values $E_{2\alpha} = 92.04 \pm 0.05$ keV and $\gamma = 5.57 \pm 0.25$ eV [27, 28]. Taking into account these considerations, a number of the two-body potentials are constructed and listed in Table I.

The set of potentials 1–11 with parameters $\mu_r^{-1} = 1.53$ fm and $\mu_a^{-1} = 2.85$ fm [26] is constructed to study the dependence on the ^{8}Be width γ, which vary within the interval from 5.1 eV to 8.53 eV (this interval corresponds to earlier experimental measurements of $\gamma = 6.8 \pm 1.7$ eV [27]). The potential 12 with parameters $\mu_r = 0.7$ fm^{-1} and $\mu_a = 0.475$ fm^{-1} [26] with ^{8}Be is used to illustrate the dependence on the potential range. The parameters of the potentials 1–12 were obtained not attempting to describe experimental α-α s-wave elastic-scattering phase shift. Therefore, the reasonable agreement with the experimental phase shift only up to energy 1-2 MeV were found. The calculated s-wave phase shifts are presented in Fig. 1. Among these potentials, the best agreement of the calculated phase shifts with the experimental data at higher energies, as shown in Fig. 1 (right panel), is obtained for the potentials 9 and 10, for which $\gamma = 6.8$ and 7.51 eV, respectively. Note a similar dependence of the phase shifts on energy, namely, the phase shifts multiplied by a proper factor coincide for different potentials 1–11.

All four parameters of the two-body potentials 13–15 were adjusted to provide the ^{8}Be width, which falls within the narrow interval of the experimental uncertainty $\gamma = 5.57 \pm 0.25$ eV, and to obtain the α-α scattering phase shift which is an agreement ones up to center-of-mass energy 12 MeV. As shown in Fig. 1, adjustment of the parameters μ_r and μ_a allows one to reach a

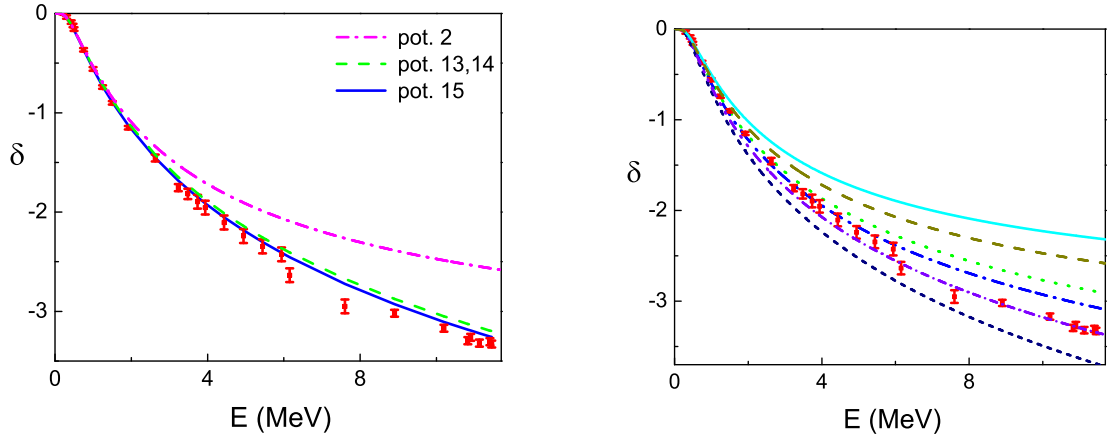

FIG. 1: The experimental and calculated α-α s-wave elastic-scattering phase shift δ versus the center-of mass energy E (MeV) for the two-body potentials 2, 13, 14, and 15 providing the ^{8}Be width within the range of the experimental uncertainty 5.57 eV $\leq \gamma \leq$ 5.82 eV (left panel) and for the two-body potentials 1, 2, 6, 9, 10, and 11 (top to bottom, right panel).

TABLE I: Parameters of the α-α potential V_s (17) providing the α-α resonance widths γ.

Potential	γ(eV)	V_r(MeV)	μ_r^{-1}(fm)	V_a(MeV)	μ_a^{-1}(fm)
1	5.11	20.012	1.53	16.5	2.85
2	5.69	35.024	1.53	19.492	2.85
3	6.20	52.772	1.53	22.344	2.85
4	6.31	57.187	1.53	22.969	2.85
5	6.37	60.051	1.53	23.359	2.85
6	6.40	61.220	1.53	23.516	2.85
7	6.50	66.028	1.53	24.141	2.85
8	6.60	71.057	1.53	24.766	2.85
9	6.80	82.563	1.53	26.1	2.85
10	7.51	136.406	1.53	31.133	2.85
11	8.53	279.206	1.53	40.0	2.85
12	5.10	197.680	1.42857	50.0	2.10526
13	5.57	284.413	1.5000	121.875	2.05500
14	5.57	295.160	1.4213	99.141	2.09455
15	5.82	283.811	1.5330	120.0	2.10021

good agreement with experiment, whereas for the potential 2 providing $\gamma = 5.7\,$eV the phase shift deviates significantly from the experimental dependence. It is worth mentioning that the present result reveals a better description of the $\alpha - \alpha$ scattering data by the harder potentials.

B. Three-body effective potentials

The three-body potentials are assumed to have a simple and convenient functional form depending only on the collective variable - the hyper-radius ρ

$$V_3(\rho) = V_0\, \mathrm{e}^{-(\rho/b_0)^2} + V_1\, \mathrm{e}^{-(\rho/b_1)^2}\ . \tag{18}$$

The parameters of the three-body potentials are chosen to obtain the experimental energies of the ground and excited states, $E_{gs} = -7.2747\,\text{MeV}$ and $E_r = 0.3795\,\text{MeV}$ [29], and r.m.s. radius of the ground state, $R^{(1)}_{exp} = 2.48 \pm 0.22\,\text{fm}$ [30, 31], of the ^{12}C nucleus. (Note that in the calculations with the two-body potentials 1-12 of Table I, the ground-state r.m.s. radius $R^{(1)}$ is fixed at the experimental value 2.47 fm [32] that does not reflect on the conclusions). As described in Section II, E_{gs}, E_r, and $R^{(1)}$ are calculated by solving a system of HRE, Eq. (4), and accurate results are obtained in the three-channel approximation.

Let us consider first the description of ^{12}C by using the one-term three-body potential (putting $V_1 = 0$). This will provide a better insight into the dependence on the three-body potential $V_3(\rho)$. For the two-parameter potentials, only the parameters V_0 and b_0 are determined by fixing E_{gs} and E_r at the experimental values. Two types of solutions are found and the corresponding parameters for the one-term three-body potentials V_0 and b_0 are presented in Table II.

For the first type of solutions, three-body potentials are rather extended with the range within the interval $4.4\,\text{fm} \leq b_0 \leq 5.4$ fm and strength $|V_0| < 40\,\text{MeV}$. The ground-state r.m.s. radius is in the range 2.2 fm $< R^{(1)} <$ 2.8 fm, which includes the experimental value for potential 5–6, nevertheless, the two-body width γ for these potentials turns out to be 6.4 eV, being well separated from the most accurate experimental value of 5.57 eV. For the second type of solutions, b_0 is about twice as small and $|V_0|$ exceeds 80 MeV. The calculated ground-state r.m.s. radius $R^{(1)}_{\text{exp}}$ underestimate the experimental value. The results for the one-term three-body potential

TABLE II: Two families of solutions with the one-term three-body potential ($V_1 = 0$) for a number of two-body potentials marked by the widths γ (eV) of the α-α resonance. Shown are the parameters b_0 (fm) and V_0 (MeV), r.m.s. radii $R^{(i)}$ (fm), width of the excited state Γ (eV), and monopole transition matrix element M_{12} (fm^2).

α-α Pot.	γ	b_0	V_0	Γ	$R^{(1)}$	$R^{(2)}$	M_{12}	b_0	V_0	Γ	$R^{(1)}$	$R^{(2)}$	M_{12}
1	5.11	4.3942	-16.067	10.3	2.24	3.5	8.14	1.9851	-81.092	6.7	1.92	3.3	5.75
2	5.69	4.5001	-18.600	13.0	2.35	3.7	8.59	2.2310	-89.941	8.2	2.02	3.4	6.46
3	6.20	4.6006	-20.824	15.9	2.45	3.8	8.87	2.3314	-113.28	9.7	2.09	3.5	6.90
4	6.31	4.6162	-21.325	16.5	2.46	3.9	8.91	2.3420	-120.30	10.1	2.11	3.5	6.97
5	6.37	4.6247	-21.643	16.9	2.48	3.9	8.93	2.3472	-125.05	10.2	2.12	3.5	7.01
6	6.40	4.6455	-21.640	17.2	2.48	3.9	8.97	2.3464	-127.48	10.4	2.12	3.5	7.03
7	6.50	4.6379	-22.297	17.6	2.50	3.9	8.97	2.3547	-135.38	10.7	2.13	3.5	7.09
8	6.60	4.6455	-22.838	18.1	2.51	3.9	8.99	2.3584	-144.47	11.0	2.14	3.6	7.13
9	6.80	4.6531	-24.047	19.3	2.55	4.0	9.03	2.3611	-166.39	11.7	2.17	3.6	7.22
10	7.51	4.6111	-29.285	22.7	2.65	4.1	9.03	2.3415	-281.63	14.4	2.25	3.7	7.37
11	8.53	4.4858	-39.948	26.1	2.77	4.3	8.85	2.2980	-621.03	18.0	2.35	4.0	7.36
12	5.10	5.3767	-15.411	13.9	2.49	3.9	8.22	1.8225	-424.426	4.6	2.04	3.2	7.04
13	5.57	5.2905	-17.409	18.5	2.56	4.0	8.39	1.8858	-562.38	6.7	2.11	3.2	7.44
14	5.57	5.2852	-17.463	18.5	2.56	4.0	8.37	1.8443	-664.91	6.7	2.10	3.2	7.38
15	5.82	5.2051	-18.724	18.8	2.58	4.0	8.47	1.9386	-559.04	7.3	2.13	3.3	7.53

($V_1 = 0$) clearly show a lack of simultaneous description for the ^{8}Be width and the ground-state size $R^{(1)}$, and thus the one-term potential is too simple to describe real nuclei. One can readily propose to use simultaneously both the short- and the long-range term in the three-body potential to obtain a compromising description of the two- and three-body characteristics.

From the above it is clear that one should perform more elaborate calculations, in which four parameters of the three-body potential in the form of Eq. (18) are used to fix the ground- and excited-state energies and the ground-state r.m.s. radius at the experimental values. Varying one remaining degree of freedom in the four-dimensional space of parameters $V_{0,1}, b_{0,1}$, one obtains

one-parameter sets of three-body potentials for a given two-body potential. In particular, the dependence of the three-body potential parameters corresponding to two-body potentials 13–15 of Table I, which provides a γ of about 5.57 eV, are shown in Fig. 2. A noticeable feature of

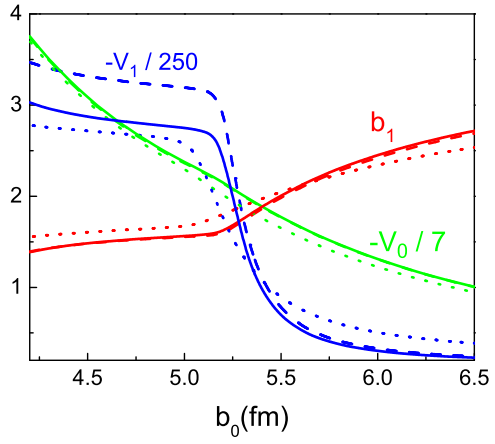

FIG. 2: Relation between the parameters of the three-body effective potentials corresponding to the two-body potentials 13, 14 and 15 plotted by solid, dashed, dotted lines, respectively.

these dependencies is that by decreasing the total range b_0 of the effective potential, a deep attractive well at short distances is obtained.

C. Properties of the 0_2^+ state

As discussed above the position of the 0_2^+ state is fixed at the experimental value. However, one should also require a description of its fine characteristics, viz., the width Γ, r.m.s. radius $R^{(2)}$ and the $0_2^+ \to 0_1^+$ monopole transition matrix element. Note that $R^{(2)}$ is not experimentally available, instead, M_{12} can be used to characterize the extension of the resonance state. Generally, a reliable calculation of the extremely small (in nuclear scale) Γ and MTME is a rather complicated task. To overcome these difficulties, it was necessary to use up to 400 trial functions in variational calculations; the solution of the four-channel system of the HRE shows that the resonance width is determined with an accuracy much better than 1 eV.

For the simple calculations with the one-term three-body potentials, Γ and M_{12} are presented in Table II. In this case, the ground-state size $R^{(1)}$ cannot be fixed at the experimental value and therefore it is not surprising that Γ and M_{12} vary in a wide range with variations of the two-body potential.

For the elaborate calculations with the three-body potentials in the form of Eq. (18), one obtains one-parameter dependence, which is suitably represented for each two-body potential by a line in the Γ–M_{12} plane. The calculated dependencies are illustrated in Fig. 3 for the comparatively soft two-body potentials 6, 7, 9 (with $6.4 < \gamma < 6.8$ eV) and for harder two-body potentials 13, 14, 15 (with $5.57 < \gamma < 5.82$ eV). The dependence of $R^{(2)}$ on γ is illustrated in the inset in Fig. 3, where it is seen that the lines lie within a narrow band in the Γ – $R^{(2)}$ plane. Recall that each line in the M_{12}–Γ plane represents the dependence on the parameter of the three-body potential, e.g., on b_0. As a matter of fact, Γ monotonically increases with increasing b_0, e. g., for the two-body potential 13 the width runs the interval 4 eV $\leq \Gamma \leq$ 17

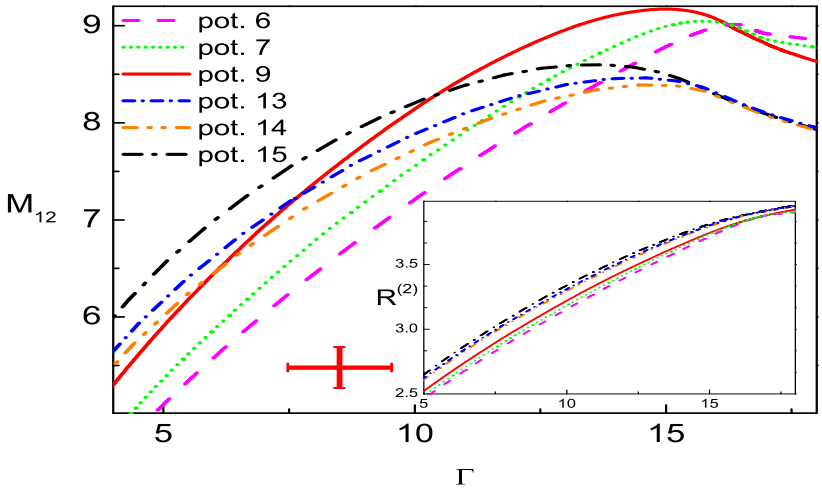

FIG. 3: Calculated M_{12}–Γ relations for the two-body potentials 6, 7, 9, 13, 14, and 15. The point with errorbars shows the experimental data $\Gamma = 8.5 \pm 1.0$ eV and $M_{12} = 5.48 \pm 0.22$ fm^2 [29]. The corresponding $R^{(2)}$–Γ relations are shown in the inset.

eV if the potential parameter runs the interval 4.5 fm $\leq b_0 \leq$ 5.5 fm. Similarly, as shown in Fig. 2, there is the dependence on the three-body-potential shape. In particular, a decrease in Γ, M_{12}, and $R^{(2)}$ corresponds to an increase in $|V_{0,1}|$ and decrease in b_1. In other words, the smaller Γ, M_{12}, and $R^{(2)}$ corresponds to three-body potentials with the stronger short-range attractive well, which give rise to a drastic modification of the excited-state wave function at short distances. In fact, if Γ decreases from 18 eV to 5 eV, $R^{(2)}$ decreases from 3.9 fm to 2.5 fm, the latter value almost coincides with the experimental ground-state r.m.s. radius $R^{(1)} = 2.48$ fm. Diminishing of $R^{(2)}$ to these small values means a comparatively compact structure of the excited state for the effective potentials with a strong short-range attraction.

IV. CONCLUSION

The method discussed in the present report provides an accurate calculation of fine characteristics of ^{12}C, viz., the extremely narrow width of the 0_2^+ state and the $0_2^+ \to 0_1^+$ MTME within the framework of the α-cluster model. A number of the effective potentials are found, which could be used in the calculations of α-cluster nuclei [21, 33]. One uses local α-α potentials, which reproduce the ^{8}Be energy and width and the α-α s-wave elastic-scattering phase shift and three-α potentials depending on the hyperradious, which reproduce the ground-state and excited-state energies and the ground-state r.m.s. radius of ^{12}C.

One of the qualitative conclusions made is that, if E_{gs}, E_r, and $R^{(1)}$ are fixed at the experimental values, a considerable short-range component of the wave function is needed to improve agreement with experiment for Γ and M_{12}. Certainly, the problem of reliable description of Γ and M_{12} in the α-cluster model deserves a thorough investigation, for example, by using the non-local three-body potential describing coupling with a twelve-nucleon channel at short distances. One of the next steps in improving the results is to start calculations with more realistic

two-body potentials, which take into account the angular-momentum dependence.

---

[1] E. E. Salpeter, Astrophys. J. **115**, 326 (1952).
[2] F. Hoyle, Astrophys. J. Suppl. **1**, 121 (1954).
[3] D.N.F. Dunbar, R.E. Pixley, W.A. Wenzel, and W. Whaling, Phys. Rev. **92**, 649 (1953).
[4] C.W. Cook, W.A. Fowler, C.C. Lauritsen, and T. Lauritsen, Phys. Rev. **107**, 508 (1957).
[5] M. Freer et al., Phys. Rev. C **49**, R1751 (1994).
[6] Y.Funaki, A.Tohsaki, H.Horiuchi, P.Schuck, and G.Röpke, Eur. Phys. J. A **24**, 368 (2005).
[7] M. Chernykh, H. Feldmeier, T. Neff, P. von Neumann-Cosel, and A. Richter, Phys. Rev. Lett. **98**, 032501 (2007).
[8] L.V. Grigorenko, R.C. Johnson, I.G. Mukha, I.J. Thomson, and M.V. Zhukov, Phys. Rev. C **64**, 054002 (2001).
[9] L.V. Grigorenko and M.V. Zhukov, Phys. Rev. C **68**, 054005 (2003).
[10] H.O.U. Fynbo et al., Phys. Rev. Lett **91**, 082502 (2003).
[11] H.O.U. Fynbo et al., Nature **433**, 136 (2005).
[12] O.I. Kartavtsev, Few-Body Systems **34**, 39 (2004).
[13] A.G.W. Cameron, Astrophys. J. **130**, 916 (1959).
[14] K. Nomoto, F.-K. Thielemann, and S. Miyaji, Astron. Astrophys. **149**, 239 (1985).
[15] K. Langanke, M. Wiescher, and F.-K. Thielemann, Z. Phys. A **324**, 147 (1986).
[16] I. Fushiki and D.Q. Lamb, Astrophys. J. **317**, 3621 (1987).
[17] S. Schramm, Astrophys. J. **397**, 579 (1992).
[18] D.V. Fedorov and A.S. Jensen, Phys. Lett. B **389**, 631 (1996).
[19] N.N. Filikhin, Yad. Fiz. **63**, 1612 (2000).
[20] S.I. Fedotov, O.I. Kartavtsev, V.I. Kochkin, and A.V. Malykh, Phys. Rev. C **70**, 014006 (2004).
[21] I. Filikhin, V.M. Suslov, and B. Vlahovic, Journ. Phys. G **31**, 1207 (2005).
[22] S.I. Fedotov, O.I. Kartavtsev, and A.V. Malykh, Eur. Phys. J. A **26**, 201 (2005).
[23] J.H. Macek, J. Phys. B **1**, 831 (1968).
[24] F.T. Smith, J. Math. Phys. **3**, 375 (1962).
[25] A. Dragt, J. Math. Phys. **6**, 533 (1965).
[26] S. Ali and A.R. Bodmer, Nucl. Phys. **80**, 99 (1966).
[27] F. Ajzenberg-Selove, Nucl. Phys. A **490**, 1 (1988).
[28] S. Wüstenbecker et al., Zeit. Phys. A **344**, 205 (1992).
[29] F. Ajzenberg-Selove, Nucl. Phys. A **506**, 1 (1990).
[30] W. Ruckstuhl et al., Nucl. Phys. A **430**, 685 (1984).
[31] E.A.J.M. Offermann, L.S. Cardman, C.W. de Jager, H. Miska, C. de Vries, and H. de Vries, Phys. Rev. C **44**, 1096 (1991).
[32] W. Reuter, G. Fricke, K. Merle, and H. Miska, Phys. Rev. C **26**, 806 (1982).
[33] Y. Ronen, N. Barnea, and W. Leidemann, Few-Body Systems **38**, 97 (2006).

Antisymmetrized Molecular Dynamics Applied to Light Nuclear System

G.J. Rampho*

Physics Department, University of South Africa, Pretoria 0003, South Africa

The Antisymmetrized Molecular Dynamics (AMD) method has been used to study various nuclear systems. Properties such as binding energies, root-mean-square radii, clustering, etc. can be obtained with accuracies comparable to most conventional methods. In contrast to other competing methods, however, with the AMD there is a possibility of tracing the positions and momenta of individual nucleons within the nucleus and thus clustering phenomena can be easily visualized. The basic ideas behind this powerful approach are discussed and some results for selected light nuclei are presented.

I. INTRODUCTION

Based on the Time-Dependent Cluster Model [1, 2], a special case of the time-dependent variational theory [3] that is applicable to fermionic systems has been proposed. This special case, called Antisymmetrized Molecular Dynamics, has two main features. One is that the spatial component of the wave function describing individual constituent particles of a system is represented by a gaussian wave packet, and the other is that the total wave function of the system is constructed as a Slater determinant of single-particle wave functions. The width parameter of the gaussian packets is treated as a real constant. AMD was used to study various nuclear systems (see Ref. [3] and references theirin) and was shown to reproduce experimental binding energies of light nuclei with reasonable accuracy. These studies, however, also highlighted the need for improvement of the AMD wave function, especially in the case of few-nucleon systems. AMD is an *ab initio* theory able to describe the dynamics of heavy ion reactions and structure attributes of many-body systems without model assumptions. The Coulomb and three-body potentials can easily be treated with AMD, and hence, properties of stable and unstable nuclear systems can be studied.

The basic notions of the AMD formulations were suggested in Ref. [4] and further elaborated in Ref. [5]. These include the construction of the wave function for many-body systems and the evaluation of the expectation values of one- and two-body operators. Incorporation of two-particle collision attributes was done in Ref. [3]. In this work the AMD method is applied to light nuclei and the corresponding binding energies and root mean square radii (rms) are calculated and cluster aspects of the nuclei considered are investigated.

In Sec. II the basic formalism of the AMD is discussed. The types of hamiltonians that can be treated, the construction of the wave function, the equations of motion of the variable parameters and the variational technique used are briefly outlined. Results and illustrations of the application of AMD to some light nuclear systems are presented in Sec III. Conclusions drawn are given in Sec IV.

*Electronic address: rampho@science.unisa.ac.za

II. FORMALISM

Consider the time-dependent Schrödinger equation

$$\left(\mathrm{i}\,\hbar \frac{\partial}{\partial\, t} - H \right) \Psi = 0 \tag{1}$$

for light nuclear systems described by a general, non-relativistic, Hamiltonian of the form

$$H = -\sum_i \frac{\hbar^2}{2\,M_i} \nabla_i^2 + \frac{1}{2!} \sum_{i \neq j} V_{ij} + \frac{1}{3!} \sum_{i \neq j \neq k} V_{ijk} \tag{2}$$

where M_i is the mass of nucleon i and V_{ij} and V_{ijk} are the two- and three-body potentials respectively. The solution Ψ is approximated by a Slater determinant of gaussian wave packets that depend on complex dynamical variables. The approximate solution is then obtained by minimizing the expectation value of the hamiltonian with respect to the dynamical variables, using a time-dependent variational method. The energy so obtained is just an upper-bound to the true energy of the system. The resulting solution Ψ can also be used to determine other properties of the system.

A. The Wave Function

The single–particle states $\phi(\boldsymbol{\upsilon})$ are assumed to be of the form [3]

$$\phi(\boldsymbol{\upsilon}) = \psi(\boldsymbol{r})\, \chi(\boldsymbol{\sigma})\, \xi(\boldsymbol{\tau}) \tag{3}$$

where $\psi(\boldsymbol{r})$, $\chi(\boldsymbol{\sigma})$, and $\xi(\boldsymbol{\tau})$ are the spatial, spin, and isospin wave functions, respectively. The spins of the nucleons are treated as fixed and only the case of parallel spins is considered. Hence $\chi = |\uparrow\rangle$ or $\chi = |\downarrow\rangle$ and $\xi = |\,\text{proton}\,\rangle$ or $\xi = |\,\text{neutron}\,\rangle$. The spatial component, $\psi(\boldsymbol{r})$, is parametrized as a normalized gaussian wave packet

$$\phi(\boldsymbol{r}) = \left(\frac{2\alpha}{\pi} \right)^{3/4} \exp\left[-\alpha \left(\boldsymbol{r} - \frac{\boldsymbol{s}}{\sqrt{\alpha}} \right)^2 + \frac{1}{2}\,\boldsymbol{s}^2 \right] \equiv |\,\boldsymbol{s}\,\rangle \tag{4}$$

where the centroid of the wave packet, $\boldsymbol{s}$, is a complex time–dependent parameter. The 'phase' $\boldsymbol{s}^2/2$ is included mainly to simplify the structure of elements of the resulting overlap matrix, $\langle\, \phi_i \,|\, \phi_j \,\rangle$. When the momentum operator of a nucleon is denoted by, say, $\boldsymbol{p}$, then the real and imaginary components of the parameter $\boldsymbol{s}$ are given by [3]

$$\mathrm{Re}(\boldsymbol{s}) = \sqrt{\alpha}\, \frac{\langle\, \boldsymbol{s} \,|\, \boldsymbol{r} \,|\, \boldsymbol{s} \,\rangle}{\langle\, \boldsymbol{s} \,|\, \boldsymbol{s} \,\rangle}\,, \qquad \mathrm{Im}(\boldsymbol{s}) = \frac{1}{2\,\hbar\,\sqrt{\alpha}}\, \frac{\langle\, \boldsymbol{s} \,|\, \boldsymbol{p} \,|\, \boldsymbol{s} \,\rangle}{\langle\, \boldsymbol{s} \,|\, \boldsymbol{s} \,\rangle} \tag{5}$$

The width parameter a is treated as a real constant and taken as common for all nucleons.

The total wave function $\Psi(\boldsymbol{\upsilon})$ of the system depends on the position $\boldsymbol{r}_i$, spin $\boldsymbol{\sigma}_i$, and isospin $\boldsymbol{\tau}_i$, $(1, 2, 3, \ldots, N)$ variables of the nucleons. Here the collective variable $\boldsymbol{\upsilon}_i$ is used to represent the set $\{\, \boldsymbol{r}_i\, \boldsymbol{\sigma}_i\, \boldsymbol{\tau}_i \,\}$. For the fermionic systems treated in this work, the total wave function of the system is required to be antisymmetric with respect to the interchange of particles. One way of constructing an antisymmetric wave function, is by using Slater determinants of single-particle states $\phi_i(\boldsymbol{\upsilon}_j)$

$$\Psi_A(\boldsymbol{\upsilon}_1, \boldsymbol{\upsilon}_2, \ldots, \boldsymbol{\upsilon}_N) \;=\; \frac{1}{\sqrt{N!}} \det[\, \phi_i(\boldsymbol{\upsilon}_j) \,]\,. \tag{6}$$

where $\phi_i(\boldsymbol{v}_j)$ depends on the degrees of freedom of the i–th particle only. The wave function is represented by $\Psi(\boldsymbol{v}, \boldsymbol{\beta})$ where β is a set of variational parameters. The excited states are constructed so that they are automatically orthogonal to the lower states. This is achieved by the use of the Gram-Schmidt orthogonalization procedure. The n-th excited trial state is therefore constructed as

$$| \Psi_n(\boldsymbol{\beta}) \rangle = \left[1 - \sum_{i=0}^{n-1} | \Psi_i(\boldsymbol{\beta}') \rangle \langle \Psi_i(\boldsymbol{\beta}') | \right] | \Psi_t(\boldsymbol{\beta}) \rangle \tag{7}$$

where $\boldsymbol{v}$ is ommited for convenience, Ψ_i are the already computed normalized lower states and Ψ_t is a trial function formulated as in the case of the ground state.

B. Binding Energies

The energy expectation value of the system is calculated using the wave function constructed as in the previous subsection. The structure of such a wave function makes it possible for the integrals involved to be evaluated analytically.

In calculating the kinetic energy of a nuclear system, the difference in mass between proton and neutron should be incorporated. Since we are interested in bound nucleons, the most realistic approach in distinguishing between the proton and the neutron mass is to separate the kinetic energy operator into a charge-independent (CI) term t_i^{CI} and a charge-symmetry-breaking (CSB) term t_i^{CSB} [6]

$$t_i = t_i^{CI} + t_i{}^{CSB} = -\frac{\hbar^2}{2\mu_i^*} \nabla_i^2 \tag{8}$$

where

$$\frac{1}{\mu_i^*} = \frac{1}{2} \left(\frac{1}{\mu_i} + \frac{\tau_{zi}}{\Delta\mu_i} \right) , \tag{9}$$

with

$$\frac{1}{\Delta\mu} = \frac{1}{m_p} - \frac{1}{m_n} . \tag{10}$$

where τ_{zi} is the isospin and μ_i the reduced mass of nucleon i. However, the term $t_i{}^{CSB}$ usually is neglected in the primary AMD. The expectation value of the kinetic energy operator of the system $\mathcal{T}$ is computed as

$$\mathcal{T} = \frac{\langle \Psi | \sum_j t_j | \Psi \rangle}{\langle \Psi | \Psi \rangle} \tag{11}$$

$$= \sum_{ij} \langle \phi_i | t_j | \phi_j \rangle B_{ji}^{-1} . \tag{12}$$

where B_{ij}^{-1} are the elements of the inverse of the overlap matrix B. The expectation values $\langle \phi_i | t_j | \phi_j \rangle$ can be analytically evaluated.

The nucleon-nucleon potentials can be expressed in the general form

$$V(\boldsymbol{r}_{ij}) = \sum_p u(\boldsymbol{r}_{ij}) \mathcal{O}_{ij}^p \tag{13}$$

where $\mathcal{O}_{ij}^{p}$ is a given two-body operator and $u(\boldsymbol{r}_{ij})$ a function depending on the relative positions of the interacting nucleons. The expectation value of spin-independent two-body potentials of the system, $\mathcal{V}_2$, is computed as

$$\mathcal{V}_2 = \frac{\langle \Psi \,|\, \sum_{ij} V_{ij} \,|\, \Psi \rangle}{\langle \Psi \,|\, \Psi \rangle} \tag{14}$$

$$= \frac{1}{2} \sum_{ijkl} \langle \phi_k \, \phi_l \,|\, V(r_{ij}) \,|\, \phi_i \, \phi_j \rangle \, \left[B_{ik}^{-1} \, B_{jl}^{-1} - B_{il}^{-1} \, B_{jk}^{-1} \right] \, . \tag{15}$$

In the case of spin-dependent potentials minor modifications are introduced in this matrix elements. There are not so many forms of the potential functions $u(r_{ij})$ for which the expectation value $\langle \phi_k \, \phi_l \,|\, u(r_{ij}) \,|\, \phi_i \, \phi_j \rangle$ can be analytically evaluated. One of such forms is the gaussian form which is used in a number of nucleon-nucleon potentials. Other forms of $u(r_{ij})$ can also be used for analytical evaluations of the integrals involved. However, this could lead to numerical instabilities (one such case is the Coulombic form). For the latter cases $u(r_{ij})$ is expanded as

$$u(r) = \sum_{n} v_n \, \mathrm{e}^{-b_n \, r^2} \tag{16}$$

to fit the potential with the parameters v_n and b_n. The three-body potential is treated in the same way as the two-body potentials.

The total energy of the system is obtained as the expectation value of the Hamiltonian $\langle H \rangle$ whence the internal energy of the system E_I can be obtained by subtracting the contribution of the center of mass motion $\mathcal{T}_{cm}$.

$$E_I = \langle H \rangle - \mathcal{T}_{cm} \, . \tag{17}$$

When there are internal clusters formed in the system, then E_I can be calculated from the number of fragments N_F, the internal energy of the fragments E^F and the inter-fragment relative energies E^R as

$$E_I = \sum_{i=1}^{N_F} E_i + \gamma \, E^R \tag{18}$$

where γ is either a constant or a linear function of N_F, depending on the form of clusterization considered. In AMD formalism $\gamma = N_F$ and $E^R = T_0$. Only N_F and E_i are actually calculated. The parameters T_0 is a constant chosen to shift binding energies of the nuclear system.

C. Equations of Motion

If the total wave function of the system is parametrized by N complex time-dependent parameters $\boldsymbol{s}$, $\Psi\left(\boldsymbol{s}_1, \boldsymbol{s}_2, \ldots, \boldsymbol{s}_N\right)$, then the time-dependent variational principle Ref. [3]

$$\delta \int_{t_1}^{t_2} \frac{\langle \Psi \,|\, \mathrm{i}\hbar \frac{\partial}{\partial t} - H \,|\, \Psi \rangle}{\langle \Psi \,|\, \Psi \rangle} \, \mathrm{d}t = 0 \tag{19}$$

with the constraints

$$\delta\Psi(t_1) = \delta\Psi(t_2) = \delta\Psi^*(t_1) = \delta\Psi^*(t_2) = 0 \tag{20}$$

can be cast in the form

$$\delta \int_{t_1}^{t_2} \left[\frac{\mathrm{i}\,\hbar}{2} \sum_j \left(\frac{\mathrm{d}\,\boldsymbol{s}_\mathrm{j}}{\mathrm{d}t} \frac{\partial}{\partial\,\boldsymbol{s}_j} - \frac{\mathrm{d}\,\boldsymbol{s}_\mathrm{j}^*}{\mathrm{d}t} \frac{\partial}{\partial\,\boldsymbol{s}_j^*} \right) \ln \mathcal{N} - E \right] \mathrm{d}t = 0 \tag{21}$$

with the corresponding constraints

$$\delta\boldsymbol{s}(t_1) = \delta\boldsymbol{s}(t_2) = \delta\boldsymbol{s}^*(t_1) = \delta\boldsymbol{s}^*(t_2) = 0 \tag{22}$$

where

$$\mathcal{N} = \langle\,\Psi\,|\,\Psi\,\rangle \tag{23}$$

is the norm of the wave function and

$$E = \frac{\langle\,\Psi\,|\,H\,|\,\Psi\,\rangle}{\langle\,\Psi\,|\,\Psi\,\rangle} \tag{24}$$

the energy functional of the system. Note that $\boldsymbol{s}$ and $\boldsymbol{s}^*$ are treated as independent variables.

The time evolution of the state Ψ is derived from the minimization of the time-dependent variational principle which leads to the coupled equations of motion of the parameters $\boldsymbol{s}$ and $\boldsymbol{s}^*$, compactly expressed in the form [7]

$$\frac{\mathrm{i}\,\hbar}{2} \begin{bmatrix} 0 & \mathcal{C} \\ -\mathcal{C}^* & 0 \end{bmatrix} \begin{bmatrix} \dfrac{\mathrm{d}\,\boldsymbol{s}^*}{\mathrm{d}\,t} \\ \dfrac{\mathrm{d}\,\boldsymbol{s}}{\mathrm{d}\,t} \end{bmatrix} = \begin{bmatrix} \dfrac{\partial\,E}{\partial\,\boldsymbol{s}^*} \\ \dfrac{\partial\,E}{\partial\,\boldsymbol{s}} \end{bmatrix} \tag{25}$$

where $\mathcal{C}$ is a hermitian matrix with elements

$$\mathcal{C}_{ij}\,(\boldsymbol{s}, \boldsymbol{s}^*) = \frac{\partial^2}{\partial\,\boldsymbol{s}_i{}^*\,\partial\,\boldsymbol{s}_j} \ln \mathcal{N} \tag{26}$$

The upper-bound to the energy of the system is obtained by solving these equations. Since the parameters $\boldsymbol{s}$ and $\boldsymbol{s}^*$ are not truly independent solving only one set of equations, say,

$$\mathrm{i}\hbar \sum_j \mathcal{C}_{i\sigma,j\tau} \frac{\mathrm{d}\,s_{j\tau}}{\mathrm{d}\,t} = \frac{\partial\,E}{\partial\,s_{i\sigma}^*} \tag{27}$$

should suffice.

An interesting minimization technique, is the use of the so-called *frictional cooling* [3] to determine the variational parameters. The technique involves introducing a "friction" coefficient to the equation of motion for the variational parameters, Eq. (27). It can be shown that multiplying the equations of motion by a complex constant, say $a + \mathrm{i}\,b$, where a and b are arbitrary real numbers, then the variation of the energy functional with time

$$\frac{\mathrm{d}\,\mathrm{E}}{\mathrm{d}\,t} < 0 \tag{28}$$

when $b < 0$, decreases with time. Therefore, the solution of the modified equation of motion results in a minimization of the energy functional, Eq. (24).

III. RESULTS AND DISCUSSIONS

To determine the variational parameters, the equations of motion, Eq. (27), are modified by replacing the matrix $\mathcal{C}$ with a unit matrix and multiplying the right-hand-side with a complex constant

$$\frac{\mathrm{d}\, s_{i\sigma}}{\mathrm{d}\, t} = \frac{(\, a - \imath\, b\,)}{\imath\hbar}\, \frac{\partial\, E}{\partial\, s^{*}_{i\sigma}}\,. \tag{29}$$

These modifications are introduced only to set up and simplify the *cooling* process. The above equations are solved with the constraint $\sum_i \boldsymbol{s}_i = 0$ so that only the zero-point oscillation of the center-of-mass need be subtracted from the expectation value of the hamiltonian of the system. Corrections for the center-of-mass and relative motion of fragments to the binding energy of the system lead to the expression [3]

$$E_b = \langle\, H\,\rangle - \frac{3\,\hbar^2\,\nu}{2\,M}\, A + T_0\ (\, A - N_F\,) \tag{30}$$

where ν and T_0 a free parameters chosen to fit the experimental binding energies of the ^{4}He and ^{12}C nuclei. The values $\nu = 0.16$ and $T_0 = 7.7\,\mathrm{MeV}$ are used with ν taken to be the same for all nucleons.

As an illustration of the AMD method, the binding energies and root-mean-square radii of selected few-nucleon systems are computed with the Volkov No. 1 potential [8],

$$V(r_{ij}) = \left[\, 144.86\,\mathrm{e}^{-\,(\,r_{ij}/0.82\,)^2} - 83.34\,\mathrm{e}^{-\,(\,r_{ij}/1.60\,)^2}\,\right]\ (\, w - m\, P_\sigma\, P_\tau\,) \tag{31}$$

where $w = 1 - m$ and $m = 0.576$. P_σ and P_τ are the spin and isospin projection operators, respectively. The Coulomb potential,

$$V_C(r_{ij}) = \frac{\mathrm{e}^2}{|\, \boldsymbol{r}_i - \boldsymbol{r}_j\,|}\, \left(\frac{1}{2} + \tau_i\right)\left(\frac{1}{2} + \tau_j\right) \tag{32}$$

where τ is the isospin of the nucleon, is approximated by seven gaussians. The accuracy of such an approximation is discussed in Ref. [9]. The matrix elements of the expectation value of these potentials are

$$\mathcal{V} = \frac{1}{2}\sum_{ijkl,n} v_n\ (\,1 - \rho_n\,)^{3/2}\, \exp\left[-\frac{\rho_n}{4}\,\boldsymbol{C}^2\right]\, R_{ki}\, R_{lj}\, \left[\, S_+\, R^{-1}_{ik}\, R^{-1}_{jl} - S_-\, R^{-1}_{il}\, R^{-1}_{jk}\,\right] \tag{33}$$

where $\boldsymbol{C} = \boldsymbol{s}^{*}_l - \boldsymbol{s}^{*}_k + \boldsymbol{s}_j - \boldsymbol{s}_i$ and $\rho_n = b_n/(b_n + \alpha)$.

The summation over spins are given by $S_\pm = (\, w \pm m\,)\left(\,1 \mp \delta_{\eta_i\eta_j}\,\right)$ in the case of the Volkov potential and $S_\pm = 1$ for the Coulomb potential; η is the spin-isospin component of the nucleon wave function. The calculated binding energies are compared with those presented in Ref. [10], which are obtained via the stochastic variational method (SVM) for the same potential.

The preliminary binding energy results obtained with the AMD method are presented in Table I with the negative sign suppressed. As can be noticed from this table the experimental binding energy of the $4N$ system is well reproduced as expected. However, the calculated binding energy of the $2N$ system is a little less than twice the value obtained via other methods. The $3N$ system on the other hand is off by about 2 MeV. Considering that the AMD wave function has only one free parameter ν and that it does not have definite parity or total angular momentum,

TABLE I: The binding energies of few-nucleon systems with the Volkov No. 1 potential.

Binding Energy (MeV)	$2N$	$3N$	$4N$
$E_{\rm AMD}$	0.969	9.984	28.290
$E_{\rm SVM}$ [11]	0.545	8.468	30.420
$E_{\rm EXP}$	2.225	8.481	28.295

this results are reasonable.

The same wave functions are used to calculate the root-mean-square radii of the $2N$, $3N$ and $4N$ nuclear systems with expression

$$\langle\, r^2 \,\rangle = \frac{\langle\, \Psi \,|\, \frac{1}{A} \sum_i \,(\, r_i - R \,)\, |\, \Psi \,\rangle}{\langle\, \Psi \,|\, \Psi \,\rangle} \tag{34}$$

where R is the center-of-mass of the system. The integrals involved are evaluated analytically. For this quantity no fitting is done and the results are shown in Table. II. As can be observed from this table the AMD theory reproduces the experimental values of the root-mean-square radii of the $2N$ and $3N$ systems. The calculated value for the $4N$ system is less than the SVM and experimental values by about 0.15 fm.

TABLE II: The root-mean-square radii of few-nucleon systems with the Volkov No. 1 potential.

r.m.s (fm)	$2N$	$3N$	$4N$
$\langle\, r^2 \,\rangle^{1/2}_{\rm AMD}$	1.91	1.56	1.35
$\langle\, r^2 \,\rangle^{1/2}_{\rm SVM}$ [11]	3.44	1.73	1.49
$\langle\, r^2 \,\rangle^{1/2}_{\rm EXP}$	1.96	1.57	1.47

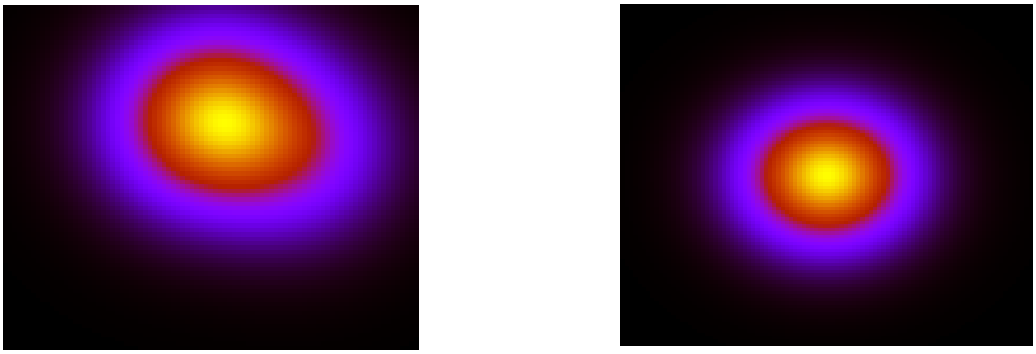

FIG. 1: The density of the $4N$ system: (a) the initial random distribution and (b) the final configuration after the variation of parameters.

In solving the cooling equations a random number generator is used to set up the initial values of the variational parameters. The initial probability density of the system is computed

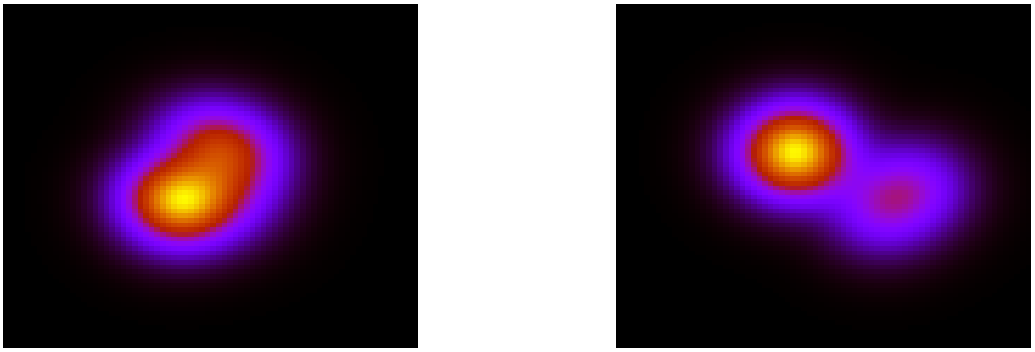

FIG. 2: The density of the ^{6}Li system: (a) the initial random distribution and (b) the final configuration after the variation of parameters.

using such values of the parameters. The initial densities for the $4N$ and $6N$ systems are shown in Fig. III(a) and Fig. III(a), respectively. The densities obtained after the cooling process are shown in Fig. III(b) for the $4N$ system and Fig. III(b) for the $6N$ system. The final densities for the $2N$ and $3N$ systems are similar to that of the $4N$ system, which appear to be, as expected, spherical. The final density for the $6N$ system, on the other hand, seem to reflect some degree of deformation as compared to that of the $4N$ system. This apparent deformation and the computed value of N_F, which is greater than one but less than two, suggest an underlying clustering structure in the $6N$ nuclear system.

IV. CONCLUDING REMARKS

It is demonstarted that the AMD method can be used to evaluate observables of light– to medium-light– nuclear systems. To obtain the binding energies of these systems, the clustering structures are considered which introduce an additional free parameter related to the energy of the relative motion of the clusters. The binding energies thus obtained, reflect to a certain extend the quality of the wave function generated by the primary AMD theory. Concerning the root-mean-square radii, they are reasonably reproduced the values being comparable to the experimental ones.

Some remarks could be passed here concerning the open questions on the AMD method. Even though the experimental values of the root-mean-square radii of few-nucleon systems can be reproduced and also the experimental binding energies with realistic nucleon-nucleon potentials [10], the generated AMD wave function of the system may not have such desired qualities as the appropriate asymptotic behavior in the case of bound states, the correct parity or being an eigenstate of the total angular momentum of the system. As a result numerous efforts for improvements have been introduced in the AMD formalism. These include representing single-particle wave functions with either deformed gaussians [12] or linear combinations of gaussians [13], or superposing several Slater determinants [14] to represent the total wave function of the system. Also, in addition to projecting the AMD wave function on to the eigenstates of parity and total angular momentum of the system [15], AMD was coupled with other methods like the generator coordinate method [16], the Hartree-Fock [13], and the incorporation of Vlasov equa-

tion [17], to study various aspects of numerous nuclear systems. These modifications generated the so-called advanced or extended versions of AMD. Further investigations and improvements along these lines are under consideration.

---

[1] S. Drożdż, J. Okolowcz, and M. Ploszajczak, Phys. Lett. B **109**, 145 (1982).
[2] E. Caurier, B. Grammaticos, and T. Sami, Phys. Lett. B **109**, 150 (1982).
[3] A. Ono, H. Horiuchi, T. Maruyama, and A. Ohnishi, Prog. Theor. Phys. **87**, 1185 (1992).
[4] D. Brink, in Proceedings of the International School of Physics "Enroco Fermi," Course 36, Edited by C. Bloch, (Academic, New York, 1965) p247.
[5] Y. Akaishi, S.A. Chin, H. Horiuchi, and K. Ikeda, Cluster Models and Other Topics, International Review of Nuclear Physics - Vol. 4 (World Scientific, Singapore, 1986).
[6] B.S. Pudliner, V.R. Pandharipande, J. Carlson, S.C. Pieper, and R.B. Wiringa Phys. Rev. C **52**, 1720 (1997).
[7] M. Saraceno, P. Kramer, and F. Fernandez, Nucl. Phys. A **405**, 88 (1983).
[8] A. Volkov, Nucl. Phys. **75**, 33 (1965).
[9] Y. Taniguchi, T. Watanabe, N. Sawado, and S. Oryu, Few-Body Systems Suppl. **15**, 247 (2003).
[10] T. Watanabe and S. Oryu, Prog. Theor. Phys. **116**, 429 (2006).
[11] K. Varga and Y. Suzuki, Phys. Rev. C **52**, 2885 (1995).
[12] M. Kimura, Phys. Rev. C **69**, 044319 (2004).
[13] A. Doté, H. Horiuchi, and Y. Kanada-En'yo Phys. Rev. C **56**, 1844 (1997).
[14] Y. Kanada-En'yo, M. Kimura, and H. Horiuchi, C. R. Physique **4**, 497 (2003).
[15] Y. Kanada-En'yo and H. Horiuchi, Phys. Rev. C **55**, 628 (1995).
[16] N. Furutachi, J. Phys.: Conf. Ser. **49**, 122 (2006).
[17] A. Ono and H. Horiuchi, Phys. Rev. C **53**, 2958 (1996).

Integrodifferential Equation Approach Applied to Hypernuclei

R.M. Adam*

Nuclear Energy Corporation of South Africa,
P.O. Box 582, Pretoria 0001, South Africa

The Integrodifferential Equation Approach (IDEA) to many-body quantum mechanical systems involves projecting the Hilbert space onto a basis set of hyperspherical harmonic functions and is exact if higher than two-body correlations are excluded from the dynamics. In the current work the IDEA is extended to systems of unequal masses and this generalized formalism is applied to some hypernuclear systems, in particular to both single and double Λ hypernuclei. The binding energies are in good agreement with those obtained with other methods. Ultimately the interesting question to be investigated theoretically is whether any stable double Λ hypernuclei are predicted to exist.

I. INTRODUCTION

A large number of short-lived hypernuclei have been detected over the past 50 years and numerous theoretical and experimental investigations were carried out concerning these systems (see, for example, Refs. [1–3] and references therein). Such hypernuclei generally contain a single "light" baryon such as Λ or Σ, e.g. ${}^{5}_{\Lambda}$He, ${}^{6}_{\Lambda}$H, ${}^{7}_{\Sigma}$Li, ${}^{209}_{\Lambda}$Pb etc. Hypernuclei with strangeness $S = 2$ hypernuclei also exist, e.g. ${}^{6}_{\Lambda\Lambda}$He. However the lifetime of most of these hypernuclei is about 10^{-10} sec. To date no stable hypernucleus has been detected. This is because the decay of the Λ and Σ particles is not kinematically suppressed in the nuclear environment, unlike the decay of the neutron. The decay energy of the Λ particle is quite large,

$$\Lambda \rightarrow p + \pi^- , \qquad \sim 40\,\mathrm{MeV} ,$$

whereas no binding energy of a single Λ particle to a nucleus has been found to exceed 27 MeV. This is unlike the case of the neutron the decay of which yields about 0.8 MeV,

$$n \rightarrow p + e + \overline{\nu}_e , \qquad 0.8\,\mathrm{MeV} ,$$

whereas the average binding energy per nucleon is about 8 MeV.

The binding energy per nucleon as a function of baryon number A peaks at $A = 56$. However, in the case of the Λ-nucleus separation energy, the peak is at $A = 209$. The reason for this difference is that the Λ particle is not affected by Pauli Principle restrictions in the nuclear medium.

It has also been found that the separation energy in double Λ hypernuclei is significantly higher than in single Λ hypernuclei. For example the Λ separation in ${}^{5}_{\Lambda}$He is 3.1 MeV, whereas the $\Lambda\Lambda$ separation energy in ${}^{6}_{\Lambda\Lambda}$He is 10.8 ± 0.6 MeV. This difference is attributed to (i) $\Lambda\Lambda$ attraction and (ii) the polarization of the ^{4}He nucleus by the Λ's. It is likely that this effect will be accentuated in higher A hypernuclei until it finally saturates at a particular value of A.

Ultimately the aim of this work is to investigate the trend of $\Lambda\Lambda$ separation energies in hypernuclei of different masses, and to examine clustering via resonances in relevant channels. This can be achieved by using the the Integrodifferential Equation Approach (IDEA) developed

*Electronic address: robadam@necsa.co.za

by Fabre de la Ripelle and co-workers [4–10]. The method is based on a hyperspherical harmonics expansion method and takes into account the two-body correlations into account exactly. Details of the formalism can be found in the aforementioned references while an extension of the method to bound systems with unequal mass particles appears in Ref. [11].

In Sec. II the IDEA formalism is presented and the most important features of it are outlined with more emphasis given to unequal mass systems. The method has been applied to the ${}^{6}_{\Lambda\Lambda}$He system and Λ and $\Lambda\Lambda$ results for separation energies in a range of hypernuclei in an α-cluster nuclear model are given. Calculations were also performed for the full $N\Lambda$ and $N\Lambda\Lambda$ models of hypernuclei. The conclusions are summarized in Sec. IV, while some technical details concerning the projection function are given in the Appendix.

II. THE INTEGRODIFFERENTIAL EQUATION APPROACH

We shall outline here the derivation of the IDEA by defining first the following chain of Jacobi coordinates for a system of $A = N + 1$ particles with masses m_i.

$$
\begin{aligned}
\vec{\xi}_N &= \left[\frac{2Am_1m_2}{M(m1+m2)}\right]^{1/2}(\mathbf{x}_2-\mathbf{x}_1)\\
\vec{\xi}_{N-1} &= \left[\frac{2A(m_1+m_2)m_3}{M(m1+m2+m3)}\right]^{1/2}\left(\mathbf{x}_3-\frac{m_1\mathbf{x}_1+m_2\mathbf{x}_2}{m_1+m_2}\right)\\
&\vdots\\
\vec{\xi}_{N-i+1} &= \left[\frac{2A(\sum_{j=1}^{i}m_j)m_{j+1}}{M\sum_{j=1}^{i}m_j}\right]^{1/2}\left(\mathbf{x}_{i+1}-\frac{\sum_{j=1}^{i}m_j\mathbf{x}_j}{\sum_{j=1}^{i}m_j}\right)\\
&\vdots\\
\vec{\xi}_1 &= \left[\frac{2A(M-m_A)m_A}{M^2}\right]^{1/2}\left(\mathbf{x}_A-\frac{\sum_{j=1}^{A-1}m_j\mathbf{x}_j}{M-m_A}\right)\\
\mathbf{X} &= \frac{1}{M}\sum_{j=1}^{A}m_j\mathbf{x}_j
\end{aligned}
\tag{1}
$$

where $\mathbf{X}$ is the center of mass , m_i the mass of the particle i, and $M = \sum_{j=1}^{A} m_j$ is the total mass of the system under consideration. The hyperradius r, which is a collective variable, is defined via

$$
r = \left[\sum_{i=1}^{N}\xi_i^2\right]^{1/2} = \left[\frac{2A}{M^2}\sum_{i<j\le A}m_im_jr_{ij}^2\right]^{1/2} \tag{2}
$$

where $\mathbf{r}_{ij} = \mathbf{x}_i - \mathbf{x}_j$. For equal masses we have

$$
r = \left[2\sum_{i=1}^{A}(\mathbf{x}_i-\mathbf{X})^2\right]^{1/2} = \left[\frac{2}{A}\sum_{i<j\le A}\mathbf{r}_{ij}^2\right]^{1/2} \tag{3}
$$

The angular coordinates over the hypersphere are defined by the the spherical coordinates ω_i of each vector ξ_i and by the $[\phi]$ coordinates, the latter being defined by

$$\begin{aligned}
\xi_N &= r\cos\phi_N \\
\xi_{N-1} &= r\sin\phi_N\cos\phi_{N-1} \\
&\vdots \\
\xi_i &= r\sin\phi_N\cdots\sin\phi_{i+1}\cos\phi_i \\
&\vdots \\
\xi_1 &= r\sin\phi_N\cdots\sin\phi_2
\end{aligned} \tag{4}$$

where we choose $\phi_1 = 0$. This is known as the standard choice of angular coordinates of Zernike and Brinkman [12].

The volume element $\mathrm{d}\tau$ is given by the product

$$\mathrm{d}\tau = \prod_{j=1}^{N} \mathrm{d}^3\xi_j = \prod_{j=1}^{N} \xi_j^2\,\mathrm{d}\xi_j\,\mathrm{d}\omega_j \tag{5}$$

where $\mathrm{d}\omega_j = \cos\phi_j\,\mathrm{d}\phi_j$. Using Eq. (4) we get

$$\mathrm{d}\tau = \mathrm{d}\omega_1 \prod_{j=2}^{N} \cos^2\phi_j(\sin\phi_j)^{3j-4}\,\mathrm{d}\phi_j d\omega_j r^{3N-1}\,\mathrm{d}r, \tag{6}$$

or using the variable $z_j = \cos 2\phi_j$,

$$\mathrm{d}\tau = d\omega_1 \prod_{j=2}^{N} 2^{-3j/2}(1-z_j)^{(3j-5)/2}(1+z_j)^{1/2} dz_j\,\mathrm{d}\omega_j r^{3N-1}\,\mathrm{d}r \tag{7}$$

The surface element is

$$\mathrm{d}\Omega = \mathrm{d}\omega_1 \prod_{j=2}^{N} 2^{-3j/2} W_j(z_j)\,\mathrm{d}z_j\,\mathrm{d}\omega_j \tag{8}$$

where the function W_j is given by

$$W_j(z_j) = (1-z_j)^{(3j-5)/2}(1+z_j)^{1/2} \tag{9}$$

and is known as weight function.

In general the surface element $\mathrm{d}\Omega_i$ is defined to be the part of the surface $\mathrm{d}\Omega$ which contains the coordinates ω_j and z_j for $j \le i$ i.e

$$\mathrm{d}\Omega_i = \mathrm{d}\omega_1 \prod_{j=2}^{i} 2^{-3j/2} W_j(z_j)\,\mathrm{d}z_j\,\mathrm{d}\omega_j \tag{10}$$

Knowing the element $d\Omega_j$ we may construct the element of $\mathrm{d}\Omega_{j+1}$ via

$$\mathrm{d}\Omega_{j+1} = \mathrm{d}\Omega_j(\sin\phi_{j+1})^{D-4}\cos\phi_{j+1}^2\,\mathrm{d}\phi_{j+1}\,\mathrm{d}\omega_{j+1} \tag{11}$$

where $D = 3(j+1)$. Thus, for the surface element $\mathrm{d}\Omega_N$ we have

$$\mathrm{d}\Omega_N = \mathrm{d}\Omega_{N-1}\sin\phi_N^{D-4}\cos\phi_N^2\,\mathrm{d}\phi_N\,\mathrm{d}\omega_N\,. \tag{12}$$

Since

$$\cos\phi_N = \left(\frac{1+z_N}{2}\right)^{1/2} \qquad \text{and} \qquad \sin\phi_N = \left(\frac{1-z_N}{2}\right)^{1/2}$$

the relation (12) can be written as

$$\mathrm{d}\Omega_N = 2^{-D/2}\,\mathrm{d}\Omega_{N-1}(1-z_N)^{(D-5)/2}(1+z_N)^{1/2}\,\mathrm{d}z_N d\omega_N\,. \tag{13}$$

Finally, we recall that the total kinetic energy operator T is given by

$$T = -\frac{\hbar^2}{2}\sum_{i=1}^{A}\frac{1}{m_i}\nabla_i^2 = -\frac{\hbar^2}{M}\left[A\sum_{i=1}^{N}\nabla_{\xi_i}^2 + \frac{1}{2}\nabla_X^2\right]. \tag{14}$$

It is noted that the latter relations are invariant under any exchange of particles.

Its basic assumption in deriving the IDEA formalism is that the particle interact via pairwise forces (for the inclusion of three-body forces see Ref. [6]) i.e, one starts from the Faddeev decomposition

$$\Psi = \psi_{12} + \psi_{23} + \psi_{31} \tag{15}$$

such that

$$(T-E)\psi_{12} = -V_{12}\Psi \tag{16}$$

For more than three particles, we assume a similar the decomposition

$$\Psi = \sum_{i<j}\psi_{ij} \tag{17}$$

such that Eq. (16) is still valid. In the general case where one deals with non-identical particle (which is the case under consideration) one has instead of (16) coupled Faddeev-type equations of the form

$$(T-E)\psi_{12}^{(c)} = -V_{12}^{(c)}\Psi \tag{18}$$

where the subscript α denotes a give type of pair (e.g., $\Lambda\Lambda$, ΛN etc.) We shall restrict ourselves here to the case where the forces are of Wigner type. Then the amplitude ψ_{ij} can be written as [6, 13]

$$\psi_{ij}(\mathbf{x}) = H_{[L_m]}(\mathbf{x})F(r_{i\,j}, r) \tag{19}$$

where $H_{[L_m]}(\mathbf{x})$ is a polynomial of minimal degree L_m characterized by a set of quantum numbers $[L_m]$. For systems such as ${}^{5}_{\Lambda}$He and ${}^{6}_{\Lambda\Lambda}$He the Pauli principle allows the different fermions to occupy single particle S-states and one has the simplification

$$H_{[L_m]}^{(c)}(\mathbf{x}) = H_{[0]}(\mathbf{x}) = \text{constant} \tag{20}$$

for all pairs involved. Then one has

$$(T-E)F^{(c)}((\xi_N^{ij})^2, r) = -V^{(c)}(r_{i\,j})\sum_{k<l}F^{(c)}((\xi_N^{k\,l})^2, r) \tag{21}$$

To proceed we project Eq. (21) onto the two-dimensional space $r \oplus \xi_N^{ij}$ by integrating over all coordinates except r and ξ_N^{ij} and setting

$$z = 2(\xi_N^{ij})^2/r^2 - 1$$

and

$$P^{(c)}(z,r) = r^{(D-1)/2} F^{(c)}(\xi_N^{ij}, r)$$

we obtain

$$\left\{ \frac{\hbar^2 A}{M} \left[-\frac{\partial^2}{\partial r^2} + \frac{\mathcal{L}(\mathcal{L}+1)}{r^2} \right. \right. - \left. \left. \frac{4}{r^2} \frac{1}{W(z)} \frac{\partial}{\partial z} (1-z^2) W(z) \frac{\partial}{\partial z} \right] - E \right\} P^{(c)}(z,r)$$
$$= -V^{(c)} \left(\frac{r}{\mu_c} \sqrt{(1+z)/2} \right) \Pi^{(c)}(r,z) \tag{22}$$

where

$$\Pi^{(c)}(r,z) = P^{(c)}(r,z) + \sum_{c'=1}^{N_p} \int_{-1}^{+1} f^{(c,c')}(z,z') P^{(c')}(r,z')\, \mathrm{d}z', \tag{23}$$

where $f^{(c,c')}(z,z')$ is a projection function arising from projecting the amplitude $F^{(c)}(\xi_N^{kl}, r)$ onto the ξ_N^{ij} space (see Appendix A), N_p is the number of coupled equations, $\mathcal{L} = (D-3)/2$, and $W(z)$, known as weight function,

$$W(z) = (1-z)^\alpha (1+z)^\beta, \qquad \alpha = (D-5)/2, \quad \beta = 1/2 \tag{24}$$

The parameter μ_c is the reduced mass for the channel c

$$\mu_c = \left[\frac{2A m_i m_j}{M(m_i + m_j)} \right]^{1/2}$$

The reduced equation, Eq. (22) is S- projected and thus it excludes the effects of higher partial waves. These effects can be included, albeit approximately and in an average way, using hypercentral potentials defined by

$$V_0^{(c)}(r) = \frac{1}{h_0^{(\alpha,\beta)}} \int_{-1}^{+1} W(z)\, V^{(c)} \left(\frac{r}{\mu_c} \sqrt{\frac{1+z}{2}} \right) \mathrm{d}z \tag{25}$$

where $h_0^{(\alpha,\beta)}$ is given by (A5) for $K = 0$. Then adding $V_0^{(c)}(r)$ to both sides of (22) we obtain the IDEA equation

$$\left\{ \frac{\hbar^2 A}{M} \left[-\frac{\partial^2}{\partial r^2} + \sum_{c'} \nu_{c'} V_0^{(c')}(r) + \frac{\mathcal{L}(\mathcal{L}+1)}{r^2} - \frac{4}{r^2} \frac{1}{W(z)} \frac{\partial}{\partial z} (1-z^2) W(z) \frac{\partial}{\partial z} \right] - E \right\} P^{(c)}(z,r)$$
$$= -\left[V^{(c)} \left(\frac{r}{\mu_c} \sqrt{(1+z)/2} \right) - V_0^{(c)}(r) \right] \Pi^{(c)}(r,z) \tag{26}$$

where ν_c is the number of pairs of a given type c. Note that $\sum_c \nu_c = A(A-1)/2$, the total number of pairs. We emphasize here the inclusion of $V_0^{(c)}$ compensates for considering only harmonic polynomials of the form (20) associated with S-states only.

From the above it is clear that the extension of the IDEA to unequal mass particles results in no major complication and that the equations to be solved are still quite simple and easy to apply to hypernuclear systems. The number of channels in the coupled system (excluding, for the moment, the matter of coupled angular momentum states), is equal to the number of different types of particles pairs, e.g. NN, $N\Lambda$ and $\Lambda\Lambda$.

The solution of Eq. (26) can be achieved either by solving it as a two-dimensional integrodifferential equation, or via adiabatic approximations [6, 8]. In the extreme adiabatic approximation (EAA) we assume that the amplitude can be written as a product

$$P^{(c)}(z,r) = P_\lambda^{(c)}(z,r)u_\lambda(r) \tag{27}$$

which means that we assume that the orbital motion is very rapid as compared to the radial motion and contains most of the energy, as for electrons in atoms. Then Eq. (26) can be split into two equations, namely,

$$\begin{aligned}\frac{\hbar^2 A}{M}\frac{4}{r^2}\frac{1}{W(z)}\frac{\partial}{\partial z}(1 &- z^2)W(z)\frac{\partial}{\partial z}P_\lambda^{(c)}(z,r) + U_\lambda(r)P_\lambda^{(c)}(z,r) \\ &= \left[V^{(c)}\left(\frac{r}{\mu_c}\sqrt{(1+z)/2}\right) - V_0^{(c)}(r)\right]\Pi_\lambda^{(c)}(r,z)\end{aligned} \tag{28}$$

from which we determine, for each r, the eigenpotential $U_\lambda(r)$ which is used to evaluate the binding energy $E_\lambda^{\rm EAA}$ from the second equation,

$$\frac{\hbar^2 A}{M}\left[-\frac{\mathrm{d}^2}{\mathrm{d}r^2} + \frac{\mathcal{L}(\mathcal{L}+1)}{r^2} + \sum_{c'}\nu_{c'}V_0^{(c')}(r) + U_\lambda(r)\right]u_\lambda(r) = E_\lambda^{\rm EAA}u_\lambda(r)\,. \tag{29}$$

The EAA provides a lower bound and the accuracy achieved for nuclear systems depends of the short range characteristics of the underlying nucleon-nucleon forces. For soft potentials the accuracy is of the order of $\sim 1\%$ and it can be further improved by using the uncoupled adiabatic approximation (UAA) [6].

III. RESULTS

We present below some results obtained via the exact solution of Eq. (26) to demonstrate the suitability of the method. In Table I the results obtained for the $\alpha\Lambda\Lambda$ model of ${}^{6}_{\Lambda\Lambda}$He system are given. The IDEA results are very close to the equivalent Harmonic Oscillator results.

TABLE I: Three-body dissociation energies for the $\alpha\Lambda\Lambda$ model of ${}^{6}_{\Lambda\Lambda}$He for Dalitz $\Lambda\Lambda$ potential [16]

$\alpha\Lambda$ Potential	IDEA	Harmonic Oscillator
Bassichis-Gal[17]	11.08	11.012
Isle [18]	9.25	9.04
Bando [19]	11.29	11.207

IV. CONCLUSIONS

It has been demonstrated, over the past two decades, that the IDEA has a wide range of applications in bound state problems, from atomic and molecular to nuclear systems as

TABLE II: Three-body dissociation energies for the $\alpha\Lambda\Lambda$ model of ${}^{6}_{\Lambda\Lambda}$He for Dalitz $\Lambda\Lambda$ potential and convoluted MT (I+ III)/2 NN potential

$N\Lambda$ Potential	MT(I + III)/2 potential
Gibson	9.23
Bassichis-Gal	10.20
Dalitz-Downs	11.21

TABLE III: Dissociation energies for the $4N\Lambda\Lambda$ model of ${}^{6}_{\Lambda\Lambda}He$ for Dalitz $\Lambda\Lambda$ potential and MT $(I + III)/2NN$ potential

$N\Lambda$ Potential	MT(I + III)/2 potential	$N\Lambda$ Overlap prob - %
Gibson	7.88	0.15
Bassichis-Gal	13.55	0.17
Dalitz-Downs	27.85	2.77

well as in three-quarks within the quark-antiquark potential model. In the present paper we demonstrated that this is the case for hypernuclear systems as well. The method is simple enough for straightforward calculations, the accuracy being comparable to other competing methods and thus it can be reliably used to extract characteristics of the system under consideration. In the present work, for example, the IDEA reveals a high degree of polarization of the nuclear core by Λ hyperons which is not revealed in the "rigid core" approximation. Furthermore, it has been shown that adiabatic approximations can also be employed in hypernuclear systems. These approximations should be accurate enough as most of the potentials involved are rather soft and thus reliable results and wave functions can be readily obtained and used in reaction processes.

In short, the IDEA is a powerful method in the context of hypernuclear problems, given that it is able to reveal the effect of interparticle correlations and clusterings for systems consisting of arbitrarily large numbers of particles. It is simple and reliable and can be used not only in bound state studies but also in locating resonances, in photoprocesses etc.

APPENDIX A: PROJECTION FUNCTION

Following the procedure of Ref. [14] we expand the pairwise amplitudes in hyperspherical harmonics functions which, for S-states are reduce to the Jacobi polynomial $P_K^{(\alpha,\beta)}(z)$

$$F(\xi_N^{kl}, r) = \sum_{K=0}^{\infty} P_K^{(\alpha,\beta)}(\cos 2\phi_N^{kl})\Phi(r) \tag{A1}$$

where $\phi_N^{kl} = \xi_N^{kl}/r$. Projecting onto the ξ_N^{ij} space we obtain

$$\langle \xi_N^{ij} | F(\xi_N^{kl}) \rangle = \sum_K \langle P_K^{(\alpha,\beta)}(\cos 2\phi_N^{ij}) | P_K^{(\alpha,\beta)}(\cos \phi_N^{kl}) \rangle P_K^{(\alpha,\beta)}(\cos 2\phi_N^{ij})\Phi_K(r) \tag{A2}$$

We recall here that $z = \cos 2\phi_N^{ij}$. The matrix elements are given in [14, 15]

$$\langle P_K^{(\alpha,\beta)}(\cos 2\phi_N^{ij}) | P_K^{(\alpha,\beta)}(\cos \phi_N^{kl}) \rangle = \frac{P_K^{(\alpha,\beta)}(\cos 2\varphi_{k,l}^{ij})}{P_K^{(\alpha,\beta)}(1)} \tag{A3}$$

The angle $\varphi^{ij}_{k,l}$ is evaluated from the kinematical rotation vector [14],

$$\begin{aligned} V(\varphi) &= \xi^{ij}_N \cos\varphi_N + \xi^{ij}_{N-1} \sin\varphi_N \cos\varphi_{N-1} + \cdots \\ &+ \xi^{ij}_{N-i+1} \sin\varphi_N \sin\varphi_{N-1} \cdots \sin\varphi_{N-i+2} \cos\varphi_{N-i+1} + \cdots + \xi^{ij}_1 \sin\varphi_N \cdots \sin\varphi_2 \end{aligned}$$

For $V(\varphi) \equiv \xi^{kl}_N$ we obtain

$$\cos 2\varphi_N = \begin{cases} +1 & \text{if } (kl) = (ij) \\ -1 & \text{if } (kl) \text{ and } (ij) \text{ are disjoint} \\ \dfrac{m_i m_k - m_j(m_i + m_j + m_k)}{m_i m_k + m_j(m_i + m_j + m_k)} & \text{if one member } (j, \text{ in this case}) \\ & \text{of the pair } (ij) \text{ coincides with} \\ & \text{one member } (l, \text{ in this case}) \text{ of} \\ & \text{the pair } (kl). \end{cases}$$

Setting $\varphi^{ij}_{kl} = \varphi_N$ [14] in Eq. (A3) and defining

$$f(z, z', \cos 2\varphi^{ij}_{kl}) = W(z') \sum_{K=0}^{\infty} \frac{P_K^{(\alpha,\beta)}(z') P_K^{(\alpha,\beta)}(z) P_K^{(\alpha,\beta)}(\cos 2\varphi^{ij}_{kl})}{P_K^{(\alpha,\beta)}(1) h_K^{(\alpha,\beta)}}, \tag{A4}$$

where

$$h_K^{(\alpha,\beta)} = \int_{-1}^{+1} W(z) [P_K^{(\alpha,\beta)}(z)]^2 \, \mathrm{d}z, \tag{A5}$$

we obtain the projection $f^{(c,c')}$

$$f^{(c,c')}(z, z') = \sum_{k\,l \equiv c'} f(z, z', \cos\varphi^{ij}_{kl}). \tag{A6}$$

The summation is over all pairs $(k\,l)$ which are of type c'. The pair $(i\,j)$ is of type c. Two more points should be clarified here. If $c = c'$ and the particles comprising the pair c are identical, (e.g. $\Lambda\Lambda$, NN etc), the projection function reads

$$f^{(c,c)}(z, z') = (n_j - 2)[2f(z, z', -1/2) + \frac{1}{2} f(z, z', -1)] \tag{A7}$$

where n_j is the total number of particles of the type comprising the pair c. If c and c' are disconnected (i.e when they have no common particles) then

$$f^{(c,c')}(z, z') = n_c n_{c'} f(z, z', -1) \tag{A8}$$

where n_c and $n_{c'}$ are the number of pairs of types c and c' respectively.

Other expressions concerning the projection function for equal mass particles and A-fermions can be found in Refs. [6, 10, 11] and will not be repeated here.

---

[1] W.M. Alberico and G. Garbarino, Physics Reports **369**, 1 (2002).
[2] H. Nemura, Y. Akaishi, and Y. Susuki, Phys. Rev. Lett. **89**, 142504 (2002).
[3] A. Gal, The hypernuclear physics heritage of Dick Dalitz (1925-2006), arXiv: physics/0701019 (2007).

[4] M. Fabre de la Ripelle and H. Fiedeldey, Phys. Lett. B **171**, 325 (1986).
[5] M. Fabre de la Ripelle, H. Fiedeldey, and S.A. Sofianos, Few–Body Systems Suppl. **2**, 493 (1987).
[6] M. Fabre de la Ripelle, H. Fiedeldey, and S.A. Sofianos, Phys. Rev. C **38**, 449 (1988).
[7] R.M. Adam, PhD Thesis, University of South Africa, 1990.
[8] W. Oehm, S.A. Sofianos, H. Fiedeldey, and M. Fabre de la Ripelle, Phys. Rev. C **43**, 25 (1991).
[9] W. Oehm, S. A. Sofianos, H. Fiedeldey, and M. Fabre de la Ripelle, Phys. Rev. C **44**, 81 (1991).
[10] M. Fabre de la Ripelle, S.A. Sofianos, R.M. Adam, Annals of Physics NY **316**, 107 (2005).
[11] R.M. Adam and H. Fiedeldey, J. Phys. G: Nucl. Part. Phys. **19**, 703 (1993).
[12] F. Zernike, H. C. Brinkman, Proc. Kon. Ned. Acad. Wetensch **33**, 3 (1935).
[13] R.M. Adam, H. Fiedeldey, S.A. Sofianos, M. Fabre de la Ripelle, J. Phys. G: Nucl. Part. Phys. **18**, 1365 (1992).
[14] M. Fabre de la Ripelle, Annals of Physics NY **147**, 281 (1983).
[15] M. Fabre de la Ripelle, *Models and Methods in Few-Body Physics (Springer Lecture Notes in Physics* **273** ed L.S. Ferreira, A.C. Fonseca, and L. Streit (Springer-Verlag, New-York, 1987) p302.
[16] R.H. Dalitz and G. Rajasekaran, Nucl. Phys. **50**, 450 (1964).
[17] K. Daskaloyannis, M. Grypeos, and H. Nassena, Phys. Rev. C **26**, 702 (1982).
[18] Y. Kurihara, Y. Akaishi, and H. Tanaka, Prog. Theor. Phys. **71**, 561 (1984).
[19] K. Ikeda, H. Bando, and T. Motoba, Prog. Theor. Phys. (Suppl.) **81**, 147 (1985).

Analyses of Low and Intermediate Energy Nucleon Scattering Data from Exotic Nuclei

S. Karataglidis*

Department of Physics and Electronics, P.O. Box 94, Rhodes University, Grahamstown, 6140, South Africa

Most data from reactions involving exotic nuclei have been analysed successfully within a cluster-model framework. This is due to such reactions, for example breakup in heavy-ion collisions, probing exclusively the long-range behaviour of the wave functions in question. However, scattering of light ions from hydrogen, which equates to proton scattering in the inverse kinematics, probes the whole of the nucleus, and so one requires a microscopic approach to analyse such data. Current models for both low and intermediate energy scattering will be presented which are able to predict scattering observables. These models may be used to sensitively test details of nuclear structure, and may elicit details of the cores of exotic nuclei. Examples will be presented for both stable and exotic nuclei. Consequences for future experiments and analyses will be discussed.

I. INTRODUCTION

That cluster models are able to explain much data involving exotic nuclei, particularly from breakup in heavy-ion collisions, may be a consequence of the property that cluster models are designed to explain the long range behaviour of nuclei by taking into account long-range correlations missing in the shell model [1]. However, internal dynamics at the nucleon level, for light nuclei at least, may now be adequately explained using no-core shell models [2], for which long-range correlations are introduced into the Hamiltonian by higher-order $\hbar\omega$ excitations beyond the $0\hbar\omega$ model space [3].

The study of exotic nuclei by standard techniques concentrating on the asymptotic region has always had one additional problem. In heavy ion collisions leading to breakup, the part of the wave function relating to the core is inaccessible and remains hidden [4, 5]. The success of cluster models in analyses of data from those reactions is due to the fact that a detailed description of the structure of the core is not required. It has also been established that the breakup of ^{6}He is a two-step process [6], with the intermediate ^{5}He surviving before the emission of the second neutron. Therefore, final state interactions play a significant role in breakup reactions. To obtain information on the ground state wave function, of the core itself, and how the neutron skin or halo may affect it, one requires reactions which probe the entire nuclear wave function.

One such reaction is the charged photopion reaction which allows for the investigation of exotic nuclei as final states after the emission of a charged pion from a stable nucleus [7]. In the case of $^{17}\mathrm{O}(\gamma,\pi^-)^{17}\mathrm{F}^*$ it was shown that the proton halo in the excited state of ^{17}F manifested itself as a depletion of the proton density in the core. While some experiments have been done (see [8] for a discussion) the range of experiments is limited to those exotic nuclei next to the valley of stability. One requires an alternative to study nuclei out to the drip lines.

Scattering of light ions from hydrogen, which equates to proton scattering in the inverse kinematics, is the best available means by which the whole of the wave functions of exotic nuclei may be investigated. Nucleon scattering probes the matter densities of the nucleus.

*Electronic address: S.Karataglidis@ru.ac.za

At intermediate energies, as the V_{pn} component of the nucleon-nucleon (NN) interaction is strongest, proton scattering primarily probes the neutron density and *vice-versa*. For neutron-rich nuclei, especially, scattering from hydrogen is a useful tool by which one may study the neutron density, particular in the interior of the nucleus.

At low energies, nucleon scattering involves the formation of compound $A+1$ nuclear states and so, for light nuclei, one may probe the structures of nuclei outside the drip lines.

In both cases, one requires a model of scattering which is predictive in order for that model to be useful as a tool for structure. Herein, models for low and intermediate energy scattering are presented which satisfy this criterion. First, the Melbourne g-folding model for intermediate energy scattering [9] is discussed. That model folds the effective NN interaction in-medium, as obtained from the relevant NN g matrices for infinite matter, with the density profile of the target ground state. Second, a new method for solving the coupled-channel Lippmann-Schwinger equations for low-energy scattering, known as MCAS [10], is presented. Therein, the coupled-channel equations are solved algebraically. Central both models is the requirement that the Pauli Principle be satisfied.

The first half of the paper will discuss the Melbourne g-folding model and present various results for angular and spin observables for scattering from both stable and exotic nuclei. The second half will discuss the MCAS model for low energy scattering and illustrate the importance of the Pauli Principle in descriptions of scattering. Results for stable nuclei and to nuclei beyond the drip line will be presented.

II. FORMAL THEORY OF THE OPTICAL POTENTIAL

The optical potential for nucleon-nucleus (NA) scattering is associated with the elastic scattering channel only. Following Feshbach [11], the Hilbert space for scattering is split into the elastic scattering channel (denoted the $\mathcal{P}$ space) and the non-elastic channels (the $\mathcal{Q}$ space). The Schrödinger equation for scattering then becomes, with P and $Q = 1 - P$ projectors onto the respective spaces,

$$\begin{aligned} (E - H_{PP})\, P \left|\Psi^{(+)}\right\rangle &= H_{PQ} Q \left|\Psi^{(+)}\right\rangle \\ (E - H_{QQ})\, Q \left|\Psi^{(+)}\right\rangle &= H_{QP} P \left|\Psi^{(+)}\right\rangle \ , \end{aligned} \tag{1}$$

where $H_{XY} = XHY$, $PQ = QP = 0$, and $Q\left|\Psi_{\rm gs}\right\rangle = 0$. Recoupling, and taking the one-body approximation gives the appropriate Schrödinger equation for the projectile wave function, *viz.*

$$\left\{E - H_0 - \left\langle \Phi_{\rm gs}\right| V \left|\Phi_{\rm gs}\right\rangle - \left\langle \Phi_{\rm gs}\right| V G^{(+)}_{QQ} V \left|\Phi_{\rm gs}\right\rangle\right\} \left|\chi^+\right\rangle = 0 \ , \tag{2}$$

where $G^{(+)}_{QQ} = [E - H_{QQ} + i\varepsilon]^{-1}$, and from which the optical potential (OMP) is defined as

$$U = \left\langle \Phi_{\rm gs}\right| V \left|\Phi_{\rm gs}\right\rangle + \left\langle \Phi_{\rm gs}\right| V G^{(+)}_{QQ} V \left|\Phi_{\rm gs}\right\rangle \ . \tag{3}$$

Specification of the OMP is a many-body problem with explicit dependence on the target ground state wave function. It is complex, nonlocal, and energy dependent, through the NN interaction V, through ensuring that the Pauli Principle is not violated, and also through $G^{(+)}_{QQ}$. The second term in Eq. (3) is termed the Dynamic Polarising Potential (DPP), and defines how coupling to nonelastic channels varies with energy. Specifically, such coupling may be cast into three broad energy regimes:

Low Energy For $E < 10$ MeV, explicit coupling to specified, discrete, low-lying excited states of the target is necessary, leading to the formation of compound states in the $A+1$ nucleus.

Giant Resonances Between 10 and 25 MeV, coupling to the giant resonances becomes important [12]. One important exception is the set of He isotopes, for which there are no giant resonances.

Intermediate and High energies At higher energies, as the level density becomes high, coupling to nonelastic channels may be handled implicitly by using folding models based on the NN g matrices for nuclear matter.

Note that these energy limits serve only as a rough guide.

The OMP of Eq. (3) may not be solved directly as, while the P space is finite, the Q space is infinite in principle, and the coupling to the Q space may not be specified exactly. Models are required to specify the optical potential.

III. INTERMEDIATE ENERGY SCATTERING, MELBOURNE g-FOLDING MODEL

The review article [9] describes the model for intermediate energy NA scattering in detail. Herein, only the main ingredients are described.

The Melbourne g-folding model for intermediate energy NA scattering takes as its basis an effective NN interaction from the g matrices of the bare NN interaction. Those g matrices are the solutions of the Brueckner-Bethe-Goldstone equation, in momentum space,

$$g\left(\mathbf{q},\mathbf{q}';\mathbf{K}\right) = V\left(\mathbf{q},\mathbf{q}'\right) + \int V\left(\mathbf{q}',\mathbf{k}'\right) \frac{Q\left(\mathbf{k}',\mathbf{K};k_f\right)}{\left[E\left(\mathbf{k},\mathbf{K}\right) - E\left(\mathbf{k}',\mathbf{K}\right)\right]} g\left(\mathbf{k}',\mathbf{q};\mathbf{K}\right)\ d\mathbf{k}' \ , \tag{4}$$

where $\mathbf{k} = (\mathbf{p}_0 - \mathbf{p}_1)$ is the relative momentum and $\mathbf{K}$ is the centre-of-mass momentum of the two particles. Primes denote the equivalent set of momenta after scattering. Q is a Pauli-blocking operator and the energies in the propagator contain auxiliary potentials which model the effect of the nuclear medium [13]. Those auxiliary potentials are sometimes modelled by effective mass operators. The Pauli operator Q and the energies E may be replaced by the angle-averaged values which has been shown to be a good approximation for nuclear densities above $\sim 15\%$ [14, 15]. This is an important consideration for scattering from exotic nuclei where scattering is observed from the core in the case of halo nuclei [8].

The g matrices so obtained are then mapped to those for finite nuclei in coordinate space [9] by folding in the specified (model) density of the target ground state. That mapping to a coordinate space representation is achieved by means of a double Bessel transform and allows for the explicit specification of central, tensor, and two-body spin-orbit terms as sums of Yukawa functions. This is also a practical consideration: the DWBA suite of programs [16] which are used to calculate the scattering observables require a coordinate-space representation of the potential. Once those effective g matrices ($g_{\rm eff}$) have been obtained, the nonlocal, complex, OMP for scattering is defined as

$$\begin{aligned} U(\mathbf{r},\mathbf{r}';E) \ &= \ \delta(\mathbf{r}-\mathbf{r}') \sum_i n_i \int \varphi_i^*(\mathbf{s}) g_D(\mathbf{r},\mathbf{s};E) \varphi_i(\mathbf{s})\, d\mathbf{s} \\ &\quad + \sum_i n_i \varphi_i(\mathbf{r}') g_E(\mathbf{r},\mathbf{r}';E) \varphi_i \\ &= \ U_D(\mathbf{r},E)\delta(\mathbf{r}-\mathbf{r}') + U_E(\mathbf{r},\mathbf{r}';E) \ , \end{aligned} \tag{5}$$

where D and E denote the direct and exchange terms of the effective interaction, respectively. Nuclear structure information enters via the occupation numbers n_i for each orbit and the single-particle (SP) wave functions φ_i. The direct term is the well-known $g\rho$ form of the optical potential and is local by construction. The nonlocality arises from the explicit exchange terms; neglecting such terms can lead to serious problems [17]. A credible model of structure is necessary in the specification of the OMP.

The SP wave functions entering Eq. (5) are usually assumed to be of harmonic oscillator (HO) form. For most nuclei this is a reasonable assumption and is consistent with the underlying shell model. However, for exotic nuclei, halos in particular, it is more appropriate to use Woods-Saxon (WS) wave functions [8] with binding energies of the orbits occupied by the halo nucleons set to the separation energy of the single nucleon in the halo. This allows for the extension of the nuclear density for loosely bound systems beyond the simple oscillator result. Such a specification was necessary to describe the anomalously large $B(E1)$ value in ^{11}Be [18].

Inelastic scattering may be calculated in a distorted-wave-approximation (DWA) with the $g_{\rm eff}$ as the operators effecting the transition. The transition amplitude may be written, with '0' and '1' denoting the projectile and bound-state nucleon, respectively, as

$$T^{M_f M_i \nu' \nu}_{J_f J_i}(\theta) = \left\langle \chi^{(-)}_{\nu'}(0) \right| \left\langle \Psi_{J_f M_f} | A g_{\rm eff}(0,1) \mathcal{A}_{01} \{ | \Psi_{J_i M_i} \rangle \left| \chi^{(+)}_{\nu}(0) \right\rangle \right\} \ , \tag{6}$$

where χ is the distorted wave function for the projectile and $\mathcal{A}_{01}$ is the antisymmetrisation operator for the projectile and bound-state nucleon. In this approach, the distorted wave functions are generated from folding of the same $g_{\rm eff}$ with the structure of the nuclear states.

A. Nuclear structure considerations

The OMP in the g-folding model is a one-body operator with respect to the target (bound) nucleons and so one requires specification of the one-body density matrix elements (OBDME), *viz.*

$$S_{\alpha_1 \alpha_2 J} = \left\langle J_f \left\| \left[a^\dagger_{\alpha_2} \times \tilde{a}_{\alpha_1} \right]^J \right\| J_i \right\rangle \ , \tag{7}$$

where $\alpha = \{l, s, j, m_\tau\}$, with m_τ denoting either a proton or neutron. Various models have been utilised but, for the most part, the shell model has been used to specify the OBDME. Others include the Skyrme-Hartree-Fock (SHF) and the RPA.

Note that in specifying the OMP one must keep to the level of the density matrix elements to preserve the nonlocality. Use of the density itself requires gross approximations to be made in the handling of the nonlocal exchange terms within a local potential. That may be problematic [17]. Note also that the specification of the structure is central to success in analyses of data. A poor structure results in poor agreement with data [19].

IV. RESULTS FROM THE MELBOURNE g-FOLDING MODEL

For the results presented herein, the BonnB NN interaction [20] was used to obtain the $g_{\rm eff}$. All NA scattering results were obtained using DWBA98 [16] from single-shot calculations: there was no fitting to any data. The review [9] presents most results obtained to that time, and includes a discussion on the connection between electron and proton scattering. Some of those results are presented here, as well as some that have been obtained since.

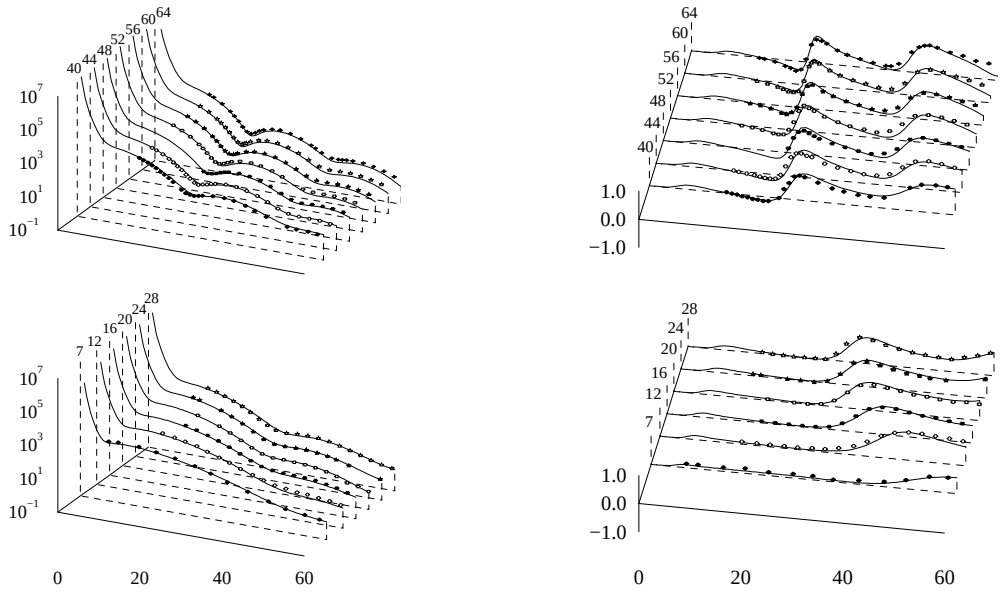

FIG. 1: Differential cross sections (left) and analysing powers (right) for the elastic scattering of 65 MeV protons from various nuclei to mass 64.

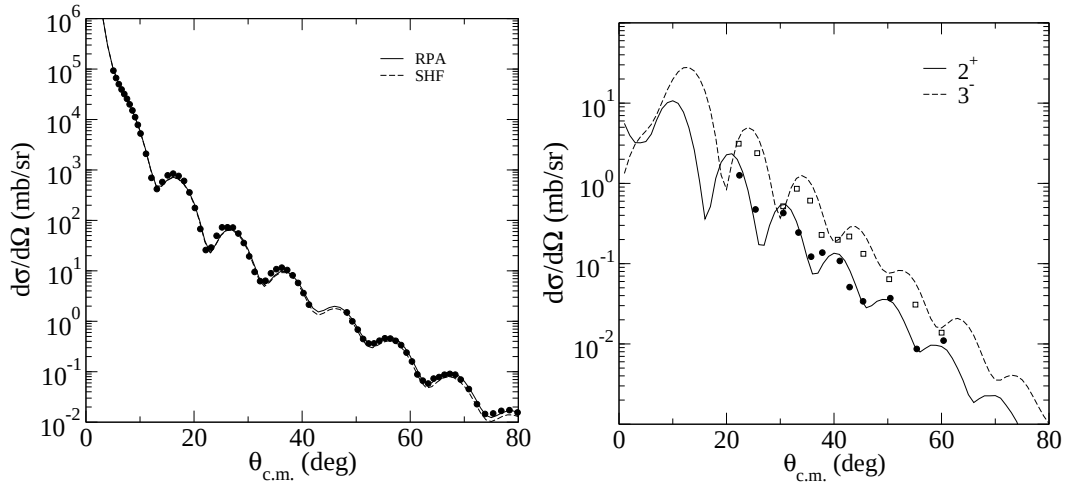

FIG. 2: Differential cross sections for 121 MeV elastic (left) and 135 MeV inelastic (right) proton scattering from ^{208}Pb.

Fig. 1 shows the differential cross sections and analysing powers for the elastic scattering of 65 MeV protons from nuclei in the mass range $7 \leq A \leq 64$. The structure models used varied from the shell model for nuclei up to ^{40}Ca, and a simple packed model for nuclei above that. Clearly, both the differential cross sections and analysing powers are well reproduced. Note the excellent reproduction of the observables' dependence with momentum transfer as one increases the mass.

Fig. 2 displays the results for the elastic [21] and inelastic [22] proton scattering from ^{208}Pb at 121 and 135 MeV, respectively. The RPA model was used with the Gongy D1S density-dependent effective interaction to obtain the ground state and transition densities as required. The elastic scattering cross section data at 121 MeV [23] are also compared to the results of an

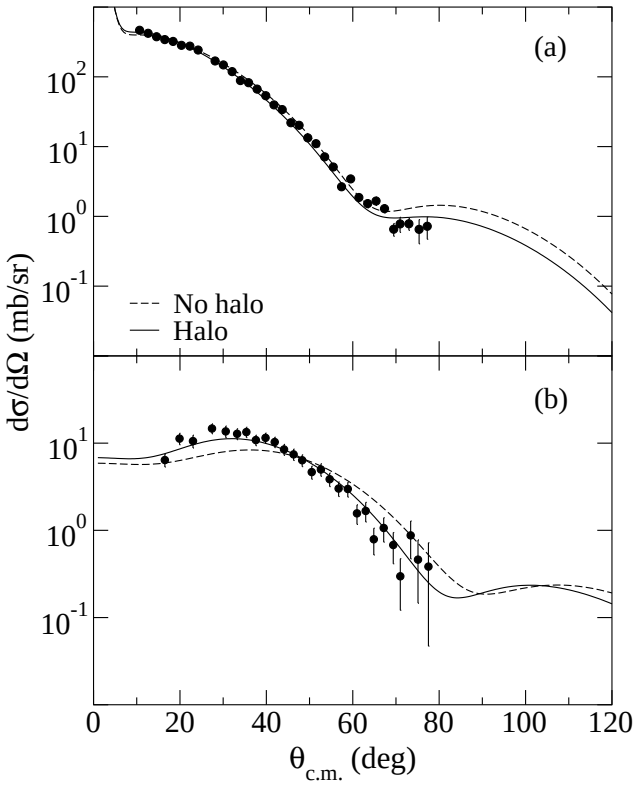

FIG. 3: Differential cross sections for the elastic (a) and inelastic (b) scattering of 41A MeV ^{6}He from hydrogen.

SHF calculation using the SkM* force [24]. The agreement between the results obtained from the RPA and SHF calculations and data for the elastic scattering illustrates that both models specify a reasonable density for the ground state of ^{208}Pb. But only the RPA gives information on the transitions to excited states, and transition densities obtained therefrom were used to obtain the results for the inelastic scattering to the 2^+_1 and 3^-_1 states in ^{208}Pb. The data [25] and results are compared in the right panel of Fig. 2. There is excellent agreement between the data and results of the RPA calculations for both the $E2$ and $E3$ cross sections, and the results clearly illustrate the phase rule of Blair [26].

These results, and similar obtained for different mass ranges and energies [9], give encouragement for the use of the model in analyses of scattering data involving exotic nuclei. Fig. 3 displays the differential cross section for the elastic scattering of ^{6}He from hydrogen at 41A MeV, as well as the inelastic scattering to the 2^+_1 state at 1.8 MeV [27]. The model used to specify the OBDME is a complete $(0+2+4)\hbar\omega$ shell model using the G matrix interaction of Zheng *et al.* [28]. Two sets of results are presented: those designated "halo" used WS SP wave functions with the binding energy for the valence neutron orbits set to the single neutron separation energy of 2 MeV, while those designated "nonhalo" are those using HO SP wave functions with an oscillator parameter $b = 1.8$ fm, consistent with the shell model used. The halo results gives better agreement with the elastic scattering data, including at large angles beyond the first diffraction minimum. There the halo result is below that of the naive oscillator, and is the only region in which the two results differ. The extension of the neutron density comes at a price: in order to conserve particle number the density must be depleted in the core [7, 8]. That is manifest at these energies as a decrease in the cross section at large momentum transfer. This is confirmed by the limited amount of data beyond the first minimum. The halo is better illustrated in the

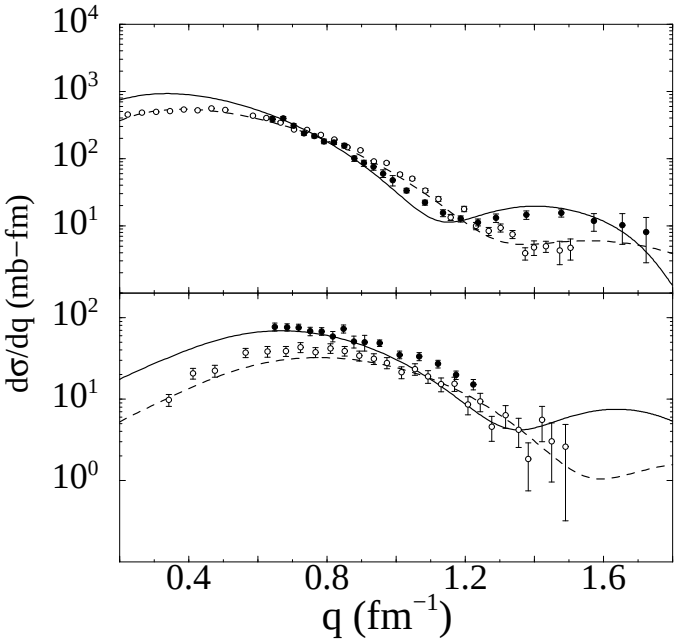

FIG. 4: Differential cross section for the elastic (top) and inelastic (bottom) scattering of $24.5A$ (full circles [30]) and $41A$ (open circles [27]) MeV ^{6}He ions from hydrogen.

inelastic scattering to the 2^+ state. As $E2$ transitions are surface-peaked, the extension of the neutron density leads to the enhancement of the cross section at $\sim 30^\circ$, in agreement with the data. Complementary to the scattering data is the reaction cross section for proton scattering from ^{6}He [27]. The predictions for the reaction cross section are 353 mb and 406 mb for the nonhalo and halo specifications of the density, respectively. The measured value is 409 ± 22 mb [29].

Fig. 4 shows the differential cross sections for the elastic and inelastic scattering of ^{6}He from hydrogen at $41A$ and $24.5A$ MeV [30], as a function of momentum transfer. Therein, only the halo results of the analyses are displayed. Not only is the dependence on momentum transfer well reproduced, but also the dependence on energy.

V. SCATTERING AT LOW ENERGY: MCAS

Low-energy facilities such as ISAC, ISOLDE, and proposed facilities such as RIA, perform experiments for nuclear structure and nuclear astrophysics with hadronic probes involving exotic nuclei. Hence, a predictive model of low-energy scattering is required, particularly with a view to obtaining reliable OMPs for use in other hadron-induced reactions.

A different formulation is required to that of the intermediate-energy folding-model approach as

- Low-energy scattering involves the formation of compound $A + 1$ nuclei;
- There are few nonelastic channels open so the mean-field approximation is not valid and the nonelastic channels must be handled explicitly;
- Knowledge of the low-energy OMP is critical to obtain reliable distorted waves for use in analyses of capture and transfer reactions;

- The structures of both the target and compound nuclei are important.

These points are addressed by the Multi-Channel Algebraic Scattering (MCAS) theory [10] used to solve the coupled Lippmann-Schwinger equations for the coupled-channels problem. Ref. [10] contains the full development of the MCAS; herein, only a brief summary is presented.

MCAS takes as its starting point the coupled Lippmann-Schwinger (LS) equations in momentum space for channels c and c', where, for scattering from a spin-zero target, $c = 1$ defines the elastic scattering channel

$$T_{cc'}(p,q;E) = V_{cc'}(p,q) + \mu \left[\sum_{c''=1}^{\rm open} \int_0^\infty V_{cc''}(p,x) \frac{1}{k_{c''}^2 - x^2 + i\varepsilon} T_{c''c'}(x,q;E)\, x^2 dx - \sum_{c''=1}^{\rm closed} \int_0^\infty V_{cc''}(p,x) \frac{1}{h_{c''}^2 + x^2} T_{c''c'}(x,q;E)\, x^2 dx \right] \quad (8)$$

for potential matrices $V_{cc'}(p,q)$, and $\mu = 2m_{red}/\hbar^2$ with m_{red} being the reduced mass. Therein the open and closed channels have been separated with the channel wave numbers being

$$k_c = \sqrt{\mu(E - \epsilon_c)} \text{ and } h_c = \sqrt{\mu(\epsilon_c - E)} \quad (9)$$

for $E > \epsilon_c$ and $E < \epsilon_c$ respectively, with ϵ_c being the threshold energy of channel c.

One may obtain algebraic solutions of the coupled LS equations by separable expansion of the potential matrix $V_{cc'}(p,q)$, *viz.*

$$V_{cc'}(p,q) \sim V_{cc'}^{(N)}(p,q) = \sum_{n=1}^{N} \hat{\chi}_{cn} \eta_n^{-1} \hat{\chi}_{c'n}(q) \ , \quad (10)$$

where

$$\hat{\chi}_{cn}(p) = \left[\frac{2}{\pi}\right]^{1/2} \frac{1}{p} \int_0^\infty F_l(pr) \chi_{cn}(r)\, dr \ . \quad (11)$$

A most useful choice of the radial factors is that linked to Sturmian functions of the chosen potential matrix, i.e.

$$\chi_{cn}(r) = \sum_{c'=1}^{C} V_{cc'} \Phi_{c'n}(r), \quad (12)$$

where $\Phi_{c'n}$ are the Sturmian functions [31], generated from the chosen potential matrix.

The optical potential for elastic scattering now contains explicit channel coupling and is defined as

$$V^{\rm opt}(r,r';E) = V_{11}(r) + \Delta U(r,r';E) \quad (13)$$

where the nonlocal DPP can be shown to be [10]

$$\Delta U(r,r';E) = \sum_{n,n'=1}^{N} \chi_{1n}(r) \frac{1}{\eta_n} \mathcal{G}_{nn'}^{(Q)}(E) \frac{1}{n'} \chi_{n'1}(r') \ . \quad (14)$$

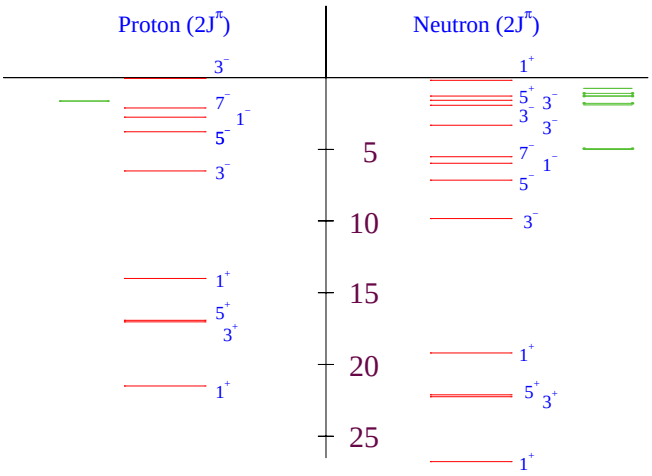

FIG. 5: Mass-13 sub-threshold spectra from the coupling of a nucleon to ^{12}C in the collective model.

The energy factor is the propagator for all excluded channels

$$\mathcal{G}^{(Q)}_{nn'}(E) = \sum_{c,c'=2}^{C} \int\int \chi_{cn}(r) G^{(Q)}_{cc'}(r,r') \chi_{c'n'}(r')\, dr\, dr', \tag{15}$$

and are defined by the linear algebraic equations

$$\mathcal{G}^{(Q)}_{nn'}(E) = \mu \left[\sum_{c=2}^{\text{open}} \int_0^\infty \frac{\hat{\chi}_{cn}(x)\hat{\chi}_{cn'}(x)}{k_c^2 - x^2 + i\varepsilon}\, x^2 dx - \sum_{c=2}^{\text{closed}} \frac{\hat{\chi}_{cn}(x)\hat{\chi}_{cn'}(x)}{h_c^2 + x^2}\, x^2 dx \right]. \tag{16}$$

There is also a new method by which the resonances in the $A+1$ compound nucleus may be found from the poles in the S matrix, once the T matrix is obtained [10]. The solution of these equations for positive E gives the resonances in the $A+1$ compound nucleus. Of note, that as the solutions are obtained in momentum space, one may also find poles in the S matrix corresponding to negative E, in which case the poles correspond to sub-threshold bound states.

VI. RESULTS FROM MCAS

Presently, the collective model is used to specify the structure by using the spectrum of the target nucleus to define the relevant open and closed channels. For ^{12}C+n, the assumed target spectrum is 0^+_1 (ground state), 2^+_1 (4.44 MeV), and 0^+_2 (7.65 MeV). The potential matrix is specified allowing for quadrupole deformation. States in the compound ^{13}C nucleus are formed by the coupling of the incident neutron to the assumed target spectrum. For negative energy, the spectrum found is shown in Fig. 5. Also shown in Fig. 5 is the subthreshold spectrum of ^{13}N found by adding the Coulomb potential to the potential matrix to account for an incident proton.

Note that in both cases, there are far more predicted states than are otherwise known. The problem is the neglect of the Pauli-blocking in forming the compound states. There is nothing in the collective model preventing the incident nucleon from coupling into an already filled orbit in the target nucleus, thus leading to many spurious states. One can account for the Pauli Principle in the collective model by adding an Orthogonalising Pseudo-Potential (OPP) [10] to

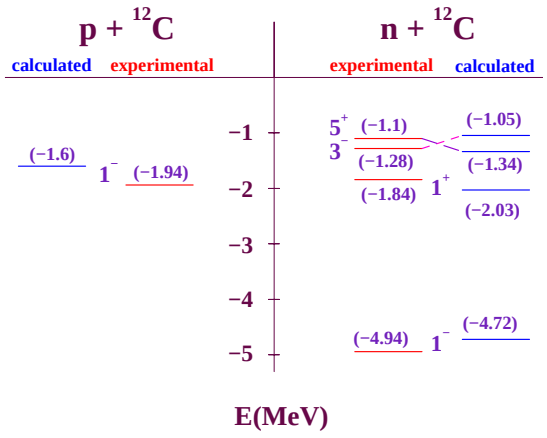

FIG. 6: Mass-13 subthreshold spectra obtained from the collective model after correcting for the Pauli Principle.

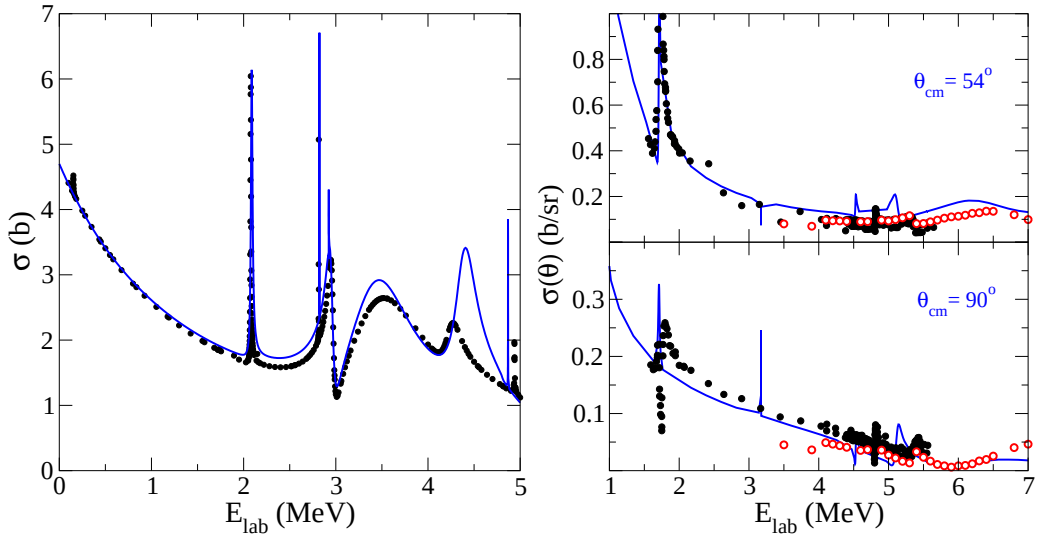

FIG. 7: Cross sections for n+^{12}C (left) and p+^{12}C (right) elastic scattering.

the potential matrix at the outset, which ensures that all Sturmian functions used are orthogonal to every function describing an occupied state in the target. Thereby all MCAS solutions of ths LS equations are orthogonal to all forbidden states in all channels. Making this correction, one obtains the mass-13 spectra shown in Fig. 6. Therein, there is one-to-one correspondence between the predicted subthreshold spectrum and data, with only a small inversion of the $\frac{5}{2}^+$ and $\frac{3}{2}^-$ states in ^{13}C.

Neglect of the Pauli Principle in coupled-channels calculations can be severe [32]. However, the severity of having spurious states is not restricted to finding the correct subthreshold spectra. While the correct scattering resonances may be found in a standard collective model coupled-channels calculation by a judicious use of parameters, the presence of spurious subthreshold states necessarily means that the underlying wave functions corresponding to those resonances are not correct [33].

The cross sections for low-energy nucleon-^{12}C elastic scattering are shown in Fig. 7. In both cases the resonances and widths are reasonably well reproduced, although the agreement

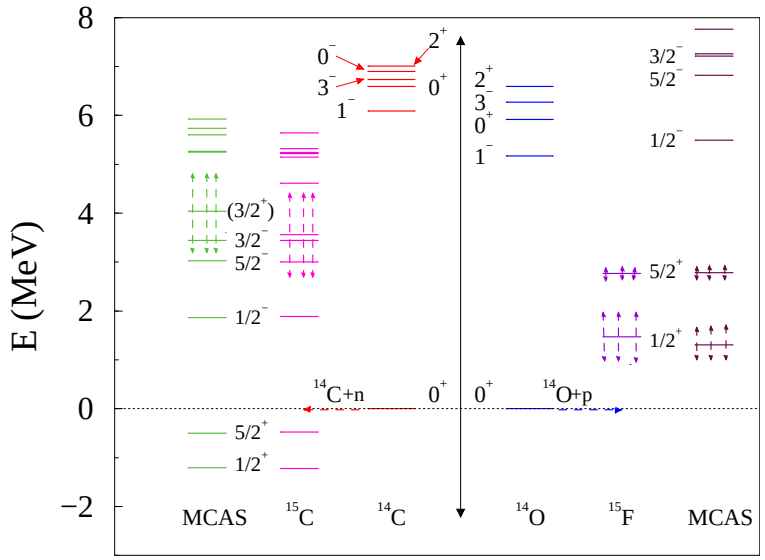

FIG. 8: Mass-15 spectra from the coupling of n+^{14}C and p+^{14}O.

weakens as one increases the energy. In that case, the influence of states in the target spectrum higher than those assumed increases and more states of the target spectrum must be taken into account.

An application of the MCAS approach to states beyond the drip line is that of ^{15}F [34], which is formed in the collective model by p+^{14}O. The mirror system is that of n+^{14}C forming ^{15}C, and the potentials are set by the mirror system before application to ^{15}F. Fig. 8 shows the mass-15 spectra formed by adding a nucleon to the mass-14 nucleus, assuming a target spectrum of 0^+_1, 0^+_2, and 2^+_1. An additional feature is needed to explain these spectra: that of Pauli-hindrance. This is an acknowledgement of partially-filled orbits in the target nucleus, and is formed by a much weaker energy for the OPP than that for Pauli-blocking. When one takes both Pauli-hindrance and Pauli-blocking into account, one obtains the spectrum of ^{15}C as shown in Fig. 8. Adding the Coulomb potential to the potential matrix found for ^{15}C gives the spectrum for ^{15}F as shown. Note that while the two bound ^{15}C states are found, the MCAS correctly predicts no bound states for ^{15}F and places the resonances in the region indicated by the measured spectrum.

The cross sections for both p+^{14}O and n+^{14}C are shown in Fig. 9. The data for the scattering of ^{14}O from hydrogen shows two resonances corresponding to the $\frac{5}{2}^+$ and $\frac{1}{2}^+$ resonances in ^{15}F. The MCAS result reasonably predicts both the energies and the widths of those states, and the level of agreement is as good as with other analyses [35, 36].

VII. CONCLUSIONS

Predictive models for both low- and intermediate-energy nucleon-nucleus scattering have been presented. These allow for facets of nuclear structure to be studied for both the target and compound nuclear states.

For intermediate energy scattering, a g-folding model approach, based on the effective NN g matrices, together with credible models of nuclear structure, is suitable to study details of the target density. Excellent agreement is achieved between data and predictions for both differential cross sections and spin observables, when reasonable descriptions of the target densities are available. For ^{208}Pb, an RPA specification of the density not only gave an excellent prediction

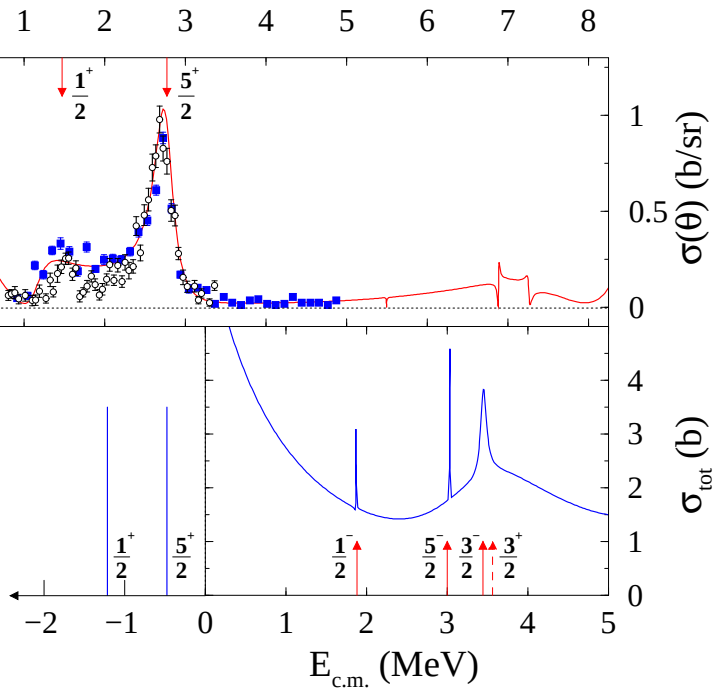

FIG. 9: The elastic cross sections from scattering of ^{14}O ions from hydrogen at 180° (top) and the predicted total cross section for the scattering of neutrons from ^{14}C (bottom) [34]. The known spectral values are indicated by the arrows.

of the elastic scattering, but also for the inelastic scattering to the 2^+_1 and 3^-_1 states as well. The model has also been applied to scattering of exotic nuclei from hydrogen. In the case of ^{6}He, the neutron halo has been identified unambiguously, with a self-consistent analysis of the data from elastic scattering, inelastic scattering and the reaction cross section.

At low energies, the MCAS approach has been applied to nucleon scattering from ^{12}C in the first instance. Using a collective model prescription of the target spectrum, bound and resonance states in the mass-13 nuclei are found in good agreement with the known spectra. Central to this approach is the requirement that the Pauli Principle be satisfied. Violation of the Pauli Principle in coupled-channels calculations leads to spurious states in the compound nucleus spectrum, and such causes severe problems both in the specification of the sub-threshold bound states and in the descriptions of the scattering.

The MCAS approach also allows for the study of nuclei beyond the drip lines. To account for partially-filled valence orbits which may appear in configurations of such nuclei, one requires also Pauli hindrance in the collective model, which acknowledges the shell effects arising from partially-filled orbits. The spectrum of ^{15}F and the p+^{14}O cross section were explained using both Pauli hindrance and Pauli blocking.

The consequences of the violation of the Pauli Principle in coupled-channels calculations are serious. Not only are spurious sub-threshold states introduced but the structures of the observed resonance states in scattering are not correct. That has implications for any parametrized local interaction for scattering abd wave functions found from them in analyses of related reactions. If the underlying wave functions are not reliable, observables obtained for reactions requiring the use of distorted wave functions from the optical potentials would also be problematic. Development of MCAS is continuing to address these problems.

With these tools, nuclear structure may be studied with nucleon probes to the same level

as that accorded to electron scattering. As electron scattering facilities to measure the form factors of exotic nuclei are not yet available, the use of nucleon probes presents the best means of studying exotic nuclei. It is hoped that experiments and theory will continue tapping into this rich vein of study.

---

[1] K. Wildemuth and Y. C. Tang, *A unified theory of the nucleus* (Academic Press, New York, 1977).
[2] S. Karataglidis, B. A. Brown, K. Amos, and P. J. Dortmans, Phys. Rev. C **55**, 2826 (1997).
[3] A. Arima, H. Horiuchi, K. Kubodera, and N. Takigawa, Adv. Nucl. Phys. **5**, 345 (1972).
[4] P. G. Hansen, Phys. Rev. Lett. **77**, 1016 (1996).
[5] H. Esbensen, Phys. Rev. C **53**, 2007 (1996).
[6] D. Aleksandrov et al., Nucl. Phys. **A633**, 234 (1998).
[7] S. Karataglidis and C. Bennhold, Phys. Rev. Lett. **80**, 1614 (1998).
[8] S. Karataglidis, P. J. Dortmans, K. Amos, and C. Bennhold, Phys. Rev. C **61**, 024319 (2000).
[9] K. Amos, P. J. Dortmans, H. V. von Geramb, S. Karataglidis, and J. Raynal, Adv. Nucl. Phys. **25**, 275 (2000).
[10] K. Amos, L. Canton, G. Pisent, J. P. Svenne, and D. van der Knijff, Nucl. Phys. **A728**, 65 (2003).
[11] H. Feshbach, Ann. Phys. (N.Y.) **19**, 287 (1962).
[12] H. V. von Geramb et al., Phys. Rev. C **12**, 1697 (1975).
[13] M. Haftel and F. Tabakin, Nucl. Phys. **A158**, 1 (1970).
[14] W. Legindgaard, Nucl. Phys. **A297**, 429 (1978).
[15] T. Cheon and E. F. Redish, Phys. Rev. C **39**, 331 (1989).
[16] J. Raynal, computer program DWBA98, NEA 1209/05 (1998).
[17] P. K. Deb and K. Amos, Phys. Rev. C **62**, 024605 (2000).
[18] D. J. Millener, J. W. Olness, E. K. Warburton, and S. S. Hanna, Phys. Rev. C **28**, 497 (1983).
[19] S. Karataglidis, P. J. Dortmans, K. Amos, and R. de Swiniarski, Phys. Rev. C **52**, 861 (1995).
[20] R. Machleidt, K. Holinde, and C. Elster, Phys. Rep. **149**, 1 (1987).
[21] M. Dupuis, S. Karataglidis, E. Bauge, J.-P. Delaroche, and D. Gogny, Phys. Rev. C **73**, 014605 (2006).
[22] M. Dupuis, S. Karataglidis, E. Bauge, J.-P. Delaroche, and D. Gogny, nucl-th/0506077.
[23] A. Nadasen et al., Phys. Rev. C **23**, 1023 (1981).
[24] S. Karataglidis, K. Amos, B. A. Brown, and P. K. Deb, Phys. Rev. C **65**, 044306 (2002).
[25] G. S. Adams et al., Phys. Lett. **B91**, 23 (1980).
[26] K. Amos, I. E. McCarthy, and K. R. Greider, Nucl. Phys. **68**, 469 (1965).
[27] A. Lagoyannis et al., Phys. Lett. **B518**, 27 (2001).
[28] D. C. Zheng, B. R. Barrett, J. P. Vary, W. C. Haxton, and C.-L. Song, Phys. Rev. C **52**, 2488 (1995).
[29] A. de Vismes et al., Phys. Lett. **B505**, 15 (2001).
[30] S. V. Stepantsov et al., Phys. Lett. **B542**, 35 (2002).
[31] S. Weinberg, Phys. Rev. **131**, 440 (1963).
[32] L. Canton, G. Pisent, J. P. Svenne, D. van der Knijff, K. Amos, and S. Karataglidis, Phys. Rev. Lett. **94**, 122503 (2005).
[33] K. Amos, S. Karataglidis, D. van der Knijff, L. Canton, G. Pisent, and J. P. Svenne, Phys. Rev. C **72**, 064604 (2005).
[34] L. Canton, G. Pisent, J. P. Svenne, K. Amos, and S. Karataglidis, Phys. Rev. Lett. **96**, 072502 (2006).
[35] V. Z. Goldberg et al., Phys. Rev. C **69**, 031302(R) (2005).
[36] D. Baye, P. Descouvement, and F. Leo, Phys. Rev. C **72**, 024309 (2005).

Nuclear Structure Calculations with Skyrme Interactions

V.V. Voronov*

Bogoliubov Laboratory of Theoretical Physics,
Joint Institute for Nuclear Research, 141980 Dubna, Moscow region, Russia

Starting from an effective Skyrme interaction we present a method that takes into account the coupling between one- and two-phonon terms in the wave functions of excited states. The approach is a development of a finite rank separable approximation for the quasiparticle RPA calculations proposed in our previous work. Some examples of such calculations for low-lying states and giant resonances are given. The influence of the phonon-phonon coupling on energies and transition probabilities for the low-lying quadrupole and octupole states in the neutron-rich Sn isotopes is studied.

I. INTRODUCTION

Experimental and theoretical studies of properties of the excited states in nuclei far from the β-stability line are presently the object of very intensive activity. The random phase approximation (RPA) [1–4] is a well-known and successful way to treat nuclear vibrational excitations. Using the Gogny's [5] or Skyrme-type [6] effective nucleon-nucleon interactions the most consistent models can describe the ground states in the framework of the Hartree-Fock (HF) and Hartree-Fock-Bogoliubov (HFB) approximations and the excited states within the RPA and quasiparticle RPA (QRPA). Such models are quite successful not only to reproduce the nuclear ground state properties [7, 8], but also to describe the main features of nuclear excitations in closed-shell [9, 10] and open-shell nuclei [11–14]. In the latter case the pairing correlations are very important.

Due to the anharmonicity of vibrations there is a coupling between one-phonon and more complex states [2, 4] and the complexity of calculations beyond standard RPA or QRPA increases rapidly with the size of the configuration space, so one has to work within limited spaces. Making use of separable forces one can perform calculations of nuclear characteristics in very large configuration spaces since there is no need to diagonalize matrices whose dimensions grow with the size of configuration space. For example, the well-known quasiparticle-phonon model (QPM) [4] can do very detailed predictions for nuclei away from closed shells [15], but it is very difficult to extrapolate the phenomenological parameters of the nuclear hamiltonian to new regions of nuclei.

That is why a finite rank approximation for the particle–hole (p-h) interaction resulting from the Skyrme forces has been suggested in our previous work [16]. Thus, the self-consistent mean field can be calculated with the original Skyrme interaction whereas the RPA solutions would be obtained with the finite rank approximation to the p-h matrix elements. It was found that the finite rank approximation can reproduce reasonably well the dipole and quadrupole strength distributions in Ar isotopes. Alternative schemes to factorize the p-h interaction were considered in [17–19].

Recently, the finite rank approximation for p-h interactions of Skyrme type has been generalized to take into account the pairing correlations [20]. The QRPA was used to describe characteristics of the low-lying 2^+ and 3^- states and giant resonances in nuclei with very dif-

*Electronic address: voronov@theor.jinr.ru

ferent mass numbers [20, 21]. It was found that there is room for the phonon-phonon coupling effects in many cases. The first calculation to estimate this effect has been done for ^{112}Sn in [22].

In Ref. [23], we extended our approach to take into account the coupling between the one- and two-phonon terms in the wave functions of excited states. As an application of the method we present results for low-lying 2^+ and 3^- states in neutron-rich Sn isotopes and compare them with recent experimental data [24] and other calculations [25–27].

This paper is organized as follows: in Sec. II a sketch of our method allowing to consider effects of the phonon-phonon coupling is presented. In Sec. III details of calculations and some examples of the RPA calculations for low-lying states and giant resonances are given. It is shown in Sec. IV how the phonon-phonon coupling can influence the properties of the quadrupole and octupole states in $^{124-134}$Sn isotopes. Conclusions are drawn in Sec. V.

II. METHOD OF CALCULATIONS

A. The model hamiltonian and QRPA

We start from the effective Skyrme interaction [6] and use the notation of Ref. [28] containing explicit density dependence and all spin-exchange terms. The single-particle spectrum is calculated within the HF method. The continuous part of the single-particle spectrum is discredited by diagonalizing the HF hamiltonian on a harmonic oscillator basis [29]. The p-h residual interaction $\tilde{V}_{\rm res}$ corresponding to the Skyrme force that includes both direct and exchange terms can be obtained as a second derivative of the energy density functional with respect to the density [30]. Following our previous papers [16] we simplify $\tilde{V}_{\rm res}$ by approximating it by its Landau-Migdal form. For Skyrme interactions all Landau parameters F_l, G_l, $F_l^{'}$, and $G_l^{'}$ with $l > 1$ are zero. Here, we keep only the $l = 0$ terms in $V_{\rm res}$ and in the coordinate representation one can write it in the following form:

$$\begin{aligned} V_{\rm res}(\mathbf{r}_1, \mathbf{r}_2) \;=\; & N_0^{-1}[F_0(r_1) + G_0(r_1)(\sigma_1 \cdot \sigma_2) \\ & +(F_0^{'}(r_1) + G_0^{'}(r_1)(\sigma_1 \cdot \sigma_2))(\tau_1 \cdot \tau_2)]\delta(\mathbf{r}_1 - \mathbf{r}_2) \end{aligned} \tag{1}$$

where σ_i and τ_i are the spin and isospin operators, and $N_0 = 2k_F m^*/\pi^2\hbar^2$ with k_F and m^* standing for the Fermi momentum and nucleon effective mass. The expressions for F_0, G_0, $F_0^{'}$, and $G_0^{'}$ in terms of the Skyrme force parameters can be found in Ref. [28]. Because of the density dependence of the interaction the Landau parameters of Eq. (1) are functions of the coordinate $\mathbf{r}$.

In what follows we use the second quantized representation and $V_{\rm res}$ can be written as:

$$\hat{V}_{\rm res} \;=\; \frac{1}{2}\sum_{1234} V_{1234} : a_1^+ a_2^+ a_4 a_3 : \tag{2}$$

where a_1^+ (a_1) is the particle creation (annihilation) operator, 1 denotes the quantum numbers $(n_1\, l_1\, j_1\, m_1)$, and

$$V_{1234} = \int \phi_1^*(\mathbf{r}_1)\phi_2^*(\mathbf{r}_2) V_{\rm res}(\mathbf{r}_1, \mathbf{r}_2)\phi_3(\mathbf{r}_1)\phi_4(\mathbf{r}_2)\mathbf{dr}_1\mathbf{dr}_2. \tag{3}$$

After integrating over the angular variables one needs to calculate the radial integrals. It is shown in [16, 20] that the radial integrals can be accurately calculated by choosing a large enough cut-off radius R and using a N-point integration Gauss formula with abscissas r_k and

weights w_k. Thus, the two-body matrix element is a sum of N separable terms, i.e., the residual interaction takes the form of a rank N separable interaction.

We employ a hamiltonian which includes an average HF field, pairing interactions, the isoscalar, and isovector particle–hole (p–h) residual forces in a finite rank separable form [20]:

$$H \;=\; \sum_{\tau}\left(\sum_{jm}^{\tau}(E_j-\lambda_\tau)a^{\dagger}_{jm}a_{jm}-\frac{1}{4}V^{(0)}_{\tau}:P^{\dagger}_0\,(\tau)P_0\,(\tau):\right)+\hat{V}_{\rm res}\,, \tag{4}$$

where

$$P^{+}_0\,(\tau)=\sum_{jm}^{\tau}(-1)^{j-m}a^{+}_{jm}a^{+}_{j-m}\,. \tag{5}$$

We sum over the proton(p) and neutron(n) indexes and the notation $\{\tau=(n,p)\}$ is used. The change $\tau\leftrightarrow-\tau$ implies that $p\leftrightarrow n$. The single-particle states are specified by the quantum numbers (jm), E_j are the single-particle energies, λ_τ the chemical potentials, and $V^{(0)}_{\tau}$ is the interaction strength in the particle-particle channel. The hamiltonian (4) has the same form as the QPM hamiltonian with N separable terms [4, 31], but the single-particle spectrum and parameters of the p-h residual interaction are calculated making use of the Skyrme forces.

In what follows we work in the quasiparticle representation defined by the canonical Bogoliubov transformation:

$$a^{+}_{jm}\;=\;u_j\alpha^{+}_{jm}\;+\;(-1)^{j-m}v_j\alpha_{j-m}\,. \tag{6}$$

The hamiltonian (4) can be represented in terms of bifermion quasiparticle operators and their conjugates [4]:

$$B(jj^{'};\lambda\mu)\;=\;\sum_{mm^{'}}(-1)^{j^{'}+m^{'}}\langle jmj^{'}m^{'}\mid\lambda\mu\rangle\alpha^{+}_{jm}\alpha_{j^{'}-m^{'}}\,, \tag{7}$$

$$A^{+}(jj^{'};\lambda\mu)\;=\;\sum_{mm^{'}}\langle jmj^{'}m^{'}\mid\lambda\mu\rangle\alpha^{+}_{jm}\alpha^{+}_{j^{'}m^{'}}\,. \tag{8}$$

We introduce the phonon creation operators

$$Q^{+}_{\lambda\mu i}\;=\;\frac{1}{2}\sum_{jj^{'}}\left(X^{\lambda i}_{jj^{'}}\,A^{+}(jj^{'};\lambda\mu)-(-1)^{\lambda-\mu}Y^{\lambda i}_{jj^{'}}\,A(jj^{'};\lambda-\mu)\right)\,. \tag{9}$$

where the index λ denotes total angular momentum and μ is its z-projection in the laboratory system. One assumes that the ground state is the QRPA phonon vacuum $\mid 0\rangle$, i.e. $Q_{\lambda\mu i}\mid 0\rangle\;=0$. We define the excited states for this approximation by $Q^{+}_{\lambda\mu i}\mid 0\rangle$. The quasiparticle energies (ε_j), the chemical potentials (λ_τ), the energy gap, and the coefficients u and v of the Bogoliubov transformations (6) are determined from the BCS equations with the single-particle spectrum that is calculated within the HF method with the effective Skyrme interaction. Making use of the linearized equation-of-motion approach [1],

$$\langle 0|\left[\delta Q_{\lambda\mu i},\left[H,Q^{+}_{\lambda\mu i}\right]\right]\mid 0\rangle=\omega_{\lambda i}\langle 0|\left[\delta Q_{\lambda\mu i},Q^{+}_{\lambda\mu i}\right]\mid 0\rangle\,, \tag{10}$$

with the normalization condition

$$\langle 0\mid\;[Q_{\lambda\mu i},Q^{+}_{\lambda\mu i^{'}}]\;\mid 0\rangle\;=\delta_{ii^{'}}\,, \tag{11}$$

one can get the QRPA equations [3, 4]

$$\begin{pmatrix} \mathcal{A} & \mathcal{B} \\ -\mathcal{B} & -\mathcal{A} \end{pmatrix} \begin{pmatrix} X \\ Y \end{pmatrix} = w \begin{pmatrix} X \\ Y \end{pmatrix} . \tag{12}$$

In QRPA problems there appear two types of interaction matrix elements, the $A^{(\lambda)}_{(j_1 j_1')(j_2 j_2')}$ matrix related to forward-going graphs and the $B^{(\lambda)}_{(j_1 j_1')_\tau (j_2 j_2')_{q\tau}}$ matrix related to backward-going graphs. Solutions of this set of linear equations yield the eigen-energies and the amplitudes X and Y of the excited states. The dimension of the matrices $\mathcal{A}, \mathcal{B}$ is the space size of the two-quasiparticle configurations. For our case expressions for $\mathcal{A}, \mathcal{B}$ and X, Y are given in [20]. Using the finite rank approximation we need to invert a matrix of dimension $4N \times 4N$ independently of the configuration space size [16, 20]. Therefore, this approach enables one to reduce remarkably the dimensions of the matrices that must be inverted to perform structure calculations in very large configuration spaces.

B. Phonon-phonon coupling

Our calculations [20] show that, for the normal parity states one can neglect the spin-multipole terms of the p-h residual interaction (1). Using the completeness and orthogonality conditions for the phonon operators one can express bifermion operators $A^+(jj';\lambda\mu)$ and $A(jj';\lambda\mu)$ through the phonon ones and the initial hamiltonian (4) can be rewritten in terms of quasiparticle and phonon operators in the following form:

$$H = h_0 + h_{QQ} + h_{QB} \tag{13}$$

$$h_0 = \sum_{jm} \varepsilon_j \, \alpha^+_{jm} \, \alpha_{jm} \tag{14}$$

$$h_{QQ} = -\frac{1}{4} \sum_{\lambda\mu i i' \tau} W^{\lambda i i'}(\tau) \, Q^+_{\lambda\mu i} Q_{\lambda\mu i'} \tag{15}$$

$$h_{QB} = -\frac{1}{2} \sum_{\lambda\mu i \tau} \sum_{jj'}{}^{\tau} \Gamma^{\lambda i}_{jj'}(\tau) \left((-)^{\lambda-\mu} Q^+_{\lambda\mu i} + Q_{\lambda-\mu i} \right) B(jj';\lambda-\mu) + h.c. \tag{16}$$

The coefficients W and Γ of the hamiltonian (13) are sums of N combinations of phonon amplitudes, the Landau parameters, the reduced matrix elements of the spherical harmonics and radial parts of the HF single-particle wave function (see Appendix A). It is worth to point out that the term h_{QB} is responsible for the mixing of the configurations and, therefore, for the description of many characteristics of the excited states of even–even nuclei [4].

To take into account the mixing of the configurations in the simplest case one can write the wave functions of excited states as

$$\Psi_\nu(\lambda\mu) = \{ \sum_i R_i(\lambda\nu) Q^+_{\lambda\mu i} + \sum_{\lambda_1 i_1 \lambda_2 i_2} P^{\lambda_1 i_1}_{\lambda_2 i_2}(\lambda\nu) \left[Q^+_{\lambda_1\mu_1 i_1} Q^+_{\lambda_2\mu_2 i_2} \right]_{\lambda\mu} \} |0\rangle \tag{17}$$

with the normalization condition

$$\sum_i R_i^2(J\nu) + 2 \sum_{\lambda_1 i_1 \lambda_2 i_2} \left(P^{\lambda_1 i_1}_{\lambda_2 i_2}(J\nu) \right)^2 = 1 \, . \tag{18}$$

Using the variational principle in the form

$$\delta\ (\langle\,\Psi_\nu(\lambda\mu)\,|H\mid\,\Psi_\nu(\lambda\mu)\rangle\ -\ E_\nu\,(\langle\,\Psi_\nu(\lambda\mu)\,|\,\Psi_\nu(\lambda\mu)\rangle\ -\ 1))\ =\ 0, \tag{19}$$

one obtains a set of linear equations for the unknown amplitudes $R_i(J\nu)$ and $P^{\lambda_1 i_1}_{\lambda_2 i_2}(J\nu)$,

$$(\omega_{Ji} - E_\nu)R_i(J\nu) + \sum_{\lambda_1 i_1 \lambda_2 i_2} U^{\lambda_1 i_1}_{\lambda_2 i_2}(J\nu)P^{\lambda_1 i_1}_{\lambda_2 i_2}(J\nu) = 0\,, \tag{20}$$

$$\sum_i U^{\lambda_1 i_1}_{\lambda_2 i_2}(Ji)R_i(J\nu) + 2(\omega_{\lambda_1 i_1} + \omega_{\lambda_2 i_2} - E_\nu)P^{\lambda_1 i_1}_{\lambda_2 i_2}(J\nu) = 0\,, \tag{21}$$

where $U^{\lambda_1 i_1}_{\lambda_2 i_2}(Ji)$ is the matrix element coupling one- and two-phonon configurations [4, 32],

$$U^{\lambda_1 i_1}_{\lambda_2 i_2}(Ji) = \langle 0|Q_{Ji}h_{QB}\left[Q^+_{\lambda_1 i_1}Q^+_{\lambda_2 i_2}\right]_J|0\rangle\,. \tag{22}$$

The expression of $U^{\lambda_1 i_1}_{\lambda_2 i_2}(Ji)$ is given in Appendix B. The number of linear equations (20), (21) equals the number of one- and two-phonon configurations included in the wave function (17).

The energies of excited states E_ν are solutions of the secular equation

$$F(E_\nu) \equiv det\left|(\omega_{\lambda i} - E_\nu)\delta_{ii'} - \frac{1}{2}\sum_{\lambda_1 i_1, \lambda_2 i_2}\frac{U^{\lambda_1 i_1}_{\lambda_2 i_2}(\lambda i)U^{\lambda_1 i_1}_{\lambda_2 i_2}(\lambda i')}{\omega_{\lambda_1 i_1} + \omega_{\lambda_2 i_2} - E_\nu}\right| = 0, \tag{23}$$

where the rank of the determinant equals the number of the one-phonon configurations. Using Eqs. (20) and (21) and the normalization condition (18), one can find the amplitudes $R_i(J\nu)$ and $P^{\lambda_1 i_1}_{\lambda_2 i_2}(J\nu)$.

It is necessary to point out that the equations derived above have the same form as the basic QPM equations [4, 32], but the single-particle spectrum and the p-h residual interaction are determined making use of the Skyrme interactions.

III. DETAILS OF CALCULATIONS

We apply the present approach to study characteristics of the low-lying vibrational states in the neutron-rich Sn isotopes. In this paper we use the parametrization SLy4 [33] of the Skyrme interaction. This parametrization was proposed to describe isotopic properties of nuclei from the β-stability line to the drip lines. Spherical symmetry is assumed for the HF ground states.

The pairing constants V^0_τ are fixed to reproduce the odd-even mass difference of neighboring nuclei. It is well known [11, 12] that the constant gap approximation leads to an overestimate of occupation probabilities for subshells that are far from the Fermi level and it is necessary to introduce a cut-off in the single-particle space. Above this cut-off subshells do not participate in the pairing effect. In our calculations we choose the BCS subspace to include all subshells lying below 5 MeV.

In order to perform QRPA calculations, the single-particle continuum is discretized [29] by diagonalizing the HF hamiltonian on a basis of twelve harmonic oscillator shells and cutting off the single-particle spectra at the energy of 100 MeV. This is sufficient to exhaust practically all the energy-weighted sum rule.

The Landau parameters F_0, G_0, $F_0^{'}$, and $G_0^{'}$ expressed in terms of the Skyrme force parameters [28] depend on k_F. As it is pointed out in our previous works [16, 20] one needs to adopt some

effective value for k_F to give an accurate representation of the original p-h Skyrme interaction. For the present calculations we use the nuclear matter value for k_F.

Our previous investigations [20] enable us to conclude that N=45 for the rank of our separable approximation is enough for multipolarities $\lambda \leq 3$ in nuclei with $A \leq 208$. Increasing N, for example, up to N=60 in ^{208}Pb changes results for energies and transition probabilities not more than 1%. Our calculations show that, for the natural parity states one can neglect the spin-multipole interactions and this reduces by a factor 2 the total matrix dimension, i.e., the matrix dimensions never exceed $2N \times 2N$ independently of the configuration space size [16, 20].

The two-phonon configurations of the wave function (17) are constructed from natural parity phonons with multipolarities $\lambda = 2, 3, 4, 5$. All one-phonon configurations with energies below 8 MeV for $^{124-130,134}$Sn and 10 MeV for ^{132}Sn are included in the wave function (17). The cut-off in the space of the two-phonon configurations is 21 MeV. An extension of the space for one- and two-phonon configurations does not change results for energies and transition probabilities practically.

IV. RESULTS OF CALCULATIONS

A. Harmonic approximation

Of great importance for us is how well the ground state properties of the stable nuclei are reproduced Therefore we pay a special attention on nuclear radii. In Fig. 1 the dependence of the difference between neutron and proton radii on the mass number is shown [34]. The difference becomes larger when the number of the neutrons is increased. The calculated charge radii are in reasonable agreement with the known experimental data [35, 36]. The radii decrease about 10% around the double magic nucleus ^{132}Sn. This is due to the vanishing of a pairing gap in this nucleus. As a first example we examine the 2_1^+ state energies and B(E2)-values in some

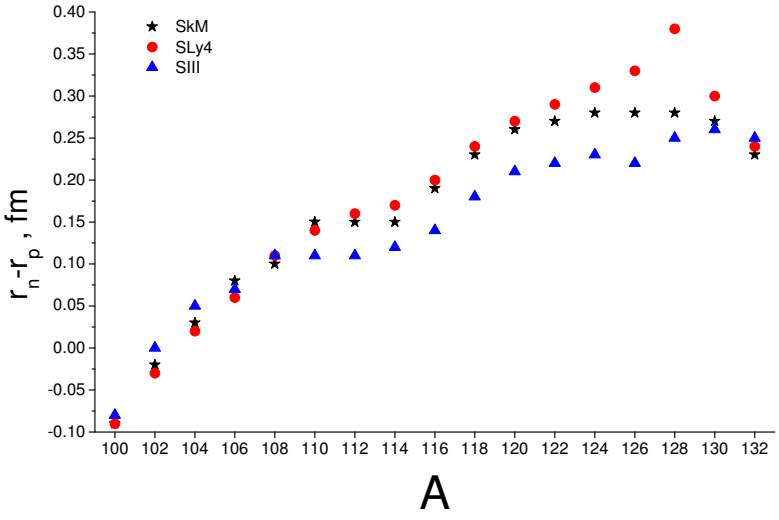

FIG. 1: The dependence of the difference between neutron and proton radii on the mass number of Sn isotopes.

Ar, Sn, and Pb isotopes [20]. The results of our QRPA calculations and the experimental data

[37] are shown in Table I. One can see that there is a satisfactory agreement with experimental data. Results of our calculations for Ar isotopes are close to those of QRPA with Skyrme forces [43]. The evolution of the B(E2)-values in the Ar isotopes demonstrates clearly the pairing effects. The experimental and calculated B(E2)-values in ^{38}Ar are three times less than those in ^{36,40}Ar. The neutron shell closure leads to the vanishing of the neutron pairing and a reduction of the proton gap. As a result there is a remarkable reduction of the E2 transition probability in ^{38}Ar. Some overestimate of the energies indicates that there is room for two-phonon effects. As

TABLE I: Energies and B(E2)-values for up-transitions to the first 2^+ states.

Nucleus	Energy (MeV)		B(E2↑) (e^2fm^4)	
	Exp.	Theory	Exp.	Theory
^{36}Ar	1.97	1.91	300±30	310
^{38}Ar	2.17	2.51	130±10	110
^{40}Ar	1.46	2.17	330±40	290
^{112}Sn	1.26	1.49	2400±140	2600
^{114}Sn	1.30	1.51	2400±500	2100
^{206}Pb	0.80	0.96	1000±20	1700
^{208}Pb	4.09	5.36	3000±300	2000

an another example of the pairing effect we examine the 2^+_1 and 3^-_1 state energies and transition probabilities in some S isotopes. The results of our QRPA calculations for the energies and B(E2)-values and the experimental data [37] are shown in Table II.

TABLE II: Energies, B(E2)-values, and $(M_n/M_p)/(N/Z)$ ratios for up-transitions to the first 2^+ states.

Nucleus	Energy (MeV)		B(E2↑) (e^2fm^4)		$(M_n/M_p)/(N/Z)$	
	Exp.	Theory	Exp.	Theory	Exp.	Theory
^{32}S	2.23	3.34	300±13	340	0.94±0.16	0.92
^{34}S	2.13	2.48	212±12	290	0.85±0.23	0.87
^{36}S	3.29	2.33	104±28	130	0.65±0.18	0.40
^{38}S	1.29	1.55	235±30	300	1.09±0.29	0.73

One can see that there is a rather good agreement with experimental data. Results of our calculations for S isotopes are close to those of QRPA with Skyrme forces [43]. The evolution of the B(E2)-values in the S isotopes clearly demonstrates the pairing effects. The experimental and calculated B(E2)-values in ^{36}S are two times less than those in ^{34,38}S. The neutron shell closure leads to the vanishing of the neutron pairing and a reduction of the proton gap. As a result there is a remarkable reduction of the E2 transition probability in ^{36}S. Some overestimate of the energies in ^{34,38}S indicates that there is room for two-phonon effects.

Results of our calculations for the 3^-_1 energies and the transition probabilities B(E3) are compared with experimental data [38] in Table III. Generally there is a good agreement between theory and experiment.

An additional information about the structure of the first 2^+ and 3^- states can be extracted by looking at the ratio of the multipole transition matrix elements M_n/M_p that depend on the relative contributions of the proton and neutron configurations. In the framework of the collective model for isoscalar excitations this ratio is equal to $M_n/M_p = N/Z$ and any deviation from this value can indicate an isovector character of the state. The M_n/M_p ratio can be

TABLE III: Energies, B(E3)-values, and $(M_n/M_p)/(N/Z)$ ratios for up-transitions to the first 3^- states.

Nucleus	Energy (MeV)		B(E3↑) (e^2fm^6)		$(M_n/M_p)/(N/Z)$
	Exp.	Theory	Exp.	Theory	Theory
^{32}S	5.01	7.37	12700±2000	8900	0.89
^{34}S	4.62	5.66	8000±2000	8500	1.06
^{36}S	4.19	3.86	8000±3000	7200	1.15
^{38}S	–	5.68	–	6200	1.01

determined experimentally by using different external probes [40–42]. Recently [43], QRPA calculations of the M_n/M_p ratios for the 2_1^+ states in some S isotopes have been done. The predicted results are in good agreement with experimental data [43]. Our calculated values of the M_n/M_p ratios for the 2_1^+ and 3_1^- states are shown in Tables II and III, respectively. Our results support the conclusions of Ref. [43] about the isovector character of the 2_1^+ states in ^{36}S. As one can see from Table III our calculations predict that the M_n/M_p ratios for the 3_1^- states are rather close to N/Z, thus indicating their isoscalar character.

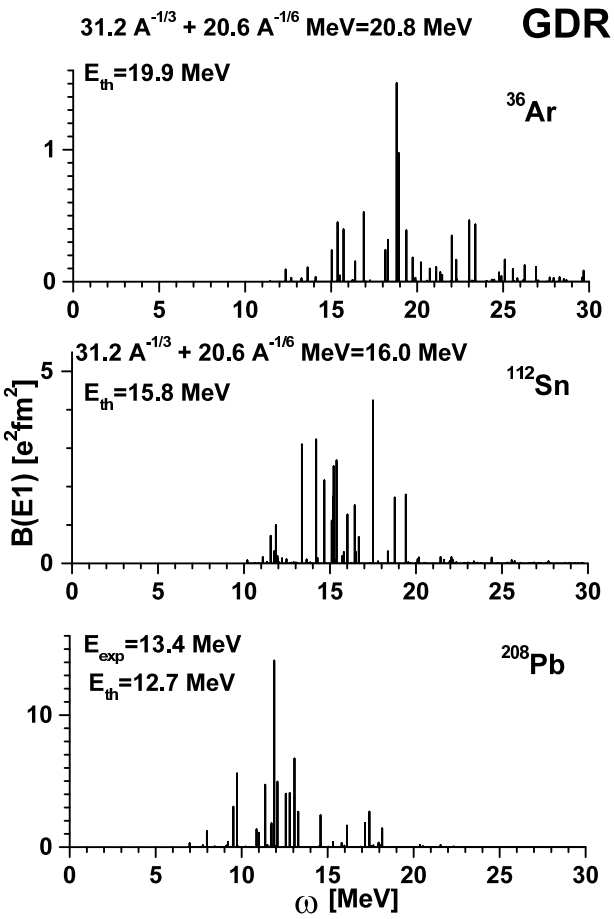

FIG. 2: The dipole strength distributions in ^{36}Ar, ^{112}Sn, and ^{208}Pb.

To test our approach for high lying states we examine the dipole strength distributions (GDR) in ^{36}Ar, ^{112}Sn, and ^{208}Pb [21] (see Fig. II). For the energy centroids (m_1/m_0) we get 19.9 MeV, 15.8 MeV, and 12.7 MeV in ^{36}Ar, ^{112}Sn, and ^{208}Pb respectively. The calculated energy

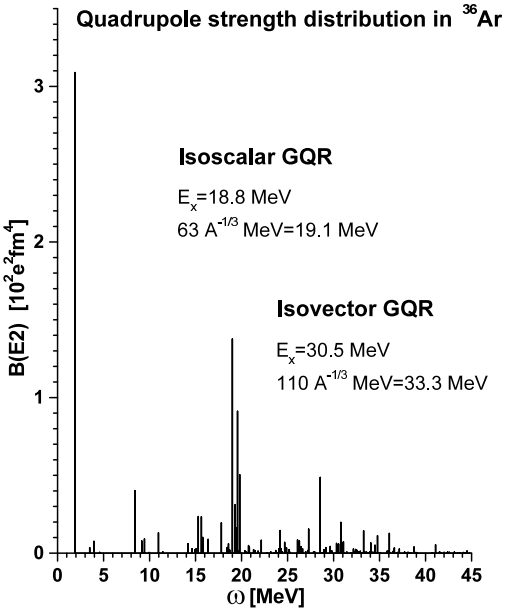

FIG. 3: The quadrupole strength distribution in ^{36}Ar.

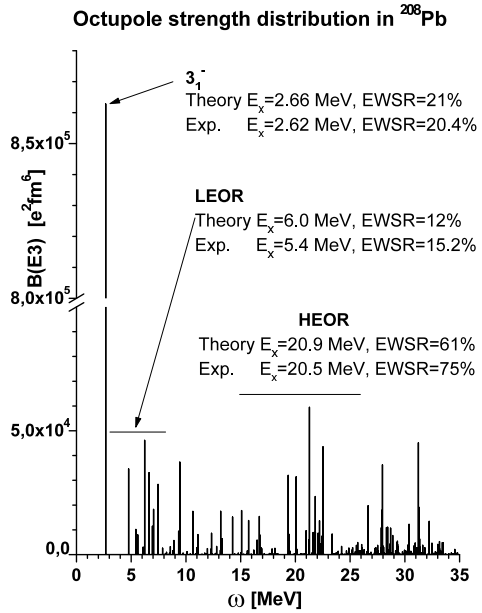

FIG. 4: The octupole strength distribution in ^{208}Pb.

centroid for ^{208}Pb is in a satisfactory agreement with the experimental value of 13.4 MeV [44]. The values of energy centroids for ^{36}Ar and ^{112}Sn are rather close to the empirical systematic $E_c = 31.2A^{-1/3} + 20.6A^{-1/6}$ MeV. As one can see from Fig. III, the calculated values for the GQR for ^{36}Ar are closed to the empirical systematic too. The octupole strength distribution in ^{208}Pb is rather well studied in many experiments [46, 48].

The calculated octupole strength distribution up to the excitation energy 35 MeV is shown in Fig. IV. According to experimental data [46] for the 3^-_1 state, in ^{208}Pb the excitation energy equals to $E_x = 2.62$ MeV and the energy-weighted sum rule (EWSR) is exhausted by 20.4% that can be compared with the calculated values $E_x = 2.66$ MeV and EWSR=21%.

TABLE IV: Energies and B(E2)-values for up-transitions to the first 2^+ states.

Nucleus	Energy (MeV)			B(E2↑) (e^2b^2)		
	Exp.	Theory		Exp.	Theory	
		QRPA	2PH		QRPA	2PH
^{124}Sn	1.13	1.92	1.03	0.1660±0.0040	0.177	0.151
^{126}Sn	1.14	1.96	1.30	0.10±0.03	0.149	0.133
^{128}Sn	1.17	2.08	1.48	0.073±0.006	0.111	0.100
^{130}Sn	1.22	2.37	1.73	0.023±0.005	0.064	0.058
^{132}Sn	4.04	4.47	4.03	0.14±0.06	0.136	0.129
^{134}Sn	0.73	1.65	1.34	0.029±0.006	0.016	0.015

For the low-energy octupole resonance below 7.5 MeV our calculation gives the centroid energy $E_c = 5.96$ MeV and EWSR=12% as compared to the experimental values of 5.4 MeV and 15.2% respectively. For the high-energy octupole resonance we get values $E_c = 20.9$ MeV and EWSR=61% that are in a good agreement with experimental findings $E_c = 20.5 \pm 1$ MeV and EWSR=75 ± 15% [48]. One can conclude that present calculations reproduce correctly not only the 3^-_1 characteristics, but the whole octupole strength distribution in ^{208}Pb.

B. Effect of phonon-phonon coupling

As an application of the method we investigate effects of the phonon-phonon coupling on energies and transition probabilities to 2^+_1 and 3^-_1 states in $^{124-134}$Sn.

Results of our calculations for the 2^+_1 energies and transition probabilities $B(E2)$ are compared with experimental data [24, 37] in Table IV. Columns "QRPA" and "2PH" give values calculated within the QRPA and taking into account the phonon-phonon coupling, respectively.

It is seen in Table IV that there is a remarkable increase of the 2^+_1 energy and $B(E2\uparrow)$ in ^{132}Sn in comparison with those in ^{130,134}Sn. Such a behavior of $B(E2\uparrow)$ is related with the proportion between the QRPA amplitudes for neutrons and protons in Sn isotopes. The neutron amplitudes are dominant in all Sn isotopes and the contribution of the main neutron configuration $\{1h_{11/2}, 1h_{11/2}\}$ increases from 81.2% in ^{124}Sn to 92.8% in ^{130}Sn when neutrons fill the subshell $1h_{11/2}$. At the same time the contribution of the main proton configuration $\{2d_{5/2}, 1g_{9/2}\}$ is decreasing from 9.3% in ^{124}Sn to 3.9% in ^{130}Sn. The closure of the neutron subshell $1h_{11/2}$ in ^{132}Sn leads to the vanishing of the neutron paring. The energy of the first neutron two-quasiparticle pole $\{2f_{7/2}, 1h_{11/2}\}$ in ^{132}Sn is greater than energies of the first poles in ^{130,134}Sn and the contribution of the $\{2f_{7/2}, 1h_{11/2}\}$ configuration in the doubly magic ^{132}Sn is about 61%. Furthermore, the first pole in ^{132}Sn is closer to the proton poles. This means that the contribution of the proton two-quasiparticle configurations is greater than those in the neighboring isotopes and as a result the main proton configuration $\{2d_{5/2}, 1g_{9/2}\}$ in ^{132}Sn exhausts about 33%. In ^{134}Sn the leading contribution (about 99%) comes from the neutron configuration $\{2f_{7/2}, 2f_{7/2}\}$ and as a result the $B(E2)$ value is reduced. Such a behavior of the 2^+_1 energies and $B(E2)$ values in the neutron-rich Sn isotopes reflects the shell structure in this region . It is worth to mention that the first prediction of the anomalous behavior of 2^+ excitations around ^{132}Sn based on the QRPA calculations with a separable quadrupole-plus-pairing hamiltonian has been done in [25].

In comparison with other QRPA calculations of Sn isotopes done with the Gogny force [27] and, especially, with Skyrme forces [26], the present QRPA results for 2^+_1 energies are in agreement but our $B(E2)$ values are somewhat larger. One possible cause for this discrepancy

TABLE V: Energies and B(E3)-values for up-transitions to the first 3^- states.

Nucleus	Energy (MeV)			B(E3↑) (e^2b^3)		
	Exp.	Theory		Exp.	Theory	
		QRPA	2PH		QRPA	2PH
^{124}Sn	2.60	3.64	3.25	0.073±0.010	0.208	0.196
^{126}Sn	2.72	4.16	3.76		0.191	0.176
^{128}Sn		4.66	4.22		0.181	0.161
^{130}Sn		5.17	4.75		0.183	0.159
^{132}Sn	4.35	5.66	5.36		0.202	0.191
^{134}Sn		5.01	4.51		0.128	0.111

TABLE VI: $(M_n/M_p)/(N/Z)$ ratios for the first 2^+ and 3^- states.

State	^{124}Sn	^{126}Sn	^{128}Sn	^{130}Sn	^{132}Sn	^{134}Sn
2^+_1	0.99	0.99	0.98	0.97	0.81	1.44
3^-_1	0.94	0.92	0.89	0.86	0.83	0.91

may lie in the fact that different prescriptions for the residual interaction in the p-p channel are adopted in Ref. [26] and in the present work.

One can see from Table IV that the inclusion of the two-phonon terms results in a decrease of the energies and a reduction of transition probabilities. Note that the effect of the two-phonon configurations is important for the energies and this effect becomes weak in ^{132}Sn. There is some overestimate of the energies for the QRPA calculations and taking into account the two-phonon terms improves the description of the 2^+_1 energies. The reduction of the $B(E2)$ values is small in most cases due to the crucial contribution of the one-phonon configuration in the wave function structure.

Results of our calculations for the 3^-_1 energies and the transition probabilities $B(E3)$ compared to experimental data [38] are shown in Table V. As for the quadrupole excitations the influence of coupling between one- and two-phonon terms in the wave functions of the 3^-_1 states leads to the decrease of the energies and the reduction of transition probabilities. In spite of the fact that the 3^-_1 states have strong collectivity and many two-quasiparticle configurations give a contribution in the QRPA wave functions in Sn isotopes the phonon-phonon coupling is not very strong in this case. Our calculation shows that the main reason is the smallness of the matrix elements coupling the one-phonon configuration $\{3^-_1\}$ and the two-phonon configuration $\{2^+_1;3^-_1\}$ ($U^{2^+_1}_{3^-_1}(3^-_1)$). As a result the decrease of the 3^-_1 energies is about 10%. In the present paper we neglect the p-p channel that can be important for collective phonons and can reduce the collectivity of states [4, 39]. This can give an additional lowering of energies and transition probabilities , but this is not the case for ^{132}Sn. Comparing with the QRPA results of Ref. [26] for 3^-_1 energies and transition probabilities we find that the energies are in general agreement whereas our calculated $B(E3)$ are larger than those of Ref. [26]. Again, the reason may be in the different treatments of the residual interaction in the p-p channel. It is worth to mention that experimental data for 3^-_1 states in the neutron-rich Sn isotopes are very scarce.

Our calculated values for the M_n/M_p ratios for the 2^+_1 and 3^-_1 states are shown in Table VI. The calculated M_n/M_p ratios are rather close to N/Z except 2^+_1 in ^{134}Sn. It is worth noting that the deviation of the ratio for 2^+_1 state in ^{132}Sn correlates with the increase of the contribution of the proton two-quasiparticle configurations.

V. CONCLUSIONS

A finite rank separable approximation for the QRPA calculations with Skyrme interactions, proposed in a previous work of ours, is extended to take into account the coupling between one- and two-phonon terms in the wave functions of excited states. The suggested approach enables one to reduce considerably the dimensions of the matrices that must be diagonalized to perform structure calculations in very large configuration spaces. As an application of the method we have studied the behavior of the energies and transition probabilities to 2_1^+ and 3_1^- states in $^{124-134}$Sn. The inclusion of the two-phonon configurations results in a decrease of the energies and a reduction of transition probabilities.

It is shown that for the 2_1^+ states, there is some overestimate of the calculated excitation energies in the QRPA calculations and the effects of the two-phonon configurations can decrease substantially these energies. These effects are weaker for 3_1^- states where the one-phonon contributions represent about 90% of the total results. In this case, the main discrepancies between measured and calculated energies are too large to be overcome by the inclusion of the two-phonon configurations and one should seek for improvements in the effective interaction used.

The inclusion of the two-phonon terms does not change the effect of a remarkable increase of the QRPA value of $B(E2; 0^+ \rightarrow 2_1^+)$ for the doubly-closed shell nucleus ^{132}Sn in comparison with its neighbors. A systematical study of the influence of the two-phonon terms taking into account the p-p channel on properties of the low-lying states is now in progress.

APPENDIX A

The coefficients of the hamiltonian (13) are given by the following expressions:

$$W^{\lambda ii'}(\tau) = \sum_{k=1}^{N} \left(\frac{D_M^{\lambda ik}(\tau)}{\sqrt{2\mathcal{Y}_\tau^{\lambda ki'}}} + \frac{D_M^{\lambda i'k}(\tau)}{\sqrt{2\mathcal{Y}_\tau^{\lambda ki}}} \right), \tag{A1}$$

$$\Gamma_{jj'}^{\lambda i}(\tau) = \sum_{k=1}^{N} \frac{f_{jj'}^{(\lambda k)} v_{jj'}^{(-)}}{\sqrt{2\mathcal{Y}_\tau^{\lambda ki}}}, \tag{A2}$$

where

$$D_M^{\lambda ik}(\tau) = \sum_{jj'}{}^{\tau} f_{jj'}^{(\lambda k)} u_{jj'}^{(+)} \left(X_{jj'}^{\lambda i} + Y_{jj'}^{\lambda i} \right),$$

$$\mathcal{Y}_\tau^{\lambda ki} = \frac{2(2\lambda+1)^2}{\left(D_M^{\lambda ik}(\tau) \left(\kappa_0^{(M,k)} + \kappa_1^{(M,k)} \right) + D_M^{\lambda ik}(-\tau) \left(\kappa_0^{(M,k)} - \kappa_1^{(M,k)} \right) \right)^2},$$

$v_{jj'}^{(-)} = u_j u_{j'} - v_j v_{j'}$ $u_{jj'}^{(+)} = u_j v_{j'} + v_j u_{j'}$.

In the above expressions, $f_{jj'}^{(\lambda k)}$ denotes the single-particle radial matrix elements [20]:

$$f_{j_1 j_2}^{(\lambda k)} = u_{j_1}(r_k) u_{j_2}(r_k) i^\lambda \langle j_1 || Y_\lambda || j_2 \rangle,$$

where $u_{j_1}(r_k)$ is the radial part of the HF single-particle wave function at the abscissas of the N-point integration Gauss formula r_k. $\kappa_0^{(M,k)}$ and $\kappa_1^{(M,k)}$ are defined by the Landau parameters as

$$\begin{pmatrix} \kappa_0^{(M,k)} \\ \kappa_1^{(M,k)} \end{pmatrix} = -N_0^{-1} \frac{Rw_k}{2r_k^2} \begin{pmatrix} F_0(r_k) \\ F_0'(r_k) \end{pmatrix}.$$

APPENDIX B

The matrix elements $U^{\lambda_1 i_1}_{\lambda_2 i_2}(Ji)$ have the following form:

$$\begin{aligned} U^{\lambda_1 i_1}_{\lambda_2 i_2}(\lambda i) \;=\; & (-1)^{\lambda_1+\lambda_2+\lambda}\sqrt{(2\lambda_1+1)(2\lambda_2+1)}\sum_{\tau}\sum_{j_1 j_2 j_3} \\ & \times \left(\Gamma^{\lambda i}_{j_1 j_2}(\tau) \begin{Bmatrix} \lambda_1 & \lambda_2 & \lambda \\ j_2 & j_1 & j_3 \end{Bmatrix} \left(X^{\lambda_2 i_2}_{j_2 j_3} Y^{\lambda_1 i_1}_{j_3 j_1} + X^{\lambda_1 i_1}_{j_3 j_1} Y^{\lambda_2 i_2}_{j_2 j_3}\right)\right. \\ & + \Gamma^{\lambda_1 i_1}_{j_1 j_2}(\tau) \begin{Bmatrix} \lambda_1 & \lambda_2 & \lambda \\ j_3 & j_2 & j_1 \end{Bmatrix} \left(Y^{\lambda_2 i_2}_{j_3 j_1} Y^{\lambda i}_{j_2 j_3} + X^{\lambda i}_{j_2 j_3} X^{\lambda_2 i_2}_{j_3 j_1}\right) \\ & \left. + \Gamma^{\lambda_2 i_2}_{j_1 j_2}(\tau) \begin{Bmatrix} \lambda_1 & \lambda_2 & \lambda \\ j_1 & j_3 & j_2 \end{Bmatrix} \left(Y^{\lambda_1 i_1}_{j_2 j_3} Y^{\lambda i}_{j_3 j_1} + X^{\lambda i}_{j_3 j_1} X^{\lambda_1 i_1}_{j_2 j_3}\right)\right). \end{aligned} \tag{B1}$$

[1] D.J.Rowe, *Nuclear Collective Motion, Models and Theory* (Barnes and Noble, 1970).
[2] A. Bohr and B. Mottelson, *Nuclear Structure* **vol.2** (Benjamin, New York, 1975).
[3] P. Ring and P.Schuck, *The Nuclear Many Body Problem* (Springer, Berlin, 1980).
[4] V.G. Soloviev, *Theory of Atomic Nuclei: Quasiparticles and Phonons* (Institute of Physics, Bristol and Philadelphia, 1992).
[5] D. Gogny, in *Nuclear Self-consistent Fields*, eds. G. Ripka and M. Porneuf (North-Holland, Amsterdam, 1975).
[6] D. Vautherin and D.M. Brink, Phys. Rev. **C 5**, 626 (1972).
[7] H. Flocard and P. Quentin, Ann. Rev. Nucl. Part. Sci. **28**, 523 (1978).
[8] J. Dobaczewski, W. Nazarewicz, T.R. Werner, J.F. Berger, C.R. Chinn, and J. Dechargé, Phys. Rev. **C 53**, 2809 (1996).
[9] G. Colò, P.F. Bortignon, Nguyen Van Giai, A. Bracco, and R.A. Broglia, Phys. Lett. **B276**, 279 (1992).
[10] G. Colò, Nguyen Van Giai, P.F. Bortignon, and R.A. Broglia, Phys. Rev. **C50**, 1496 (1994).
[11] E. Khan and Nguyen Van Giai, Phys. Lett. **B 472**, 253 (2000).
[12] G. Colò, Nguyen Van Giai, P.F. Bortignon, and M.R. Quaglia, Phys. Lett. **B485**, 362 (2000).
[13] G. Colò and P.F. Bortignon, Nucl. Phys. A **696**, 427 (2001).
[14] E. Khan, N. Sandulescu, M. Grasso, and Nguyen Van Giai, Phys. Rev. C **66**,024309 (2002).
[15] S. Galès, Ch. Stoyanov, and A.I. Vdovin, Phys. Rep. **166**, 127 (1988).
[16] Nguyen Van Giai, Ch. Stoyanov, and V.V. Voronov, Phys. Rev. C **57**,1204 (1998).
[17] T. Suzuki and H. Sagawa, Prog. Theor. Phys., **65**, 565 (1981).
[18] P. Sarriguren, E. Moya de Guerra, and A. Escuderos, Nucl. Phys., A **658**, 13 (1999).
[19] V.O. Nesterenko, J. Kvasil, and P.-G. Reinhard, Phys. Rev. C **66**, 044307 (2002).
[20] A.P. Severyukhin, Ch. Stoyanov, V.V. Voronov, and Nguyen Van Giai, Phys. Rev. C **66**, 034304 (2002).
[21] A.P. Severyukhin, V.V. Voronov, Ch. Stoyanov, and Nguyen Van Giai, Physics of Atomic Nuclei **66**, 1434 (2003).

[22] A.P. Severyukhin, V.V. Voronov, Ch. Stoyanov, and Nguyen Van Giai, Nucl. Phys. A **722**, 123c, (2003).
[23] A.P. Severyukhin, V.V. Voronov, and Nguyen Van Giai, Eur. Phys. J. A **22**, 397 (2004).
[24] D.C. Radford *et al.*, Phys. Rev. Lett. 88, 22501 (2002); Eur. Phys. J. A **15**, 171 (2002); http:// www.phy.ornl.gov, HRIBF Newsletter, July 2003.
[25] J. Terasaki, J. Engel, W. Nazarewicz, and M. Stoitsov, Phys. Rev. C **66**, 054313 (2002).
[26] G. Colò, P.F. Bortignon, D. Sarchi, D. T. Khoa, E. Khan, and Nguyen Van Giai, Nucl. Phys. A **722**, 111c (2003).
[27] G. Giambrone *et al.*, Nucl. Phys. A **726**, 3 (2003).
[28] Nguyen Van Giai and H. Sagawa, Phys. Lett. B **106**, 379 (1981).
[29] J.P. Blaizot and D. Gogny, Nucl. Phys. A **284**, 429 (1977).
[30] G.F. Bertsch and S.F. Tsai, Phys. Reports C **18**, 126 (1975).
[31] V.G. Soloviev, Yad. Fiz. **50**, 40 (1989).
[32] V.V. Voronov and V.G. Soloviev, Phys. of Part. & Nucl. **14**, 583 (1983).
[33] E. Chabanat , P. Bonche, P. Haensel, J. Meyer, and R. Schaeffer, Nucl. Phys. A **635**, 231 (1998).
[34] D. Tarpanov, Ch. Stoyanov, and V.V. Voronov, BgNS TRANSCATIONS **10**, No 2, 285 (2005).
[35] E. Nadzakov *et al.*, At. Data Nucl. Data Tables **56**, (1) (1994).
[36] F. Le Blanc *et al.*, Phys. Rev. C **72**, 034305 (2005).
[37] S. Raman, C.W. Nestor Jr., and P. Tikkanen, At. Data and Nucl. Data Tables **78**, 1 (2001).
[38] T. Kibedi and R.H. Spear, At. Data and Nucl. Data Tables **80**, 35 (2002).
[39] T. Kubo, H. Sakamoto, T. Kammuri, and T. Kishimoto, Phys. Rev. C **54**, 2331 (1996).
[40] A.M. Bernstein, V.R. Brown, and V.A. Madsen, Comments Nucl. Part. Phys., **11**, 203 (1983).
[41] M.A. Kennedy, P.D. Cottle, and K.W. Kemper, Phys. Rev. C **46**, 1811 (1992).
[42] J.K. Jewell *et al.*, Phys. Lett. B **454**, 181 (1999).
[43] E. Khan *et al.*, Nucl. Phys. A **694**, 103 (2001).
[44] S.S. Dietrich and B.L.Berman, At. Data and Nucl. Data Tables **38**, 199 (1988).
[45] A. Van der Woude, Prog. in Part. and Nucl. Phys. **18**, 217 (1987).
[46] Y. Fujita *et al.*, Phys. Rev. C **32**, 425 (1985).
[47] H.P. Morsch *et al.*, Phys. Rev. Lett. **45**, 337 (1980); Phys. Rev. C **22**, 489 (1980).
[48] T.Yamagata *et al.*, Phys. Rev. C **23**, 937 (1981).

Fragment Correlations in Breakup Reactions of Two-neutron Halo Nuclei

S.N. Ershov*

Joint Institute for Nuclear Research, Dubna 141980, Russia

One of the most interesting questions in the physics of radioactive beams is that of the structure of halo nuclei at the limits of nuclear existence. In Borromean two-neutron halo nuclei the nature of the three-body continuum is currently most intriguing. The concentration of transition strength, experimentally observed in these nuclei at low excitation energy, may contain three-body resonances or new kinds of collective motion, such as a soft dipole mode corresponding to oscillations of the core against the halo neutrons. The continuum is usually explored via responses induced by transitions from the ground state to the continuum. A viable way to study the continuum properties is to explore nuclear reactions under conditions where one-step transitions dominate. This is still a rather comprehensive task, because of the intertwining of the ground state and continuum structures, influenced by reaction mechanisms. In kinematically complete experiments, in parallel to the excitation spectrum, we can study many different angular and energy correlations between fragments. Thus continuum spectroscopy implies a consistent analysis of a variety of exclusive and inclusive cross sections accessible in kinematically complete experiments. Fragment correlations of two-neutron halo nuclei in breakup reactions induced by collisions with electrons and heavy ions are discussed and compared with experimental data where it is possible.

I. INTRODUCTION

One of the most interesting questions in the physics of radioactive beams is that of the structure of nuclei at the limits of nuclear existence, where a new type of nuclear structure, halo, has been found in some light nuclei [1]. Peculiarities of halos are revealed in the specific structure of the ground state (loosely bound, abnormal spatial extension with extreme clusterization) as well as in low-energy excitations above the breakup threshold where concentration of transition strength is observed. The nature and properties of the three-body continuum for two-neutron halo nuclei is currently a most intriguing question.

The breakup into three fragments is richer and also more complicated compared with the breakup into two fragments. The nuclear excitation energy fixes only the total phase volume accessible for the fragments. Kinetic energies for fragments have continuous distributions within this volume. In addition, two (Jacobi) relative orbital angular momenta characterize their motion. The specific structure of the continuum defines the accessible excitation modes. Finally, continuum excitations and the structure of the ground state are tightly interwined by reaction mechanisms.

The experimental study of three-body correlations of halo fragments in breakup reactions demands kinematically complete measurements when three particles, halo neutrons and core, are detected in coincidence [2]. Then it is possible to reconstruct the spectrum of the halo nucleus and select events that correspond to low-energy excitations. For fixed excitation energy, the three fragments can still move relative to each other in a variety of ways. Thus in parallel to the excitation spectrum we can study many different angular and energy correlations between fragments. They are sensitive to different aspects of reaction dynamics. Thus con-

*Electronic address: ershov@theor.jinr.ru

tinuum spectroscopy implies a consistent analysis of a variety of exclusive and inclusive cross sections accessible in kinematically complete experiments. The theoretical analysis of such reactions involves the strong nucleon-nucleon interactions. The strength and complicated character of strong interactions bring ambiguities in disentangling the reaction mechanism and nuclear structure. In spite of a considerable amount of nuclear structure information on halo nuclei extracted from collisions with other nuclei, cleaner ways for a study of their structures, like electron scattering, are greatly needed. Electron scattering is one of the most powerful and proven methods for nuclear structure investigations. At the present moment there is no ready installation for performing electron scattering experiments on unstable nuclei. Electron-nucleus collider experiments are however planned for the future installations at RIKEN and GSI.

In this work we present a theoretical analysis concerning energy and angular correlations between fragments of ^{6}He obtained from breakup reactions induced by collisions with electrons and heavy ions. The structure of the ground state and continuum excitations of ^{6}He is calculated in a three-body model [3–6] using the method of hyperspherical harmonics. The reaction mechanisms are described within the microscopic four-body distorted wave theory [7–14] which has been successfully developed and used for the description of different reactions with two-neutron halo nuclei.

II. BREAKUP REACTIONS OF HALO NUCLEI

A. Breakup reaction mechanism

Fragmentation reactions have complicated dynamics where nuclear structure and reaction mechanism are tightly intertwined. Our discussion will be confined by dissociation reactions with undestroyed core leading to the low-energy halo excitations. The cross section of the elastic breakup $a + A \to 1 + 2 + C + A$, involving collision of projectile a (two-neutron halo nucleus breaking into three fragments 1, 2 and C) with target A, is given by [15]

$$\sigma = \frac{(2\pi)^4}{\hbar v_i} \sum_\alpha \int \mathrm{d}\boldsymbol{k}_1 \, \mathrm{d}\boldsymbol{k}_2 \, \mathrm{d}\boldsymbol{k}_C \, \mathrm{d}\boldsymbol{k}_A \; \delta(E_i - E_f) \; \delta(\boldsymbol{P}_i - \boldsymbol{P}_f) \; |T_{fi}|^2 \tag{1}$$

where v_i is the relative velocity of the colliding systems in the initial channel, $\boldsymbol{k}_i$, $i = 1, 2, C$, are the wave numbers of the neutrons and the core, and $\boldsymbol{k}_A$ is the target wave number in the final channel. The sum over α is over all quantum numbers which are necessary to characterize the reaction and includes, if particles have spin, the averaging of the initial spin projections and the sum over the final spin projections. The exact transition matrix T_{fi} can be written as

$$T_{fi} = \langle \Psi_\alpha^{(-)}(\boldsymbol{k}_x, \boldsymbol{k}_y, \boldsymbol{k}_f) \; | \sum_{p,t} V_{pt} - U_{aA} | \; \Psi_0, \; \Phi_A, \; \chi_i^{(+)}(\boldsymbol{k}_i) \rangle \tag{2}$$

where $\Psi_\alpha^{(-)}$ is the full scattering solution with ingoing wave boundary condition and Ψ_0 and Φ_A are ground state wave functions of the halo and the target, respectively. The distorted wave $\chi_i^{(+)}$ describing the relative motion of nuclei in the initial channel is a solution of the Schrödinger equation with optical potential U_{aA}. V_{pt} is NN interaction between the projectile and target nucleons. Due to the translational invariance only relative wave numbers can characterize reaction dynamics; $\boldsymbol{k}_x$, $\boldsymbol{k}_y$, and $\boldsymbol{k}_{i,f}$ are the relative wave numbers between a pair of fragments, between the center of mass of a pair and the third fragment, and between the center of masses of halo and target nuclei in the initial and final channels, respectively. In the halo rest frame, $\hbar\boldsymbol{k}_y$ corresponds to the momentum of the third fragment.

The exact T-matrix (2) can not be calculated without approximations. Since our main goal is the study of the halo structure, the reaction is considered at conditions that allow a simplified treatment of the reaction mechanism making it both tractable and transparent. Hence, we study the collisions at high enough energies (large momenta $\hbar\boldsymbol{k}_i$ and $\hbar\boldsymbol{k}_f$) leading to low-energy halo excitations where one-step processes are dominant. The low-energy halo excitations correspond to small values of the relative momenta $\hbar\boldsymbol{k}_x$ and $\hbar\boldsymbol{k}_y$. Therefore the halo fragments spend some time together and interact between themselves. There is no spectators and all fragments are participants. At such conditions a distorted wave treatment of reaction dynamics can be used and the exact scattering wave function $\Psi_\alpha^{(-)}(\boldsymbol{k}_x, \boldsymbol{k}_y, \boldsymbol{k}_f)$ can be written as a product of the wave function of the projectile, target, and of their relative motion. Then the reaction amplitude (2) reduces to

$$T_{fi} = \langle \chi_f^{(-)}(\boldsymbol{k}_f),\ \Phi_A,\ \Psi^{(-)}(\boldsymbol{k}_x, \boldsymbol{k}_y)\ |\sum_{p,t} V_{pt}|\ \Psi_0,\ \Phi_A,\ \chi_i^{(+)}(\boldsymbol{k}_i)\rangle \tag{3}$$

where $\chi_f^{(-)}(\boldsymbol{k}_f)$ is the distorted wave describing the relative motion of nuclei in the final channel, $\Psi^{(-)}(\boldsymbol{k}_x, \boldsymbol{k}_y)$ is the halo three-body continuum wave function. In calculating $\Psi^{(-)}(\boldsymbol{k}_x, \boldsymbol{k}_y)$ all fragment pairwise interactions should be taken into account, i.e. final state interactions should be fully included. The term with optical potential U_{aA} does not contribute to the T-matrix (3) due to the orthogonality between the halo bound state Ψ_0 and the continuum $\Psi^{(-)}(\boldsymbol{k}_x, \boldsymbol{k}_y)$ wave functions. This low-energy region of nuclear excitations is the most sensitive to the three-body correlations and consequently it is the most interesting in halo structure studies. Such investigations, however, require a special selection of experimental data. This can be achieved by performing kinematically complete experiments in which the energies and momenta of all halo fragments are measured in coincidence. Then it is possible to describe the energy spectrum of the halo nucleus and select only events which correspond to low-energy excitations. At the same time, a variety of different energy and angular correlations become available and thus the possibility to describe them within the same model is a thorough test to our understanding of nuclear structure and reaction dynamics. The reaction model based on approximation (3) was successfully applied for the description of many reactions with halo nuclei [7–14].

B. Electron scattering

Electron scattering is one of the most powerful methods for nuclear structure investigations. The electromagnetic interactions of electron with nuclear charges and currents, unlike the strong interaction between nucleons, are well known and weak. Thus the reaction mechanism can be disentangled, in principle, from the nuclear structure effects. The ultrarelativistic electrons are used in the study of nuclear structure. Since the charge of halo nuclei is small, multiple scattering effects can safely be neglected and the interactions can be well described by one-photon exchange terms [16]. Then the initial and final electron states are known and described by the plane wave Dirac spinors. For small energy and momentum transfers, considered here, the contributions from convection and magnetization currents can be neglected in comparison with the Coulomb interaction. If $\varepsilon_{i,f}$ and $\hbar\boldsymbol{k}_{i,f}$ denote an electron energy and momentum, the exclusive cross section of electron scattering, leading to the low-energy halo excitations, can be written [13] as

$$\frac{\mathrm{d}^8\sigma}{\mathrm{d}\hat{\mathbf{k}}_f\,\mathrm{d}\hat{\mathbf{k}}_x\,\mathrm{d}\hat{\mathbf{k}}_y\,\mathrm{d}\varepsilon_x\,\mathrm{d}\varepsilon_y} = f_R\ \sigma_M\ 2\left(\frac{\mu_x\mu_y}{\hbar^4}\right)^{3/2}\sqrt{\varepsilon_x\varepsilon_y}\ \frac{Q^4}{|\mathbf{q}|^4}\ W_{00} \tag{4}$$

where f_R is a recoil factor, σ_M is the Mott cross section which describe the electron scattering on a point-like nucleus, $\boldsymbol{q} = \boldsymbol{k}_i - \boldsymbol{k}_f$ is the three-dimensional momentum transfer, and $Q =$

$((\varepsilon_i - \varepsilon_f)/(\hbar c), \boldsymbol{q})$ is the Lorentz-invariant four-momentum transfer. The factor $\sqrt{\varepsilon_x \varepsilon_y}$ is the phase space accessible to decay into fragments. The nuclear structure function W_{00} is given by

$$W_{00} = \sum \; |\langle \Psi^{(-)}(\boldsymbol{k}_x, \boldsymbol{k}_y) \mid \hat{\rho}(\boldsymbol{q}) \mid \Psi_0 \rangle|^2 \tag{5}$$

where $\hat{\rho}(\boldsymbol{q})$ is the charge operator. The sum in hadron tensor (5) assume the averaging on spin projections of the halo nucleus and the summing over spin projections of halo fragments. The explicit expression of the nuclear structure function can be found in [13]. The function W_{00} contains all information about the nuclear structure, energy, and angular correlations of the fragments.

At the present moment there is no ready installations for performing the electron scattering experiments with unstable nuclei. But due to the new developments for intense beams of radioactive isotopes, electron-nucleus collider experiments become feasible in future on the new installations in RIKEN and GSI. The first measurements will be done for the processes with the largest cross sections: elastic and inclusive inelastic electron scattering. Detecting electrons means that we know the momentum $\mathbf{q}$ transferred to the halo nucleus and the excitation energy. If, in addition, the core momentum $\mathbf{k}_C$ is measured, we also know the relative momentum $\mathbf{k}_y$ and the absolute value $|\mathbf{k}_x|$. The corresponding cross section is obtained by integration (4) over the unobserved direction $\hat{\mathbf{k}}_x$. This integration destroys the angular correlation of the $\mathbf{k}_x$-motion. The obtained cross section depends on the angle between the transferred momentum $\hat{\mathbf{q}}$ and the direction $\hat{\mathbf{k}}_y$ of the core fragment decay.

C. Basic dynamics of halo nuclei

The basic dynamics of halo nuclei can be characterized [3] as a coexistence of two subsystems: one which consists of core nucleons and the other of halo neutrons moving relative the core center of mass. Some arguments [17] support such a decoupling of core and halo degrees of freedom: i) Wave function components that correspond to partition into breakup fragments must dominate in the ground state of a weakly bound system. ii) The interaction cross section of high-energy halo nuclei on light targets, which is approximately equal to the sum of interaction cross section of core nucleus and two-neutron removal cross section, indicates that the reaction process take place separately on the core and halo subsystems. iii) The core nucleus and halo nucleus both have similar magnetic dipole and quadrupole moments. These arguments back up the assumption that the core is not significantly perturbed by the valence neutrons located far away from it. Thus with good accuracy the wave functions Ψ of the two-neutron halo nucleus can be written as a product of two functions

$$\Psi(\mathbf{r}_1, \ldots, \mathbf{r}_A) \;=\; \varphi_c(\boldsymbol{\xi}_1, \ldots, \boldsymbol{\xi}_{A_c}) \; \psi(\mathbf{x}, \; \mathbf{y}) \tag{6}$$

The function $\varphi_c(\boldsymbol{\xi}_1, \ldots, \boldsymbol{\xi}_{A_c})$ describes the internal structure of the core while $\psi(\mathbf{x}, \; \mathbf{y})$ describe the relative motion of halo neutrons around the core c.m. In (6) the coordinate $\boldsymbol{\xi}_j$ denotes the position of a core nucleon relative the core c.m., $\mathbf{x}$ is the relative distance between halo neutrons and $\mathbf{y}$ is the distance between the core and the center of mass of the two halo neutrons. Neglect of explicit considerations for internal core degrees of freedom is the main approximation in (6). These effects are treated approximately through the effective nucleon-core interaction. Such factorization is a starting point for application of three-body models to the description of the halo structure [3–5]. Few-body models avoid the complicated and still partly open questions concerning the development of nuclear clustering, and instead calculate halo wave functions $\psi(\mathbf{x}, \; \mathbf{y})$ directly. Within such models extended for an approximate treatment of the Pauli

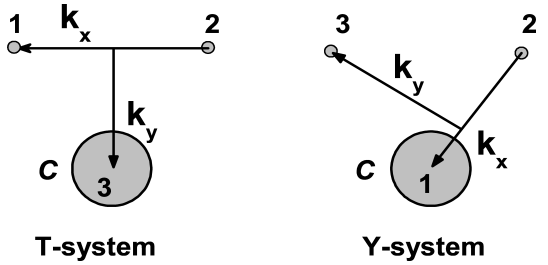

FIG. 1: The **T** and **Y** Jacobi coordinate systems for two-neutron halo nucleus.

principle, it is possible to give a consistent description of the main properties of both the ground state and the low-energy continuum wave functions of halo nuclei.

To characterize the relative motion of the three fragments we need two relative Jacobi momenta: $\hbar\mathbf{k}_x$ between two constituents and $\hbar\mathbf{k}_y$ between the third constituent and the center of mass of the first pair. Since two of the three (constituents) are identical neutrons, there exists only two different Jacobi coordinate systems, shown in Fig. 1. One, labeled **T** ('cluster' representation), corresponds to the case when 1 and 2 are neutrons with relative momentum $\hbar\mathbf{k}_x$, while particle 3 is the core C. In the second case called **Y** ('shell-model' representation), the relative momentum $\hbar\mathbf{k}_x$ is defined by the core C with index 1 and a neutron with index 2, while the other neutron has index 3. The excitation energy E_κ of the halo nucleus above threshold is equal to the sum of kinetic energies for the fragments' relative motion, $E_\kappa = \varepsilon_x + \varepsilon_y = (\hbar^2/2)(\mathbf{k}_x^2/\mu_x + \mathbf{k}_y^2/\mu_y)$. The energy E_κ and the three-body phase space $\sqrt{\varepsilon_x\varepsilon_y}\,\mathrm{d}\varepsilon_x\,\mathrm{d}\varepsilon_y$ are invariant, i.e. independent of Jacobi system. For future reference we also introduce the variable $\epsilon = \varepsilon_x/E_\kappa$ (ε_y/E_κ = 1 - ϵ) which describes the share of the relative kinetic energy residing within a pair of particles (or the third particle and the center mass of the pair), at energy E_κ.

Relative momenta of fragments and neutron spin projections $\nu_{1,2}$ on a quantization axis (we assume for simplicity that the spin of the core is zero) are used to characterize uniquely the final continuum state $\Psi \equiv \Psi^{(\pm)}_{\nu_1,\nu_2}(\mathbf{k}_x, \mathbf{k}_y; \mathbf{r}_1, \ldots \mathbf{r}_A)$, while the initial nuclear total angular momentum J_i and its projection M_i are sufficient for the ground state identification, $\Psi \equiv \Psi_{J_iM_i}(\mathbf{r}_1, \ldots \mathbf{r}_A)$. A three-body continuum wave function $\Psi^{(+)}_{\nu_1\nu_2}(\mathbf{k}_x, \mathbf{k}_y)$ has the following decomposition within the method of hyperspherical harmonics [11]

$$\Psi^{(+)}_{\nu_1\nu_2} = \sum_{\alpha\mu\nu M} (\frac{1}{2}\nu_1\ \frac{1}{2}\nu_2 \mid S\nu)\ (L\mu\ S\nu \mid JM)\ \imath^K\ \psi_K^{l_xl_y}(\epsilon)\ [Y_{l_x}(\mathbf{k}_x) \otimes Y_{l_y}(\mathbf{k}_y)]^*_{L\mu}\ \Psi^{\beta LS}_{JM}(E_\kappa, \mathbf{r}_i) \tag{7}$$

In the decomposition (7) $\alpha = \{J, L, S \text{ and } \beta\}$, $\beta = \{l_x, l_y, K\}$ are abbreviations for sets of quantum numbers. Here, J, L, and S describe the total angular momentum, the total orbital angular momentum, and total spin in the final continuum state of the halo nucleus, respectively, while l_x and l_y denote the orbital angular momenta corresponding to the $\mathbf{k}_x$ and $\mathbf{k}_y$ linear momenta, and K is the hypermoment, $K = l_x + l_y + 2n$, ($n = 0, 1, \ldots$). The quantum numbers (J, S, L, l_x, l_y, K) describe all possible elementary modes of the relative motion in the three-body continuum state of the halo nucleus. $\psi_K^{l_xl_y}(\epsilon)$ is the hyperangular part of the hyperharmonic [3, 5, 14],

$$\psi_K^{l_xl_y}(\epsilon) = \sqrt{\epsilon^{l_x}(1-\epsilon)^{l_y}}\ M_n^{l_xl_y}(\epsilon), \qquad M_n^{l_xl_y}(\epsilon) = N_n^{l_xl_y}\ P_n^{(l_x+1/2, l_y+1/2)}(1-2\epsilon) \tag{8}$$

where $M_n^{l_x l_y}(\epsilon)$ is simply the product of the normalization coefficient $N_n^{l_x l_y}$ of a hyperharmonic (8) and the Jacobi polynomial $P_n^{(\sigma,\tau)}$ of order n. Sometimes we will use $n = (K - l_x - l_y)/2$ as summation index instead of K. The function $\Psi_{JM}^{\beta LS}(E_\kappa, \mathbf{r}_i)$ is the coordinate part of wave function $\Psi_{\nu_1\nu_2}^{(+)}$ at continuum energy E_κ, and depends on the quantum numbers (β, L, S, J), projection M of the total angular momentum, and the translation invariant space coordinates $\mathbf{r}_i$ of the nucleons in halo nucleus a,

$$\begin{aligned}\Psi_{JM}^{\beta LS}(E_\kappa, \mathbf{r}_i) \;&=\; \frac{1}{(\kappa\rho)^{5/2}} \sum_{\gamma'} \chi_{\gamma,\gamma'}^{J}(\kappa,\rho)\; \psi_{K'}^{l'_x,l'_y}(\sin^2\theta_\rho)\; [Y_{l'_x}(\hat{\mathbf{x}}) \otimes Y_{l'_y}(\hat{\mathbf{y}})]_{L'M_{L'}} \\ &\times\; (L'M_{L'}S'M_{S'}|JM)\; |\chi_{S'M_{S'}}\rangle\; \varphi_c(\boldsymbol{\xi}_1, \ldots, \boldsymbol{\xi}_{A_c}) \end{aligned} \tag{9}$$

where

$$\tan\theta_\rho = \frac{\sqrt{\mu_x}\,|\mathbf{x}|}{\sqrt{\mu_y}\,|\mathbf{y}|}, \qquad \text{and} \qquad \rho = \sqrt{\frac{\mu_x|\mathbf{x}|^2 + \mu_y|\mathbf{y}|^2}{m_n}}$$

and where $|\chi_{S'M_{S'}}\rangle$ is a coupled spin function for the two halo neutrons. The hyperradial wave function $\chi_{\gamma,\gamma'}^{J}(\kappa,\rho)$ is a solution of a set of the coupled K-harmonic equations. The ground state wave function $\psi_{J_iM_i}(\mathbf{x},\mathbf{y})$ has a similar decomposition (9) to $\psi_{\gamma,JM}(\kappa,\mathbf{x},\mathbf{y})$ but now with $\kappa = \sqrt{2m_n|E_B|/\hbar^2}$, with separation energy $|E_B|$. The necessary details on how to solve a system of K-harmonic equations and on how to choose the nucleon-nucleon and nucleon-core potentials of the three-body bound and continuum wave functions of the ^{6}He can be found in [5].

III. RESULTS

A. Breakup of halo nuclei in collisions with electrons

As an example of electron scattering, we consider the collision with ^{6}He at an initial energy $\varepsilon_i = 500\,\text{MeV}$ which will become available at GSI. Fig. 2 shows the calculated inclusive spectra of low-energy excitations for a few electron scattering angles θ corresponding to transferred momenta $|\mathbf{q}| < 80$ (MeV/c). The absolute cross sections depend strongly on the momentum transfer $|\mathbf{q}|$ and decrease rapidly with increasing electron scattering angle θ. The multipole composition of the excitation spectra depends on the properties of the Coulomb interaction and the nuclear structure. In the multipole decomposition of the Coulomb interaction the monopole term decreases most slowly with the distance between electron and the nuclear center of mass, then follow terms with higher angular momenta, dipole, quadrupole and so on. At small momentum transfer the reaction amplitude obtains its main contribution from large distances where, however, the monopole excitations are strongly suppressed by the orthogonality of the ground and continuum halo states. As a result the dipole excitations dominate at low excitation energies for small $|\mathbf{q}|$ (see Fig. 2a). The modes which give the main contributions to excitations, with hypermoments $K = 1$ and 3, are shown by the dashed and dot-dashed lines in Fig. 2a. In Fig. 2(b,c) the solid, dashed, dot-dashed, and thin solid lines are the total, dipole, quadrupole, and monopole excitations of ^{6}He, respectively. With increasing momentum transfer the well-known three-body 2^+ resonance at $E^* = 1.8$ MeV appears (Fig. 2b) and soon becomes a pronounced feature (Fig. 2c) in the low-energy spectrum. The concentration of the dipole transition strength near threshold does not mean that dipole excitations have a collective nature and represent a resonance. As seen from Figs. 2a-c, the energy position and the shape of the dipole excitations show a strong dependence on transferred momentum while for a genuine three-body resonance, like the 2^+ at $E^* = 1.8$ MeV, the peak position is fixed. To further clarify

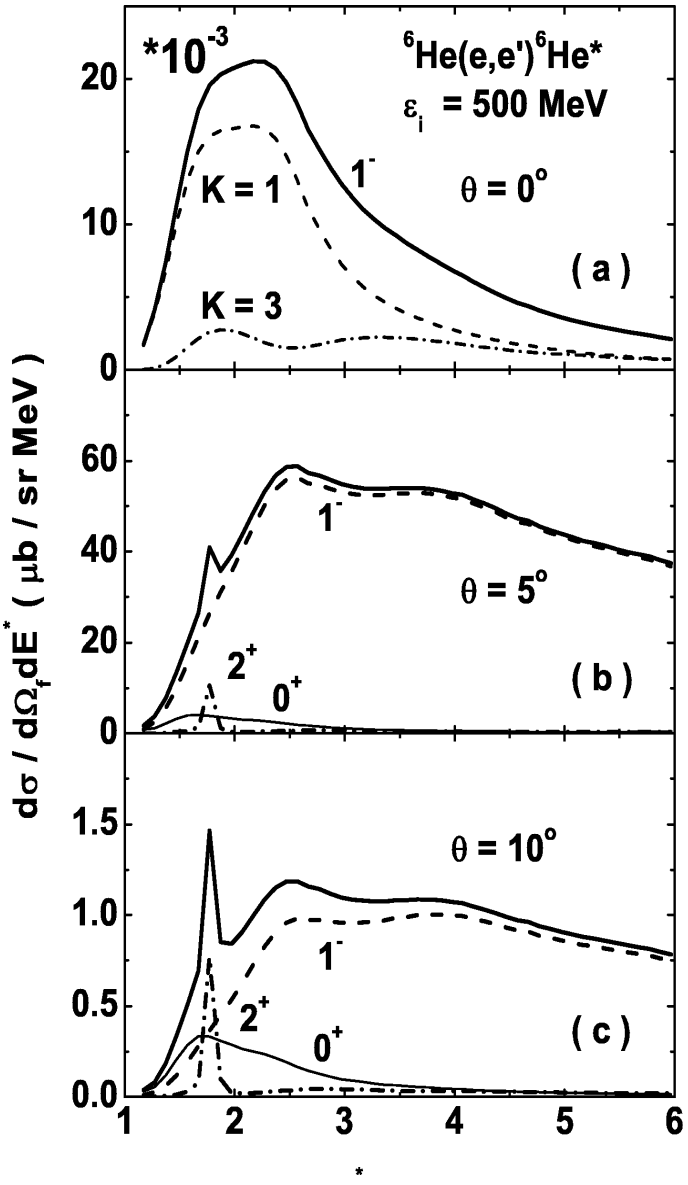

FIG. 2: Inclusive inelastic electron scattering on ^{6}He for $\varepsilon_i = 500$ MeV and various scattering angles. (a): The solid line is the total (dipole) cross section. The dashed and dot-dashed lines are contributions to the dipole excitation from modes with orbital momenta $l_x = 0$, $l_y = 1$, spin S =0, and hypermoments $K = 1$ and 3, respectively. (b) and (c): The solid, dashed, dot-dashed and thin solid lines are the total, dipole, quadrupole, and monopole cross sections, respectively.

the true nature of the observed 1^- peak, more complicated energy correlations of the fragments must be studied. We now turn to breakup cross sections where the α-particle is detected in coincidence with the scattered electron. Then the energy and angle of the α-particle characterize the cross section in addition to the electron degrees of freedom. Since we consider processes with small momentum and energy transfers for which the Coulomb interaction dominates, the coincidence cross section does not depend on the orientation of the ejectile plane relative to the scattering plane. The reaction dynamics, in addition to the electron variables, depends on the relative angle between the momenta $\hbar\mathbf{k}_y$ and $\hbar\mathbf{q}$, and the α-particle energy. To further reduce the number of independent variables, we consider distributions over the relative energy $E_{\alpha-(nn)}$

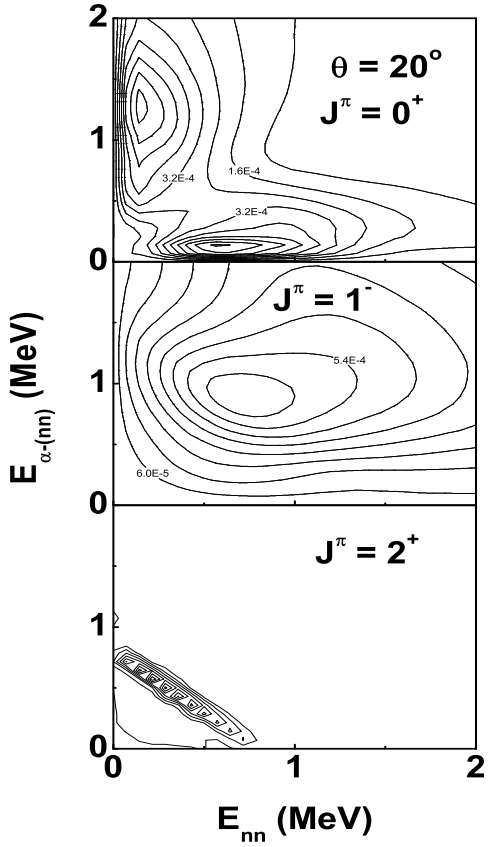

FIG. 3: Contour plots of electron cross sections for separate multipole excitations for scattering angle θ = 20° as function of the relative energy between the two halo neutrons E_{nn} and their energy relative the α-particle $E_{\alpha-(nn)}$.

($= \varepsilon_y$) between the α-particle and the c.m. of the halo neutron pair, $\mathrm{d}^3\sigma/\,\mathrm{d}\Omega_f\,\mathrm{d}E_{\alpha-(nn)}$, which is obtained by integrating the exclusive cross sections over the α-particle direction $\hat{\mathbf{k}}_y$ and over the total nuclear excitation energy E^* from the breakup threshold up to 6 MeV. To better demonstrate the decay properties of multipole excitations, we show in Fig. 3 contour plots of cross sections for separate multipolarities as a function of the relative energies E_{nn} ($= \varepsilon_x$) and $E_{\alpha-(nn)}$. The decay patterns of the energy correlations are distinctly different for the different multipole excitations. For the quadrupole case the decays are stretched along a straight line which is a clear signal of resonance behavior (see [12] and relevant discussions there). Monopole correlations reveal two peaks: One where the α particle is at rest and the two neutrons carry all excitation energy, and the other where the two neutrons have small relative energy and the excitation energy is defined by the relative motion between the α and the neutron pair. This picture keeps an imprint of the "cigar" and "dineutron" configurations in the ground state structure of ^{6}He [3].

Next we consider the angular correlations in coincidence cross sections $\mathrm{d}^5\sigma/\,\mathrm{d}\Omega_f\,\mathrm{d}\Omega_y dE^*$ as function of the angle $\theta_{\alpha q}$ between the α-particle and the transferred momentum $\mathbf{q}$. Fig. 4 shows examples of the $\theta_{\alpha q}$ angular correlations for two different excitation energies in ^{6}He: The 2^+ resonance is largest in part (a) and the dipole excitation dominates in (b). The shapes of the distributions are different for different multipolarities, and symmetric relative 90°. The monopole

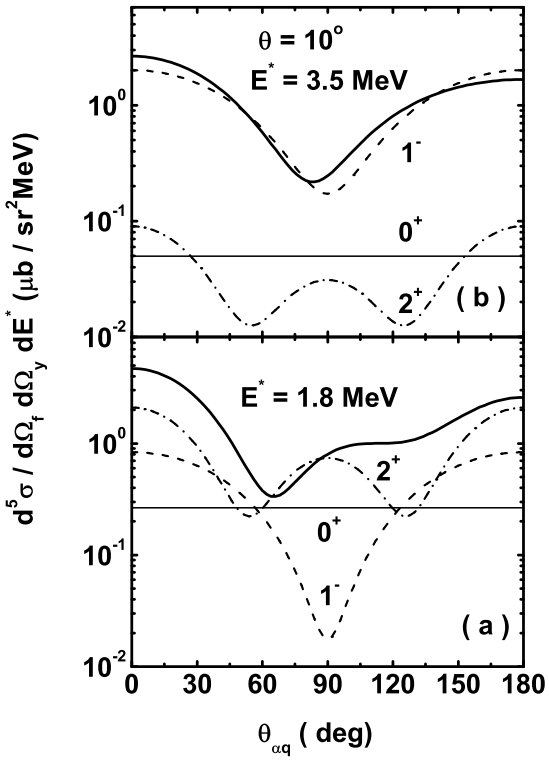

FIG. 4: Cross sections $\mathrm{d}^5\sigma/\,\mathrm{d}\Omega_f\,\mathrm{d}\Omega_y\,\mathrm{d}E^*$ for electrons with energy $\varepsilon_i = 500\,\mathrm{MeV}$ and scattering angle $\theta = 10^\circ$ as function of the relative angle $\theta_{\alpha q}$ between α-particle and transferred momentum $\mathbf{q}$. Parts (a) and (b) correspond to 1.8 MeV and 3.5 MeV excitation energies in ^{6}He, respectively. The solid, dashed, dot-dashed, and thin solid lines are the total, dipole, quadrupole, and monopole contributions.

has an isotropic distribution. The dipole has a pronounced minimum at 90° while the quadrupole has two minima near 60° and 120° and maximum at 90° with height a few times less then at 0° or 180°. The total distribution includes contributions not only from separate multipole excitations but also their interference. As a result, the total distribution is not symmetrical relative 90° and can have a rather complicated shape as, for example, in Fig. 4(a) where dipole and quadrupole are excited with comparable strength. In cases when one multipole excitation dominates as, for example, in Fig. 4(b), the total distribution keeps a shape which is specific for the single multipole and only slightly distorted. Thus it can give a clear signal on the multipole nature of dominant nuclear excitations.

B. Breakup of halo nuclei in collisions with heavy ions

The *exclusive* breakup cross section (i.e. when energies and momenta of all fragments are observed), averaged over initial and summed over final spin projections, depends on eight independent variables and can be calculated within the four-body microscopic distorted wave model [11]. This cross section contains the most complete information that can be extracted from a reaction between unpolarized nuclei. At present time there are no experimental data to compare with. Also, this cross section depends on too many variables to offer a meaningful analysis of the important correlations. More instructive is to integrate out most of the independent variables

and analyze various *semi-inclusive* cross sections that can be compared with experiment, and thus clarify the underlying dynamics.

Recently, experimental data on different angular and energy correlations of the three fragments from breakup of ^{6}He on lead target at collision energy 240 MeV/nucleon, obtained at GSI, have been published [18]. They reveal a very interesting picture. The *low-energy spectrum* of ^{6}He shows a smooth behavior [19], while with increasing excitation energy, the shape of some *correlations* changes dramatically along the spectrum. To be in compliance with the published experimental data, we will consider at most triple differential cross sections and will keep $\mathbf{k}_x$ and $\mathbf{k}_y$ as independent variables. The vectors $\mathbf{k}_x$ and $\mathbf{k}_y$, describing the relative motion of halo fragments, lie in a plane. Only the angle between $\mathbf{k}_x$ and $\mathbf{k}_y$, ($\cos\theta = (\hat{\mathbf{k}}_x \cdot \hat{\mathbf{k}}_y)$), has a physical meaning. The orientation of the plane does not play any role and can be integrated out. Thus we can write the triple cross section in the following way [11]

$$\frac{\mathrm{d}^3\sigma}{\mathrm{d}\cos\theta\ \mathrm{d}\epsilon\ \mathrm{d}E_\kappa} = \sqrt{\epsilon\ (1-\epsilon)}\ \sum_\lambda\ P_\lambda(\cos\theta)\ \frac{1}{2}\ \sum_{L\beta\beta'} \psi_K^{l_x l_y}(\epsilon)\ \psi_{K'}^{l'_x l'_y}(\epsilon)$$
$$\times\ \imath^{(K'-K)}\ C_{l'_x l'_y L}^{l_x l_y \lambda}\ \sum_\delta\ A_{\delta\, n}^{l_x l_y L}(E_\kappa)\ A_{\delta\, n'}^{l'_x l'_y L}(E_\kappa)^* \qquad (10)$$

where the coefficients $C_{l'_x l'_y L}^{l_x l_y \lambda}$ are defined by

$$C_{l'_x l'_y L}^{l_x l_y \lambda} = (-1)^{\lambda+L}\ \hat{l}_x \hat{l}_y \hat{l}'_x \hat{l}'_y \begin{Bmatrix} l_x & l'_x & \lambda \\ l'_y & l_y & L \end{Bmatrix} (l_x 0\ l'_x 0 \mid \lambda 0)\ (l_y 0\ l'_y 0 \mid \lambda 0) \qquad (11)$$

and $\hat{l}_i = \sqrt{2l_i+1}$. In (10) $\delta = \{J, S, \gamma\}$ is a shorthand notation for a set of quantum numbers, while γ denotes some additional quantum numbers defined by the reaction mechanism [11]. The reaction amplitude $A_{\delta\, n}^{l_x l_y L}(E_\kappa)$ which contains all reaction dynamics, depends only on the continuum energy E_κ and is proportional to the matrix element that includes integration over all space coordinates. The function $\Psi_{JM}^{\beta LS}(E_\kappa, \mathbf{r}_i)$ in expression (7) enters this matrix element for the reaction amplitude. The magnitude of $A_{\delta\, n}^{l_x l_y L}(E_\kappa)$, describing the strength of different elementary modes for fragment motions, is defined by the reaction mechanism that couples the wave functions of the ground and excited states of the halo nucleus. Only elementary modes defined by quantum numbers l_x, l_y and K give coherent contributions to the cross section (10), while all other are added independently. The derivation of cross section (10) and the explicit expressions for the nuclear amplitude can be found in [11, 14].

The cross section that includes only energy correlations in the relative motion of fragments can be obtained by integration over angle θ

$$\frac{\mathrm{d}^2\sigma}{\mathrm{d}\epsilon\ \mathrm{d}E_\kappa} = \sqrt{\epsilon\ (1-\epsilon)} \sum_{l_x l_y L}\ \sum_{KK'} \psi_K^{l_x l_y}(\epsilon)\ \psi_{K'}^{l_x l_y}(\epsilon)\ (-1)^{(n'-n)}\ \sum_\delta A_{\delta\, n}^{l_x l_y L}(E_\kappa)\ A_{\delta\, n'}^{l_x l_y L}(E_\kappa)^* \qquad (12)$$

Angular averaging destroys correlations in l_x and l_y motions and keeps coherent contributions only in the hypermoment K. Note that, as a rule, at low excitation energy the largest components of the halo continuum wave function have $n = 0$. Only for monopole excitations the component with the lowest possible value $K = l_x = l_y = 0$ is suppressed due to the Pauli principle, and $K = 2$ with $n = 1$ dominates. Since the function $M_n^{l_x l_y}(\epsilon)$ (i.e. the Jacobi polynomial) for $n = 0$ is a constant, we may expect that the dominant energy dependence near threshold is defined by the mixture of factors $\epsilon^{l_x}\ (1-\epsilon)^{l_y}$ weighted with the probability of these excitations. The factor $\sqrt{\epsilon\ (1-\epsilon)}$ describes the phase space accessible for fragment relative motion at fixed

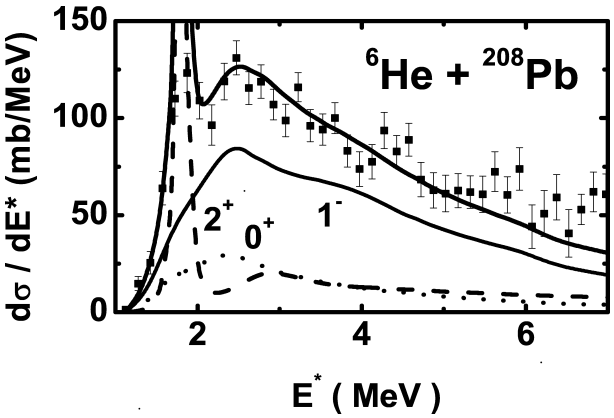

FIG. 5: Comparison of the theoretical ^{6}He excitation spectrum (thick solid line) for ^{6}He + ^{208}Pb breakup at 240 MeV/nucleon with experimental data [19]. The thin solid, dashed and dotted lines show the dipole 1^-, quadrupole 2^+, and monopole 0^+ contributions.

excitation energy, and is *a common factor for all nuclear excitations*. The deviation from phase space distributions is defined by the partial content of continuum excitations, namely what combinations of the l_x and l_y orbital angular momenta dominate. In order to reveal the spectroscopic content more clearly, we remove the important but trivial phase space energy dependence from the energy correlations (12), and rather discuss the double cross section: $\mathrm{d}^2\sigma/\sqrt{\epsilon(1-\epsilon)}\ \mathrm{d}\epsilon\ \mathrm{d}E_\kappa$. This modified cross section, as distinct from (12), is not necessarily equal to zero at $\epsilon = 0$ or 1 and has finite values at these points if the modes with l_x or $l_y = 0$ are excited. If we integrate the triple differential cross section (10) over the energy distribution ϵ, we obtain the fragment angular correlations.

The formulas given above apply to cross section calculations in both coordinate systems, **T** and **Y**. Since the transformation of hyperspherical harmonics in transition from one Jacobi system to another is a simple rotation, the connection between the reaction amplitudes $A^{l_x l_y L}_{\delta K}(E_\kappa)$ in the two systems is unitary and provided by the Raynal-Revai coefficients $\langle l_x^{\mathbf{T}} l_y^{\mathbf{T}} \mid l_x^{\mathbf{Y}} l_y^{\mathbf{Y}} \rangle_{K\,L}$ [20, 21],

$$A^{l_x^{\mathbf{Y}} l_y^{\mathbf{Y}} L}_{\delta K} = \sum_{l_x^{\mathbf{T}} l_y^{\mathbf{T}}} \langle l_x^{\mathbf{T}} l_y^{\mathbf{T}} \mid l_x^{\mathbf{Y}} l_y^{\mathbf{Y}} \rangle_{K\,L}\ A^{l_x^{\mathbf{T}} l_y^{\mathbf{T}} L}_{\delta K} \tag{13}$$

where the **T** or **Y** indices on orbital angular momenta denote the coordinate system where these momenta are defined. Since in the **T** system the permutation of the two halo neutrons only results in reversing the direction of their relative Jacobian **x** coordinate, the three-body wave function has a particular simple symmetry property for this operation. Due to this symmetry the number of allowed wave function components is reduced. Hence amplitudes are initially calculated in the **T** system. For calculations in the **Y** system the amplitudes are obtained using Eq. (13). This means that the angular and energy distributions in one Jacobi system are connected unambiguously to the other and their simultaneous description in both systems is a thorough check on correct knowledge about the partial content, absolute values, and relative phases of amplitudes in continuum excitations.

The experimental excitation spectrum for ^{6}He inelastic scattering in collision with ^{208}Pb at 240 MeV/nucleon has been published in [19]. Our theoretical analysis of these data within the four-body microscopic distorted wave theory was reported in [11]. The reaction amplitude in this model has three ingredients: i) The structure of the target nucleus (matter density) and of the halo system (transition densities). ii) The nucleon-nucleon effective interactions between

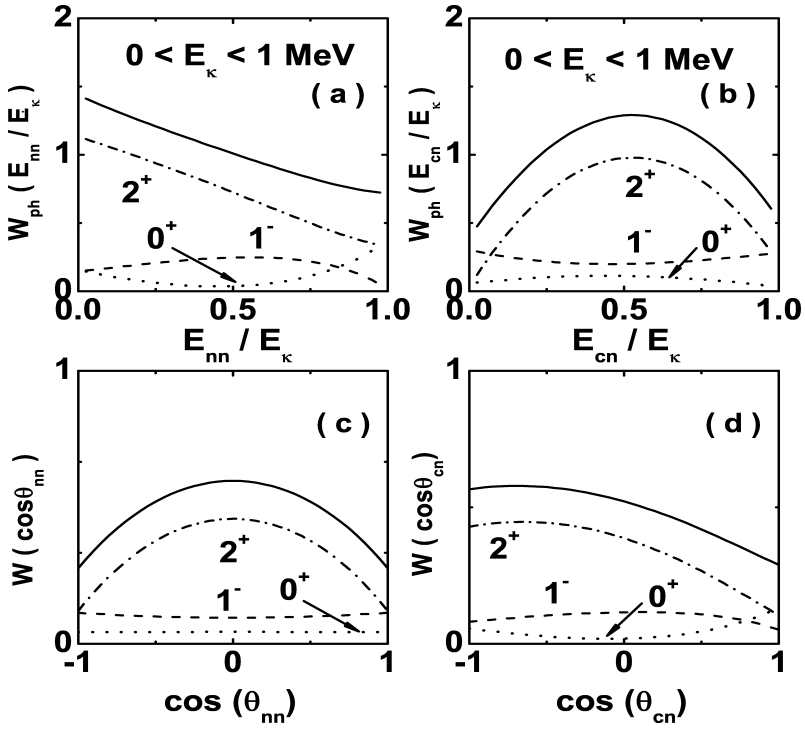

FIG. 6: Energy ((a) and (b)) and angular ((c) and (d)) fragment correlations (solid line) in the ^{6}He+^{208}Pb breakup at 240 MeV/nucleon for excitation energy region $0 < E_\kappa < 1$ MeV. (a) and (c) are shown in Jacobi configuration **T**, (b) and (d) in configuration **Y**. The dashed, dotted, and dash-dotted lines show the dipole 1^-, monopole 0^+, and quadrupole 2^+ contributions, respectively.

projectile and target nucleons. iii) The optical potentials for relative motion of projectile and target nuclei. In the calculations presented below we have used the same parameters as in the Ref. [11].

In Fig. 5 another comparison of the calculated ^{6}He excitation spectrum (thick solid line) with experimental data is given. (Note that E^* is the excitation energy from the ground state and shifted by the separation energy $S_b = 0.97$ MeV relative to the continuum energy E_κ, $E^* = E_\kappa + S_b$.) The thin solid, dashed and dotted lines show the dipole 1^-, quadrupole 2^+, and monopole 0^+ contributions, respectively. The shape of the experimental spectrum shows a peak at the position of the well-known 2^+ resonance at 1.8 MeV, a bump near 3 MeV and subsequently the strength decreases with increasing excitation energy. The calculations reproduce both the shape and absolute value of the inclusive spectrum and display a small monopole contribution. The dipole dominates and the three-body 2^+ resonance at 1.8 MeV is strongly excited.

In a recent experimental analysis of correlation data [18], the excitation spectrum as a function of the energy E_κ has been separated into bins. The obtained experimental distributions were integrated over the finite energy regions of E_κ within these bins and normalized to unity. Accordingly, the same procedure has been used for our theoretical calculations. Four energy regions have been singled out in the ^{6}He excitation spectrum: The first, from $0 < E_\kappa < 1$ MeV, contains the 2^+ resonance, the others cover the energy intervals $1 < E_\kappa < 3$ MeV, $3 < E_\kappa < 6$ MeV and $6 < E_\kappa < 9$ MeV. To increase the sensitivity to the spectroscopic content of the continuum excitations, we calculate the modified energy correlations between fragments (as discussed previously and denoted by W_{ph} in the figures) where the phase space energy factor $\sqrt{\epsilon(1-\epsilon)}$ has been divided out. The experimental data for energy correlations [18] were scaled accordingly.

Fig. 6 shows theoretical calculations of the energy and angular fragment correlations in the

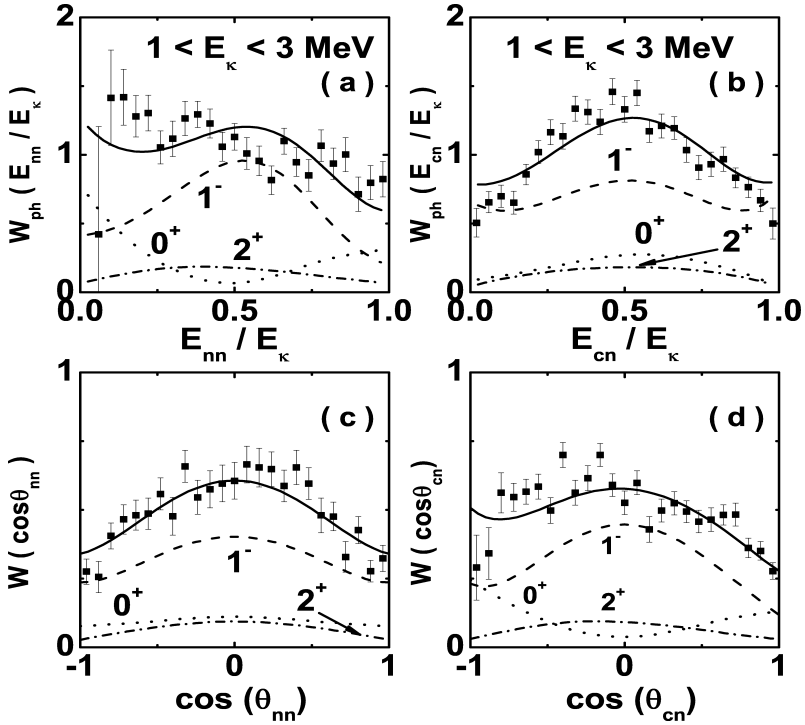

FIG. 7: Energy and angular fragment correlations in ^{6}He $+^{208}$ Pb breakup at 240 MeV/nucleon for excitation energy region $1 < E_\kappa < 3$ MeV. Notations are the same as in Fig. 6.

energy region $0 < E_\kappa < 1$ MeV where the 2^+ resonance dominates the spectrum. Parts (a) and (c) correspond to calculations in the Jacobi coordinate system **T** while (b) and (d) are for **Y**. The dashed, dotted and dashed-dotted lines show contributions from the dipole 1^-, monopole 0^+ and quadrupole 2^+ excitations, respectively. In the **T** system the energy correlation has unsymmetrical shape. At $\epsilon = 0$ and 1 it has nonzero values. This shows unambiguously the presence of excitations with orbital angular momenta $l_x^{\mathbf{T}}$ and $l_y^{\mathbf{T}} = 0$. Since $W_{ph}(0)$ is larger than $W_{ph}(1)$, the total weight of modes with $l_x^{\mathbf{T}} = 0$, $l_y^{\mathbf{T}} > 0$ is bigger than the weights for $l_y^{\mathbf{T}} = 0$ and $l_x^{\mathbf{T}} > 0$. The 2^+ resonance (dash-dotted line) dominates in this energy region.

Fig. 7 compares the theoretical calculations of energy and angular fragment correlations in the energy interval $1 < E_\kappa < 3$ MeV with the experimental data of [18]. Notations are the same as in Fig. 6. Qualitatively the shapes of various correlations in this energy interval are similar to the shapes in the previous one but the partial multipole content is different. From calculations follows that dipole excitations dominate at these energies. The bell shape of the dipole energy correlation in Fig. 7(a) is largely due to excitation of the $l_x^{\mathbf{T}} = 0$, $l_y^{\mathbf{T}} = 1$, and $S = 0$ component with hypermoment $K = 1$ and its interference with the one having $K = 3$. The nonzero value at $\epsilon = 1$ reflects the contribution from the excitation of the $l_x^{\mathbf{T}} = 1$, $l_y^{\mathbf{T}} = 0$, and $S = 1$ elementary mode. In spite of the dipole domination, other multipolarities still play an important role in modifying the shape of total distributions. For example, the monopole excitations are important near $\epsilon = 0$ and 1. Hence, omitting this contribution may lead to significant distortion of an analysis of partial content. Energy correlations in the **Y** system, Fig.7(b), have almost symmetrical shape since due to the Raynal-Revai transformation the strong excitation with $l_x^{\mathbf{Y}} = 1$ and $l_y^{\mathbf{Y}} = 0$ quantum numbers appears in addition to the $l_x^{\mathbf{Y}} = 0$ and $l_y^{\mathbf{Y}} = 1$ mode. Angular correlations in both systems, Figs. 7(c) and (d)), are mainly described by the Legendre polynomial of second order. Comparing with the experimental data of [18] for this energy interval we conclude that the theoretical calculations of angular and energy

correlations describe measurements in both **T** and **Y** systems rather well. It indicates that our model assumptions concerning the reaction mechanism and nuclear structure are correct.

The situation in the next energy bin is, however, more perplexing. Fig. 8 shows comparison of theoretical calculations of energy and angular correlations with the experimental data of [18] for the energy interval $3 < E_\kappa < 6\,\mathrm{MeV}$. The theoretical calculations show that dipole excitations also dominate in this region. In contrast, the relative contribution from different multipolarities has become larger. The calculations describe reasonably well the experimental data for the energy distribution in the **T** system (Fig. 8(a)) and the angular correlations in the **Y** system (Fig. 8(d)). The angular correlation in the **T** system (Fig. 8(c)) and for energy in **Y** (Fig. 8(b)) deviate however strongly from experiment. Note that the shapes of the experimental distributions described by the calculations (Fig. 8(a) and Fig. 8(d)) are qualitatively similar to the shapes of the previous energy interval, while the correlations that are not described by theory (Fig. 8(b) and Fig. 8(c)) have changed dramatically. The most striking difference is for the angular dependence in the **T** system. The calculations have convex behavior while the experimental data show a concave shape, and taking into account the first and last points, create a wavy curve. Such wiggling can be obtained by Legendre polynomials of order four and higher with large weights. But to have such terms large relative orbital momenta $l_x^{\mathbf{T}}$ and $l_y^{\mathbf{T}}$ must be excited with sizable weights in the continuum wave function. It requires large amplitudes of wave function components with $K = 4$ (positive parity) and $K = 5$ (negative parity) or higher. The higher K the more the centrifugal barrier suppresses the corresponding wave function component at fixed excitation energy. With increasing excitation energy, however, the modes with higher hypermoment become more significant. To illustrate this point, Fig. 9 shows calculations of correlations in the energy region $6 < E_\kappa < 9\,\mathrm{MeV}$. In this region the dipole excitation is largest as before, but the relative contribution from other multipolarities becomes bigger in comparison with previous energy intervals. The angular correlation in the **T** system (Fig. 9(c)) and energy distribution in **Y** (Fig. 9(b)) start to develop features similar to the experimental data of Fig. 8(c) and Fig. 8(b), but still components with large K are not excited with sufficient intensity to produce a sizable oscillation.

In Ref. [18] a phenomenological analysis of the experimental distributions on angular and energy three-body correlations was presented. The data were described by disintegration of dipole excitations with amplitudes restricted within the method of hyperharmonics by the lowest hypermomenta $K = 1$ and 3 and fitted to the experiment. In phenomenological analysis of angular correlations in the **T** system the concave shape, but without wiggles at forward and backward directions, was reproduced for the energy interval $3 < E_\kappa < 6$ MeV. The phenomenological amplitudes were compared with amplitudes from our microscopic calculations [5] of dipole transitions within the method of hyperspherical functions. The theoretical dipole amplitudes for energy interval $1 < E_\kappa < 3$ MeV need some adjustment to agree with the phenomenological results, while they strongly deviate for interval $3 < E_\kappa < 6\,\mathrm{MeV}$. In our present calculations, which take into account excitations with a number of multipolarities (dipole, quadrupole and monopole), we have a good description of experimental correlations for $1 < E_\kappa < 3\,\mathrm{MeV}$ without any necessity to modify the dipole transitions from the microscopic calculations. The description of a wiggling shape requires, as we mentioned above, to take into account excitations with higher values of hypermomentum K, that however were not included in the fitting procedure of the phenomenological analysis.

It is an open question which model features may be responsible for the disagreements in the excitation energy interval $3 < E_\kappa < 6\,\mathrm{MeV}$, and what should be done to improve calculations. One possibility is decays from the octupole and higher multipolarities. Our calculations of the 3^- excitations show that their absolute values are more then one order of amplitude lower in comparison with dipole, and thus can not significantly modify the theoretical description.

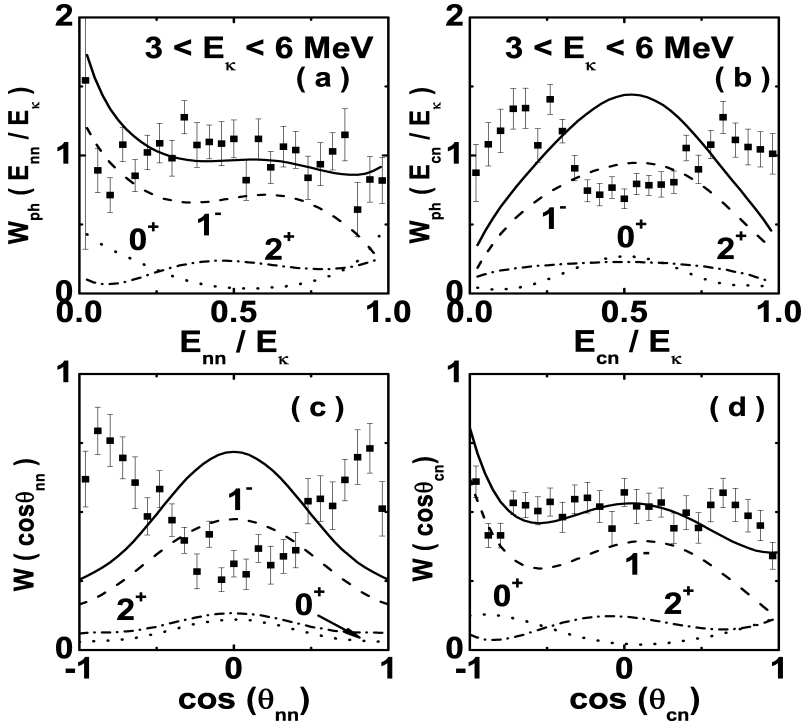

FIG. 8: Energy and angular fragment correlations in ^{6}He + ^{208}Pb breakup at 240 MeV/nucleon for excitation energy region $3 < E_\kappa < 6$ MeV. Notations are the same as in Fig. 6.

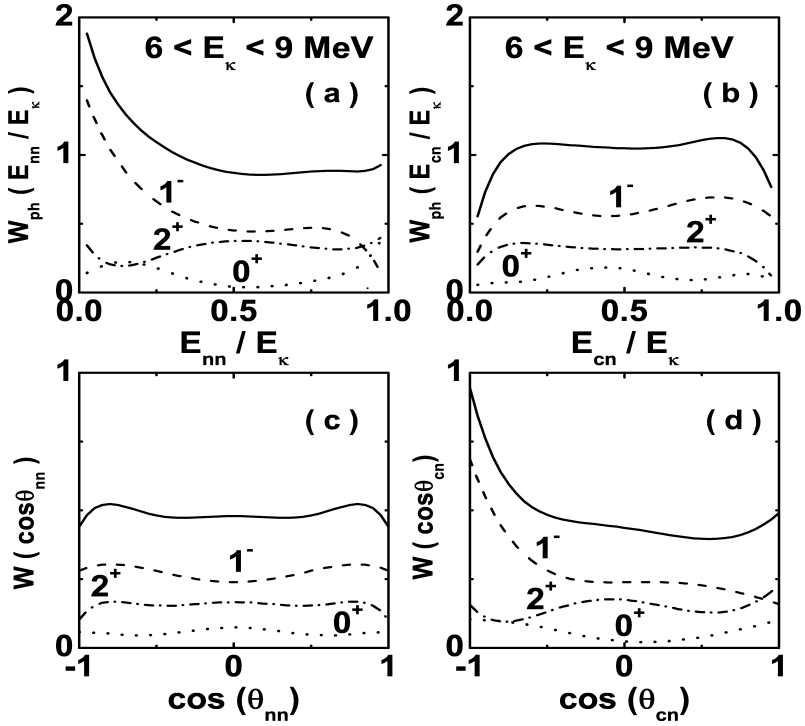

FIG. 9: Energy and angular fragment correlations in ^{6}He +^{208} Pb breakup at 240 MeV/nucleon for excitation energy region $6 < E_\kappa < 9$ MeV. Notations are the same as in Fig. 6.

In the theoretical three-body model the neutron-neutron and neutron-core effective interactions determine properties of nuclear structure and the way that the structure changes with increasing excitation energy. Thus one option is to modify the interactions to increase the share with large K hypermoment in the continuum wave functions. But this modification must not destroy the description obtained for the nuclear structure at lower excitation energies and must not seriously worsen the quality of agreement with the two-body data on which the effective interactions are based. We have not succeeded in improving the calculations in this direction.

Another possibility consists of scrutinizing the way experimental data and theoretical calculations are being compared. Experiments with radioactive beams are done in inverse kinematics where the exotic nucleus collides with target and breakup fragments are kinematically focused in forward direction and detected with high efficiency. The theoretical calculations described above, involve integrations over all unobserved momenta and assume a 4π measurements of the fragments. But due to the geometry of the performed experiments this is only experimentally fulfilled for the lowest excitation energies. Recently T. Aumann stated [2]: "The angular range for fragments and neutrons covered by the detectors corresponds to a 4π measurement of the breakup in the rest frame of the projectile for fragment neutron relative energies up to 5.5 MeV (at 500 MeV/nucleon beam energy)". In our case the collision energy per nucleon is half this value. Hence the boundary for 4π measurement is moved closer to threshold and the second interval $3 < E_\kappa < 6$ MeV does not satisfy the condition for complete averaging over unobserved degrees of freedom assumed in the theory. That means that the correct way to compare theoretical calculations with measured data should be the following: The exclusive eight folded breakup cross section has to be calculated and its numerical six-dimension integration done over the part of the allowed phase space that corresponds to experimental conditions for fragment detection. Without such calculations it is difficult to estimate the influence of the experimental geometry on the shape of angular and energy theoretical correlations and get a concise assessment of the underlying nuclear structure model.

IV. CONCLUSIONS

The three-body breakup is an essentially richer but also more complicated process than binary breakup into two fragments. At fixed continuum energy the relative motions of the three fragments have continuous distributions of kinetic energies, but it appear that at low excitation energies the leading physics for Borromean nuclei can be extracted from a few elementary modes characterized by a few orbital angular momenta. The task of continuum spectroscopy is to define the dominant excitations (multipolarities) and their quantum numbers (elementary modes). The way to achieve this task is to explore the world of various correlations in fragment motions. This demands kinematically complete experiments and theoretical understanding of the underlying reaction dynamics and nuclear structure. The first steps have now been taken in this direction.

Theoretical calculations of the ^{6}He breakup on the ^{208}Pb target reproduce quite well the low-lying excitation spectrum and fragment angular and energy correlations near breakup threshold. While dipole dominates at most excitation energies other multipolarities can significantly distort the dipole correlation pictures and for a consistent analysis of experimental data all multipole excitations have to be taken into account. With increasing continuum energy ($3 < E_\kappa < 6$ MeV) some angular and energy correlations are described within the theoretical model while some are not.

Future measurements of electrons in coincidence with fragments promise to give valuable information about halo structure. The pattern of energy and angular correlations are rather specific for different multipole excitations. Correlation measurements in general provide a unique

tool for revealing the complex dynamics of nuclear excitations and pave the way to spectroscopy of the continuum, provided that rather small cross sections can be measured.

Acknowledgements

The author are greatly thankful to B.V. Danilin and J.S. Vaagen for their invaluable contributions to the presented results.

[1] I. Tanihata, J. Phys. **G22**, 157 (1996).
[2] T. Aumann, Eur. Phys. J. A **26**, 441 (2005).
[3] M.V. Zhukov, B.V. Danilin and D.V. Fedorov et al., Phys. Rep. **231**, 151 (1993).
[4] B.V. Danilin and M.V. Zhukov, Yad. Phys. **56**, 67 (1993) [Phys. At. Nucl. **56**, 460 (1993)].
[5] B.V. Danilin, I.J. Thompson, M.V. Zhukov, and J.S. Vaagen, Nucl. Phys. A **632**, 383 (1998).
[6] B.V. Danilin, S.N. Ershov, and J.S. Vaagen, Phys. Rev. C **71**, 057301 (2005).
[7] B.V. Danilin et al., Phys. Rev. C **43**, 2835 (1991).
[8] S.N. Ershov et al., Phys. Rev. C **56**, 1483 (1997).
[9] S.N. Ershov, B.V. Danilin, T. Rogde, and J.S. Vaagen, Phys. Rev. Lett. **82**, 908 (1999).
[10] S.N. Ershov, B.V. Danilin, and J.S. Vaagen, Phys. Rev. C **62**, 041001(R) (2000).
[11] S.N. Ershov, B.V. Danilin, and J.S. Vaagen, Phys. Rev. C **64**, 064609 (2001).
[12] S.N. Ershov, B.V. Danilin, J.S. Vaagen, A.A. Korsheninnikov, and I.J. Thompson, Phys. Rev. C **70**, 054608 (2004).
[13] S.N. Ershov, B.V. Danilin, and J.S. Vaagen, Phys. Rev. C **72**, 044606 (2005).
[14] S.N. Ershov, B.V. Danilin, J.S. Vaagen, Phys. Rev. C **74**, 014603 (2006).
[15] M.L. Goldberger and K.W. Watson, Collision Theory (New-York, 1964).
[16] J.D. Bjorken, S.D. Drell, Relativistic Quantum Mechanics (McGraw Hill, New York, N.Y., 1964).
[17] A.S. Jensen, M.V. Zhukov, Nucl. Phys. A **693**, 411 (2001).
[18] L.V. Chulkov et al., Nucl. Phys. A **759**, 23 (2005).
[19] T. Aumann et al, Phys. Rev. C **59**, 1252 (1999).
[20] J. Raynal, J. Revai, Nuovo Cimento A **68**, 612 (1970).
[21] Yu.A. Smorodinskii, V.D. Efros, Yad. Fiz. **17**, 210 (1973) [Sov. J. Nucl. Phys. **17**, 107 (1973)].

Resonances of Multichannel Systems

Alexander K. Motovilov*

Bogoliubov Laboratory of Theoretical Physics,
JINR Joliot-Curie 6, 141980 Dubna, Moscow Region, Russia

We describe the structure of the T-matrices, scattering matrices, and Green functions on unphysical energy sheets in multichannel scattering problems with binary channels and in the three-body problem. Based on the explicit representations obtained for the values of T- and S-matrices on the unphysical sheets, we prove that the resonances belonging to an unphysical sheet are just those energies where the correspondingly truncated scattering matrix, taken in the physical sheet, has eigenvalue zero. We show, in addition, that eigenvectors of the truncated scattering matrix associated with its zero eigenvalue are formed of the breakup amplitudes for the respective resonant states.

I. INTRODUCTION

Resonances of multichannel systems play a crucial role in various problems of nuclear, atomic, and molecular physics. In a wider sense, resonances represent one of the most interesting and intriguing phenomena observed in scattering processes, and not only in quantum physics but also in optics, acoustics, radiophysics, mechanics of continua etc. Literature on resonances is enormous and in this short introduction we have a chance to mention only several key points in the history of the subject and to refer only to a few key approaches to quantum-mechanical resonances, necessarily leaving many others a part.

With a resonance of a quantum system one usually associates an unstable state that only exists during a certain time. The original idea of interpreting resonances in quantum mechanics as complex poles of the scattering amplitude (and hence, as those of the scattering matrix) goes back to G. Gamov [1]. For radially symmetric potentials, the interpretation of two-body resonances as poles of the analytic continuation of the scattering matrix has been entirely elaborated in terms of the Jost functions [2]. Beginning with E. C. Titchmarsh [3] it was also realized that the S-matrix resonances may show up as poles of the analytically continued Green functions.

Another, somewhat distinct approach to resonances is known as the complex scaling (or complex rotation) method. The complex scaling makes it possible to rotate the continuous spectrum of the N-body Hamiltonian in such a way that resonances in certain sectors of the complex energy plane turn into usual eigenvalues of the scaled Hamiltonian. In physics literature the origins of such an approach are traced back at least to C. Lovelace [4]. A rigorous approval of the complex scaling method has been done by E. Balslev and J. M. Combes [5]. A link between the S-matrix interpretation of resonances and its complex rotation counterpart was established by G. A. Hagedorn [6] who has proven that for a reasonable class of quickly decreasing potentials at least a part of the scaling resonances for an N-body system ($N \leq 4$) turns to be also the scattering matrix resonances. We remark that the complex scaling seems to be the most popular approach to practical calculation of resonances, particularly in atomic and molecular systems (see, e.g., Refs. [7–11] and references cited therein).

If support of the interaction is compact, the resonances of a two-body system can be treated within the approach created by P. Lax and R. Phillips [12]. An advantage of the Lax-Phillips

*Electronic address: motovilv@theor.jinr.ru

approach is in the opportunity of giving an elegant operator interpretation of resonances. The two-body resonances show up as the discrete spectrum of a dissipative operator which is the generator of the compressed evolution semigroup. An operator interpretation of resonances in multichannel systems, based on a 2×2 operator matrix representation of a rather generic Hamiltonian, can be found in [13].

For more details on the history of the subject and other approaches to resonances, as well as for the bibliography we refer to books [14–19] (it might also be useful to look through the review parts of papers [20] and [21]). Here we only notice that, in contrast to the "normal" bound and scattering states, the resonant ones still remain a quite mysterious object and many questions related to resonances are still unanswered. This is partly related to the fact that, unlike the "normal" spectrum, resonances are not a unitary invariant of a self-adjoint (Hermitian) operator. Moreover, following to J. S. Howland [22] and B. Simon [23], one should conclude that no satisfactory definition of resonance can rely on a single operator on an abstract Hilbert space and always an extra structure is necessary. Say, an unperturbed dynamics (in quantum scattering theory) or geometric setup (in acoustical or optical problems). Resonances are as relative as the scattering matrix is itself.

In the present approach we follow the typical setup where the resonances arising due to an interaction V are considered relative to the unperturbed dynamics described by the kinetic energy operator H_0. The resolvent $G(z) = (H - z)^{-1}$ of the total Hamiltonian $H = H_0 + V$ is an analytic operator-valued function of $z \in \mathbb{C} \setminus \sigma(H)$. The spectrum $\sigma(H)$ of H is a natural boundary for holomorphy domain of $G(z)$ considered as an operator-valued function. However the kernel $G(\cdot, \cdot, z)$ may admit analytic continuation through the continuous spectrum of H. Or the form $\langle G(z)\varphi, \psi\rangle$ may do this for any φ, ψ of a dense subset of the Hilbert space $\mathfrak{H}$. Or the "augmented" resolvent $PG(z)P$ admits such a continuation for P the orthogonal projection onto a subspace of $\mathfrak{H}$. In any of these cases one deals with the Riemann surface of an analytical function.

In the simplest example with $H = H_0 = -\Delta$, the two-body kinetic energy operator in coordinate representation, we have

$$G(\boldsymbol{x}, \boldsymbol{x}', z) = \frac{1}{4\pi} \frac{\mathrm{e}^{\mathrm{i}z^{1/2}|\boldsymbol{x}-\boldsymbol{x}'|}}{|\boldsymbol{x} - \boldsymbol{x}'|},$$

where $\boldsymbol{x}, \boldsymbol{x}'$ are three-dimensional vectors. Clearly, $G(\boldsymbol{x}, \boldsymbol{x}', z)$ as a function of the energy z has a two-sheeted Riemann surface which simply coincides with that of the function $z^{1/2}$.

In this way one arrives at the concept of the unphysical energy sheet(s). The copy of the complex energy plane where the resolvent $G(z)$ is considered initially as an operator-valued function is called the physical sheet. The remainder of the Riemann surface is assumed to consist of the unphysical sheets (in general, an unphysical sheet may only be a small part of the complex plane).

Meanwhile, any analytic function is uniquely defined by its values given for an infinite set of points belonging to its initial domain and having at list one limiting point. Usually one knows the T-matrix or Green function on the whole physical sheet which means that, at least in principle, it should be possible to express their values on unphysical sheets through the ones on the physical sheet.

In [21, 24] (see also [25, 26]) we have found such expressions. More precisely, we have derived explicit representations for the values of the two- and three-body $G(z)$, $T(z)$, and $S(z)$ on unphysical energy sheets in terms of these quantities themselves only taken on the physical sheet. The same has been also done for analogous objects in multichannel scattering problems with binary channels [24]. The representations obtained not only disclose the structure T-matrices, scattering matrices, and Green functions on unphysical energy sheets but they also show which

blocks of the scattering matrix taken in the physical sheet are "responsible" for resonances on a certain unphysical sheet. This result paves the way to developing new methods for practical calculation of resonances in concrete multichannel systems and, in particular, in the three-body ones (see, e.g. [27–29]). As a matter of fact we reduce all the study of resonances to a work completely on the physical sheet. The present report essentially extends the presentation given recently in [30].

II. TWO-BODY PROBLEM

In general, we assume that the interaction potential v falls off in coordinate space not slower than exponentially. When studying resonances of a two–body system with such an interaction one can employ equally well both coordinate and momentum representations. However, in the three-body case it is much easier for us to work in the momentum space (for an explanation see [21], p. 149). This is one of the reasons why we proceed in the same way in the two-body case. Thus, for the two-body kinetic energy operator h_0 we set $(h_0 f)(\boldsymbol{k}) = \boldsymbol{k}^2 f(\boldsymbol{k})$ where $\boldsymbol{k} \in \mathbb{R}^3$ stands for the reduced relative momentum. In case of a local potential we have $v(\boldsymbol{k}, \boldsymbol{k}') = v(\boldsymbol{k} - \boldsymbol{k}')$ and $v(\boldsymbol{k}) = \overline{v(-\boldsymbol{k})}$.

Surely, we need to add some requirements on the analyticity of the potentials in their complex momentum variables as well as on their fall-off as the real parts of the momenta approach infinity (see [21] and [24] for details). For simplicity, through all this presentation we assume that the potentials involved are holomorphic functions of the momenta on the corresponding whole complex spaces (that is, on the whole $\mathbb{C}^3$ in the two-body case).

The transition operator (T-matrix) reads

$$t(z) = v - vg(z)v, \tag{2.1}$$

where $g(z) = (h - z)^{-1}$ denotes the resolvent of the perturbed Hamiltonian $h = h_0 + v$. The operator t is the solution of the Lippmann-Schwinger equation

$$t(z) = v - vg_0(z)t(z), \tag{2.2}$$

that is, in terms of the its kernel we have

$$t(\boldsymbol{k}, \boldsymbol{k}', z) = v(\boldsymbol{k}, \boldsymbol{k}') - \int_{\mathbb{R}^3} \mathrm{d}\boldsymbol{q} \frac{v(\boldsymbol{k}, \boldsymbol{q}) t(\boldsymbol{q}, \boldsymbol{k}', z)}{\boldsymbol{q}^2 - z} \tag{2.3}$$

taking into account that the free Green function g_0 reads

$$g_0(\boldsymbol{k}, \boldsymbol{k}', z) = \frac{\delta(\boldsymbol{k} - \boldsymbol{k}')}{(\boldsymbol{k}^2 - z)}.$$

Clearly, all dependence of t on z is determined by the integral term on the right-hand side of (2.3) that looks like a particular case of the Cauchy type integral

$$\Phi(z) = \int_{\mathbb{R}^N} \mathrm{d}\boldsymbol{q} \frac{f(\boldsymbol{q})}{\lambda + \boldsymbol{q}^2 - z} \tag{2.4}$$

for $N = 3$. Cauchy type integrals of the same form but for various N we will also have below when considering a multichannel problem with binary channels in Sec. III and the three-body problem in Sec. IV.

Let $\mathfrak{R}_\lambda$, $\lambda \in \mathbb{C}$, be the Riemann surface of the function

$$\zeta(z) = \begin{cases} (z - \lambda)^{1/2} & \text{if } N \text{ is odd,} \\ \log(z - \lambda) & \text{if } N \text{ is even.} \end{cases} \tag{2.5}$$

If N is odd, $\mathfrak{R}_\lambda$ is formed of two sheets of the complex plane. One of them, where $(z-\lambda)^{1/2}$ coincides with the arithmetic square root $\sqrt{z-\lambda}$, we denote by Π_0. The other one, where $(z-\lambda)^{1/2} = -\sqrt{z-\lambda}$, is denoted by Π_1.

If N is even, the number of sheets of $\mathfrak{R}_\lambda$ is infinite. In this case as the index ℓ of a sheet Π_ℓ we take the branch number of the function $\log(z-\lambda)$ picked up from the representation $\log(z-\lambda) = \log|z-\lambda| + \mathrm{i}\,2\pi\ell + \mathrm{i}\phi$ with $\phi \in [0, 2\pi)$. Usually the point λ is called the branching point of the Riemann surface $\mathfrak{R}_\lambda$.

The following statement can be easily proven by applying the residue theorem (if necessary, consult [24] for a proof).

Lemma 1. *For a holomorphic $f(\boldsymbol{q})$, $\boldsymbol{q} \in \mathbb{C}^N$, the function $\Phi(z)$ given by* (2.4) *is holomorphic on $\mathbb{C} \setminus [\lambda, +\infty)$ and admits the analytic continuation onto the unphysical sheets Π_ℓ of the Riemann surface $\mathfrak{R}_\lambda$ as follows*

$$\Phi(z|_{\Pi_\ell}) = \Phi(z) - \ell\,\pi\mathrm{i}(\sqrt{z-\lambda}\,)^{N-2} \int_{S^{N-1}} \mathrm{d}\widehat{\boldsymbol{q}}\, f(\sqrt{z-\lambda}\widehat{\boldsymbol{q}}), \tag{2.6}$$

where S^{N-1} denotes the unit sphere in $\mathbb{R}^N$ centered at the origin.

Notice that in (2.6) and further on the writing $z\big|_{\Pi_\ell}$ means that position of z is taken on the unphysical sheet Π_ℓ. If the reference to Π_ℓ is not present and we write simply z than one understands that we deal with exactly the same energy point but lying on (dropped onto) the physical sheet Π_0.

Let us return to the two-body problem and set

$$\big(g_0(z)f_1, f_2\big) \equiv \int_{\mathbb{R}^3} \mathrm{d}\boldsymbol{q}\, \frac{f_1(\boldsymbol{q})f_2(\boldsymbol{q})}{\boldsymbol{q}^2 - z},$$

where f_1 and f_2 are holomorphic. Then by Lemma 1

$$\big(g_0(z|_{\Pi_1})f_1, f_2\big) = \big(g_0(z|_{\Pi_0})f_1, f_2\big) - \pi\mathrm{i}\sqrt{z} \int_{S^2} \mathrm{d}\widehat{\boldsymbol{q}}\, f_1(\sqrt{z}\widehat{\boldsymbol{q}})f_2(\sqrt{z}\widehat{\boldsymbol{q}}),$$

which means that the continuation of the free Green function $g_0(z)$ onto the unphysical sheet Π_1 can be written in short form as

$$g_0(z|_{\Pi_1}) = g_0(z) + \mathrm{a}_0(z) j^\dagger(z) j(z), \tag{2.7}$$

where $\mathrm{a}_0(z) = -\pi\mathrm{i}\sqrt{z}$ and $j(z)$ is the operator forcing a (holomorphic) function f to set onto the energy shell, i.e. $\big(j(z)f\big)(\widehat{\boldsymbol{k}}) = f(\sqrt{z}\widehat{\boldsymbol{k}})$.

Taking into account (2.7), on the unphysical sheet Π_1 the Lippmann-Schwinger equation (2.2) turns into

$$t' = v - v(g_0 + \mathrm{a}_0 j^\dagger j)t', \qquad t' = t|_{\Pi_1}.$$

Hence $(I + vg_0)t' = v - \mathrm{a}_0 j^\dagger j\, t'$. Invert $I + vg_0$ by using the fact that $t(z) = v - vg_0 t$ and, hence, $(I + vg_0)^{-1}v = t$:

$$t' = t - \mathrm{a}_0 t j^\dagger j t'. \tag{2.8}$$

Apply $j(z)$ to both sides of (2.8) and obtain $jt' = jt - \mathrm{a}_0\, jtj^\dagger\, jt'$, which means

$$(\widehat{I} + \mathrm{a}_0\, jtj^\dagger)\, jt' = jt, \tag{2.9}$$

where $\widehat{I}$ stands for the identity operator in $L_2(S^2)$. Then observe that $\widehat{I} + \mathrm{a}_0\, jtj^\dagger$ is nothing but the two-body scattering matrix $s(z)$ since the kernel of the latter for $z \in \Pi_0$ is known to read

$$s(\widehat{\boldsymbol{k}}, \widehat{\boldsymbol{k}}', z) = \delta(\widehat{\boldsymbol{k}}, \widehat{\boldsymbol{k}}') - \pi \mathrm{i}\sqrt{z}\; t(\sqrt{z}\widehat{\boldsymbol{k}}, \sqrt{z}\widehat{\boldsymbol{k}}', z).$$

Hence

$$jt' = [s(z)]^{-1} jt. \tag{2.10}$$

Going back to (2.8) and using (2.10) we get $t' = t - \mathrm{a}_0\; tj^\dagger [s(z)]^{-1} jt$, that is,

$$t(z|_{\Pi_1}) = t(z) - \mathrm{a}_0(z)\; t(z) j^\dagger(z) [s(z)]^{-1}\, j(z) t(z). \tag{2.11}$$

All entries on the right-hand side of (2.11) are on the physical sheet. This is just the representation for the two-body T-matrix on the unphysical sheet we looked for.

From (2.11) one immediately derives representations for the continued resolvent,

$$g(z|_{\Pi_1}) = g + \mathrm{a}_0\, (I - gv) j^\dagger\, [s(z)]^{-1} j (I - vg), \tag{2.12}$$

and continued scattering matrix,

$$s(z|_{\Pi_1}) = \mathcal{E}\, [s(z)]^{-1}\, \mathcal{E}, \tag{2.13}$$

where $\mathcal{E}$ is the inversion, $(\mathcal{E} f)(\widehat{\boldsymbol{k}}) = f(-\widehat{\boldsymbol{k}})$. Hence, the resonances are nothing but zeros of the scattering matrix $s(z)$ in the physical sheet. That is, the energy z on the unphysical sheet Π_1 is a resonance if and only if there is a non-zero vector $\mathcal{A}$ of $L_2(S^2)$ such that

$$s(z)\mathcal{A} = 0 \tag{2.14}$$

for the same z on the physical sheet.

We remark that this fact is rather well known for the partial-wave Schrödinger equations in case of centrally-symmetric potentials. In this case the statement that the resonances correspond to zeros of the partial-wave scattering matrix s_l on the physical sheet of the complex energy plane follows from its representation (see, e.g., [16])

$$s_l(p) = (-1)^l\, \frac{f_l(p)}{f_l(-p)}$$

in terms of the Jost function $f_l(p)$ where l stands for the angular momentum and p for the (scalar) complex momentum. This property of $s_l(p)$ was explicitly noticed in the review article [20, p. 1357]. Generalizations of the statement to the case of multichannel problems with binary channels and to the three-body problem have been given in [24] and [21], respectively. We will discuss them below in Sec. III and IV.

The eigenfunction $\mathcal{A}$ in (2.14) represents the breakup amplitude of an unstable state associated with the resonance z. This means that in coordinate space the corresponding "Gamov vector", i.e. the resonance solution to the Schrödinger equation, has the following asymptotics

$$\begin{aligned} \psi_{\mathrm{res}}(\boldsymbol{x}) \underset{\boldsymbol{x}\to\infty}{\sim}\; & \mathcal{A}(-\widehat{\boldsymbol{x}})\; \frac{\exp\bigl(\mathrm{i} z^{1/2}\big|_{\Pi_1} |\boldsymbol{x}|\bigr)}{|\boldsymbol{x}|} \\ & \mathcal{A}(-\widehat{\boldsymbol{x}})\; \frac{\exp\bigl(-\mathrm{i}\sqrt{z}|\boldsymbol{x}|\,\bigr)}{|\boldsymbol{x}|}, \qquad \widehat{\boldsymbol{x}} = \boldsymbol{x}/|\boldsymbol{x}|. \end{aligned} \tag{2.15}$$

This claim is a particular case of the statement of Lemma 2 below.

It should be stressed that the asymptotics (2.15) contains no term with the incoming spherical wave

$$\frac{\exp\bigl(-\mathrm{i}z^{1/2}\big|_{\Pi_1}|\boldsymbol{x}|\bigr)}{|\boldsymbol{x}|}.$$

We conclude the section with a remark that in [31] (see also [32, Section 2] and [20, Section 3]) Yu. V. Orlov was very close to obtaining a representation that would be a version of the representation (2.11) for partial-wave two-body T-matrices in the case of centrally-symmetric potentials. As a matter of fact, only the last step has not been done in [31, 32], the one analogous to the transition from equation (2.8) to equation (2.11) by using relation (2.10).

III. MULTICHANNEL PROBLEM WITH BINARY CHANNELS

From now on assume that h is an $m\times m$ matrix Schrödinger operator of the form

$$h=\begin{pmatrix} \lambda_1+h_0^{(1)}+v_{11} & v_{12} & \dots & v_{1m} \\ v_{21} & \lambda_2+h_0^{(2)}+v_{22} & \dots & v_{2m} \\ \dots & \dots & \dots & \dots \\ v_{m1} & v_{m2} & \dots & \lambda_m+h_0^{(m)}+v_{mm} \end{pmatrix}, \tag{3.1}$$

written in the momentum representation. Thus, we assume that

$$(h_0^{(\alpha)}f_\alpha)(\boldsymbol{k}_\alpha)=\boldsymbol{k}_\alpha^2 f_\alpha(\boldsymbol{k}_\alpha),\quad \boldsymbol{k}_\alpha\in\mathbb{R}^{n_\alpha},\quad f_\alpha\in L_2(\mathbb{R}^{n_\alpha}),\quad \alpha=1,2,\dots,m.$$

We restrict ourselves to the case where the channel dimensions n_α satisfy the inequalities $n_\alpha\geq 3$, $\alpha=1,2,\dots,m$, and $1\leq m<\infty$. For simplicity, we assume that the potential/coupling terms $v_{\alpha\beta}(\boldsymbol{k}_\alpha,\boldsymbol{k}'_\beta)$ are holomorphic functions of their variables $\boldsymbol{k}_\alpha\in\mathbb{C}^{n_\alpha}$ and $\boldsymbol{k}'_\beta\in\mathbb{C}^{n_\beta}$, sufficiently rapidly decreasing as $\operatorname{Re}\boldsymbol{k}_\alpha\to\infty$ or $\operatorname{Re}\boldsymbol{k}'_\beta\to\infty$ (see [24]). The thresholds $\lambda_1,\lambda_2,\dots,\lambda_m\in\mathbb{R}$ are assumed to be distinct and arranged in ascending order: $\lambda_1<\lambda_2<\ldots<\lambda_m$.

We also introduce the notations

$$h_0=\begin{pmatrix} \lambda_1+h_0^{(1)} & 0 & \dots & 0 \\ 0 & \lambda_2+h_0^{(2)} & \dots & 0 \\ \dots & \dots & \dots & \dots \\ 0 & 0 & \dots & \lambda_m+h_0^{(m)} \end{pmatrix} \quad\text{and}\quad v=\begin{pmatrix} v_{11} & v_{12} & \dots & v_{1m} \\ v_{21} & v_{22} & \dots & v_{2m} \\ \dots & \dots & \dots & \dots \\ v_{m1} & v_{m2} & \dots & v_{mm} \end{pmatrix}$$

for the unperturbed Hamiltonian and the total interaction, respectively. By $g_0(z)$ and $g(z)$ we denote the corresponding resolvents,

$$g_0(z)=(h_0-z)^{-1}\quad\text{and}\quad g(z)=(h-z)^{-1}.$$

Similarly to the one-channel (i.e. two-body) case of Sec. II, we again begin with the study of the T-matrix

$$t(z)=v-vg(z)v$$

that is the solution to the Lippman-Schwinger equation

$$t(z)=v-vg_0(z)t(z). \tag{3.2}$$

The kernels $t_{\alpha\beta}(\boldsymbol{k}_\alpha, \boldsymbol{k}'_\beta, z)$ of the block entries $t_{\alpha\beta}(z)$ of the operator matrix $t(z)$ satisfy the equation system

$$t_{\alpha\beta}(\boldsymbol{k}, \boldsymbol{k}', z) = v_{\alpha\beta}(\boldsymbol{k}, \boldsymbol{k}') - \sum_{\gamma=1}^{m} \int_{\mathbb{R}_{n\gamma}} \mathrm{d}\boldsymbol{q} \frac{v_{\alpha\gamma}(\boldsymbol{k}, \boldsymbol{q}) t_{\gamma\beta}(\boldsymbol{q}, \boldsymbol{k}', z)}{\lambda_\gamma + \boldsymbol{q}^2 - z}. \tag{3.3}$$

As in the two-body T-matrix in equation (2.3), the dependence of the kernels $t_{\alpha\beta}(\boldsymbol{k}, \boldsymbol{k}', z)$ on z is determined by the integrals on the right-hand-side of (3.3), which are Cauchy type integrals of the form (2.4).

In contrast to the two-body case, for $m \geq 2$ we arrive at a multi-sheeted Riemann surface with number of sheets greater than two. The reason is simple: Every threshold λ_α, $\alpha = 1, 2, \ldots, m$, turns into a branching point. If all channel dimensions n_α are odd, the number of sheets should be equal to 2^m, that is, in addition to the physical sheet the Riemann surface will contain $2^m - 1$ unphysical ones. If at least one of n_α's is even, we will have a logarithmic branching point and the number of unphysical sheets will be necessarily infinite. In fact, this Riemann surface simply coincides with the Riemann surface $\mathfrak{R}$ of the vector-valued function

$$\boldsymbol{\zeta}(z) = \big(\zeta_1(z), \zeta_2(z), \ldots, \zeta_m(z)\big),$$

where (cf. formula (2.5))

$$\zeta_\alpha(z) = \begin{cases} (z - \lambda_\alpha)^{1/2} & \text{if } n_\alpha \text{ is odd,} \\ \log(z - \lambda_\alpha) & \text{if } n_\alpha \text{ is even,} \end{cases}$$
$$\alpha = 1, 2, \ldots, m.$$

To enumerate the sheets of $\mathfrak{R}$ it is natural to use a multi-index

$$\ell = (\ell_1, \ell_2, \ldots, \ell_m),$$

where each ℓ_α coincides with the branch number for the corresponding function ζ_α, $\alpha = 1, 2, ..., m$. In particular, if n_α is odd then ℓ_α may get only two values: either 0 or 1. For even n_α the value of ℓ_α is allowed to be any integer. The sheets of $\mathfrak{R}$ are denoted by Π_ℓ. The physical sheet corresponds to the case where all components of ℓ are equal to zero and thus it is denoted simply by Π_0.

Each sheet Π_ℓ is a copy of the complex plane $\mathbb{C}'$ cut along the ray $[\lambda_1, +\infty)$. The sheets are pasted to each other in a suitable way along edges of the cut segments between neighboring points in the set of the thresholds λ_α, $\alpha = 1, 2, \ldots, m$. In particular, if coming from the sheet $\Pi_{(\ell_1, \ell_2, \ldots, \ell_m)}$ the energy z crosses the interval $(\lambda_\alpha, \lambda_{\alpha+1})$, $\alpha = 1, 2, \ldots, m$, $\lambda_{m+1} \equiv +\infty$, in the upward direction (i.e. passes from the region $\operatorname{Im} z < 0$ to the region $\operatorname{Im} z > 0$), then it arrives at the sheet $\Pi_{(\ell'_1, \ell'_2, \ldots, \ell'_\alpha, \ell_{\alpha+1}, \ldots, \ell_m)}$ with all indices beginning from $\ell_{\alpha+1}$ remaining the same while the first α indices ℓ_j, $1 \leq j \leq \alpha$, change by unity. If n_j is odd then $\ell'_j = 1$ for $\ell_j = 0$ and $\ell'_j = 0$ for $\ell_j = 1$; if n_j is even then $\ell'_j = \ell_j + 1$. In the case where the energy z passes the same interval $(\lambda_\alpha, \lambda_{\alpha+1})$ downward, it arrives at the sheet $\Pi_{(\ell'_1, \ell'_2, \ldots, \ell'_\alpha, \ell_{\alpha+1}, \ldots, \ell_m)}$ where for odd n_j the indices ℓ'_j are the same as in the previous case and for even n_j they change according to the rule $\ell'_j = \ell_j - 1$. The indices ℓ_j with numbers $j \geq \alpha + 1$ remain unchanged.

Under the assumption that the kernels $t_{\alpha\beta}(\sqrt{z - \lambda_\alpha}\,\widehat{\boldsymbol{k}}, \boldsymbol{k}', z)$ admit the analytic continuation in z through the cuts (the existence of such a continuation may be rigorously approved, see [24]) one can perform analytic continuation of the Lippman-Schwinger equation (3.3) from the physical sheet Π_0 onto any unphysical sheet Π_ℓ of the surface $\mathfrak{R}$. Of course, the trajectory along

which we pull z should avoid the branching points λ_α. Applying after each crossing the interval $(\lambda_1,+\infty)$ the corresponding variant of formula (2.6) we arrive at the following result

$$t_{\alpha\beta}(\boldsymbol{k},\boldsymbol{k}',z\big|_{\Pi_\ell}) = v_{\alpha\beta}(\boldsymbol{k},\boldsymbol{k}') - \sum_{\gamma=1}^{m}\int_{\mathbb{R}_{n_\gamma}} \mathrm{d}\boldsymbol{q}\frac{v_{\alpha\gamma}(\boldsymbol{k},\boldsymbol{q})t_{\gamma\beta}(\boldsymbol{q},\boldsymbol{k}',z\big|_{\Pi_\ell})}{\lambda_\gamma+\boldsymbol{q}^2-z} \tag{3.4}$$
$$-\sum_{\gamma=1}^{m}\ell_\gamma\, A_\beta(z)\int_{S^{n_\gamma-1}}\mathrm{d}\widehat{\boldsymbol{q}}\;\, v_{\alpha\gamma}(\boldsymbol{k}_\alpha,\sqrt{z-\lambda_\gamma}\widehat{\boldsymbol{q}})\, t_{\gamma\beta}(\sqrt{z-\lambda_\gamma}\widehat{\boldsymbol{q}},\boldsymbol{k}'_\beta,z\big|_{\Pi_\ell}),$$

where

$$A_\gamma(z) = -\pi\mathrm{i}(\sqrt{z-\lambda_\gamma})^{n_\gamma-2} \tag{3.5}$$

Notice that the second integral term on the right-hand side of (3.4) includes the half-on-shell values $t_{\gamma\beta}(\sqrt{z-\lambda_\gamma}\widehat{\boldsymbol{q}},\boldsymbol{k}'_\beta,z\big|_{\Pi_\ell})$ of the T-matrix kernels $t_{\gamma\beta}(\boldsymbol{q},\boldsymbol{k}'_\beta,z\big|_{\Pi_\ell})$ taken on the unphysical sheet Π_ℓ. Thus, like in the two-body case of Sec. II, it is convenient to introduce operators $j_\gamma(z)$ forcing a holomorphic function $f(\boldsymbol{q})$, $\boldsymbol{q}\in\mathbb{C}^n$, to set onto the corresponding energy shell, i.e.

$$\big(j_\gamma(z)f\big)(\widehat{\boldsymbol{q}}) = f(\sqrt{z-\lambda_\gamma}\widehat{\boldsymbol{q}}),\quad \gamma=1,2,\ldots,m.$$

From these operators we construct a block diagonal matrix

$$J(z) = \begin{pmatrix} j_1(z) & 0 & \ldots & 0\\ 0 & j_2(z) & \ldots & 0\\ \ldots & \ldots & \ldots & \ldots\\ 0 & 0 & \ldots & j_m(z)\end{pmatrix}.$$

Using this notation one easily rewrites equation (3.4) in the matrix form

$$t(z\big|_{\Pi_\ell}) = v - vg_0(z)t(z\big|_{\Pi_\ell}) - vJ^\dagger(z)LA(z)J(z)t(z\big|_{\Pi_\ell}), \tag{3.6}$$

where L and $A(z)$ are diagonal $m\times m$ matrices with scalar entries,

$$L = \begin{pmatrix} \ell_1 & 0 & \ldots & 0\\ 0 & \ell_2 & \ldots & 0\\ \ldots & \ldots & \ldots & \ldots\\ 0 & 0 & \ldots & \ell_m\end{pmatrix}\quad\text{and}\quad A(z) = \begin{pmatrix} A_1(z) & 0 & \ldots & 0\\ 0 & A_2(z) & \ldots & 0\\ \ldots & \ldots & \ldots & \ldots\\ 0 & 0 & \ldots & A_m(z)\end{pmatrix}, \tag{3.7}$$

and $J^\dagger(z)$ is the "transpose" of $J(z)$ which means that the product $t(z)J^\dagger(z)$ has half-on-shell kernels of the form $v_{\alpha\beta}(\boldsymbol{k},\sqrt{z-\lambda_\beta}\boldsymbol{k}')$.

When rearranging (3.6) we first transfer the term $vg_0(z)t(z\big|_{\Pi_\ell})$ to the left-hand side of (3.6) and obtain

$$\big(I+vg_0(z)\big)t(z\big|_{\Pi_\ell}) = v - vJ^\dagger(z)LA(z)J(z)t(z\big|_{\Pi_\ell}). \tag{3.8}$$

Our next step is to invert the operator $\big(I+vg_0(z)\big)$ (of course, this is only possible for z not belonging to the discrete spectrum of h). Here, we keep in mind that the energy z in this operator is from the physical sheet where the Lippmann-Schwinger equation (3.2) holds and thus $\big(I+vg_0(z)\big)^{-1}v = t(z)$. Using this inversion formula we then derive from (3.8) that

$$t(z\big|_{\Pi_\ell}) = t(z) - t(z)J^\dagger(z)LA(z)J(z)t(z\big|_{\Pi_\ell}). \tag{3.9}$$

At this point it is convenient to introduce another diagonal scalar $m \times m$ matrix

$$\widetilde{L} = \begin{pmatrix} \widetilde{\ell}_1 & 0 & \dots & 0 \\ 0 & \widetilde{\ell}_2 & \dots & 0 \\ \dots & \dots & \dots & \dots \\ 0 & 0 & \dots & \widetilde{\ell}_m \end{pmatrix} \tag{3.10}$$

whose diagonal entries are

$$\widetilde{\ell}_\alpha = \begin{cases} 0 & \text{if } \ell_\alpha = 0, \\ \mathrm{Sign}(\ell_\alpha) = \dfrac{\ell_\alpha}{|\ell_\alpha|} & \text{if } \ell_\alpha \neq 0. \end{cases}$$

Clearly, the matrices L, $\widetilde{L}$, and $A(z)$ commute. Moreover, $L\widetilde{L} = L$. Using these facts one rewrites (3.9) in a slightly different form

$$t(z\big|_{\Pi_\ell}) = t(z) - t(z)J^\dagger(z)LA(z)\widetilde{L}J(z)t(z\big|_{\Pi_\ell}). \tag{3.11}$$

which means that the value $t(z\big|_{\Pi_\ell})$ of the T-matrix t at a point z on the unphysical sheet Π_ℓ is expressed through the value of t itself taken at the same point z on the physical sheet as well as through the half-on-shell value $J(z)t(z\big|_{\Pi_\ell})$ taken still for $z\big|_{\Pi_\ell}$ and, in addition, multiplied by $\widetilde{L}$ from the left. Applying the product $\widetilde{L}J(z)$ to both side of (3.11) we arrive at a closed equation for $\widetilde{L}J(z)t(z\big|_{\Pi_\ell})$,

$$\big[\widehat{I} + \widetilde{L}J(z)t(z)J^\dagger(z)LA(z)\big]\widetilde{L}J(z)t(z\big|_{\Pi_\ell}) = \widetilde{L}J(z)t(z), \tag{3.12}$$

where $\widehat{I}$ denotes the identity operator in the sum Hilbert space

$$\mathfrak{G} = L_2(S^{n_1-1}) \oplus L_2(S^{n_2-1}) \oplus \ldots \oplus L_2(S^{n_m-1}). \tag{3.13}$$

Therefore, at any point z in the physical sheet where the operator

$$s_\ell(z) = \widehat{I} + \widetilde{L}J(z)t(z)J^\dagger(z)LA(z) \tag{3.14}$$

is invertible, we will have

$$\widetilde{L}J(z)t(z\big|_{\Pi_\ell}) = [s_\ell(z)]^{-1}\widetilde{L}J(z)t(z). \tag{3.15}$$

Notice that $s_\ell(z)$ commutes with $\widetilde{L}$, i.e.

$$\widetilde{L}s_\ell(z) = s_\ell(z)\widetilde{L},$$

and hence

$$LA(z)s_\ell(z)^{-1}\widetilde{L} = LA(z)s_\ell(z)^{-1}. \tag{3.16}$$

Taking into account equalities (3.15) and (3.16) we obtain from (3.12) the following result:

$$t\big(z\big|_{\Pi_\ell}\big) = t(z) - t(z)J^\dagger(z)LA(z)[s_\ell(z)]^{-1}\widetilde{L}J(z)t(z) \tag{3.17}$$

$$= t(z) - t(z)J^\dagger(z)LA(z)[s_\ell(z)]^{-1}(z)J(z)t(z). \tag{3.18}$$

These are just the representations for $t\big(z\big|_{\Pi_\ell}\big)$ we look for: In (3.17) and (3.18) values of the multichannel T-matrix on an arbitrarily chosen unphysical energy sheet Π_ℓ are explicitly written

in terms of the entries whose values are taken from the physical sheet. Formulas (3.17) and (3.18) are just the ones that represent a generalization of the two-body representation (2.11) to the case of multichannel Schrödinger operators with binary channels. A slightly different version of the representations (3.17) and (3.18) was first published in [24].

The operator matrix $s_\ell(z)$ given by (3.14) is closely related to the total scattering matrix for the problem which reads

$$s(z) = \widehat{I} + J(z)t(z)J^\dagger(z)A(z), \tag{3.19}$$

Of course, the total scattering matrix contains neither entry L nor entry $\widetilde{L}$. For the matrix $s_\ell(z)$ these entries play an important role. Depending on the unphysical sheet Π_ℓ under consideration, certain rows and columns of the difference matrix $\big(s_\ell(z) - \widehat{I}\,\big) = \widetilde{L}J(z)t(z)J^\dagger(z)L$ completely consist of zero entries. Nullification takes place for those rows and columns of the difference matrix $\big(s(z) - \widehat{I}\,\big) = J(z)t(z)J^\dagger(z)$ whose numbers α are such that the corresponding indices ℓ_α equal zero. This is a reason why we call $s_\ell(z)$ the truncated scattering matrix associated with the unphysical sheet Π_ℓ.

Notice that if instead of (3.2) we start with the transposed Lippmann-Schwinger equation

$$t(z) = v - t(z)g_0(z)v\,,$$

then in the same way we obtain for $t\big(z\big|_{\Pi_\ell}\big)$ another representation that can be considered as a transposed version of the representation (3.17):

$$t\big(z\big|_{\Pi_\ell}\big) = t(z) - t(z)J^\dagger(z)\widetilde{L}[s_\ell^\dagger(z)]^{-1}A(z)LJ(z)t(z) \tag{3.20}$$

$$= t(z) - t(z)J^\dagger(z)[s_\ell^\dagger(z)]^{-1}A(z)LJ(z)t(z), \tag{3.21}$$

where

$$s_\ell^\dagger(z) = \widehat{I} + LA(z)J(z)t(z)J^\dagger(z)\widetilde{L}\,.$$

The operator $s_\ell^\dagger(z)$ represents the result of truncation of the transposed S-matrix

$$s^\dagger(z) = \widehat{I} + A(z)J(z)t(z)J^\dagger(z).$$

From the uniqueness of the analytic continuation by (3.17) and (3.20) it immediately follows that

$$t(z)J^\dagger(z)LA(z)s_\ell(z)^{-1}J(z)t(z) = t(z)J^\dagger(z)[s_\ell^\dagger(z)]^{-1}A(z)LJ(z)t(z).$$

To describe structure of the scattering matrices $s(z)$ or $s^\dagger(z)$ analytically continued to an unphysical sheet Π_ℓ we need some more notations. First, introduce a block diagonal operator matrix $\mathcal{E}(\ell)$ of the form $\mathcal{E} = \operatorname{diag}\big(\mathcal{E}_1, \mathcal{E}_2, \dots, \mathcal{E}_m\big)$ where $\mathcal{E}_\alpha$ is the identity operator on $L_2(S^{n_\alpha-1})$ if ℓ_α is even and $\mathcal{E}_\alpha$ is the inversion, $(\mathcal{E}_\alpha f)(\widehat{\boldsymbol{k}}) = f(-\widehat{\boldsymbol{k}})$, if ℓ_α is odd. Second, let $\mathrm{e}(\ell)$ be a scalar diagonal matrix, $\mathrm{e} = \operatorname{diag}\big(\mathrm{e}_1, \mathrm{e}_2, \dots, \mathrm{e}_m\big)$, with the main diagonal entries e_α defined by

$$\mathrm{e}_\alpha = \begin{cases} +1 \ \text{ for any } \ell_\alpha = 0, \pm1, \pm2, \dots \ \text{ if } \ \ n_\alpha \ \text{ is even}\,, \\ +1 \ \text{ if } \ n_\alpha \ \text{ is odd and } \ \ell_\alpha = 0, \\ -1 \ \text{ if } \ n_\alpha \ \text{ is odd and } \ \ell_\alpha = 1. \end{cases}$$

That is, e_α only depend on the corresponding n_α and ℓ_α. It is obvious that if a matrix-valued function $A(z)$ is defined on the physical sheet of the Riemann surface $\mathfrak{R}$ by formulas (3.5) and (3.7), then after the analytic continuation to the sheet Π_ℓ it acquires the form

$$A(z)\big|_{\Pi_\ell} = A(z)\mathrm{e}(\ell). \tag{3.22}$$

Now we are ready to present our main result concerning the S-matrices. We claim that after continuation to the sheet Π_ℓ their values are expressed by the formulas

$$s\big(z\big|_{\Pi_\ell}\big) = \mathcal{E}\left[\widehat{I} + \overline{\overline{t}}\,A\mathrm{e} - \overline{\overline{t}}\,LAs_\ell^{-1}\overline{\overline{t}}\,A\mathrm{e}\right]\mathcal{E}\,, \tag{3.23}$$

$$s^\dagger\big(z\big|_{\Pi_\ell}\big) = \mathcal{E}\left[\widehat{I} + \mathrm{e}A\overline{\overline{t}} - \mathrm{e}A\overline{\overline{t}}\,[s_\ell^\dagger]^{-1}AL\,\overline{\overline{t}}\right]\mathcal{E}\,, \tag{3.24}$$

where we use another shorthand notation

$$\overline{\overline{t}}\,(z) = J(z)t(z)J^\dagger(z).$$

The argument z of the operator-valued functions $s_\ell(z)$, $s_\ell^\dagger(z)$, $J(z)$, $J^\dagger(z)$, and $A(z)$ on the right-hand sides of (3.23) (3.24) is a point on the physical sheet Π_0 having just the same position on the complex plane as the point $z\big|_{\Pi_\ell}$ on the sheet Π_ℓ on the left-hand sides of (3.23) and (3.24), respectively.

At last, we present the representation for the continued resolvent on the sheet Π_ℓ:

$$g\big(z\big|_{\Pi_\ell}\big) = g + \big(I - gv\big)J^\dagger ALs_\ell^{-1}J\big(I - vg\big), \tag{3.25}$$

$$= g + \big(I - gv\big)J^\dagger[s_\ell^\dagger]^{-1}ALJ\big(I - vg\big). \tag{3.26}$$

In this report we skip derivation of the representations (3.23)–(3.26). The interested reader may find it in [25, Sections 1.4 and 1.5] (see also [24]). Here we only remark that the derivation is rather straightforward being based directly on the representations (3.20) or (3.21) for the T-matrix.

The most important consequence of the representations (3.23)–(3.26) is the fact that all energy singularities of the T-matrix, scattering matrices, and resolvent on an unphysical sheet Π_ℓ, differing of those in the physical sheet, are just the singularities of the inverse truncated scattering matrix $[s_\ell(z)]^{-1}$ (or, and this is the same, the ones of its transpose $[s_\ell^\dagger(z)]^{-1}$). This means that

resonances on sheet Π_ℓ correspond exactly to the points z on the physical sheet where the operator $s_\ell(z)$ has eigenvalue zero, (R)

i.e. the resonances on Π_ℓ are those energies z on Π_0 where equation

$$s_\ell(z)\mathcal{A} = 0 \tag{3.27}$$

has a non-trivial solution $\mathcal{A} \neq 0$ in the sum Hilbert space $\mathfrak{G}$ given by (3.13).

Eigenvectors of the truncated scattering matrices $s_\ell(z)$ associated with resonances have a quite transparent physical meaning. Assume that z is a resonance on the unphysical sheet Π_ℓ. This implies that for the same energy z on the physical sheet Π_0 equation (3.27) has a solution $\mathcal{A} \neq 0$, $\mathcal{A} = (\mathcal{A}_1, \mathcal{A}_2, \ldots, \mathcal{A}_m)^\dagger$. Clearly, the components $\mathcal{A}_\alpha$ of the vector $\mathcal{A}$ are non-zero only for the channels α such that $l_\alpha \neq 0$. Taking into account that (3.27) can be written in the equivalent form

$$\mathcal{A} = -\widetilde{L}Jt(z)J^\dagger LA(z)\mathcal{A}, \tag{3.28}$$

this conclusion follows from

$$(I - \widetilde{L})\mathcal{A} = 0.$$

Notice that the latter holds since $\widetilde{L}(I - \widetilde{L}) = 0$.

Along with the vector $\mathcal{A}$ we also consider an "extended" vector $\widetilde{\mathcal{A}}$ that is obtained of $\mathcal{A}$ as a result of replacing the projection $\widetilde{L}$ on the right-hand side of (3.28) with the identity operator, i.e.

$$\widetilde{\mathcal{A}} = -Jt(z)J^\dagger LA(z)\mathcal{A}. \tag{3.29}$$

Clearly, $\mathcal{A} = \widetilde{L}\widetilde{\mathcal{A}}$.

We claim that up to scalar factors the components $\widetilde{\mathcal{A}}_1(\widehat{\boldsymbol{k}}_1)$, $\widetilde{\mathcal{A}}_2(\widehat{\boldsymbol{k}}_2)$, …, $\widetilde{\mathcal{A}}_m(\widehat{\boldsymbol{k}}_m)$ of the eigenvector $\widetilde{\mathcal{A}}$ make sense of the breakup amplitudes of the corresponding resonance state in channels 1, 2,…, and m, respectively. In particular, these amplitudes determine angular dependence of coefficients at the spherical waves in the asymptotics of the channel components of the resonant solution to the Schrödinger equation in coordinate representation.

To give some details, let us denote by $h_0^\#$ and $v^\#$ the coordinate-space version (Fourier transform) of the operators h_0 and v, respectively. Namely, let

$$h_0^\# = \operatorname{diag}(\lambda_1 - \Delta_{\boldsymbol{x}_1}, \lambda_2 - \Delta_{\boldsymbol{x}_2}, \dots, \lambda_m - \Delta_{\boldsymbol{x}_m}),$$

where $\Delta_{\boldsymbol{x}_\alpha}$, $\alpha = 1, 2 \dots, m$, stands for the Laplacian in variable $\boldsymbol{x}_\alpha \in \mathbb{R}^{n_\alpha}$.

In the statement below we restrict ourselves to the case where absolute values of the unphysical-sheet indices corresponding to the even-dimensional channels are less than or equal unity, i.e. we assume that if n_α is even then $|l_\alpha| \le 1$. Recall that if n_α is odd then automatically $l_\alpha = 0$ or $l_\alpha = 1$.

Lemma 2. *Assume that z is a resonance on an unphysical sheet Π_ℓ with multi-index $\ell = (\ell_1, \ell_2, \dots, \ell_m)$ such that $|\ell_\alpha| \le 1$ for all $\alpha = 1, 2, \dots, m$. Let $\mathcal{A} \in \mathfrak{G}$ be a non-zero solution to equation* (3.27) *for the same energy z but belonging to the physical sheet. Then for this z the Schrödinger equation*

$$\left(h_0^\# + v^\#\right)\psi^\# = z\psi^\# \tag{3.30}$$

has a non-zero (resonant) solution $\psi^\#_{\mathrm{res}} = (\psi^\#_{\mathrm{res},1}, \psi^\#_{\mathrm{res},2}, \dots, \psi^\#_{\mathrm{res},n})^\dagger$ whose components $\psi^\#_{\mathrm{res},\alpha}(x_\alpha)$ for $\ell_\alpha \ne 0$ possess exponentially increasing asymptotics,

$$\psi^\#_{\mathrm{res},\alpha}(\boldsymbol{x}_\alpha) \underset{\boldsymbol{x}_\alpha \to \infty}{=} C_\alpha(z, \ell_\alpha)\big(\mathcal{A}_\alpha(-\widehat{\boldsymbol{x}}_\alpha) + o(1)\big)\frac{\mathrm{e}^{-\mathrm{i}\sqrt{z-\lambda_\alpha}|\boldsymbol{x}_\alpha|}}{|\boldsymbol{x}_\alpha|^{(n_\alpha-1)/2}}, \tag{3.31}$$

while for $\ell_\alpha = 0$ their asymptotics is exponentially decreasing,

$$\psi^\#_{\mathrm{res},\alpha}(\boldsymbol{x}_\alpha) \underset{\boldsymbol{x}_\alpha \to \infty}{=} C_\alpha(z, \ell_\alpha)\big(\widetilde{\mathcal{A}}_\alpha(\widehat{\boldsymbol{x}}_\alpha) + o(1)\big)\frac{\mathrm{e}^{+\mathrm{i}\sqrt{z-\lambda_\alpha}|\boldsymbol{x}_\alpha|}}{|\boldsymbol{x}_\alpha|^{(n_\alpha-1)/2}}, \tag{3.32}$$

where $\widetilde{\mathcal{A}}(\widehat{\boldsymbol{k}}_\alpha)$ stand for the corresponding components of the extended vector (3.29) *and*

$$C_\alpha(z, \ell_\alpha) = \sqrt{\frac{\pi}{2}}\,\mathrm{e}^{\mathrm{i}(n_\alpha-3)(2\ell_\alpha-1)\pi/4}\,(z-\lambda_\alpha)^{(n_\alpha-3)/4} \tag{3.33}$$

For the function $(z-\lambda_\alpha)^{\frac{n_\alpha-3}{4}}$ on the right-hand side of (3.33) *the main branch is chosen.*

Complete proof of this statement may be found in [25, Section 1.6].

The functions $\psi^\#_{\mathrm{res},\alpha}(x_\alpha)$ taken altogether form the Gamov vector corresponding to the resonance energy z (see, e.g. [15, 17]). Just asymptotic formulas (3.31) and (3.32) prove that the functions $\mathcal{A}_\alpha(\widehat{k}_\alpha)$, $\ell_\alpha \ne 0$, and $\widetilde{\mathcal{A}}_\alpha(\widehat{k}_\alpha)$, $\ell_\alpha = 0$, make sense of the breakup amplitudes describing decay of the resonant state along open and closed channels, respectively.

IV. THREE-BODY PROBLEM

In this section we give a sketch of our results on the structure of the T-matrix, scattering matrices, and Green function on unphysical energy sheets in the three-body problem. For detail exposition of this material see Refs. [21] or [25].

Let H_0 be the three-body kinetic energy operator in the center-of-mass system. Assume that there are no three-body forces and thus the total interaction reads $V = v_1 + v_2 + v_3$ where v_α, $\alpha = 1, 2, 3$, are the corresponding two-body potentials having just the same properties as in Sec. II.

The best way to proceed in the three-body case is to work with the Faddeev components [33]

$$M_{\alpha\beta} = \delta_{\alpha\beta} v_\alpha - v_\alpha G(z) v_\beta \quad (\alpha, \beta = 1, 2, 3)$$

of the T-operator $T(z) = V - VG(z)V$ where $G(z)$ denotes the resolvent of the total Hamiltonian $H = H_0 + V$. The components $M_{\alpha\beta}$ satisfy the Faddeev equations

$$M_{\alpha\beta}(z) = \delta_{\alpha\beta} \mathbf{t}_\alpha(z) - \mathbf{t}_\alpha(z) G_0(z) \sum_{\gamma \neq \alpha} M_{\gamma\beta}(z) \tag{4.1}$$

with $G_0(z) = (H_0 - z)^{-1}$ and

$$\mathbf{t}_\alpha(P, P', z) = t_\alpha(\boldsymbol{k}_\alpha, \boldsymbol{k}'_\alpha, z - \boldsymbol{p}_\alpha^2) \delta(\boldsymbol{p}_\alpha - \boldsymbol{p}'_\alpha)$$

where $\boldsymbol{k}_\alpha, \boldsymbol{p}_\alpha$ denote the corresponding reduced Jacobi momenta (see [21] for the precise definition we use) and $P = (\boldsymbol{k}_\alpha, \boldsymbol{p}_\alpha) \in \mathbb{R}^6$ is the total momentum.

Assume that any of the three two-body subsystems has only one bound state with the corresponding energy $\varepsilon_\alpha < 0$, $\alpha = 1, 2, 3$. Assume in addition that all of these three binding energies are different. It is easy to see that the thresholds ε_1, ε_2, ε_3, and 0 are associated with particular Cauchy type integrals in the integral equations (4.1). By Lemma 1 the two-body thresholds ε_α appear to be square-root branching points while the three-body threshold 0 is the logarithmic one. In order to enumerate the unphysical sheets we introduce the multi-index $\ell = (\ell_0, \ell_1, \ell_2, \ell_3)$ with $\ell_0 = \ldots, -1, 0, 1, \ldots$ and $\ell_\alpha = 0, 1$ if $\alpha = 1, 2, 3$. Clearly, only encircling the two-body thresholds one arrives at seven unphysical sheets. The three-body threshold generates infinitely many unphysical sheets. (There might also be additional branching points on the unphysical sheets, in particular due to two-body resonances.)

It turns out that the analytically continued Faddeev equations (4.1) can be explicitly solved in terms of the matrix $M = \{M_{\alpha\beta}\}$ itself taken only on the physical sheet, just like in the case of the two-body T-matrix in Sec. II and multichannel T-matrix in Sec. III. The result strongly depends, of course, on the unphysical sheet Π_ℓ concerned. More precisely, the resulting representation reads as follows

$$M|_{\Pi_\ell} = M + Q_M \, L \, S_\ell^{-1} \, \widetilde{L} \, \widetilde{Q}_M. \tag{4.2}$$

In the particular case we deal with, L and $\widetilde{L}$ are 4×4 diagonal scalar matrices of the form $L = \operatorname{diag}(\ell_0, \ell_1, \ell_2, \ell_3)$ and $\widetilde{L} = \operatorname{diag}(|\ell_0|, \ell_1, \ell_2, \ell_3)$, respectively; $S_\ell(z) = I + \widetilde{L}(S(z) - I)L$ is a truncation of the total scattering matrix $S(z)$ and the entries Q_M, $\widetilde{Q}_M$ are explicitly written in terms of the half-on-shell kernels of M (see formula (7.34) of [21]). From (4.2) one also derives explicit representations for $G(z|_{\Pi_\ell})$ and $S(z|_{\Pi_\ell})$ similar to those of (3.25) and (3.23), respectively.

Thus, to find resonances on the sheet Π_ℓ one should simply look for the zeros of the truncated scattering matrix $S_\ell(z)$, that is, for the points z on the physical sheet where equation $S_\ell(z)\mathcal{A} = 0$

has a non-trivial solution $\mathcal{A}$. The vector $\mathcal{A}$ will consist of amplitudes of the resonance state to breakup into the various possible channels. Within such an approach one can also find the three-body virtual states.

In order to find the amplitudes involved in S_ℓ, one may employ any suitable method, for example the one of Refs. [27–29] based on the Faddeev differential equations. In these works the approach we discuss has been successfully applied to several three-body systems. In particular, the mechanism of emerging the Efimov states in the ^{4}He trimer has been studied [27, 28].

Acknowledgments

The author kindly acknowledges support of this work by the Russian Foundation for Basic Research, the Deutsche Forschungsgemeinschaft (DFG) and the South African-JINR collaborative agreement.

---

[1] G. Gamow, Z. Phys. **51**, 204 (1928).
[2] R. Jost, Helv. Phys. Acta. **20**, 250 (1947).
[3] E.C. Titchmarsh, *Eigenfunction Expansions Associated with Second Order Differential Equations*, Vol. II (Oxford U. P., London, 1946).
[4] C. Lovelace, Phys. Rev. B **135**, 1225 (1964).
[5] E. Balslev and J.M. Combes, Commun. Math. Phys. **22**, 280 (1971).
[6] G.A. Hagedorn, Commun. Math. Phys. **65**, 181 (1979).
[7] E. Brändas and N. Elander (Eds.), *Resonances: The Unifying Route Towards the Formulation of Dynamical Processes — Foundations and Applications in Nuclear, Atomic, and Molecular Physics*, Lect. Notes Phys. **325** (Springer-Verlag, Berlin, 1989).
[8] D.V. Fedorov, E. Garrido, and A.S. Jensen, Few-Body Syst. **33**, 153 (2003).
[9] C.Y. Hu and A.K. Bhatia, Muon Catalyzed Fusion **5/6**, 439 (1990/91).
[10] V.I. Korobov, Phys. Rev. A **67**, 062501 (2003).
[11] N. Moiseyev, Phys. Rep. **302**, 211 (1998).
[12] P.D. Lax and R.S. Phillips, *Scattering Theory* (Academic Press, N.Y.–London, 1967).
[13] R. Mennicken and A. K. Motovilov, Math. Nachr. **201**, 117 (1999).
[14] A. Baz, Ya. Zeldovich, and A. Perelomov, *Scattering, Reactions and Decays in Nonrelativistic Quantum Mechanics* (Israel Program for Scientific Translations, Jerusalem, 1969).
[15] A. Böhm, *Quantum Mechanics: Foundations and Applications* (Springer-Verlag, 1986).
[16] V. de Alfaro and T. Regge, *Potential scattering* (North-Holland, Amsterdam, 1965).
[17] R.G. Newton, *Scattering Theory of Waves and Particles*, 2nd ed. (McGraw Hill, N. Y., 1982).
[18] M. Reed and B. Simon, *Methods of Modern Mathematical Physics, IV: Analysis of Operators* (Academic Press, N. Y., 1978).
[19] M. Reed and B. Simon, *Methods of Modern Mathematical Physics, III: Scattering Theory* (Academic Press, N. Y., 1979).
[20] K. Möller and Yu.V. Orlov, Fiz. Elem. Chast. At. Yadra **20**, 1341 (1989)(Russian).
[21] A.K. Motovilov, Math. Nachr. **187**, 147 (1997).
[22] J.S. Howland, Pacific J. Math. **55**:1, 157 (1974).
[23] B. Simon, Int. J. Quant. Chem. **14**, 529 (1978).
[24] A.K. Motovilov, Theor. Math. Phys. **97**, 692 (1993).
[25] A.K. Motovilov, *Theory of Resonances in Multichannel Systems*, D.Sc. Thesis (JINR, Dubna, 2006; in Russian).
[26] A.K. Motovilov, Fiz. Elem. Chast. At. Yadra **32**:7, 144 (2001) (in Russian).
[27] E.A. Kolganova and A.K. Motovilov, Comp. Phys. Comm. **126**, 88 (2000).
[28] E.A. Kolganova and A.K. Motovilov, Phys. Atom. Nucl. **62**, 1179 (1999).
[29] E.A. Kolganova and A.K. Motovilov, Phys. Atom. Nucl. **60**, 177 (1997).

[30] A.K. Motovilov, Few-Body Syst. **38**, 115 (2006).
[31] Yu. V. Orlov, Pis'ma v ZhETF **33**:7, 380 (1981)(in Russian).
[32] Yu.V. Orlov and V.V. Turovtsev, ZhETF **86**, 1600 (1984)(in Russian).
[33] L.D. Faddeev, *Mathematical Aspects of the Three-Body Problem in Quantum Mechanics* (Israel Program for Scientific Translations, Jerusalem, 1965).

Dynamics of Molecular Trimers: Configuration Space Faddeev Calculations

M.L. Lekala*

Department of Physics, University of South Africa,
P O Box 392, Pretoria 0003, South Africa

We present a method for solving the configuration space Faddeev equations as three-dimensional equations, i.e. without resorting to an explicit partial wave decomposition. The method is employed in bound state calculations to obtain vibrational states of several molecules consisting of three atoms.

I. INTRODUCTION

Clusters of molecules consisting of few atoms attract a great deal of attention in the past years by both theoreticians and experimentalists (see e.g. [1] and references therein). One of the reasons for this interest is the understanding of the dynamical behavior and properties of trimers under changing thermodynamical environment. This will enable us to shed some light of how the individual molecular properties are connected to the bulk behavior of materials such as the super-fluidity, phase transitions and phase coexistence, melting, *etc.*

Several methods have been used in the past to study the dynamics of trimers. These methods follow, in general, a two-step process, namely: First, the wave function is expanded in terms of some finite basis representation, from which the potential energy surfaces are extracted (known as adiabatic potentials). Second, once the potential energy surfaces are obtained, the bound and scattering states are calculated. However, the underlying pairwise van der Waal forces for molecular trimers have a hard repulsive core and the accuracy of adiabatic approximations is not guaranteed. Furthermore, the strong repulsive potential gives rise, in turn, to strong two-body correlations and, therefore, to obtain converged results, a large number of partial waves must be included. As a result, one has to deal with a huge computational problem that makes the calculations difficult and tedious.

In the present work we employed the three-dimensional three-body Faddeev-type equations in configuration space within the framework of the total-angular-momentum representation [2, 3] thus avoiding the cumbersome partial wave decomposition.

This paper is organized as follows. In Sec. II we briefly discuss the formalism of the Faddeev equations, whereas in Sec. III the numerical method employed is presented. Various aspects of the method as applied to noble-gas trimers are discussed here, with more emphasis given to numerical stabilities especially when three-molecular forces are included. The results of calculations for the various systems considered are presented in Sec. IV. Concluding remarks are passed in Sec. V.

II. FADDEEV EQUATIONS

We consider a bound system of three non-relativistic particles α, β, and γ, in the presence of both two- and three-body forces. Kinematically the system is described in terms of a set of

*Electronic address: lekala@science.unisa.ac.za

Jacobi coordinates, schematically shown in Fig. 1, defined in terms of the particle masses as follows [4]

$$\mathbf{r}_\alpha = \sqrt{\frac{2m_\beta m_\gamma}{m_\beta + m_\gamma}}(\mathbf{r}_\beta - \mathbf{r}_\gamma) \tag{1}$$

$$\rho_\alpha = \sqrt{\frac{2m_\alpha(m_\beta + m_\gamma)}{m_\alpha + m_\beta + m_\gamma}}\left(\mathbf{r}_\alpha - \frac{m_\beta \mathbf{r}_\beta + m_\gamma \mathbf{r}_\gamma}{m_\beta + m_\gamma}\right) \tag{2}$$

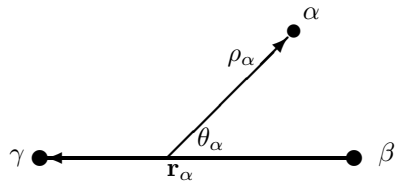

FIG. 1: Jacobi coordinates for three particles

The different Jacobi coordinates are related to each other and are obtained via cyclic permutation as

$$\begin{pmatrix} \mathbf{r}_\beta \\ \\ \rho_\beta \end{pmatrix} = \begin{pmatrix} C^{11}_{\beta\alpha} & C^{12}_{\beta\alpha} \\ \\ C^{21}_{\beta\alpha} & C^{22}_{\beta\alpha} \end{pmatrix} \begin{pmatrix} \mathbf{r}_\alpha \\ \\ \rho_\alpha \end{pmatrix} \tag{3}$$

where the coefficients $C^{ij}_{\beta\alpha}$ are functions of the masses of the particles, given by

$$C^{11}_{\beta\alpha} = \sqrt{\frac{m_\beta m_\alpha}{(m_\alpha + m_\gamma)(m_\beta + m_\gamma)}}\,, \tag{4}$$

$$C^{12}_{\beta\alpha} = (-1)^{\alpha-\beta}\mathrm{sign}(\alpha - \beta)\sqrt{\frac{m_\gamma(m_\alpha + m_\beta + m_\gamma)}{(m_\alpha + m_\gamma)(m_\beta + m_\gamma)}} \tag{5}$$

with $C^{22}_{\beta\alpha} = C^{11}_{\beta\alpha}$ and $C^{21}_{\beta\alpha} = -C^{12}_{\beta\alpha}$.

The Hamiltonian for the systems in the presents of both two- and three-body forces reads

$$\mathrm{H}_3 = \mathrm{H}_0 + \sum_i v_i^{(\mathrm{2BF})} + V^{(\mathrm{3BF})}\,; \qquad\qquad i = \alpha, \beta, \gamma \tag{6}$$

and leads to a set of coupled differential Faddeev-type equations

$$\left[\mathrm{H}_0 + v_i^{(\mathrm{2BF})}(\mathbf{r}_i) + V^{(\mathrm{3BF})}(\mathbf{r}_i, \rho_i) - E_3\right]\Phi_i(\mathbf{r}_i, \rho_i) = -v_i^{(\mathrm{2BF})}(\mathbf{r}_i)\sum_{j\neq i}\Phi_j(\mathbf{r}_j, \rho_j) \tag{7}$$

where $i, j = \alpha, \beta, \gamma$, Φ_i is the i^{th} Faddeev component describing the subsystem $(j, k), i \neq j, k$, and H_0 is the free Hamiltonian; $v_i^{(\mathrm{2BF})}$ and $V^{(\mathrm{3BF})}$ are the two- and three-body potentials respectively while E_3 is the binding energy. As usual the total wave function Ψ_3 for the system is given by

$$\Psi_3(\mathbf{r}_i, \rho_i) = \sum_i \Phi_i(\mathbf{r}_i, \rho_i)\,, \qquad i = \alpha, \beta, \gamma \tag{8}$$

A. Total-angular-momentum representation

When the particles interact via spherically symmetric forces, the Hamiltonian commutes with the total orbital angular momentum, and one of its projection. As a result the separation of variables describing the rotation of the system as a whole and the intrinsic variables defined by the size of the triangle formed by the three-particles is possible. Accordingly, following [2, 3], Φ can be expanded in terms of the Wigner functions $\mathcal{D}^L_{\alpha M_L M}(\zeta_\alpha, \vartheta_\alpha, \varphi_\alpha)$ (i.e. eigenfunctions of the total angular momentum L) as follows

$$\Phi_\alpha(\mathbf{r}_\alpha, \rho_\alpha) = \sum_{L, M_L, M} \frac{\phi^L_{\alpha M_L M}(r_\alpha, \rho_\alpha, z_\alpha)}{r_\alpha \rho_\alpha} \mathcal{D}^L_{\alpha M_L M}(\zeta_\alpha, \vartheta_\alpha, \varphi_\alpha)\,, \tag{9}$$

where $\phi^L_\alpha(r_\alpha, \rho_\alpha, z_\alpha)$ are the projections of the Faddeev components (sometimes called Faddeev amplitudes) on subspaces with a fixed angular momentum L, and r_α, ρ_α are the magnitudes of the Jacobi vectors, i.e. $r_\alpha = |\mathbf{r}_\alpha|$, etc.; $z_\alpha = (\mathbf{r}_\alpha \cdot \rho_\alpha)/r_\alpha\rho_\alpha$ is the angle between the two Jacobi vectors, and $z_\alpha \in (-1, 1)$. The corresponding projected free Hamiltonian is

$$\mathrm{H}^L_0 = \mathcal{D}^L_{\alpha M_L M}(g^{-1}_\alpha) r_\alpha \rho_\alpha \mathrm{H}_0 \frac{1}{r_\alpha \rho_\alpha} \mathcal{D}^L_{\alpha M_L M}(g_\alpha)\,, \tag{10}$$

where $g_\alpha = (\zeta_\alpha, \vartheta_\alpha, \varphi_\alpha)$ stands for the coordinates describing the angular motion of the system. Substituting Eq. (9) into Eq. (7) and projecting on the subspace of the fixed angular momentum L, one obtains

$$\left[\mathrm{H}^L_0 + v^{(2\mathrm{BF})}_\alpha(r_\alpha) + V^{(3\mathrm{BF})}(r_\alpha, \rho_\alpha, z_\alpha) - E_3\right] \phi^L_\alpha(r_\alpha, \rho_\alpha, z_\alpha) = -v^{(2\mathrm{BF})}_\alpha(r_\alpha) \sum_{\beta \neq \alpha} \phi^L_\beta(r_\beta, \rho_\beta, z_\beta) \tag{11}$$

Equations (11) are the Faddeev equations in the total-angular-momentum representation. They describe three-body states with fixed total angular momentum L, leading to a set of $(6L + 3)$ coupled three-dimensional partial differential equations.

For identical particles (i.e. $m_\alpha = m_\beta = m_\gamma$) and for $L = 0$ the different Faddeev amplitudes are related as follows

$$\phi^0_\beta(r_\beta, \rho_\beta, z_\beta) \;=\; P^+ \phi^0_\alpha(r_\alpha, \rho_\alpha, z_\alpha) = r_\alpha \rho_\alpha \frac{\phi^0(r^+_\alpha, \rho^+_\alpha, z^+_\alpha)}{r^+_\alpha \rho^+_\alpha}\,, \tag{12}$$

$$\phi^0_\gamma(x_\gamma, y_\gamma, z_\gamma) \;=\; P^- \phi^0_\alpha(r_\alpha, \rho_\alpha, z_\alpha) = r_\alpha \rho_\alpha \frac{\phi^0(r^-_\alpha, \rho^-_\alpha, z^-_\alpha)}{r^-_\alpha \rho^-_\alpha}\,, \tag{13}$$

where P^+ (P^-) is the cyclic (anticyclic) permutation operator acting on the coordinates. The coordinates $r^\pm$, $\rho^\pm$, $z^\pm$ are given by

$$r^\pm(r, \rho, z) \;=\; \left(\frac{1}{4} r^2 + \frac{3}{4}\rho^2 \mp \frac{\sqrt{3}}{2} r\rho z\right)^{1/2} \tag{14}$$

$$\rho^\pm(r, \rho, z) \;=\; \left(\frac{3}{4} r^2 + \frac{1}{4}\rho^2 \pm \frac{\sqrt{3}}{2} r\rho z\right)^{1/2} \tag{15}$$

$$z^\pm(r, \rho, z) \;=\; \frac{\pm\frac{\sqrt{3}}{4} r^2 \mp \frac{\sqrt{3}}{4}\rho^2 - \frac{1}{2} r\rho z}{r^\pm(r, \rho, z)\rho^\pm(r, \rho, z)}\,, \tag{16}$$

where the subscript α, which is redundant for identical particles, is dropped. Substitution of Eqs. (12) and (13) into (11) leads to a single equation for the amplitude ϕ^0, namely

$$\left[\mathrm{H}_0^0 + v^{(2\mathrm{BF})}(1 + P^+ + P^-) + V^{(3\mathrm{BF})} - E_3\right]\phi^0(r,\rho,z) = 0\,, \tag{17}$$

where the arguments have been suppressed for clarity. Also

$$\mathrm{H}_0^0 = -\frac{\partial^2}{\partial r^2} - \frac{\partial^2}{\partial \rho^2}\left(\frac{1}{r^2} + \frac{1}{\rho^2}\right)\frac{\partial}{\partial z}(1-z^2)^{1/2}\frac{\partial}{\partial z} \tag{18}$$

In the case of non-identical particles (e.g. $m_\alpha = m_\beta \neq m_\gamma$), Eq. (11) has two independent Faddeev solutions, i.e. ϕ_γ associated with the (α,β) subsystem and ϕ_α associated with the pair (β,γ). The third component ϕ_β, associated with the subsystem (γ,α), is obtained from ϕ_α by a simple rotation of the coordinate space. Thus, in this case one solves a set of two coupled equations for the amplitudes.

III. NUMERICAL METHOD

Our objective is to obtain a regular solution to the set of coupled differential equations (11) or equivalently Eq. (17) for identical particles. To this end ϕ is expanded in terms of a set of square integrable basis functions S_i [5]

$$\phi(r,\rho,z) = \sum_{l=1}^{L}\sum_{m=1}^{M}\sum_{n=1}^{N}\mathcal{C}_{lmn}\mathrm{S}_l(r)\mathrm{S}_m(\rho)\mathrm{S}_n(z)\,. \tag{19}$$

The subscripts (L, M, N) refer to the number of basis functions in the three variables (r,ρ,z), respectively. Substituting Eq. (19) into Eq. (17), followed by the orthogonal collocation procedure [6] gives a system of linear algebraic equations

$$[\hat{\mathrm{H}}_1 + \hat{\mathrm{H}}_2 - E_3\hat{I}]\mathcal{C} = 0\ , \tag{20}$$

for the expansion coefficients $\mathcal{C}$, where $\hat{\mathrm{H}}_1 = \hat{\mathrm{H}}_0 + \hat{v}^{(2\mathrm{BF})} + V^{(3\mathrm{BF})}$ and $\hat{\mathrm{H}}_2 = \hat{v}^{(2\mathrm{BF})}(\hat{P}^+ + \hat{P}^-)$. Treating E_3 as a parameter, (20) is turned into an eigenvalue equation

$$-(\hat{\mathrm{H}}_1 - E_3\hat{I})^{-1}\hat{\mathrm{H}}_2\mathcal{C} = \Lambda(E_3)\mathcal{C}\,, \tag{21}$$

where $\Lambda(E_3)$ is the eigenvalue, and for physical solutions $\Lambda(E_3) = 1$.

A. Discussion on Convergence Properties of the Method

The problem of obtaining eigensolutions to Eq. (21) is equivalent to that of finding the discrete spectrum of the operator

$$\hat{\mathcal{F}} = -(\hat{\mathrm{H}}_1 - E_3\hat{I})^{-1}\hat{\mathrm{H}}_2\,. \tag{22}$$

which can be realized using standard methods for large matrices such as the iterative Arnoldi method. In the nuclear case, due to the short-ranged nature of the forces, the Arnoldi method works satisfactorily for a wide range of potentials. However, in the case of molecular trimers, the

underlying interatomic potentials are for all practical purposes of hard-core nature. This leads to several problems. For example, in the case of trimers relatively larger than the helium trimer, the spectra contain in general a large number of positive and negative eigenvalues, some of which lie very close to one. The large number of negative eigenvalues suppresses the convergence of the Arnoldi algorithm. On the other hand, the existence of several eigenvalues close to one makes it difficult to pinpoint a physical solution.

To address the aforementioned convergence problems we adopt the approach described in Refs. [5, 7], in which the negative eigenvalues are eliminated from the spectrum by considering instead of $\hat{\mathcal{F}}$ the spectrum of the operator

$$\hat{\mathcal{M}}(z) = (\hat{\mathrm{H}}_0 + \hat{V} + \hat{V}_m - z)^{-1}(\hat{V}_m - \hat{V}\hat{P})\,, \tag{23}$$

where $\hat{V}_m$ is a strong short-ranged potential. Of importance is that the positive eigenvalues of $\hat{\mathcal{M}}$ in the vicinity of 1 are identical to those of $\Lambda_{i,\mathcal{F}} = 1$, and are independent of the modifying potential. On the other hand, the eigenvalues $\mu_i(z_i) = -1$ correspond to eigenvalues of the equation

$$[\hat{\mathrm{H}}_0 + 2\hat{V}_m + \hat{V}(1 - \hat{P}) - z_i]\mathcal{C} = 0\,, \tag{24}$$

and depend on the modifying potential $\hat{V}_m$. Thus by a proper choice of $\hat{V}_m$ they can be eliminated. According to Arnoldi algorithm convergence estimations, see for example [8], this feature of $\hat{\mathcal{M}}$ should improve dramatically the convergence of the eigenvalues.

The aforementioned features can be demonstrated by considering the spectra of $\mathcal{F}$ and $\mathcal{M}$, for the strongly repulsive LM2M2 potential in the case of helium trimer, shown in Fig. 2 and Fig. 3, respectively.

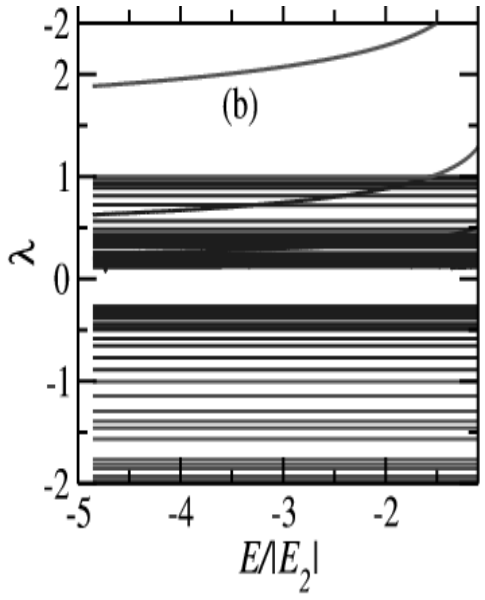

FIG. 2: Spectrum of $\mathcal{L}(E)$ for the LM2M2 potential as given in Ref. [5].

B. Diagonalization

Due to the large sizes of the matrices involved, it is not easy to solve directly the eigenvalue problem (21). To address this problem we use the tensor-trick technique [9]. According to

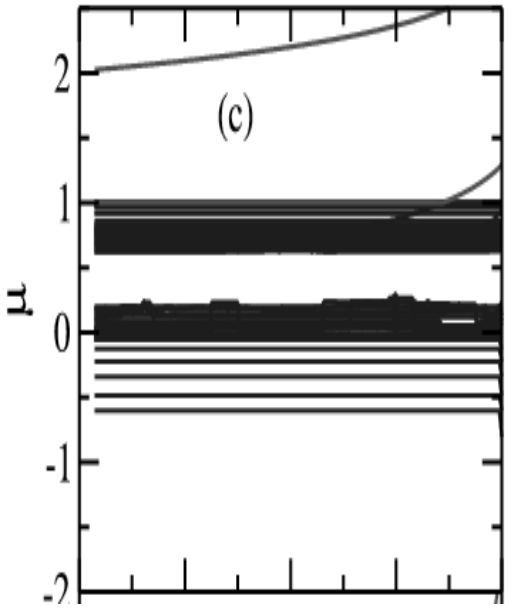

FIG. 3: Same as in Fig. 2 but for $\mathcal{M}(E)$.

this technique diagonalization can be simplified if the matrix $(\hat{\mathrm{H}}_1 - E_3\hat{I})^{-1}$ can be written as a product of simpler matrices. For example, following [7], we write

$$(\hat{\mathrm{H}}_1 - E_3\hat{I})^{-1} = \hat{B}\hat{G}^{-1}\hat{B}^* \,, \tag{25}$$

which has a band structure, and where the matrix $\hat{B}$ is given

$$\hat{B} \equiv \prod_{i=1}^{N_z} \oplus(\hat{B}_r^i \otimes \hat{B}_\rho^i) \otimes [\hat{B}_z]_i \,, \tag{26}$$

and $\hat{G}$ is diagonal matrix $\hat{G} = \mathrm{diag}\{g_{111}, g_{112}, \cdots, g_{i_r i_\rho i_z}, \cdots g_{N_r N_\rho N_z}\}$ with $g_{i_r i_\rho i_z}$ given by $g_{i_r i_\rho i_z} = E^{i_z}_{r i_\rho} + E^{i_z}_{r i_\rho} - E_3$.

In this work, we solve the eigenvalue problem using the Restarted Arnoldi algorithm.

C. Minimization Approach

In cases where a plethora of closely lying states exist, such as in the case of the Ozone molecule considered in this work, convergence challenges increase formidably. As a result it becomes practically impossible to discriminate levels definitely. In order to address this question we employed an optimization method called MERLIN [10]. Merlin is an optimization package and supports many optimization algorithms such as direct, gradient, and conjugate gradient methods. Examples of the first type of methods include the Simplex method, and gradient methods include the so-called BFGS update methods. The Fletcher-Reeves and Polak-Ribiere methods are examples of conjugate gradient methods included. The combination of these strategies that makes MERLIN highly effective and robust, in contrast to, for example, library routines that implement a single algorithm.

The Merlin optimization is applied to solve Faddeev equations by transforming eigenvalue problem (21) into a minimization problem as follows

$$I(E_\lambda; \mathbf{p}) = \frac{\sum_i [\mathcal{F}\phi_\lambda(r_i, \rho_i, z_i; \mathbf{p}) - \Lambda_\lambda(E_\lambda)\phi_\lambda(r_i, \rho_i, z_i; \mathbf{p})]^2}{\sum_i [\phi_\lambda(r_i, \rho_i, z_i; \mathbf{p})]^2} \,, \tag{27}$$

where the trial eigenfunction ϕ_λ is defined on the collocation points (r_i, ρ_i, z_i), and $\mathbf{p}$ is the parameter vector.

D. Algorithm Implementation

The choice of the r-grid is very crucial in the implementation of our algorithm. This grid must be optimized to always reproduce the two-body binding. This is achieved by dividing the space $\Omega_r = [a_0, r_{\max}]$ (a_0 is the first nonzero grid point from $r = 0$) into two sub-domains, namely, the interior domain $\Omega_{r,I}$ and the exterior domain $\Omega_{r,J}$, separated by some carefully chosen break-point r_B carefully chosen to eliminate numerical noise associated with the $r \to 0$ behavior. That is, we partition as follows: $a_0 = r_0 < r_1 < \cdots < r_B < \cdots < r_{N_r} = r_{\max}$. In general, $\Omega_{r,I}$ is relatively dense compared to $\Omega_{r,J}$. Moreover, it must have small separation between grid points, and contain a sufficient number of points to describe well the most important ranges affecting the physical quantities involved. In other words the grid must be constructed such that the density of the points is higher where the wave functions are important. For bound states, the wave function has more structure at small values of r. In this work, it was found that the transformation

$$r_{i+1} = a_0 + i\delta r_i^{(I)}, \qquad i = 1, 2, \cdots, N_{r,I} - 1, \tag{28}$$

$$r_i = r_{i-1} + \delta r_i^{(J)}, \quad i = N_{r,I}, \cdots, N_r, \tag{29}$$

where the $\delta r_i{}'$s are the scaling functions, and $N_{r,I}$ is the number of interior points in the domain $\Omega_{r,I}$, fulfills the requirements described. As a rule of thumb the break point r_B is chosen in such a way that roughly two-thirds of the r-grid points are interior points. The ρ-grid is defined similarly with $\Omega_{\rho,I}$.The z-grid, $z_0 < z_1 < \cdots < z_{N_z}$, is obtained by the transformation

$$z_i = g(t_i), \qquad i = 0, \cdots\cdots, N_z, \tag{30}$$

where $t_i = -1 + i\delta z$ and the function g is given by $g(t) = (t + C_0 t^3)/(1 + C_0)$, with $z_0 = -1$ and $z_{N_z} = 1$, and the control parameter is chosen within $-1 < C_0 \leq 0$.

We interpolate using the quintic Hermite splines. We employ the orthogonal collocation method with three Gaussian quadrature points per subinterval. This means that for a basic grid with N points there are $(3N + 3)$ collocation points. Once the collocation points are obtained, the matrix elements of the operators in (17) are easily constructed, leading to $(3N+3)$ equations. However, in the r and ρ direction, collocation method supplemented by the boundary conditions reduces the number of equations from $3N + 3$ to $3N$. For the z coordinate the number remains $3N_z + 3$. Thus the dimension of the system of equations to be solved is rather large and equals $N_T = 3N_r \times 3N_\rho \times 3(N_z + 1)$.

IV. RESULTS AND DISCUSSION

We calculated the binding energies for the $^4He_3$, $^{40}Ar_3$, and the Ozone molecule. In the case of $^4He_3$ only two-body interactions are employed since it is known three-body forces contribute $<1\%$ to the binding [11]. We used HFD-B, LM2M2 potentials [12], and the so-called TTY potential of Tang *et. al* [13]. Our converged results are given in Table I, where N_r (N_ρ, N_z) refers to the number of the mesh points for the $r-$ $(\rho-, z-)$ grid. For the HFD-B potential, our results are compared with those of Refs. [5, 14], both of which use forms of the differential Faddeev equations, and of Refs. [11, 15] in which hyperspherical harmonics expansion methods are used.

In the case of Ar_3, we use the HFD-C potential [13] for the two-body force. For the three-body forces we consider the first few dominant ones, namely triple-dipole (DDD), dipole-dipole-quadrupole (DDQ), and dipole-quadrupole-quadrupole (DQQ). With these inputs we calculate systematically the low-lying states for the trimer. In Table II we present our results. We used $\hbar^2/\mu = 1.21381149\,\mathrm{K}\cdot\mathrm{\AA}^{-2}$. The results compared well with those of [16, 17].

Finally, we calculated the low-lying states for the Ozone molecule. Here, we use the potential given in [18] for two-body forces, and the dominant tripole dipole forces [19] for three-body potential. The results are given in Table III.

V. CONCLUSIONS

We presented a reliable three-dimensional method for solving The Faddeev-type equations applied to molecular three-body bound state problems. The method is applied to obtain spectra for various trimers.

We calculated the binding energies for the ground state and some low-lying excited states for heavier trimers using two- and three-body potentials. The results obtained using a combination of two- and three-body forces are in fair agreement with, e.g. those of Refs. [16] and [17], which were obtained using different formalisms. It is thus clear that the Faddeev-type formalism employed here is suitable for studies of trimers and the question of handling the multitude of coupled equations for the various partial waves can be avoided by solving the three-dimensional equations directly. Finally, our results show that three-body forces have a significant contribution, especially in heavier molecular trimers, to the binding should, in general, be included.

TABLE I: The binding energies (in K) of the ground state $^4He_3$ for the potentials: HFD-B, LM2M2, and TTY. The top part of the table gives results obtained in this work as a function of the grid sizes. The bottom part of the table give results obtained by others using different methods.

N_r	N_ρ	N_z	HFD-B	LM2M2	TTY
50	50	3	-0.1385316	-0.1218115	-0.1209365
100	100	3	-0.1350168	-0.1269019	-0.1268981
150	150	3	-0.1324774	-0.12641587	-0.12642109
200	200	3	-0.1321926	-0.12641020	-0.12641001
	Ref. [11]		–	-0.1061	–
	Ref. [15]		–	-0.1252	–
	Ref. [14]		-0.131	–	–
	Ref. [5]		-0.13298	-0.1264	-0.1264

TABLE II: The binding energies (in eV) for the Ar_3 obtained with HFD-C as a pairwise potential (v_{2BF}) and with a combination of v_{2BF} and the DDD, DDQ, and DQQ three-body forces.

ν	v_{2BF}	v_{2BF}+DDD	v_{2BF}+DDD+DDQ	v_{2BF}+DDD+DDQ+DQQ
0	-0.0327	-0.0363	-0.0381	-0.0381
1	-0.0295	-0.0325	-0.0340	-0.0343
2	-0.0262	-0.0291	-0.0305	-0.0311
3	-0.0246	-0.0270	-0.0283	-0.0290

TABLE III: The binding energies (in eV) for the Ozone obtained with pairwise potential (v_{2BF}) and DDD three-body forces.

ν	v_{2BF} ($\times 10^2$)	v_{2BF}+DDD ($\times 10^2$)
0	-0.1005	-0.1342
1	-0.0990	-0.1209
2	-0.0851	-0.1143
3	-0.0809	-0.1129
4	-0.0800	-0.1052

[1] D. E. Manolopoulos, J. Chem. Soc. Faraday Trans. **93**, 673 (1997).
[2] V.V. Kostrykin, A.A. Kvitsinsky, and S.P. Merkuriev, Few-Body Systems **6**, 97 (1989).
[3] A.A. Kvitsinsky, V.V. Kostrykin, and S.P. Merkuriev, Sov. J. Part. Nucl. **21**, 553 (1990).
[4] L.D. Faddeev and S.P. Merkuriev, *Quantum Scattering Theory for Several Particle Systems* (Kluwer, Dordrecht, 1993).
[5] V.A. Roudnev, S.L. Yakovlev, and S.A. Sofianos, Few-Body Systems **37**, 179 (2005).
[6] C. de Boor, B. Swartz, SIAM J. Numer. Anal. **10**, 582 (1973).
[7] V. Roudnev and S. Yakovlev, Comp. Phys. Comm. **126**, 162 (2000).
[8] Y. Saad, Numerical Methods for Large Eigenvalue Problems, (*Algorithms and Architectures for Advanced Scientific Computing*, New York, Manchester University Press, 1992).
[9] N.W. Schellingerhout, L.P. Kok, and G.D. Bosveld, Phys. Rev. A **40**, 5568 (1989); L.P. Kok, N.W. Schellingerhout, Few-Body Systems **11**, 99 (1991).
[10] D.G. Papageorgiou, I.N. Demetropoulos, and I.E. Lagaris, Comput. Phys. Commun. **109**, 227 (1998).
[11] B.D. Esry, C.-D. Lin, and C.H. Greene, Phys. Rev. **54**, 394 (1996).
[12] R.A. Aziz and M.J. Slaman, J. Chem. Phys. **94**, 8047 (1991); R.A. Aziz, J. Chem. Phys. **99**, 4518 (1993).
[13] K.T. Tang, J.P. Toennis, and C.L. Yiu, Phys. Rev. Lett. **74**, 1546 (1995).
[14] A.K. Motovilov, S.A. Sofianos, and E.A. Kolganova, Chem. Phys. Lett. **275**, 168 (1997).
[15] E. Nielsen, D.V. Fedorov, and J.S. Jensen, J. Phys. **B31**, 4085 (1998).
[16] D.M. Leitner and J.D. Doll, J. Chem. Phys. **94**, 6644 (1994); D.M. Leitner, J.D. Doll, and R.M. Whitnell, J. Chem. Phys., **94**, 6644 (1991).
[17] A.R. Cooper and J.M. Hutson, J. Chem. Phys. 98, 2160 (1998); A.R. Cooper, S. Jain, and J. M. Hutson, J. Chem. Phys. **98**, 2160 (1993).
[18] J.N. Murrell, S. Carter, S.C. Farantos, P. Huxley, and A.J.C. Varandas, *Molecular Potential Energy Functions*, (John Wiley & Sons, 1984).
[19] B.M. Axilrod and E. Teller, J. Chem. Phys. 11, 2299 (1943).

Towards Multi-Band Inversion in Semiconductor Heterostructures

André E. Botha*

Physics Department, P.O. Box 392, University of South Africa, 0003

The relationship between two well-known methods in physics is studied: the $\boldsymbol{k}\cdot\boldsymbol{p}$ method for semiconductors and the Marchenko inversion method from nuclear physics. Two possibilities are suggested for adapting the coupled-channel Marchenko method to the design of semiconductor heterostructures. Some preliminary results are presented for a 2-band model.

I. INTRODUCTION

In view of ongoing research into new, potentially useful, spintronic devices, which can be manufactured from carefully designed semiconductor heterostructures, it is currently of interest to investigate whether well-established techniques in nuclear physics can be applied profitably to the emerging fields of spintronics [1, 2] and heterostructure design via inversion [3, 4].

In nuclear physics the inverse scattering problem on the line has received numerous theoretical treatments and several important questions concerning the inversion procedure have been addressed successfully. These include the numerical solution of the Marchenko integral equation for constant effective mass, dealing with bound states and the successful solution of the coupled-channel problem with thresholds and bound states [4].

In semiconductor physics however, only limited use has been made of inverse scattering techniques in one dimension; despite their huge prospects for the design of heterostructures [5, 6]. Notwithstanding the old problem of phase reconstruction [7], the lack of progress may be attributed to the fundamental difference between the nuclear and semiconductor cases. In the latter case the inversion procedure must take into account the periodic nature of the semiconductor lattice potential, which gives rise to interband $\boldsymbol{k}\cdot\boldsymbol{p}$ coupling. In heterostructures with abrupt transitions from one material to another, the degree of interband coupling may not be the same in each constituent bulk material. The inverse problem is thus considerably more complicated. It consists not only of determining the heterostructure profile, but also of finding the key material dependent $\boldsymbol{k}\cdot\boldsymbol{p}$ parameters that govern the electron transport. Since both the $\boldsymbol{k}\cdot\boldsymbol{p}$ method [8–11] and Marchenko inversion [12–15] are well documented in the literature, a review of these two methods will not be provided here.

In the present article, inversion in semiconductor heterostructures is considered. Section II starts with a brief review of recent developments in single-band inversion. A solution to the important problem of variable effective mass is recalled. In Sec. III a general formalism is developed for solving the multi-band $\boldsymbol{k}\cdot\boldsymbol{p}$ equation. The formal similarity between the coupled-channel Schrödinger equation (in the nuclear case) and the multi-band $\boldsymbol{k}\cdot\boldsymbol{p}$ equation (in the semiconductor case), facilitates the derivation of a modified Riccati equation which can be used to calculate the reflection matrix. Although the Riccati equation is well-known in nuclear physics, the basic technique presented in Sec. III is entirely new to semiconductor physics. In Sec. IV an important question is posed: Is it possible to extend the coupled-channel Marchenko inversion method to include the interband coupling in semiconductors? Due to the complexity of this question it remains, for the moment, unanswered. However, at the end of Sec. IV, two possible ways forward are suggested. Finally, in Sec. V some preliminary numerical results are

*Electronic address: bothaae@unisa.ac.za

presented for a two-band model. These results will serve as input to the anticipated solution of the multi-band inverse problem in semiconductor heterostructures.

II. SINGLE-BAND INVERSION WITH VARIABLE EFFECTIVE MASS

As a first approximation the time independent Schrödinger equation for a single electron inside a semiconductor heterostructure can be written as

$$-\frac{1}{2m_0}\varphi''(z) + V_S(z)\,\varphi(z) = E\varphi(z)\ . \tag{1}$$

In this approximation the electron is assumed to have a constant effective mass m_0 throughout the entire heterostructure. The objective of inversion is to recover the potential profile $V_S(z)$ from either of the two reflection amplitudes, $R_\pm(k)$. For a constant effective mass the inversion of Eq. (1) is well known [12].

In real heterostructures however, the effective mass of the electron varies from one material to the next. Therefore, a better approximation consists of writing the effective mass as $m_0 m(x)$, where $m(x)$ is a function of position along the growth direction of the heterostructure. In this

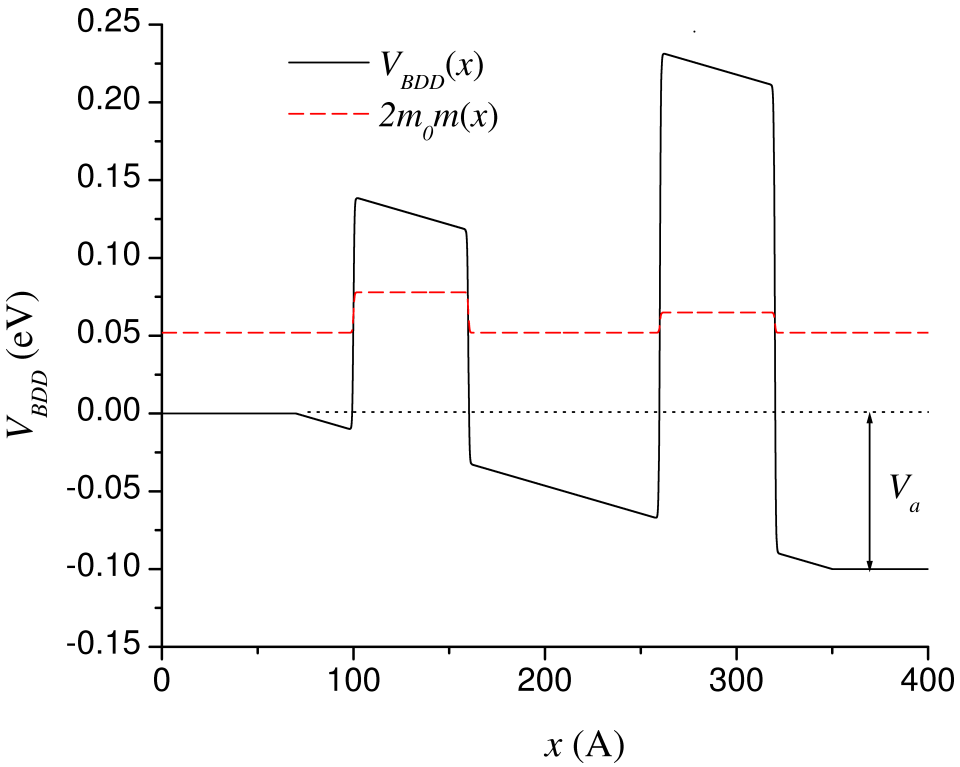

FIG. 1: Potential profile and variable effective mass $m_0 m(x)$ for a biased heterostructure. V_a is an applied (bias) potential.

case the Hermiticity of the kinetic energy operator can be ensured by writing the Schrödinger equation in the BenDaniel-Duke form [11]

$$-\frac{1}{2m_0}\left[\frac{\chi'(x)}{m(x)}\right]' + V_{BDD}(x)\,\chi(x) = E\chi(x)\ . \tag{2}$$

It is possible to transform Eq. (2) into the form of Eq. (1) via a unitary transformation, effected by [7]

$$\chi(x) = m_0 \sqrt{X'(x)}\varphi(z) \ , \tag{3}$$

with $z = X(x)$. Differentiating $\chi(x)$ with respect to x gives

$$\chi'(x) = \frac{m_0}{2}\left[X'(x)\right]^{-\frac{1}{2}} X''(x)\,\varphi(z) + m_0\left[X'(x)\right]^{\frac{3}{2}} \frac{\mathrm{d}\varphi}{\mathrm{d}z} \ . \tag{4}$$

Dividing Eq. (4) by $2m_0\left[X'(x)\right]^2$, differentiating a second time and making use of Eq. (1), then produces

$$-\frac{1}{2m_0}\left[\frac{\chi'(x)}{\left[X'(x)\right]^2}\right]' + \underbrace{\left(V_S(X(x)) + \frac{X'''(x)}{4\left[X'(x)\right]^3} - \frac{5\left[X''(x)\right]^2}{8\left[X'(x)\right]^4}\right)}_{V_{BDD}(x)}\chi(x) = E\chi(x) \ . \tag{5}$$

Equation (5) has the same form as Eq. (2), provided the identification $m(x) = \left[X'(x)\right]^2$ is made. Thus, as long as $m(x) \geq 0$, it is possible to map the problem of inverting Eq. (2), for an unknown potential $V_{BDD}(x)$, to an equivalent, much simpler problem of inverting Eq. (1) to obtain the potential $V_S(z)$. By solving a differential equation for the monotonically increasing function $X(x)$, the potential $V_{BDD}(x)$ can be recovered from

$$V_{BDD}(x) = V_S(X(x)) + \frac{X'''(x)}{4\left[X'(x)\right]^3} - \frac{5\left[X''(x)\right]^2}{8\left[X'(x)\right]^4} \ . \tag{6}$$

As an example of the above procedure, the transmission probability corresponding to the heterostructure in Fig. 1 has been plotted as a function of electron energy, in Fig. 2. The equivalent constant effective mass potential, as calculated from Eq. (6), is shown in Fig. 3. Note that the potential profiles shown in Figs. 1 and 3 both produce the transmission probability shown in Fig. 2. In Fig. 3 it can be seen that the equivalent constant effective mass potential is considerably more demanding, from a numerical point of view, than the variable effective mass potential. The height of the peaks in the equivalent potential, at each interface, depends on the sharpness of the transition in effective mass. In Fig. 3 the peaks are unusually high because the transition in effective mass takes place over a distance of approximately 1 Å (cf. Fig. 1), which is less than the lattice constant ($a \approx 6$ Å) for a typical III-V semiconductor.

Even though a numerical implementation of the above inversion procedure is possible, it should be borne in mind that the variable effective mass model can only provide qualitative information about the electron tunneling in heterostructures. It can be shown that a two-band model is the *minimum* structure that can quantitatively model the dominant physical process in electron tunneling, i.e. interband coupling. Therefore, any multi-band inversion procedure, even for two bands, would indeed be very useful for more realistic heterostructure design.

III. MULTI-BAND RICCATI METHOD FOR CALCULATING $\boldsymbol{R}(E)$

In the multi-band case the inverse problem starts from a reflection matrix $\boldsymbol{R}(E)$. To develop the theory one thus needs a reliable method of calculating $\boldsymbol{R}(E)$.

The following multi-band Riccati method is based on the multi-band $\boldsymbol{k}\cdot\boldsymbol{p}$ equation. Its main advantage is that, unlike the transfer matrix method for example, the Riccati method has been found to work extremely well in type-II heterostructures [16].

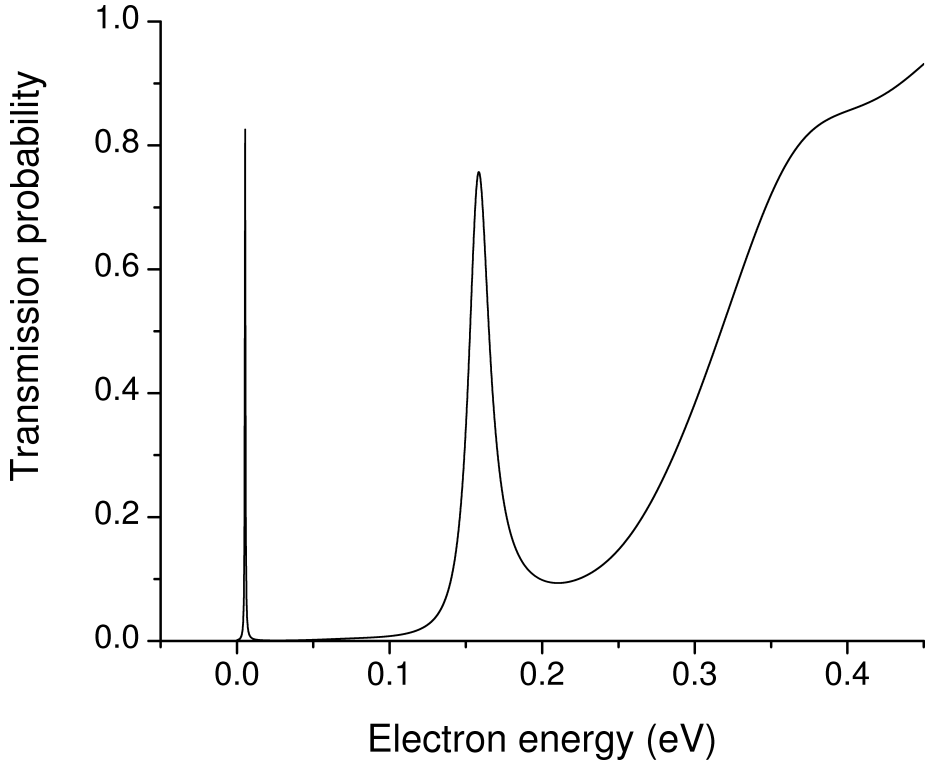

FIG. 2: Transmission probability as a function of electron energy for the heterostructure in Fig. 1.

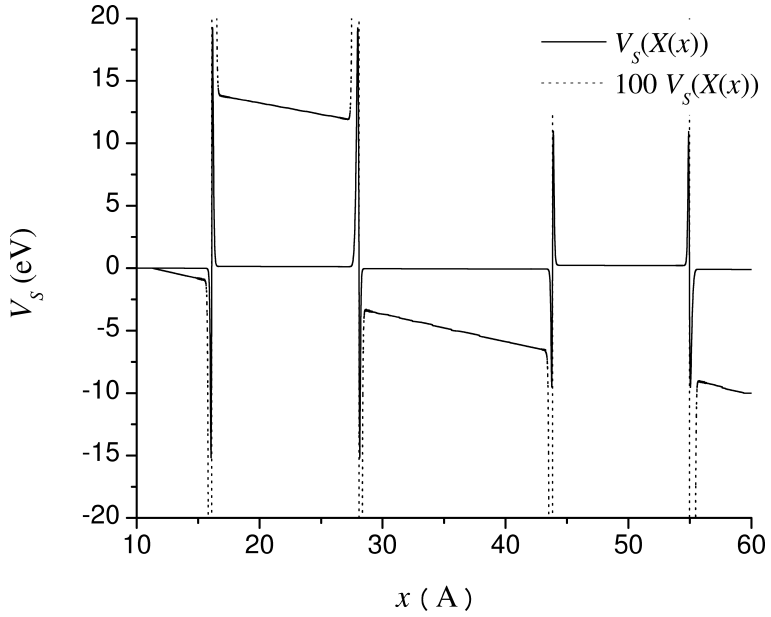

FIG. 3: Equivalent constant effective mass potential, as calculated from Eq. (6), and corresponding to the potential shown in Fig. 1. The dotted curve shows a magnified view.

In natural units (see Appendix A) the N-band $\boldsymbol{k} \cdot \boldsymbol{p}$ equation describing an electron in a

heterostructure grown in the x-direction (see Fig. 4) can be written as

$$\left[-\boldsymbol{H}_2\frac{\partial^2}{\partial x^2}+\boldsymbol{H}_1\frac{\partial}{\partial x}+\boldsymbol{V}(x)+\boldsymbol{\mathcal{E}}\right]\boldsymbol{F}(x)=E\boldsymbol{F}(x)\ . \tag{7}$$

where $\boldsymbol{V}(x)$ is a real diagonal $N\times N$ potential matrix and $\boldsymbol{\mathcal{E}}$ contains the band-edge energies at $\boldsymbol{k}=0$ (threshold energies). The additional term $\boldsymbol{H}_1\partial/\partial x$ in Eq. (7) represents the $\boldsymbol{k}\cdot\boldsymbol{p}$ coupling. Note that $\boldsymbol{H}_1$ is a real anti-symmetric $N\times N$ matrix.

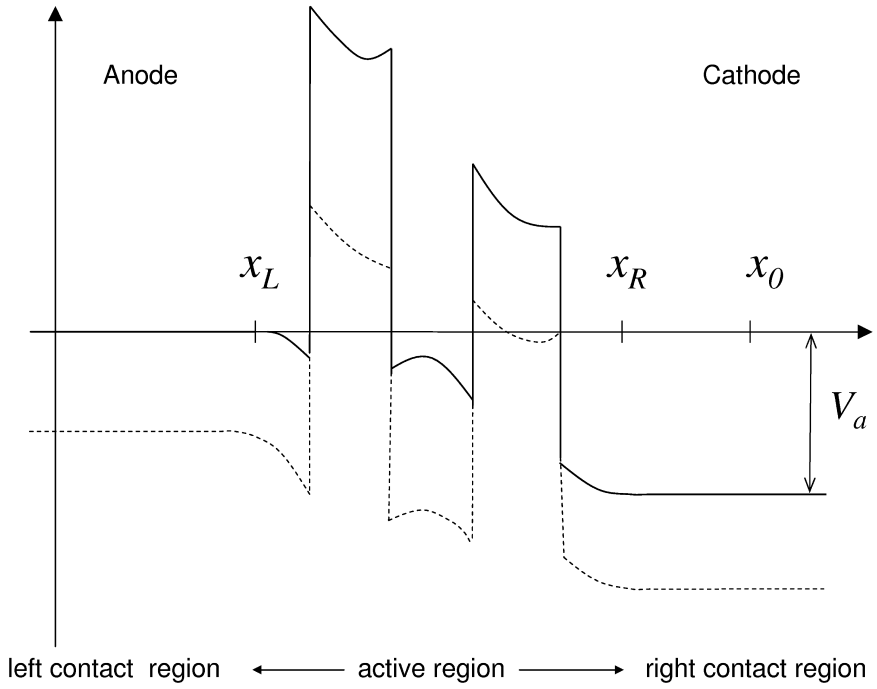

FIG. 4: Schematic multi-band potential profile (showing two bands) along the growth direction of a heterostructure. Within the active region, i.e. between x_L and x_R, the potential may vary arbitrarily. To the left and right of the active region are two contact (flat-band) regions. V_a is an applied (bias) potential.

Following the method of Ref. [16], the multi-band $\boldsymbol{k}\cdot\boldsymbol{p}$ Riccati equation corresponding to Eq. (7) may be derived as

$$\frac{\partial\boldsymbol{Y}}{\partial x}=\boldsymbol{H}_2^{-1}\left(\boldsymbol{V}(x)+\boldsymbol{\mathcal{E}}-k^2+\boldsymbol{H}_1\boldsymbol{Y}\right)-\boldsymbol{Y}^2\ , \tag{8}$$

were $\boldsymbol{Y}=\boldsymbol{F}'\boldsymbol{F}^{-1}$.

The solution to Eq. (7), to the left of the active region, can be written in the form

$$\boldsymbol{F}_L(x)=\left[\exp(i\boldsymbol{K}x)+\exp(-i\boldsymbol{K}x)\,\boldsymbol{R}\right]\boldsymbol{C}\qquad(x\le x_L) \tag{9}$$

where $\boldsymbol{C}$ is an arbitrary constant matrix. By making the usual assumption, that there are no incident waves from the right, the solution to the right can be written as

$$\boldsymbol{F}_R(x)=\exp(i\boldsymbol{K}x)\,\boldsymbol{T}\boldsymbol{C}\qquad(x_R\le x) \tag{10}$$

Here $\boldsymbol{T}(E)$ and $\boldsymbol{R}(E)$ are the, as yet unknown, transmission and reflection matrices, respectively. Evaluation of $\boldsymbol{F}_L$ and its first derivative at $x=0$ (using Eq. (9)) yields

$$\boldsymbol{F}_L(0)\,\boldsymbol{C}^{-1}\ =\ 1+\boldsymbol{R}\,, \tag{11}$$

$$\boldsymbol{F}_L'(0)\,\boldsymbol{C}^{-1}\ =\ i\boldsymbol{K}(0)\,(1-\boldsymbol{R})\ . \tag{12}$$

Multiplication of Eq. (12) from the right by $\left(\boldsymbol{F}_L(0)\,\boldsymbol{C}^{-1}\right)^{-1} = \boldsymbol{C}\boldsymbol{F}_L(0)^{-1}$ produces

$$\boldsymbol{F}_L^{'}(0)\,\boldsymbol{C}^{-1}\boldsymbol{C}\boldsymbol{F}_L^{-1}(0) = \boldsymbol{F}_L^{'}(0)\,\boldsymbol{F}_L^{-1}(0) = \boldsymbol{Y}(0) = i\boldsymbol{K}(0)\,(1-\boldsymbol{R})\,(1+\boldsymbol{R})^{-1}\ . \tag{13}$$

The reflection matrix,

$$\boldsymbol{R} = \left[i\boldsymbol{K}(0) + \boldsymbol{Y}(0)\right]^{-1}\left[i\boldsymbol{K}(0) - \boldsymbol{Y}(0)\right]\ , \tag{14}$$

is found by solving for $\boldsymbol{R}$ in Eq. (13).

In Eq. (14) the matrix $\boldsymbol{K}(0)$ is obtained from the energy-dispersion relation

$$\boldsymbol{H}_2\boldsymbol{K}^2 + i\boldsymbol{H}_1\boldsymbol{K} = k^2\mathbf{1} - \boldsymbol{\mathcal{E}}\ . \tag{15}$$

Equation (15) is the result of substituting the trial solution $\exp(i\boldsymbol{K}x)$ into Eq. (7) for $\boldsymbol{V}(0) = \mathbf{0}$. In Eq. (14) $\boldsymbol{Y}(0)$ is obtained by integrating Eq. (8) from $x = x_0$ to $x = 0$, as described in Ref. [16]. The boundary condition for this integration is $\boldsymbol{Y}(x_0) = i\boldsymbol{K}(x_0)$.

A. Example: A two-band model

For a two-band model the required matrices in Eq. (7) are given by

$$\boldsymbol{H}_2 = \begin{pmatrix} +1/2 & 0 \\ 0 & -1/2 \end{pmatrix},\ \boldsymbol{H}_1 = \begin{pmatrix} 0 & +P/\sqrt{2} \\ -P/\sqrt{2} & 0 \end{pmatrix} \text{ and } \boldsymbol{\mathcal{E}} = \begin{pmatrix} 0 & 0 \\ 0 & -E_g \end{pmatrix}\ , \tag{16}$$

where E_g is the fundamental energy gap of the material and P is the interband momentum matrix element. The latter parameter is a characteristic of the material. Physically, P describes the coupling between the two bands and is also responsible for the non-parabolicity in the energy band structure. In this model the non-parabolicity can clearly be seen from the energy-dispersion relation

$$E = -\frac{E_g}{2} \pm \frac{E_g}{2}\sqrt{1 + \frac{2\left(E_g + P^2\right)k^2}{E_g^2} + \frac{k^4}{E_g^2}}\ . \tag{17}$$

In Eq. (17) the + sign is for the conduction band and the − sign for the valence band and E is the electron energy measured from the minimum in the conduction band of the material.

On the other hand, the solution to Eq. (15) yields $K_{11} = K_{22} = 0$,

$$K_{12} = \frac{1}{\sqrt{2}P}\left(-P^2 - \sqrt{4E^2 + 4EE_g + E_g^2 - 2P^2E_g + P^4}\right)\ , \tag{18}$$

$$K_{21} = K_{12} + \frac{2E + E_g}{\sqrt{2}P}\ . \tag{19}$$

As may be expected from the form of the matrices in Eq. (16), the $\boldsymbol{K}$ matrix in this case contains only off-diagonal entries. This observation is however not generally true in models with more than two bands.

IV. MULTI-BAND INVERSION IN THE PRESENCE OF INTERBAND COUPLING

In this section the following important question is posed: Is it possible, in general, to recover all the structural and compositional data from the reflection matrix? Or in the context of the

exemplary two-band model: Is it possible to recover $V_1(x)$, $V_2(x)$ *and* P from the 2×2 reflection matrix, $\boldsymbol{R}(E)$?

From the above considerations it is clear that, even for the two-band case, the objective of inversion in semiconductors is more challenging. Because of the $\boldsymbol{k}\cdot\boldsymbol{p}$ coupling term, represented by $\boldsymbol{H}_1\partial/\partial x$ in Eq. (7), there is an additional complication. $\boldsymbol{H}_1$ contains the momentum matrix element P, which is an empirical material parameter characterizing the material. Therefore, in much the same way as the variable effective mass had to be recovered from the differential equation for $\chi(x)$, a two-band inversion procedure should recover P, *in addition to* the potential profiles $V_1(x)$ and $V_2(x)$. As noted in Ref. [6], in general, multi-band inverse methods should be able to produce all the structural and compositional data which characterizes the heterostructure through which the electron tunnels.

Now consider the general solution to Eq. (7). With the choice $\boldsymbol{C}=\boldsymbol{T}^{-1}$ in Eqs. (9) and (10), the general solution to Eq. (7) can be written as

$$\boldsymbol{F}(x)=\boldsymbol{F}_+(E,x)=\left(\tilde{\boldsymbol{F}}_-(E,x)+\boldsymbol{F}_-(E,x)\,\boldsymbol{R}\right)\boldsymbol{T}^{-1}\,, \tag{20}$$

where the solutions $\boldsymbol{F}_\pm(E,x)$ and $\tilde{\boldsymbol{F}}_\pm(E,x)$ satisfy the boundary conditions

$$\boldsymbol{F}_+(E,x) = \exp(+i\boldsymbol{K}x) \quad \text{and} \quad \tilde{\boldsymbol{F}}_+(E,x)=\exp(-i\boldsymbol{K}x) \qquad \text{for } x_R<x \tag{21}$$

$$\boldsymbol{F}_-(E,x) = \exp(-i\boldsymbol{K}x) \quad \text{and} \quad \tilde{\boldsymbol{F}}_-(E,x)=\exp(+i\boldsymbol{K}x) \qquad \text{for } x<x_L \tag{22}$$

The above boundary conditions ensure that $\boldsymbol{F}_\pm(E,x)$ and $\tilde{\boldsymbol{F}}_\pm(E,x)$ are the Jost solutions to Eq. (7).

For the case when $\boldsymbol{H}_1=0$ and $\boldsymbol{H}_2=\mathbf{1}$, Eq. (7) reduces to

$$\left[-\mathbf{1}\frac{\partial^2}{\partial x^2}+\boldsymbol{V}(x)+\boldsymbol{\mathcal{E}}\right]\boldsymbol{F}(x)=E\boldsymbol{F}(x) \tag{23}$$

It is know that the Jost solutions to Eq. (23) have the Levin representations

$$\boldsymbol{F}_+(E,x) = \exp(+i\boldsymbol{K}x)+\int_x^\infty \boldsymbol{G}_+(x,y)\exp(+i\boldsymbol{K}y)\,\mathrm{d}y\,, \tag{24}$$

$$\tilde{\boldsymbol{F}}_+(E,x) = \exp(-i\boldsymbol{K}x)+\int_x^\infty \boldsymbol{G}_+(x,y)\exp(-i\boldsymbol{K}y)\,\mathrm{d}y\,, \tag{25}$$

$$\boldsymbol{F}_-(E,x) = \exp(-i\boldsymbol{K}x)+\int_{-\infty}^x \boldsymbol{G}_-(x,y)\exp(-i\boldsymbol{K}y)\,\mathrm{d}y\,, \tag{26}$$

$$\tilde{\boldsymbol{F}}_-(E,x) = \exp(+i\boldsymbol{K}x)+\int_{-\infty}^x \boldsymbol{G}_-(x,y)\exp(+i\boldsymbol{K}y)\,\mathrm{d}y\,, \tag{27}$$

where the potential matrix $\boldsymbol{V}(x)$ is related to either of the kernels $\boldsymbol{G}_\pm$ via

$$\boldsymbol{V}(x)=\mp 2\frac{\partial}{\partial x}\boldsymbol{G}_\pm(x,x)\,. \tag{28}$$

The differential equations satisfied by the kernels $\boldsymbol{G}_\pm(x,y)$ are

$$\left(\frac{\partial^2}{\partial x^2}-\frac{\partial^2}{\partial y^2}\right)\boldsymbol{G}_\pm(x,y)=\boldsymbol{V}(x)\,\boldsymbol{G}_\pm(x,y)+\left[\boldsymbol{\mathcal{E}},\boldsymbol{G}_\pm(x,y)\right]\,. \tag{29}$$

Equivalently, the Marchenko integral equations for $\boldsymbol{G}_{\pm}$ can be derived as in Ref. [14].

In the present case, which includes the additional terms $\boldsymbol{H}_1 \partial/\partial x$ and $\boldsymbol{H}_2 \neq \boldsymbol{1}$, the procedure that was used for Eq. (23) is not immediately possible. In fact, its generalization turns out to be a formidable problem and one which will require further investigation.

It may be possible to generalize the representation of the Jost-like solutions, so as to take into account the interband coupling term. Alternatively, it may be possible to develop a folding procedure [17] which, similarly to the unitary transformation that was used in the single band case, can transform Eq. (7) into the form of Eq. (23), which can be solved according to the method of Ref. [14].

In conclusion of this section it is noted that the multi-band $\boldsymbol{k} \cdot \boldsymbol{p}$ method restricts the wave vector to lie within the first Brillouin zone. As such the carrier energy can not be identified uniquely with the magnitude of the electron momentum k (compare, for example, Eqs. (A1) and (A2)). This is because, in essence, the $\boldsymbol{k} \cdot \boldsymbol{p}$ method exploits the periodicity of the bulk effective lattice potential, via the Bloch theorem, to reduce the problem of an electron inside an infinite crystal to an equivalent problem which takes place entirely within a single unit cell.

V. PRELIMINARY NUMERICAL RESULTS

In this section a numerical implementations of the theory in Sec. III is made for the two-band model which is discussed in Sec. III A. The preliminary results presented here will be useful in future work as input to the, as yet unsolved, multi-band inverse problem.

In Fig. 5, Eq. (17) has been used to plot the conduction and valence band for InAs, which is a typical, technologically important, III-V semiconductor.

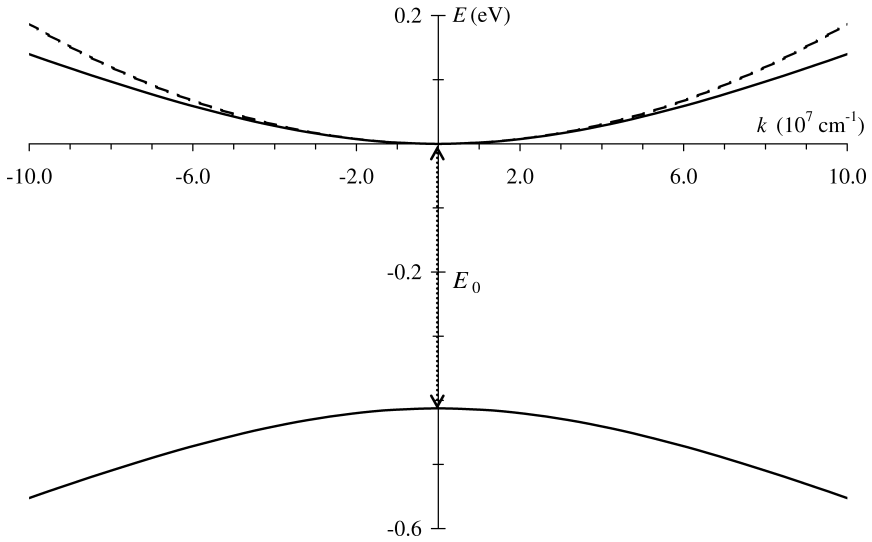

FIG. 5: Conduction and valence bands for bulk InAs as calculated from Eq. (17) for $T = 0\,\mathrm{K}$. To illustrate the non-parabolicity in the energy band structure, the parabolic conduction band has been shown by the dashed curve.

In a bulk semiconductor such as InAs, the temperature dependence of the fundamental energy gap E_g can often be approximated by the empirical Varshni formula

$$E_g\,(T) = E_0 - \frac{\alpha T^2}{\beta + T}\ . \tag{30}$$

For InAs the parameter values are: $E_0 = 0.417\,\mathrm{eV}$, $\alpha = 2.76 \times 10^{-4}\,\mathrm{eVK}^{-1}$ and $\beta = 93\,\mathrm{K}$. The momentum matrix element ($P = 0.753$ in natural units) is chosen so that the effective mass in the two-band model, which is given by $m^* \approx E_g/P^2$, agrees with the experimental value at low temperature. The value of P is usually assumed to be independent of temperature. Thus the temperature variation of the effective mass arises purely through the temperature dependence of E_g, as given by Eq. (30). The experimental value of the effective mass of an electron in InAs is given by $m^* = 0.026$ at $T = 0\,\mathrm{K}$ [18]. Parameter values appropriate to other important III-V compound semiconductors and their alloys can be found in Ref. [18].

As an example of the method described in Sec. III, $\boldsymbol{R}(E)$ has been calculated for the heterostructure shown in Fig. 6.

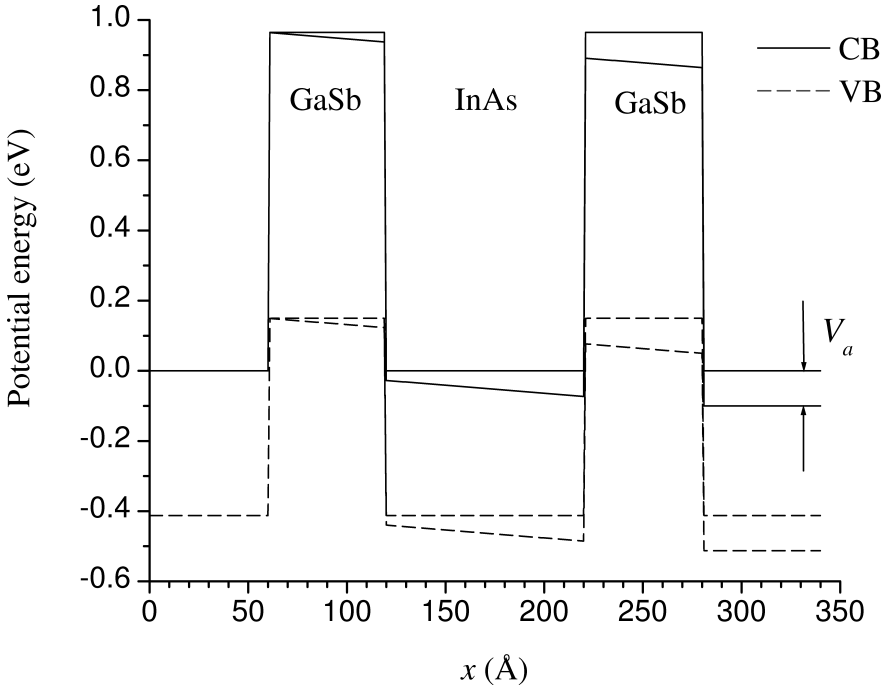

FIG. 6: Confining potential profile of an InAs/GaSb double quantum well. The solid lines are for the conduction bands (CB) and the dashed curves for the valence bands (VB). Two case are show: one for zero applied voltage and the other for an applied voltage $V_a = 0.1\,\mathrm{eV}$.

For this structure only the conduction band is open to transmit incident electrons with energy $E > 0$. The transmission probability as a function of E is shown in Fig. 7 for two different values of applied voltage V_a. It is apparent, in Fig. 7 that, even though the singe-band and two-band models contain exactly the same effective mass at the zone center ($k = 0$), the transmission probabilities predicted by these two models are not in good agreement. This observation reemphasizes the need for a multi-band formulation. Even if an energy-dependent effective mass correction is made, by using Eq. (11) and the definition

$$m^* = \left(\frac{\mathrm{d}^2 E}{\mathrm{d}k^2}\right)^{-1} \tag{31}$$

the resulting transmission probability differs imperceptibly from that shown in Fig. 7 for the 1-band case.

In comparison to higher-band models the two-band model also has shortcomings, though it is substantially more realistic than a single-band model. Provided the energy associated with the applied voltage is not too great, the electron transport behavior is governed by a local

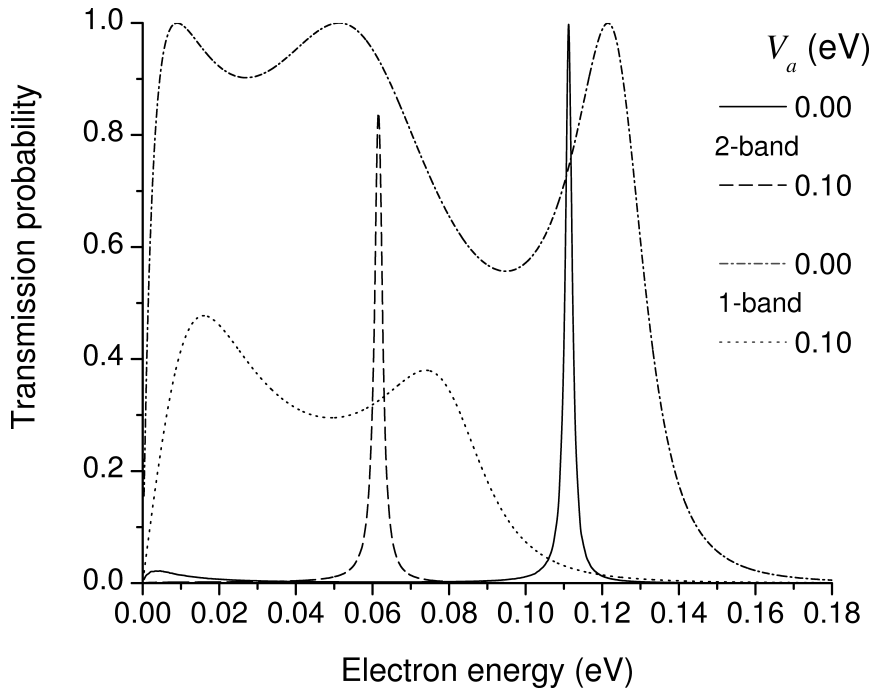

FIG. 7: Transmission probability for the GaSb/InAs/GaSb double quantum well shown in Fig. 6. The solid and dashed curves were calculated using the two-band model. The remaining two curves were calculated by using a single-band effective mass model.

neighborhood in the dispersion relation, which is represented quite accurately by the two-band model. In practice the two-band model thus captures most of the essential physics relating to charge transport. It is interesting to note that the kinetic energy terms appearing in $\boldsymbol{H}_2$ play only a minor role in the electron transport. They effectively give rise to a very small increase in the band-gap; the fractional change being on the same order as the effective mass relative to the free electron mass. It is therefore not surprising that the energy-dependent effective mass correction makes almost no difference to the results obtained from the single-band model in Fig. 7. The dominant effect is that of interband coupling.

VI. CONCLUSION

An alternative method has been developed and implemented numerically to calculate the electronic structure and quantum transport properties of type-II heterostructures. In order to test the theory and to provide input for future calculations, a numerical implementation has been made using a two-band model.

Because the theory presented in Sec. III has been based on the familiar $\boldsymbol{k}\cdot\boldsymbol{p}$ method, it may easily be extended to include the additional bands required to model other phenomena such as band anisotropy, spin-splitting (bulk, structural and due to an applied magnetic field), lattice strain, band bending, etc. [19].

The considerations of Sec. IV have shown that, in the case of semiconductors heterostructures, the main obstacle for inversion is the presence of interband coupling, i.e. the additional term $\boldsymbol{H}_1\partial/\partial x$ in Eq. (7). It remains unclear, for the moment, whether or not there exists an alternative representation, perhaps similar to Eq. (24) to (27), which can solve the more complicated problem posed by Eq. (7). Another way forward might be via a suitable unitary transformation which could eliminate the interband coupling term in Eq. (7), and thus reduce

the problem to one which has been solved previously.

APPENDIX A: NATURAL UNITS

By convention, the natural units [20] in semiconductor physics are those in which length is measured in terms of Bohr radii and energy in terms of the Hartree energy (See Table 1). In

TABLE I: Natural units of length and energy in semiconductor physics. The Bohr radius a_0 is the most likely distance at which the electron orbits the nucleus of a hydrogen atom in its ground state and the Hartree energy is equal to the absolute value of the electric potential energy of the hydrogen atom in its ground state.

Bohr radius:	$4\pi\varepsilon_0\hbar^2/\left(m_e e^2\right) = 0.0529177249\,\mathrm{nm}$
Hartree energy:	$\hbar^2/\left(m_e a_0^2\right) = 27.2113961\,\mathrm{eV}$

these units the Schrödinger equation for a single electron of mass m_e $(= \hbar = c = 1)$ has the form

$$-\frac{1}{2}\varphi''(x) + V(x)\,\varphi(x) = E\varphi(x) \tag{A1}$$

In the work on inversion however (See, for example, Ref. [4].), the Schrödinger equation is written in units for which

$$-\varphi''(x) + V(x)\,\varphi(x) = k^2\varphi(x) \tag{A2}$$

and the potential energy of the electron is measured in units of nm^{-2}. The appropriate conversion factor between the two systems of units is therefore given by

$$\frac{\hbar^2}{2m_e} = \frac{\hbar^2 c^2}{2m_e c^2} = \frac{(197.327054\,\mathrm{MeV\,fm})^2}{2\,(0.51099906\,\mathrm{MeV})} = 0.038099841\,\mathrm{eV\,nm}^2$$

For example, a typical potential of $V = 1.0\,\mathrm{eV}$ in Eq. (A1) is equivalent to

$$V = \frac{1\,\mathrm{eV}}{0.0381\,\mathrm{eV\,nm}^2} \approx 30\,\mathrm{nm}^{-2}$$

in the units of Ref. [4]. Note that all of the potentials considered in Ref. [4] are on the order of $0.3\,\mathrm{nm}^{-2}$, which is an order of magnitude smaller than the typical potentials which occur in semiconductor heterostructures.

ACKNOWLEDGMENTS

The author is grateful to Prof. S.A. Sofianos for fruitful discussions concerning this work.

[1] X. Cartoixa, D. Z. Y. Ting, and T. McGill, Nanotechnology **14**, 308 (2003).
[2] I. Zutić, J. Fabian, and S. Das Sarma, Rev. Mod. Phys. **76**, 323 (2004).
[3] D. Bessis, G. Mantica, G. A. Mezincescu, and D. Vrinceanu, Europhys. Lett. **37**, 151 (1997).
[4] S. A. Sofianos *et al.*, Microelectronics Journal **38**, 235 (2007), and references therein.
[5] Microelectronics Journal **30** (1999), edited by E. N. Glytsis. This entire volume is devoted to various aspects of semiconductor quantum devices.

[6] L. Perotti and D. Bessis, Microelectronics Journal **34**, 1037 (2003).
[7] D. Bessis and G. A. Mezincescu, Microelectronics Journal **30**, 953 (1999).
[8] D. M. Wood and A. Zunger, Phys. Rev. B **53**, 7949 (1996).
[9] P. Y. Yu and M. Cardona, *Fundamentals of Semiconductors: physics and material properties*, 3rd ed. (Springer, New York, 2001).
[10] R. Winkler, *Spin-Orbit Coupling Effects in Two-Dimensional Electron and Hole Systems* (Springer, Berlin, 2003).
[11] P. Harrison, Quantum Wells, Wires and Dots, 2nd ed. (Wiley, New York, 2005).
[12] K. Chadan and P. C. Sabatier, *Inverse Problems in Quantum Scattering Theory*, 2nd ed. (Springer, Berlin, 1989).
[13] D. N. Ghosh Roy, *Methods of Inverse Problems in Physics* (CRC Press, Boca Raton, 1991).
[14] S. Sofianos, M. Braun, R. Lipperheide, and H. Leeb, *Lecture Notes in Physics*, edited by B. Apagyi, G. Endredi, and P. Levay (Springer, Berlin, 1997), Vol. 488, p. 54.
[15] G. Reiss and R. Lipperheide, Phys. Rev. B **53**, 8157 (1996).
[16] A. E. Botha, Microelectronics Journal **38**, in press (2007).
[17] M. E. Flatté, et al., Phys. Rev. B **53**, 1963 (1996).
[18] I. Vurgaftman, J. R. Meyer, and L. R. Ram-Mohan, Applied Physics Review **89**, 5815 (2001).
[19] A. E. Botha and M. R. Singh, Phys. Rev. B **67**, 195334 (2003).
[20] R. McWeeny, Nature **243**, 196 (1973).

Searching for Multi-Body Decays pf Low and Middle Excited Activities

D.V. Kamanin[1], Yu.V. Pyatkov[1,2], W.H. Trzaska[3], and W. von Oertzen[4*]

[1] *Joint Institute for Nuclear Research, 141980 Dubna, Moscow region, Russia*

[2] *Moscow Engineering Physics Institute, 115409 Moscow, Russia*

[3] *Department of Physics of University of Jyväskylä, FIN-40014 Jyvškylä; Finland Helsinki Institute of Physics, Finland and*

[4] *Hahn-Meitner-Institute GmbH Str. 100, 14109 Berlin, Germany*

In our experiments devoted to investigation of the rare decay modes in the ^{252}Cf (sf) at the FOBOS set up we have found experimental indications of a new type of nuclear transformation. The mass-energy correlations for these rare collinear events observed at the yield level of about 10^{-5} with respect to the binary fission allowed one to associate them with the decay of the system into three or more fragments of comparable masses via an elongated chain-like configuration. In each such mode revealed, at least two of the partners are the magic nuclei, thus clustering of the decaying system gives rise to the effect observed. For these reasons we have called this effect "Collinear Cluster Tripartition" (CCT). The CCT products form different structures in the mass plots look like the rectangles and the lines, which map presumably an evolution of the multi-components heavy nuclear molecules onto the space of mass-asymmetry *vs* deformation. The effect at hand was confirmed recently in a series of experiments of our collaboration in JYFL (Jyväskylä, Finland). Multiple attempts to discover similar decay channel ("true ternary fission") for low excited nuclei did not succeed in the past. The special features of the equipment used and the new data processing procedures developed, will allow an observation of very interesting cluster effects for the first time.

I. EXPERIMENTAL AND THEORETICAL BACKGROUND

It is well known that the energy release (Q-value) calculated within the framework of the liquid drop model for the fission mode with three fragments, is larger than for binary fission [1]. Within the same approach, the theory also predicts the shape of the fissioning system which could lead to ternary and even quaternary fission [2]. This is illustrated in Fig. 1. As, however, was stressed in the cited work, two and three-neck shapes are less favorable as compared to the conventional dumbbell-like configurations. An additional obstacle for emitting even rather light particles from the body of the mother system, is the necessity to penetrate the potential barrier due to the interaction of two partners, if we mean two-neck prescission shape.

In reality, the particle-accompanied fission (or ternary fission) discovered in 1946 [3] is a rather rare process. Several such processes, in which the charged particle is a proton, deuteron, triton, $^{3-8}$He, $^{6-11}$Li, $^{7-14}$Be, $^{10-17}$B, $^{13-20}$C, $^{15-20}$N, or $^{15-22}$O, have been detected in spontaneous and neutron-induced fission. Many other heavier isotopes of F, Ne, Na, Mg, Al, Si, P, S, Cl, Ar, and even Ca were recently mentioned [4]. The details of the ternary fission mechanism are still unclear. It is generally believed that light charged particles, which once in a few hundreds of cases accompany fission, are born in the vicinity of scission and subsequently accelerated and

*Electronic address: kamanin@jinr.ru

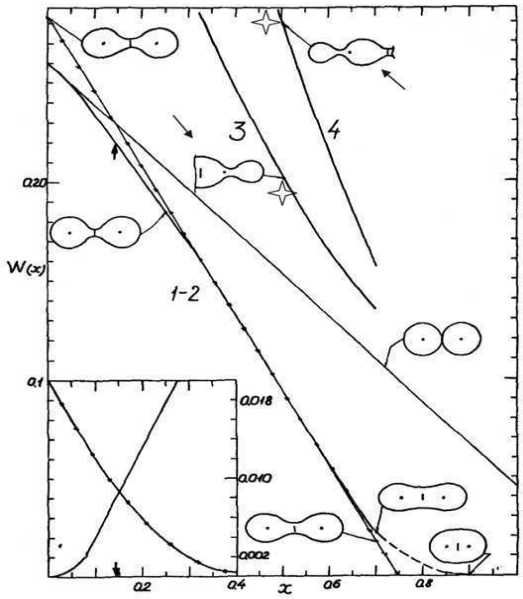

FIG. 1: Symmetrical shapes of equilibrium for a liquid drop model [2]. Abscissa is an $X \sim Z^2/A$ (liquid drop model parameter X to be proportional to nuclear charge Z and mass number A of the nucleus). $W(X)$ which is the difference of the potential energy of the deformed nucleus and that of the initial sphere is plotted along the vertical axis. Two-neck shapes (3) and three-neck shapes (4) are marked by the arrows. The stars are the most favorable points for the formation of a "quasi-molecule".

focused almost perpendicularly to the fission axis by the Coulomb field of the fission fragments [5]. In spite of this simple picture, it was found that a surprisingly high portion of alphas (the dominating tripartition particles) can be recorded in the vicinity of the fission axis [6]. This phenomenon occurring once per 10^5 fissions was called "polar emission". So far, polar emission of α, p, t, and d were observed in the reactions $^{235,\ 233}$U$(n_{\rm th}, f)$, ^{252}Cf (sf), ^{238}U+p(42 MeV) and some preliminary models of the phenomenon were proposed.

Along with ternary decays quaternary ones are also known [7]. In this case two light charged particles (predominantly alphas) are detected in coincidence with two heavy fragments. The ratio of the yields quaternary to binary fission is about 10^{-6}. In theory a more general "multi-cluster accompanied fission" was analyzed [8]. Some typical prescission configurations are shown in Fig. 2. The strong shell effect corresponding to the doubly magic heavy fragment ^{132}Sn is emphasized. As can be inferred from the figure's potential barrier, the polar emission (1st column, 2nd row) is much higher than that of the emission from the neck (1st column, 1st row), which explains the low yield of the polar emission as compared to that of the conventional ternary fission. The above processes are different from cluster radioactivity predicted at first theoretically [9] and discovered later experimentally [10]. The term "cluster radioactivity" is applied for spontaneous emission of light fragments heavier than α-particle in the decays of heavy nuclei. Nowadays there are known 18 nuclides from ^{231}Fr to ^{242}Cm emitting light nuclei from ^{14}C to ^{34}Si. The heavy fragments are grouped in the vicinity of the double magic ^{208}Pb that is why this domain of cluster decays is known as "lead radioactivity". Lead radioactivity is far from being unique. Many other combinations of daughter nuclei are allowed energetically to be emitted including the formation of the products of comparable masses named cold fission. However, cluster radioactivity is a very rare process with a probability 10^{-10}- 10^{-17} to those of α-decays. In all known cases, except one, the products of cluster radioactivity are formed in their ground states in contrast to conventional binary fission fragments. The question, on whether the mech-

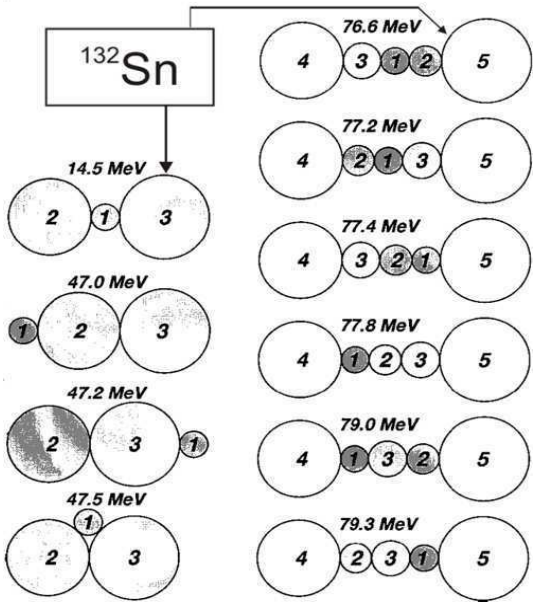

FIG. 2: Aligned and compact configurations for α-accompanied and α+^{6}He+^{10}Be accompanied cold fission of ^{252}Cf [8]. the corresponding light particles are sketched as circles marked by numbers 1, 2, and 3 respectively. The potential barrier for emitting light particles is shown above each nuclear configuration.

anism of cluster radioactivity resembles to that of α-decay or to that of superasymmetric fission is still under discussion.

Cluster radioactivity is a binary process. Nevertheless, we mention it in the context of this report due to the following reason. Bearing in mind that a magicity of one of the decay partners plays a key role in the process, a natural question arises whether multicluster decays appear to occur. In other words a decay of heavy nucleus into magic constituents (clusters by definition) should be searched for. At least one example of dicluster decay is well known, namely ^{258}Fm(sf) $\rightarrow$ 2Sn with two magic fragments in the exit channel [11].

Searching for ternary cluster decays is a challenge very close to the "true ternary fission problem" which has a long history. Multiple attempts (see, for instance, the most reported ones [12, 13]) to discover a decay of low excited nuclei into three fragments of comparable masses did not succeed so far. Except of the radio-chemical and mass-spectrometric techniques, being selective reference to revealed nuclides, all the experiments performed aimed at detecting three moving fragments emitted at some angles to each other (equal angles for equal fragments). Being pretty expected from the symmetry point of view, such an experimental design contradicts theoretical estimations. Within the liquid drop approach [14] and, recently, within its extended version [15], it was shown that the chain-like (prolate) configuration is prefered as compared to oblate shapes for realizing true ternary fission (Fig. 3). This is quite understandable bearing in mind that the Coulomb component of the potential barrier has to be overcome for the triple decay. The elongated (prolate) configuration with two necks for the fissioning ^{252}Cf nucleus was demonstrated recently in our work [16] where the shell corrections were taken into account. This result was obtained in our more detailed calculations of the potential energy surface of the ^{252}Cf nucleus carried out in the framework of the procedure presented in [17, 18] based on the Strutinsky method. Fig. 4a depicts the shape of the fissioning nucleus at the bottom of the "symmetry" valley with the quadrupole moment $Q_2 = 7.52$ a.u. (see Fig. 8 in [18]). As was already pointed out in our previous works [18–21], the system that fissions in the vicinity of the bottom of the potential valley, constitutes two magic nuclei (clusters) connected by a

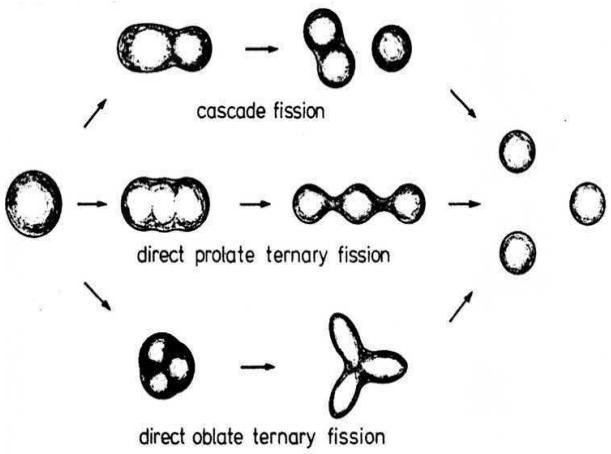

FIG. 3: Possible ways leading to true ternary fission [14].

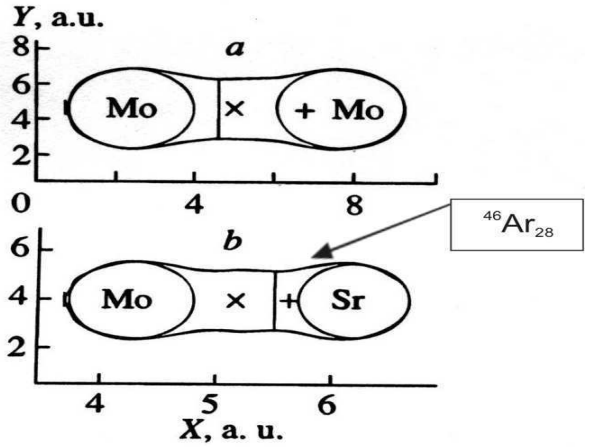

FIG. 4: a) The shape of the nucleus at the bottom of the "symmetric" valley at the point $Q_2 = 7.52$ a.u. and $n = 0.074$; b) The same system at the point $Q_2 = 7.52$ a.u. and $n = 0.208$. See text for details.

neck. In Fig. 4a, these clusters are the deformed magic nuclei of ^{108}Mo ($\beta_2 \sim 0.58$). In the calculations, the shape of the system was varied in such a way that the value of Q_2 remained constant while the mass-asymmetry n changed starting from the value corresponding to the valley's bottom. By definition, $n = (M_1 - M_2)/Mc$, where M_1 and M_2 are the masses of the system concentrated, respectively, on the left and on the right sides of the varied boundary, which divides the nuclear body into two parts (marked by vertical lines in Fig. 4), and Mc is the mass of the fissioning nucleus. As a result, the new shape of the system shown in Fig. 4b, was revealed for the first time. The energy of the system is only slightly higher (by ~ 2 MeV) than the corresponding value at the bottom. The distinguishing feature of the shape observed is the double waist which vividly divides the system into three parts of comparable sizes namely $^{108}Mo_{66}$, $^{98}_{38}Sr$, $^{46}Ar_{28}$. Magic numbers are marked at the bottom of the element symbol. Thus, all three constituents are the magic nuclei. It would appear reasonable to identify the double rupture of such a configuration as the true ternary fission (ternary cluster decay) so long sought.

What can one learn from the theoretical and experimental background in the field under discussion? Ternary decay of low or middle excited nucleus via chain-like prescission configuration into magic fragments of comparable masses seems to be reasonable from a theoretical point of view. It is also reasonable to search for experimental manifestations of such decay channel by

analyzing almost collinear multibody events. It is just our experimental program during the last few years. Some experiments within the framework of this program are reported below.

II. EXPERIMENTS AND RESULTS

A. Velocity, momentum, and neutron multiplicity gating in searching for CCT

The first one to be presented was performed at the modified 4π-spectrometer FOBOS installed at the FLNR of the JINR [22]. In our preliminary experiments at FOBOS setup, the total mass of two complementary detected fragments in a new exotic decay mode amounted to about 70% of the initial mass of the fissioning nuclei (^{252}Cf or ^{248}Cm). Mass-energy correlations for these rare events allow one to associate them with the decay of the system via an elongated three-body chain-like configuration. At least one of the detected fragments formed in each event under discussion was a magic nucleus. Two fragments arisen at the outmost left and the outmost right positions fly apart along the chain axis, i.e. collinear, while the middle fragment can stay almost at rest. Due to these features we called the decay channel observed collinear cluster tripartition (CCT). Evaluated excitation energy let one to expect the middle fragment of the chain to be an isotropic neutron sours of high multiplicity (≤ 10). In order to verify this prediction, the FOBOS setup has been equipped with neutron detectors.

The experimental layout of the modified spectrometer is shown in Fig. 5. Two groups containing five big and one small FOBOS modules each were used as a double-armed TOF-E (time-of-flight-energy) spectrometer which covered $\sim 29\%$ of the hemisphere in each arm and thus the energies and the velocity vectors of the coincident fragments were detected. The neutron detector consisting of 140 separate hexagonal modules comprising ^{3}He-filled proportional counters in a moderator covered altogether $\sim 19\%$ of the complete solid angle of 4π. The electronics of the "neutron belt" were operated in the slave mode being triggered by the event selector of the gas part of the FOBOS detector. The number of tripped ^{3}He neutron counters was added to the data stream as an additional parameter for each registered fission event. A special procedure of mass reconstruction as well as a numerical model of the neutron registration channel were designed [23]. Simulations within the model help one to fill peculiarities of neutron detection (Fig. 6).

The mass-mass plot of the coincident fragments with the high multiplicity of neutrons (at least 3 of them should be detected) is shown in Fig. 7a. It is easy to recognize the rectangular-shaped structure below the locus of conventional binary fission. This structure becomes more conspicuous (Fig. 7b) if the velocity cut shown in Fig. 8 is applied to the distribution. The clearing effect can be explained in the following terms.

Fragments scatter both at the electrodes of the "stop" avalanche counter and at the supporting grids of the ionization chamber that provides the main part of the faulty events which imitate the CCT effect searched for. Indeed, the mass of the heavy fragment calculated from the true velocity value but from incorrect (reduced) value of the energy diminishes proportionally to the latter. Therefore a pair of the fragments originated from conventional binary fission could reveal the mass defect similar to that characterizing a CCT event. However, if one rejects the events corresponding to the sufficient mass asymmetry determined by means of the ratio of the velocities which occurred beyond the velocity-window selected (Fig. 8), the notable part of the scattered events under consideration are also discriminated automatically. This selection cuts off a part of the binary events loci due to velocity gating. Also their "scattered projections", i.e. the tails in the direction of smaller masses, disappear. A special attention should be paid to the rectangle in Fig. 7b which is bounded by the clusters from at least three sides. The

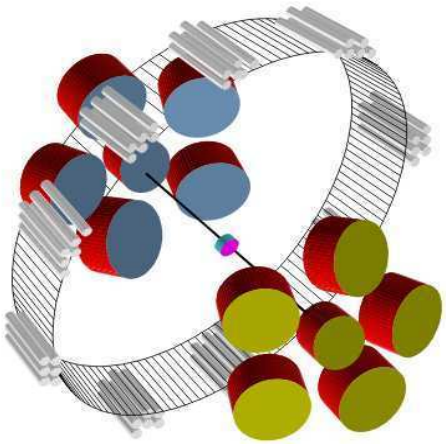

FIG. 5: Schematical view of the modified FOBOS setup. The spontaneous fission source is placed inside the start detector in the middle. The belt consisting of 140 ^{3}He neutron counters is placed perpendicular to the mean fission axis of the registered fragments, which are analyzed by 12 standard FOBOS modules consisting of the position-sensitive avalanche counters (PSAC) and the Bragg ionization chambers (BIC).

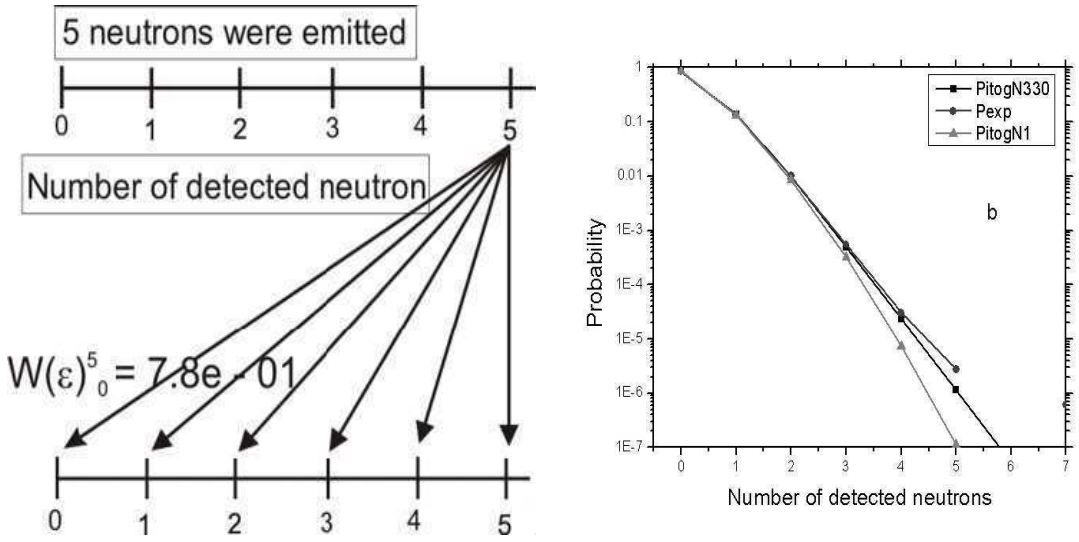

FIG. 6: a) Peculiarities of the neutron registration channel. Even if five neutrons were emitted, the most probable result is that any neutrons will be detected due to actual registration efficiency. b) Comparison of the experimental spectrum (points) with the calculated ones for the source intensity $n = 330\,\mathrm{sec}^{-1}$ (used in experiment, shown by the rectangles) and $n = 1\,\mathrm{sec}^{-1}$, when the rate of random coincidences is negligible (triangle). For 3 detected neutrons the contribution of the random events is about 35%.

corresponding magic numbers are marked in this figure at the bottom of the element symbols. More complicated structures (marked by the arrows a, b, and c in Fig. 7c) are observed in the mass-mass plot if the events with 2 fired neutron counters are also taken into play. Omitting for a moment physical treating of the structures observed, we attract ones attention to the specific peculiarity of some lines constituted the structures b and c. The sum of the masses along them remains constant, see the dashed line in the lower left corner of Fig. 7c for comparison. Fig. 10a represents a similar structure to that shown in Fig. 7a except that it is not gated by neutrons

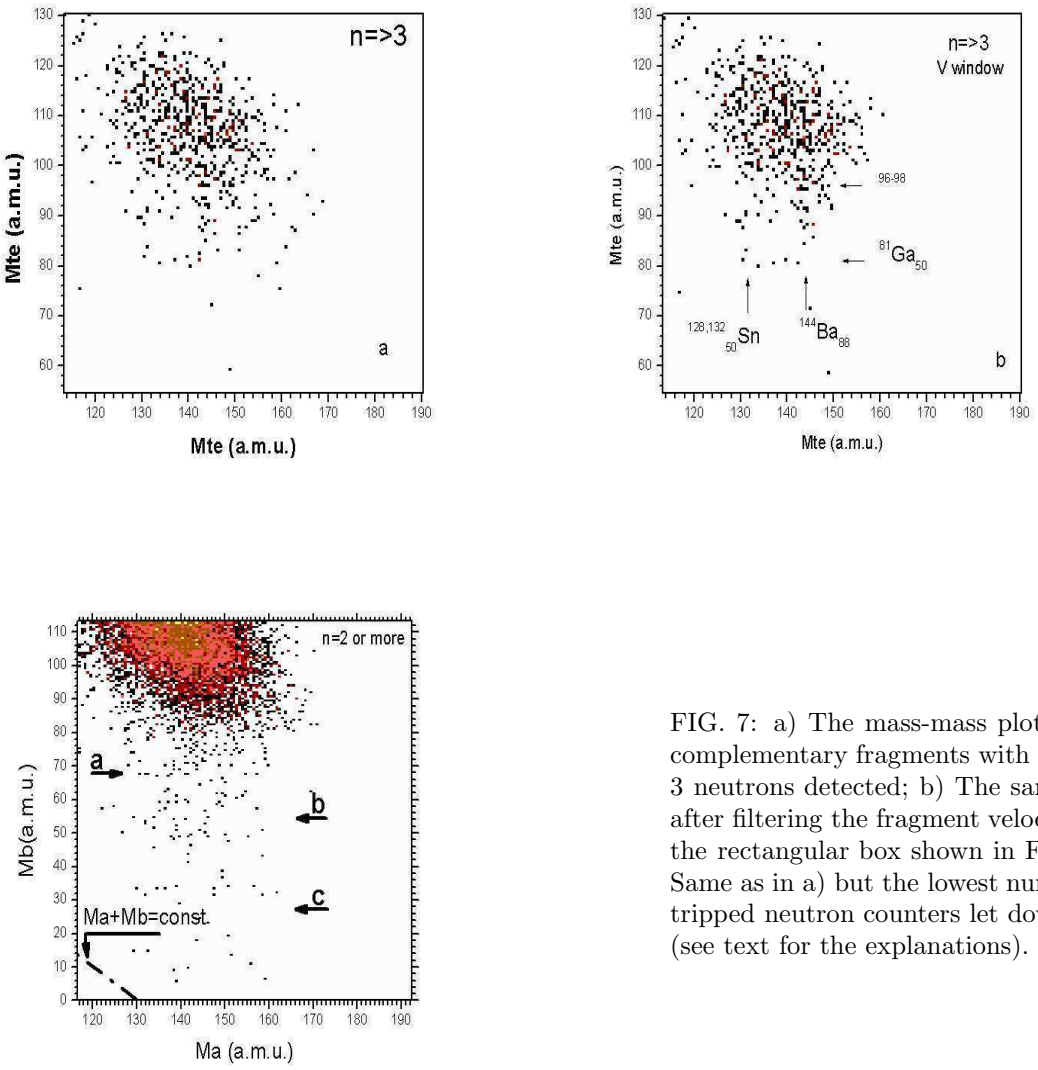

FIG. 7: a) The mass-mass plot of the complementary fragments with at least 3 neutrons detected; b) The same plot after filtering the fragment velocities in the rectangular box shown in Fig.8; c) Same as in a) but the lowest number of tripped neutron counters let down to 2 (see text for the explanations).

and both the velocity and the momentum windows are used here to reveal the mass-symmetric partitions. The corresponding momentum distribution of the fragments and the selection applied are shown in Fig. 10. The plot in Fig. 10b obtained on conditions of the momentum selection solely is not so clear.

Like in the previous case, however, the rectangular structure observed is bounded by the magic fragments, namely ^{68}Ni (the spherical proton shell Z=28 and the neutron sub-shell $N = 40$) and ^{84}Se (the spherical neutron shell $N = 50$). Each structure revealed, maps an evolution of the decaying system onto the mass space. Reconstruction of the evolution scenarios is a goal of the forthcoming analysis. The events at the lower left corner of the rectangle attract special attention as they form well-separated blocks in the matrices of the experimental observables (velocity and energy). Table I exemplifies the parameters of three most symmetric events. One can judge from this table that the cluster masses obtained by the TOF-E analysis are located in the vicinity of the mass numbers 68 and 72. Both nuclei are attributed presumably to the magic Ni isotopes. The content of neutrons for the fragments whose masses are close to 72 complies then with the prediction of the unchanged charge density hypotheses. The surprising fact is that the evaluated TKE value even for the chain Ni-C-Zn-C-Ni exceeds the

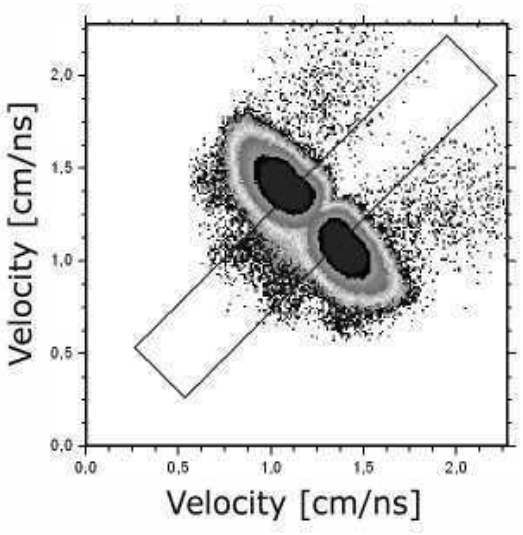

FIG. 8: Velocity matrix of the complementary fragments. The events falling into the rectangular box were used to compose the final mass-mass plot in Fig. 10.

experimental findings (~ 100 MeV). The next point to be stressed is that the observed neutron multiplicity (the number of tripped neutron counters in Table I) is low and, hence, the number of emitted neutrons could not be high. This contradicts the expectations put forward earlier. The discrepancies reported may be an indication of more complicated decay scenario, for instance, decay of the middle fragment in chain.

B. Comparative study of the ^{252}Cf (sf) collinear tripartition at different spectrometers

In this subsection we describe the results of three experiments devoted to a search for collinear tri-partition of the ^{252}Cf nucleus. It should be stressed once more that among all known methods

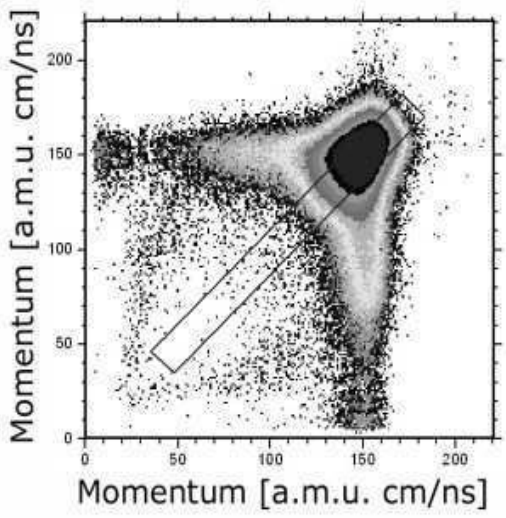

FIG. 9: Momentum-momentum plot. The events falling into the rectangular box were used to compose the final mass-mass plot in Fig. 10.

TABLE I: Experimental parameters of true tripartition events.

Parameter	Event No 1	Event No 2	Event No 3
Number of tripped neutron counters	0	0	1
Velocity in the arm "a" (Va) cm/ns	1.147	1.102	1.135
Velocity in the arm "b" (Vb) cm/ns	1.173	1.141	1.23
TOF-TOF mass (Mtta) a.m.u.	127.4	128.2	131.1
TOF-TOF mass (Mttb) a.m.u.	124.6	123.8	120.9
Momentum (Pa) (cm/ns)* (a.m.u.)	79.6	80.7	7.8
Momentum (Pb) (cm/ns)* (a.m.u.)	84.7	78.3	83.4
TOF-E mass (Mtea) a.m.u.	69.4	73.2	69.4
TOF-E mass (Mteb) a.m.u.	72.2	68.6	67.8
Etea (emission energy) MeV	47.5	46.3	46.5
Eteb MeV	51.7	46.5	53.4
TKEte (total kinetic energy) MeV	99.1	92.7	99.9

of measuring the masses of nuclear reaction products, the TOF-E (time-of-flight versus energy) method is the only one, which uniquely allows the study of multibody decays. In this method both, the fragment velocities V, obtained by means of TOF, and the energy E are measured for each fragment individually. The fragment mass M is calculated simply using $M = 2E/V2$. Three different TOF-E spectrometers with the detector arms placed opposite to each other and symmetric to the ^{252}Cf source were used in our experiments as described below. In the first experiment (Ex1, Fig. 11a), performed at the FOBOS setup in the Flerov Laboratory (FLNR) of the Joint Institute for Nuclear Research in Dubna, about 13*106 coincident binary fission events were recorded (the numbers in parenthesis refer to labels in the figure). The TOF of the fragments was measured over a flight path of 50 cm between the "start" detector (3) based on the micro–channel plates (MCP) placed next to the ^{252}Cf-source (1) and the "stop" position-sensitive avalanche counters (PSAC, 4). The latter provided through the measurements of the position also the fragment emission angle with a precision of 0.20. The energies of the coincident fragments, which passed through the PSACs were measured in the Bragg ionization chambers

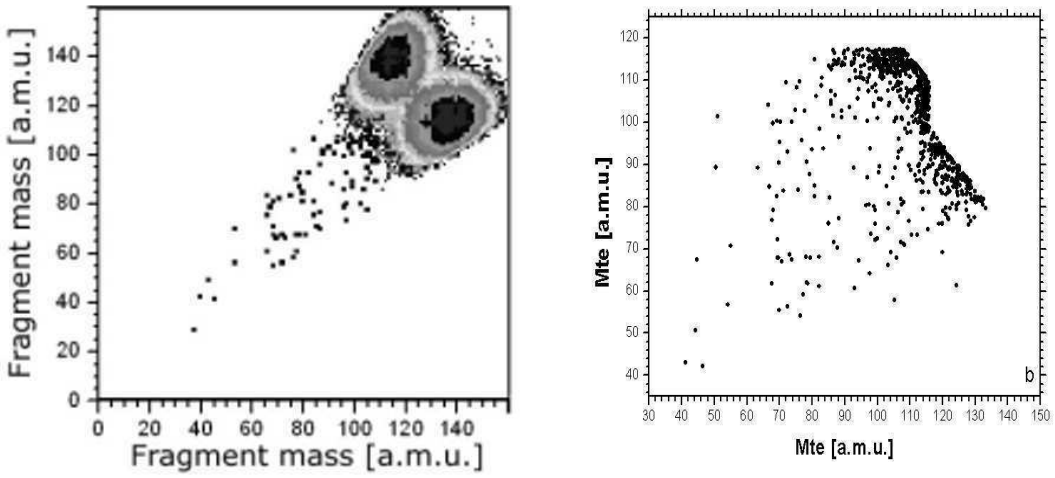

FIG. 10: a) The mass matrix of the complementary fragments selected by requirement of their approximately equal velocities and momenta; b) the same matrix if only momentum selection is assumed.

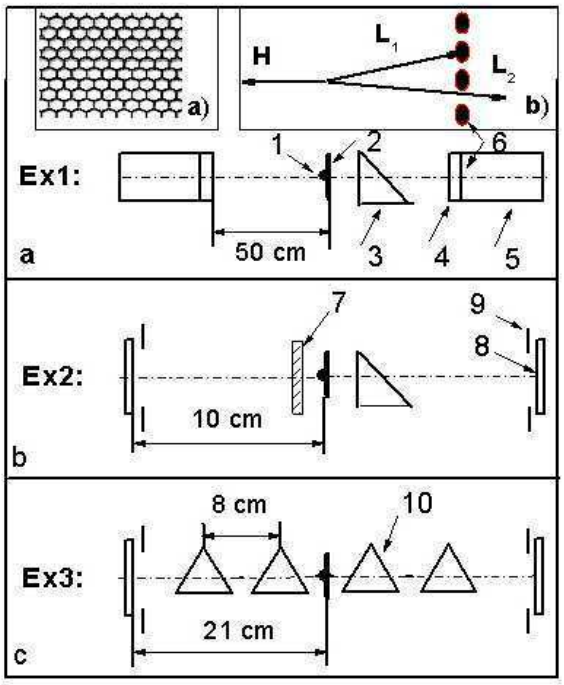

FIG. 11: A scheme of coincident measurements of two fragments of the collinear tri-partition partners for the three experiments. First experiment Ex1 (a) was performed at the FOBOS setup. Here: 1 is a Cf source, 2 is a source backing; 3 is a microchannel plate (MCP) based timing "start" detector; 4 is a position sensitive avalanche counter as "stop" detector; 5 is an ionization chamber with the supporting grid 6 on the entrance window. The side view of the grid is shown in the insert (left). Second and third experiments Ex2, Ex3 (b and c) were performed at the spectrometers based on MCP detectors (2, 10) and PIN diodes (8) bounded by frame (9). The scheme of detecting the tripartition partners is shown in the insert (right). After passage of the dispersion foil two light fragments (L1 and L2) obtain a small angle divergence due to multiple scattering. One of the fragments (L1) can be lost hitting the separating block, while the fragment L2 reaches the energy detector.

(BIC, 5) with entrance windows supported by a grid (6) with 70% transparency. The geometrical structure of the grid is hexagonal, the side view is shown in the insert (left) of Fig. 11.

This mechanical structure of the detectors is essential for the registration of the effect described below. The ^{252}Cf source is mounted on a Al_2O_3 backing (2) of a thickness 50 μg/cm^2, the other side was free or coated with a layer of Au of 20 μg/cm^2 thickness. In Fig. 11 (top) the primary heavy fragment (H) is emitted to the left from the free side of the ^{252}Cf-source, the two light fragments (L1 and L2) are emitted in the same direction. As explained below, scattering processes will separate the two light fragments in a small angular separation, and only one of them is likely to be registered. If both fragments enter only the total energy is measured.

A similar source of ^{252}Cf was used in further experiments performed in the Accelerator Laboratory of the University of Jyväskylä (JYFL). In the second experiment (Ex2, Fig.11b) we used a different TOF-E-spectrometer based on one MCP "start" detector and two PIN diodes (8), the latter provided both time and energy signals. The active area of each PIN diode was bounded by the frames (9). The flight-paths here were10 cm for each detector arm. An Al-foil (7), 5μm thick has been placed just near active ^{252}Cf layer. In this experiment, 2*106 binary events were registered.

In the third experiment (Ex3, Fig. 11c) two pairs of the MCP-based timing detectors (10) provided signals for measuring TOF's with flight paths of 8 cm each. The fragment energy was

measured by PIN diodes. The total transparency of each arm amounted to 70% due to the grids of the electrostatic mirrors (four per detector, instead of two as in the Ex1 and Ex2) of the timing detectors. In this third experiment, 2*106 of binary events were collected.

In Fig. 12a, left, we show in a logarithmic scale the two-dimensional (2D) distribution of the two registered masses of the coincident fragments in the experiment (Ex1) at the FOBOS set up. Only collinear events in both identical spectrometer arms with a relative angle of ($180 \pm 1^{\circ}$) were selected, this value is within the angular resolution, and it is in the range of a typical angular spread for conventional binary fission fragments.

The "tails" in the mass distributions marked 3-6 in Fig. 12, left, extending from the loci (1 and 2) used to mark the conventional binary fission, are mainly due to the scattering of the fragments on both the foils and on the grid edges of the "stop" avalanche counters and the ionization chambers. An astonishing difference in the shapes of the "tails" (3 and 4) attracts attention. The only asymmetry, albeit small but important, between the two arms to be emphasized consists in a very thin source backing for the "rear side" and the "start" detector foil located in the arm b only (Fig. 11, top). There is a distinct bump, marked (7), on the latter "tail" (4), oriented approximately parallel to the line defining a constant sum of masses, $M_a + M_b$ =const, i.e., tilted by 450 with respect to the abscissa axis. The explanation of this bump is the essence of our analysis. The bump is located in a region corresponding to a large "missing" mass. In Fig. 12, left, we show the line for the total mass $M_{\rm total} = 225$ as a border line to separate these interesting events from normal binary fission. A statistical significance of the events in the structure (7) can be deduced from Fig. 12, right. There the spectra of total masses, $M_{\rm total} = M_a + M_b$, for the "tails" (4 and 3), spectrum a and spectrum b, respectively, are compared. The difference spectrum of b and the tail (3) is marked c, the integral of these events is 4.7×10^{-3} relative to the conventional fission events contained in the locus (2), shown in Fig. 12, left. The corresponding ratio for the gross peak of the curve a (shown by the dashed line) is smaller and amounts to about 2.7×10^{-3}. A background as shown was defined by a polynomial fit (curve d) using the points outside of the peak. In order to explain the differences in the "tails" (3 and 4) mentioned above, the following scenario is proposed, the geometry is shown in Fig.11 (insert top, right). In ternary fission, the three fragments are emitted collinearly and two of the fragments are emitted in one direction but become separated with an angle less than 1° after passing a dispersing media, due to multiple scattering [24]. These materials are the backing of the source (located only on the side of tail (4) or the Al foil placed deliberately in the path). If both fragments pass on and enter into the (BIC), we register a signal corresponding to the sum of the energies of the two fragments. The event is registered as binary fission with almost usual parameters. In the other scenario only a proper energy (mass) of one of the light fragments is measured, because the second one is stopped (lost) in the supporting grid of the ionization chamber, or for the other cases on the frame of the PIN diode, playing the role of the separating element.

In order to verify whether the dispersive scattering through a transparent foil can give rise to the effect discussed, we have performed a special experiment (Ex2, Fig.11b) at the JYFL spectrometer. One side of the Cf-source was covered by an Al foil (7) of a $5\,\mu$m thickness. This thickness corresponds approximately to a half of the range of a typical heavy fragment. A bump similar to that shown in Fig. 11a is observed. The result of this experiment is shown in Fig.13, which depicts the spectra analogous to those presented in Fig.12 right. The bump obtained with the difference marked c, again appears in the arm pointing to the scattering foil. The integrated yield of the spectrum c confined within the masses of 180-220 a.m.u. amounts to 2.4×10^{-3} relative to the corresponding locus of conventional binary fission. These events typically correspond to a mass loss of 40-70 a.m.u., as in the other case, the positions in the mass scale of the peaks c agree well in both experiments. This result also shows that the effect of the dispersive scattering considered, does not depend on the foil thickness.

In the third experiment (Ex3, Fig. 11c) the grids supporting the foils of the two MCPs used as timing detectors in each arm, served both as a separating mesh and as a dispersing media, the system has 72% total transparency within the geometrical solid angle. The energy was obtained by PIN diodes. Again the separation of the two lighter partners of the tripartition decay was achieved by scattering in a dispersive foils and the blocking one of the two fragments (scattered at a very small relative angle) in the frames. We observe again the bump in the sum spectrum of $M_{\rm total} = M_a + M_b$ confined within 180-220 a.m.u. as shown in Fig. 14. Spectrum a) corresponds to the arm facing the source backing, which acts as scattering medium. The additional yield in the same mass range as previously, relative to binary events, amounts to 2.7×10^{-3}. The best mass resolution among our experiments (< 2.5 a.m.u.) was achieved in this case. This is due to the better measurement of TOFs by the MCP-detectors and the absence of straggling in the energy channel. Unfortunately, the spectrum suffers from low statistics, this is partially overcome by applying a simple averaging procedure of the counts in three adjacent channels (curve b). This procedure smoothes the background fluctuations and produces two statistically reliable wide peaks in this spectrum, marked by arrows indicating "missing" $^{70,\ 68}$Ni fragments, and also the total mass of two registered fragments amounting to 204-208 a.m.u., respectively. The symmetry of the two spectrometer arms is reflected in the result, that the spectrum a) and the complementary one obtained in the second arm of the spectrometer depicted in Fig. 14 as curve c, give the same result. The statistically significant regions centered at $M_{\rm total} = 204 - 212$ a.m.u. are marked by arrows in Fig. 14. We note that the same effect of an enhanced yield corresponding to a missing mass defined by a region of $M_{\rm total} = M_a + M_b = 180 - 212$ has been observed in the three independent experiments described. The small variation of the yields relative to the total binary events can be traced back to the different geometries. Possible uncertainties in the yields obtained from the experiments at hand need some comments. The statistical error in any cases does not exceed 2.5%. At the same time a systematic component is difficult to estimate.

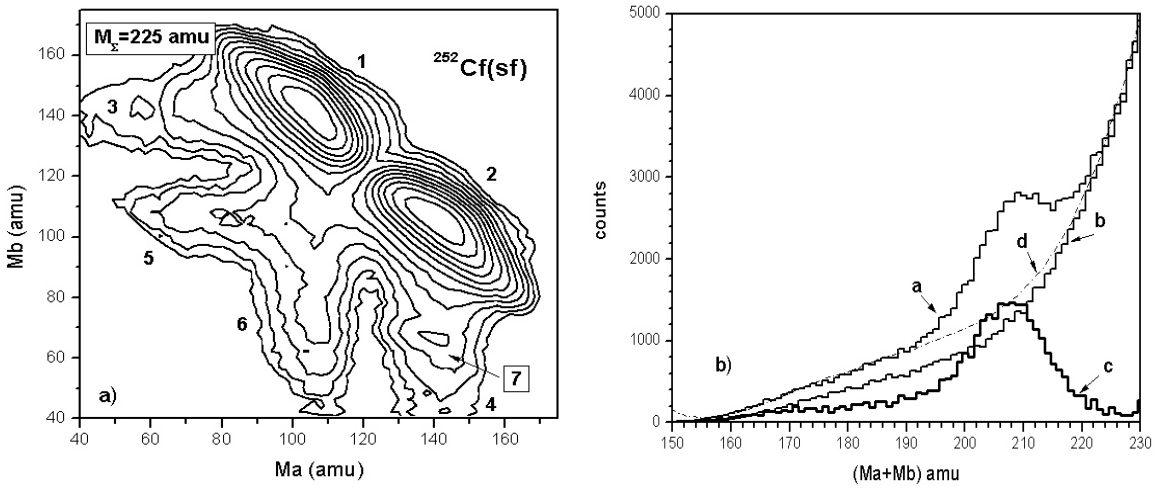

FIG. 12: Experimental evidence of the collinear tripartiton of μg/cm^{2}Cf obtained at the FOBOS setup. Contour map (in logarithmic scale) of the mass-mass distribution of the collinear fragments detected in coincidence in the opposite arms (marked by letters a and b) of the spectrometer (top). The loci of conventional binary fission events 1, 2 are prolonged by the "tails" marked 3-6 due to the scattered fragments. Bump 7 located below the line of the sum $M_a + M_b = 225$ a.m.u. is analyzed (bottom). There the spectra of total masses for the "tails" (3 and 4), spectrum a and spectrum b, respectively, are compared. The difference spectrum is marked c. Curve d is a polynomial fit using the points outside of the gross peak on spectrum a.

The ratio "number of ternary events per binary fission" is governed by the multiple scattering angles of the mass-energy-charge distribution of the ternary decay products unknown in detail. Thus we can only claim the effect to be not less than 4×10^{-3} per binary fission.

The experimental observations will be interpreted as a collinear ternary decay with three fragments of similar mass, a decay which is different to the previously reported "ternary" fission, where the third light fragment (typically He or Be-isotopes) is emitted perpendicular to the axis spanned by the heavy fission fragments [25]. For a more detailed discussion we come back to the results obtained in Ex1. The contour map of the two-dimensional mass-mass distribution obtained by subtraction of the "tail" (3) from "tail" (4), already defined in Fig. 11a, is shown in Fig. 15a. This distribution shows the contour of the ternary mass splits more clearly, it is almost free from further experimental background originating from scattered fragments of the normal binary fission. Some features of this 2D-plot can be further emphasized by a process, where a second derivative filter is applied, a method which is typically used in the search for peaks in gamma-spectra [26, 27] (Fig. 15b). The scale of the squares is defined in the insert to this figure. The tops of the peaks are found over certain linear sections of $M_a = \text{const}$ with intersections with the discrete diagonal lines, as marked in Fig. 15b, they correspond to the total masses $M_{\text{total}} = \text{const.}$ with values of 204, 208 and 212 a.m.u., respectively. The listed peaks have already been marked in Fig. 14. Thus, the bump (7) seen in Figs. 11a and 15a consists mainly of the three overlapping ridges oriented along the lines $M_{\text{total}} = \text{const}$.

From the observed mass spectra we will have to consider a ternary fission process with one heavier and two lighter fragments. The missing masses in the sum spectra of the experiment (Ex1) suggest subsystems with particular masses. The same mass values are observed as distinct peaks in Fig. 14 (from Ex3); these are also seen as ridges in Fig.15b. We note that from these data the shell closures [28] in proton and neutron number are decisive for the formation of the emitted subsystems. As can be deduced from Fig. 15a the ridges (marked by the dashed lines) go through crossing points corresponding to different combinations of two fragments with "magic" nucleon numbers (marked by the dash-and-dot arrows). These marked points could be related to mass values with magic subsystems well known from binary fission [28, 29] as follows: 204 $\rightarrow$ ^{70}Ni+^{134}Te or ^{72}Ni+^{132}Sn ("missing" ^{48}Ca), 208 $\rightarrow$ ^{80}Ge+^{128}Sn ("missing" $^{44}S_{28}$) and

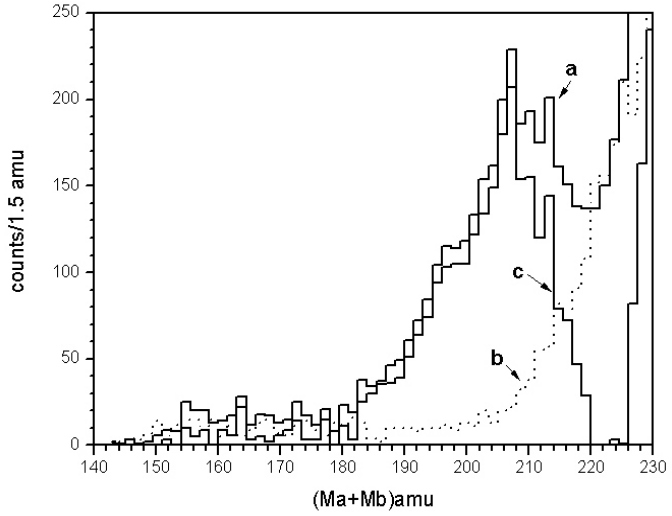

FIG. 13: Spectrum of sum of masses ($M_b + M_a$) from experiment Ex2, for two registered fragments for the gate similar to the "tail"4 from Fig. 12, left. Spectrum b corresponds to the "clean" opposite arm free from dispersion foil, c is the difference spectrum.

for $M_{\rm total} = 212 \rightarrow {}^{80}$Ge+^{132}Sn or ^{78}Ni+^{134}Te or ^{68}Ni+^{144}Ba.

It should be noted that the central peak in the Fig. 14a (marked as $\Sigma = 204 - 208$) is likely a triplet which includes the peak centered at 206 a.m.u. It could be related to magic subsystem: $206 \rightarrow$ 72Ni+^{134}Te ("missing" $^{46}Ar_{28}$). Thus, three subsystems from these proposed above consist of three magic clusters each. The ridges discussed are crossed as well by the horizontal ridge (seen via bunching of contour lines in Fig. 11c), this effect can be linked with the isotopes of $^{68,\ 70}$Ni which are also magic [29]. This observation would imply that the detected light fragment from the two L1, L2 fragments (see Fig. 11b) is always a Ni-isotope. Due to the symmetry of the detector setup, namely that the two L1, L2 fragments are always detected in coincidence with the same heavy fragments, one should also observe events with a "missing" Ni-fragment. This is indeed observed, and the peak corresponding to "missing" masses of 70 and 68 a.m.u. is well seen in Fig. 14 (curve b). Thus all different peaks in the "missing"- mass spectrum correspond, consistently, to the ternary decay scenario proposed. Inspecting the lower part of Fig.15a, we observe a gross bump, which is well bounded by the mass of the double magic nucleus of ^{48}Ca. Further there is a strong manifestation for the formation of the deformed magic ^{150}Ce nucleus [30], which is seen as two peaks (all in all 355 events) in the upper right corner of Fig. 15a ($^{72,\ 78}$Ni/^{150}Ce). Also a weak trace of a vertical ridge in the vicinity of the well known magic $^{144}Ba_{88}$ nucleus should be noted.

We would also like to stress that the observation of structures for the masses of the emitted fragments and the "missing" masses corresponding to known shells should be seen as a decisive argument in favor of the physical origin of the effect of tripartition. No experimental feature can emphasize these mass values, the experiment does not "know" magic numbers. The role of nuclear shells in the effect observed appears in analogy with known molecular like states in light alpha-cluster nuclei which can also form strongly deformed hyper-deformed resonances. Recent theoretical studies of multicluster accompanied fission [8] and binary clusterization of the ^{252}Cf nucleus [31] emphasize the role of the double magic nuclei ^{132}Sn and ^{48}Ca in these processes.

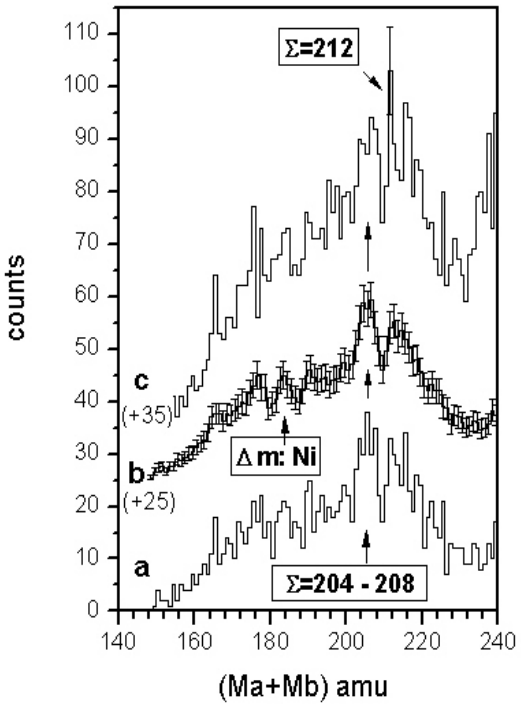

FIG. 14: Spectrum of sum of masses of two detected fragments obtained in our third experiment Ex3: a) From the arm facing the source backing; b) the same spectrum smoothed by means of averaging of counts in three adjacent channels (shifted up by 25 counts); c) the sum of spectrum a and a complementary spectrum obtained in the second arm of the spectrometer (shifted up by 35 counts). The sums marked in the panels correspond to different pairs of magic nuclei (see text). The peak in spectrum b) marked by arrow is due to the doublet of "missing" $^{70,\ 68}$Ni fragments.

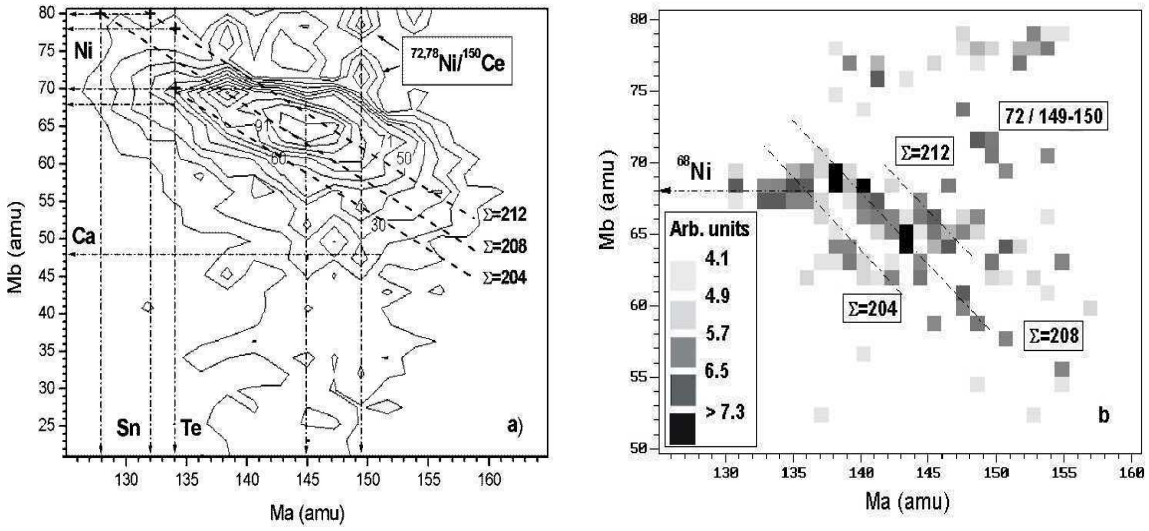

FIG. 15: a) The figure depicts as a 2D-contour map (M_b versus M_a) the difference between the "tails" 4 and 3, of the events measured with the FOBOS-detector system shown in Fig. 11a; note the expanded scale for the lighter mass fragments. Dashed lines tilted by 450 with respect to the M_a axis correspond to the fixed total mass of detected fragments (see the text for more details); b) same as in a), however, passed through a filter which emphasizes the two dimensional structures.

The observed ternary decay must be viewed as sequence of two neck ruptures of a hyper-deformed shape, and strongly deformed sub-structures may be created in the first step. In the ternary decay modes first a heavy fragment may be created, equal by mass to the sum of two magic clusters (consisting of Sn, Te for the heavy and of Ge, Ni, as the light ones) and a complementary light fragment L1. The following rupture of the heavy fragment, created in the first stage, leads to the formation of cluster L2 and complimentary one being heavier than Sn or Te. An alternative scenario leading to the horizontal ridge in Fig. 15, a differs by the creation of Ni-cluster at the first step.

We can consider a preformation of two magic clusters in the body of the fissioning system at the early stage of its elongation. This was shown in the framework of Strutinsky procedure in [18] to occur by the formation of a potential valley in a multi-dimensional deformation space. Descending from the fission barrier along a specific valley is accompanied by tunneling of the system into the valley of separated fragments [32]. This path is described by a continuous trajectory in the space of observables [33] relevant for the experiment, such as energy, mass, etc. We can propose that the ternary decays follow the path along the most populated valley based on the Ge-Sn clusters revealed in Ref. [18] and those energetically close by. All these valleys give rise to trajectories which are united in the gross bump marked (7) in Figs. 12a and 15a.

Two important facts should be emphasized to explain the occurrence of the ternary fission in the specific mode observed here. We already know from the liquid drop model, that the Q-value for the fission mode with three fragments is larger than that for binary fission. Similarly to the latter, ternary fission is preferred for masses where magic numbers of the shell model are possible. The mentioned fission valleys are thus deeper than for binary fission and are deepest for ternary fission with at least two magic (or semi-magic) clusters. The Coulomb interaction between the two clusters give the minimum energy value (deepest valley) for the collinear configuration. Deviations from these two conditions have very large effect in the reduction of the fission probabilities.

III. CONCLUSION

An understanding of the physical mechanism of the CCT will require additional efforts in experiment and theory, but some conclusions can already be drawn. The results presented here for the decay of the nucleus of ^{252}Cf show, for the first time, the true ternary spontaneous decay channel has been observed with good statistical accuracy in agreement with recent theoretical expectations [15]. The decay fragments with the masses in the vicinity of magic ^{132}Sn, ^{70}Ni and ^{48}Ca isotopes fly apart almost collinearly and we call such decay "collinear cluster tripartition" (CCT). The probability of this new effect is not less than 4×10^{-3} with respect to the normal binary fission. This implies that its probability is much larger than of the known "ternary fission" accompanied by the light charged particles. It seems now clear that the effect is due to the formation of the multi-component nuclear molecules based on magic nuclei as clustered substructures in the body of the decaying heavy system. This observation points to the need of an essential refinement of the actual fission theory.

Acknowledgments

The work was partially supported by Russian Foundation for Basic Research grant 05-02-17493.

[1] W.J. Swiatecki, Proc. of the 2nd UN Int. Conf. on the Peaceful Uses of Atomic Energy (United Nations, Geneva, 1958), Vol. 15, p. 248.
[2] V.M. Strutinsky *et al.*, Nucl. Phys. **46**, 639 (1963).
[3] T. San-Tsiang *et al.*, Seances Acad. Sci. **223**, 986 (1946).
[4] F. Goennenwein *et al.*, Nuovo Cimento A **110**, 1089 (1997).
[5] I. Halpern, Annu. Rev. Nucl. Sci.**21**, 245 (1971).
[6] E. Piasecki *et al.*, Phys. Lett. **33B**, 568 (1970).
[7] S.K. Kataria *et al.*, "Physics and chemistry of fission", Vienna: IAEA, Vol. 2, 13-17 August 1973, p. 389.
[8] D.N. Poenaru *et al.*, Phys. Rev. C **59**, 3457 (1999).
[9] A. Sandulesku *et al.*, Fiz. Elem. Chastits At Yadra **11**, 1334 (1980).
[10] H.J. Rose and G.A. Jones, Nature **307**, 245 (1984).
[11] E.K. Hulet *et al.*, Phys. Rev. Lett. **56**, 313 (1986).
[12] . M.L. Muga *et al.*, Phys. Rev. **161**, 1266 (1967).
[13] P. Schall *et al.*, Phys. Let. B **191**, 339 (1987).
[14] H. Diehl and W. Greiner, Nucl. Phys. A **229**, 29 (1974).
[15] D.N. Poenaru *et al.*, Proc. Symp. On Nuclear Clusters, Rauschholzhaussen, Germany, 5-9 August 2002, p.283
[16] Yu. V. Pyatkov *et al.*, Physics of Atomic Nuclei **66**, 1631 (2003).
[17] V.V. Pashkevich, Nucl. Phys. A **169**, 275 (1971).
[18] Yu.V. Pyatkov *et al.*, Nucl. Phys. A **624**, 140 (1997).
[19] Yu.V. Pyatkov and R. A. Shekhmamet'ev, Phys. At. Nucl. **57**, 1116 (1994).
[20] Yu.V. Pyatkov *et al.*, Izv. Ross. Akad. Nauk, Ser. Fiz. **60**, 30 (1996) (in Russian).
[21] Yu. V. Pyatkov *et al.*, Nucl. Phys. A **611**, 355 (1996).
[22] H.-G. Ortlepp *et al.*, Nucl. Instr. and Meth. A **403**, 65 (1998).
[23] D.V. Kamanin *et al.*, Physics of Atomic Nuclei **66**, 1655 (2003).
[24] L. Meyer, Phys. Stat. Sol. (b) **44**, 253 (1971).
[25] F.Goennenwein *et al.*, Europhysics News **36**, 11 (2005).
[26] M.A. Mariscotti, Nucl. Instr. and Meth. **50**, 309 (1967).
[27] Yu.V.Pyatkov *et al.*, Nucl. Instr. and Meth. A **488**, 381 (2002).

[28] B.D. Wilkins *et al.*, Phys. Rev. C **14**, 1832 (1976).
[29] D. Rochman *et al.*, Nucl. Phys. A **735**, 3 (2004).
[30] H. Mrton, Private communication.
[31] J. Cseh *et al.*, Phys. Rev. C **70**, 034311 (2004).
[32] J.F. Berger *et al.*, Nucl. Phys. A **428**, 23 (1984).
[33] Yu.V.Pyatkov *et al.*, Physics of Atomic Nuclei **67**, 1726 (2004).

Radioactive Ion Beam Research Done in Dubna

G.M. Ter-Akopian,* A.S. Fomichev, M.S. Golovkov, A.V. Gorshkov, V.A. Gorshkov, L.V. Grigorenko, S.A. Krupko, Yu.Ts. Oganessian, A.M. Rodin, S.I. Sidorchuk, R.S. Slepnev, and S.V. Stepantsov

Flerov Laboratory of Nuclear Reactions, JINR, Dubna, RU-141980 Russia

R. Wolski

Flerov Laboratory of Nuclear Reactions, JINR, Dubna, RU-141980 Russia and

The Henryk Niewodniczański Institute of Nuclear Physics, Kraków, Poland

A.A. Korsheninnikov and E.Yu. Nikolskii

RIKEN, Hirosawa 2-1, Wako, Saitama 351-0198, Japan and

C "The Kurchatov Institute", Kurchatov sq. 1, 123182 Moscow, Russia

V.A. Kuzmin, B.G. Novatskii, and D.N. Stepanov

C "The Kurchatov Institute", Kurchatov sq. 1, 123182 Moscow, Russia

P. Roussel-Chomaz and W. Mittig

GANIL, BP 5027, F-14076 Caen Cedex 5, France

Experiments carried out using ^{3}H, ^{6}He and ^{8}He beams available from the ACCULINNA separator are briefly reviewed. In more detail results obtained recently in three experiments are presented.

Attempt to observe a ^{7}H resonance produced in the reaction ^{2}H(^{8}He, ^{3}He)^{7}H resulted only in setting a limit $\mathrm{d}\sigma/\mathrm{d}\Omega \leq 20$ μb/sr for the reaction exit channel which could populate a resonance lying between 0 and 3 MeV above the ^{7}H decay threshold.

The spectrum of ^{9}He was studied by means of the ^{2}H(^{8}He, p)^{9}He reaction at a lab energy of 25 MeV/amu and small center-of-mass angles. Energy and angular correlations were obtained for the ^{9}He decay products by complete kinematic reconstruction. The lowest resonant state of ^{9}He is found at 2.0±0.2 MeV with a width of ∼2 MeV and is identified as $1/2^{-}$. The observed angular correlation pattern is uniquely explained by the interference of the $1/2^{-}$ resonance with a virtual $1/2^{+}$ state (a limit $a > -20$ fm is obtained for the scattering length), and with a $5/2^{+}$ resonance at energy ≥ 4.2 MeV.

Quasi-free scattering of the α core bound in ^{6}He was explored keeping in mind the possible study of the cluster structure of this halo nucleus. For the first time coincident particles emitted in the ^{4}He(^{6}He, 2α)nn reaction were detected in wide angular ranges giving a wide kinematical range of the measured angular and momentum distributions. The contribution of processes, competing with the quasi-free $\alpha - \alpha$ scattering in the $\alpha + \alpha + n + n$ output channel, was considerably suppressed by the selection of events with $\mathrm{E}_{\alpha 1(2)-nn} > 10$ MeV. Experimental distributions, relevant to the reaction mechanism and to the ^{6}He structure, were compared with the results of Monte-Carlo simulations based on the Plane Wave Impulse Approximation (PWIA) formalism. The PWIA predictions showed consistency with the experimental data.

I. INTRODUCTION

Secondary radioactive ion beams (RIBs) obtained with the use of intermediate energy primary beams of heavy ions were used extensively to investigate the structure of light halo nuclei. Mostly, nuclear matter radii and momentum distributions of fragmentation reaction products were carried out at the RIB energy >40 MeV/amu to extract information about halo nuclei (see e.g. Ref. [1]). The study of the lightest halo nuclei done by means of direct reactions produced by lower energy RIBs available from the separator ACCULINNA [2] is an essential part of the research program carried out at the G.N. Flerov Laboratory of JINR (Dubna).

The finding of a two-neutron exchange process resulting in a large cross section value for the backward direction ^{6}He + ^{4}He elastic scattering at E_{lab} = 25 MeV/amu made the first experimental proof of the "di-neutron" configuration in ^{6}He [3]. The known extended distribution of neutron matter in ^{6}He was explored with the ^{6}He + ^{1}H elastic and inelastic scattering measured in a broad angular range with a 24.5 MeV/amu beam of ^{6}He nuclei [4] . Data acquired about elastic scattering and 1n and 2n transfer reactions observed for the ^{6}He + ^{1}H system testified to a large "di-neutron" spectroscopic factor in ^{6}He and a low probability for a t+t clustering in its structure [5]. A similar study made for the ^{8}He + ^{1}H reaction resulted in the estimation of spectroscopic factors for the ^{6}He(0^+g.s.) and ^{6}He(2^+) subsystems in ^{8}He and in the observation of a ^{5}H+t clustering in the ^{8}He structure [6, 7]. Search for a four-neutron exchange in the ^{8}He + ^{4}He reaction fixed only an upper limit of 1 μb/sr for the cross section of backward direction elastic scattering of 25 MeV/amu ^{8}He nuclei [6].

Due to their inherent transparency and not too low cross sections, transfer reactions induced by RIBs were proven to be effective in the study of resonance states of particle unstable drip-line nuclei. Cryogenic tritium targets [8] and a 58 MeV beam of ^{3}H nuclei accelerated at the Dubna U-400M cyclotron [9] played essential role in this work, alongside with the ^{6}He and ^{8}He beams delivered by ACCULINNA. The energy and width of the ^{4}H ground state (g.s.) resonance were finally determined in a complete kinematic study made for the transfer reactions ^{2}H(t,p)^{4}H and ^{3}H(t,d)^{4}H [10]. The ^{5}H puzzle was resolved in experiments where the ground state resonance of this nuclear system was investigated using the ^{1}H(^{6}He,^{2}He)^{5}H [11] and ^{3}H(t,p)^{5}H [12, 13] reactions. It is worth noting that a T=3/2 isobaric analog state of the ^{5}H g.s. was for the first time obtained in the ^{5}He spectrum populated in the transfer reaction ^{2}H(^{6}He,^{3}He)^{5}He [14].

These results give us inspiration to employ RIB transfer reactions in order to get even more neutron-excess nuclei of hydrogen and helium. Quite recently we completed an experiment combining the conditions necessary for detecting ^{7}H and ^{9}He nuclei emerging as products in the ^{8}He + ^{2}H reaction. Sect. II gives an account of this experiment. Results derived for ^{9}He are presented in Sect. III.

Exploratory study was undertaken for the (α,2α) knock-out occurring when a helium target was bombarded with a 25 MeV/amu ^{6}He beam. Conditions adopted in this experiment facilitated the observation of quasi-free scattering (QFS) of helium target nuclei from the α-cluster core of the ^{6}He halo nucleus. These results are presented in Sect. IV.

II. SEARCH FOR ^{7}H MANIFESTATION IN THE ^{8}He + ^{2}H REACTION

Motivation. —In Ref. [15] we revisited the long-standing issue of the ^{7}H nucleus setting an upper limit of 3 nb/sr for the cross section of the ^{2}H(^{8}He,^{3}He)^{7}H reaction which could populate a (hypothetical) quasi stable ($T_{1/2} \geq 1$ ns) resonance state in ^{7}H. One could not

*Electronic address: gurgen@jinr.ru

a priory exclude such a long life time for ^{7}H without checking this experimentally because, most likely, this nucleus undergoes an unique decay - the four neutron emission (five-body decay). Estimates [15] show that the width of the ^{7}H g.s. resonance will be less than 1 MeV, if its decay energy is less than 2–3 MeV. In the experiment discussed here, we made an attempt to observe the ^{7}H resonance which could come to light in the missing mass spectrum derived from the kinematical characteristics of ^{3}He nuclei emitted in the ^{2}H(^{8}He,^{3}He)^{7}H reaction.

Experiment. — We used a 34 MeV/amu primary beam of ^{11}B accelerated by the U-400M cyclotron to bombard the production target of ACCULINNA (Be, 370 mg/cm^2). At a typical primary beam intensity of 4 pμA a 25 MeV/amu secondary beam of ^{8}He nuclei was delivered by the separator to a target positioned in a reaction chamber at a distance of $\sim$ 20ṁ from the production target. Roughly one half of this distance was occupied by the ACCULINNA separator, whereas the second half was a straight beam line used for the beam diagnostics.

A set of beam detectors was installed on the straight section of the beam line. Two thin plastic scintillators placed on a 8 m base were used for the energy measurement and particle identification. These measurements were done individually for any beam particle. The overall time-of-flight (TOF) resolution was 0.8 ns. Beam tracking was done by two multi-wire chambers installed 26 and 80 cm upstream of the target. Each chamber had two planes of wires with a 1.25 mm pitch. The beam energy spread and angular divergence on the target were about 8.5% and 0.23°, respectively. For each projectile nucleus hitting the target the energy, the hit position on the target and the inclination angle of the trajectory were defined with accuracy 1.4%, 1.5 mm and 0.1°, respectively.

The ^{8}He beam intensity was typically 2×10^{4} s^{-1} at if the separator was tuned for a beam energy of 25-28 MeV/amu. By tuning the separator for 25-28 MeV/amu ^{6}He beam we could have 2×10^{6} s^{-1} ^{6}He nuclei on the target. However conditions implied by the beam diagnostics compelled us to limit the ^{6}He beam intensity to 3×10^{5} s^{-1}. Being focused in a 20 mm circle on the target window, both beams, ^{6}He and ^{8}He, had a purity of $\geq$ 95%.

The target used in this experiment was a gas cell filled with deuterium at 1020 mPa and cooled down to 25 K. The 4 mm thick target cell was supplied with 6 μm stainless steel windows. The target thickness was 2.5×10^{20} cm^{-2}. In the present experiment, the energy of the ^{8}He beam in the middle of the target was $\sim$25 MeV/nucleon.

Slow ^{3}He nuclei escaping from the target in the forward direction were detected by a telescope composed of a front array of 8 sector type 40 μm thick Si detectors followed by an annular 300 μm Si detector having an active area of the outer and inner diameters of 82 mm and 32 mm, respectively. It was segmented in 16 rings on one side and 16 sectors on the other side providing a good position resolution. The array of 40 μm Si detectors matched the active area of the annular detector. The telescope was installed 100 mm downstream of the target. The ΔE-E particle identification, provided by the telescope, was essential since the overwhelming majority of detected charged particles were tritons and ^{4}He nuclei. This background was suppressed by detecting the ^{3}He nuclei in coincidence with the the ^{3}H nuclei resulting from the ^{7}H decay.

The ^{3}H nuclei resulting from the ^{9}He decay were detected by a Si-CsI telescope installed 55 cm downstream of the target. The telescope consisted of two 1 mm thick silicon detectors and 16 CsI crystals coupled with pin-diodes. The 6×6 cm Si detectors were segmented in 32 strips both in horizontal and vertical directions, providing position resolution and particle identification (by the ΔE-E method together with the CsI detectors). The CsI crystals ($1.5 \times 2 \times 2$ cm) were arranged as a 4×4 wall just behind the Si detectors.

Results. — A beam dose of 2×10^{10} ^{8}He nuclei passing through the deuterium target was accumulated in this experiment. A ^{7}H missing mass spectrum resulting from the detected ^{3}He-

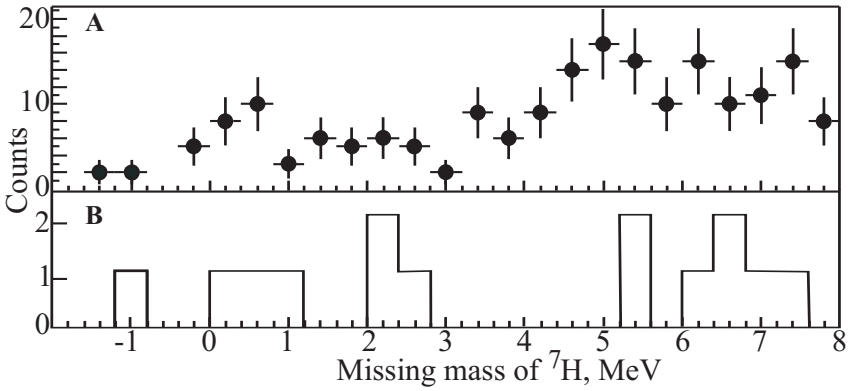

FIG. 1: Missing mass spectrum of ^{7}H derived from the ^{2}H(^{8}He,^{3}He)^{7}H reaction data. A - ^{3}He events, B - ^{3}He-^{3}H events.

^{3}H coincidence events is presented in Fig. 1, panel B. Panel A in Fig. 1 shows the ^{7}H spectrum derived from the data collected for single ^{3}He nuclei. Evidently, the more rich pattern seen in the spectrum of panel A was due to the ^{4}He background which partly could fall into the ^{3}H locus on the ΔE-E identification plot. From the few events observed in the spectrum of Fig. 1, panel B, only a cross section limit $d\sigma/d\Omega \leq 20$ μb/sr follows for the reaction ^{2}H(^{8}He,^{3}He)^{7}H populating a resonance lying between 0 and 3 MeV above the ^{7}H decay threshold.

III. NEW INSIGHTS INTO THE ^{9}He LOW-ENERGY SPECTRUM

Motivation. — Since the first observation of ^{9}He reported in Ref. [16] it was studied in relatively small number of works compared to the neighboring exotic nuclei. This could be connected with the technical difficulty of this study. On the other hand, the low-energy resonant states of ^{9}He were considered to be well established experimentally. The observations made in Ref. [16] were confirmed in Ref. [17], where the ^{9}Be(^{14}C,^{14}O)^{9}He reaction was used.

A recent experiment [18] was focused on the search for a virtual s-wave state in ^{9}He. An upper limit on the scattering length $a < -10$ fm was set in this work. Also, in Ref. [19] the properties of states in ^{9}He were inferred basing on the studies of isobaric partners in ^{9}Li. The available results are summarized in Table I.

The interpretation of the ^{9}He spectrum as provided in [16, 17] faces certain difficulties which did not go unnoticed (Ref. [20]). Indeed, the authors of Ref. [17] reported on the observation of

TABLE I: Experimental positions of states in ^{9}He relative to the ^{8}He+n threshold (energies and widths are given in MeV).

	$1/2^+$	$1/2^-$		$3/2^-$		$5/2^+$	
Ref.	a (fm)	$E_{^9\mathrm{He}}$	Γ	$E_{^9\mathrm{He}}$	Γ	$E_{^9\mathrm{He}}$	Γ
[16]		1.13(10)	small[b]	2.3	small[b]	4.9	
[17]		1.27(10)	0.10(6)	2.4(1)	0.7(2)	4.3	small
[18]	<-10						
[19][a]		1.1		2.2		4.0	
Present work	>-20	2.0(2)	2			≥ 4.2	> 0.5

[a] Inferred from isobaric symmetry.
[b] Observed peak width is equal to the declared resolution.

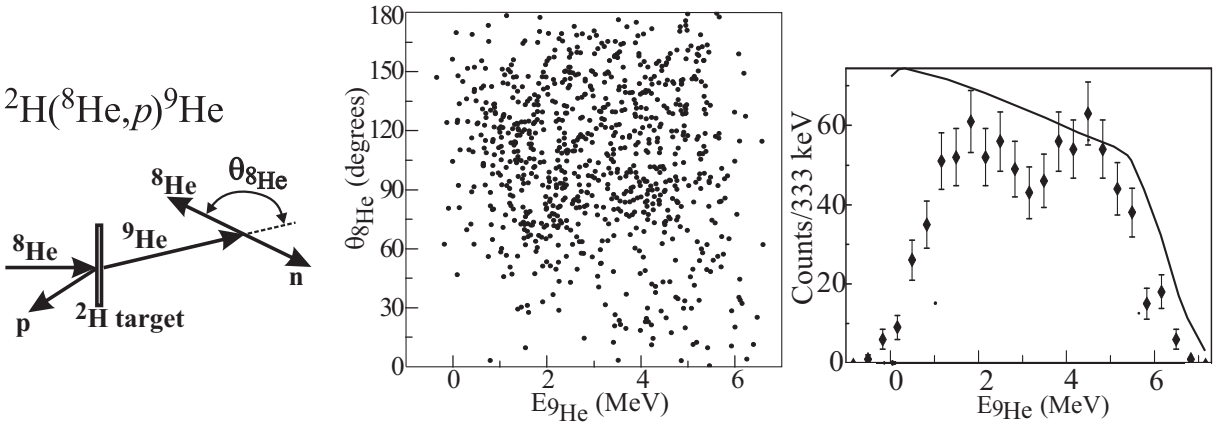

FIG. 2: *L*eft panel: Kinematical diagram showing momentum vectors for the ^{2}H(^{8}He,p)^{9}He reaction (see text). *C*entral panel: Experimental data in the $\{E_{^9\mathrm{He}}, \theta_{^8\mathrm{He}}\}$ plane. *R*ight panel: The missing mass spectrum of ^{9}He. The curve shows the total detection efficiency in arbitrary units.

a narrow [$\Gamma = 0.10(6)$ MeV] ^{9}He resonance at energy 1.27(10) MeV above the ^{8}He+n threshold with spin and parity assigned as $J^\pi = 1/2^-$. However, a much larger width, $0.8 - 1.3$ MeV was estimated in Ref. [20] for such a resonance assuming, as expected, that this is a single particle state. The observations reported in Refs. [16, 17] require a spectroscopic factor of ≤ 0.1 for the first resonant state of ^{9}He what conflicts with the idea that this is a single-particle state. F. Barker in Ref. [20] concludes on this point that "some configuration mixing in either the ^{9}He($1/2^-$) or ^{8}He(0^+) state or both is possible, but is unlikely to be large enough to reduce the calculated width to the experimental value".

The second ^{9}He resonance was found at 2.4 MeV [17]. In order to explain the width [$\Gamma = 0.7(1)$ MeV] reported for this resonance one should suppose a quite large spectroscopic factor $S \sim 0.3 - 0.4$. However, being assumed to be a $3/2^-$ state [17], it should be a complicated particle-hole excitation as the $p_{3/2}$ sub-shell is occupied in ^{9}He.

Having in mind the mentioned issues we decided to study the ^{9}He in the "classical" (d,p) reaction well populating single particle states. In contrast with the previous works complete kinematics measurements were foreseen to reveal the low-energy s-wave mode. Following the experimental concept of Ref. [13], where the ^{5}H continuum was studied, the so called "zero geometry" was used in this work. So, the ^{2}H(^{8}He,p)^{9}He reaction was employed in the experiment presented below.

Experiment. — Conditions of the beam production and diagnostics, as well as parameters inherent to the deuterium target, were identical to those existing in the ^{7}H experiment. Kinematical diagram for the ^{2}H(^{8}He,p)^{9}He reaction is shown in Fig. 2 (left panel). Slow protons escaping from the target in the backward direction hit against an annular 300 μm silicon detector with an active area of the outer and inner diameters of 82 mm and 32 mm, respectively. Being installed 100 mm upstream of the target this detector provided for the study of the ^{2}H(^{8}He,p)^{9}He reaction at center-of-mass (c.m.) angles $3^\circ \leq \theta \leq 7^\circ$. It was segmented in 16 rings on one side and 16 sectors on the other side. A veto detector was installed upstream of the proton detector to eliminate signals coming from the beam halo.

The ^{8}He nuclei resulting from the ^{9}He decay were detected by the Si-CsI telescope described in Section II. We did not use particle identification in the proton detector because, due to the kinematical constraints of the ^{8}He+^{2}H collisions, only protons could be emitted in the backward direction. The main cause of the background was due to the evaporation protons originating

from the interaction of ^{8}He beam with the target windows. This background was almost completely suppressed by the p$-^8$He coincidence. Such coincidence fixed complete kinematics for the experiment. Finally, an empty target run showed only $\sim 2\%$ of background events.

Experimental results are presented in Fig. 2 (central panel) as a $E_{^9\mathrm{He}}$ *vs.* $\theta_{^8\mathrm{He}}$ plot and its projections on the $E_{^9\mathrm{He}}$ axis (see Fig. 2, right panel). Hereafter, we denote by $E_{^9\mathrm{He}}$ the ^{9}He missing mass energy and by $\theta_{^8\mathrm{He}}$ the ^{8}He angle in the ^{9}He c.m. system (see Fig. 2). Detection threshold set for the protons (~ 1.2 MeV) led to the efficiency fall for the missing mass of ^{9}He above 5 MeV (see Fig. 2, right panel). Monte-Carlo (MC) procedures were used to estimate all experimental details. Energy resolution was found to be 0.65 MeV (FWHM) for the ^{9}He missing mass energy $0 \geq E_{^9\mathrm{He}} \leq 3.0$ MeV. The main contributions to this value were due to the target thickness ($\sim 75\%$) and the precision of the beam energy measurement ($\sim 20\%$). In the full range of measured $E_{^9\mathrm{He}}$ values efficiency achieved in the p-^{8}He coincidence detection approached 100% for $\theta_{^8\mathrm{He}} < 45°$ and $\theta_{^8\mathrm{He}} > 135°$. At $E_{^9\mathrm{He}} \geq 4$ MeV and $60° < \theta_{^8\mathrm{He}} < 120°$ this efficiency fell down to $\sim$60%. The resolution in $\theta_{^8\mathrm{He}}$ had FWHM $\leq 12°$ at $E_{^9\mathrm{He}} \geq 3$ MeV, $\leq 15°$ at $E_{^9\mathrm{He}} \sim 2$ MeV, and $\leq 35°$ at $E_{^9\mathrm{He}} \sim 0.25$ MeV. This resolution was mainly defined by the precision of the beam energy measurement ($\sim 70\%$) and particle tracking ($\sim 25\%$).

Qualitative considerations. — The total number of counts presented in Fig. 2 (~ 900) corresponds to a reaction cross section of $\sim$7 mb/sr. This value is consistent with the direct one-neutron transfer reaction mechanism at forward angles implied in this work.

The narrow states known from literature do not show up in the data. Instead, we see in Fig. 2 (right panel) two broad peaks at about 2.0 and 4.2 MeV. Near the threshold, the ^{9}He spectrum exhibits behavior which is consistent rather with s-wave ($\sigma \sim \sqrt{E_{^9\mathrm{He}}}$) then with p-wave only ($\sigma \sim E_{^9\mathrm{He}}^{3/2}$). This is an indication for a possible virtual state in ^{9}He.

An important feature of the data is a prominent forward-backward asymmetry with ^{8}He flying preferably in the backward direction in the ^{9}He c.m. system. To describe such an asymmetry the interference of opposite parity states is unavoidable. As far as the asymmetry is observed even at low $E_{^9\mathrm{He}}$, the s-p interference is compulsory (see Fig. 3 a1-a3). Such an interference can provide only a very smooth distribution described by the first order polynomial (see below Eq. 2). Since above 3 MeV the distribution character changes to a higher polynomial, but asymmetry does not disappear, the p-d interference is also needed (see Fig. 3 a5). This defines the minimal set of states as s, p, and d.

Theoretical model. — In the zero geometry approach the resonant states of interest are identified by the observation of the recoil particle (here proton) at zero [in reality small, $3° \leq \theta_p(\mathrm{c.m.}) \leq 7°$] angle. This means that the angular momentum transferred to the studied system should have zero projection on the momentum transfer axis. As a result we get a complete (strong) alignment for states with $J > 1/2$ in the produced system. In the ^{9}He case only the magnetic sub states with $M = \pm 1/2$ should be populated for $J^\pi = 5/2^+$, $3/2^-$, and $3/2^+$ states. This strongly reduces ambiguity in the analysis of correlation patterns. For instance, in the case of zero-spin particles the zero geometry experiments give very clear pictures with angular distributions described by pure Lagrange polynomial $|P_l^0|^2$. The situation in the case of nonzero spin particles involved is more complicated (see detailed discussion and further references in [13]), and diverse correlation patterns are possible.

We have found that our experimental data can be well explained in a simple model involving only three low-lying states: $1/2^+$, $1/2^-$, and $5/2^+$. The reaction cross section in the DWBA

ansatz is written as

$$\frac{\mathrm{d}\sigma(\Omega_{^9\mathrm{He}})}{\mathrm{d}E_{^9\mathrm{He}}\,\mathrm{d}\Omega_{^8\mathrm{He}}} \sim \frac{v_f}{v_i}\sqrt{E_{^9\mathrm{He}}}\sum_{MM_S}\Big|\sum_J\langle\Psi_f^{JMM_S}\,|V|\,\Psi_i\rangle\Big|^2$$
$$= \frac{v_f}{v_i}\sum_{MM_S}\sum_{JJ'}\sum_{M_l'M_l}\rho_{JM}^{J'M}C_{l'M_l'SM_S}^{J'M'}C_{lM_lSM_S}^{JM}\,Y_{lM_l'}^{*}Y_{lM_l}. \quad (1)$$

For density matrix the generic symmetries are

$$\rho_{JM}^{J'M'} = \left(\rho_{J'M'}^{JM}\right)^* \quad ; \qquad \rho_{JM}^{JM'} = (-)^{M+M'}\rho_{J-M'}^{J-M}\,,$$

and properties specific to the coordinate choice (spirality representation) and setup (zero geometry) are

$$\rho_{JM}^{J'M'} \sim \delta_{M,M'}(\delta_{M,1/2}+\delta_{M,-1/2})\,.$$

For the density matrix parametrization we use the following model for the transition matrix. The wave function (WF) Ψ_f is calculated in the l-dependent square well (with depth parameters V_l). The well radius is taken $r_0 = 3$ fm, what is consistent with the typical R-matrix phenomenology $1.4A^{1/3}$. The energy dependence of the velocities v_i, v_f (in the incoming ^{8}He-d and outgoing ^{9}He-p channels) and WF Ψ_i is neglected for our range of ^{9}He energy. The term $V\,|\Psi_i\rangle$, describing the reaction mechanism, is approximated by radial θ-function:

$$V\,|\Psi_i\rangle \to C_l\,r^{-1}\,\theta(r_0-r)\,[Y_l(\hat{r})\otimes\chi_S]_{JM}\,,$$

where C_l is a (complex) coefficient defined by the reaction mechanism. With $|\rho_{J\pm1/2}^{J'\pm1/2}|$ denoted as $A_{l'l}$, the cross section as a function of energy $E_{^9\mathrm{He}}$ and $x = \cos(\theta_{^8\mathrm{He}})$ is

$$\frac{\mathrm{d}\sigma(\Omega_{^9\mathrm{He}})}{dE_{^9\mathrm{He}}\,\mathrm{d}x} \sim \frac{1}{\sqrt{E_{^9\mathrm{He}}}}\Big[4A_{00}+4A_{11}+3(1-2x^2+5x^4)A_{22}$$
$$+\;8\,x\cos(\phi_{10})A_{10}+4\sqrt{3}\,x(5x^2-3)\cos(\phi_{12})A_{12}\Big]\,. \quad (2)$$

Here

$$A_{l'l} = |A_{l'}||A_l|\,, \qquad A_l = C_lN_l(E)\,\mathrm{e}^{i\delta_l(E)}\int_0^{r_0}\mathrm{d}r\,j_l(q_lr)\,,$$
$$q_l = \sqrt{2M(E-V_l)}\,, \qquad \phi_{l'l}(E) = \phi_{l'l}^{(0)}+\delta_{l'}(E)-\delta_l(E)\,,$$

where N_l is defined by matching condition on the well boundary for internal function $j_l(q_lr)$. The three coefficients C_l give rise to the two phases $\phi_{10}^{(0)}$ and $\phi_{12}^{(0)}$. Positions and widths of the states are fixed by the three parameters V_l. Their relative contributions to the missing mass spectrum are fixed by the three parameters $|C_l|$. Phase $\phi_{10}^{(0)}$ is fixed by the angular distributions at $E_{^9\mathrm{He}} < 2.2\,\mathrm{MeV}$, where the contribution of the d-wave resonance is small. After that, phase $\phi_{12}^{(0)}$ was varied to fit the angular distributions at higher energies. So, the model does not have redundant parameters and the ambiguity of the theoretical interpretation is defined by the data quality. In Figs. 3a, b, and c, model calculations with different s-wave contributions are compared with the experimental data.

We have found that the weight and interaction strength for the $1/2^+$ state can be varied in a relatively broad range, still providing a reasonable description of the data. The parameter sets of the model are given in Table II; sets 1 and 2 correspond to a small negative scattering length

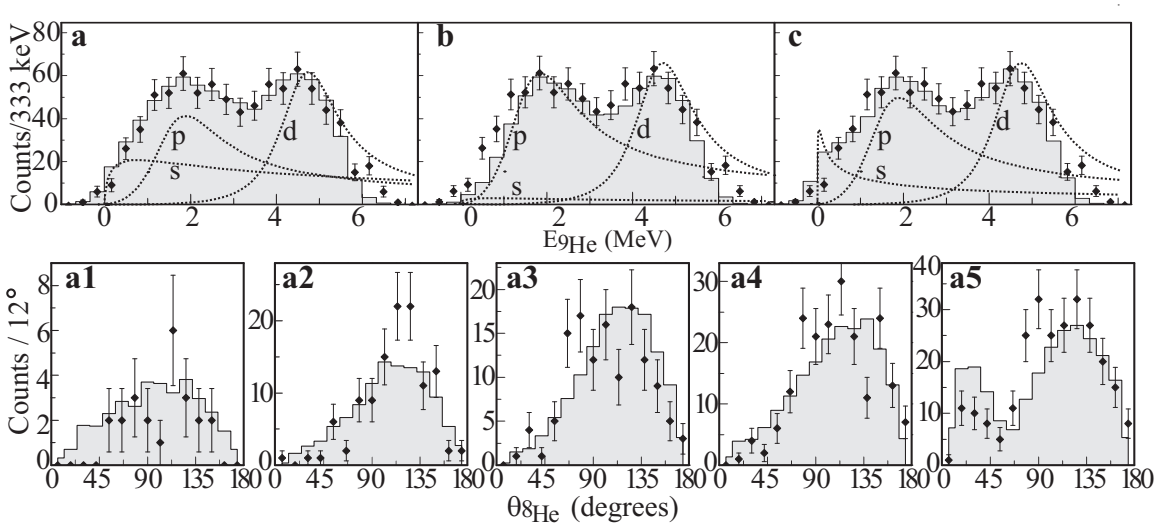

FIG. 3: Panels **a**, **b**, and **c** show fits to the ^{9}He missing mass spectrum presented by diamonds with error bars. Fits were made with different assumptions about the properties of the s-wave (see parameter sets 1, 2, and 3 in Table II). Curves **s**, **p**, and **d** represent the $1/2^+$, $1/2^-$, and $5/2^+$ states, respectively. Panels **a1**, **a2**, **a3**, **a4**, and **a5** in bottom show distributions in angle $\theta_{^8\mathrm{He}}$ obtained for ^{9}He events in energy bins $E_{^9\mathrm{He}} = -0.5$–0.5, 0.5–1.4, 1.4–2.2, 2.2–3.5, and 3.5–7.0 MeV, respectively. Gray histograms show the MC simulation of results. The simulations shown in the five bottom panels were done for parameter set 1.

($a = -4$ fm) and different weights of s-wave (the largest and the lowest possible weights), set 3 has $a = -25$ fm and the largest possible weight for s-wave. It can be seen (comparing Figs. 3a and b that agreement with the data becomes poor when the population of the s-wave continuum falls below $15 - 25\%$ of the p-wave. On the other hand, a large negative scattering length has a drastic effect below 0.5 MeV (see Fig. 3c). The data quality is not sufficient to derive the exact properties of the s-wave contribution. Situations with the large contribution of the s-wave state but with moderate scattering length (say $a > -20$ fm) seem to be more plausible. Measurements with better resolution are required to refine the properties of the $1/2^+$ continuum.

The experimental data allowed us to well fix the energy and width for the p-wave resonance (E_{res}=2.0±0.2 MeV, Γ_{res} ∼2 MeV) whereas the position of the d-wave resonance is not well defined in our analysis due to the efficiency fall in the high-energy side of the spectrum. A broader energy range measured for ^{9}He is needed to resolve the $5/2^+$ state completely.

Discussion. — It should be noted that the interference of any other combination of s-, p-, and d-wave states *can not* lead to the required forward-backward asymmetry in the whole energy range. The correlation terms (square brackets in Eq. (2)) are

$$\left[\ldots\right] \;=\; 2A_{00} + 2A_{11} + (1+3x^2)A_{22} + 4x\cos(\phi_{10})A_{10}$$

TABLE II: Parameters of the theoretical model used in this work. V_i values are in MeV and weight coefficients for different states are normalized to unity $\sum |C_i|^2 = \sum W_i = 1$.

Set	W_0	W_1	V_0	V_1	V_2	$\phi_{10}^{(0)}$	$\phi_{12}^{(0)}$
1	0.26	0.35	−4.0	−20.7	−43.4	0.80π	-0.03π
2	0.03	0.52	−4.0	−20.7	−43.4	0.85π	-0.02π
3	0.12	0.43	−5.817	−20.7	−43.4	1.00π	-0.03π

$$
\begin{aligned}
&+\ 2\sqrt{2}(3x^2-1)\cos(\phi_{20})A_{20}\,,\\
\big[\ldots\big] &= 4A_{00}+2(1+3x^2)A_{11}+3(1-2x^2+5x^4)A_{22}\,,\\
\big[\ldots\big] &= 2A_{00}+(1+3x^2)(A_{11}+A_{22})+2\,x(9x^2-5)\\
&\times\ \cos(\phi_{12})A_{12}+2\sqrt{2}(3x^2-1)\cos(\phi_{20})A_{20}\,,
\end{aligned}
$$

respectively, for the $\{s_{1/2}, p_{1/2}, d_{3/2}\}$, $\{s_{1/2}, p_{3/2}, d_{5/2}\}$, and $\{s_{1/2}, p_{3/2}, d_{3/2}\}$ sets of states. The asymmetric term ($\sim x$) is present here either for the s-p interference only or for the p-d only or for neither.

Results obtained in the present work are generally consistent with the existing data. The virtual s-state obtained in the present work was reported earlier in Ref. [18]. Our lower limit of 4.2 MeV for the d-wave resonance is in agreement with the values found in Refs [12, 17]. The present work gives definite proofs for the $1/2^-$ resonance at $E_{^9He}$=2.0 MeV with the width of $\sim$ 2 MeV. Positions (2.4 and 2.2 MeV) found for a wide resonance in Refs. [12, 17] are compatible with our result.

A remark should be made about the issue of a possible narrow resonance in the low energy spectrum of ^{9}He. The ^{2}H(^{8}He, p)^{9}He reaction employed in our experiment well populates single particle resonances. A resonance of a more complicated structure (and, hence, characterized with a small single particle spectroscopic factor) should be populated with a low probability in this reaction. Therefore it might be that we could not reveal such a resonance in our data. It is worth noting the case of a more narrow $p_{1/2}$ state imposed on the wide, single particle state having the same quantum numbers. Whatever weakly such a narrow resonance is populated, the phase shift for the $p_{1/2}$ continuum changes across this resonance by a value close to π and the character of angular distribution, built on the $s_{1/2}$-$p_{1/2}$ interference, should change drastically within this energy range. No trend of this kind is observed in Fig. 3. The data, however, do not exclude a weak population of a $p_{1/2}$ state having a width $\Gamma \leq 0.3$ MeV. The phase shift of the *broad* $1/2^-$ state changes slowly and hardly achieves $\pi/2$ in our calculations. This allows us to explain the smooth asymmetry behavior obtained at $E_{^9He} \leq 3$ MeV.

The idea that only the $1/2^-$ single-particle resonance state can be found in the low energy region of ^{9}He not only looks natural, but also finds support in the recent theoretical papers. In Ref. [21] dealing with the whole chain of helium isotopes in continuum shell model, the $1/2^-$ state is located at 1.6 MeV above the ^{8}He+n threshold and its width is $\sim$ 0.6 MeV indicating a dominant single particle component in the WF. The $3/2^-$ state is predicted to be at 6.6 MeV and relatively narrow ($\sim$ 2.5 MeV), what is natural for a complicated particle-hole excitation.

Conclusions. — We would like to emphasize the following results of our studies of ^{9}He:

i) Our data show two broad overlapping peaks (at 2.0 and 4.2 MeV) in the ^{9}He spectrum.

ii) An essential contribution of the s-wave $1/2^+$ state is evident from the data. It is manifested in two ways: (a) large forward-backward asymmetry at $E \leq 3$ MeV and (b) accumulation of counts around the decay threshold of ^{9}He, which should not take place for the cross section behavior for higher l-values. A limit $a > -20$ fm is obtained for the scattering length of this state, which is consistent with the limit of Ref. [18].

iii) The proposed spin assignment $\{s_{1/2}, p_{1/2}, d_{5/2}\}$ is unique, as no other reasonable set of low-lying states can give the observed correlation pattern.

iv) The experimental data are well described in a simple single-particle potential model, involving only basic theoretical assumptions about the reaction mechanism and the low-energy spectrum of ^{9}He. This supports the idea that ^{8}He (having closed $p_{3/2}$ sub shell) represents a "good" core in the ^{9}He structure.

IV. QUASI-FREE SCATTERING IN THE ^{4}He(^{6}He, 2α)2n REACTION

Quasi-free scattering of nucleons and clusters bound in nuclei is acknowledged as a tool for nuclear structure studies (see e.g. [22–24]). Along with the use of electron beams, QFS induced by beams of protons and α particles has been extensively studied. Momentum distributions and spectroscopic factors were extracted in these experiments for the knocked-out particles. Usually, the remaining third body (spectator) was either a stable nucleus or it was found in a quasi-stationary state. The data were mostly analyzed using PWIA and a better correspondence between experimental data and theory predictions was achieved at higher collision energies. The Distorted Wave Impulse Approximation (DWIA) was shown [25] to be more reliable in getting correct values for spectroscopic factors even from the QFS data acquired with the use of rather low energy beams. In Ref. [26] the QFS reaction ^{6}Li(α, 2α)d was investigated at ^{4}He beam energies around 100 MeV. The authors analyzed their data by means of PWIA and DWIA showing that the two approaches lead to quite similar conclusions about the momentum distribution of the α cluster in the ^{6}Li nucleus and both results were in accord with the wave function of ^{6}Li given by theory. Most likely, the reason why the PWIA analysis appeared to be correct in this case is associated with the small binding energy of the α cluster in ^{6}Li. Such a situation seems to be even more reasonable for the weakly bound drip-line nuclei.

To check this assumption we carried out a test experiment dedicated to the observation of the QFS of the ^{6}He α core showing up in the ^{4}He(^{6}He,2α)nn reaction. It was tempting to know from this experiment whether the study of QFS can be used for direct observations of three-body correlations specific for the ground state of Borromean nuclei. ^{6}He is a convenient object for such a study because one can believe that its WF is well established in theory [27].

The peculiarity of the ^{4}He(^{6}He,2α)nn reaction consists in the lack of a bound state for the two neutrons becoming free after the knock-out of the ^{6}He α core. Similar situation occurred when the QFS reactions ^{6}Li(α,2α)pn and ^{6}Li(p,pα)pn were investigated [28, 29]. These experiments were performed in coplanar geometry with the use of small-aperture detectors.

We studied the ^{4}He(^{6}He,2α)nn reaction at a ^{6}He beam energy of 25A MeV/amu. The secondary beam of ^{6}He nuclei with intensity of $2 \times 10^4\,\mathrm{s}^{-1}$ bombarded a helium gas target cooled down to 16 K. The target thickness was $2 \times 10^{20}\,\mathrm{cm}^{-2}$. The beam diagnostics array was outlined in Sect. II.

Coincident α particles emitted from the target in angular ranges of $15^\circ - 55^\circ$ were detected by two position sensitive ΔE-E telescopes installed symmetrically in respect to the beam direction. Each telescope had a pair of Si strip detectors (one of these detectors had a thickness of 70 μm and another one was 1 mm thick). Behind of this pair, a 6.2 mm Si(Li)detector was installed in each telescope. The measured α particle energies and angles allowed us to calculate relative momentum values, $\mathrm{P_{n-n}}$, observed for the two spectator neutrons in their c.m. system, and momentum vectors $\mathbf{P}_{\mathrm{nn}}$ characterizing the motion of their c.m. in the projectile reference frame. Resolution attained in the momentum values was about 15 MeV/c. With Z axis chosen to coincide with the projectile trajectory, the polar and azimuthal angles of momentum vector $\mathbf{P}_{\mathrm{nn}}$ were determined with errors of $\leq 1.5^\circ$. A quite low background level was observed in a run made with empty target.

Two bumps are seen in Fig. 4 (left panel) showing the $\mathrm{P}^Z_{\mathrm{nn}}$ distribution observed in the reaction ^{4}He(^{6}He,2α)nn [1]. Spectator neutrons originating from "real" $\alpha - \alpha$ QFS are in the event group centered around the $\mathrm{P}^Z_{\mathrm{nn}}$=0 point. The maximum rising nearby $\mathrm{P}^Z_{\mathrm{nn}} = -200$ MeV/c is populated by different processes, e.g. the 1n or α transfer from ^{6}He to ^{4}He and inelastic

[1] $\mathrm{P}^Z_{\mathrm{nn}}$ is longitudinal (Z) component of momentum $\mathbf{P}_{\mathrm{nn}}$.

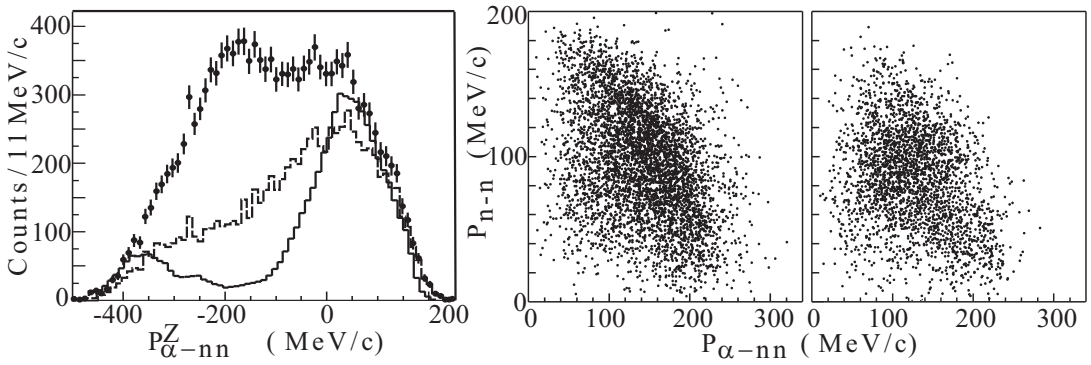

FIG. 4: *L*eft panel: Distribution in momentum component P^Z_{nn} observed in the reaction ^{4}He(^{6}He,2α)nn. Points with error bars show the total distribution. Events corresponding to the $\alpha-\alpha$ CM scattering angle $\theta_{CM} = 60°-120°$ and to $E_{\alpha 1(2)-nn}$ >10 MeV are shown by the histograms drawn by the dashed and solid lines, respectively. *C*entral panel: Joint momentum distribution $S^2(\mathbf{P}_{n-n}\ vs.\ \mathbf{P}_{\alpha-nn})$ extracted from the experimental data. *R*ight panel: The $S^2(\mathbf{P}_{n-n}\ vs.\ \mathbf{P}_{\alpha-nn})$ distribution obtained by MC simulation. (See explanations in text).

scattering of ^{6}He projectiles on ^{4}He nuclei. The contribution of these reaction channels extends rather far to the right side of the $P^Z_{nn} = -200$ MeV/c point with a tail reaching P^Z_{nn}=0. Selecting events with $\theta_{\alpha-\alpha} = 60° - 120°$ we reduced considerably the part of these interfering processes. Their contribution was suppressed further by the choice of events with large energy values characterizing the relative motion in the $\alpha 1-$nn and $\alpha 2-$nn subsystems. The two distributions obtained for events selected according to these criteria are presented in Fig. 4 (left panel). After such selection of detected events, the contribution of all interfering reaction channels in the obtained spectra was well described by a four-body phase space (PS).

To analyze these data, we performed complete MC simulations using a standard PWIA factorization for the transition matrix:

$$\left(\frac{d\sigma}{d\Omega}\right)^{QFS}_{\alpha-\alpha} \sim S^2(\mathbf{P}_{n-n}, \mathbf{P}_{\alpha-nn}) \left(\frac{d\sigma}{d\Omega}\right)_{\alpha-\alpha} F_{PS}\, dE_{n-n}\, dE_{\alpha-\alpha}\, d\Omega_{\alpha\alpha-nn}\, d\Omega_{n-n}, \qquad (3)$$

where $F_{PS} = \sqrt{E_{n-n}E_{\alpha-\alpha}(E_0 + Q - E_{n-n} - E_{\alpha-\alpha})}$ is a phase space factor that accounts for energy conservation, $E_0 = E_{n-n} + E_{\alpha-\alpha} + E_{\alpha\alpha-nn} - Q$ is the CM energy of the whole $\alpha-\alpha-n-n$ system ($E_{\alpha\alpha-nn}$ stands for the energy of relative motion of the $\alpha\alpha$ and nn centers-of-mass). The $\alpha-\alpha$ elastic scattering cross section, $(d\sigma/d\Omega)_{\alpha-\alpha}$, was calculated for the relative energy $E_{\alpha-\alpha}$ measured in the reaction exit channel. This implied the use of the final-state energy prescription.

Due to the large acceptance provided by the detection system the two α particles were observed in a wide range of their relative energy $E_{\alpha-\alpha}$ =(5 – 60) MeV and the observed scattering angle $\theta_{\alpha-\alpha}$ covered a range of 30° - 150°. The dependence of cross-section $(d\sigma/d\Omega)_{\alpha-\alpha}$ on $E_{\alpha-\alpha}$ and $\theta_{\alpha-\alpha}$ was derived from the known set of phase shifts measured in a proper energy range.

Function $S^2(\mathbf{P}_{n-n}, \mathbf{P}_{\alpha-nn})$, entering into Eq. 3, contains nuclear structure information relevant to ^{6}He [2]. Taking into account the n-n final state interaction (FSI), this function was calculated as

$$S(\mathbf{P}_{n-n}, \mathbf{P}_{\alpha-nn}) = \int d\mathbf{r}_{n-n}\, d\mathbf{r}_{\alpha-nn} \psi^*_{n-n}(\mathbf{P}_{n-n}, \mathbf{r}_{n-n}) e^{-i\mathbf{P}_{\alpha-nn}\mathbf{r}_{\alpha-nn}}\, \psi_{6He}(\mathbf{r}_{n-n}\mathbf{r}_{\alpha-nn}), \qquad (4)$$

[2] In Jacobi co-ordinates, adopted in the three-body model of Borromean nuclei, the momenta $\mathbf{P}_{n-n}$ and $\mathbf{P}_{\alpha-nn}$ have conventional notations $\mathbf{p}_x$ and $\mathbf{p}_y$, respectively.

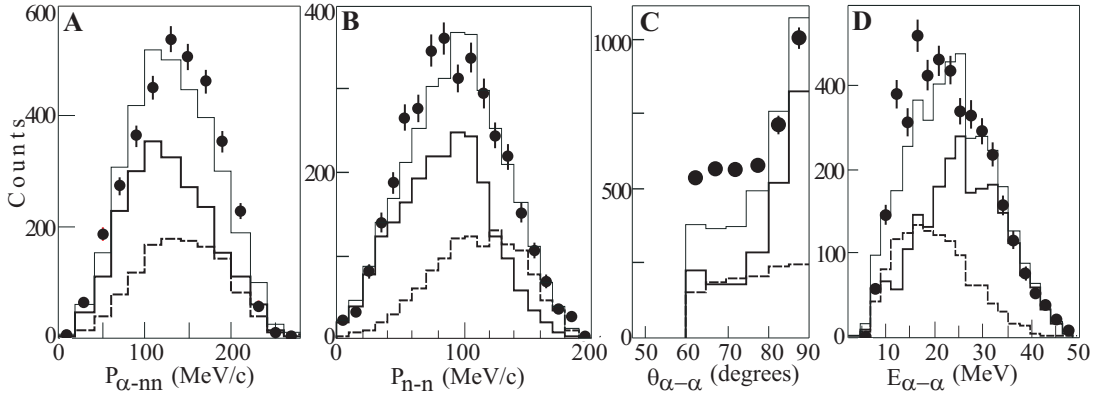

FIG. 5: Result of fits made to four distributions obtained from the experimental data. Panels **A** and **B** present the two projections of the distribution shown in Fig. 4 (central panel). Panels **C** and **D** show the event distributions in $\alpha-\alpha$ CM scattering angle $\theta_{\alpha-\alpha}$ and in energy $E_{\alpha-\alpha}$. Points with error bars show the experimental data. The fit results obtained for the QFS and PS spectra are shown by histograms drawn by thick solid line and dashed line, respectively. The sums of the QFS and PS distributions are shown by histograms drawn by thin lines.

where $\psi_{6\mathrm{He}}(\mathbf{r}_{\mathrm{n-n}}\mathbf{r}_{\alpha-nn})$ is the three-body wave function of ^{6}He [27]. Joint momentum distribution $S^2(\mathbf{P}_{\mathrm{n-n}}, \mathbf{P}_{\alpha-nn})$ was extracted from the measured data with the use of Eq. 3. The data were selected with the simultaneous imposition of the two criteria presented in Fig. 4, left panel. Additionally, condition $P^Z_{nn} \geq 0\,\mathrm{MeV/c}$ was imposed. The obtained experimental distribution is shown in Fig. 4 (central panel) together with a MC simulation made with the use of Eq. 4 (see Fig. 4, right panel). The two distributions are similar in the widths of their projections to the axes $P_{\mathrm{n-n}}$ and $P_{\alpha-nn}$. To check whether the QFS part is considerable in the experimental distribution we fitted a set of experimentally measured distributions by the sums of MC simulations made for the QFS and PS spectra. Some of these fits are shown in Fig. 5. One can make sure that the fits provide a good description of the experimental distributions.

This inference seems to be not trivial in the light of the fact that the QFS process was treated here in the framework of the model based on assumptions inherent to Eq. 3. It is remarkable that the final state energy prescription, employed for the calculation of $(\mathrm{d}\sigma/\mathrm{d}\Omega)_{\alpha-\alpha}$, lead to a reasonably good fit to the experimental $\theta_{\alpha-\alpha}$ distribution obtained as a sum of QFS events characterized by the so different values of final state energy $E_{\alpha-\alpha}$ (see Fig. 5, panels **C** and **D**).

In Fig. 6 we show three distributions in $\theta_{\alpha-\alpha}$ obtained from different cuts made in $E_{\alpha-\alpha}$. These spectra were built from the bulk of detected events selected to satisfy the conditions $E_{\alpha 1(2)-nn} > 10\,\mathrm{MeV}$ and $P_{\mathrm{n-n}} < 100\,\mathrm{MeV/c}$. From panel **B** of Fig. 5 one can see that the choice of events with $P_{\mathrm{n-n}} < 100\,\mathrm{MeV/c}$ results in a relative increase of the QFS part in the data. Strong variations visible in the angular dependencies presented in Fig. 6 are all due to the behavior of the QFS cross section (the phase-space spectra are smooth). The excellent fits made to these experimental spectra make us confident that the effect of QFS has been well revealed in this experiment.

Summarizing, we note that in our experiment the QFS of the α core bound in ^{6}He was explored keeping in mind the possible study of the cluster structure of this halo nucleus. The possible use of QFS measurements for revealing momentum correlations specific for three-body Borromean nuclei was the subject of our interest. The three-body WF of ^{6}He is believed to be well established in theory and a comparison of theoretical predictions with experimental data could be a good test for the use of QFS for the study of clustering states in halo nuclei.

For the first time coincident particles emitted in the ^{4}He(^{6}He,2α)nn reaction were detected

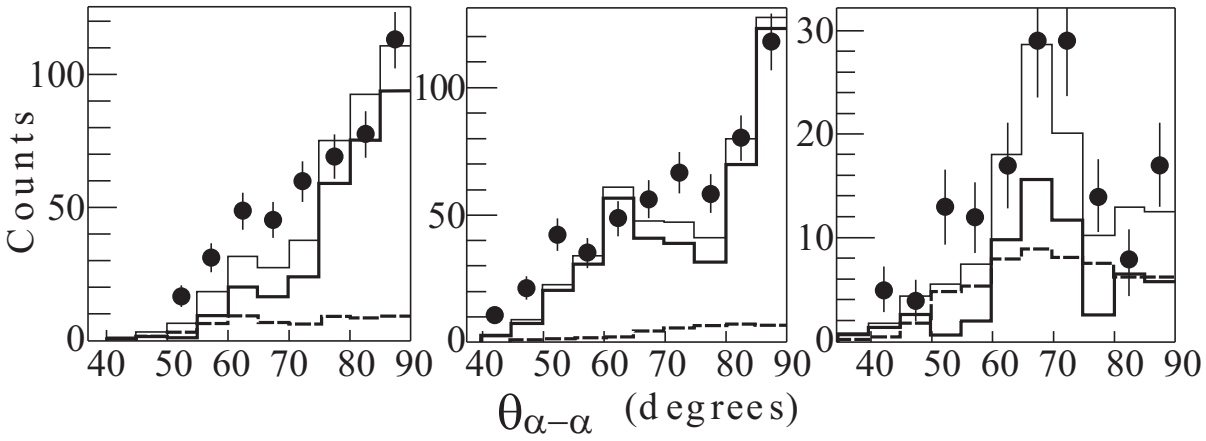

FIG. 6: Angular dependence obtained for QFS events with values of $E_{\alpha-\alpha}$ chosen in the range of 15–20, 30–35, and 45–50 MeV (see panels **A, B**, and **D**, respectively. Experimental data were selected to satisfy the conditions $E_{\alpha 1(2)-nn} > 10$ MeV and $P_{n-n} < 100$ MeV/c. (See notations in the caption of Fig. 4).

in wide angular ranges giving a wide kinematical range of the measured angular and momentum distributions. The contribution of processes competing with the $\alpha-\alpha$ QFS in the $\alpha+\alpha+n+n$ output channel were considerably suppressed by the selection of events with $E_{\alpha 1(2)-nn} > 10$ MeV. This condition provided a reliable separation of events corresponding to QFS. Experimental distributions relevant to the reaction mechanism and to the ^{6}He structure, was compared with the results of MC simulations based on the PWIA formalism. The PWIA predictions showed consistency with the experimental data. One should note that the n-n FSI is the only distorting factor involved in the data analysis. We assume that the influence of the n-n FSI will be less significant at higher energies of bombarding ^{6}He nuclei.

The ratio of the cross-section $(\mathrm{d}\sigma/\mathrm{d}\Omega)_{\alpha-\alpha}$ emerging from our data to the cross section value of the free $\alpha-\alpha$ elastic scattering was found to be constant in energy ranges $10 < E_{\alpha-\alpha} < 50$ MeV and $0 < E_{n-n} < 40$ MeV. The angular distributions of quasi-free $\alpha-\alpha$ scattering measured for different energies $E_{\alpha-\alpha}$ were well reproduced by MC simulation while the relative values of the four-body breakup and $\alpha-\alpha$ elastic scattering cross-sections varied by more than two orders of magnitude in the energy and angular ranges allowed by the used detector array.

[1] B. Jonson, Pysics Reports **389**, 1 (2004).
[2] A.M. Rodin *et al.*, Nucl. Instr. Meth. B **204**, 114 (2003).
[3] G.M. Ter-Akopian *et al.*, Phys. Lett. B **426**, 151 (1998).
[4] S.V. Stepantsov *et al.*, Phys. Lett. B **542**, 35 (2002).
[5] R. Wolski *et al.*, Phys. Lett. B **467**, 8 (1999).
[6] R. Wolski *et al.*, Nucl. Phys. A **701**, 29c (2002).
[7] G.M. Ter-Akopian *et al.*, Nucl. Phys. A **734**, 295 (2004).
[8] A.A. Yukhimchuk *et al.*, Nucl. Instr. Meth. A **513**, 439 (2003).
[9] Yu.Ts. Oganessian *et al.*, Bull. Rus. Acad. Sci. Phys. **66**, 676 (2002).
[10] S.I. Sidorchuk *et al.*, Phys. Lett. B **594**, 54 (2004).
[11] A.A. Korsheninnikov *et al.*, Phys. Rev. Lett. **87**, 092501 (2001).
[12] M.S. Golovkov *et al.*, Phys. Lett. B **566**, 70 (2003).
[13] M.S. Golovkov *et al.*, Phys. Rev. C **72**, 064612 (2005).
[14] G.M. Ter-Akopian *et al.*, Eur. Phys. J. A **25**, s01, 315 (2005).
[15] M.S. Golovkov *et al.*, Phys. Lett. B **588**, 163 (2004).

[16] K. Seth, *et al.*, Phys. Rev. Lett. **58**, 1930 (1987).
[17] H.G. Bohlen, *et al.*, Prog. Part. Nucl. Phys. **42**, 17 (1999).
[18] L. Chen, *et al.*, Phys. Lett. **B505**, 21 (2001).
[19] G.V. Rogachev, *et al.*, Phys. Rev. C **67**, 041603R (2003).
[20] F.C. Barker, Nucl. Phys. A **741**, 42 (2004).
[21] A. Volya and V. Zelevinsky, Phys. Rev. Lett. **94**, 052501 (2005).
[22] P.G. Roos *et al.*, Phys. Rev. C **15**, 69 (1977).
[23] C.W. Wang *et al.*, Phys. Rev. C **21**, 1705 (1980).
[24] G. Jacob *et al.*, Rev. of Mod. Phys. **38**, 121 (1966).
[25] N.S. Chant and P.G. Roos, Phys. Rev. C **15**, 57 (1977).
[26] A. Okihana *et al.*, Nucl. Phys. A **549**, 1 (1992).
[27] B.V. Danilin *et al.*, Yad. Fiz. **48**, 1206 (1988).
[28] R.F. Warner *et al.*, Nucl. Phys. A **503**, 161 (1989).
[29] R.F. Warner *et al.*, Phys. Rev. C **42**, 2143 (1990).

Search for Effects of Nucleon Polarized Hidden Strangeness in Nucleon-Nucleon Interactions at JINR Nuclotron: The NIS project

V.P. Balandin, O.V. Borodina, Yu.L. Chentsov, A.A. Fechtchenko, V.N. Lysyakov, A.I. Maksimchuk, I.V. Ostrovsky, A.N. Parfenov, E.E. Perepelkin, S.N. Plyashkevich, S.V. Rabtsun, V.L. Rapatsky, N.S. Rossijskaya, R.A. Salmin, M.G. Sapozhnikov, E.A. Strokovsky, Y.A. Tchentsov, I.G. Voloshina, I.P. Yudin

(LPP JINR)

S.A. Avramenko, V.D. Aksinenko, A.E. Baskakov, Yu.T. Borzunov, S.N. Bazylev, V.F. Chumakov, L.B. Golovanov, R.I. Kukushkina, A.Litvinenko, J. Lukstins, I.I. Migulina, V.N. Ramzhin, P.A. Rukoyatkin, I.V. Slepnev, V.M. Slepnev, N.A. Shutova, L.S. Zolin

(VBLHE JINR)

B.A. Popov, V.V. Tereschenko

(DLNP JINR)

A.P. Kobushkin

BINP, Kiev, Ukraine

B. Kamys, J. Smyrski

Jagellonian University, Cracow, Poland

T. Nakano, M. Yosoi, N. Muramatsu, M. Sumihama, Y. Maeda

RCNP, Osaka University, Japan

M. Faessler, A. Zvyagin

Ludwig-Maksimilian University, Munich, Germany

The experimental program of the NIS project is aimed to search for effects of nucleon polarized strangeness in production of ϕ and ω mesons in pp and np scattering. It implies (i) comparison of production cross sections of ϕ and ω mesons near their thresholds in proton-proton interactions and (ii) measurement of ϕ production in np interactions. NIS experiment will provide data on the magnitude of the effect of the OZI violation in pp interactions in a vicinity of the threshold ($\varepsilon \sim 83 \div 120\,\mathrm{MeV}$).

To realize this program, it was proposed to construct a new magnetic spectrometer NIS with particle identification system based of TOF measurements at Nuclotron. At the Phase I of the experiment it was suggested to use multiwire proportional chambers of 2m×1m in size from EXCHARM experiment as trackers. At the Phase II of the experiment, it was planned to replace these MPWCs with large straw chambers to be produced in JINR LPP. Commissioning of the setup is expected at 2007, with subsequent start of physical measurements.

I. INTRODUCTION

We would like to measure the cross sections of the ϕ and ω meson production in pp and np scattering

$$p + p \to p + p + \phi \tag{1}$$

$$p + p \to p + p + \omega \tag{2}$$

$$d + p \to n + p + \phi + p_s \tag{3}$$

at 83, 100, and 120 MeV above their thresholds. The measurements are planned at the extracted beam of the JINR Nuclotron.

The physics motivation is to verify to what extent the large OZI-rule violation seen in some reactions of the antiproton annihilation at rest (see Sec. II A) preserves in the nucleon-nucleon interaction. The first measurement at energies below 10 GeV was made in the DISTO experiment [1, 2]. Indication on the OZI-rule violation of factor 10 was observed. Strong violation of the OZI-rule may be connected with the nucleon intrinsic strangeness, as discussed in details in Sec. II B.

At present, the first stage of the construction of the experimental apparatus is finished. The commissioning of the spectrometer and start of the data taking for the reactions (1)-(3) is scheduled for 2007. It will be possible at the same time to study a_0/f_0 production and to search for exotic baryons in ϕp system. The same setup configuration will be used in search for $\Theta^+(1540)$ pentaquark in the reaction:

$$p + p \to \Theta^+ + K^- + \pi^+ + p \ , \ \Theta^+ \to K^+ + n \tag{4}$$

At the cross section level of 0.07 μb, the NIS spectrometer can detect more than 1000 reconstructed Θ^+ events per week with the beam intensity of 10^7 s^{-1}.

II. PHYSICS MOTIVATION

The interest to study the ϕ and ω meson production in the nucleon-nucleon interactions is motivated by some unexpected results obtained in the LEAR experiments with stopped antiprotons, where, in some reactions of antinucleon-nucleon annihilation, anomalously large yield of the ϕ mesons was observed.

A. Apparent OZI-violation in antiproton annihilation at rest

The production of the ϕ mesons in hadron interactions is obeying the OZI rule [3]. This rule states that the reactions with disconnected quark lines should be suppressed. It forbids creation of $\bar{s}s$ mesons in the interaction of hadrons composed from u and d quarks. According to the OZI rule, the production of the $\bar{s}s$ mesons is possible only due to admixture of u and d quarks in the $\bar{s}s$-meson wave function. The amount of this admixture is determined for each meson nonet by the value of the mixing angle, providing quantitative predictions for the $\bar{s}s$ states production. The ratio between cross sections of the ϕ and ω in the interactions of non-strange hadrons for the vector meson nonet should be

$$R(\phi/\omega)_{\rm OZI} = 4.2 \cdot 10^{-3} \, . \tag{5}$$

This prediction has been tested in a number of experiments (for review, see, [4, 5]). Different probes were used in a wide interval of energies. It was found that (practically) everywhere the OZI rule is fulfilled well, within few percent accuracy.

In this situation it was quite surprising to see the discovery made at LEAR experiments, namely, that in some annihilation channels the ϕ-meson production significantly exceeds the prediction of the OZI rule. The main features of this effect are shown at the Fig. 1 and are summarized below. **1)** The deviation from the OZI–rule predictions is unusually strong.

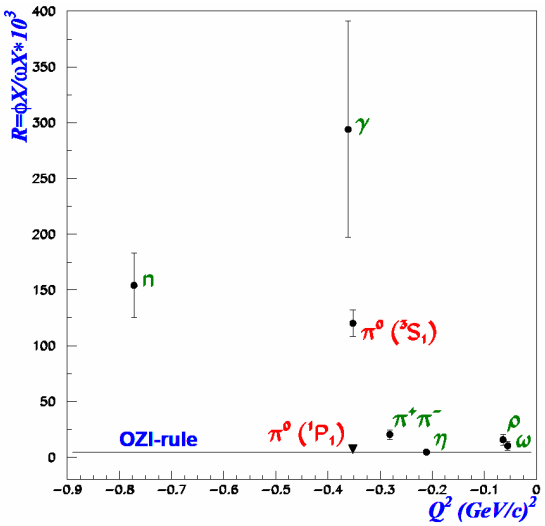

FIG. 1: The ratio $R = \phi X/\omega X \cdot 10^3$ of yields for different reactions of $\bar{p}p \to \phi(\omega)X$ annihilation at rest as a function of the momentum transfer to ϕ . The solid line shows the prediction of the OZI rule.

The largest OZI rule violation is observed in the $\bar{p}p \to \phi\gamma$ channel, where the Crystal Barrel collaboration has found [5, 6] that the ratio of the yields of the corresponding processes after phase space corrections is

$$R_\gamma = \frac{Y(\bar{p}p \to \phi\gamma)}{Y(\bar{p}p \to \omega\gamma)} = (294 \pm 97) \cdot 10^{-3}, \tag{6}$$

which is about 70 times larger than the OZI prediction (5).

Another very strong apparent violation of the OZI rule was found by OBELIX and Crystal Barrel collaborations for the $\bar{p} + p \to \phi(\omega) + \pi^0$ channels, where the corresponding quantity is

$$R_\pi = \frac{Y(\bar{p}p \to \phi\pi)}{Y(\bar{p}p \to \omega\pi)} = (106 \pm 12) \cdot 10^{-3} \tag{7}$$

for annihilation in a liquid-hydrogen target [5] and

$$R_\pi = (114 \pm 10) \cdot 10^{-3} \tag{8}$$

for annihilation in a hydrogen-gas target [7]. These ratios are about a factor of 30 higher than the OZI rule prediction (5).

2) This effect is not universal for all annihilation channels of the ϕ production but mysteriously occurs only in some of them. For instance, no enhancement of the ϕ production is observed for the $\phi\,\omega$ or $\phi\,\rho$ channels where $(R(\phi\omega/\omega\omega) = (19 \pm 7) \cdot 10^{-3}$ and $R(\phi\rho/\omega\rho) = (6.3 \pm 1.6) \cdot 10^{-3}$ [4]).

3) There is a strong dependence of the strength of the OZI–rule violation on the quantum

numbers of the initial $\bar{p}p$ state. It was clearly demonstrated by the OBELIX collaboration results [8]:

$$R_\pi(\phi/\omega,\ ^3S_1) \ = \ (120 \pm 12) \cdot 10^{-3} \ , \tag{9}$$

$$R_\pi(\phi/\omega,\ ^1P_1) \ < \ 7.2 \cdot 10^{-3} \qquad \text{with 95\% CL} \tag{10}$$

4) There is a serious indication that the degree of the OZI rule violation depends on the momentum transfer (see, Fig. 1).

5) The apparent OZI-violation was found not only for the ϕ meson production but also for the tensor $\bar{s}s$ state - $f_2'(1525)$-meson. As in a case of ϕ meson, the apparent OZI violation for tensor mesons turns out to be extremely sensitive to the quantum numbers of the initial state.

Using the f_2' yield from the analysis of the $K^+K^-\pi^0$ channel and f_2 from the $\pi^+\pi^-\pi^0$ one, it was obtained [8] that

$$R(f_2'(1525)\pi^0/f_2(1270)\pi^0) \ = \ (47 \pm 14) \cdot 10^{-3} \ , \quad \text{S-wave} \tag{11}$$

$$= \ (149 \pm 20) \cdot 10^{-3} \ , \quad \text{P-wave} \tag{12}$$

The OZI–rule prediction for the tensor mesons is $R(f_2'/f_2) = (3 - 16) \cdot 10^{-3}$.

B. Polarized nucleon strangeness model

An explanation of these facts was provided by the model of polarized nucleon strangeness [9, 10]. The main idea is that the OZI rule, by itself, is always valid. Some deviations from this rule are only apparent. They are due to a non-trivial dynamics of the process, which cannot be described by diagrams with disconnected quark lines.

For instance, the OZI rule forbids the production of a pure $\bar{s}s$ state in the nucleon-nucleon interaction, if there are no strange quarks in the nucleon. Only in this case the production of the $\bar{s}s$ pair is described by a disconnected diagram. But if the strange quarks in the nucleon play a non-negligible role, then the $\bar{s}s$ pair could be produced in the nucleon-nucleon interaction via shake-out or rearrangement of the strange quarks already stored in the nucleon. This process is described by a connected diagram and the OZI rule suppression is not applicable in this situation. Therefore the observed violation of the OZI rule is only *apparent*. It means that the ϕ meson may be created from the strange quarks already stored in the nucleon.

It turns out that the polarization of the nucleon strange sea may naturally explain the observed dependence of the degree of the OZI rule violation from the initial state quantum numbers, initial energy, and the final state content. A number of tests of the model was proposed [9–11]; part of them was already successfully confirmed by the experiment. The main assumptions of the model are the following:

- Negative polarization of the strange quarks in the nucleon,
- formation of the $\bar{s}s$ meson via rearrangement processes, and
- the quantum numbers of the $\bar{s}s$ pair in the nucleon is $J^{PC} = 0^{++}$.

It was assumed that the formation of the $\bar{s}s$ mesons is going via rearrangement diagrams, shown in Fig. 2. It means that the **two** nucleons must take part in the $\bar{s}s$ production If the nucleon spins are parallel (Fig. 2, then the spins of the $\bar{s}$ and s quarks in both nucleons are also parallel. If the polarization of the strange quarks is not changed during the interaction, then the $\bar{s}$ and

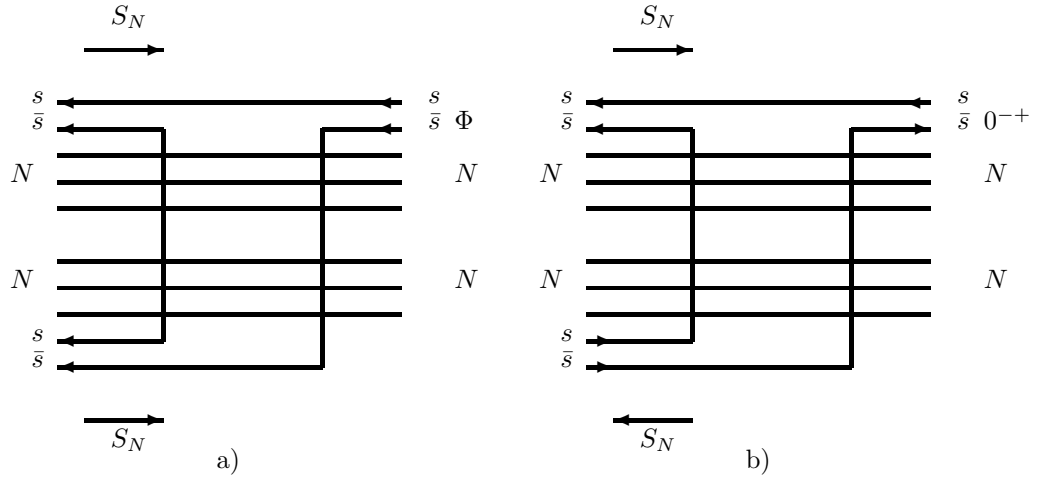

FIG. 2: Production of the $\bar{s}s$ mesons in NN interaction from the spin-triplet (a) and spin-singlet (b) states. The arrows show the direction of spins of the nucleons and strange quarks.

s quarks could keep parallel spins in the final state. The total spin of $\bar{s}s$ quarks will be $S = 1$ and if their relative orbital momentum is $L = 0$, what means that the strangeonium has the ϕ quantum numbers; if $L = 1$, it will correspond to the creation of tensorial strangeonium, $f_2'(1525)$.

Another important assumption of the polarized intrinsic strangeness model [10] is that the quantum numbers of the $\bar{s}s$ pair in the nucleon is $J^{PC} = 0^{++}$. The shake-out of such pairs will not create ϕ or tensor $f_2'(1525)$ meson, but a scalar strangeonium.

The polarized intrinsic strangeness model gives rather definite predictions for the ϕ meson production in nucleon-nucleon collisions:

1) If the $\bar{s}s$ pair has $J^{PC} = 0^{++}$ quantum numbers the apparent OZI violation for ϕ production in NN collisions must exist at energies where spin-triplet initial states dominate. At these energies the ratio

$$R_{pp} = \frac{\sigma(pp \to pp\phi)}{\sigma(pp \to pp\omega)}$$

is expected to be much higher than the value predicted by the OZI rule (5).

2) It was conjectured [9] that the degree of OZI rule violation might depend on the momentum transfer. In Fig. 1 the compilation of the data on the ratio $R = (\phi X/\omega X) \cdot 10^3$ of yields for different reactions of $\bar{p}p \to \phi(\omega)X$ annihilation at rest is shown as a function of the momentum transfer to ϕ . The solid line corresponds to the prediction of the OZI rule (5).

One could see that the largest OZI-violation has been observed for the reactions with the largest momentum transfer to ϕ. That is, first of all, the Pontecorvo reaction $\bar{p}d \to \phi n$ and $\bar{p}p \to \phi\gamma, \phi\pi$ processes. The degree of the violation smoothly decreases with increase of the mass of the X-system created with the ϕ, i.e. with decreasing of the momentum transfer to ϕ. Thus for the $\phi\pi\pi$ final state with light effective masses of the two-pions system around 300-400 MeV, the deviation from the OZI rule is significant, whereas for the $\phi\eta$ final state there is no problem with the OZI rule.

The polarized strangeness model explained this trend as appearing due to the rearrangement nature of the ϕ production. The rearrangement mechanism implies that **two** nucleons should participate in the ϕ production. This means a dependence on quantum numbers of both nucleons as well as appearance of some minimal momentum transfer from which this additional mechanism becomes important.

3) The ratio between the total cross sections of ϕ production on neutron and on proton is:

$$R_{np} = \frac{\sigma(np \to np\phi)}{\sigma(pp \to pp\phi)} = \frac{1}{2}\left(1 + \frac{|f_0|^2}{|f_1|^2}\right) \tag{13}$$

where f_1 and f_0 are the amplitudes corresponding to total isospin $I = 1$ and $I = 0$, respectively.

At threshold, when the orbital momentum of two nucleons in the final state is $l_1 = 0$ and the orbital momentum of the produced meson relative to the center-of-mass system of these two nucleons also vanishes, the connection between the isospin and the total spin of the two nucleons in the initial state is fixed. The amplitude f_1 corresponds to the spin-triplet initial nucleon state, and the amplitude f_0 corresponds to the spin-singlet one. Therefore, using the experimental data on the pp and np cross sections, it is possible to estimate the ratio between spin-singlet and spin-triplet amplitudes.

In the case of dominance of the production from $^3S_1$ state one must observe that ϕ production in pp interaction will be higher than in np with ratio

$$R_{np} = \frac{\sigma(np \to np\phi)}{\sigma(pp \to pp\phi)} \approx \frac{1}{2}\,.$$

C. Experiments on ϕ and ω production

The predictions of the polarized strangeness model were confirmed in part by the DISTO Collaboration measurements [1] of the ϕ and ω production at the proton energy of 2.85 GeV, i.e. at 83 MeV above the ϕ production threshold.

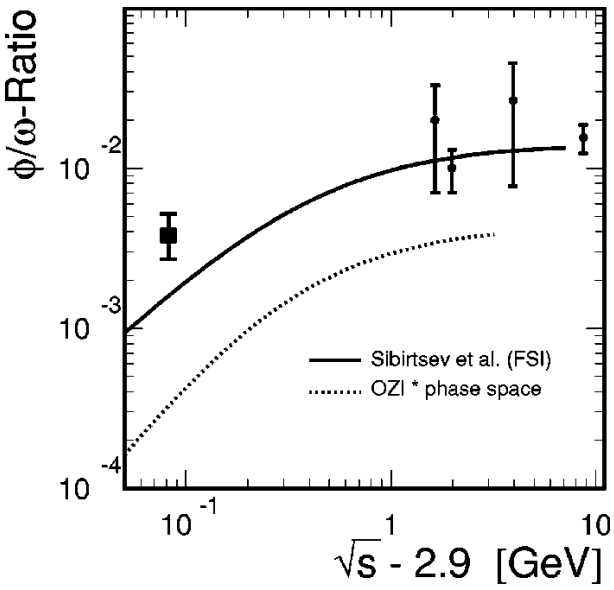

FIG. 3: Result of the DISTO experiment at SATURNE-II [1].

It was found that (see also Fig. 3)

$$R_{pp} = \frac{\sigma(pp \to pp\phi)}{\sigma(pp \to pp\omega)} = (3.7 \pm 0.7^{+1.2}_{-0.9}) \cdot 10^{-3}\,. \tag{14}$$

One can see that (up to 2 years ago) the DISTO measurement was the only one at the energies less than 10 GeV. The solid line in Fig. 3 shows the result of the fit of the experiments at high

energies. The dotted line shows prediction of the OZI rule corrected for the phase space. The ϕ cross section was measured at 83 MeV above the threshold whereas ω cross section was taken at 320 MeV above the corresponding threshold. Therefore the difference in the (ϕpp) and (ωpp) phase spaces is quite high and the corrected ratio (14) is by a factor 13 larger than the OZI–rule prediction.

The cross section of the ω production (2) near the threshold was measured by the SPES-III and COSY-TOF collaborations [12, 13]. The data base for the energy dependence of the cross section (2) of the ω production can be found in Refs. [1, 12–15]. The data from SPES-III and COSY-TOF collaborations (Ref. [12, 13]) allowed to find a smooth phenomenological approximation (see Ref. [16, 23] and ANKE proposal #104 [16]).

Basing on DISTO data [1] for ϕ production cross section at $\varepsilon \approx 83$ MeV and on COSY-TOF data [13] for ω cross section at $\varepsilon \approx 92$ MeV, the degree of the OZI-rule violation was estimated as $R_{pp} \sim 7$.

Beside the DISTO measurement, up to the last year, the ϕ production in pp interaction (1) had been investigated only in two other experiments, at 10 and 24 GeV/c ([14, 15]). In the current year (2006), the results from the ANKE collaboration [1] were published in Ref. [18]. The cross section of the ϕ production in reaction (1) was measured at 18.5, 34.6, and 83 MeV above the threshold. The typical statistics comprises 200-250 events. The published results reported by the ANKE collaboration agree with DISTO data (see Fig. 4) and demonstrate a substantial OZI-rule violation (14).

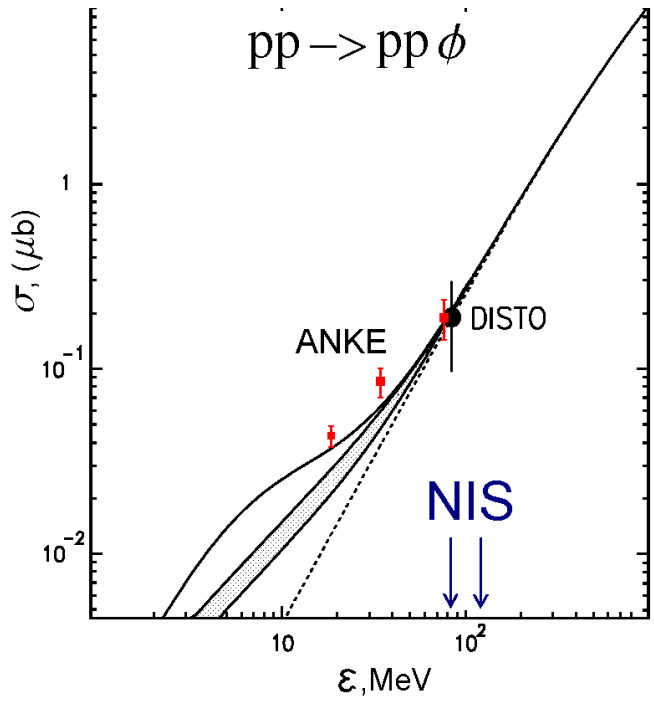

FIG. 4: Data from ANKE published recently in [18]. The topmost solid line: fit to the $p(p,p)p\omega$ data,normalized to the DISTO point.

However, it is interesting that the strength of the OZI-rule violation is energy dependent, which is easily seen in Fig. 4. Being averaged over all the 3 energies the ANKE data give for

[1] apparently influenced by the NIS project, see [17]

$R_{\phi/\omega}$

$$R_{\phi/\omega} = (3.3 \pm 0.6) \cdot 10^{-2} \sim 8 \times R_{\rm OZI} \tag{15}$$

In addition, results of ANKE indicate that the FSI effects in (ωpp) and (ϕpp) systems are significantly different, which discards the assumption about a similarity between the ε-dependence of the ω and ϕ production cross sections close to their thresholds.

It is interesting, that the DISTO collaboration [2] has observed also differences between the angular distributions of ϕ and ω mesons produced in (1)-(2). The ϕ meson angular distribution is flat, whereas to fit the ω angular distribution the first three even Legendre polynomials are needed (Ref. [1]). This was confirmed by the COSY-TOF collaboration [13], where it was found that that the angular dependence of the ω meson production is not isotropic at the energy excess of about $\sim$ 173 MeV.

In general, the difference in angular distributions of ϕ and ω meson is an indication of different production mechanisms. It contradicts the OZI rule prediction that ϕ could be formed in pp interactions only via ω-ϕ mixing. However, to demonstrate this, one should compare ϕ and ω meson distributions at the same energy above the corresponding thresholds.

D. Comparison with conventional models

Calculations of ϕ production in near-threshold NN reactions within the framework of conventional boson exchange mechanism were done ([20–23]). Two mechanisms of ϕ production were analysed, namely, the one due to the $\phi\rho\pi$ coupling and the other due to the direct ϕNN interaction. It turns out that the former dominates.

It was shown that the ϕ production in pp interaction is dominated by the spin-triplet $^3S_1$ initial state till 20-50 MeV above the threshold. Even at 100 MeV above the threshold the role of the spin-triplet initial state is still dominant. It is predicted [20] that the ratio

$$R_{np} = \frac{\sigma(np \to np\phi)}{\sigma(pp \to pp\phi)} \approx 3 - 7 \tag{16}$$

depending on the set of parameters used.

The energy dependence of ϕ production measured by the ANKE collaboration [18] disagrees with the calculations of [24] (note that parameters of this calculation has been fitted to reproduce the DISTO point).

E. Polarized strangeness model with $J^{PC}(s\bar{s}) = O^{-+}$

The quantum numbers of the $\bar{s}s$ pair in the nucleon are not fixed *a priory*. In the original version of the polarized strangeness model [9, 10] it was assumed that J^{PC} of the $\bar{s}s$ pair has the vacuum quantum numbers O^{++}. It turns out that for better description of some new experiments one should assume that the $\bar{s}s$ system has $^1S_0$ quantum numbers $J^{PC} = O^{-+}$ and the quantum numbers of the us system are also $J^{PC} = O^{-+}$. Schematically, the configuration looks as follows:

$$N \overset{\uparrow}{\bullet} \overset{\circ}{\downarrow} s \overset{\circ}{\uparrow} \bar{s} \tag{17}$$

In the case of antiproton annihilation the choice of 0^{-+} wave function for $\bar{s}s$ system leaves intact all predictions of the original model [9, 10] concerning suppression of the ϕ production

from the spin-singlet initial state or enhancement of $f_2'(1525)$ strangeonium from initial states with $L = 1$ and $S = 1$. However, for the nucleon-nucleon scattering the situation will change. The corresponding rearrangement diagram is shown in Fig. 5.

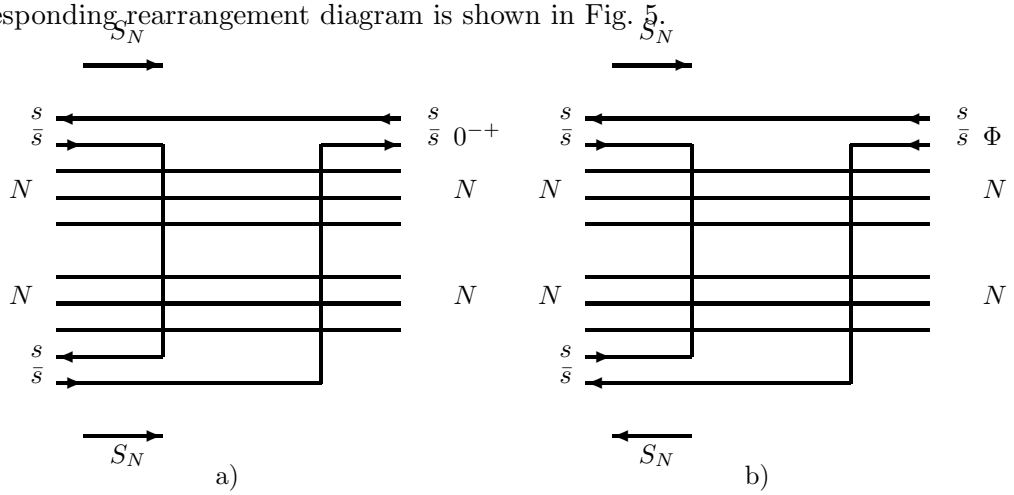

FIG. 5: Production of the $\bar{s}s$ mesons in NN interaction, assuming $J^{PC}(s\bar{s}) = O^{-+}$, from spin-triplet (a) and spin-singlet (b) initial states. The arrows show the direction of spins of the nucleons and strange quarks.

It is clear that in this model the ϕ is formed from the spin-singlet initial state. From the spin-triplet initial state the rearrangement diagram of Fig. 5 will increase production of the strangeonium with the $J^{PC} = O^{-+}$.

It means, that at small energy above the threshold, where initial spin-triplet state is dominant, one could not expect large apparent OZI violation. This effect must appear at highest energies, where spin-singlet states will start to work. At large energies, above the threshold, the connection between the spin and isospin amplitudes is not as simple as in Eq. (13). To disentangle the models more experimental data are needed.

Summarizing, one can conclude that there are sharp distinctions between polarized strangeness model predictions and conventional approaches. The differences are:

- Predicted value of ϕ/ω cross section ratio,
- momentum transfer dependence of the ϕ/ω cross section ratio, and
- different values for R_{np}.

It is necessary to measure cross-sections and isospin correlations (spin-spin correlations might be useful as well) for ϕ and ω meson production keeping the same energy excess above the thresholds for both ϕ and ω production. The first step towards this task is already done by ANKE collaboration in a study concerning the $p(n, d)\phi$ reaction.

F. Search for the pentaquark baryon production.

About 3 year ago an exotic and narrow baryon resonance in the K^+n and K^0p systems (the Θ^+ baryon) was observed in four independent experiments [25] but with limited statistics (from 20 to 60 events in the peak above a background for each of them). In one of the experiments the resonance was produced by the hadron beam ($K^+Xe \to K^0pXe'$ with the bubble chamber DIANA at ITEP (Moscow) in Russia); in the three other experiments the resonance

was found in the photoproduction reactions ($\gamma n \to nK^+K^-$, with LEPS at SPring-8 electron accelerator (Osaka University), $\gamma d \to K^+K^-pn$ with CLAS at JLAB in USA, $\gamma p \to K^0_S K^+ n$ with SAPHIR at ELSA (Bonn) in Germany). Inspection of the old BEBC data for ν_μ and $\bar{\nu}_\mu$ interactions with hydrogen, deuterium, and neon nuclei, done by the ITEP group, resulted in an additional signal for the K^0p resonance [27]. Masses of $1540\pm10\,\mathrm{MeV/c^2}$, $1540\pm4\pm2\,\mathrm{MeV/c^2}$, $1539\pm2\,\mathrm{MeV/c^2}$, $1543\pm5\,\mathrm{MeV/c^2}$, and $1533\pm5\,\mathrm{MeV/c^2}$ were reported with the resonance width estimations somewhere between $(9 \div 22)\,\mathrm{MeV}$.

These messages were exciting because it was the first evidence for the existence of baryons with positive strangeness (the narrow width, by itself, is not so much surprising). Up to now, only negative strangeness baryons were known. Baryons with positive strangeness cannot be built from 3 quarks: it can only be for at least a five quark system within the standard quark theory. The popular interpretation of the reported Θ^+ (initially called Z^+) resonance is that it is a 5-quark system $uudd\bar{s}$. Another unexpected and exciting feature of the new data [25–29] was that the possible new baryon is rather light. At the moment, the experimental data are controversial (see, for example, Ref. [36]) and the problem remains unsolved.

G. Present status of the pentaquarks.

Since the first claims, both positive and negative results on the Θ^+ pentaquark production were published. As a rule, experiments with positive signals have low statistics. A common features of these experiments are: they are of exclusive type, event multiplicity is low, and the data were taken at intermediate energies. In contrast, experiments with negative results are mostly of inclusive type, event multiplicity is high, and the center of mass energy is high as well, but the collected statistics are very high. Concerning the claimed Ξ^{--} pentaquark baryon, there is only a single positive result reported by NA-49 collaboration: no other experiments reported a positive evidence for the existence of this baryon.

Up to now the quantum numbers (spin, parity, and isospin) of Θ^+-baryon are not determined experimentally. The only attempt to estimate spin of the Θ^+ was done in Ref. [30], where the authors claimed that the spin value of 1/2 is excluded. Moreover, even the value of Θ^+ mass became a puzzle: in the $\Theta^+ \to nK^+$ decay channel it is slightly higher than in the $\Theta^+ \to pK^0_s$ one.

Nevertheless, a number of theoretical papers about the quark structure, properties, and production mechanisms of such baryons is already huge. Theorists discuss even the possibility of "penta"-nuclei existence.

The recent result from CLAS [31] at high statistical level discards the low statistics result of Ref. [26]: no Θ^+ production was observed in the photoproduction off protons in the reaction $\gamma p \to \Theta^+ \bar{K}^0$, while the same CLAS group reported [29] observation of the Θ^+ in the reaction $\gamma p \to \Theta^+ K^- \pi^+$. This challenge was taken by theorists. First, it was immediately noticed that if the spin of the Θ^+ is not 1/2 but rather 3/2, than the contact (Kroll-Ruderman like) term works for neutron target and is absent for proton target in the photoproduction reaction $\gamma N \to \Theta^+ K$ (an analogy with $\Lambda(1520)$ photoproduction where such an asymmetry is known experimentally); see [33].

It should be mentioned that a more general spin/isospin analysis of $\gamma N \to \Theta^+ K$ reaction was done in Ref. [34]. It was noticed that:

- A photon which turns into K^+K^- (ϕ in the vector meson dominance picture) can make a $\Theta^+ K$ directly on a neutron but cannot make it on a proton. (Again, the asymmetry in production of $\Lambda(1520)$ in γp and γn gives the basis. The $\gamma K^0 \bar{K}^0$ vertex is forbidden by an $SU(3)_f$ flavor selection rule.)

- Interference between resonances and background can result in differences between K^+n and K^0p modes of detecting the Θ^+, including the "visible" shift in its mass. Here the ϕ-component of the photon plays again a crucial role.

An interesting search for Θ^+ in pion induced reaction $\pi^-p \to K^-X$ was done recently (as a by-product) in Ref. [38].

A new view on structure of baryons was suggested recently by D. Diakonov and V. Petrov [35], where a new estimation of Θ^+ width is given: $\Gamma_\Theta \sim 2 \div 4\,\mathrm{MeV}$.

Summarizing, one can conclude that the very existence of the pentaquark baryons remains a question but it seems rather natural from a theoretical point of view. This means that new experiments in this direction are necessary. We have proposed to perform dedicated search for Θ-baryon production in proton-proton interactions at the Nuclotron using the setup being constructed for the NIS project.

III. DETECTOR CONFIGURATION

The initial goal of the NIS project was to search for effects of nucleon polarized strangeness in production of ϕ and ω mesons in pp and np scattering (II). To realize this program, it was proposed to built a magnetic spectrometer with trackers based on the multiwire proportional chambers of 2m×1m in size from the EXCHARM experiment[39], (Phase I; at Phase II these MPWCs should be replaced by a modern tracker system based on straw tubes) and with the particle identification system based on TOF measurements (Fig. 6). The spectrometer is placed at Nuclotron extracted beam in the LHE Building 205.

The typical signature of the $pp \to \phi pp$ event planned to be used in the main event selection trigger is $pp \to (K^+K^-) + pp$ with 3 positively and 1 negatively charged tracks (4-prongs signature).

A similar 4-prong signature corresponds to the production of the Θ^+ baryon with positive strangeness in reaction (4) and (18) when it decays into the nK^+ channel:

$$pp \to \Theta^+ + K^- + p + \pi^+ \ , \ \ \Theta \to pK^0 \ , \ \ K^0_S \to \pi^+\pi^- \ . \tag{18}$$

Although its decay into pK^0 channel with subsequent $K^0_S \to \pi^+\pi^-$ decay corresponds to the 6-prongs signature with 4 positively charged and 2 negatively charged tracks, it is not necessary to detect pions from the K^0_S decay explicitly in order to select this channel: one can select it demanding that the missing mass reconstructed on 4 charged particles must be the kaon mass.

It is necessary to note that the threshold of the reactions (4) and (18) is about ≈216 MeV (in the c.m.) above the ϕ-meson production threshold for pp interaction.

Due to the difference with ϕ-production in kinematics, pions are too "soft" (in most cases) to escape the volume of the analysing magnet. In order to detect these pions, 3 minidrift wire chambers (MDC) with multitrack resolution capability will be installed into the analyzing magnet. One of the MDCs, with an insensitive zone for the beam passing, will be installed immediately after the target perpendicularly to the beam direction (the "forward MDC") while the two others (the "side MDCs") will be installed in the free space between the pole tips and the yoke as shown schematically in Fig. 6.

The "forward" MDC will significantly improve the tracking capability of the NIS setup as well as the background suppression, because it will provide for each track an additional space point measured with good accuracy in the magnetic field region near the target. Thus it will be possible to reconstruct tracks originating from "secondary" vertices (not from the target region), for example, from $\Lambda \to p\pi^-$ decays.

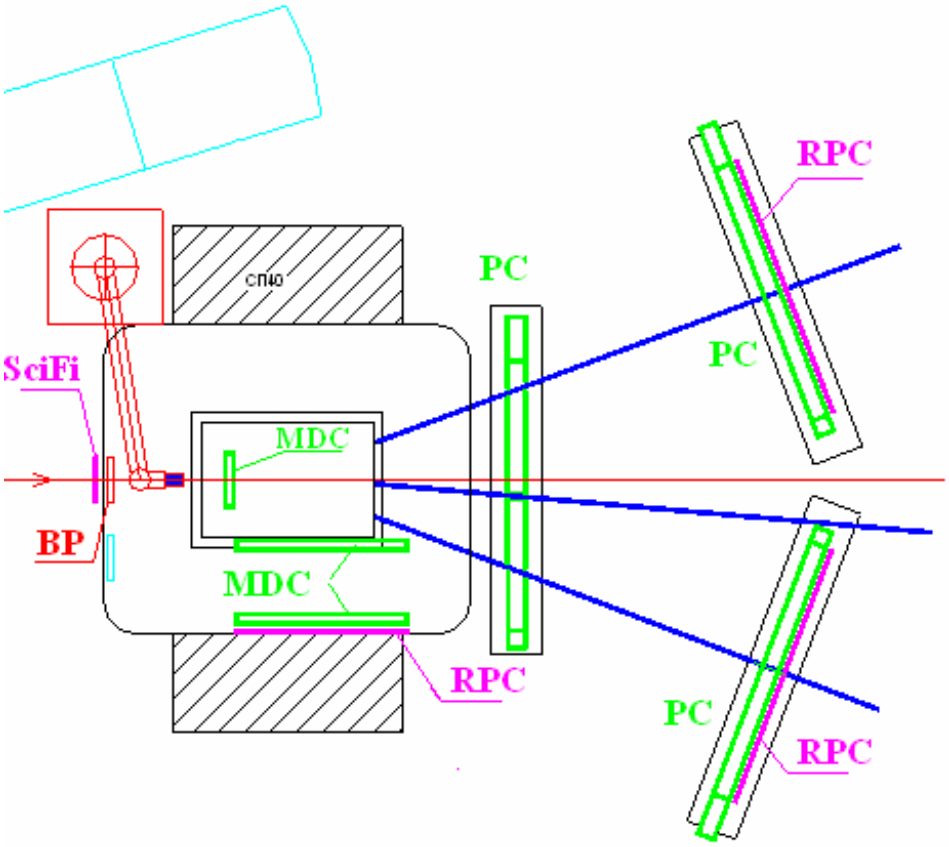

FIG. 6: Layout of the NIS spectrometer. The tracker stations (PC, MDC) and the TOF stations (based on RPC detectors) are shown schematically. SciFi (scintillation fibre counter) will provide timing signal for TOF measurements and beam parameters monitoring. Two positions of the beam profilometer (BP) are shown: in blue - during measurements, in red - during beam tuning before the measurements. The unscattered beam passes through the holes between the last detector stations; the coordinate detectors of the 1-st station have holes (insensitive zones) to pass the beam. The volume of the magnetic field is $100{\times}68{\times}150\,\mathrm{cm}^3$ ($X \times Y \times Z$). The maximal strength of the field is 0.8 T.

With this setup it is possible to perform the search of the Θ-baryons in other production channels. A very attractive option is the production of the Θ-baryon in neutron-proton interactions. It can be investigated by making use of the reaction

$$dp \to \Theta^+ + p_S + \Lambda\,, \qquad \Lambda \to p\pi^-\,. \tag{19}$$

Here p_S is the proton-spectator. It must be detected in coincidences with the Λ decay products, the proton and π^-. The "forward" MDC is of vital importance for this experiment.

IV. EXPECTED EVENT RATES OF ϕ PRODUCTION AT NIS

The event rates were estimated for ϕ-production using Monte-Carlo simulation of the reaction for the layout outlined in Fig. 6. The factor called below as $\varepsilon_{acceptance}$ includes both the geometrical acceptance of the setup and kaon losses due to their decays. For the "minimal"

configuration of the setup (i.e. the 1-st MDC is installed, the side MDCs are not) it is about of $\varepsilon_{acceptance} \approx 7 \cdot 10^{-3}$. Below this value is taken conservatively. Other factors are:

- 10 cm liquid hydrogen target i.e. $N_{targ} \approx 4.26 \cdot 10^{23}$ protons/cm^2.
- The proton beam intensity: $10^7\,\mathrm{s}^{-1}$ with the burst duration of 5 sec (the duty factor is δ =0.5); this corresponds to the integrated proton flux through the target of $I_{\mathrm{hour}} \sim 1.8 \cdot 10^{10}$ particles per hour.
- Due to the time needed for machine maintenance during a calendar day, the working time of the machine (the "live" beam time) may be conservatively estimated as 20 hours per day; (actually it means that the overall duty factor should be taken as $\delta \times 20/24 \approx 0.42$); it results in the integrated proton flux through the target of $I_{\mathrm{day}} = 24 \cdot 0.83 \cdot 1.8 \cdot 10^{10} = 3.58 \cdot 10^{11}$ particles per day.
- The overall estimated "luminosity" $L = N_{\mathrm{targ}} \cdot I_{\mathrm{day}} \approx 1.53 \cdot 10^{35}\,\mathrm{cm}^{-2}\mathrm{day}^{-1}$ or $1.53 \cdot 10^5\,\mu\mathrm{b}^{-1}\,\mathrm{day}^{-1}$. For the excess over the ϕ threshold ε = 83, 100, and 120 MeV, the estimated ϕ production cross section σ_{prod} is to be 0.19, 0.28, and $\sim$0.35 μb, respectively; below the value of $\sigma_{\mathrm{prod}} = 0.2$ is taken conservatively, what gives the estimate $L \cdot \sigma \approx 3.1 \cdot 10^4\,\mathrm{day}^{-1}$.
- An event of ϕ production in reaction (1) with all 4 tracks inside the setup acceptance can be treated as "found" after off-line analysis, when all 4 tracks are reconstructed, all 4 particles are identified and the effective mass of the found K^+K^- is within the ϕ peak in the corresponding distribution. Because of detectors (PCs, RPCs) inefficiencies, losses of events due to cuts during particle identification and ϕ-selection procedures, the probability $w_{\mathrm{find}\ \phi}$ is to be about of $w_{\mathrm{find}\ \phi} \sim 0.5$.

Taking all the factors together one gets the number $\mathrm{N}_\phi^{\mathrm{reconstructed}}$/day of ϕ mesons, detected and selected off-line in the K^+K^- effective mass distribution per calender day of the data taking,

$$N_\phi^{\mathrm{reconstructed}} \frac{1}{\mathrm{day}} = w_{\mathrm{find}\ \phi} \cdot \varepsilon_{\mathrm{acceptance}} \cdot L \cdot \sigma_{\mathrm{tot}} \approx 110 \frac{\mathrm{events}}{\mathrm{day}}\,.$$

In order to get R_{pp} with $\delta R_{pp} \sim 2\%$ one needs $\geq$ 2500 detected ϕ's. To evaluate the ϕ-production cross section we use below very conservative estimation concerning the value of OZI-rule violation, i.e. that the cross section of ω-production is about of 40 times bigger than that of ϕ.

The corresponding beam time necessary to find in off-line analysis of about of 2500 ϕ-mesons per one ε point is estimated to be $\sim$ 22 days. Taking into account that the acceptance for the detection of the ω-meson in the channel $pp \to pp + \omega \to pp + \pi^+ + \pi^- + \pi^\circ$ is less than for the detection of ϕ, the time sharing between measurements of ϕ and ω production cross sections can be taken as 3:1, i.e. $\sim$ 7 days of data taking for ω production. Thus, the corresponding beam time needed for data taking at one ε point in reactions (1) - (2) is $\approx$ 30 days. If the relation (16) is valid, the beam time needed for measurement of reaction (3) should be of $\sim$ 7 days.

The total beam time necessary for calibrating and background measurements, setting up the apparatus in the begin of runs and the tuning of the accelerator, we estimate conservatively as $\sim$30 days.

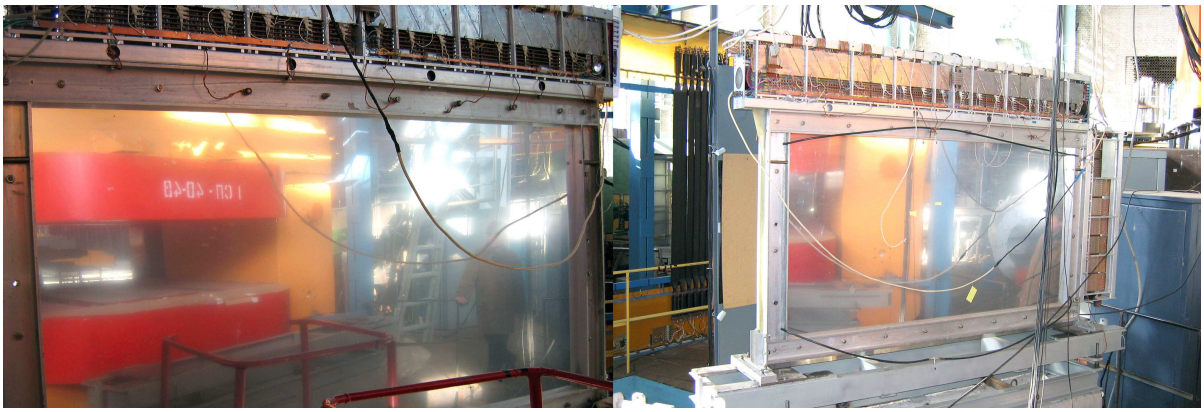

FIG. 7: Rear NIS proportional chambers in place.

V. DETAILS OF THE APPARATUS

The main components of the spectrometer are mounted in place and were tested at Nuclotron beam in several runs.

- **The tracking subsystem** is based on the large area multiwire proportional chambers (MWPC), Fig. 7 and on MDC chambers which are in production.

  The tracking system will allow reconstruction of $\geq$4 tracks with 3 tracks of positive and one of negative charged particles. The idea of the track reconstruction is similar to that of Saclay experiment E278 [40] with SPES4-π setup: the measured track, traced backward through the magnetic field, must match coordinates measured in MDC1 and hit a small size ($\sim$3 cm) target placed in front of the magnetic field.

- **The PID and trigger subsystems** will be based on RPC modules. The idea of the particle identification is based on measurements of the time of flight (TOF) measurements on the base between the RPC stations (Fig.6) and momentum-TOF correlation with the measured track length on the TOF baseline taken into account. The time resolution of the RPC modules was measured at test-bench with cosmic rays and at Nuclotron beam. In this study two RPC modules were placed close to each other; a pad of the first one gave "start" signal, the conjugated pad of the second module gave "stop" signal. The time resolution of $\sim$0.2 ns was obtained(without correction for signal propagation time in 20 cm RPC pads).

- The main criterium for **trigger selecting the events** will be the multiplicity condition: $\geq$3 particles (with positive electric charge) in the one arm and one negatively charged particle in the other one.

VI. CONCLUSIONS

The search for effects of nucleon polarized hidden strangeness in production of ϕ and ω mesons in pp and np scattering was first proposed in 2000. At present time, the measurements of the cross sections of the ϕ and ω meson production in pp and np scattering

$$p + p \to p + p + \phi \qquad (1)$$

$$p + p \to p + p + \omega \qquad (2)$$

$$d + p \to n + p + \phi + p_s \quad (3)$$

at 83, 100, and 120 MeV above their thresholds are planned at the extracted beam of the JINR Nuclotron.

The total beam time needed for data taking at one ε point in reactions (1) - (2) is ≈ 30 *days. The beam time for measurement of reaction (3) should be of* ~ 7 *days.*

The cross sections of ϕ and ω production were measured ([1]) in DISTO experiment at SATURNE-II. Measurements of ω production were published from SPES-III [12] and COSY-TOF [13] collaborations. Evidence on OZI-rule violation (factor 6 to 13) was observed.

It should be emphasized that to find the OZI-rule violation in proton-proton interaction is crucially important for the very notion of the nucleon polarized hidden strangeness. This violation was found in anitproton-proton interaction and it is important to see whether this effect exists in nucleon-nucleon system also.

Significance of the OZI-violation problem remains high, what is well emphasized by the fact that in the last two years investments were made to increase the energy limit of COSY accelerator over its nominal project energy, up to 3.8 GeV, in order to allow measurements of ϕ meson production in reaction (1) at ANKE setup [16–18].

The NIS experimental setup at Phase I will include tracking system based on MWPCs and newly produced MDC chambers inside the gap of the analyzing magnet; straw tube chambers should be added at Phase II. Particle identification system based on time-of-flight measurements in combination with measured momenta will be used.

At present, the NIS setup is at final stage of the assembling. The main detectors (MWPC, TOF-detectors based on RPC) have been mounted.Methodical studies are in progress (tests of detectors, studies of backgrounds) on the Nuclotron beam and on the test-benches (with r/a sources and with cosmic rays). The liquid hydrogen target is ready. Manufacturing of the first MDC is almost completed; works on preparation of the start-detector based of scintillation fibres is close to the end. The first beam profilometer was manufactured, tested and is ready for use; elements of the other 2 profilometers are being produced. R&D and tests of multichannel TDC and QDC modules in VME standard are finished; their mass-production is started. R&D on high voltage cells for RPC and MDC is completed; mass production of the cells and control modules is completed on 80%. Front-end pre-amplifiers for MDC and SciFi detectors are being prototyped. Modules of trigger logics are at the production stage. Completion of their production is being determined only by available funding. Necessary software tools have been developed; software for on-line data taking was developed for test-benches and for the work at the beam. Monte-Carlo tools were developed; new tools for the event reconstruction are created.

The main components of the NIS setup were successfully tested at extracted Nuclotron beams. Commissioning of the setup is planned for the 2007 with start of calibrating measurements at the Nuclotron beam with subsequent start of the data taking according the physical program of the project.

---

[1] F. Balestra *et al.*, Phys. Rev. Lett. **81** (1998) 4572; F. Balestra *et al.*, NIM **A 426**, (1999) 385.

[2] F. Balestra *et al.*, Phys. Rev. C **63**, (2001) 024004.
[3] S. Okubo, Phys.Lett. B **5**, 165 (1963); G. Zweig CERN Report No.8419/TH412 (1964); I. Iizuka. Prog. Theor. Phys. Suppl. **37**, 21 (1966).
[4] V.P. Nomokonov and M. G. Sapozhnikov, Physics of Elementary Particles and Atomic Nuclei **34**, 184 (2003); hep-ph/0204259, 2002.
[5] C. Amsler, Rev. Mod. Phys. **70**, 1293 (1998).
[6] C. Amsler *et al.*, Phys. Lett. B **346**, 363 (1995).
[7] V.G. Ableev *et al.*, Nucl.Phys. A **594**, 375 (1995).
[8] The OBELIX collaboration, A. Alberico *et al.*, Phys. Lett. B **438**, 430 (1998); R. Donά, Proc. LEAP'98 Conference, Villasimius, 1998; Nucl. Phys. A **655**, 213c (1999).
[9] J. Ellis, M. Karliner, D. Kharzeev, and M.G. Sapozhnikov, Phys. Lett. B **353**, 319 (1995).
[10] J. Ellis, M. Karliner, D. Kharzeev, and M.G. Sapozhnikov, Nucl. Phys. A **673**, 256 (2000).
[11] J. Ellis, D. Kharzeev, and A. Kotzinian, Z. Phys. C **65**, 189 (1995).
[12] F. Hibou *et al.*, Phys. Rev. Lett. **83**, 492 (1999).
[13] S. Abd El-Samad et al, Phys. Lett. B **522**, 16 (2001); A. Boehm *et al.*, NIM A **443**, 238 (2000).
[14] R. Baldi *et al.*, Phys. Lett. B **68**, 381 (1977).
[15] V. Blobel *et al.*, Phys. Lett. B **59**, 88 (1975).
[16] ANKE COSY proposal #104, 2001 year.
[17] M. Hartmann, Proc. "Baryons 2004" Conf., Paleseau, 2004; IKP/COSY Annual report 2004, p.12.
[18] M. Hartmann *et al.*, Phys. Rev. Lett. **96**, 242301 (2006); Y. Maeda at al., nucl-ex/0607001 (2006).
[19] IKP/COSY Annual report 2004, p.12.
[20] A.I. Titov, B. Kaempfer, and B.L. Reznik, Eur. Phys. J. A **7**, 543 (2000).
[21] A.I. Titov, B. Kaempfer, and V.V. Shklyar, Phys. Rev. C **59**, 999 (1999).
[22] N. Kaiser, Phys. Rev. C **60**, 057001 (1999).
[23] K. Nakayama *et al.*, Phys. Rev. C **60**, 055209 (1999); Phys. Rev. C **63**, 015201 (2000); Phys. Rev. C **57**, 1580 (1998).
[24] K. Tsushima and K. Nakayama, Phys. Rev. C **68**, 034612 (2003).
[25] V.V. Barmin *et al.*, The DIANA collaboration, hep-ex/0304040 (reported as a talk at Session of Nuclear Division of Russian Academy of Sciences, Dec. 3, 2002, to appear in proceedings, Phys. Atom. Nuclei, 2003); T. Nakano *et al.*, Phys. Rev. Lett. **91** (2003), in print; S. Stepanyan *et al.*, The CLAS collaboration, hep-ex/0307018;
[26] J. Barth *et al.*, The SAPHIR Collaboration, hep-ex/0307083.
[27] A.A. Asratyan, A.G. Dolgolenko and M.A. Kubantsev, hep-ex/0309042.
[28] C. Alt *et al.*, Phys. Rev. Lett. **92**, 042003 (2004).
[29] V. Kubarovsky *et al.*, Phys. Rev. Lett. **92**, 032001 (2004).
[30] Yu.A. Troyan *et al.*, JINR Comm. D1-2004-39, JINR, Dubna, 2004.
[31] R. de Vita *et al.*, APS talk, Apr. 16, 2005.
[32] D. Diakonov, V. Petrov, and M. Polyakov, Z. Phys. A 359 (1997) 305; M.V. Polyakov *et al.*, Eur. Phys. J. A **9**, 115 (2000).
[33] A. Hosaka, hep-ph/0506138; S. Nam *et al.*, hep-ph/0505134.
[34] M. Karliner and H.J. Lipkin, hep-ph/050684.
[35] D. Diakonov and V. Petrov, hep-ph/0505201.
[36] K. Seth, hep-ex/0504051; K.H. Hicks, hep-ex/0504028.
[37] M. Abdel-Bary *et al.*, hep-ex/0403011.
[38] K. Miwa *et al.*, nucl-ex/0601032.
[39] A.N. Aleev et al,, Instr. and. Exp. Techn. **38** $N°$**4**, 425 (1995); Instr. and. Exp. Techn. **42**, 481 (1999).
[40] L.V. Malinina *et al.*, Phys. Rev. C **64**, 064001 (2001); L.V. Malinina *et al.*, JINR preprint E1-2001-12, JINR, Dubna, 2001; L.S. Azhgirey *et al.*, JINR Rapid Comm. **2[94]-99**, 5 (1999); G.D. Alkhazov *et al.*, preprint EP-9-2000 No. 2352 (2000), PNPI, Gatchina.
[41] A.N. Walenta, NIM **217**, 65 (1983).
[42] I. Chirikov-Zorin *et al.*, NIM A **260**, 142 (1987).
[43] Preprint CERN/EP80-99, 1980.
[44] K. Ackerstaff *et al.*, NIM A **417**, 230 (1998).

On Computer Algebra Application to Simulation of Quantum Computation

V.P. Gerdt[1)], R. Kragler[2)], and A.N. Prokopenya[3)]

[1)] *Joint Institute for Nuclear Research, 141980 Dubna, Russia*[*]

[2)] *University of Applied Sciences, D-88241 Weingarten, Germany*[†] *and*

[3)] *Brest State Technical University, Moskowskaya 267, 224017 Brest, Belarus*[‡]

In the present paper which is an extended version of paper [1] we consider a *Mathematica*-based package for simulation of quantum circuits. It provides a user-friendly graphical interface to specify a quantum circuit, to draw it, and to construct the unitary matrix for quantum computation defined by the circuit. The matrix is computed by means of the linear algebra tools built-in *Mathematica*. For circuits composed from the Toffoli and Hadamard gates the package can also output the corresponding multivariate polynomial system over $\mathbb{F}_2$ whose number of solutions in $\mathbb{F}_2$ determines the circuit matrix. Thereby the matrix can also be constructed by applying to the polynomial system the Gröbner basis technique based on the corresponding functions built-in Mathematica. We illustrate the package and the method used by a number of examples.

I. INTRODUCTION

Quantum computations is a topic of great interest for the last two decades. One reason for this is a potential ability of a quantum computer to do a certain computational task much more efficiently than can be done by any classical computer [2, 3]. Two of the most famous examples of such calculations are Shor's algorithm [4] for efficient factorization of large integers and Grover's algorithm [5] of element search in an unsorted list. Nevertheless, despite of considerable efforts in the quantum computing community, the number of such efficient quantum algorithms which have been discovered still remains rather small. For this reason a search for other problems which may be efficiently solved with a quantum computer and developing the corresponding quantum algorithms, as well as the physical question of the feasibility of building a quantum computer, is of great interest in present-day investigations.

Since realistic quantum computers have not yet been built, it is worthwhile to simulate quantum computation on a classical computer, and there is quite a number of such simulators (see, for example, [6, 7]). Among two equivalent models of quantum computation – quantum Turing machine and the circuit model – the last one is more convenient both for simulation and application [2].

The circuit model of computation was introduced first for a classical computer that can be considered as an electrical circuit made up of wires and logical gates. The wires are used to carry information around the circuit, while the logic gates perform manipulations of the information, converting it from one form to another. Note that inside a classical computer any information is encoded into a sequence of bits which are the elementary units of information. And any complex logic operation can be represented as an ordered sequence of some elementary logic gates which

[*]Electronic address: gerdt@jinr.ru
[†]Electronic address: kragler@hs-weingarten.de
[‡]Electronic address: prokopenya@brest.by

act on single bits or pairs of bits. Using special notation for these gates, one can easily visualize a circuit and clearly show a structure of computations. Thus, the circuit model turned out to be very convenient and realistic for many applications and is widely used in computer science.

In the present paper we use the computer algebra system *Mathematica* [8] for simulation of quantum computation and develop a package which provides a user-friendly graphical interface to specify a quantum circuit, to draw the circuit specified, and to construct a unitary $2^n \times 2^n$ matrix U defined by the circuit with n qubits. In Sec. II we discuss general structure of an arbitrary quantum circuit and introduce the basic logical gates commonly used in the quantum circuit model. In Sec. III we describe an algorithm for the quantum circuits generation with *Mathematica*. And in Sec. IV we develop an algorithm for computing the unitary matrix defined by the circuit and implement it with *Mathematica*. In Sec. V circuits of special type are considered which are composed from the Hadamard and Toffoli gates only. If a circuit is of this type our Mathematica package can generate the system of polynomial equations over $\mathbb{F}_2$ whose solution space in $\mathbb{F}_2$ uniquely determines the circuit matrix [9]. We show in Sec. VI how the built-in *Mathematica* Gröbner bases module can be used to to construct the circuit matrix in terms of the polynomial system. Throughout the paper we illustrate the methods used and the package by simple examples.

II. STRUCTURE AND BASIC ELEMENTS OF QUANTUM CIRCUITS

The circuit model is easily transferred to quantum computations by means of creating quantum analogues for the basic components of a classical computer [2]. Quantum information is represented as a sequence of quantum bits or *qubits* which are the elementary units of quantum information. A qubit is a two-level quantum system that can be prepared, manipulated and measured in a controlled way. The state of a qubit is denoted as $|a\rangle$ corresponding to standard Dirac notation for quantum mechanical states. Two possible states for a qubit are usually denoted as $|0\rangle$ and $|1\rangle$, which correspond to the states 0 and 1 for a classical bit. But in contrast to classical bits, qubit as a quantum system may exist not only in one of the states $|0\rangle$ or $|1\rangle$ but also in the state $|a\rangle$ being a superposition of these states

$$|a\rangle = \alpha|0\rangle + \beta|1\rangle \ , \tag{1}$$

where α and β are complex numbers constrained by the normalization condition $|\alpha|^2 + |\beta|^2 = 1$. Thus, the state of a qubit is represented by the vector (1) in the two-dimensional complex vector space, where the special states $|0\rangle$ and $|1\rangle$ form an orthonormal basis and are known as computational basis states [2].

A set of n qubits forms a quantum memory register, where the input data and any intermediate results of computations are held. It is shown on diagrams as a column of states of the form $|a_j\rangle$ $(j = 1, 2, ..., n)$ from which quantum wires start. Although a quantum circuit doesn't contain any wires as such, the term "wires" is merely used to show evolution of qubits acted on by various quantum gates. General structure of any quantum circuit can be readily understood from Fig. 1, where a very simple quantum circuit containing two qubits and two quantum gates is depicted. The circuit is to be read from left-to-right. It means that a column of two qubits $|a_1\rangle$ and $|a_2\rangle$ in the left-hand side of the diagram in Fig. 1 corresponds to the initial state of quantum register. Then it is successively acted on by two quantum gates and its final state is shown on the right-hand side of the diagram as the column of qubits $|b_1\rangle$ and $|b_2\rangle$. Note that a quantum circuit containing more qubits and quantum gates can be built in a similar way.

As in the case of classical computation, there are two groups of the elementary quantum gates which perform manipulation of quantum information. The first group consist of the single-qubit gates. Such gates have only one input and one output wires and are depicted by some

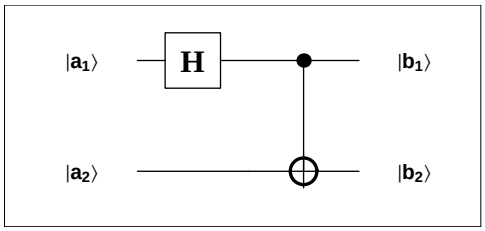

FIG. 1: A simple quantum circuit.

Hadamard gate	Pauli – X	Pauli – Y	Pauli – Z	Phase	π / 8 – gate
H	X	Y	Z	S	T
$\frac{1}{\sqrt{2}}\begin{pmatrix}1 & 1\\ 1 & -1\end{pmatrix}$	$\begin{pmatrix}0 & 1\\ 1 & 0\end{pmatrix}$	$\begin{pmatrix}0 & -i\\ i & 0\end{pmatrix}$	$\begin{pmatrix}1 & 0\\ 0 & -1\end{pmatrix}$	$\begin{pmatrix}1 & 0\\ 0 & i\end{pmatrix}$	$\begin{pmatrix}1 & 0\\ 0 & e^{i\frac{\pi}{4}}\end{pmatrix}$

FIG. 2: Single-qubit gates.

capital letter placed into a square. Following [2], we'll use here only six non-trivial single-qubit quantum gates which are shown in Fig. 2 together with their matrix representation with respect to the computational basis states. Using this set of single-qubit matrices one can construct any operation on a single qubit. Note that the matrix of any single-qubit gate shows how the gate acts on the states of the computational basis, for example,

$$H|0\rangle = \frac{1}{\sqrt{2}}(|0\rangle + |1\rangle) \ , \ H|1\rangle = \frac{1}{\sqrt{2}}(|0\rangle - |1\rangle) \ . \tag{2}$$

The second group of elementary quantum gates consists of the gates acting on two and more qubits, i.e., the multi-qubit gates. Let us consider first two-qubit quantum gates. Remember that the state of one qubit is represented by the vector (1) in the two-dimensional complex vector space with the basis vectors $|0\rangle$ and $|1\rangle$. Hence, the state of the system of two independent qubits may be determined as a direct (tensor) product of two two-dimensional spaces associated with each qubit. Such a space has four basis vectors

$$|0\rangle_1 \otimes |0\rangle_2 \equiv |00\rangle \ , \ |0\rangle_1 \otimes |1\rangle_2 \equiv |01\rangle \ ,$$

$$|1\rangle_1 \otimes |0\rangle_2 \equiv |10\rangle \ , \ |1\rangle_1 \otimes |1\rangle_2 \equiv |11\rangle \ , \tag{3}$$

where the symbol $\otimes$ denotes a direct product of basis states associated with the first $(|0\rangle_1, |1\rangle_1)$ and the second $(|0\rangle_2, |1\rangle_2)$ qubits. Thus, the system of two qubits has a four-dimensional space of states with computational basis states (3), an arbitrary state of such a system may be represented as superposition of the form

$$|\psi\rangle = \alpha|00\rangle + \beta|01\rangle + \gamma|10\rangle + \delta|11\rangle \ , \tag{4}$$

where coefficients $\alpha, \beta, \gamma, \delta$ are complex numbers constrained by the normalization condition $|\alpha|^2 + |\beta|^2 + |\gamma|^2 + |\delta|^2 = 1$. Hence, any two-qubit quantum gate can be represented as a 4×4 matrix in the computational basis states (3). One of the useful two-qubit gates is a controlled-NOT or CNOT gate, its graphical and matrix representation is shown in Fig. 3. This gate has two input qubits, known as the control qubit ($|a_1\rangle$ with black dot on the corresponding wire)

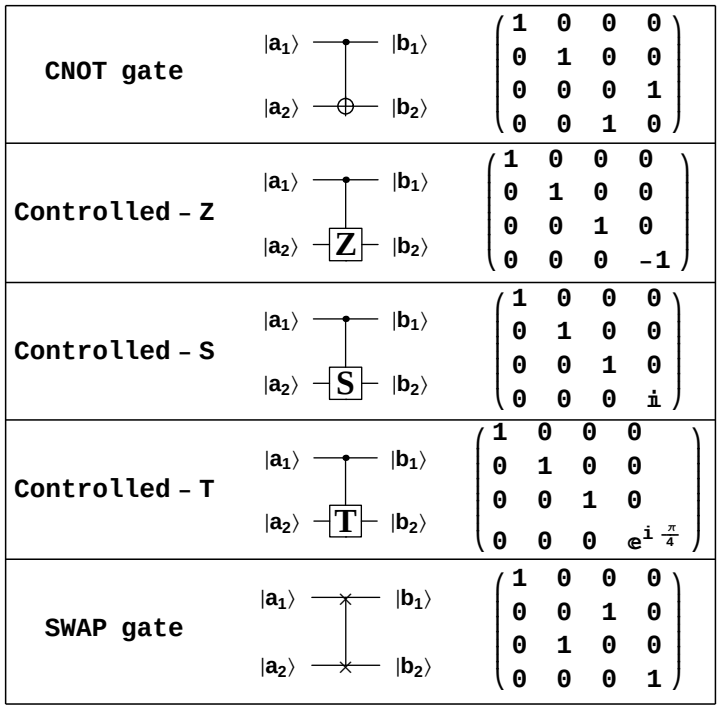

FIG. 3: Controlled two-qubit gates and swap gate.

and the target qubit ($|a_2\rangle$ marked with the sign $\oplus$). It flips the state of the target qubit if the control qubit is in the state $|1\rangle$ and does nothing if the control qubit is in the state $|0\rangle$. In other words, if the control qubit is in the state $|1\rangle$ the Pauli-X gate is applied to the target qubit. Other controlled gates shown in Fig. 3 act similarly as the CNOT gate: if the control qubit is in the state $|1\rangle$ then the corresponding Z, S or T gate is applied to the target qubit, otherwise the target qubit is left alone. Another example of the two-qubit gate is the SWAP gate (see Fig. 3) which interchanges the states of two input qubits.

The set of six single-qubit gates shown in Fig. 2 together with the CNOT-gate is a universal set of gates [2]. It means that any quantum computation can be decomposed in terms of this set gates. In practice, however, there may be more specialized quantum gates that would enable us to construct more compact circuits for specific computations, some of them are shown in Fig. 3. We'll use also the Toffoli gate (Fig. 4) or controlled-controlled-gate [2]. It can be considered as a generalization of CNOT-gate and has three input qubits and three output qubits: two of them are the control qubits and one is the target qubit. And it flips the state of the target qubit only if both control qubits are in the state $|1\rangle$. Note that other two-qubit gates in Fig. 3 may be generalized to the three-qubit gates in a similar way.

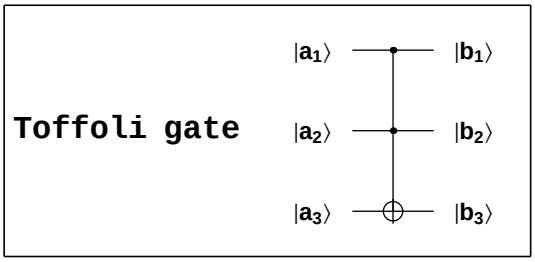

FIG. 4: Toffoli gate.

III. BUILDING OF QUANTUM CIRCUITS

Before describing an algorithm for generating quantum circuits let us note that any quantum circuit may be represented as a rectangular table. The number of rows in the table is equal to the number of qubits in the circuit, while the number of columns depends on the number of quantum gates and their arrangement. Consider, for example, a quantum circuit containing three qubits and six quantum gates (see diagram in the left-hand side of Fig. 5). Drawing dashed lines, we can separate neighboring rows and columns in the table in such a way that each of its cell would contain some elementary gate (wires without any gates can be considered as the identity quantum gates, i.e., the gates making identical transformation of the corresponding qubits).

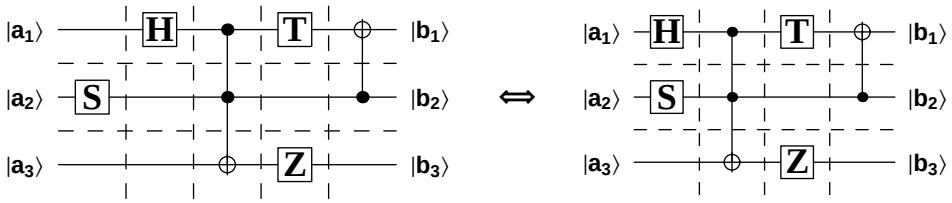

FIG. 5: Table representation of the quantum circuit.

Obviously, we can shift the S-gate to the second column in the table without any disturbance of the circuit. Then the first column will contain only three identity gates and it can be removed from the table. Hence, two diagrams in Fig. 5 represent the same circuit but the table in the right-hand side is smaller and simpler. In general, drawing the circuit, we'll adhere the following convention: *each column in the table can contain either one multi-qubit gate or only single-qubit gates and there are not any neighboring columns containing only single-qubit gates acting on different qubits*. Note, that according to this convention, we can not shift the Pauli-Z gate in Fig. 5 to the last column because it would turn out to be in the same column together with multi-qubit CNOT gate.

Thinking of any quantum circuit as a table of elementary quantum gates, we can define a matrix whose elements are some symbols, denoting the gates, and this matrix will contain all information on the circuit. An example of such matrix is shown in Fig. 6, where C and X correspond to the control and target qubits, respectively (the symbols corresponding to the single-qubit gates are obvious). Obviously, this matrix completely determines the structure of the quantum circuit.

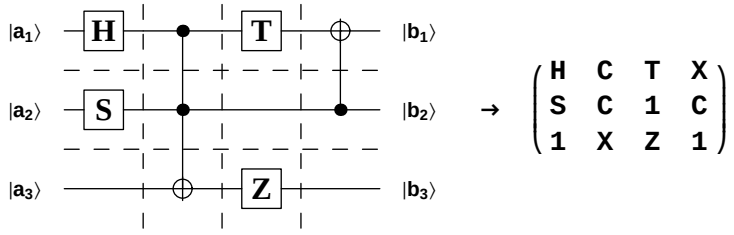

FIG. 6: Matrix representation of the quantum circuit.

In our *Mathematica* package we just use such matrix representation for quantum circuits and define the function $circuit[mat\_?MatrixQ]$ which generates the quantum circuit, corresponding to any given matrix mat. It is quite cumbersome and we do not describe it here. Of course,

before evaluating this function, we should choose a set of symbols, denoting different quantum gates, and define the functions, determining the corresponding graphical objects. One possible function, generating the Hadamard gate, is shown in Fig. 7 (the corresponding expression is written in *Mathematica* code).

```
hadamardGate[yy_, xx_] := Block[ {x, y},
        x = 0.1 (xx - 1); y = 0.1 (1 - yy);
  { Line[{{x, y}, {x + 0.025, y}}],
    Line[{{x + 0.075, y}, {x + 0.1, y}}],
    Line[{{x + 0.025, y - 0.025}, {x + 0.025, y + 0.025},
          {x + 0.075, y + 0.025}, {x + 0.075, y - 0.025},
          {x + 0.025, y - 0.025}}], Text[
     StyleForm["H", FontFamily → "Times", FontSize → 18,
            FontWeight → "Bold"], {x + 0.05, y - 0.003}]} ]
```

FIG. 7: Function generating the Hadamard gate.

Here the integers yy, xx correspond to the row and column numbers, respectively, and determine the position of the Hadamard gate in the matrix *mat*. Note that other single-qubit gates are defined in a similar way.

Then we define a function *matrixGenerating* which generates a cell, containing two *Mathematica* expressions: the matrix *mat* with given number of rows and columns all of its elements are equal to 1 and function *circuit*[*mat*] (Fig. 8).

$$\texttt{mat} = \begin{pmatrix} 1 & 1 & 1 & 1 \\ 1 & 1 & 1 & 1 \\ 1 & 1 & 1 & 1 \end{pmatrix} \texttt{; circuit[mat]}$$

FIG. 8: Function for generating the quantum circuits.

Now, in order to generate a quantum circuit, it is sufficient to change units in the matrix *mat* by symbols, corresponding to constituent quantum gates, and evaluate the cell. If the matrix *mat* in Fig. 8 has been changed in such a way that it would coincide with the matrix given in Fig. 6, for example, then, as a result, we obtain the circuit shown in Fig. 6 as a result. It should be noted that, using the functions *matrixGenerating* and *circuit*, we can generate any quantum circuit.

IV. COMPUTING THE CIRCUIT MATRIX

A system of n qubits has 2^n basis states of the form $|a_1 a_2 \dots a_n\rangle$, where $a_j = 0, 1$ ($j = 1, \dots, n$). They are obtained as direct product of basis states $(|0\rangle_j, |1\rangle_j)$ associated with all n qubits [2]. In the case of $n = 2$ the corresponding basis states have been written in (3). Hence, the unitary matrix U defined by the quantum circuit with n qubits may be represented as a $2^n \times 2^n$ matrix with respect to these basis states.

As the circuit is read from left-to-right and we use the matrix *mat* to represent the circuit, then the matrix U can be written as the following product

$$U = U_m U_{m-1} \dots U_1 \ , \tag{5}$$

where U_j $(j = 1, 2, \ldots, m)$ is the $2^n \times 2^n$ matrix defined by the quantum gates being in the jth column of the matrix mat and m is a number of columns.

If the column contains only single-qubit gates then its matrix U_j may be constructed as a direct product of all 2×2 matrices corresponding the gates available in this column. For example, the first column of the matrix in Fig. 6 contains Hadamard (H), phase (S) and identity gates (matrices of H and S gates are shown in Fig. 2 while the matrix of the identity gate is just the 2×2 unity one). Then the matrix U_1 defined by this column is determined by the following *Mathematica* command

$$Fold[BlockMatrix[Outer[Times, \#1, \#2]]\&, \{\{1\}\}, \{matH, matS, matI\}]$$

where $matH$, $matS$, $matI$ are the matrices of the corresponding gates.

```
gateCN[n_, kn_, kc_?ListQ] :=
 Block[ {basisOld, basisNew, u0, rules},
  basisOld =
   Table[IntegerDigits[j, 2, n], {j, 0, 2^n - 1}];
  basisNew = Map[ReplacePart[#,
      Mod[Apply[Times, #[[kc]]] + #[[kn]], 2],
      kn] &, basisOld, 1];
  rules = Table[{Position[basisNew, basisOld[[j]] ][[
       1, 1]], j} → 1, {j, 2^n}];
  u0 = SparseArray[rules, {2^n, 2^n}] ;
  u0  ]
```

FIG. 9: Function for computing the matrix of CNOT and Toffoli gates.

$$\texttt{gateCN[3, 3, \{1, 2\}]} \rightarrow \begin{pmatrix} 1 & 0 & 0 & 0 & 0 & 0 & 0 & 0 \\ 0 & 1 & 0 & 0 & 0 & 0 & 0 & 0 \\ 0 & 0 & 1 & 0 & 0 & 0 & 0 & 0 \\ 0 & 0 & 0 & 1 & 0 & 0 & 0 & 0 \\ 0 & 0 & 0 & 0 & 1 & 0 & 0 & 0 \\ 0 & 0 & 0 & 0 & 0 & 1 & 0 & 0 \\ 0 & 0 & 0 & 0 & 0 & 0 & 0 & 1 \\ 0 & 0 & 0 & 0 & 0 & 0 & 1 & 0 \end{pmatrix}$$

FIG. 10: Matrix corresponding to the Toffoli gate.

Matrices defined by the multi-qubit gates can not be, in general, found as direct product of some 2×2 matrices and we need to compute them separately. For example, the function $gateCN[n\_\,,\ kn\_\,,\ kc\_?ListQ]$ shown in Fig. 9 computes the $2^n \times 2^n$ matrix U_j corresponding to CNOT and Toffili gates. It has three arguments: integer n, the number of qubits in the circuit; number kn and the list of numbers kc determine position of the target qubit and the controlled qubits, respectively. To compute the matrix corresponding to the Toffoli gate we have to evaluate the function $gateCN[3, 3, \{1, 2\}]$ (see Fig. 10). The matrix defined by the last column of mat shown in Fig. 6 is computed by the command $gateCN[3, 1, \{2\}]$. Similarly, one can compute matrices corresponding to other controlled gates.

As soon as all matrices defined by the columns of the primary matrix mat are computed, we can evaluate the matrix U defined by the corresponding quantum circuit. This task is fulfilled

$$\frac{1}{\sqrt{2}}\begin{pmatrix} 1 & 0 & 0 & 0 & 1 & 0 & 0 & 0 \\ 0 & -1 & 0 & 0 & 0 & -1 & 0 & 0 \\ 0 & 0 & 0 & i\,e^{\frac{i\pi}{4}} & 0 & 0 & 0 & -i\,e^{\frac{i\pi}{4}} \\ 0 & 0 & -i\,e^{\frac{i\pi}{4}} & 0 & 0 & 0 & i\,e^{\frac{i\pi}{4}} & 0 \\ e^{\frac{i\pi}{4}} & 0 & 0 & 0 & -e^{\frac{i\pi}{4}} & 0 & 0 & 0 \\ 0 & -e^{\frac{i\pi}{4}} & 0 & 0 & 0 & e^{\frac{i\pi}{4}} & 0 & 0 \\ 0 & 0 & i & 0 & 0 & 0 & i & 0 \\ 0 & 0 & 0 & -i & 0 & 0 & 0 & -i \end{pmatrix}$$

FIG. 11: Matrix defined by the circuit of Fig. 6.

by the function $matrixU[mat\_?MatrixQ]$, whose argument is just the matrix mat which we use to define a quantum circuit. For the circuit shown in Fig. 6 the corresponding matrix U given in Fig. 11.

In order to demonstrate that with the package developed we can easily simulate any quantum circuit, let us consider the circuit for a 3 qubit quantum Fourier transformation [2]. To generate this circuit and compute its unitary matrix U we have to evaluate the following *Mathematica* commands. First of all, we generate a skeleton 3×7 matrix with the function *matrixGenerating* (see Fig. 12).

$$\texttt{mat} = \begin{pmatrix} 1 & 1 & 1 & 1 & 1 & 1 & 1 \\ 1 & 1 & 1 & 1 & 1 & 1 & 1 \\ 1 & 1 & 1 & 1 & 1 & 1 & 1 \end{pmatrix}\texttt{; circuit[mat]}$$

FIG. 12: A skeleton 3×7 matrix.

Then we replace some units in the matrix mat according to the algorithm of quantum Fourier transformation [2] (see Fig. 13) and evaluate the function $circuit[mat]$. As a result, the corresponding quantum circuit is obtained as output.

$$\texttt{mat} = \begin{pmatrix} H & S & T & 1 & 1 & 1 & SW \\ 1 & C & 1 & H & S & 1 & 1 \\ 1 & 1 & C & 1 & C & H & SW \end{pmatrix}\texttt{; circuit[mat]}$$

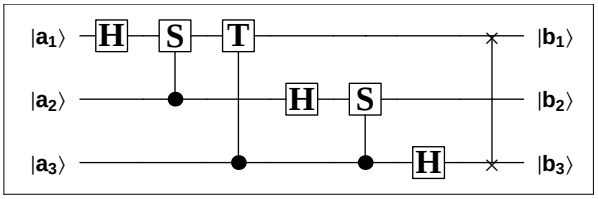

FIG. 13: Circuit for 3 qubit quantum Fourier transform.

At last, we evaluate the function $matrixU[mat]$ and obtain the matrix U (see Fig. 14) defined by the circuit of Fig. 13 (cf. [2]).

$$\frac{1}{2\sqrt{2}}\begin{pmatrix}
1 & 1 & 1 & 1 & 1 & 1 & 1 & 1\\
1 & e^{\frac{i\pi}{4}} & i & i\,e^{\frac{i\pi}{4}} & -1 & -e^{\frac{i\pi}{4}} & -i & -i\,e^{\frac{i\pi}{4}}\\
1 & i & -1 & -i & 1 & i & -1 & -i\\
1 & i\,e^{\frac{i\pi}{4}} & -i & e^{\frac{i\pi}{4}} & -1 & -i\,e^{\frac{i\pi}{4}} & i & -e^{\frac{i\pi}{4}}\\
1 & -1 & 1 & -1 & 1 & -1 & 1 & -1\\
1 & -e^{\frac{i\pi}{4}} & i & -i\,e^{\frac{i\pi}{4}} & -1 & e^{\frac{i\pi}{4}} & -i & i\,e^{\frac{i\pi}{4}}\\
1 & -i & -1 & i & 1 & -i & -1 & i\\
1 & -i\,e^{\frac{i\pi}{4}} & -i & -e^{\frac{i\pi}{4}} & -1 & i\,e^{\frac{i\pi}{4}} & i & e^{\frac{i\pi}{4}}
\end{pmatrix}$$

FIG. 14: Matrix defined by the circuit of Fig. 13.

V. POLYNOMIAL EQUATIONS DESCRIBING CIRCUITS BUILT FROM HADAMARD AND TOFFOLI GATES

If a circuit contains only the Toffoli and Hadamard gates, then one can construct its circuit matrix by the alternative method [9, 10] that does not use the above method based on the straightforward linear algebra. Instead, the alternative method exploits algebra of multivariate polynomials associated with the circuit. With all this going on, it should be noted that the Toffoli and Hadamard gates form a universal gate set [11] and that there is a famous Soloway-Kitaev algorithm requiring software [2, 12, 13] for conversion of circuits composed from other gates for its implementation.

To construct the system of multivariate polynomials one can apply the quantum-mechanical Feynman's sum-over-paths approach to a quantum circuit [9]. This means for every path any quantum gate in the circuit under consideration acts as its classical counterpart. In doing so, the classical gate for the quantum Hadamard gate outputs the path variable $x \in \mathbb{F}_2$ [9] irrespective of the input. Its value determines one of the two possible paths of computation. Thereby, the classical Hadamard gate acts as

$$a_1 \mapsto x\,, \qquad a_i, x \in \mathbb{F}_2\,,$$

whereas the classical Toffoli gate acts as

$$(a_1, a_2, a_3) \mapsto (a_1, a_2, a_3 \oplus a_1 a_2)$$

where $\oplus$ denotes addition modulo 2.

Let us now consider as an example the 3 qubit circuit built from the Hadamard and Toffoli gates [9]. Again we generate, first, the 3×4 matrix corresponding to this example by means of the function *matrixGenerating* as shown in Fig. 15 which is the output of the circuit of Fig. 16. Its circuit matrix computed by the function *matrixU*[*mat*] as described in of Sec. IV is given by Fig. 17.

$$\texttt{mat} = \begin{pmatrix} \texttt{H} & \texttt{C} & \texttt{H} & \texttt{X} \\ \texttt{H} & \texttt{C} & \texttt{1} & \texttt{C} \\ \texttt{1} & \texttt{X} & \texttt{H} & \texttt{C} \end{pmatrix}\texttt{; circuit[mat]}$$

FIG. 15: 3×4 matrix generating the example from [9].

Turning back to Feynman's sum-over-paths approach, a classical path is defined by a sequence of classical bit strings $\mathbf{a}, \mathbf{a_1}, \mathbf{a_2}, \ldots, \mathbf{a_m} = \mathbf{b}$ produced from action of the classical gates. Each

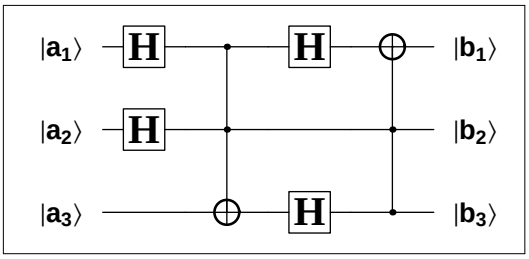

FIG. 16: The circuit example from [9].

$$\begin{pmatrix} \frac{1}{2} & \frac{1}{2} & \frac{1}{2} & \frac{1}{2} & 0 & 0 & 0 & 0 \\ \frac{1}{2} & -\frac{1}{2} & \frac{1}{2} & -\frac{1}{2} & 0 & 0 & 0 & 0 \\ \frac{1}{2} & \frac{1}{2} & -\frac{1}{2} & -\frac{1}{2} & 0 & 0 & 0 & 0 \\ \frac{1}{2} & -\frac{1}{2} & -\frac{1}{2} & \frac{1}{2} & 0 & 0 & 0 & 0 \\ 0 & 0 & 0 & 0 & \frac{1}{2} & \frac{1}{2} & \frac{1}{2} & \frac{1}{2} \\ 0 & 0 & 0 & 0 & \frac{1}{2} & -\frac{1}{2} & \frac{1}{2} & -\frac{1}{2} \\ 0 & 0 & 0 & 0 & \frac{1}{2} & \frac{1}{2} & -\frac{1}{2} & -\frac{1}{2} \\ 0 & 0 & 0 & 0 & \frac{1}{2} & -\frac{1}{2} & -\frac{1}{2} & \frac{1}{2} \end{pmatrix}$$

FIG. 17: Matrix for circuit of Fig. 16 computed by linear algebra.

set of values of the path variables x_i gives a sequence of classical bit strings which is called an admissible classical path. All path variables and, thus, all admissible classical paths for Fig. 16 are explicitly shown in Fig. 18. The corresponding sequence of classical bit strings is $\mathbf{a} = \{a_1, a_2, a_3\}$, $\mathbf{a_1} = \{x_1, x_2, a_3\}$, $\mathbf{a_2} = \{x_1, x_2, a_3 \oplus x_1 x_2\}$, $\mathbf{a_3} = \{x_3, x_2, x_4\}$, $\mathbf{a_4} = \{x_3 \oplus x_2 x_4, x_2, x_4\} = \mathbf{b}$.

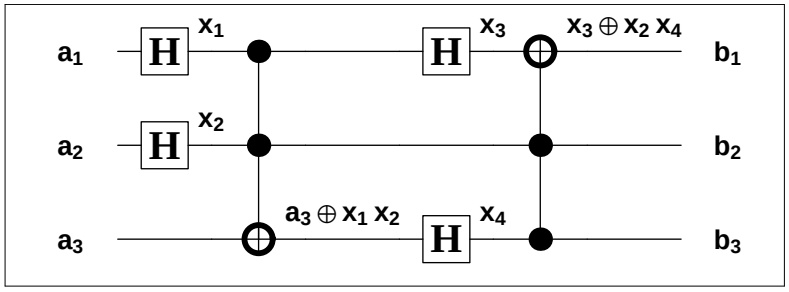

FIG. 18: The admissible paths for the circuit of Fig. 16.

Each admissible classical path is provided with a phase which is determined by the Hadamard gates applied [9]. The phase is changed only when the input and output of the Hadamard gate are simultaneously equal to 1. Thereby, this gives the formula

$$\varphi(\mathbf{x}) = \sum_{\text{Hadamard gates}} input \bullet output \qquad (1)$$

with the sum evaluated in $\mathbb{F}_2$. As to Toffoli gates, they do not change the phase.

In the example of Fig. 16 the phase of the path $\mathbf{x}$ reads

$$\varphi(\mathbf{x}) = a_1x_1 \oplus a_2x_2 \oplus x_1x_3 \oplus a_3x_4 \oplus x_1x_2x_4\,.$$

According to the Feynman's sum-over-paths method the matrix element of a quantum circuit is the sum over all the allowed paths from the classical state $\mathbf{a}$ to $\mathbf{b}$

$$\langle \mathbf{b}|\, U_f\, |\mathbf{a}\rangle = \frac{1}{\sqrt{2^h}} \sum_{\mathbf{x}:\mathbf{b}(\mathbf{x})\mathbf{b}} (-1)^{\varphi(\mathbf{x})}\,,$$

where h is the number of Hadamard gates. Apparently, the terms in the sum have the same absolute value but may vary in sign.

Let N_0 be the number of positive terms in the sum and N_1 be the number of negative terms:

$$N_0 = |\,\{\ \mathbf{x} \mid \mathbf{b}(\mathbf{x}) = \mathbf{b} \quad \textbf{and} \quad \varphi(\mathbf{x}) = 0\ \}\,|\,, \tag{2}$$

$$N_1 = |\,\{\ \mathbf{x} \mid \mathbf{b}(\mathbf{x}) = \mathbf{b} \quad \textbf{and} \quad \varphi(\mathbf{x}) = 1\ \}\,|\ . \tag{3}$$

Hence, N_0 and N_1 count the number of solutions for the indicated systems of $n+1$ polynomials in h variables over $\mathbb{F}_2$. Then the matrix element may be written as

$$\langle \mathbf{b}|\, U_f\, |\mathbf{a}\rangle = \frac{1}{\sqrt{2^h}}\,(N_0 - N_1)\ . \tag{4}$$

In our *Mathematica* package there is function $polynomials[mat\_?MatrixQ]$ which constructs and outputs the set of polynomials over $\mathbb{F}_2$ which follows from the bit string of the form $\mathbf{b}(\mathbf{x}) = \mathbf{b}$ that relates the output bits with the path variables. Here we denoted by $\mathbf{b}(\mathbf{x})$ the last bit string $\mathbf{a_m}$ in the admissible path set which depends polynomially on the path variables $\mathbf{x} = \{x_1, \ldots, x_h\}$. Since in constructing the circuit matrix we have to count the number of solutions for polynomial systems (2) and (3) in $\mathbb{F}_2$, and input and output bit variables a_i, b_i also take values in $\mathbb{F}_2$, function $polynomials[mat\_?MatrixQ]$ outputs the polynomials in the form $\mathbf{b}(\mathbf{x}) + \mathbf{b} = 0$ and adds the phase polynomial (1) to the system.

For the circuit of Fig. 16 function $polynomials[mat\_?MatrixQ]$ outputs

$$\begin{aligned}
&\boldsymbol{x_3 \oplus x_2}\ \ \boldsymbol{x_4 \oplus b_1}\\
&\boldsymbol{x_2 \oplus b_2}\\
&\boldsymbol{x_4 \oplus b_3}\\
&\boldsymbol{a_1\ x_1 \oplus a_2\ x_2 \oplus x_1\ x_3 \oplus a_3\ x_4 \oplus x_1\ x_2\ x_4}
\end{aligned}$$

FIG. 19: Polynomial system for the circuit of Fig. 16.

The upper tree polynomial in Fig. 19 are those generated by the output bit string relating the input and output qubit values for admissible paths coded in terms of the variables $\{x_1, x_2, x_3, x_4\}$. The bottom polynomial is the phase polynomial defined by formula (1).

VI. SOLVING CIRCUIT POLYNOMIAL SYSTEM

To count the number of solutions in $\mathbb{F}_2$ for the polynomial systems (2) and (3) in order to apply formula (4) we rewrite them into the form

$$F_0 = \{\mathbf{b}(\mathbf{x}) + \mathbf{b}, \phi(\mathbf{x})\}\,, \tag{5}$$

$$F_1 = \{\mathbf{b}(\mathbf{x}) + \mathbf{b}, \phi(\mathbf{x}) + 1\}\,. \tag{6}$$

Here F_0 denotes the output of the function $polynomials[mat\_?MatrixQ]$ in our *Mathematica* package. It is convenient to transform the system into the canonical Gröbner basis form [14]. The Gröbner basis method invented in [15] is the most universal algorithmic tool for investigation and solving multivariate polynomial systems.

To compute N_0 and N_1 one can convert F_0 and F_1 into an appropriate triangular form [16] providing elimination of the path variables $x_1, ..., x_h$. One of such triangular forms is the pure lexicographical Gröbner basis that can be computed by means of *Mathematica* which has a built-in module for computing polynomial Gröbner bases.

For the system of polynomials F_0 in (5) shown in Fig. 19 the lexicographical Gröbner basis for the ordering on the variables $x_1 \succ x_2 \succ x_3 \succ x_4$ is given by

$$G_0 : \begin{cases} g_1 = a_1x_1 \oplus b_1x_1 \oplus a_2b_2 \oplus a_3b_3 \,, \\ g_2 = x_2 \oplus b_2 \,, \\ g_3 = x_3 \oplus b_1 \oplus b_2b_3 \,, \\ g_3 = x_4 \oplus b_3 \,, \end{cases} \tag{7}$$

The Gröbner basis (7) can easily be obtained with *Mathematica*. To do this it is sufficient to define the polynomial set (5) as *Mathematica* polynomial list by the command

```
F0 = {x3 + x2 * x4 + b1, x2 + b2, x4 + b3,
  a1 * x1 + a2 * x2 + x1 * x3 + a3 * x4 + x1 * x2 * x4}
```

FIG. 20: Input *Mathematica* form for F_0 in (5).

and invoke the *Mathematica* function $GroebnerBasis$ with the arguments specified as follows

```
GB0 = GroebnerBasis[F0, {x1, x2, x3, x4},
  MonomialOrder → Lexicographic, Modulus → 2]
```

FIG. 21: *Mathematica* command for computation of (7).

The last option in Fig. 21 says to the function that coefficient field is $\mathbb{F}_2$. As a result *Mathematica* will output the Gröbner basis (7)

```
{b3 + x4, b1 + b2 b3 + x3, b2 + x2, a2 b2 + a3 b3 + a1 x1 + b1 x1}
```

FIG. 22: The *Mathematica* output for the command of Fig. 21.

Similarly, for the system F_1 in (6) the Gröbner basis is

$$G_1 : \begin{cases} g_1 = a_1x_1 \oplus b_1x_1 \oplus a_2b_2 \oplus a_3b_3 \oplus 1 \,, \\ g_2 = x_2 \oplus b_2 \,, \\ g_3 = \ x_3 \oplus b_1 \oplus b_2b_3 \,, \\ g_3 = x_4 \oplus b_3 \,. \end{cases} \tag{8}$$

The lexicographical Gröbner bases (7) and (8) immediately yield the following conditions on the parameters:

$$G_0 : \quad a_1 \oplus b_1 = a_2b_2 \oplus a_3b_3 = 0 \,, \tag{9}$$

$$G_1 : \quad a_1 \oplus b_1 = 0 \,, \ a_2b_2 \oplus a_3b_3 = 1 \,. \tag{10}$$

It is immediately followed that if conditions (9) are satisfied then the polynomial system G_0 (resp. F_0) has two common roots in $\mathbb{F}_2$ and G_1 (resp. F_1) has no common roots, and, vise-versa, if conditions (10) are satisfied then G_0 has no roots and G_1 has two roots. In all other cases there is one root of G_0 and one root of G_1.

In that way, the 8×8 matrix for the circuit of 16 is easily determined by the formulae (4) where the numbers N_0 and N_1 are defined from systems (7) and (8). As a result, the matrix of Fig. 17 is obtained.

A $n-$qubit circuit with $h-$Hadamard gates the polynomial systems (5) and (6) contains $n+1$ polynomials in $h-$variables $\mathbf{x} = \{x_1, x_2, \ldots, x_h\}$ and $2n-$parameters $\mathbf{a} = \{a_1, a_2, \ldots, a_n\}$, $\mathbf{b} = \{b_1, b_2, \ldots, b_n\}$. These parameters determine the values of the input and output qubits, respectively. To apply formula (4) for computing the circuit matrix by the Gröbner bases method one needs to take into account that both variables and parameters are elements in the finite field $\mathbb{F}_2$. By this reason, generally, to increase efficiency of computation with the use of *Mathematica* function *GroebnerBasis* (Fig. 21) one should add to every of the systems (5) and (6) the binomials of the form

$$x_i^2 + x_1 \quad (i = 1, \ldots, h)\,. \tag{11}$$

and also take into account the restrictions

$$a_j^2 + a_j = 0, \quad b_j^2 + b_j = 0 \quad (j = 1, \ldots, n)\,.$$

Due to the last restrictions all the intermediate polynomials arising at the Gröbner basis construction by Buchberger's algorithm [14, 15] admit substantial simplification.

It turns out that if one uses another algorithmic approach to construction of Gröbner bases called involutive (see [17] and references therein), then this makes possible to avoid handling extra polynomials (11). In doing so, one can work with variables directly as with elements in $\mathbb{F}_2$. The first implementation in C++ of an involutive algorithm for computation of Gröbner basis over $\mathbb{F}_2$ with polynomial variables from $\mathbb{F}_2$ described in [18]. After proper optimization it is planned to incorporate that C++ code into the open source software GINV [19] which is a C++ module of Python and oriented to computation of Gröbner bases for polynomial ideals and modules by involutive methods.

It should be noted that solving systems of multivariate polynomial equations variables over $\mathbb{F}_2$ whose variables take values in $\mathbb{F}_2$ is also of interest in cryptanalysis. One of the attacks of a HFE (Hidden Fields Equations) public key cryptosystem is based on construction of a Gröbner basis for multivariate polynomial system over finite fields [20]. In particular, quadratic n polynomials in n with $n \geq 80$, variables over field $\mathbb{F}_2$ was recommended as a public key, and $n = 80$ was suggested as the first challenge. In paper [21] his challenge was broken by the Gröbner basis computation by means of the C program implementing author's algorithm [22]. This remarkable computational result gives a hope that construction of the circuit matrices by means of polynomial systems (5) and (6) may be computationally superior to the linear algebra based method (Sec. IV) for circuits with $n \gg h$ where n and h are, as above, the numbers of qubits and Hadamard gates.

Acknowledgements

The contribution of one of the authors (V.P.G.) was partially supported by grant 07-01-00660 from the Russian Foundation for Basic Research and by grant 5362.2006.2 from the Ministry of

Education and Science of the Russian Federation.

---

[1] V.P. Gerdt, R. Kragler, and A.N. Prokopenya, On Simulation of Quantum Circuits with *Mathematica*. Proceedings of the 4th International Workshop on Computer Algebra Systems in Teaching and Research, Siedlce, Poland, 2007, p. 135–144.

[2] M. Nielsen and I. Chuang, Quantum Computation and Quantum Information (Cambridge University Press, 2000).

[3] C.P. Williams and S.H. Clearwater, Explorations in Quantum Computing (Springer-Verlag, New York, 1997).

[4] P.W. Shor,SIAM J. Comp. **26**(5), 1484 (1997).

[5] L.K. Grover, Phys. Rev. Lett. **79**, 325 (1997).

[6] H. De Raedt and K. Michielsen, Computational Methods for Simulating Quantum Computers. In: Handbook of Theoretical and Computational Nanotechnology, Vol.3, M.Rieth and W.Schommers (Eds.), Forschungszentrum Karlsruhe (2006); arXiv:quant-ph/0406210.

[7] B. Julia-Diaz, J.M. Burdis, and F. Tabakin, QDENSITY – A Mathematica quantum computer simulation (Elsevier Science, 2005); http://www.pitt.edu/∼tabakin/QDENSITY.

[8] S. Wolfram, The Mathematica book (Wolfram Media/Cambridge University Press, 1999).

[9] C.M. Dawson et al., arXiv:quant-ph/0408129.

[10] V.P. Gerdt and V.M. Severyanov, An Algorithm for Constructing Polynomial Systems Whose Solution Space Characterizes Quantum Circuits. In: "Quantum Informatics 2005", Yu.I. Ozhigov (Ed.), SPIE Proceedings, Vol. 6264, 2006

[11] D. Aharonov, arXiv:quant-ph/0301040.

[12] C.M. Dawson and M.A. Nielsen,arXiv: quant-ph/0505030.

[13] A.B. Nagy, arXiv:quant-ph/0606077.

[14] B. Buchberger and F. Winkler, (eds.) Gröbner Bases and Applications (Cambridge University Press, 1998).

[15] B. Buchberger, An Algorithm for Finding a Basis for the Residue Class Ring of a Zero-Dimensional Polynomial Ideal. PhD Thesis, University of Innsbruck, 1965 (in German).

[16] D. Wang Elimination Methods (Springer-Verlag, Berlin, 1999).

[17] V.P. Gerdt, Involutive Algorithms for Computing Gröbner Bases. In: "Computational commutative and non-commutative algebraic geometry", IOS Press, Amsterdam, 2005, pp. 199–225; arXiv:math.AC/0501111

[18] V.P. Gerdt and M.V. Zinin, On computation of Gröbner bases over $\mathbb{F}_2$. Submitted to the International Workshop on Computer Algebra and Differential Equations (Turku, Finnland, February 20-23, 2007).

[19] `http://invo.jinr.ru`

[20] J. Patarin, Hidden fields equations (HFE) and isomorphisms of polynomials (IP): Two new families of asymmetric algorithms. In: EUROCRYPT'96, volume 1070 of LNCS 1070, (Springer-Verlag, 1996) pp. 33-48.

[21] J.C. Faugère and A. Joux, Algebraic cryptanalysis of Hidden Field Equations (HFE) Using Gröbner Bases. LNCS 2729, (Springer-Verlag, 2003) pp. 44–60.

[22] J.C. Faugère A new efficient algorithm for computing Gröbner bases without reduction to zero (F_5). In: Proceedings of Issac'2002, (ACM Press, New York, 2002) pp. 75–83.

Python: The Pocket Knife of Scientific Computing

M. Braun*

Department of Physics, University of South Africa,
P O Box 392, Pretoria 0003, South Africa

In this contribution a short introduction to the main features of the object oriented scripting language Python will be given and the libraries, tools, and modules of interest for computational physics will be discussed. Using well known subroutines written in Fortran it will be shown, how to access a Fortran77 code from Python using the versatile automatic connection tool f2py. The benefits of having a mixed application where the initialization, outer loops, flow control, and file handling are coded in Python and only the serious number crunching is delegated to Fortran, are outlined.

I. INTRODUCTION

The modern object oriented scripting language Python [1, 2] has recently attracted a lot of attention by computational scientists from many disciplines [3], especially from computational physics. The traditional work horse for the latter discipline is the Fortran77 language which is efficient for numerical tasks and an abundant treasure of well tested and reliable libraries exists. However, it lacks many modern features, such as efficient I/O and object orientation, to only name two of them. With Fortran90 and Fortran95 some features such as modular programming and operator overloading were added, which made them more suitable for complex programming tasks. These languages still do not support object orientated programming. The very popular compiled language C++ is object orientated but, in my view, rather tedious to program. Since it would be wasteful to throw away the well tested and efficient libraries that have been programmed in Fortran, C, and C++, it is imperative that these libraries can be accessed from scripting languages, for which a number of tools have been developed for this purpose.

With the ever increasing speed of CPUs, scripting languages such as Matlab/Octave, Perl, Python, and Ruby have emerged as tools for many tasks, including scientific computing. Their advantages include: i) No declaration of variables is needed, ii) increased speed of development, and iii) many advanced language features. Concerning the Python language, we mention that it was originally developed as glue language for the distributed Operating System Amoeba by Guido van Rossum at the Dutch Centrum voor Wiskunde en Informatica (CWI) and named after "The Monty Python Show". Its suitability for tasks unconnected to the original purpose became soon evident and thus it was released as open source in 1991. The design was inspired by the language ABC that van Rossum had been involved with in the 1980s. Python is by now the second most popular scripting language worldwide after Perl. It is undergoing constant development by a large team of volunteers and reached version 2.5. It is estimated that, nowadays, Python is used by ∼500 000 programmers. Companies using Python include the search engine Google, the peer-to-peer file sharing protocol Bittorrent, the web framework Zope, and the video sharing platform youtube.com.

There are a lot of reasons for choosing Python as scripting language. To start with, it has an efficient modular system, it has a clean syntax, it is easy to extend, and the implementation

*Electronic address: braunm@science.unisa.ac.za

of objects is easy. Furthermore, Python comes with Libraries/Modules for close to everything and it can be used with Unix, Linux, Win32, MacOSX, Symbian (Cellphones!), and many other OSs while implementations exist in C, Java, and NET as well. At a personal level, I have also experienced that a code can be developed more quickly than in Fortran so that many tasks can be expressed in a convenient manner, which is easy to remember and understand when looked at later. Finally, I have found that for extensions and use of libraries, it is better suited to the purposes of scientific computing than is the case with some of the competing scripting languages.

In Sec. II we present an overview of the Python language, in Sec. III we demonstrate its use in few examples, while in Sec. IV we draw our conclusions.

II. LANGUAGE OVERVIEW

The most striking features of Python for somebody who programmed in C/C++/Java are the importance of white space and the definition of blocks via indentation, which enforce readability of loops and conditional expressions. Admittedly, these features take some getting used to. The object model is quite similar to the one of Java, and (close to) everything is an object. Just as in Java there are no pointers, but there is really no need for them.

The primary building blocks for data structures are lists, i.e. mutable arrays of arbitrary Python objects, tuples. i.e. immutable lists, and associative arrays, i.e. arrays with arbitrary immutable objects as indices. Python has built-in types for integer, double precision, complex and (arbitrarily) long integer. The interactive use of Python on the command line is convenient for testing and development and provides easy access to built in documentation via doc-strings that are embedded in the source code.

There are a great variety of libraries and extension available for close to every computer related task [4], a selection of which is summarized below:

1. Operating System services: OS system etc.
2. GUI interfaces: Tkinter (build on Tcl/TK). included, bindings to Qt, Gnome, and many other toolkits exist as well.
3. Modules for standard networking protocols.
4. NumPy (Numerical Python) which includes also f2py.
5. Gnuplot: Pipe based interface to Gnuplot.
6. Scientific Python: Nomen est Omen.
7. Ipython: Improved Python shell.

Concerning the tools of special interest to computational physicists we mention here the most essential extension for computational tasks, namely *NumPy*, which provides multidimensional arrays, ufuncs, overloaded arithmetic operators, matlab-like syntax, and linear algebra operations via *Lapack*. In addition, the included tool *f2py* creates shared libraries to access Fortran77/Fortran90 functions and subroutines. Thus Python+NumPy+Gnuplot can (mostly) replace Matlab/Octave. Many additional extensions are provided by *Scientific Python* such as automatic derivatives, fitting, handling of vectors, and an interface to MPI.

III. EXAMPLES

A. Using f2py

The tool *f2py* which is part of *NumPy*, automatically creates shared libraries for Fortran subroutines as demonstrated in the following for the subroutine `GAULEG.F` from *Numerical Recipes* [5]. To indicate which arguments are input and which are output the lines starting with cf2py have been inserted in the source code as shown below:

```
      SUBROUTINE GAULEG(X1,X2,X,W,N)
%     ============================
cf2py intent(in) x1,x2
cf2py intent(out) x,w
      .
      .
      .

      RETURN
      END
```

The shared library and Python module is then created via

```
f2py -m gauleg -c gauleg_f2py.f
```

and can be loaded into a interactive python session and the points and weights of 8th order accessed as follows:

```
Python 2.4.3 (#2, Sep 18 2006, 21:07:35)
[GCC 4.1.1 20060724 (prerelease) (4.1.1-3mdk)] on linux2
Type "help", "copyright", "credits" or "license" for more information.
>>> from gauleg import gauleg
>>> x,w=gauleg(0.0,1.0,8)
>>> print x
[ 0.01985507  0.10166676  0.2372338   0.40828268  0.59171732  0.7627662
  0.89833324  0.98014493]
>>> print w
[ 0.05061427  0.11119052  0.15685332  0.18134189  0.18134189  0.15685332
  0.11119052  0.05061427]
>>>
```

B. Cubic spline interpolation subroutines and serialization of a spline object

As above the subroutines `SPLINE.F` and `SPLINT.F` are from Numerical Recipes and they can be used for cubic spline interpolation [5].

```
      SUBROUTINE SPLINE(x,y,n,yp1,ypn,y2)
C     ==================================
      INTEGER n,NMAX
      DOUBLE PRECISION yp1,ypn,x(n),y(n),y2(n)
cf2py intent(out) y2
cf2py intent(in)  yp1,yp2,x,y
```

```
      .
      .
      .
      END

      SUBROUTINE SPLINT(xa,ya,y2a,n,x,y)
c     ==================================
cf2py intent(in) xa,ya,y2a,n,x
cf2py intent(out) y
      .
      .
      .
      END
```

As in the previous example the shared library is obtained via

```
f2py -m cubic_spline -c cubic_splines.f
```

and the cf2py lines contain the information as to the intent of the variables.

The following python code encapsulates cubic spline interpolation in a convenient class and also provides for serialization, i.e saving to disk.

```
from cubic_spline import *
from numpy import *
import pickle
import sys
class spline_int:
    def __init__(self,xi,yi):
        self.xi,self.yi=xi,yi
        self.n=len(xi)
        self.y2=spline(self.xi,self.yi,1e40,1e40)
    def __call__(self,x):
        if isscalar(x):
            return splint(self.xi,self.yi,self.y2,x)
        else:
            tmp=[]
            for xx in x:
                tmp.append(splint(self.xi,self.yi,self.y2,xx))
            return array(tmp)
    def pickle(self,fname):
        wf=open(fname,"w")
        pick=pickle.Pickler(wf)
        pick.dump(self)
        wf.close()
```

This class can be used as follows

```
>>> from numpy import *
>>> x=arange(0.0,2*pi+1e-6,2*pi/512)
>>> y=sin(x)
>>> from spline_int import spline_int
>>> s=spline_int(x,y)
>>> s.pickle("sin.dat")
```

to create a cubic spline interpolating $\sin x$ on $[0, 2\pi]$ and to dump the spline object to disk in the file "sin.dat". Subsequently the following script can be used to read a spline from disk and plot it using Gnuplot:

```
#!/usr/bin/env python
# script to read a pickled spline and plot it
import Gnuplot
from numpy import *
import pickle
import sys,time
sfile = sys.argv[1]
fp=open(sfile,"r")
s=pickle.Unpickler(fp).load()
xmin=s.xi[0]
xmax=s.xi[-1]
h=xmax-xmin
xp=xmin+arange(0.0,1.0001,1./512)*h
yp=s(xp)
ymin=min(yp)
ymax=max(yp)
zxy=zip(xp,yp)
hy=ymax-ymin
g=Gnuplot.Gnuplot()
g("set style data lines")
g("set xrange[%f : %f]" % (xmin-0.1*h,xmax+0.1*h))
g("set yrange[%f : %f]" % (ymin-0.1*hy,ymax+0.1*hy))
g("set xzeroaxis linetype 3")
g("set yzeroaxis linetype 3")
g.plot(zxy)
raw_input("")
```

via

```
spline_plot.py sin.dat
```

on the command line.

C. Scripting Java using jython

The jython-project [6] has created a Python interpreter written in pure Java, which allows for the efficient scripting of Java. All Java classes can be dynamically loaded. The following example shows how to draw a simple graph using jython+Java

```
from java import awt
from math import *
from jarray import array
class Graph(awt.Canvas):
def __init__(self):
self.function = None

def paint(self, g):
if self.function is None:
```

```
return self.error(g)

sz = self.size
xs = range(0, sz.width, 2)

xscale = 4*pi/sz.width
xoffset = -2*pi

yscale = -sz.height/2.
yoffset = sz.height/2.

ys = [ ]
for x in xs:
x = xscale*x + xoffset
y = int(yscale*self.function(x)+yoffset)
ys.append(y)
g.drawPolyline(array(xs, 'i'), array(ys, 'i'), len(xs))

def error(self, g):
message = "Invalid Expression"
g.font = awt.Font('Serif', awt.Font.BOLD, 20)
width = g.fontMetrics.stringWidth(message)

x = (self.size.width-width)/2
y = (self.size.height+g.fontMetrics.height)/2
g.drawString("Invalid Expression", x, y)

def setExpression(self, e):
"@sig public void setExpression(java.lang.String e)"
try:
self.function = eval('lambda x: '+e)
except:
self.function = None
self.repaint()


if __name__ == '__main__':
def enter(e):
graph.setExpression(expression.text)
expression.caretPosition=0
expression.selectAll()

p = awt.Panel(layout=awt.BorderLayout())
graph = Graph()
p.add(graph, 'Center')

expression = awt.TextField(text='(sin(3*x)+cos(x))/2', actionPerformed=enter)
p.add(expression, 'South')

import pawt
pawt.test(p, size=(300,300))

enter(None)
```

Saving this code as *Graph.py* it can be run from the command line via

```
jython Graph.py
```

and creates the window shown below:

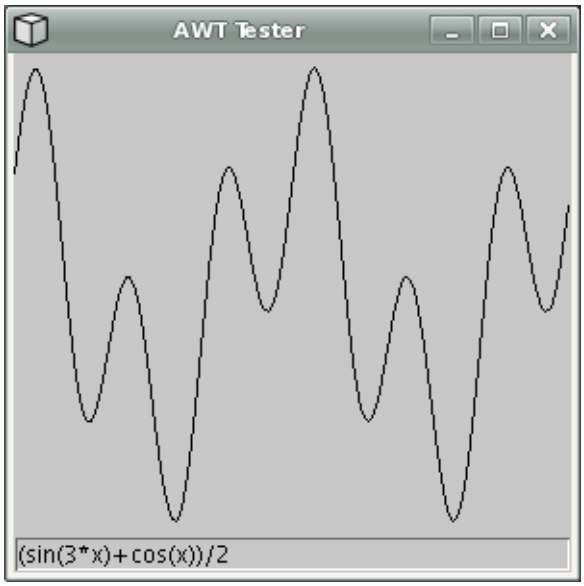

D. Graphical User Interface for finite element method

A graphical user interface was developed that uses a finite element engine written in Python and Fortran77 connected via f2py to solve the one dimensional eigenvalue equation

$$\left[-\frac{1}{w(x)}\frac{\partial}{\partial x}w(x)\frac{\partial}{\partial x}+v(x)\right]\psi(x)=\lambda\psi(x)$$

with either open or zero boundary conditions at $x=a$ and $x=b$

A screen-shot of the GUI is given below, where the five lowest eigenvalues for the harmonic oscillator potential $V(x)=x^2$ on $[-5,5]$ have been calculated and the wave function of the third excited state is plotted:

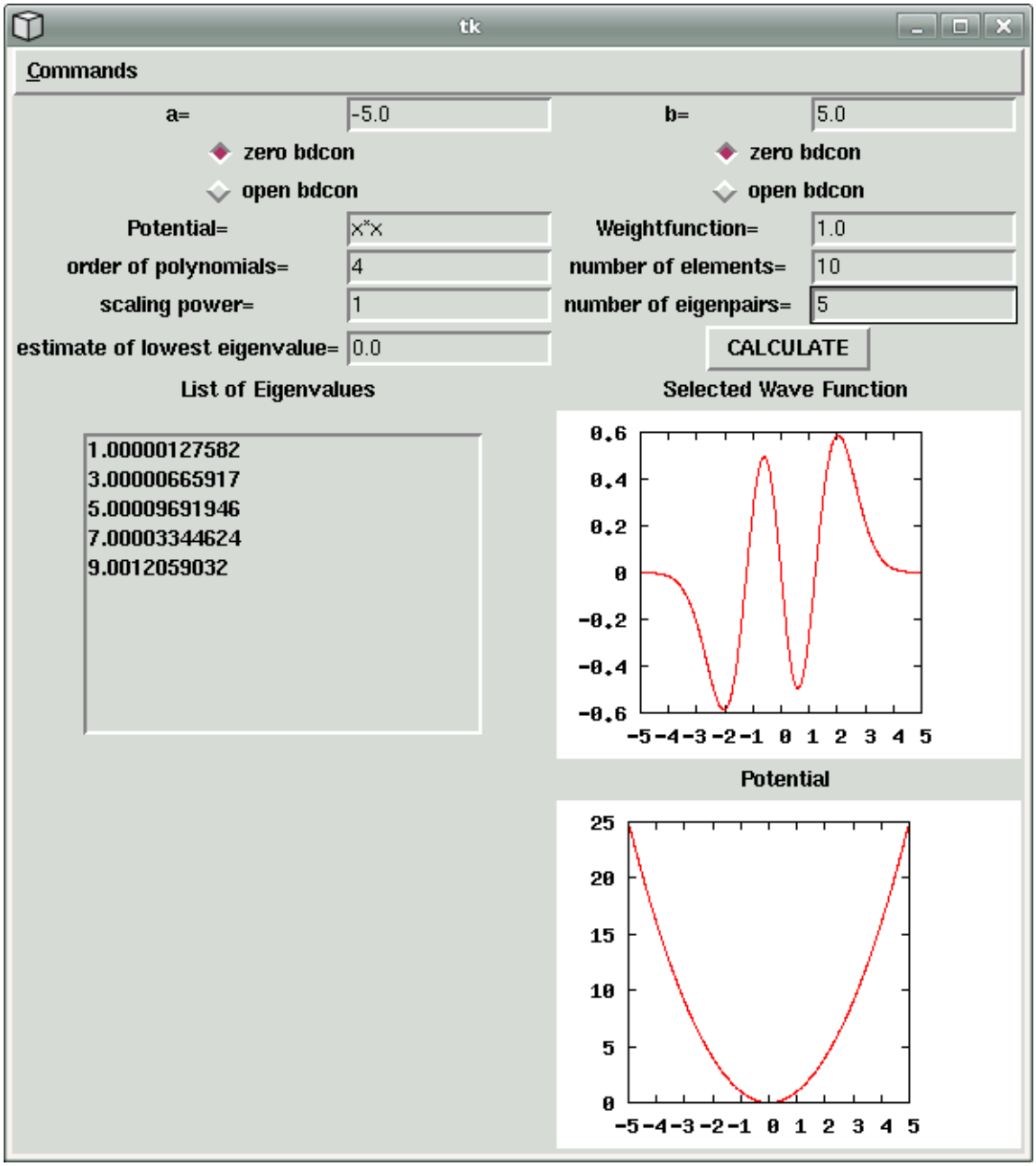

The Python code for this user interface consists of less then 200 lines of code. Thus this demonstrates how user interfaces can be constructed quite easily.

IV. CONCLUSIONS

It has been demonstrated why Python deserves to be called the "pocket knife of Computational Physics". Some examples of a mixed/hybrid approach to Computational Physics tasks were given for this purpose. The approach uses the most convenient and efficient tools for different tasks such as the control and administration of the calculation for simple numerical tasks while the heavy number crunching is done in Fortran to achieve maximum performance. It is also important to note that data structures and file handling via Python result in a modern and object oriented code, while still using the high performance libraries written in Fortran, C,

C++, etc.

---

[1] *http://www.python.org*
[2] A. Martelli, Python in a nutshell (O'Reilly and Associates, Sebastopol, USA, 2003).
[3] H.P. Langtangen, Python scripting for computational science (Springer Verlag, Berlin, 2004).
[4] D.M. Beazley, Python: Essential Reference, Third Edition (Sams Publishing, Indianapolis, USA, 2006).
[5] H.W. Press, S.A. Teukolsky, W.T. Vetterling, and B.P. Flannery, Numerical Recipes in FORTRAN, 2nd ed. (Cambridge Univ. Press, Cambridge, 1992).
[6] *http://www.jython.org*

Additive Numerical Method for Modeling Nonlinear Propagation of Two-component Waves

I.G. Zakharova,* I.G. Chernykh, and A.P. Sukhorukov

Faculty of Physics, Lomonosov Moscow State University, Moscow, Russia

We constructed an additive numerical method for systems of nonlinear evolutionary equations containing first derivatives in a divergent form. The main idea of our approach is to integrate differential equations and then use a well-known difference scheme which possesses the property of having fixed sign. The properties of conservation of movement integrals and convergence to the solution of the initial differential problem are proved. Next we studied a coupled shock waves' evolution in nonlinear viscous medium and described it by the system of two coupled Burgers equations. We applied our scheme to this system and revealed some new effects. It was also found that our scheme prevents the smearing of the shock waves.

I. INTRODUCTION

Multidimensional second-order parabolic equations containing divergent first-order differential forms are rather common in mathematical models used for numerical modeling of a wide range of nonlinear problems emerging in acoustics, optics, solid state physics, etc. As a rule, much attention is given to preservation of the most important characteristics of the studied phenomena in the process of computation. This requires a development of numerical methods which could combine the whole range of specific features, such as stability, conservativeness, fixed sign property, etc.

When constructing difference schemes for systems of nonlinear coupled evolutionary equations one often meets serious difficulties in attempting to bring together all these properties in a single scheme. Thus, for instance, the property of fixed sign is in conflict with the conservativeness. This may result in a loss of computation accuracy and even faulty solutions. A technique which may cope with most of these difficulties in designing accurate and effective numerical schemes has been introduced in [1]. This approach makes it possible to develop additive difference schemes which hold the property of having fixed sign for non-negative solutions and difference analogs of conservation laws as well.

In this paper we demonstrate how to apply our method to the mathematical modeling of dynamics of two-component coupled waves in nonlinear viscous medium. Waves' propagation in quadratically nonlinear viscous non-dispersive medium is described by Burgers equations for slowly varying profiles. In many cases one should consider a wave in air or liquid. Burgers and Korteweg de Vries-Burgers equations are actively engaged in fluid mechanics. These equations are known to posses exact solutions which can be found by rather sophisticated methods or quite easily, for instance, with the help of tanh method [2]. In solid state and plasma physics as well as in nonlinear optics and acoustics one usually deals with several waves of different polarization. Since waves interact with each other through a quadratic nonlinearity, the models consisting of coupled equations are dominant. A system of coupled Burgers equation is used in [3] to study longitudinal density variations of fluid particles. Properties of coupled viscous Burgers equations are considered also in [4]. The author of [5] used a classification of the symmetric integrable coupled equations of Burgers type. In a previous paper [6], we investigated the dynamics of

*Electronic address: zaharova@phys.msu.ru

two-component coupled waves in a nonlinear viscous medium. We found that the stationary solutions corresponding to trajectories on a phase plane between singular points and specified the existence domains for solutions of kink type. Furthermore, we revealed the shock wave profile dependence on a type of singular point and demonstrated that properties of shock wave fronts formed from initial harmonic signals are sufficiently well described by the derived stationary solutions.

This paper is organized as follows. To begin with we give, in Sec. II, a brief description of a general approach to the construction of conservative difference schemes for systems of nonlinear evolutionary equations containing first derivatives in a divergent form. Then, in Sec. III, we show how to apply our method to the system of quadratically nonlinear Burgers equations. In Sec. IV we present results for a two-component dissipative solutions, shock waves, and short video-pulses as well. Finally our conclusions are summarized in Sec. V.

II. BRIEF DESCRIPTION OF THE ADDITIVE DIFFERENCE METHOD FOR PARABOLIC EQUATIONS

We consider the following p-Dimensional (p-D) parabolic equation

$$\frac{\partial u}{\partial z} = \frac{\partial^2 u}{\partial x_\alpha^2} + \frac{\partial}{\partial x_\alpha}\left(r^{(\alpha)}(x,z,u)u\right) + f(x,u,z) \tag{1}$$

with initial

$$u(x,0) = u_0(x) \tag{2}$$

and boundary conditions

$$\frac{\partial u}{\partial x_\alpha} + r^{(\alpha)} u_{|x_\alpha=0,1} = 0 \tag{3}$$

Here $x = (x_1, \ldots, x_p),\ 0 < x_\alpha < 1$.

For clarity, let us confine ourselves to the 1-D case by assuming $x = x_1$ and thus omitting the lower index of x. Integrating (1) with respect to x and taking into account (3) we find the following conservation law

$$\frac{\mathrm{d}}{\mathrm{d}z}\int_x u(x,z)\ \mathrm{d}x = \int_x f(x,z,u)\,\mathrm{d}x \tag{4}$$

For real physical problems the right-hand side of (4) is, usually, equal to zero. Then this equality takes the form of the conservation law

$$\int_x u(x,z)\,\mathrm{d}x = \int_x u_0(x)\,\mathrm{d}x\,, \qquad z \in (0, Z]$$

Moreover, if $u_0(x) \geq 0$ and $f(x,z,u) \geq 0$ then the solution of (1)–(3) is non-negative.

To solve (1)–(3) numerically we proceed as follows. Let

$$U(x,z) = \int_0^x u(\zeta,z)\,\mathrm{d}\zeta\,. \tag{5}$$

Then the problem (1)–(3) is equivalent to

$$\frac{\partial U(x,z)}{\partial z} = \frac{\partial^2 U(x,z)}{\partial x^2} + r(x,z)\frac{\partial U(x,z)}{\partial x} + \int_0^x f(\zeta,z)\,\mathrm{d}\zeta \tag{6}$$

$$U|_{x=0} = 0\,, \qquad \left.\frac{\partial U}{\partial z}\right|_{x=1} = \int_0^1 f(\zeta, z)\,\mathrm{d}\zeta, \qquad u = \frac{\partial U}{\partial x} \tag{7}$$

To approximate (6)–(7) and, hence, also (1)–(3) let us construct the grids

$$\begin{gathered}\omega_z = \{z = z_n = n\tau,\ n = 0, \ldots, N,\ \tau = Z/N\};\\ \omega_x = \{x = x_i = ih,\ i = 0, \ldots, N_x,\ h = 1/N_x\};\\ \omega'_x = \{x' = x'_i = (i - 0.5)h,\ i = 1, \ldots, N_x,\ h = 1/N_x\}\end{gathered}$$

and the grid functions for y and Y. These functions are, respectively, the analogs of u and U on the grids $\omega_z \times \omega'_x$ and $\omega_z \times \omega_x$.

To calculate the values of y at z_n-layer for $n = 0, \ldots, N-1$ we apply the following procedure. It starts with the initial values $y_i^0 = u_0(x'_i) \geq 0$ and passes on to the next z-layer in three stages. At first the values

$$Y_i^n = \sum_{k=1}^{i} y_k^n h,\ Y_0^n = 0 \tag{8}$$

are computed. Then the function Y_i^{n+1} is obtained from the following difference scheme

$$(Y_i^{n+1} - Y_i^n)/\tau = \Lambda Y_i^{n+1} + F_i^{n+1}, \tag{9}$$

with $Y_0^{n+1} = 0$ and $(Y_{N_x}^{n+1} - Y_{N_x}^n)/\tau = F_{N_x}^{n+1}$ (see [7] for details). Finally, at the third stage we determine the grid analog of the solution to the problem (1)–(3) at the z_{n+1}-layer by means of discrete differentiation $y_i^{n+1} = Y_{\bar{x},i}^{n+1}$.

The grid operator Λ and the grid function F_i^n are defined as follows:

$$\Lambda Y_i \;=\; \kappa_i Y_{\bar{x}x,i} + r_i^+ Y_{x,i} + r_i^- Y_{\bar{x},i}\,, \tag{10}$$

$$F_i^n \;=\; F(x_i, z_n, y_i^n) = \sum_{k=1}^{i} f_k^n h\,, \tag{11}$$

where

$$r_i^{\pm} = \frac{\overline{r}_i \pm |\overline{r}_i|}{2}\,, \qquad \overline{r}_i = \frac{r(x_i, z_n, y_i^n) + r(x_{i+1}, z_n, , y_{i+1}^n)}{2}\,, \qquad \kappa_i = \frac{1}{1 + 0.5|\overline{r}_i|h}\,.$$

The solution of the above non-linear difference scheme can be obtained iteratively,

$$\frac{{}^{s+1}Y_i^{n+1} - Y_i^n}{\tau} = \Lambda\, {}^{s+1}Y_i^{n+1} + {}^{s}F_i^{n+1}\,, \qquad {}^{s+1}Y_0^{n+1} = 0, \tag{12}$$

$$\frac{{}^{s+1}Y_{N_x}^{n+1} - Y_{N_x}^n}{\tau} = {}^{s}F_{N_x}^{n+1}\,, \qquad {}^{0}Y_i^{n+1} = Y_i^n \tag{13}$$

We recall here the following relevant theorems:

Theorem 1 (Iteration convergence, existence, and uniqueness:) [1]
Let $|f(x, z, u)| < M(1 + |u|^m)$, m is integer, $M = const$. Then the iteration process converges to a unique solution of the numerical problem on the current layer at the rate of a geometric progression.

Sketch of the proof: We show that iterations are uniformly bounded above in the grid norm L_2, i.e. assuming $\| g \|^2_{L_2} = \| g \|^2 = \sum\limits_{k=1}^{N} |g_k|^2 h$. Then we obtain the inequality $\| \overset{s+1}{Y}{}^{n+1} - \overset{s}{Y}{}^{n+1} \| \leq K\tau \, \| \overset{s}{Y}{}^{n+1} - \overset{s-1}{Y}{}^{n+1} \|$, $K = const$. When $K\tau < 1$, i.e. τ is sufficiently small, this inequality means that the transform of $\overset{s}{Y}{}^{n+1}$ into $\overset{s+1}{Y}{}^{n}$ is a contraction operator. Thus, the theorem statement follows from the contraction principle.

Lemma 1 (Monotonicity) [1]
Provided that $u_0(x) \geq 0$ and $f(x, z, u) \geq 0$, the solution of the difference scheme is non-negative:

$$y_n^i \geq 0, \qquad n = 0, \ldots, N_T \ .$$

Proof: By induction on n. The basis of induction is trivial. Assume $y_i^n \geq 0$. Then, from (8), the function Y_i^n is non-negative and nondecreasing in x direction. Using non-negativity of $f(x, z, u)$ and the scheme construction it is easy to show that $Y_i^{n+1} \geq 0$ (see [7] for details). Hence, in view of $Y_0^{n+1} = 0$, we have $Y_1^{n+1} \geq Y_0^{n+1}$. Thus, to prove that $y_i^{n+1} \geq 0$ it suffices to show that Y_i^{n+1} has no local maxima. Assume for contradiction that $x_{i_{rmmax}}$ is a local maximum point for Y_i^{n+1}. Then three possible alternative cases of Y_i^{n+1} behavior should be considered in turn.

(i) $Y_{i_{\max}}^{n+1} \leq Y_{i_{\max}}^{n}$. According to the boundary condition $Y_{N_x}^{n+1} \geq Y_{N_x}^{n}$ the function Y_i^{n+1} has $x_{i_{\min}}$ as its local minimum point, where $i_{\min} > i_{\max}$. Since, by (9), we get $Y_{i_{\min}}^{n+1} \geq Y_{i_{\min}}^{n}$, contrary to the assumption for the point $x_{i_{\max}}$.

(ii) $Y_{i_{\max}}^{n+1} \geq Y_{i_{\max}}^{n}$ and Y_i^{n+1} decreases to for $i > i_{\max}$. Comparing the right boundary condition with (9) at the point $x_{i_{\max}}$, we obtain $Y_{N_x}^{n+1} \geq Y_{i_{\max}}^{n+1}$. This inequality contradicts the assumption of the decrease of Y_i^{n+1}.

(iii) $Y_{i_{\max}}^{n+1} \geq Y_{i_{\max}}^{n}$ and Y_i^{n+1} has a local minimum for $i > i_{\max}$. Using (9), monotonicity of Y_i^n, F_i^{n+1}, and taking into account $\Lambda Y_{i_{\min}}^{n+1} \geq 0$, $\Lambda Y_{i_{\max}}^{n+1} \leq 0$ we have the obvious contradiction $Y_{i_{\min}}^{n+1} \geq Y_{i_{\max}}^{n+1}$.

Thus, Y_i^{n+1} is nondecreasing function and, hence, $y_i^{n+1} = Y_{\bar{x},i}^{n+1} \geq 0$.

Theorem 2 (Conservativeness)
Difference analog of the conservative law holds:

$$\sum_{k=1}^{N_x} y_k^{n+1} h = \sum_{k=1}^{N_x} y_k^n h + \tau \sum_{k=1}^{N_x} f_k^{n+1} h \, .$$

This equality follows from the right boundary condition.

Theorem 3 (Convergence) [1]
The solution of the difference problem converges to the continuous solution in the grid norm L_2 at the rate $O(\tau + h^2)$.

Proof. We introduce the discrepancies $z_i^n = y_i^n - u_i^n$ and $Z_i^n = Y_i^n - \overline{U}_i^n$, where u_i^n is the projection of the solution to (1)–(3) on the grid $\omega_z \times \omega_x'$, and $\overline{U}_i^n = \sum\limits_{k=1}^{i} u_k^n h$. One can easily

derive from (8)–(11) the system of equations for Z_i^n and z_i^n. By using Conservativeness Theorem we estimate z_i^n in the grid norm L_2

$$\| z^n \| \leq M_1(\tau + h^2),\ M_1 = const.$$

This proves the theorem statement.

The method introduced above can be easily extended to the case of p-D equations [1]. Instead of the problem (1)–(3) we solve the sequence of the problems

$$\frac{1}{p}\frac{\partial \tilde{u}}{\partial z} = \frac{\partial^2 \tilde{u}}{\partial x_\alpha^2} + \frac{\partial}{\partial x_\alpha}\left(r^{(\alpha)}(x,z,\tilde{u})\tilde{u}\right) + \frac{1}{p}f(x,\tilde{u},z), \qquad \alpha = 1,\ldots,p\,, \quad z \in (z_{n+\alpha-1}, z_{n+\alpha}].$$

For each subproblem we introduce the integral function $U^{(\alpha)}(x,z)$ and construct a scheme of the form (8)–(11).

III. DIFFERENCE SCHEME FOR THE SYSTEM OF TWO COUPLED BURGERS EQUATIONS

We study a dynamics of two-component coupled waves in nonlinear viscous medium on the base of two Burgers equations.

$$\frac{\partial u(x,z)}{\partial z} = \frac{\partial(\alpha u^2(x,z) + (\beta/2)v^2(x,z))}{\partial x} + \Gamma_1 \frac{\partial^2 u(x,z)}{\partial x^2}\,, \tag{14}$$

$$\frac{\partial v(x,z)}{\partial z} + \mu\frac{\partial v(x,z)}{\partial x} = \beta\frac{\partial(u(x,z)v(x,z))}{\partial x} + \Gamma_2 \frac{\partial^2 u(x,z)}{\partial x^2}\,. \tag{15}$$

As can be seen from this system, one of the wave components has a quadratic nonlinearity whereas the other possesses a nonlinearity of parametric type. The meaning of variables and parameters is as follows: z is the propagation coordinate, $x = \omega(t - z/c_i)$ stands for the time in a moving coordinate system, c_1 is the velocity of the component u, $\mu = 1/c_2 - 1/c_1$ is the mismatch of reverse velocity values, α and β are nonlinear coefficients, and $\Gamma_{1,2}$ characterize the viscosity. The following initial signals are launched in the input of nonlinear medium

$$u(x, z=0) = U_0(x), \quad v(x, z=0) = V_0(x) \tag{16}$$

while the boundary conditions are given by

$$u(x=0,z) = u(x=L_x,z) = v(x=0,z) = v(x=L_x,z) = 0 \tag{17}$$

To apply the scheme we introduce the integral functions

$$U(x,z) = \int_0^x u(\zeta,z)\,\mathrm{d}\zeta\ , \qquad V(x,z) = \int_0^x v(\zeta,z)\,\mathrm{d}\zeta\ . \tag{18}$$

Then the system (14)–(15) is transformed to

$$\frac{\partial U(x,z)}{\partial z} = \alpha u\frac{\partial U(x,z)}{\partial x} + (\beta/2)v\frac{\partial V(x,z)}{\partial x} + \Gamma_1\frac{\partial^2 U(x,z)}{\partial x^2}, \tag{19}$$

$$\frac{\partial V(x,z)}{\partial z} + \mu\frac{\partial V(x,z)}{\partial x} = \beta u\frac{\partial(V(x,z))}{\partial x} + \Gamma_2\frac{\partial^2 V(x,z)}{\partial x^2}\,, \tag{20}$$

the new boundary conditions being

$$U(x,z)|_{x=0} = V(x,z)|_{x=0} = 0\,, \qquad \left.\frac{\partial U(x,z)}{\partial z}\right|_{x=0} = \left.\frac{\partial V(x,z)}{\partial z}\right|_{x=0} = 0\,.$$

To solve this system numerically, we adapt the difference scheme described in the previous section:

$$U_i^n = \sum_{k=1}^{n} u_k^n h\,, \qquad V_i^n = \sum_{k=1}^{n} v_k^n h\,, \tag{21}$$

$$\frac{U_i^{n+1} - U_i^n}{\tau} = \Lambda_u U_i^{n+1}, \qquad \frac{V_i^{n+1} - V_i^n}{\tau} = \Lambda_v V_i^{n+1}\,, \tag{22}$$

with

$$U_0^{n+1} = 0, \quad V_0^{n+1} = 0, \quad \frac{U_{N_x}^{n+1} - U_{N_x}^n}{\tau} = 0\,, \qquad \text{and} \qquad \frac{V_{N_x}^{n+1} - V_{N_x}^n}{\tau} = 0\,,$$

$$u_i^{n+1} = \frac{U_i^{n+1} - U_{i-1}^{n+1}}{h}, \qquad v_i^{n+1} = \frac{V_i^{n+1} - V_{i-1}^{n+1}}{h} \tag{23}$$

The grid operators in (22) are defined by

$$\Lambda_u U_i^{n+1} = \kappa_{u_i}\Gamma_1 U_{\bar{x}x,i}^{n+1} + \alpha\left[(u_i^n)^+ U_{x,i}^{n+1} + (u_i^n)^- U_{\bar{x},i}^{n+1}\right] + \frac{\beta}{2}\left[(v_i^n)^+ V_{x,i}^{n+1} + (v_i^n)^- V_{\bar{x},i}^{n+1}\right] \tag{24}$$

$$\Lambda_v V_i^{n+1} = \kappa_{v_i}\Gamma_2 V_{\bar{x}x,i}^{n+1} + (\beta(u_i^n)^+ - \mu) V_{x,i}^{n+1} + (\beta(u_i^n)^- - \mu) V_{\bar{x},i}^{n+1} \tag{25}$$

IV. MODELING TWO-COMPONENT DISSIPATIVE SOLUTIONS, SHOCK WAVES, AND PULSE DIFFERENTIATION

Let us first compare our results based on the difference scheme (21)–(23) with the analytical estimations presented in [6]. In order to provide an accurate comparison, we have chosen $\Gamma_1 = \Gamma_2 = \Gamma$, $\mu = 0$, and the initial harmonic signals

$$u(x,0) = -u_0 \sin(2\pi x), \qquad v(x,0) = -v_0 \sin(2\pi x)\,. \tag{26}$$

It is known that propagation of the signals of the form (26) in a nonlinear viscous medium results in two identical shock waves which become smooth while they propagate under dissipative effects. The shock wave front has the maximum slope at the moment of the dynamic balance between dissipative and nonlinear effects. This moment corresponds to the stationary profiles which are the solutions of the stationary Eqs. (14)– (15) (see [6]). Fig. 1 illustrates the results of our computations (a) and the analytical prediction (b). One can see that they are in a good agreement.

We also studied a spectrum of the signal and observed excitation of high harmonics which rise while the steady-state profile is being generated by the shock front. This means that nonlinear effects dominate by dissipative ones. After the process of shock formation is completed, the dissipative spreading becomes more essential than non-linear influence, the high harmonics decay, and finally the signal takes the initial sinusoidal shape. To model formation and interaction of two shock fronts in non-dispersive medium we use the system (14)– (15) with different viscous coefficients and $\mu = 0$. This corresponds to the case when the energy exchange is taken into account, and losses of each component are strongly different. The input signals are still the same as they appear in (26). To show an accuracy of our method we computed the values of the maximum slope of shock wave fronts defined by the derivatives $\partial u/\partial x$ and $\partial v/\partial x$. In Table I the numerical results are compared with the analytical estimations of the shock wave slopes [8]. Note

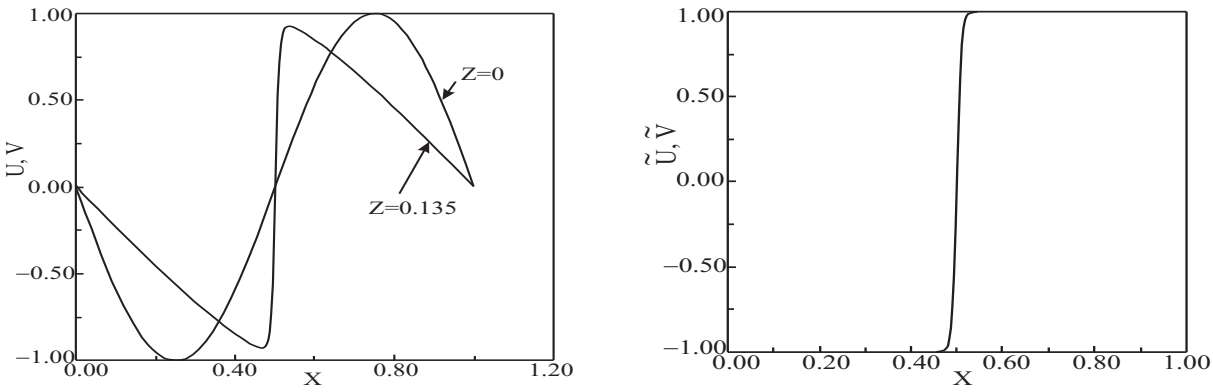

FIG. 1: a) Computed evolution of the signal of the form (26). b) Stationary analytical solution of the kink form. Both components u and v have the same profile.

that in the second column of the Table I the initial values of amplitudes are shown (see (26)), and the third column displays the computed equilibrium values, i.e. the asymptotes of amplitudes while $x \to \infty$. We should emphasize that the results of Table I demonstrate the accuracy of our modeling for various viscous coefficients and initial amplitudes. Shapes of shock profiles formed from the incident harmonic signals (26) are well described by the stationary solutions given in [8]. Let us consider the dynamics of ultra-short pulses in quadratically nonlinear medium. In

TABLE I: Results of our calculations for various viscous coefficients.

Viscous coefficients	Initial amplitudes	Equilibrium amplitudes	Slope of component U		Slope of component V	
			Numerical experiments	Analytic estimation	Numerical experiments	Analytic estimation
$\Gamma_1 = 0.1$	$u_0 = 10$	$u_{eq} = 8.8$				
	$v_0 = 1$	$v_{eq} = 1.4$	397	387	1149	1232
$\Gamma_2 = 0.01$	$u_0 = 1$	$u_{eq} = 2.0$				
	$v_0 = 10$	$v_{eq} = 8.1$	376	400	1602	1600
$\Gamma_1 = 0.01$	$u_0 = 10$	$u_{eq} = 9.8$				
	$v_0 = 1$	$v_{eq} = 1.1$	4864	4850	121	112
$\Gamma_2 = 0.1$	$u_0 = 1$	$u_{eq} = 6.7$				
	$v_0 = 10$	$v_{eq} = 6.1$	2420	2200	310	400

contrast to both previous examples that correspond to acoustic waves, we now deal with light waves. When studying the case of an ultra-short pulse, i.e. the pulse with length less than ten periods, we should utilize the approach of slowly varying profile. This approach leads to the system of equations (14)–(15) with $\Gamma_1 = \Gamma_2 = 0$ and $\mu \neq 0$.

Let us discuss now the results of our numerical experiments on the analysis of effects of short video-pulse differentiation and frequency duplication of few-cycle wave-packet. Suppose that $v \gg u$. In this case the general solution of (14)–(15) can be written as follows

$$u = \frac{\beta}{2\mu}[v_0^2(x) - v_0^2(x - \mu z)]. \tag{27}$$

where we let

$$v = v_0(x - \mu z)\,.$$

If the distance is sufficiently small, i. e. $z \ll T_0/\mu$, then the effect of signal duplication is

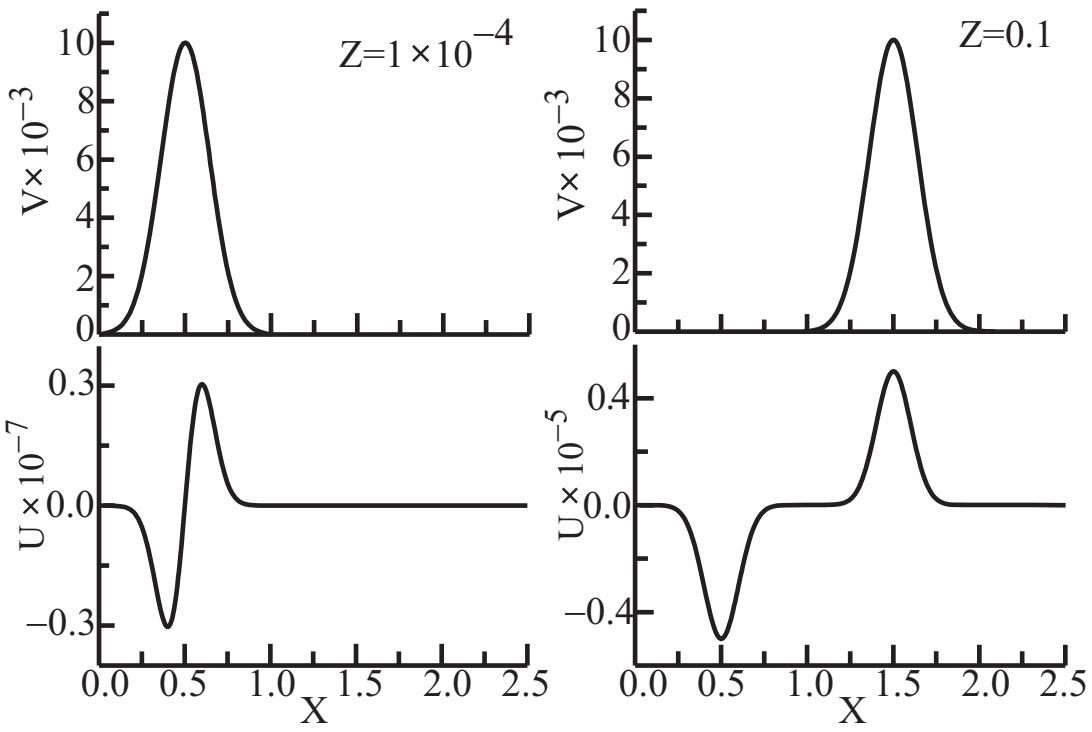

FIG. 2: Gaussian video-pulse differentiation. Left-hand side: the moment of duplication: $z \ll T_0/\mu$. Right-hand side: duplicated pulse propagation: $z \gg T_0/\mu$.]

possible, i.e

$$u = \frac{\beta}{2} \frac{\partial v_0^2(x)}{\partial x}$$

Thus, when the initial pulse has the Gaussian form

$$v_0 = V_0 \exp(-x^2/T_0^2)$$

the generated profile is given by the simplified formula

$$u = \beta V_0^2 z (x/T_0^2) \exp(-x^2/T_0^2)\,.$$

For longer distances, $z \gg T_0/\mu$, a part of the generated pulse travels at the velocity of v component while another part has the velocity of u component. This process is described by the equation (27) which, for Gaussian pulses, gives

$$u = \frac{\beta}{2\mu} v_0^2 \left\{\exp(-x^2/T_0^2) - \exp[-(x-\mu z)^2/T_0^2]\right\}$$

Fig. 2 demonstrates a bipolar pulse formation and propagation. The graphs illustrate our computer modeling based on the difference scheme (21)–(23). Note that the numerical results reflect exactly the scenario outlined above although dissipation terms are negligible in this example.

Using the initial few-cycle wave-packet,

$$v = V_0 \exp(-x^{10}/T_0^{10}) \sin(\omega x)$$

we observed an effect of doubled frequency harmonic generation. If the propagation length is small then dispersion is negligible and the harmonic amplitude increases in proportion to the passed distance. Next, the coherence of frequency doubling is broken due to the velocity mismatch, and spatial pulsations of the second harmonic amplitude manifest themselves. At the same time a differentiation of the harmonic profile is observed. In this example analytical prediction and computer modeling are also in good agreement.

V. CONCLUSION

We applied the conservative monotone difference scheme to the nonlinear system of Burgers equations. It is shown that the resources of our numerical approach provide an accurate mathematical modeling of complicated processes described by the quadratically nonlinear coupled Burgers equations. We revealed new effects of a short video-pulse differentiation and a frequency duplication of few-cycle wave-packet. Analytical results of the process are in good agreement with the results of our numerical calculations.

[1] Yu. N. Karamzin and I.G. Zakharova, Mathematical Models and Methods in Applied Sciences **6**, 353 (1996).
[2] W. Malfliet and W. Hereman, Physica Script **54**, 563 (1996).
[3] S.E. Esipov, Phys. Rev. E **52**, 3711 (1995).
[4] J. Nee and J. Duan, Applied Math. Lett. **11**, 57 (1998).
[5] M.V. Foursov, Phys. Lett. A **272**, 57 (2000).
[6] V.A. Chernykh, A.P. Sukhorukov, and I.G. Zakharova, Nonlinear propagation of two-component waves, Nonlinear Acoustics at the Beginning of the 21st Century, edited by O.V. Rudenko and O.A. Sapozhnikov (Moscow State University, Moscow, 2002) V.1, 85-88.
[7] A.A. Samarskii, The theory of difference schemes (Marcel Dekker, New York, 2001).
[8] V.A. Chernykh and A.P. Sukhorukov, Bullet. of the Russian Academy of Sciences, Physics **68**, 1943 (2004).

Closing Remarks

S. Karataglidis*

Department of Physics and Electronics, P.O. Box 94,
Rhodes University, Grahamstown, 6140, South Africa

This Symposium is not of the same format as most other conferences. First, it is on a small scale with limited participants. Second, the interests of the participants are quite varied from a number of disparate fields, as was noted by Rakityansky. It is then a problem for this humble scribe to try and find some common thread among the varied topics that were discussed during the course of this meeting.

The first general topic was that of nuclear structure, which included a number of topics:

Few-Body Models: These largely concentrated on the use of Faddeev-type and AGS calculations in 3- and 4-body systems (Sofianos) or cluster models (Malykh, Ershov).

Many-body models: Various models were described: the generalisation of Faddeev by the IDEA (Adam); the AMD (Rampho); the Shell model (Karataglidis); Skyrme-Hartree-Fock and (Q)RPA (Karataglidis, Voronov).

Exotic nuclei: Few- (Ershov) and many-body (Karataglidis) descriptions of ^{6}He particularly; the role of the continuum in models (Ershov).

Hypernuclei: Calculations of ΛN and ΛNN effective interactions (Adam, Rakityansky).

Experiments: Search for unbound neutron-rich isotopes of H (Ter-Akopian).

As Karataglidis pointed out, the common thread through all this is the idea of correlations in nuclear systems where the natural degrees of freedom are the nucleons. The various models treat correlations differently, from the use *a priori* of clusters to the calculation and use of effective interactions in many-body theories. The search for the unbound isotopes of H is predicated on the interest in finding correlations in pure neutron matter.

The second general topic is that of nuclear reactions. The talks covered several classes of reactions, which were:

Photoabsorption: Sum rules in photoabsorption (Gerasimov).

Astrophysics: Low-energy capture reactions (Belyaev).

Applied physics: Use of neutron capture in detection of suspect materials (Sapozhnikov).

Unbound systems: Reactions to find the unboound resonances of neutron-rich isotopes of H (Ter-Akopian);

Scattering: Elastic and inelastic scattering of exotic nuclei (Karataglidis, Ershov).

Fission: Fission in the actinide region (Kamanin);

Resonances: Definition and identification in reactions (Motovilov).

*Electronic address: S.Karataglidis@ru.ac.za

Finding a common thread through all these disparate topics is not so easy: some relate back to structure and the use of reactions therein. Others are applications of nuclear reactions to other phenomena. There is scope for commonality among these.

The third topic dealt with the application of nuclear theory tools in other fields of physics. Lekala discussed the use of Faddeev approaches to atomic systems, while Botha discussed the use of nuclear techniques in Solid State physics.

Particle Physics was also represented: Saphoznikov discussed the search for strangeness in the nucleon, while baryon structure and photoexcitations were discussed by Matamba.

Finally, more mathematical and numerical in scope: Gerdt discussed quantum computing, Braun discussed computing tools for use in nuclear physics, while Numerical techniques were discussed by Zakharova.

Quite a variety of topics covered by our small gathering, certainly. What may come of this diversity of ideas would be innovative applications of research in other areas, as was discussed by Botha and Lekala. This has a positive feedback inasmuch as we may draw on ideas from other fields in our own work. The hope is that this begins a process for a longlasting and productive collaboration between the two communities.